M. Lesieur

Fluid Mechanics and its Applications

Turbulence in Fluids

4th Edition

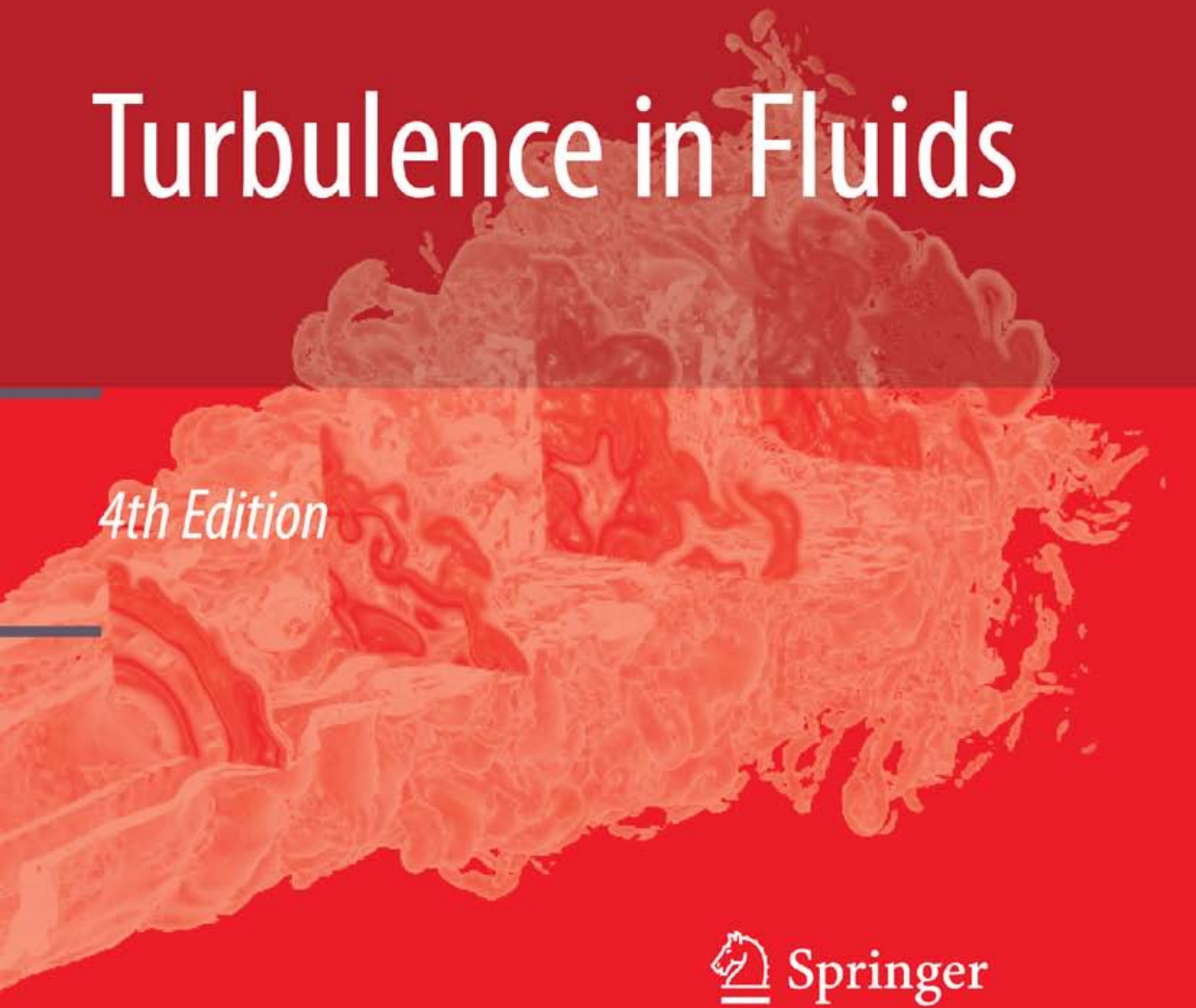

Springer

TURBULENCE IN FLUIDS

FLUID MECHANICS AND ITS APPLICATIONS
Volume 84

Series Editor: R. MOREAU
MADYLAM
Ecole Nationale Supérieure d'Hydraulique de Grenoble
Boîte Postale 95
38402 Saint Martin d'Hères Cedex, France

Aims and Scope of the Series

The purpose of this series is to focus on subjects in which fluid mechanics plays a fundamental role.

As well as the more traditional applications of aeronautics, hydraulics, heat and mass transfer etc., books will be published dealing with topics which are currently in a state of rapid development, such as turbulence, suspensions and multiphase fluids, super and hypersonic flows and numerical modeling techniques.

It is a widely held view that it is the interdisciplinary subjects that will receive intense scientific attention, bringing them to the forefront of technological advancement. Fluids have the ability to transport matter and its properties as well as to transmit force, therefore fluid mechanics is a subject that is particularly open to cross fertilization with other sciences and disciplines of engineering. The subject of fluid mechanics will be highly relevant in domains such as chemical, metallurgical, biological and ecological engineering. This series is particularly open to such new multidisciplinary domains.

The median level of presentation is the first year graduate student. Some texts are monographs defining the current state of a field; others are accessible to final year undergraduates; but essentially the emphasis is on readability and clarity.

For a list of related mechanics titles, see final pages.

Turbulence in Fluids

Fourth Revised and Enlarged Edition

By

MARCEL LESIEUR

Fluid Mechanics Professor,
Grenoble Institute of Technology,
Member of the French Academy of Sciences

Springer

A C.I.P. Catalogue record for this book is available from the Library of Congress.

ISBN 978-1-4020-6434-0 (HB)
ISBN 978-1-4020-6435-7 (e-book)

Published by Springer,
P.O. Box 17, 3300 AA Dordrecht, The Netherlands.

www.springer.com

Cover figure: Numerical simulation of positive-Q isosurfaces and passive-scalar cross sections in coaxial jets of same uniform density (courtesy G. Balarac).

Printed on acid-free paper

Library of Congress Control Number: 2007941158

This fourth edition would have never been possible without the love, enthusiasm and support of my children Alexandre, Guillaume, Juliette and Stéphanie.

Contents

Preface xvii

1 Introduction to Turbulence in Fluid Mechanics 1
1.1 Is it possible to define turbulence? 1
1.2 Examples of turbulent flows 4
1.3 Fully-developed turbulence 13
1.4 Fluid turbulence and "chaos" 14
1.5 "Deterministic" and statistical approaches 16
1.5.1 Mathematical and philosophical considerations 17
1.5.2 Numerical simulations 18
1.5.3 Stochastic tools 19
1.6 Why study isotropic turbulence? 20
1.7 One-point closure modelling 21
1.8 Outline of the following chapters 21

2 Basic Fluid Dynamics 25
2.1 Eulerian notation and Lagrangian derivatives 25
2.2 The continuity equation 27
2.3 The conservation of momentum 27
2.3.1 Variable dynamic viscosity 29
2.3.2 Navier–Stokes and Euler equations 30
2.3.3 Geopotential form 31
2.3.4 First Bernoulli's theorem 31
2.4 The thermodynamic equation 33
2.4.1 Second Bernoulli's theorem 35
2.4.2 Liquid 35
2.4.3 Ideal gas 36
2.5 Compressible Navier–Stokes equations in flux form 38
2.6 The incompressibility assumption 38

2.6.1 Liquid 39
2.6.2 Ideal gas 39
2.7 The dynamics of vorticity 41
2.7.1 Helmholtz–Kelvin theorems 42
2.8 Potential vorticity and Rossby number 44
2.8.1 Absolute vortex elements 44
2.8.2 Ertel's theorem 45
2.8.3 Molecular diffusion of potential vorticity 47
2.8.4 The Rossby number 48
2.8.5 Proudman–Taylor theorem 50
2.8.6 Taylor column 51
2.9 Boussinesq approximation 52
2.9.1 Liquid 53
2.9.2 Ideal gas 53
2.9.3 Vorticity dynamics within Boussinesq 54
2.10 Internal-inertial gravity waves 55
2.10.1 Internal gravity waves 57
2.10.2 Role of rotation 60
2.11 Barré de Saint-Venant equations 62
2.11.1 Derivation of the equations 62
2.11.2 The potential vorticity 64
2.11.3 Surface inertial-gravity waves 65
2.12 Gravity waves in a fluid of arbitrary depth 69
2.12.1 Supersonic shocks and wakes of floating bodies 71

3 Transition to Turbulence 73
3.1 Introduction 73
3.2 The Reynolds number 74
3.3 Linear-instability theory 76
3.3.1 Two-dimensional temporal analysis 77
3.3.2 The two-dimensional Orr–Sommerfeld equation 79
3.3.3 The Rayleigh equation 80
3.3.4 Three-dimensional temporal normal-mode analysis 83
3.3.5 Non-normal analysis 87
3.4 Transition in free-shear flows 91
3.4.1 Mixing layers 91
3.4.2 Round jets 104
3.4.3 Plane jets and wakes 104
3.4.4 Convective and absolute instabilities 107
3.5 Wall flows 108
3.5.1 The boundary layer 108
3.5.2 Poiseuille flow 112
3.6 Thermal convection 114

3.6.1 Rayleigh–Bénard convection . . . 114
3.6.2 Other types of thermal convection . . . 118
3.7 Transition, coherent structures and Kolmogorov spectra . . . 118

4 Shear Flow Turbulence . . . 121
4.1 Introduction . . . 121
4.1.1 Use of random functions . . . 121
4.2 Reynolds equations . . . 121
4.2.1 The mixing-length theory . . . 122
4.2.2 Application of mixing length to turbulent-shear flows . . . 123
4.3 Characterization of coherent vortices . . . 135
4.3.1 The Q criterion . . . 136
4.4 Coherent vortices in free-shear layers . . . 136
4.4.1 Spatial mixing layer . . . 136
4.4.2 Plane spatial wake . . . 138
4.4.3 Round jets . . . 140
4.4.4 Coaxial jets . . . 145
4.5 Coherent vortices in wall flows . . . 145
4.5.1 Vortex control . . . 151
4.6 Turbulence, order and chaos . . . 151

5 Fourier Analysis of Homogeneous Turbulence . . . 155
5.1 Introduction . . . 155
5.2 Fourier representation of a flow . . . 155
5.2.1 Flow "within a box" . . . 155
5.2.2 Integral Fourier representation . . . 157
5.3 Navier–Stokes equations in Fourier space . . . 158
5.4 Boussinesq equations in Fourier space . . . 160
5.5 Craya decomposition . . . 161
5.6 Complex helical-waves decomposition . . . 163
5.7 Utilization of random functions . . . 166
5.8 Moments of the velocity field, homogeneity and stationarity . . . 167
5.9 Isotropy . . . 169
5.9.1 Definition . . . 169
5.9.2 Longitudinal velocity correlation . . . 169
5.9.3 Transverse velocity correlation . . . 170
5.9.4 Cross velocity correlation . . . 170
5.9.5 Helicity . . . 170
5.9.6 Velocity correlation tensor in physical space . . . 171
5.9.7 Scalar-velocity correlation . . . 173
5.9.8 Velocity spectral tensor of isotropic turbulence . . . 174
5.10 Kinetic-energy, helicity, enstrophy and scalar spectra . . . 176
5.10.1 Kinetic energy spectrum . . . 176

5.10.2 Helicity spectrum . . . 177
5.10.3 Enstrophy . . . 177
5.10.4 Scalar spectrum . . . 178
5.11 Alternative expressions of the spectral tensor . . . 179
5.12 Axisymmetric turbulence . . . 182
5.13 Rapid-distorsion theory . . . 184

6 Isotropic Turbulence: Phenomenology and Simulations . . . 187
6.1 Introduction . . . 187
6.2 Triad interactions and detailed conservation . . . 187
6.2.1 Quadratic invariants in physical space . . . 190
6.3 Transfer and flux . . . 193
6.4 Kolmogorov's 1941 theory . . . 196
6.4.1 Kolmogorov 1941 in spectral space . . . 197
6.4.2 Kolmogorov wave number . . . 199
6.4.3 Integral scale . . . 199
6.4.4 Oboukhov's theory . . . 200
6.4.5 Kolmogorov 1941 in physical space . . . 201
6.5 Richardson law . . . 202
6.6 Characteristic scales of turbulence . . . 205
6.6.1 Degrees of freedom of turbulence . . . 205
6.6.2 Taylor microscale . . . 207
6.6.3 Self-similar spectra . . . 208
6.7 Skewness factor and enstrophy divergence . . . 209
6.7.1 Skewness factor . . . 209
6.7.2 Does enstrophy blow up at a finite time in a perfect fluid? . . . 211
6.7.3 The viscous case . . . 215
6.8 Coherent vortices in 3D isotropic turbulence . . . 216
6.9 Pressure spectrum . . . 220
6.9.1 Noise in turbulence . . . 220
6.9.2 Ultraviolet pressure . . . 220
6.10 Phenomenology of passive scalar diffusion . . . 221
6.10.1 Inertial-convective range . . . 223
6.10.2 Inertial-conductive range . . . 224
6.10.3 Viscous-convective range . . . 227
6.11 Internal intermittency . . . 227
6.11.1 Kolmogorov–Oboukhov–Yaglom theory . . . 229
6.11.2 Novikov–Stewart (1964) model . . . 230
6.11.3 Experimental and numerical results . . . 231

7 Analytical Theories and Stochastic Models 237
7.1 Introduction 237
7.2 Quasi-Normal approximation 239
7.2.1 Gaussian random functions 239
7.2.2 Formalism of the Q.N. approximation 240
7.2.3 Solution of the Q.N. approximation 242
7.3 Eddy-Damped Quasi-Normal type theories 243
7.3.1 Eddy damping 243
7.3.2 Markovianization 244
7.4 Stochastic models 245
7.5 Closures phenomenology 250
7.6 Decaying isotropic non-helical turbulence 253
7.6.1 Non-local interactions 255
7.6.2 Energy spectrum and skewness 257
7.6.3 Enstrophy divergence and energy catastrophe 261
7.7 Burgers-M.R.C.M. model 264
7.8 Decaying isotropic helical turbulence 265
7.9 Decay of kinetic energy and backscatter 270
7.9.1 Eddy viscosity and spectral backscatter 270
7.9.2 Decay laws 273
7.9.3 Infrared pressure 277
7.10 Renormalization-Group techniques 277
7.10.1 R.N.G. algebra 278
7.10.2 Two-point closure and R.N.G. techniques 282
7.11 E.D.Q.N.M. isotropic passive scalar 284
7.11.1 A simplified E.D.Q.N.M. model 287
7.11.2 E.D.Q.N.M. scalar-enstrophy blow up 289
7.11.3 Inertial-convective and viscous-convective ranges 291
7.12 Decay of temperature fluctuations 292
7.12.1 Phenomenology 293
7.12.2 Experimental temperature decay data 299
7.12.3 Discussion of LES results 301
7.12.4 Diffusion in stationary turbulence 302
7.13 Lagrangian particle pair dispersion 303
7.14 Single-particle diffusion 305
7.14.1 Taylor's diffusion law 305
7.14.2 E.D.Q.N.M. approach to single-particle diffusion 306

8 Two-Dimensional Turbulence 311
8.1 Introduction 311
8.2 Spectral tools for two-dimensional isotropic turbulence 314
8.3 Fjortoft's theorem 316
8.4 Enstrophy cascade 317

8.4.1 Forced case . . . 317
8.4.2 Decaying case . . . 318
8.4.3 Enstrophy dissipation wave number . . . 319
8.4.4 Discussion on the enstrophy cascade . . . 320
8.5 Coherent vortices . . . 322
8.6 Inverse energy transfers . . . 325
8.6.1 Inverse energy cascade . . . 325
8.6.2 Decaying case . . . 328
8.7 The two-dimensional E.D.Q.N.M. model . . . 330
8.7.1 Forced turbulence . . . 334
8.7.2 Freely-decaying turbulence . . . 334
8.8 Diffusion of a passive scalar . . . 339
8.8.1 E.D.Q.N.M. two-dimensional scalar analysis . . . 341
8.8.2 Particles-pair dispersion in 2D . . . 342
8.9 Pressure spectrum in two dimensions . . . 343
8.9.1 "Ultraviolet" case . . . 343
8.9.2 Infrared case . . . 344
8.10 Two-dimensional turbulence in a temporal mixing layer . . . 346

9 Beyond Two-Dimensional Turbulence in GFD . . . 349
9.1 Introduction . . . 349
9.2 Geostrophic approximation . . . 350
9.2.1 Hydrostatic balance . . . 351
9.2.2 Geostrophic balance . . . 352
9.2.3 Generalized Proudman-Taylor theorem . . . 353
9.2.4 Atmosphere versus oceans . . . 354
9.2.5 Thermal wind equation . . . 354
9.3 Quasi geostrophic potential vorticity equation . . . 354
9.4 Baroclinic instability . . . 357
9.4.1 Eady model . . . 357
9.4.2 Displaced fluid particle . . . 358
9.4.3 Hyperbolic-tangent front . . . 359
9.4.4 Dynamic evolution of the baroclinic jets . . . 360
9.4.5 Baroclinic instability in the ocean . . . 364
9.5 The N-layer quasi geostrophic model . . . 366
9.5.1 One layer . . . 368
9.5.2 Two layers . . . 369
9.5.3 Spectral vertical expansion . . . 371
9.6 Ekman layer . . . 372
9.6.1 Geostrophic flow above an Ekman layer . . . 373
9.6.2 The upper Ekman layer . . . 376
9.6.3 Oceanic upwellings . . . 377
9.7 Tornadoes . . . 378

9.7.1 Lilly's model . . . 378
9.7.2 A hairpin-vortex based model . . . 379
9.8 Barotropic and baroclinic waves . . . 379
9.8.1 Planetary Rossby waves . . . 379
9.8.2 Reflection of Rossby waves . . . 381
9.8.3 Topographic Rossby waves . . . 382
9.8.4 Baroclinic Rossby waves . . . 383
9.8.5 Other quasi geostrophic waves . . . 384
9.9 Quasi geostrophic turbulence . . . 386
9.9.1 Turbulence and topography . . . 386
9.9.2 Turbulence and Rossby waves . . . 387
9.9.3 Charney's theory . . . 389

10 Statistical Thermodynamics of Turbulence . . . 393
10.1 Truncated Euler equations . . . 393
10.1.1 Application to three-dimensional turbulence . . . 393
10.1.2 Application to two-dimensional turbulence . . . 397
10.2 Two-dimensional turbulence over topography . . . 399
10.3 Inviscid statistical mechanics of two-dimensional point vortices 402

11 Statistical Predictability Theory . . . 403
11.1 Introduction . . . 403
11.2 E.D.Q.N.M. predictability equations . . . 407
11.3 Predictability of three-dimensional turbulence . . . 408
11.4 Predictability of two-dimensional turbulence . . . 412
11.4.1 Predictability time in the atmosphere . . . 413
11.4.2 Predictability time in the ocean . . . 414
11.4.3 Unpredictability and cohence . . . 414
11.5 Two-dimensional mixing-layer unpredictability . . . 415
11.5.1 Two-dimensional unpredictability and three-dimensional growth . . . 416

12 Large-Eddy Simulations . . . 419
12.1 DNS of turbulence . . . 419
12.2 LES formalism in physical space . . . 420
12.2.1 Large and subgrid scales . . . 420
12.2.2 LES of a transported scalar . . . 422
12.2.3 LES and the predictability problem . . . 423
12.2.4 Eddy-viscosity assumption . . . 424
12.2.5 Eddy-diffusivity assumption . . . 425
12.2.6 LES of Boussinesq equations . . . 425
12.2.7 Compressible turbulence . . . 426
12.2.8 Smagorinsky model . . . 426

12.3 LES in spectral space 428
12.3.1 Sharp filter in Fourier space 428
12.3.2 Spectral eddy viscosity and diffusivity 428
12.3.3 LES of isotropic turbulence 431
12.3.4 The anomalous spectral eddy diffusivity 435
12.3.5 Alternative approaches 437
12.3.6 Spectral LES for inhomogeneous flows 438
12.4 New physical-space models 440
12.4.1 Structure-function model 440
12.4.2 Selective structure-function model 443
12.4.3 Filtered structure-function model 444
12.4.4 Scale-similarity and mixed models 446
12.4.5 Dynamic model 448
12.4.6 Other approaches 451
12.5 LES of two-dimensional turbulence 452

13 Towards "Real World Turbulence" 455
13.1 Introduction 455
13.2 Stably-stratified turbulence 456
13.2.1 The so-called "collapse" problem 456
13.2.2 Numerical approach to the collapse 460
13.2.3 Other configurations 466
13.3 Rotating turbulence 467
13.3.1 From low to high Rossby number 467
13.3.2 Linear instability 468
13.3.3 Mixing layers and wakes 468
13.3.4 Channels 475
13.3.5 Some theoretical considerations 479
13.3.6 Initially three-dimensional turbulence 482
13.4 Separated flows 483
13.4.1 Mean reattachment length 484
13.4.2 Coherent vortices 485
13.4.3 Instantaneous reattachment length 487
13.4.4 Rotating backstep 488
13.5 Compressible flows 489
13.5.1 Compressible mixing layer 489
13.5.2 Baroclinic effects in free-shear flows 494
13.5.3 Compressible wake 496
13.5.4 Boundary layer upon a heated plate 496
13.5.5 Compression ramp 497
13.5.6 Compressible boundary layer 499
13.6 Book's conclusions 502

References 509

Index 545

Preface

Turbulence is a dangerous topic which is often at the origin of serious fights in the scientific meetings devoted to it since it represents extremely different points of view, all of which have in common their complexity, as well as an inability to solve the problem. It is even difficult to agree on what exactly is the problem to be solved.

Extremely schematically, two opposing points of view had been advocated during these last thirty years: the first one was "statistical", and tried to model the evolution of averaged quantities of the flow. This community, which had followed the glorious trail of Taylor and Kolmogorov, believed in the phenomenology of cascades, and strongly disputed the possibility of any coherence or order associated to turbulence.

On the other bank of the river standed the "coherence among chaos" community, which considered turbulence from a purely deterministic point of view, by studying either the behaviour of dynamical systems, or the stability of flows in various situations. To this community were also associated the experimentalists and computer simulators who sought to identify coherent vortices in flows.

Situation is more complex now, and the existence of these two camps is less clear. In fact a third point of view pushed by people from the physics community has emerged, with the concepts of renormalization group theory, multifractality, mixing, and Lagrangian approaches.

My personal experience in turbulence was acquired in the first group since I spent several years studying the stochastic models (or two-point closures) applied to various situations such as helical turbulence, turbulent diffusion, or two-dimensional turbulence. These techniques were certainly not the ultimate solution to the problem, but they allowed me to get acquainted with various disciplines such as aeronautics, astrophysics, hydraulics, meteorology, oceanography, which were all, for different reasons, interested in turbulence. It is

certainly true that I discovered the fascination of fluid dynamics through the somewhat abstract studies of turbulence.

This monograph is in fact an attempt to reconcile the statistical point of view and the basic concepts of fluid mechanics which determine the evolution of flows arising in the various fields envisaged above. These basic principles, accompanied by the instability-theory predictions and the results of numerical simulations, give valuable information on the behaviour of turbulence and of the structures which compose it. But a statistical analysis of these structures can, at the same time, supply information about strong nonlinear energy transfers within the flow.

I have tried to present here a synthesis between two graduate courses given in Grenoble during these last years, namely a "Turbulence" course and a "Geophysical Fluid Dynamics" course. I would like to thank my colleagues of the Ecole Nationale d'Hydraulique et Mécanique and Université Joseph Fourier, who offered me the opportunity of giving these two courses. The students who attended these classes were, through their questions and remarks, of great help. I took advantage of a sabbatical year spent at the Aerospace-Engineering Department of University of Southern California to write the first draft of this monograph: this was rendered possible by the generous hospitality of John Laufer and his collaborators. The second edition benefitted also from a graduate course taught at Stanford University during a visit to the Center for Turbulence Research. The support and extra time offered through my appointment to the "Institut Universitaire de France" made the third edition possible. The fourth edition was written thanks to a CNRS delegation and a sabbatical semester offered by Grenoble Institute of Technology (INPG).

The organization into 13 chapters of the third edition has been kept: 1. Introduction to turbulence in fluid mechanics; 2. Basic fluid dynamics; 3. Transition to turbulence; 4. Shear-flow turbulence; 5. Fourier analysis for homogeneous turbulence; 6. Isotropic turbulence: phenomenology and simulations; 7. Analytical theories and stochastic models; 8. Two-dimensional turbulence; 9. Beyond two-dimensional turbulence in geophysical fluid dynamics; 10. Statistical thermodynamics of turbulence; 11. Statistical predictability theory; 12. Large-eddy simulations; 13. Towards real-world turbulence.

In Chapter 1, the book introduces clear definitions of turbulence in fluids and of coherent vortices. It provides several industrial and environmental examples, with numerous illustrations. Chapter 2 develops at lenght equations of fluid dynamics (velocity and energy) for flows of arbitrary density (incompressible and compressible), including Boussinesq equations (with a study of internal-gravity waves). It reviews the main theorems of vorticity dynamics and scalar transport for non-rotating or rotating flows. It looks also in details at Barré de Saint-Venant equations for shallow layers. Chapter 3 studies linear-instability theory of parallel shear flows (free and wall-bounded) in two

and three dimensions (with effects of rotation), as well as thermal convection. It provides an experimental and numerical review of transition in shear flows. Chapter 4 is devoted to free or wall-bounded turbulent shear flows. They are studied both statistically (we derive for instance the logarithmic boundary layer profile) and deterministically, with emphasis put on coherent vortices and coherent structures. Recent results illuminating the structure of round jets and turbulent boundary layer without pressure gradient are given. Chapter 5 gives mathematical details on Fourier analysis of turbulence, with informations on rapid-distorsion theory. Chapter 6 is devoted to three-dimensional isotropic turbulence, looked at phenomenologically and from a coherent-vortex point of view. Passive-scalar diffusion, important for combustion studies, is included in the chapter. It contains also new results concerning noise in turbulence, associated with pressure spectrum. Chapter 7 contains the two-point closure approaches of three-dimensional isotropic turbulence, with applications to passive scalars. The closure derivation of an helicity cascade superposed to the Kolmogorov kinetic-energy cascade, and verified by numerical large-eddy simulations, is certainly an important result of the book. Helicity is important in the generation of atmospheric tornadoes and of Earth magnetic field (dynamo effect). The chapter underlines also the important role of spectral backscatter, which is confirmed by numerical simulations. Chapter 8 is devoted to strictly two-dimensional turbulence from a phenomenological, closure and numerical viewpoint. It gives a clear theoretical exposition of the double enstrophy and inverse-energy cascades, with experimental validations. It gives new numerical results on energy and pressure spectra. Chapter 9 deals essentially with quasi two-dimensional turbulence from an external-geophysical point of view. It contains a very detailed presentation of difficult questions: quasi-geostrophic theory, baroclinic instability, atmospheric storms, N-layer models, Rossby waves (including topographic ones), Ekman layers. It discusses also of tornado generation, and finishes with Charney's theory of quasi-geostrophic turbulence. Chapter 10 presents the statistical thermodynamics of truncated Euler equations. In fact it turns out that such an approach is far from the reality of turbulence. Chapter 11, on statistical unpredictability in three and two dimensions, is mostly unchanged with respect to former editions. The role of spectral backscatter in the inverse error cascade is very important. Results of this chapter show that a deterministic numerical simulation of a turbulent flow is subject to important errors beyond the predictability time. Chapter 12 is an up to date review of large-eddy simulation techniques, which are becoming extremely powerful. It contains a detailed presentation of "classical models" such as Smagorinsky's or Kraichan's, as well as new "dynamic" or "selective" models allowing the eddy coefficients to adjust automatically to the local turbulence. Finally, Chapter 13 presents turbulence in more practical situations. We consider successively the effects of stratification, rotation

(universality of free- and wall-bounded shear flows in anticyclonic regions is astonishing), separation and compressibility. Here again, our concern is both statistical and structural.

This book is of great actuality on a topic of upmost importance for engineering and environmental applications, and proposes a very detailed presentation of the field. The fourth edition incorporates new results coming from research works which have been done since 1997, and revisits the older points of view in the light of these results. Many come from direct and large-eddy simulations methods, which have provided significant advances in most challenging problems of turbulence (isotropy, free-shear flows, boundary layers, compressibility, rotation). The book proposes many aerodynamic, thermal-hydraulics and environmental applications.

It is obvious that problems are evolving, and so do the applications: developing faster planes may be less crucial (except for defense problems) than clean, economic and silent engines. Energy issues such as fusion will push the numerical modellers towards much more complicated problems involving very hot plasma. Alarming questions posed by climate evolution about a global warming will oblige to develop full three-dimensional atmospheric and oceanic codes based at least on Boussinesq equations. This will be eased by the continuous spectacular development of computers.

Particular thanks go to the staff and graduate students of the team MOST ("Modélisation et Simulation de la Turbulence") at the Laboratory for Geophysical and Industrial Flows (LEGI, sponsored by CNRS, INPG and UJF), for their important contribution (visual in particular) to the book. Pierre Comte and Olivier Métais provided their great expertise in the domains of transition, coherent vortices, compressible, stratified or rotating turbulence, and numerical methods. I am also indebted to all the sponsoring agencies and companies who showed a continuous interest during all these years in the development of fundamental and numerical research on Turbulence in Grenoble.

Rosanne Alessandrini, Patrick Bégou, Eric Lamballais and Akila Rachedi were very helpful for handling figures, and Yves Gagne, Jack Herring, Sherwin Maslowe and Jim Riley for editing part of the material (first three editions). I am greatly indebted to Frances Métais who corrected the English style of the first edition. I also hope that this monograph will help the diffusion of some French contributions to turbulence research.

I am grateful to numerous friends around the world who encouraged me to undertake this work.

The first three editions were written using the TEX system. This would not have been possible without the help of Claude Goutorbe and Evelyne Tournier, of Grenoble Applied Mathematics Institute.

Finally I thank René Moreau and Springer for offering me the possibility of presenting these ideas.

Grenoble, May 2007

Plates

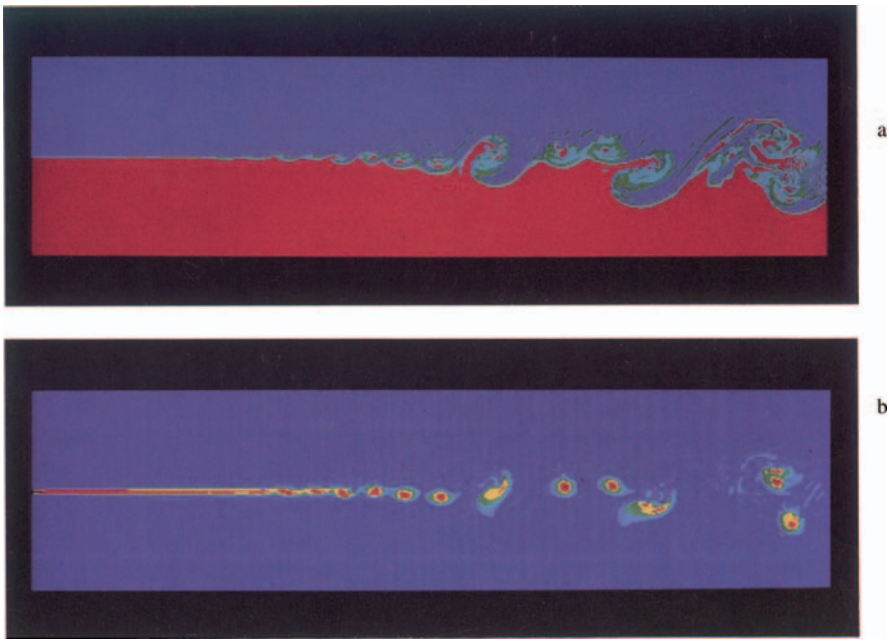

Plate 1: Two-dimensional numerical simulation of Brown and Roshko's experiment shown in Fig. 1.4. Top: passive dye contours. Bottom: vorticity contours (courtesy X. Normand).

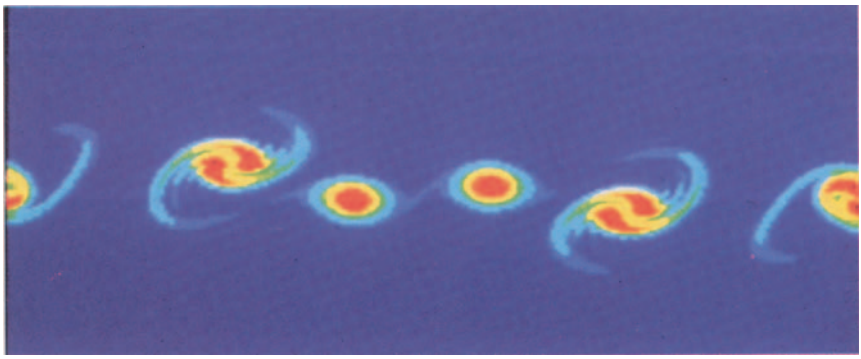

Plate 2: Vorticity contours in the two-dimensional numerical simulations of the mixing layer reported in Lesieur et al. [420] and Comte [134].

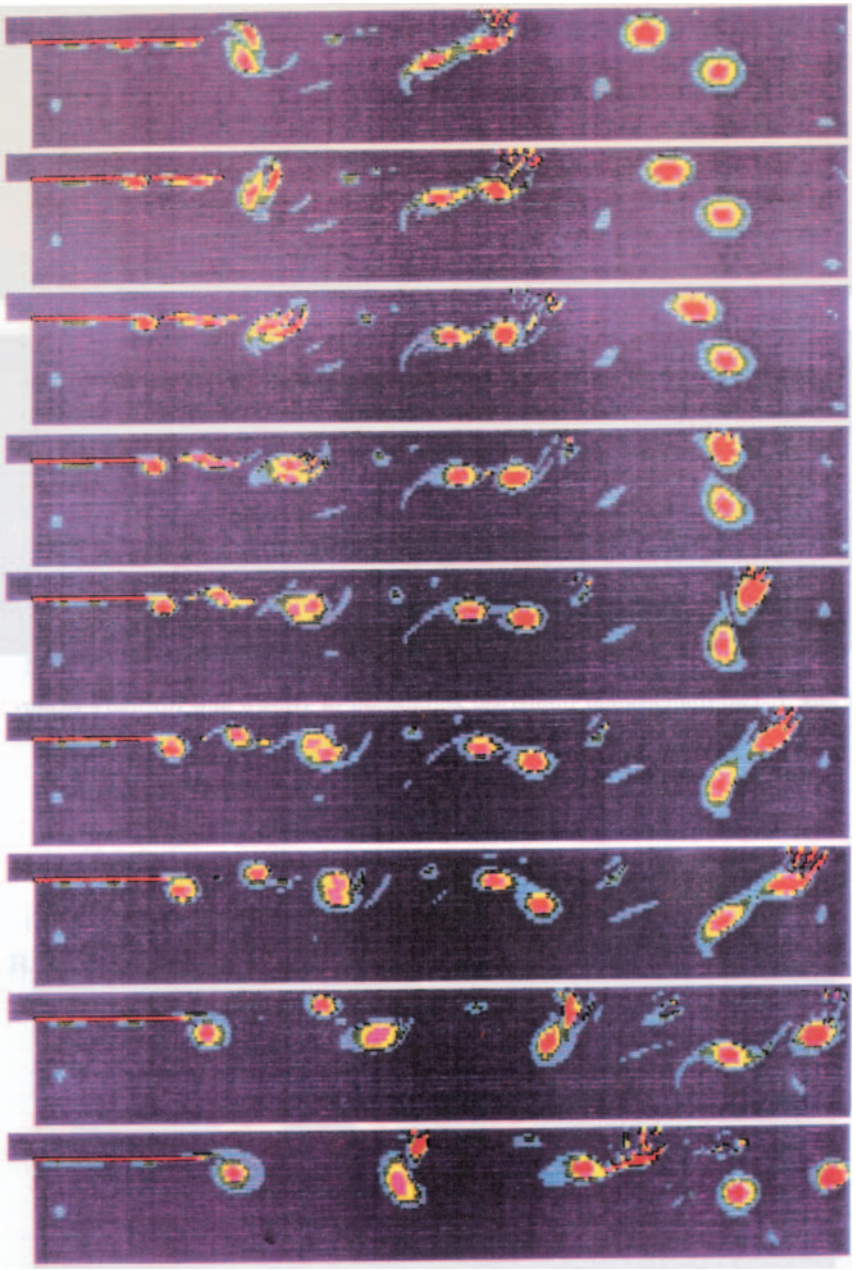

Plate 3: Evolution with time of the vorticity field in a two-dimensional direct-numerical simulation of the flow above a backward-facing step (courtesy A. Silveira, C.E.N.G. and I.M.G.).

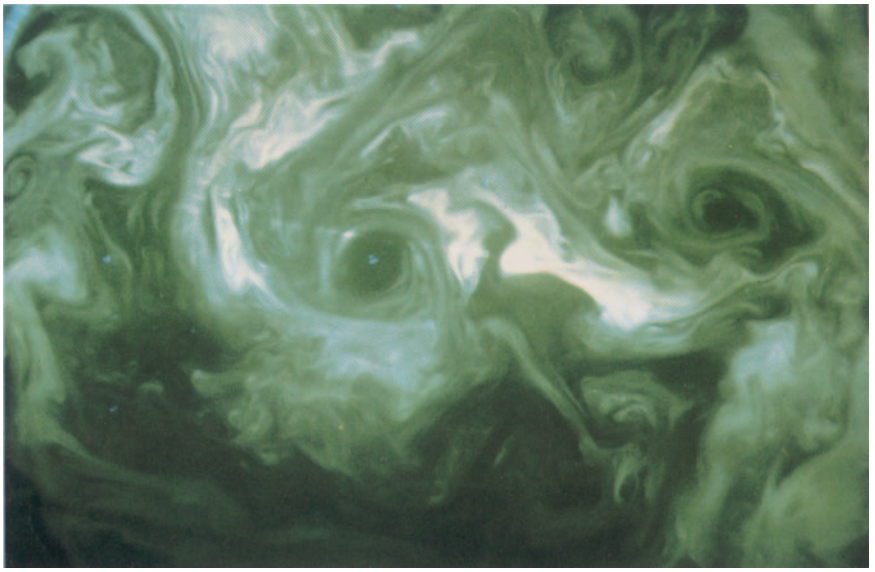

Plate 4: Visualization of a horizontal section of turbulence in a tank rotating fastly about a vertical axis: the eddies shown are quasi-two-dimensional, due to the effect of rotation (courtesy E.J. Hopfinger).

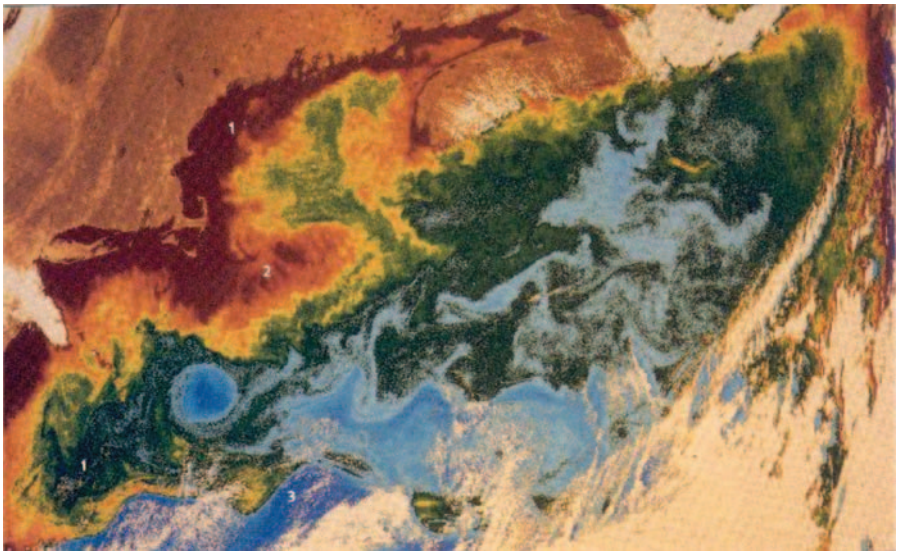

Plate 5: Satellite picture of the temperature field on the surface of the Atlantic ocean close to the Gulf Stream (courtesy NASA and EDP-Springer [424]).

Plate 6: Circulation on Jupiter (courtesy Jet Propulsion Laboratory, Pasadena, and EDP-Springer [424]).

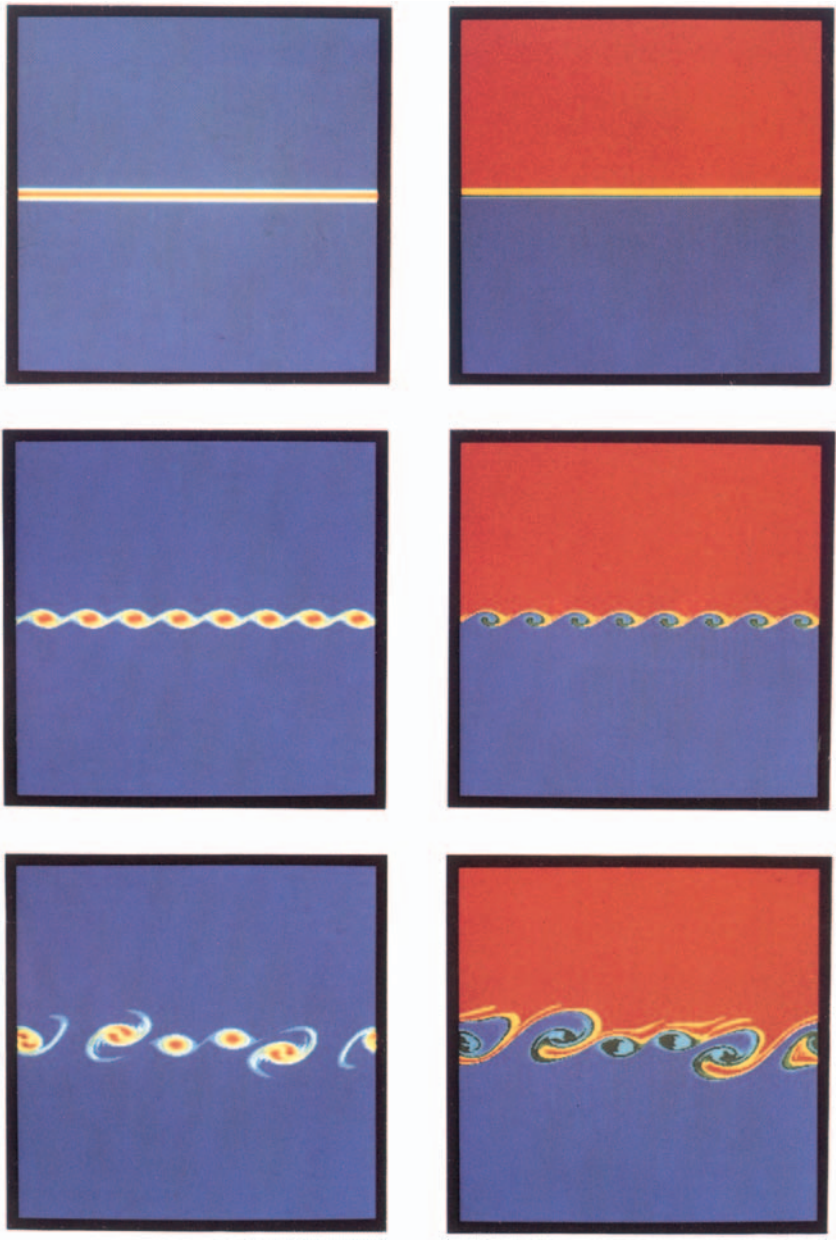

Plate 7: Direct-numerical simulation of a two-dimensional temporal mixing layer: left, vorticity field; right, passive scalar field; one can see the formation of the primary vortices, and the subsequent pairings; (from Comte [134]).

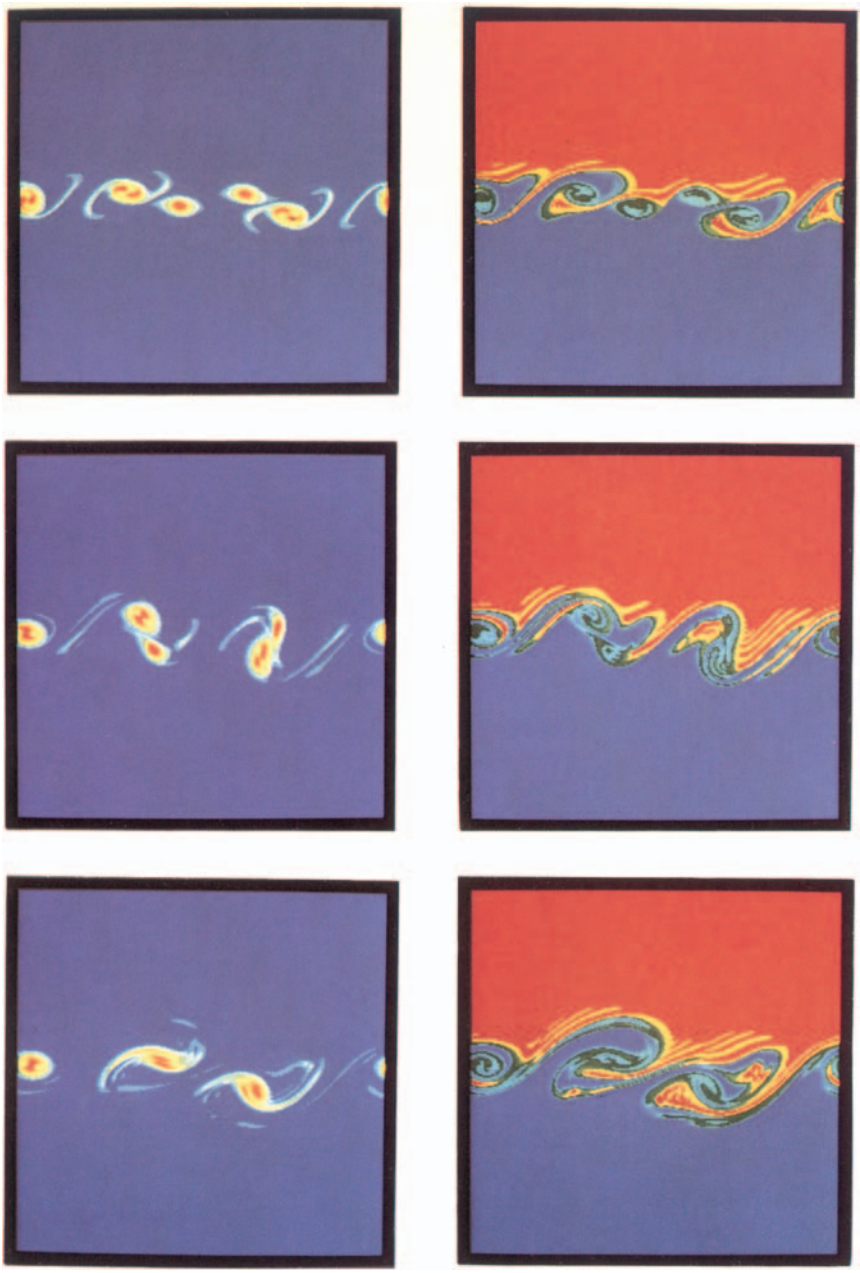

Plate 8: Same calculation as in Plate 7: end of the evolution.

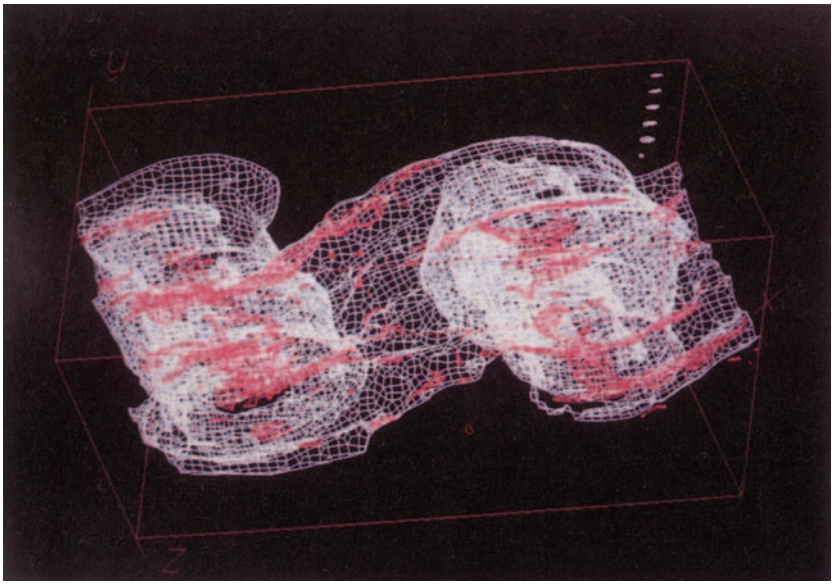

Plate 9: Large-eddy simulation of a temporal mixing layer forced quasi two-dimensionally; interface at the end of the rollup, visualized with a numerical dye; in red is shown the positive longitudinal vorticity. From Comte and Lesieur [136]).

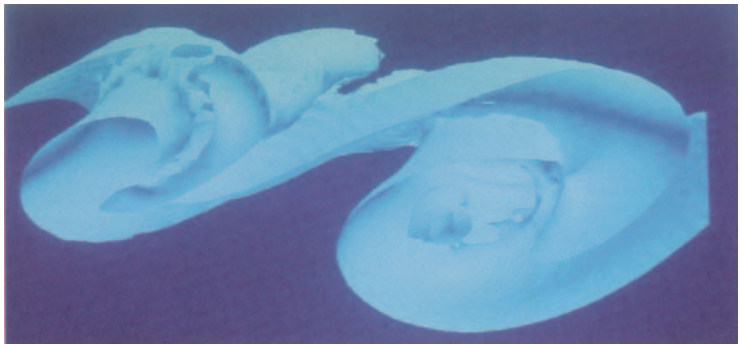

Plate 12: Same calculation as in Plate 11: vertical (in the x, y plane) cross section of the interface (courtesy P. Comte).

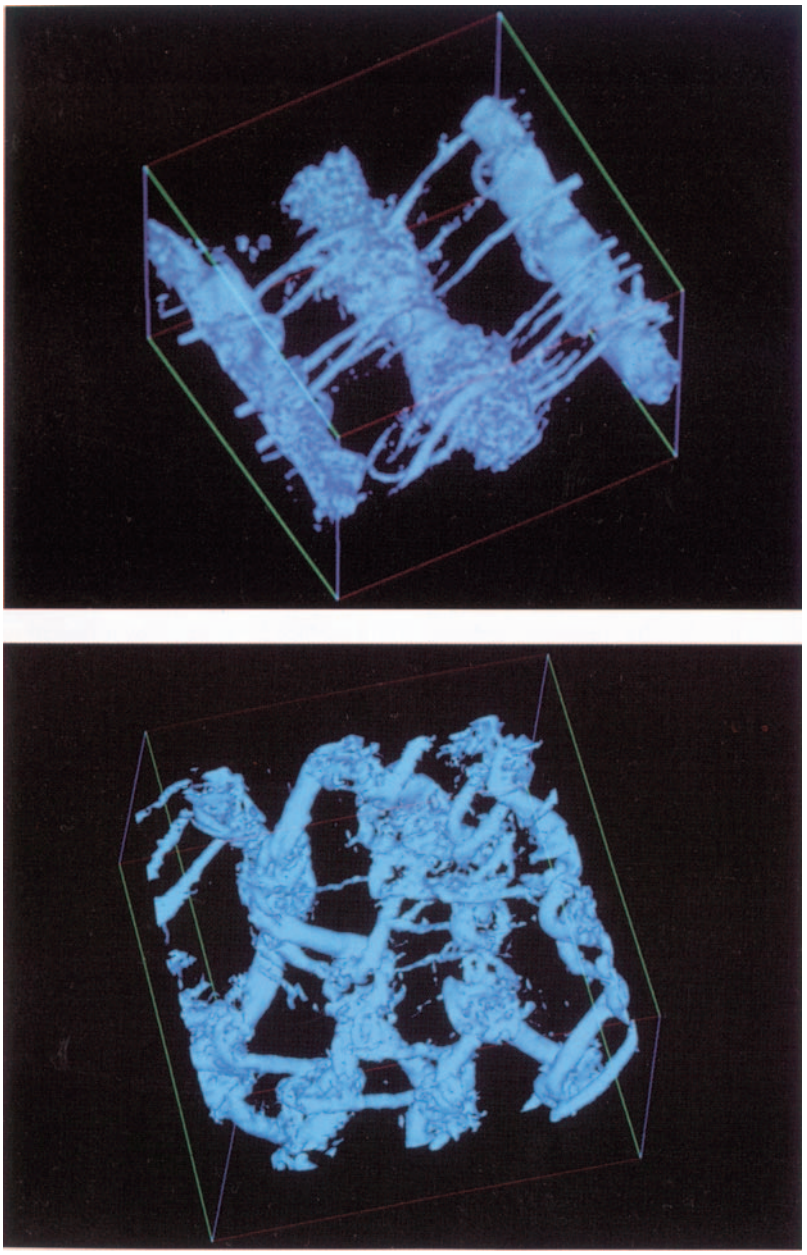

Plate 10: Vorticity modulus in the LES of a temporal mixing layer; (a) quasi two-dimensional random initial forcing; (b) 3D isotropic forcing (courtesy J. Silvestrini).

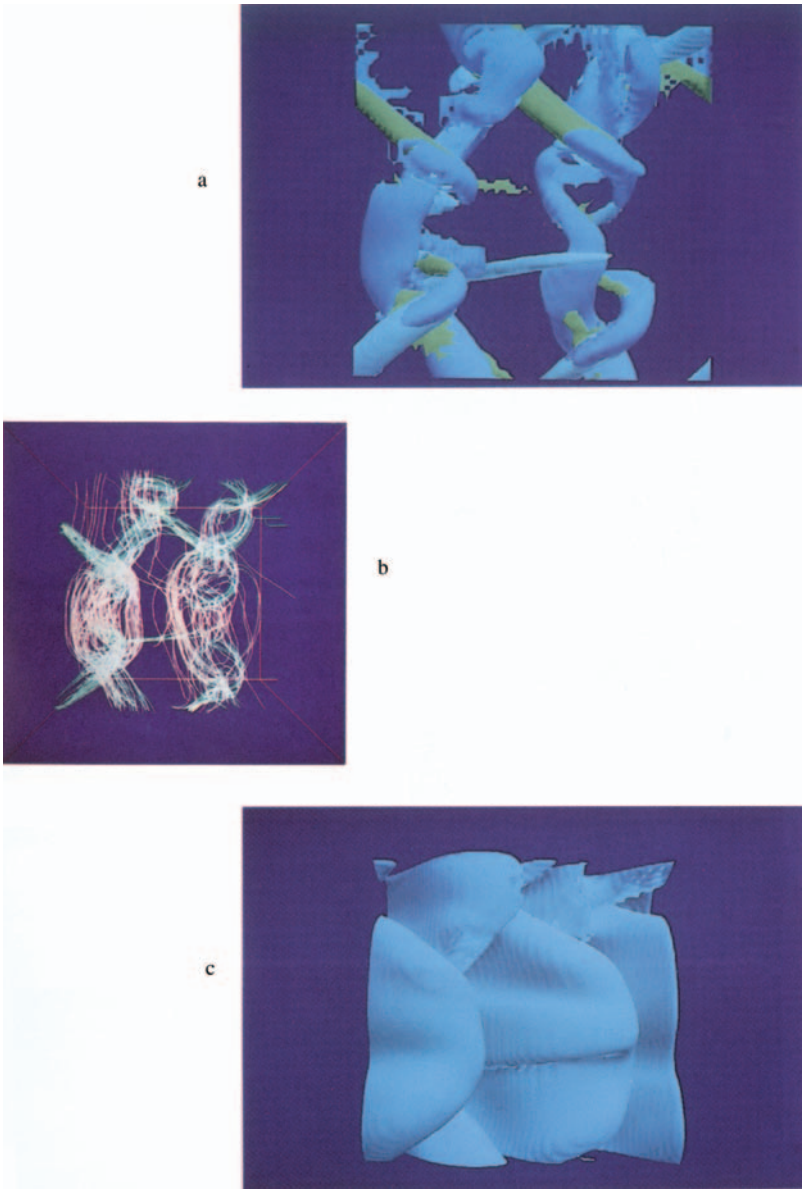

Plate 11: Direct-numerical simulation of the periodic mixing layer forced by a small random three-dimensional perturbation done by Comte et al. [137]; top view of: (a) vortex structures; (b) vortex lines; (c) passive scalar at the interface. The resolution is 128^3 Fourier wave vectors, and the Reynolds number $U\delta_i/\nu = 100$.

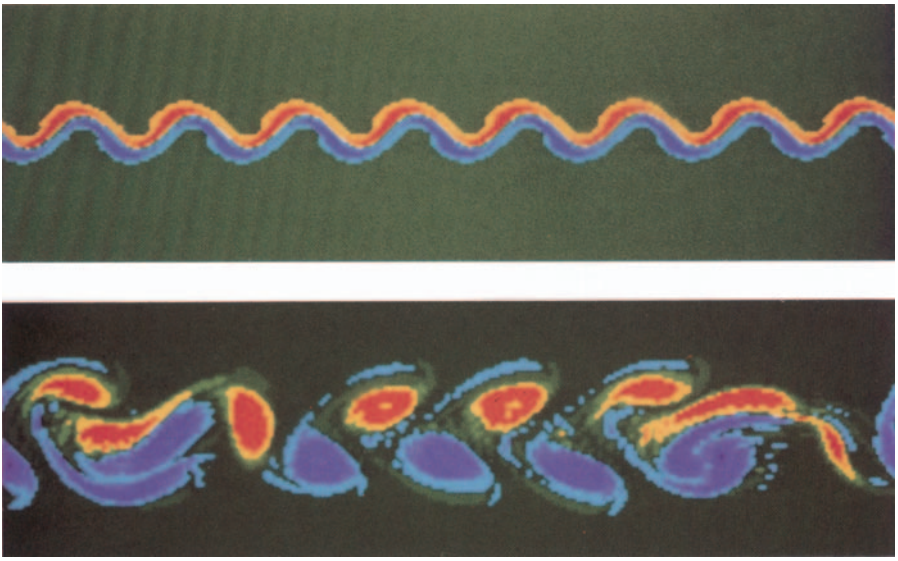

Plate 13: Vorticity field in a direct-numerical simulation of a two-dimensional temporal Bickley jet: one can see the growth of the sinuous instability, and the formation of a Karman street, with alternate eddies of positive (red) and negative (blue) vorticity (from Comte et al. [133]).

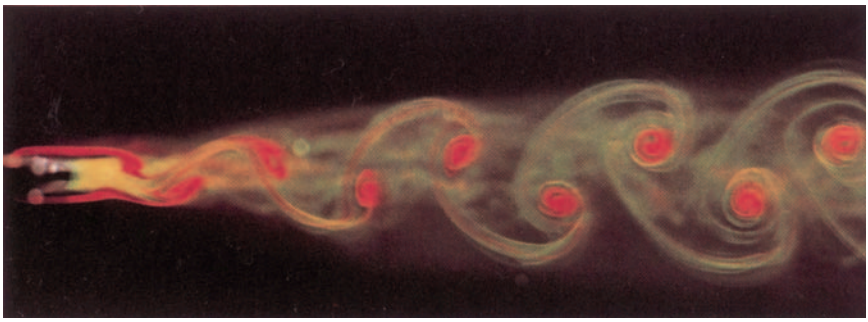

Plate 14: Experimental wake behind a splitter plate in a hydrodynamic tunnel (courtesy H. Werlé, ONERA).

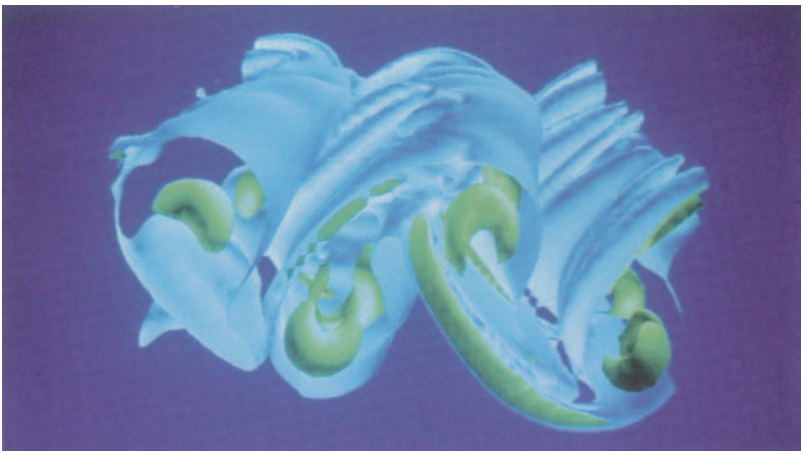

Plate 15: Vorticity components in the DNS a temporal wake, showing the formation of hairpins between the Karman billows (courtesy M.A. Gonze).

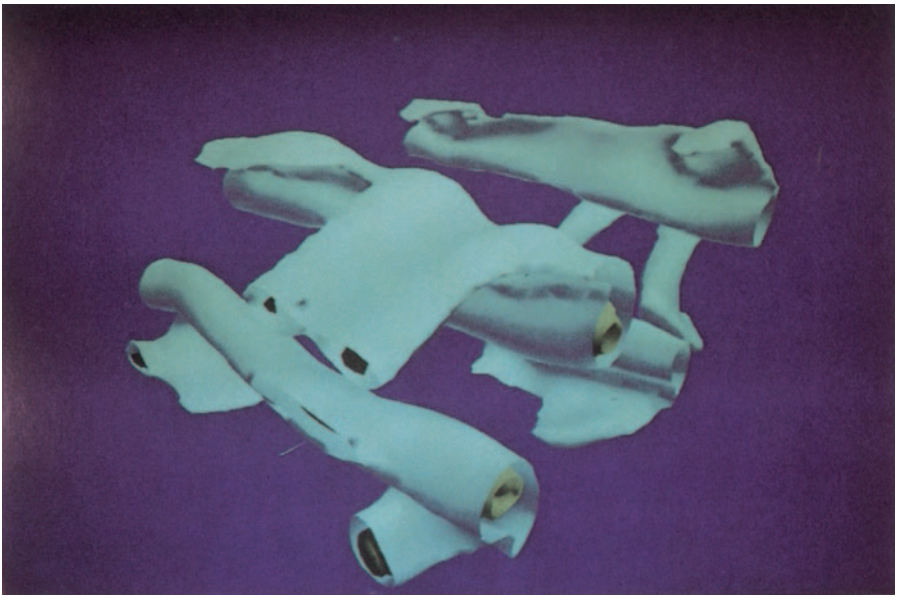

Plate 16: Same simulation as in Plate 15, showing a passive-scalar field at a later time, and the longitudinal stretching of hairpins.

Plate 17: LES of an inviscid incompressible mixing layer forced upstream by a quasi two-dimensional random perturbation; the vorticity modulus is shown at a threshold $(2/3)\omega_i$ (courtesy G. Silvestrini).

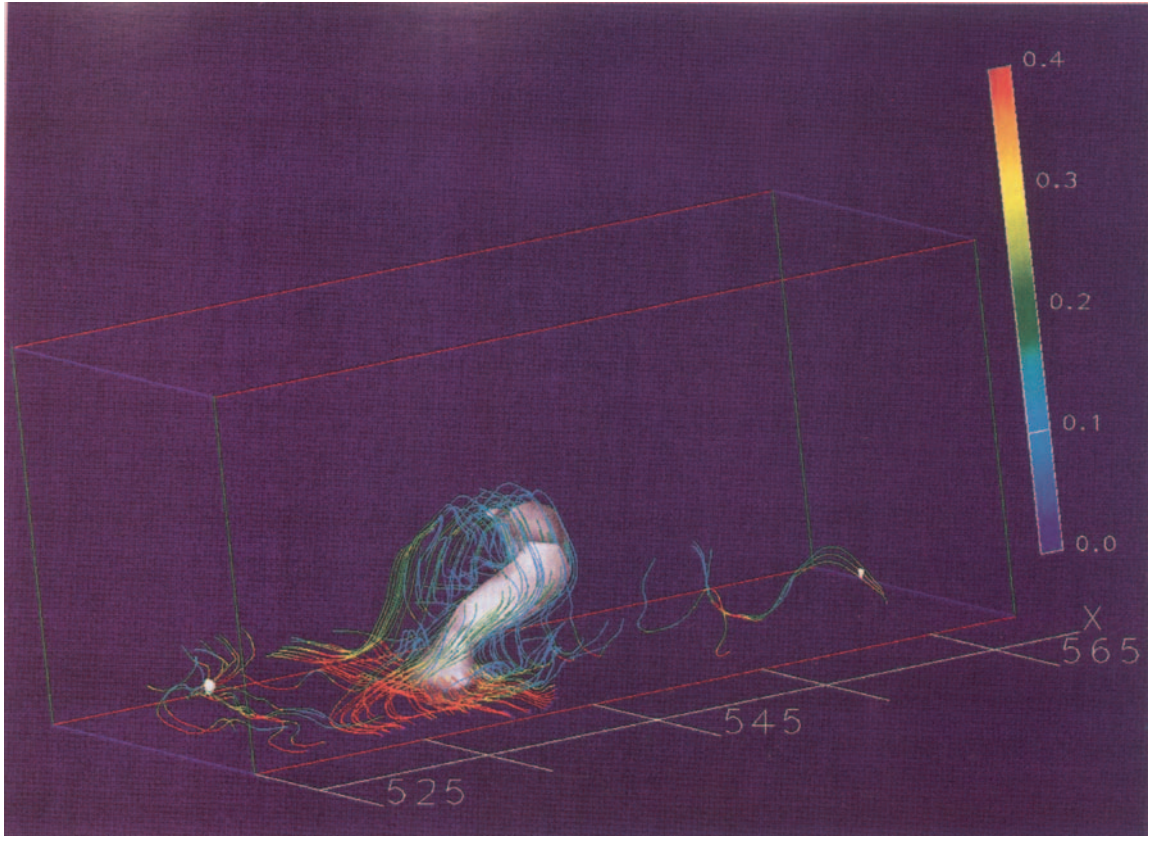

Plate 18: Hairpin vortex ejected in the LES of a spatially-developing turbulent boundary layer (from Ducros et al. [180], courtesy *J. Fluid Mech.*).

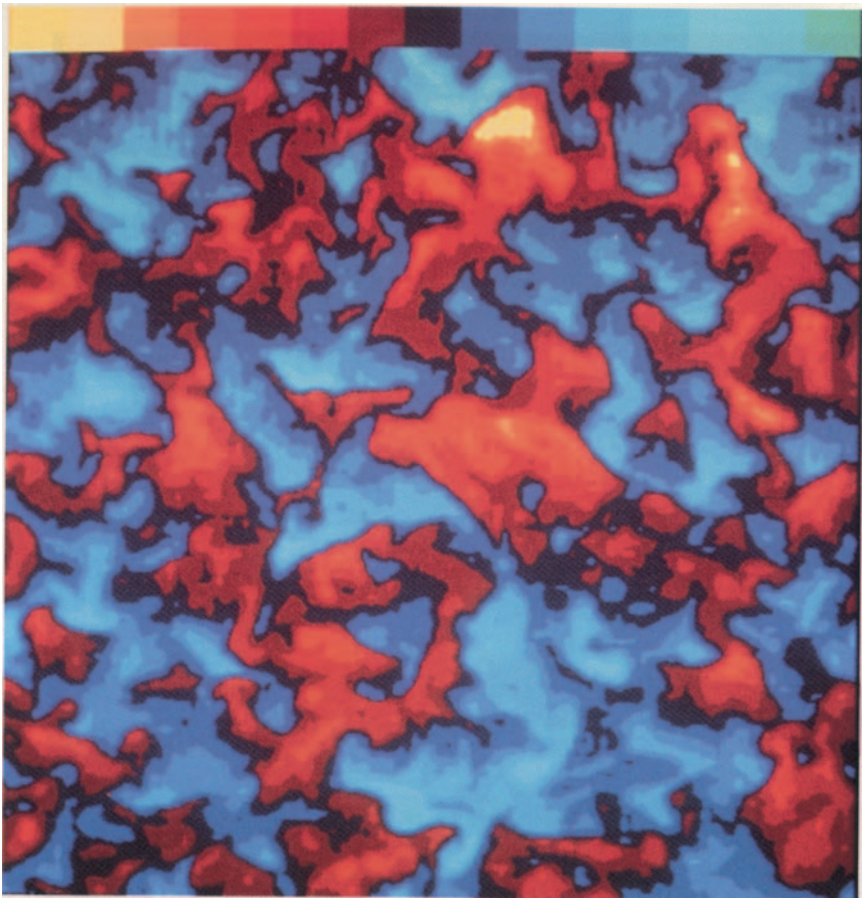

Plate 19: Cross section of the temperature distribution in the direct-numerical simulation of isotropic turbulence done by Métais and Lesieur [496]; the resolution is 128^3 Fourier modes.

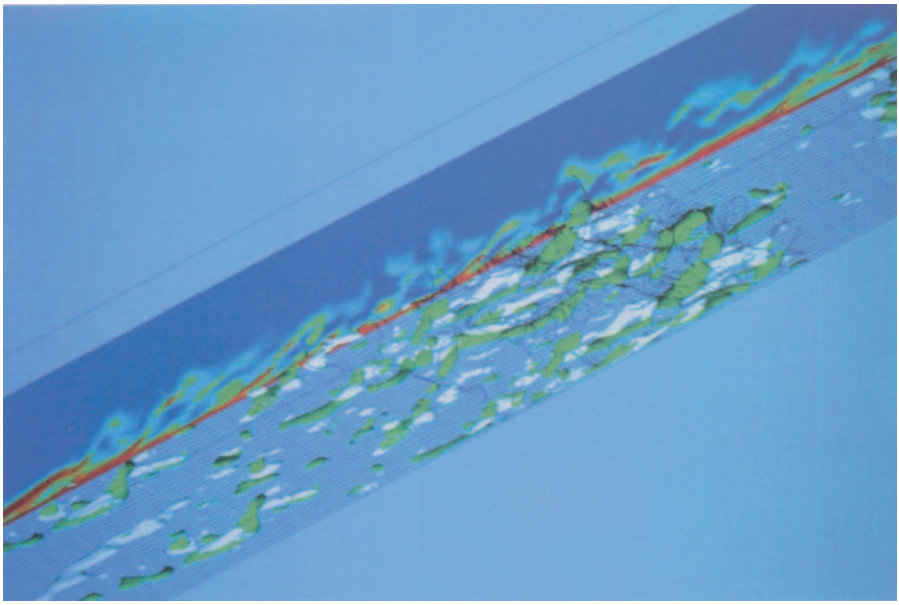

Plate 20: FSF model based LES of a spatial boundary layer; isosurfaces of longitudinal vorticity (green $+0.15U_\infty/\delta_i$, white $-0.15U_\infty/\delta_i$, see text for details (courtesy P. Comte).

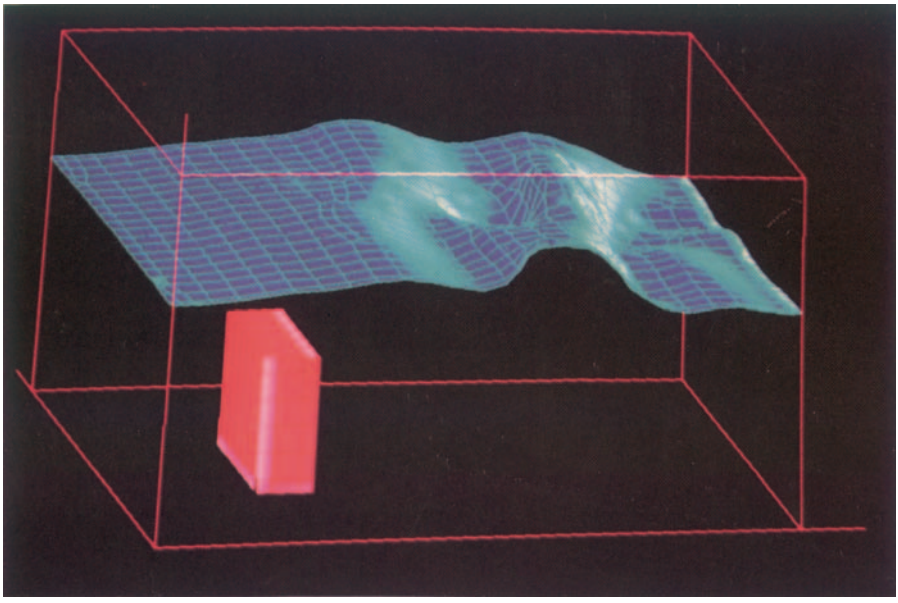

Plate 21: Isopycnal surface in a finite-volume direct-numerical simulation of a strongly-stratified flow above an obstacle (courtesy H. Laroche).

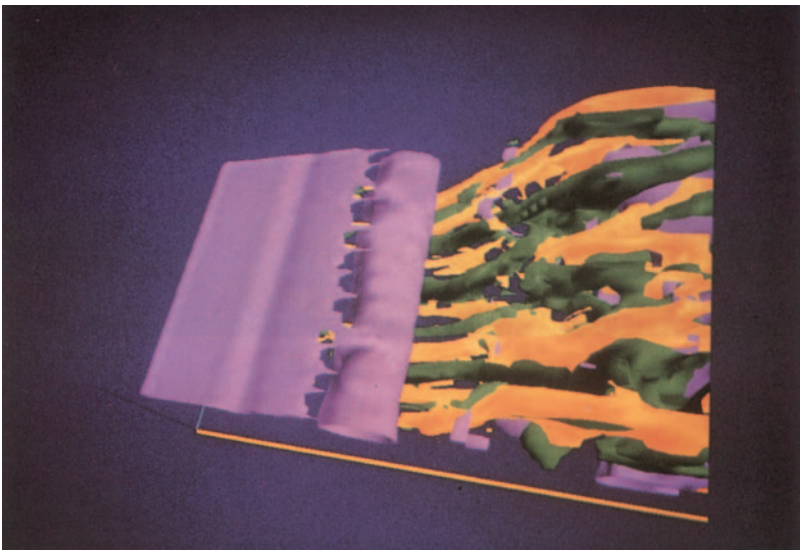

Plate 22: longitudinal (yellow and green) and spanwise (violet) vorticity components in the LES of a backwards-facing step flow at an expansion ratio of 5. This transient state will eventually degenerate into a helical-pairing configuration (courtesy A. Silveira).

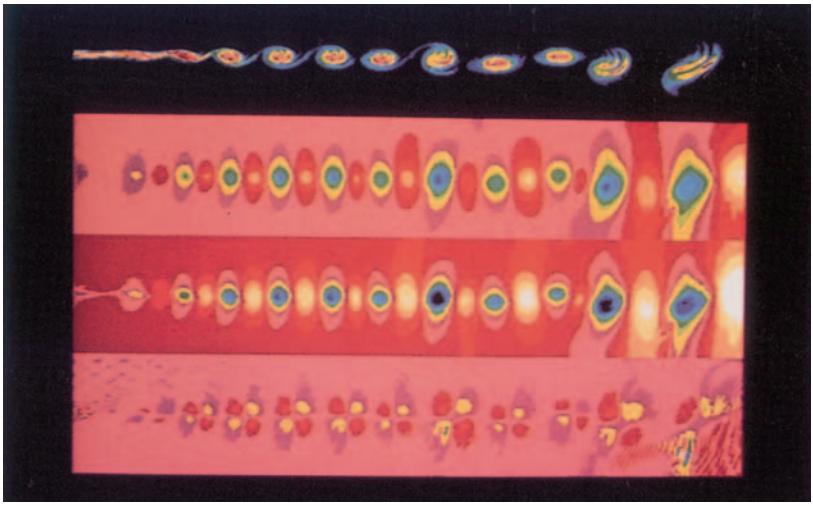

Plate 23: Direct-numerical simulation of a two-dimensional spatially-growing compressible mixing layer. The Mach numbers of the two streams are 2 and 1.2. The vorticity, pressure, density and divergence fields are shown (courtesy Y. Fouillet et X. Normand).

1

Introduction to Turbulence in Fluid Mechanics

1.1 Is it possible to define turbulence?

Everyday life gives us an intuitive knowledge of turbulence in fluids: the smoke of a cigarette or over a fire exhibits a disordered behaviour characteristic of the motion of the air which transports it. The wind is subject to abrupt changes in direction and velocity, which may have dramatic consequences for the seafarer or the hang-glider. During air travel, one often hears the word turbulence generally associated with the fastening of seat-belts. Turbulence is also mentioned to describe the flow of a stream, and in a river it has important consequences concerning the sediment transport and the motion of the bed. The rapid flow of any fluid passing an obstacle or an airfoil creates turbulence in the boundary layers and develops a turbulent wake which will generally increase the drag exerted by the flow on the obstacle (and measured by the famous C_x coefficient): so turbulence has to be avoided in order to obtain better aerodynamic performance for cars or planes. The majority of atmospheric or oceanic currents cannot be predicted accurately and fall into the category of turbulent flows, even in the large planetary scales. Small-scale turbulence in the atmosphere can be an obstacle towards the accuracy of astronomic observations, and observatory locations have to be chosen in consequence. The atmospheres of planets such as Jupiter and Saturn, the solar atmosphere or the Earth's outer core are turbulent. Galaxies look strikingly like the eddies which are observed in turbulent flows such as the mixing layer between two flows of different velocity, and are, in a manner of speaking, the eddies of a turbulent universe. Turbulence is also produced in the Earth's outer magnetosphere, due to the development of instabilities caused by the interaction of the solar wind with the magnetosphere. Numerous other examples of turbulent flows arise in aeronautics, hydraulics, nuclear and chemical engineering, oceanography, meteorology, astrophysics and internal geophysics.

It can be said that a turbulent flow is a flow which is disordered in time and space. But this, of course, is not a precise mathematical definition. The flows one calls "turbulent" may possess fairly different dynamics, may be three-dimensional or sometimes quasi two-dimensional, may exhibit well organized structures or otherwise. A common property which is required of them is that they should be able to mix transported quantities much more rapidly than if only molecular diffusion processes were involved. It is this latter property which is certainly the more important for people interested in turbulence because of its practical applications: the engineer, for instance, is mainly concerned with the knowledge of turbulent heat diffusion coefficients, or the turbulent drag (depending on turbulent momentum diffusion in the flow). The following definition of turbulence can thus be tentatively proposed and may contribute to avoiding the somewhat semantic discussions on this matter:

- Firstly, a turbulent flow must be *unpredictable*, in the sense that a small uncertainty as to its knowledge at a given initial time will amplify so as to render impossible a precise deterministic prediction of its evolution (a).
- Secondly, it has to satisfy the increased mixing property defined above (b).
- Thirdly, it must involve a wide range of spatial wave lengths (c).

Such a definition allows in particular an application of the term "turbulent" to some two-dimensional flows. It also implies that certain non-dimensional parameters characteristic of the flow should be much greater than one: indeed, let l be a characteristic length associated to the large energetic eddies of turbulence, and v a characteristic fluctuating velocity; a very rough analogy between the mixing processes due to turbulence and the incoherent random walk allows one to define a turbulent diffusion coefficient proportional to $l\ v$. As will be seen later on, l is also called the integral scale. Thus, if ν and κ are respectively the molecular diffusion coefficients[1] of momentum (called below the kinematic molecular viscosity) and heat (the molecular conductivity), the increased mixing property for these two transported quantities implies that the two dimensionless parameters $R_l = lv/\nu$ and lv/κ should be much greater than one. The first of these parameters is called the Reynolds number, and the second one the Peclet number. Notice finally that the existence of a large Reynolds number implies, from the phenomenology developed in Chapter 6, that the ratio of the largest to the smallest scale is of the order of $R_l^{3/4}$. In this respect, the property b) stressed above implies c).

A turbulent flow is by nature unstable: a small perturbation will generally, due to the nonlinearities of the equations of motion, amplify. The contrary

[1] These coefficients will be accurately defined in Chapter 2.

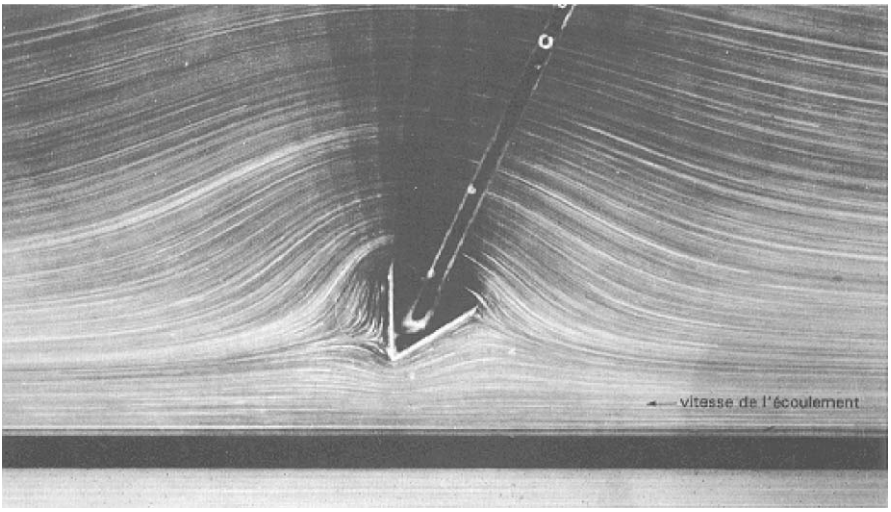

Figure 1.1. Stokes flow of glycerin past a triangular obstacle (picture by S. Taneda, Kyushu University; from Lesieur [416], courtesy S. Taneda and "La Recherche").

occurs in a "laminar" flow, as can be seen in Figure 1.1, where the streamlines, perturbed by the small obstacle, reform downstream. The Reynolds number of this flow, defined as

$$Re = [\text{fluid velocity}] \times [\text{size of the obstacle }]/\nu \tag{1.1}$$

is in this experiment equal to $2.26\ 10^{-2}$. This Reynolds number is different from the turbulent Reynolds number introduced above, but it will be shown in Chapter 3 that they both characterize the relative importance of inertial forces over viscous forces in the flow. Here the viscous forces are preponderant and will damp any perturbation, preventing a turbulent wake from developing.

There is a lot of experimental or numerical evidence showing that turbulent flows are rotational, that is, their vorticity $\vec{\omega} = \vec{\nabla} \times \vec{u}$ is non zero, at least in certain regions of space. Therefore, it is interesting to ask oneself how turbulence does in fact arise in a flow which is irrotational upstream.[2] It is obviously due to the viscosity, since an immediate consequence of Helmholtz–Kelvin's theorem, demonstrated in Chapter 2, is that zero-vorticity is conserved following the motion in a perfect fluid:[3] the presence of boundaries or obstacles imposes a zero-velocity condition which produces vorticity. Production of vorticity will then be increased by various phenomena, in particular the vortex

[2] For instance, a uniform flow.

[3] The perfect fluid is an approximation of the flow where molecular viscous effects are ignored.

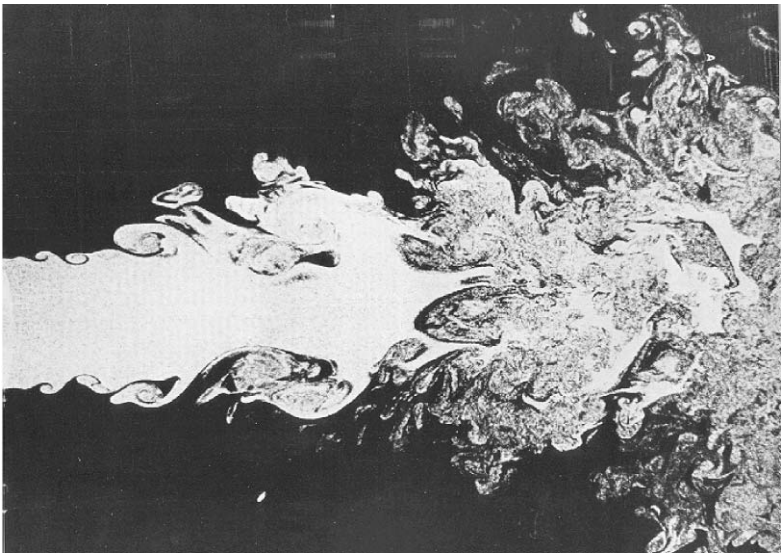

Figure 1.2. Turbulent jet (picture by J.L. Balint, M. Ayrault and J.P. Schon, Ecole Centrale de Lyon; from Lesieur [416], courtesy J.P. Schon and "La Recherche").

filaments stretching mechanism to be described later, to such a point that the flow will generally become turbulent in the rotational regions.

In what is called grid turbulence for instance, which is produced in the laboratory by letting a flow go through a fixed grid, the rotational vortex streets behind the grid rods interact together and degenerate into turbulence. Notice that the same effect would be obtained by pulling a grid through a fluid initially at rest, due to the Galilean invariance of the laws of motion. In some situations, the vorticity is created in the interior of the flow itself through some external forcing or rotational initial conditions (as in the example of the temporal mixing layer presented later on).

1.2 Examples of turbulent flows

To illustrate the preceding considerations, it may be useful to display some flows which come under our definition of turbulence. Figure 1.2 shows a turbulent air jet marked by incense smoke and visualized thanks to a technique of laser illumination. Figure 1.3 shows a "grid turbulence" described above. Figure 1.4, taken from Brown and Roshko [88], shows a mixing layer between two flows of different velocities (here helium and nitrogen), coming from the trailing edge of a thin plate: they develop at their interface a Kelvin–Helmholtz

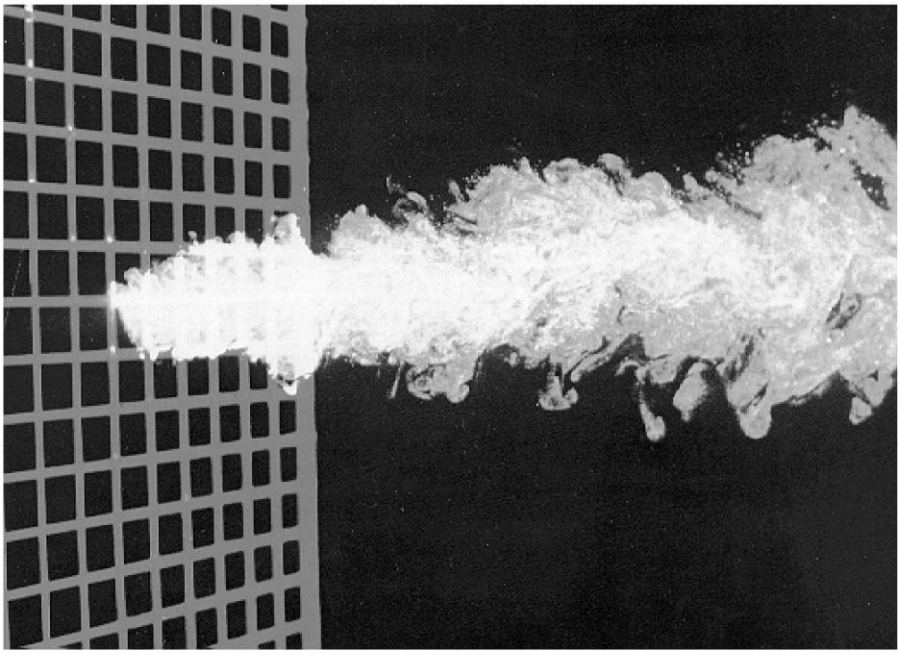

Figure 1.3. Turbulence created in a wind tunnel behind a grid. Here turbulence fills the whole apparatus, and a localized source of smoke has been placed on the grid to visualize the development of turbulence (picture by J.L. Balint, M. Ayrault and J.P. Schon, Ecole Centrale de Lyon; from Lesieur [416], courtesy "La Recherche").

instability. This instability is eventually responsible for the generation of large quasi two-dimensional vortices, which are referred to as coherent. When looking at pictures taken at different times, it is obvious that the vortices pair and amalgamate following the downstream motion. The pairing interaction between same-sign vortices when they are close enough will be discussed in Chapter 3. Upon these vortices are superposed three-dimensional turbulent small scales which seem to be more active when the Reynolds number is increased.

We will show in Chapters 3 and 4 that a contribution to three-dimensionality comes from the longitudinal stretching of hairpin vortices between the big coherent billows. Another factor of three-dimensionalization may be the occurrence of spanwise dislocations affecting the big billows themselves. This is due to helical-pairing interactions, discussed also in Chapters 3 and 4.

Plate 1(a) (see the colour plates section at the beginning of the book) shows a two-dimensional simulation of the diffusion of a passive dye by the

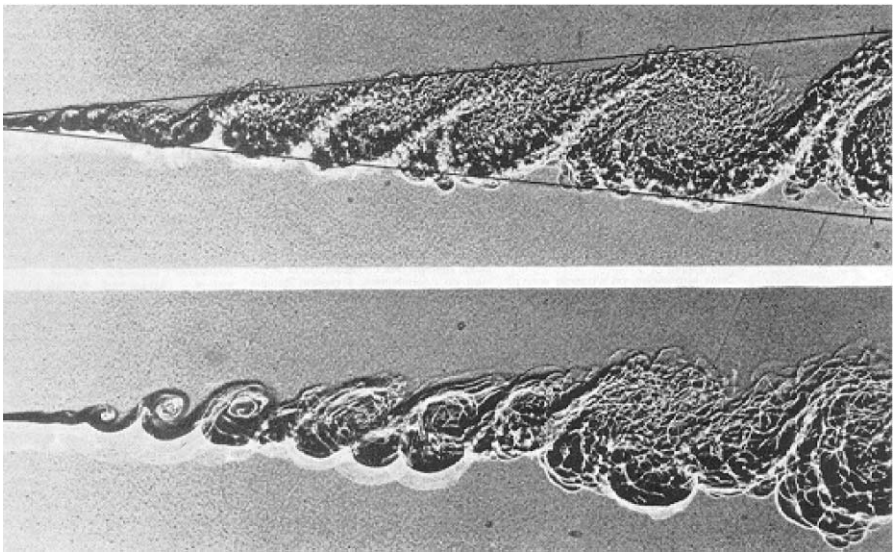

Figure 1.4. Turbulence in a mixing layer (Brown and Roshko [88]). On the top, the Reynolds number (based on the velocity difference and the width of the layer at a given downstream position) is twice that of the bottom (courtesy A. Roshko and *J. Fluid Mech.*).

large structures of the mixing layer presented in Figure 1.4, in a numerical resolution of the equations of the flow motion performed by Normand et al. [536]: the faster fluid is shown in blue, while the slower fluid is in red. The same coherent structures as in the experiment are present, which proves that the dynamics of these structures is essentially dominated by quasi two-dimensional mechanisms. We will come back often to this discussion throughout the book. An advantage of the calculation over the experiment is to provide also the vorticity field very accurately. In fact, experimental vorticity measurements are difficult to perform. However, modern particle image velocimetry techniques (called PIV or DPIV) allow now to determine the projection of the velocity fields on some planes from the displacement of particles, and hence the vorticity component perpendicular to this plane. Informations on these techniques may be found in the well-documented book of Bernard and Wallace [57]. The question which is now posed concerns the precision of these methods. On the other hand, probes using several hot wires may also provide informations on the vorticity (Balint et al. [29, 30], Vukoslavcevic et al. [708], Tsinober et al. [694]).

Comparison between the vorticity and passive dye contours provided by Plate 1(b) indicates that the coherent vortices consist here in spiral concentra-

tions of vorticity around which the convected scalar winds up. Finally, Plate 2 (see colour plates section) shows the vorticity field in a two-dimensional numerical simulation of a temporal mixing layer (that is, periodic in the mean flow direction), where the upper and lower currents are driven with respective velocities $U\vec{x}$ and $-U\vec{x}$ (see Lesieur et al. [420], and Comte [134]). As already stressed, the resemblance of the pairing eddies to the spiral galaxies is striking. This is in agreement with the fact that many galaxies are known to contain black holes, which are huge vortices which will pair if they turn in the same sense. Notice also that in Figure 1.2, in the upstream region of the jet, one can see the formation of quasi axisymmetric vortex rings.[4] Further downstream, the vortices seem to undergo some sort of pairing, as in the plane mixing layer. Then the jet breaks down into small-scale turbulence. Numerical simulations tend to indicate also the occurrence of alternate pairing of vortex rings, a mechanism resembling helical pairing in mixing layers (see e.g. Fouillet [211], and the discussion in Lesieur et al. [431]).

All these structures are called coherent because they can be found extremely far downstream, with approximately the same shape. It is possible for these coherent vortices to become irregular and unpredictable, and thus constitute a turbulent field, even if the flow is quasi two-dimensional. Evidence for that is presented in Figure 1.5, showing the vorticity contours in a two-dimensional calculation of a temporal mixing layer taken from Staquet et al. [668]: the evolution of the flow after 30 characteristic dynamic initial times is presented for four independent initial small random perturbations superimposed upon the basic inflectional velocity shear. The vortices display some important differences, since there are for instance four eddies in Figure 1.5-d and only three eddies in Figure 1.5-b. They therefore show some kind of unpredictability. Let us stress that these temporal mixing layer simulations followed the pioneering calculations of Riley and Metcalfe [599], who showed how, in two dimensions, Kelvin–Helmholtz vortices could emerge from the instability of an inflectional velocity profile perturbed deterministically or randomly.

Now we define a *coherent vortex* as a region of space:

- Where vorticity ω concentrates enough so that fluid trajectories can wind around (a).[5]

[4] They are the axisymmetric equivalent of Kelvin–Helmholtz vortices, and explain for instance why a smoker can create smoke rings.

[5] It is a very simple application of Stokes circulation theorem to show that the vorticity concentration inside a coherent vortex will tend to entrain the low-vorticity fluid surrounding it in a motion of rotation. This phenomenon will be referred to as velocity induction, and exists even in the absence of viscosity.

- Which keeps (following the flow motion) a characteristic shape during a life time T_c longer enough in front of their local turnover time ω^{-1} (b).
- Which is unpredictable (c).

In this respect, Kelvin–Helmholtz vortices in a mixing layer, or Karman vortices in a wake, are coherent. Longitudinal hairpin vortices ejected in turbulent boundary layers or channel flows are coherent as well. Still in the boundary layers, let us consider the low- and high-speed streaks observed experimentally close to the wall by Klebanoff et al. [334] during transition, and by Kline et al. [337] in the turbulent stage. Numerical simulations were carried out by Spalart [663], Robinson [609], and Ducros et al. [180] for the boundary layer, as well as by Moin and Kim [513] and Kim et al. [330] for the turbulent channel. These simulations show that the streaks do not correspond to important longitudinal and vertical vorticity concentrations, but the high-speed streaks induce high spanwise vorticity fluctuations at the wall (see Chapter 4). However, the fluid parcels do not wind around the streaks, so that condition a) is not satisfied, and they cannot be called a coherent vortex. The quasi stationary apex vortices attached to a Delta wing cannot as well, since they are predictable.

A coherent structure will just be defined as a region of space which, at a given time, has some kind of organization regarding any quantity related to the flow (velocity, vorticity, pressure, density, temperature, etc.). This is a much broader definition. In this sense, any coherent vortex is a coherent structure, but the reverse is not always true, as shown by the examples of streaks close to a wall and apex vortices.

When two coherent vortices of parallel axis and same sign are close enough, they will tend to rotate about each other, due to the velocity-induction effect just mentioned above, and will merge: this is the cause of the pairing already encountered. As stressed in Lesieur et al. [431, p. 26]: *during the process, they form spiral arms reminiscent of galaxies owing to the differential rotation, since the the angular velocities involved are proportional to* r^{-2} (where r is the distance from the fluid to the vortex centre.

If the vortices are antiparallel, the two mutual induced velocities will be of same sign, and the two vortices will move together forming a dipole. These dipoles have been found in experiments and numerical simulations done by Couder and Basdevant [150] (see also the compressible simulations of Fouillet [211]). They are usually called Batchelor's couples, from a dipole-like exact solution of Euler equation discussed in Batchelor [50].

Generally, a coherent vortex corresponds to a low pressure field, since a fluid parcel in the vortex is in approximate balance (in a frame moving with the fluid) between the centrifugal force and the pressure gradient. This is no more true if the fluid is submitted to a strong system rotation, such as large-scale atmospheric motions: there, the balance, called *geostrophic balance*, involves

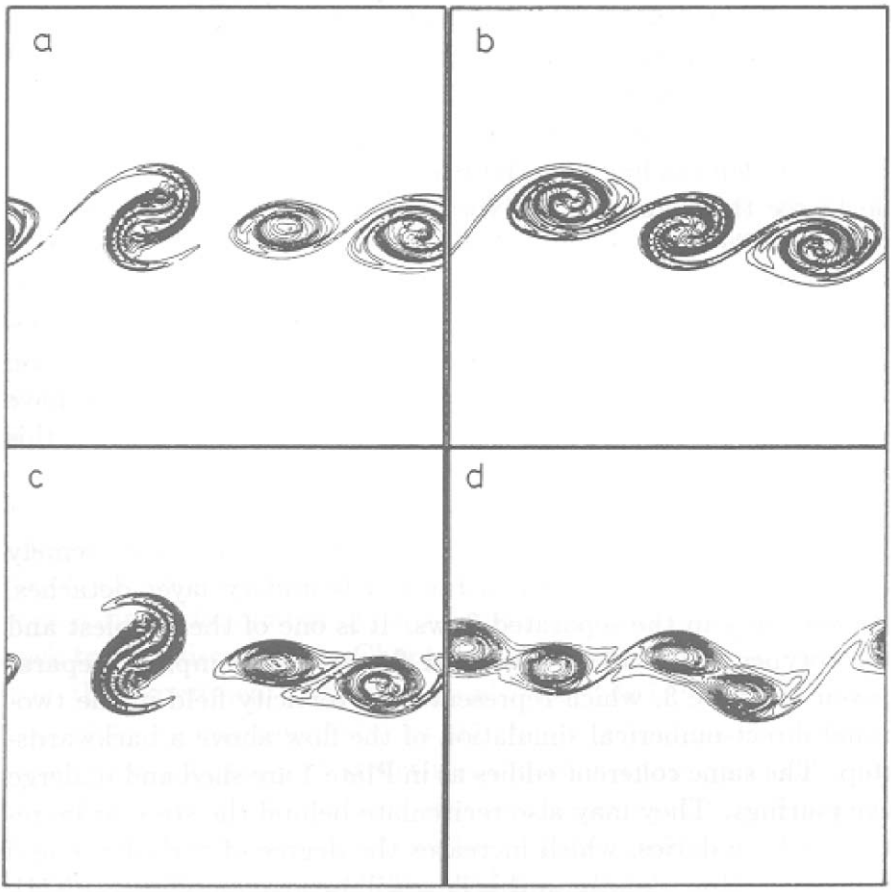

Figure 1.5. Isovorticity lines, in a two-dimensional periodic mixing-layer calculation: with four initial velocity fields differing only slightly, a decorrelation develops. This indicates that the coherent vortices are unpredictable (courtesy C. Staquet, Institut de Mécanique de Grenoble).

Coriolis force and pressure gradients, in such a way that cyclonic vortices[6] correspond to low pressure and anticyclonic vortices to high pressure.

The experimental and numerical visualizations shown in Figure 1.4 and Plate 1 are a very good example of the revolution which has occurred in our

[6] On a rotating sphere of angular rotation vector $\vec{\Omega}$, cyclonic eddies are defined in order to have a relative vorticity $\vec{\omega}$ such that $\vec{\omega}.\vec{\Omega} > 0$. Therefore, they rotate anticlockwise in the Northern hemisphere and clockwise in the Southern hemisphere.

understanding of turbulence over the last 20 years: we are now able to see the details of the vortices which form inside the flow. Before, we were like blind people, clumsily trying to develop global theories from measurements or calculations we could not really interpret. Now, the increasingly fast development of visualization devices, both in Computational and Experimental Fluid Dynamics, sheds a totally new light upon the dynamics of turbulence. It does not mean that former statistical theories have become obsolete, but they have to be re-interpreted with the aid of this new knowledge.

Let us stress that mixing-layer formation is extremely common in aeronautics, when for instance a boundary layer detaches, and more generally in the separated flows. It is one of the simplest and richest prototypes of turbulent free-shear flows. An example of separation is given in Plate 3, which represents the vorticity field in the two-dimensional direct-numerical simulation of the flow above a backward-facing step. The same coherent vortices as in Plate 1 are shed and undergo successive pairing. They may also be trapped in the recirculation zone behind the step, or bounce upon the boundaries, which increases the degree of turbulence and unpredictability. More details on this flow will be given in Chapter 13.

In the mixing-layer experiment of Figure 1.4, the turbulence in the very small scales is called fully-developed turbulence. It has some characteristics of three-dimensional isotropic turbulence (see below). This does not imply that it has totally forgotten the mechanisms of generation of turbulence, i.e. the basic inflectional shear, since the longitudinal velocity fluctuations are larger than their transverse and spanwise counterparts. As far as the large structures are concerned, they depend crucially on the basic shear, and the terminology of "developed" cannot be used for them.

Returning to large-scale coherent vortices, they can be found in the turbulence generated in a rapidly rotating tank by an oscillating grid located at the bottom of the tank. Plate 4 shows a section of the tank perpendicular to the axis of rotation. Here, the effect of rotation is to induce two-dimensionality in the flow, and to create strongly-concentrated eddies with axes parallel to the axis of rotation (Hopfinger et al. [296]). In fact, it will be shown in Chapter 13 that if the rotation rate[7] is not too high, this favours the formation of cyclonic vortices, whereas anticyclonic vortices reform together with cyclonic ones at low Rossby number.

As already mentioned earlier, atmospheric and oceanic flows are highly unpredictable and fall into the category of turbulent flows. Their dynamics in the large scales is strongly influenced by their shallowness (the ratio of vertical scales to the horizontal extension of planetary scales is of the order of 10^{-2} in the Earth's atmosphere), by the Earth's sphericity and rotation, by differential heating between the equator and the poles, and by topography. As

[7] Measured in terms of a vorticity-based Rossby number $|\omega|/2\Omega$.

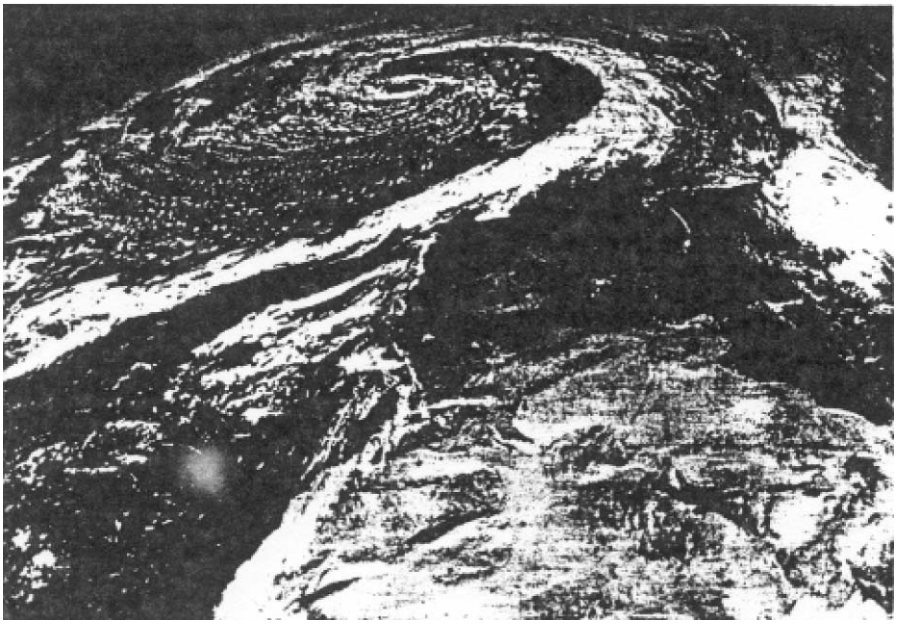

Figure 1.6. Image taken by METEOSAT II on 18th September 1983, and showing a strong depression above the Atlantic, centered 58° north and 18° east (courtesy METEO-FRANCE).

stressed above, the pressure highs or lows that can be observed every day on the meteorological maps in the medium latitudes correspond to respectively anticyclonic or cyclonic large-scale vortices in the atmosphere. They are approximately in geostrophic balance. Figure 1.6 shows for example an impressive vortex associated to a depression above the Atlantic. To illustrate what has been stressed above about the change of hemisphere on Earth, Figure 1.7 displays a meteorological map borrowed from an australian newspaper, showing an anticyclonic perturbation rotating anti-clockwise around a pressure high (H), and a cyclonic perturbation rotating clockwise around a pressure low (L).

Plate 5 shows also the eddy field which can be seen from the temperature measured by satellites on the surface of the Atlantic ocean close to the Gulf Stream. One can observe similar vortices in the Alboran sea, west of the Mediterranean. As for the synoptic atmospheric large scales just discussed above, they result from baroclinic instability, due to the conjugate effects of rotation and horizontal thermal gradients. It converts flow potential energy into horizontal kinetic energy (see Chapter 9). Numerous oceanic eddies develop in the Gulf Stream, and in the Kuroshio extension, east of Japan. They

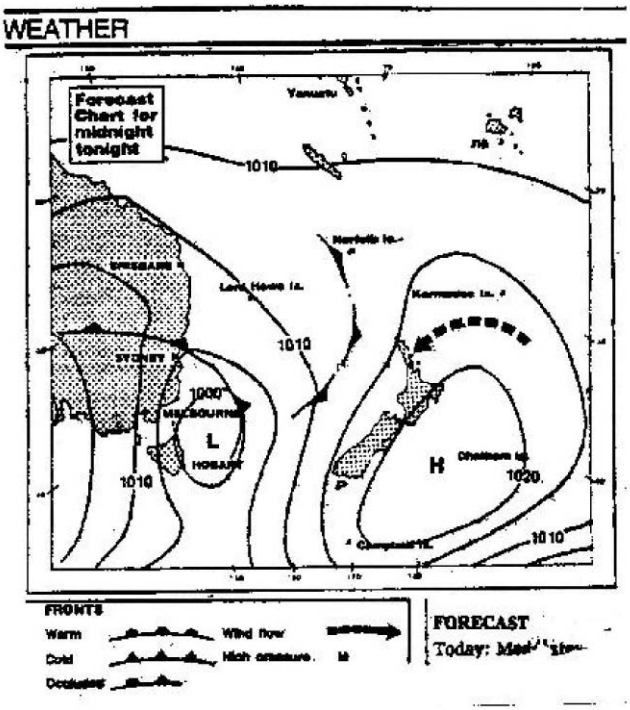

Figure 1.7. Weather map in an Australian newspaper.

are extremely important for the development and transport of phyto- and zooplancton.

In the atmospheres or oceans of rotating planets, the concept of rapid rotation can be measured by considering the smallness of a dimensionless parameter, the Rossby number, which is defined here as $R_o = U/|f|L$, where U and L are a typical horizontal velocity and length, respectively, and $f = 2\Omega \sin\varphi$ the Coriolis parameter (φ is the local latitude). The simplified models of two-dimensional or geostrophic turbulence will be considered in Chapter 9 as a first step towards the understanding of these flows. We will show that the precision of geostrophic approximation is of order R_o. Estimations of this number are given in Somméria [662] and Lesieur et al. [431]. For L corresponding to large planetary scales (1000 km), $U = 30$ m/s and at midlatitudes ($f = 10^{-4}$ rd/s), one finds 0.3 in Earth's atmosphere. We have $R_o = 0.05$ for oceanic mesoscale vortices with (scale 100 km, velocity 5 cm/s). This explains why geostrophic approximation applies better to the oceans than the atmosphere. In fact, certain developing operational oceanic prediction numerical codes are based on this approximation. However, the oceanic models have to

be modified to account for the sinking of cold salty water in the conveyor belt at the level of northern Atlantic ocean. This phenomenon is crucial, since the puzzling melting of polar ice with production of fresh water in this region might stop it. This would have dramatic consequences for the existence of the Gulf Stream north branch which might disappear, with a severe cooling of Northern Europe.

We can calculate also Jupiter Rossby number at midlatitude. Since the planet rotates in 10 h, we have $f \approx (24/10)10^{-4}$. With a velocity of 100 m/s and a scale of 10 000 km (the width of the great red spot, see below), we have $R_o = 0.04$. This is very close to the ocean. On Jupiter the mean circulation of the gaseous outer envelope is strikingly simple, since it consists of zonal jets going eastwards or westwards. The most convincing interpretation is based on anisotropic effects due to Rossby waves, arising in inverse energy cascades of geostrophic turbulence (see Rhines [593], Williams [717,718] and Chapter 9). Others propose an interaction mechanism between internal thermal convection and rotation (Busse [90]). Plate 6 shows the global circulation of Jupiter. On can see in particular the great red spot. The origin of the latter, which is anticyclonic and has been observed for many centuries, is also quite mysterious, and not well understood yet. It might result from a mixing-layer instability between the two neighbouring jets, the spot forming after successive pairings of the vortices. But it is difficult to understand why no other big eddy of this type is found. The width of the jets is of the same order as the great red spot. Smaller vortices exist also. Notice that the same kind of intense vortex as the great red spot has been discovered in 1989 on Neptune (great dark-blue spot) by NASA's Voyager 2 probe. Notice also that Jupiter's gaseous atmosphere depth is of the order of 1.5% of its radius, which might justify the use of shallow-water theories in this case. Laboratory experiments on rotating tanks have been carried out by Sommeria et al. [661] in order to identify mechanisms leading to the great red spot formation.

1.3 Fully-developed turbulence

The word "developed" has already been employed for the small-scale three-dimensional turbulence which appears in the mixing-layer experiments. Fully-developed turbulence is a turbulence which is free to develop without imposed constraints. The possible constraints are boundaries, external forces, or viscosity. One can easily observe that the structures of a flow of scale comparable with the dimensions of the domain where the fluid evolves cannot deserve to be categorized as "developed".

The same remark holds for the structures directly created by the external forcing, if any. So no real turbulent flow, even at a high Reynolds number, can be "fully developed" in the large energetic scales. At smaller scales, however,

turbulence will be fully developed if the viscosity does not play a direct role in the dynamics of these scales.[8] This will be true if the Reynolds number is high enough so that an "inertial-range" can develop.[9] In the preceding experimental examples of the jet and the mixing layer, one actually obtains fully-developed turbulence at scales smaller than the large energetic scales and larger than the dissipative scales. On the contrary, in the majority of grid-turbulence experiments, the Reynolds number is not high enough to enable an inertial range to develop. The small three-dimensional turbulent scales of the Earth's atmosphere and oceans, or Jupiter and Saturn, are certainly fully developed. But the planetary scales of these flows are not, because of constraints due to the rotation, thermal stratification and finite size of planets. In this monograph, the term "developed" will mainly be used for three-dimensional flows, though it could be generalized to some high Reynolds number two-dimensional flows constrained to two-dimensionality by some external mechanism which does not affect the dynamics of the two-dimensional eddies once created.

An interesting issue about the structure of fully-developed turbulence concerns the possibility of fractal or multi-fractal distributions. This problem has been studied by Mandelbrot [469] and Frisch [229].

Finally, we stress that it is possible, for theoretical purposes, to assume that turbulence is fully developed in the large scales also, when studying a freely-evolving statistically homogeneous turbulence (without any mean shear): there is in this case no external force or boundary action.

1.4 Fluid turbulence and "chaos"

The definition of turbulence we have given here is extremely broad, and there does not seem to be a clear distinction between "turbulence" and "chaos". Nevertheless, the word chaos is now mainly used in mechanics to describe a particular behaviour pertaining to dynamical systems with a limited number of degrees of freedom: some of these systems, under particular conditions, exhibit solutions which are chaotic in the sense that two points in the phase space, initially very close, will separate exponentially. The characteristic rate of evolution of the exponential is called a Liapounov exponent, and must be positive in order to obtain a chaotic behaviour. In the case of dissipative systems, this behaviour is generally associated with the existence of strange

[8] It will be seen in Chapter 6 that the concept of local energy cascade in high Reynolds number three-dimensional turbulence implies that inertial forces transfer energy from large to small scales without any influence of viscosity, up to the so called "dissipative scales" where the kinetic energy is finally dissipated by viscous forces.

[9] See Chapter 6.

attractors around which the trajectory of the point representing the system will wind up. One of the most famous examples of that is the Lorenz attractor, a three-mode dynamical system derived from the equations of thermal convection (Lorenz [453]). Figure 1.8, taken from Lanford [373], shows for instance a numerical simulation of the Lorenz attractor for values of the parameters corresponding to the following dynamical system:

$$\begin{aligned} \frac{dx}{dt} &= -10\ x + 10\ y \\ \frac{dy}{dt} &= 28\ x - y - xz \\ \frac{dz}{dt} &= -\frac{8}{3}\ z + xy \end{aligned} \tag{1.2}$$

In fact, the first historical example of unpredictability was given by the mathematician Henri Poincaré [579] in 1889: he discovered a deterministic chaotic behaviour in the frame of a three-body problem (e.g. Earth-Moon-Sun) in celestial mechanics. Poincaré applied also this concept to discuss the formation of hurricanes, and why natural phenomena were apparently random. He proposed that uncertainties in the observations of an initial state would forbid a precise deterministic prediction.

Chaos has now become an entire discipline in itself, covering domains that are sometimes extremely far from fluid dynamics. Its relations with the latter are up to now limited to some aspects of the transition to turbulence, in the thermal convection problem in particular, and it is not our intention to include this topic in the present monograph. The reader is referred to Bergé et al. [55] for further details on this point of view. An attempt to apply it to the wall-region in the developed turbulent boundary layer has been undertaken by Lumley and colleagues (see Aubry et al. [21]), who use a Galerkin projection of the velocity field on a proper set of eigenmodes of the Reynolds tensor $\langle u_i' u_j' \rangle$, where the u' refer to the fluctuations of the velocity with respect to the mean velocity $\langle u \rangle$: once having been properly truncated in order to retain only longitudinal modes,[10] the system exhibits a chaotic behaviour resembling the occurrence of intermittent bursts in a turbulent boundary layer. More details may be found in the very original book of Holmes et al. [293]. The difficulty with this approach lies in the necessity of knowing in advance the eigenmodes, which requires the knowledge of the Reynolds tensor, either from experiments or numerical simulations: hence, the analysis is not predictive in the sense that

[10] That is, independent of the flow direction. It is in fact an important issue to know in which conditions these modes are dominant or not. This question will be addressed at several occasions throughout the present book.

it needs the problem to have already been investigated experimentally or numerically. It necessitates also the modelling of small-scale turbulence, as in the subgrid-scale modelling problem which will be discussed in Chapter 12. These so-called proper orthogonal decompositions (POD) have also been applied to the mixing layer by Delville et al. [166], and to the round jet by Glauser et al. [259]. They show that the first mode in the expansion contains most of the energy, and that the associated spectrum is not far from Kraichnan's k^{-3} enstrophy cascade spectrum of two-dimensional turbulence (see Chapter 8). As for the second mode (associated to small scales), its spectrum is close to Kolmogorov's $k^{-5/3}$ energy cascade characteristic of three-dimensional turbulence (see Chapter 6). More recent works based on this analysis concern the plane mixing layer (Druault et al. [175]), and a mixing layer/wake interaction (Braud et al. [79]).

An important outcome of POD is the fact that most of the informations relative to a given complicated random signal can be kept in a small number of modes, so that POD have become in signal processing a powerful and cheap way of compressing the data. Another manner for doing that is the wavelet approach, for which the reader is referred to the book of Meyer [502].

Another chaotic approach to turbulence introduces the concept of chaotic advection (see Aref [12, 13] for a review), where even a low number of point vortices in a two-dimensional flow can stir passive tracers in a chaotic manner. However, it is not clear, up to now, how these concepts can be applied to developed turbulence.

We would like to stress, however, that there is a-priori no contradiction between the "chaos philosophy" and the point of view which will be presented here: while dynamical systems limit their space dependance to a small number of degrees of freedom, and are only chaotic in time, a turbulent flow has generally a large number of spatial degrees of freedom and exhibits a chaotic behaviour in both time and space. As a matter of fact, fluid turbulence is sometimes referred to as a "spatio-temporal chaos" (see Favre et al. [200–202] for a discussion on this point). Like chaotic dynamical systems, fluid turbulence also displays unpredictability, as already stressed: the degree of unpredictability can be measured locally in space for a given spatial wave length, and exchanges of predictability exist between the spatial scales (see also Chapter 11).

1.5 "Deterministic" and statistical approaches

We will show in Chapter 2 how the fluid satisfies, for macroscopic scales large in front of the microscopic molecular scales, partial-differential equations called the Navier–Stokes equations. There is ample evidence that these equations describe properly turbulent flows, even in hypersonic flow situations

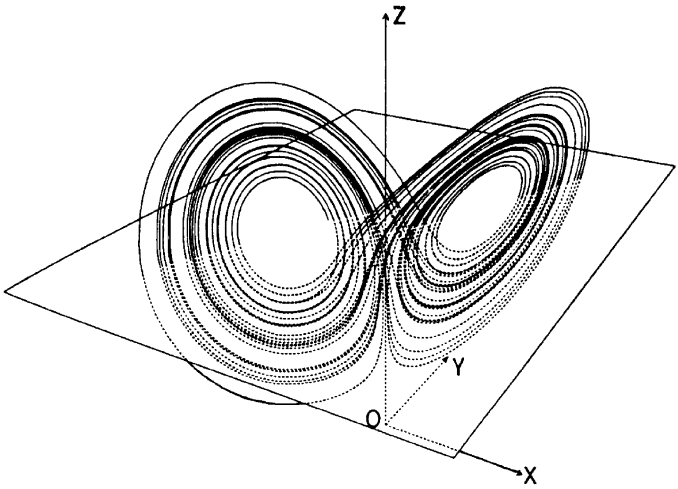

Figure 1.8. Computer plot of the Lorenz attractor, from Lanford [373] (courtesy Springer-Verlag).

up to a Mach number of the order of 15. The smallest macroscopic scale δl is smaller than the Kolmogorov dissipative scale l_d, characteristic of the dissipative scales already introduced, and much larger than the mean-free path of molecules. In fact, Navier–Stokes equations refer to quantities such as the velocity, pressure, temperature, density, which are spatially averaged on elementary control volumes of size $\sim \delta l$. From a mathematical viewpoint, however, the spatial scales in these equations can be as low as necessary.

1.5.1 Mathematical and philosophical considerations

We begin with the postulate that fluid turbulence satisfies Laplace principle of determinism (see Gayon [245]): if the initial positions and velocities were known, for a given time t_0, at all scales,[11] then there exists only one possible state for the flow at any time $t > t_0$. Laplace [376] formulated this idea in 1814 in his *Philosophical essay on probabilities*. As recalled by Gayon, this is a quotation of Laplace:

> We must envisage the universe present state as the effect of its anterior state, and as the cause of the following one. If an intelligence knew at a given time all the forces which animate nature, and the respective situations of beings which compose it, if it was vast enough to submit these data to analysis, then it would embrace in the same formula

[11] With a given set of boundary conditions and a proper external forcing.

> motions of the largest bodies of universe and those of the lightest atom: nothing would be uncertain to it, and the future together with the past would be present in front of its eyes.

Laplace thought also that man could never have all the required knowledge in all details for that, which justified the use of probability theories.

Mathematically, Laplace principle is nothing more than an assumption of existence and uniqueness for the solutions of the Navier–Stokes equations:[12] such a result exists in two dimensions (Lions [450]), but holds only for finite times in three dimensions (Leray [409], see Temam [682] for a review[13]). Physically, it is nevertheless to be expected that the presence of molecular viscosity in the Navier–Stokes equations will smooth the solutions sufficiently, in order to prevent the appearance of any singularity and the bifurcation[14] to another solution.

1.5.2 Numerical simulations

We conclude from these considerations that fluid turbulence is a deterministic phenomenon, although it evolves with time in a very complicated way, due to the nonlinear interactions. It seems of course impossible to consider theoretically for arbitrary times the deterministic evolution of a given turbulent flow, starting with a given field of initial conditions. Nevertheless such an approach will be shown here as becoming promising from a numerical viewpoint, due to the significant recent development of scientific calculators: indeed, these last two decades have seen extraordinary progress in the speed and capacity of computers, to such a degree that the numerical resolution of the Navier–Stokes equations is now at hand in some turbulent situations: it is based on a proper discretization of the space-time on a grid of mesh $\Delta x, \Delta t$. The spatial and temporal partial-derivative operators are evaluated with the aid of appropriate algorithms (spectral, or finite-difference, or finite-volume, or finite-elements methods are used). Starting from a given initial state, and with a given set of boundary conditions, one can thus calculate deterministically the time evolution of the flow. If the spatial mesh size is taken small enough to capture the finest scales (e.g. the Kolmogorov dissipative scale), one will talk of a direct-numerical simulation (DNS). Such an approach is

[12] Remark also that Laplace spoke of being able to predict the future and the past.

[13] These solutions have to be understood *in the weak sense*: one just considers space integrals of the solution multiplied by a regular test function, and allows to use part-integration rules.

[14] Here, we consider the evolution of a time-dependent system with fixed external parameters. The theory of "bifurcations" concerns the exchange from one to another stationary solution in a system when one of the external parameters is varied (see Iooss and Joseph [310] for a review).

generally limited to moderate Reynolds number flows, otherwise it becomes too costly. Let us consider for instance a typical simulation of isotropic turbulence carried out using pseudo-spectral methods at a resolution of 128^3 collocation points. If five scalar fields need to be stored at two time steps t and $t - \Delta t$, this represents about 20 Megawords to store in central memory, each word corresponding to 64 bits in double precision. Such a resolution requires about 3.6 billions of operations per time step. A complete evolution involves several thousands of time-steps, and will therefore take several hours on a 2 Gigaflops machine. This was done in 1995. Now (in 2006) it is possible to run DNS of isotropic turbulence at a resolution of $\approx 1000^3$ on the japonese machine "Earth Simulator", which has a power of more than 30 Teraflops (see Ishida et al. [311]). One sees that it takes about 10 years to multiply the resolution by ten in each direction of space. This is very slow, and still too low to expect to solve soon by DNS realistic flows at high Reynolds number (see the discussion on that in Lesieur et al. [431]).

A promising approach at high Reynolds numbers is the large-eddy simulation (LES), where the small scales are filtered out, and only the evolution of the large scales is computed, with a proper modelling of the subgrid scales. Decisive advances have been made with this tool these last years. Indeed, LESs allow to determine the dynamics of coherent vortices and the statistical quantities of turbulence for a large class of flows ranging from isotropic turbulence to mixing layers, jets, separated flows, boundary layers, rotating flows, both in the incompressible and compressible cases. LES is about $[10 \sim 100]$ times faster than the DNS when the latter is possible. The reader is referred for that to the book of Lesieur et al. [431], whose formalism and techniques are borrowed from the present book. Other useful references are the books of Geurts [252], Sagaut [624] and Pope [583].

In fact LES contain some errors due to the inaccuracy of the numerical schemes, to our current ignorance vis-à-vis the small scales, and to the lack of detail concerning the initial and boundary conditions. These errors are generally amplified by the nonlinearities of the equations, and after a period of time the predicted turbulent flow will differ significantly from the actual field. It follows that, even for a deterministic system, unpredictability and randomness will be introduced. The large-eddy simulations are nevertheless extremely useful, for they generally predict the shape (but not the phase – or exact position) of the large vortices existing in the flow. They also often contain the statistical information needed by the engineer, which can be derived from a single realization without any recourse to a costly ensemble averaging.

1.5.3 Stochastic tools

It is also very useful to employ stochastic tools and consider the various fluctuating quantities as random functions. For fully-developed turbulence,

these functions will be assumed to be statistically invariant under translations (homogeneity) and rotations (isotropy). This monograph will extensively study the dynamics of isotropic turbulence, in particular the energy transfers between the various scales of motion. Emphasis will be given to the analytical statistical theories (also called stochastic models or two-point closures) developed in particular by Kraichnan and Orszag. More details on these methods can also be found in Leslie [432] and Orszag [553].

To conclude this section, and at the risk of becoming repetitive, we stress again that it might be erroneous to oppose the so-called deterministic and statistical points of view of turbulence: the deterministic approach can be, computationally speaking, extremely expensive, and a statistical theory or modelling may prove to be very useful in the isotropic case. We discuss below the use of statistical theories for inhomogeneous turbulence.

1.6 Why study isotropic turbulence?

One might argue that no real turbulent flow is isotropic or even homogeneous in the large scales. Isotropy and homogeneity can even be questionable in the small scales. But these assumptions will allow us to employ easily the analytical statistical theories mentioned above. Such theories are extremely powerful in the sense that they permit one to deal with strong nonlinearities when departures from Gaussianity are not too high. The point of view developed here is that these techniques describe satisfactorily the dynamics of the small three-dimensional scales of a turbulent flow at the level of second-order statistical moments, and also allow one to model their action on the anisotropic large scales. The latter will generally require the numerical large-eddy simulations mentioned above and which will be discussed in Chapter 12. In those particular cases when the turbulence is constrained to quasi two-dimensionality, such as in large-scale atmospheric or oceanic situations, the two-point closures may also be a good tool to study the statistics of the large scales and their degree of predictability: it is by using one of these closures[15] that Lorenz [454] could show how, in two-dimensional isotropic turbulence, the initial uncertainty in the small scales was transferred to the large scales in a period of time which, converted into atmospheric parameters, gave a limit of 10 days to the predictability of the Earth's atmosphere (see Chapter 11 for details). Such information about the spatial inverse cascade of error could never have been obtained from the dynamical system approach followed earlier by Lorenz [453].

[15] The Quasi Normal approximation, see Chapter 7.

1.7 One-point closure modelling

There is another approach of turbulence, mainly developed in order to model inhomogeneous flows in practical applications, known as "one-point closure modelling": it starts with the exact Reynolds equations for the mean motion $\langle \vec{u} \rangle$, where the turbulent fluctuations are introduced through their second-order moments at the same point in space (see Chapter 4). The latter need to be modelled in terms of the mean flow, and the simplest way for doing that is to use an eddy-viscosity assumption, where the eddy viscosity is calculated with the aid of Prandtl's mixing-length concept [587] (see Schlichting [635] for details). This allows one to calculate the mean characteristics (velocity profiles, spreading rates) of simple turbulent shear layers such as jets, wakes, mixing layers, or boundary layers on flat plates, as is done in Chapter 4. More refined modelling techniques involve supplementary evolution equations allowing one to determine either the eddy viscosity, such as the $K - \epsilon$ model (see Launder and Spalding [388]), or the second-order moments themselves (see Lumley [456] and Launder [389]). Recent developments can be found in the books of Pope [583], as well as Durbin and Pettersson Reif Chichester [182]. These techniques, which will not be discussed here, can be extremely efficient for flows of engineering interest when numerous similar calculations under various conditions have to be repeated, in order to find a quick optimal solution to a problem such as the design of an airfoil or of a heat exchanger in a nuclear plant. But they do not give one a detailed understanding of the physical processes really involved, and pose problems for a large class of flows (separated, heated, rotating, compressible, etc.). Informations or new concepts derived from two-point closure approaches may be useful for one-point closure modelling. This is true in particular for the decay laws of kinetic energy and passive scalar variance, obtained in Chapter 7 with the aid of stochastic models, and which are useful in the implementation of the $K - \epsilon$ method. It is certain that the development of DNSs and LESs is of upmost importance to assess and improve the classical one-point closures, by allowing a direct calculation of the various Reynolds stresses and pressure-velocity correlations in some simplified test cases.

1.8 Outline of the following chapters

The present monograph is organized as follows: we give in Chapter 2 a review of the basic equations of Fluid Dynamics, focusing on the various approximations relating both to compressible gases and to Geophysical-Fluid Dynamics situations. We will put emphasis on the dynamics of vorticity and potential vorticity, and the role of rotation and stratification. Internal and external inertial or gravity waves will also be considered from a linear point of view.

Chapter 3 will consider the problem of transition to turbulence: we will first summarize some basic results of the linear hydrodynamic instability theory in two or three dimensions, applied to parallel free or wall-bounded shear flows. This will allow us to introduce a discussion on the various instabilities participating in the process of transition to turbulence in shear flows, and the associated vortex dynamics. Instabilities leading to aligned and staggered patterns will be considered as well. The role of viscosity will be discussed. We will consider also transition in thermal convection, mostly within the frame of Rayleigh–Bénard instability.

Chapter 4 will deal with developed free-shear and wall-bounded turbulence. It will be considered successively from the statistical (mixing-length theory) and the coherent vortices point of views. We will look at spiral and longitudinal vortices forming in mixing layers, jets and wakes, as well as possible occurrence of dislocations through helical pairing or alternate pairing. In boundary layers, we will discuss the relation between streaks and longitudinal vortices. We will also try to point out the analogies which may exist with the transition stage. We will finally push further the discussion about the concepts of coherence, order and chaos, and how they can apply to fluid turbulence.

Chapter 5 will introduce the mathematical tools of the spectral statistical analysis of turbulence, which are needed in the remainder of the study. One will introduce in particular Navier–Stokes equations in Fourier space, homogeneity, isotropy, axisymmetry, Craya decomposition,[16] and helical-wave decomposition. Chapter 6 will present isotropic turbulence, mainly from the point of view of phenomenological theories (Kolmogorov-type theories) and direct-numerical simulations. Turbulence diffusion and noise generated by turbulence will also be considered in this chapter.

Chapter 7 will still deal with isotropic turbulence, and present statistical models based on two-point closures, as well as related stochastic models. They will again be applied to turbulent diffusion problems. A presentation of the Renormalization Group Techniques will be given as well.

Two-dimensional turbulence corresponds to a lowest-order approximation of the dynamics of atmospheres and oceans on a rapidly-rotating planet, and applies also to M.H.D. turbulence and plasma physics. It will be extensively studied in Chapter 8, with presentation of new DNS and LES results. The so-called "quasi geostrophic" (or simply "geostrophic") approximation, which takes into account some coupled effects of stratification and rotation within a two-dimensional formalism, will be looked at in Chapter 9. In this chapter, one- and multilevel shallow-water equations will be also studied. Finally, we will consider many aspects of baroclinic instability, leading to storms in Earth atmosphere. We will study Ekman layers and Rossby waves propagation. Somme applications to Jupiter will be given.

[16] Also called vortex-wave expansion.

Chapter 10 will present the statistical thermodynamics of truncated Euler equations, and discuss to what extent this study applies to real dissipative systems, both in three and two dimensions. It is accompanied by Chapter 11, which will consider the problem of turbulence from the point of view of statistical unpredictability theory. This addresses the question of the meaning of deterministic numerical simulations. Chapter 12 will present the techniques of large-eddy simulations, which, as already stressed, open new tracks for understanding coherent-vortex dynamics and modelling industrial or environmental flows, both in incompressible and compressible cases.

The last chapter will consider turbulence in four situations of great practical importance: stable stratification, solid-body rotation, separation, and compressibility. The dynamics of these flows is not, up to now, completely understood, and they constitute challenging examples of application for the numerical simulations. We will see in particular how the coherent vortices and structures are modified. The first two examples relate mainly to oceans-atmosphere dynamics,[17] and the last two concern internal or external aerodynamics. Understanding the effect of compressibility on shear layers is of prior importance for the design of hypersonic or supersonic planes.

In summary, this unique textbook starts from basic principles of fluid dynamics for flows of arbitrary density (incompressible and compressible). It reviews the main theorems of vorticity dynamics and scalar mixing for non-rotating or rotating flows, as well as basis of linear-instability theory (including thermal convection). It introduces clear definitions of turbulence in fluids and of coherent vortices. Then it presents from a physical point of view based on experiments and numerical simulations transition and developed turbulence in shear flows (free or wall-bounded). The latter do show an astonishing universality when submitted to rotation. A substantial part is devoted to stochastic spectral theories of isotropic turbulence called two-point closures, in which the author is expert. The book shows how these closures help deriving advanced models for the very important problem of large-eddy simulations, where the small scales may be eliminated, implying major time savings in the computations. Applications given are of great interest for aeronautics and space, combustion, chemical engineering, nuclear engineering, hydraulics, meteorology, oceanography and astrophysics. The latter applications are reinforced by two chapters on two-dimensional and quasi geostrophic turbulence, very important for large-scales atmosphere and ocean dynamics.

[17] Although the effect of rotation may be important in turbomachinery.

2

Basic Fluid Dynamics

As already stressed in Chapter 1, the validity of the Navier–Stokes equations in describing the phenomenon of turbulence in fluids is no longer a topic for serious debate. Further arguments are that very well-resolved direct-numerical simulations of these equations applied to turbulent flows such as jets or channels give good results by comparison with experiments, as far as statistical quantities such as mean and rms velocities or Reynolds stresses are concerned.

We will recall in this chapter the basic equations of fluid mechanics and the dynamics of vorticity. One will look in particular to the possible influence of a solid-body rotation of angular velocity $\vec{\Omega}$, due for instance to the rotation of the Earth (when one considers the motion of the atmosphere, the oceans, the outer core), a planet, a star, or a turbomachine. We will discuss the approximation of incompressibility for the velocity field, which will be often used in this book: it will allow us to discard the acoustic waves, while taking into consideration various heated or stable density-stratified flows. The Boussinesq approximation, in particular, allows one to study the effects of buoyancy. The reader is referred to numerous textbooks (see e.g. Batchelor [50] and Gill [258]) for the complete derivation of these equations.

2.1 Eulerian notation and Lagrangian derivatives

Let us consider an orthonormal reference frame which can be at rest (that is, Galilean) or rotating with a solid-body rotation $\vec{\Omega}$ with respect to a "fixed" frame. A "fluid particle", of size large in comparison to the molecular scales and small in comparison to the Kolmogorov dissipation scale introduced in Chapter 1, and located in $\vec{x}$ at time t, will have a velocity $\vec{u}(\vec{x}, t)$ with respect to the reference frame.[1] The components of the velocity will be $u_i(\vec{x}, t)$.

[1] In fact, $\vec{x}$ should be considered as the gravity centre of the fluid particle.

Let $\rho(\vec{x},t)$ be the density of the fluid element passing by $\vec{x}$ at time t. This notation corresponds to the Eulerian formulation. Let $A(\vec{x},t)$ be any quantity associated with the motion of the fluid. When the fluid particle considered above moves, it produces a variation of A , and the derivative of A following the fluid motion in the reference frame will be denoted DA/Dt. The operator D/Dt is the Lagrangian derivative ("Lagrangian" means here "following the motion", and is not to be confused with Lagrange variational approaches in analytical mechanics). One can show very easily that

$$\frac{DA}{Dt} = \frac{\partial A}{\partial t} + \vec{u}.\vec{\nabla}A \ . \tag{2.1}$$

In a given Cartesian frame of coordinates x_i, and if the velocity-vector components are u_i, we have

$$\vec{u}.\vec{\nabla} = u_1\frac{\partial}{\partial x_1} + u_2\frac{\partial}{\partial x_2} + u_3\frac{\partial}{\partial x_3} \ .$$

Let us consider now a vector field $\vec{a}(\vec{x},t)$ moving with the flow. One has in the same way

$$\frac{D\vec{a}}{Dt} = \frac{\partial \vec{a}}{\partial t} + (\vec{u}.\vec{\nabla})\vec{a} = \frac{\partial \vec{a}}{\partial t} + \vec{\nabla}\vec{a}\otimes\vec{u} \ ,$$

where $\otimes$ stands for a tensorial product, and $\vec{\nabla}\vec{a}$ is a tensor whose components are given by the matrix $[\partial a_i/\partial x_j]$. Let us consider in particular the velocity-gradient tensor $\vec{\nabla}\vec{u}$. The acceleration of the fluid is given by

$$\frac{D\vec{u}}{Dt} = \frac{\partial \vec{u}}{\partial t} + (\vec{u}.\vec{\nabla})\vec{u} = \frac{\partial \vec{u}}{\partial t} + \vec{\nabla}\vec{u}\otimes\vec{u} \ . \tag{2.2}$$

The velocity-gradient tensor may be split into its symmetric $\overline{\overline{S}}$ and antisymmetric $\overline{\overline{\omega}}$ parts, such that

$$\vec{\nabla}\vec{u} = \overline{\overline{S}} + \overline{\overline{\omega}}$$
$$\overline{\overline{S}} = \frac{1}{2}[\vec{\nabla}\vec{u} + \vec{\nabla}\vec{u}|^t] \ , \quad \overline{\overline{\omega}} = \frac{1}{2}[\vec{\nabla}\vec{u} - \vec{\nabla}\vec{u}|^t] \ .$$

where $\vec{\nabla}\vec{u}|^t$ is the transposed velocity gradient tensor. Introducing the vorticity vector $\vec{\omega} = \vec{\nabla}\times\vec{u}$, one can show that

$$\overline{\overline{\omega}}\otimes = \frac{1}{2}\vec{\omega}\times \ , \tag{2.3}$$

where the tensorial product applies here to a vector.

Now let δV be the volume of the small fluid particle. It can easily be shown, for instance by the change of coordinates $\vec{x} \to \vec{x}_0$, where $\vec{x}_0$ is the original position at some initial time t_0 of the fluid particle located in $\vec{x}$ at time $t \geq t_0$ (see Lamb [365]), that the divergence of the velocity is given by

$$\vec{\nabla}.\vec{u} = \frac{1}{\delta V}\frac{D\ \delta V}{Dt} \tag{2.4}$$

2.2 The continuity equation

This equation is the mass conservation equation: let $\delta m = \rho\ \delta V$ be the mass of the fluid particle. It is conserved following the fluid motion, since average exchanges of mass with the surrounding fluid, which are due to molecular diffusion across the boundary $\partial(\delta V)$ of δV, will be zero for macroscopic time scales large in comparison to the molecular time scales. Hence, the logarithmic Lagrangian derivative of δm will also be zero, and one obtains

$$\frac{1}{\rho}\frac{D\rho}{Dt} + \frac{1}{\delta V}\frac{D\ \delta V}{Dt} = 0 \tag{2.5}$$

or equivalently, because of Eq. (2.4)

$$\frac{1}{\rho}\frac{D\rho}{Dt} + \vec{\nabla}.\vec{u} = 0 \tag{2.6}$$

which is the continuity equation. The particular case of incompressibility (conservation of volumes following the fluid motion) reduces to

$$\vec{\nabla}.\vec{u} = 0, \text{ or } \frac{D\rho}{Dt} = 0 \tag{2.7}$$

Notice that, at this level, incompressibility does not imply *a-priori* that the density is uniform in space: a counter example is given in ocean dynamics,[2] where the motion is approximately incompressible, but where there exists a thermal stratification responsible for spatial density variations.

2.3 The conservation of momentum

The second law of motion is obtained by applying to the fluid particle the fundamental principle of Newtonian mechanics, namely

$$\delta m\ \frac{D\vec{u}}{Dt} = [\text{body forces}] + [\text{surface forces}]\ . \tag{2.8}$$

The body forces applied to the fluid particle are gravity $\delta m\ \vec{g}$, the Coriolis force (if any) $-2\ \delta m\ \vec{\Omega} \times \vec{u}$, and possible other external forces (like the Lorentz force in the case of an electrically-conducting flow). We recall that $\vec{\Omega}$ may be Earth (or another planet) angular rotation vector, or the rotation of an experimental apparatus in the laboratory, and that we are working in a relative reference frame rotating with this angular velocity $\vec{\Omega}$. The gravity $\vec{g}$

[2] If salt budget is considered, salt exchanges across $\partial(\delta V)$ should be taken into account in the mass budget of the fluid.

is irrotational, and includes both the Newtonian gravity and the centrifugal force implied by the frame rotation. Thus, $\vec{g}$ may have spatial variations while being irrotational. The possible variation of $\vec{\Omega}$ with time has been neglected. Notice that such an assumption might be questionable in the context of Earth for studies related to climate or to magnetic-field generation, which may involve periods of time of several thousand years or more. The reader is referred to Munk and MacDonald [528] for a detailed discussion of the variation of $\vec{\Omega}$.

As shown in Batchelor [50], the fact that the surface forces applied to the fluid particle have to be proportional to δV in order to balance the two other terms of Eq. (2.8) implies the existence of a stress tensor $\overline{\overline{\sigma}} = [\sigma_{ij}]$ such that the force exerted by the fluid on one side of a small surface $d\Sigma$ oriented by a normal unit vector $\vec{n}$ (pointing towards the region of fluid considered) is

$$d\vec{f} = \overline{\overline{\sigma}} \otimes \vec{n} \; d\Sigma \; . \tag{2.9}$$

This yields in Cartesian coordinates

$$df_i = \sigma_{ij} \; n_j \; d\Sigma \; . \tag{2.10}$$

In a Newtonian fluid, the stress tensor is assumed to be linear with respect to the deformation tensor

$$S_{ij} = \frac{1}{2} \left(\frac{\partial u_i}{\partial x_j} + \frac{\partial u_j}{\partial x_i} \right) \tag{2.11}$$

and isotropic. Hence, it is found (see e.g. Batchelor [50]) that

$$\sigma_{ij} = -p \; \delta_{ij} + \mu \left[\left(\frac{\partial u_i}{\partial x_j} + \frac{\partial u_j}{\partial x_i} \right) - \frac{2}{3} \vec{\nabla}.\vec{u} \; \delta_{ij} \right] \tag{2.12}$$

where δ_{ij} is the Kronecker tensor and μ the dynamic viscosity. Following Batchelor [50], we have defined the pressure p with the aid of the trace of the stress tensor ($p = -(1/3)\sigma_{ii}$, with summation upon the i). Furthermore, we will identify this pressure with the thermodynamic pressure (static pressure). This permits to avoid the use of a second viscosity coefficient in Eq. (2.12). The dynamic viscosity μ may vary with the physical properties of the fluid, as in gases at high temperature, or Earth outer mantle, where cellular thermal convective motions are responsible for the sea floor spreading and the existence of dorsal and subduction zones (see e.g. Allègre [5]).

In fact, the notion of a viscous stress is in Newton's principles, recalled in Rouse and Ince [619], which state that

> the resistance arising [...] in the parts of a fluid is [...] proportional to the velocity with which the parts of the fluid are separated from one another.

Such a simple idea leads in particular to the significant result that, in the case of a parallel flow along a material plane surface, the tangential force exerted per unit surface area by the flow on the surface and which tends to entrain it is proportional to $\mu\ \partial U/\partial n$, where $\vec{n}$ is the unit vector normal to the surface (directed towards the flow) and U the velocity component normal to $\vec{n}$. This result can be easily deduced from Eq. (2.12), to which it gives a firm physical basis. In this case, the normal force exerted on the surface is $-p\ \vec{n}$, in agreement with the physical role of the pressure. Notice also that, in the general case, the force normal to $d\Sigma$ is equal to $-[p + (2/3)\mu\vec{\nabla}.\vec{u}]\ \vec{n}$, and contains a small viscous contribution which is zero only when the fluid is non-divergent.

Therefore Eq. (2.8) becomes, after integration of the surface forces over the surface of the fluid particle

$$\frac{Du_i}{Dt} = (\vec{g} - 2\vec{\Omega} \times \vec{u})_i + \frac{1}{\rho}\frac{\partial \sigma_{ij}}{\partial x_j} \tag{2.13}$$

or equivalently

$$\frac{Du_i}{Dt} = (\vec{g} - 2\vec{\Omega} \times \vec{u})_i - \frac{1}{\rho}\frac{\partial p}{\partial x_i} + \frac{1}{\rho}\frac{\partial}{\partial x_j}\mu\left[\left(\frac{\partial u_i}{\partial x_j} + \frac{\partial u_j}{\partial x_i}\right) - \frac{2}{3}\vec{\nabla}.\vec{u}\ \delta_{ij}\right] \tag{2.14}$$

which is the momentum equation for a compressible fluid.

2.3.1 Variable dynamic viscosity

In general, the viscosity μ is a function of temperature. This is the case in aerodynamics when the Mach number is close to one or higher, or when the fluid is strongly heated by some source. In this case, we have to know the function $\mu(T)$ in Eq. (2.14). For air, it is called Sutherland's empirical law, and writes (see e.g. Lesieur et al. [431])

$$\begin{aligned} \mu(T) = \ & \mu(273.15)\left(\frac{T}{273.15}\right)^{1/2}\ \frac{1 + S/273.15}{1 + S/T} \\ & \text{with } \mu(273.15) = 1.711\ 10^{-5} Pl \\ & \text{and } S = 110.4K\ , \end{aligned} \tag{2.15}$$

There is an extension to temperatures lower than $120K$ in the form

$$\mu(T) = \mu(120)\ T/120 \quad \forall\ T < 120\ . \tag{2.16}$$

The viscosity μ is then an increasing function of T. For temperatures higher than $120K$, this yields in particular

$$\frac{\mu(T)}{\mu(293)} \approx \left(\frac{T}{293}\right)^{1/2} \frac{1.38}{1+110/T} \ . \tag{2.17}$$

$293K$ is the temperature of air in a room at ambient temperature. Eq. (2.17) shows that the relative molecular viscosity with respect to this state is 1.06 with $T = 313$ K (atmosphere close to the tropics, or during a heat wave), 1.20 with $T = 373$ K (temperature of steam in a pressure cooker jet), 1.42 with $T = 473$ K (temperature of a cooking oven), and 3.42 with $T = 2000$ K (temperature outside a space shuttle during reentry). Remark that some authors take $\mu(T) \propto T^{0.7}$ (see e.g. Coleman et al. [130]).

For flows for which we may neglect spatial variations of temperature T, Eq. (2.14) yields

$$\frac{D\vec{u}}{Dt} = \vec{g} - 2\vec{\Omega} \times \vec{u} - \frac{1}{\rho}\vec{\nabla}p + \nu \left[\nabla^2\vec{u} + \frac{1}{3}\vec{\nabla}(\vec{\nabla}.\vec{u})\right] \ , \tag{2.18}$$

with

$$\frac{D\vec{u}}{Dt} = \frac{\partial\vec{u}}{\partial t} + \vec{u}.\vec{\nabla}\vec{u} \ , \tag{2.19}$$

where $\nu = \mu/\rho$ is called the kinematic viscosity. It is this viscosity that has already been introduced in Chapter 1 to define the Reynolds number. The term proportional to ν in the r.h.s. of Eq. (2.18) characterizes the diffusion of momentum due to molecular exchanges between the fluid particle and the fluid surrounding it. When the velocity is non-divergent, which will very often be the case in the present monograph, the dissipative term reduces to $\nu\nabla^2\vec{u}$. Notice that if other driving forces exist, they have to be added to the r.h.s. of Eq. (2.18).

2.3.2 Navier–Stokes and Euler equations

The system of equations (2.6) and (2.14) (or Eq. (2.18)), supplemented by an energy equation (see next section) is called the Navier–Stokes equations. The momentum equation Eq. (2.14) without the viscous terms is called the Euler equation, and was derived by Leonhard Euler in the middle of the 18th century. He did not consider the effect of rotation. Let us quote Lesieur [424, p. 33]:

> Leonhard Euler, a famous swiss mathematician, spent 15 years in Russia as physics and mathematics professor, thanks to Daniel Bernoulli (see below) who had recommended him to Catherine the 1st. He left Russia in 1741, to come back in 1766 upon invitation of Catherine the great. The equation of fluids motion which brings his name is the first historic example of partial-differential equations (...). This equation, proposed as soon as 1750, is only valid for a "perfect fluid", that is to say where viscous effects are neglected.

History has been quite unfair to Euler, since the only role of Navier was, 70 years later, to model approximately the missing viscous term of the Euler equation, using physical ideas contained in Newton's principles. As for Stokes, the latter had no role in the establishment of the equations of motion, but studied them in strongly viscous cases, where the quadratic term $\vec{u}.\vec{\nabla}\vec{u}$ in the r.h.s. of Eq. (2.19) is discarded. For more details on these historic aspects of fluid dynamics, the reader is referred to the very interesting book by Rouse and Ince [619].

2.3.3 Geopotential form

Eq. (2.18) can be written in an alternative way, by introducing the geopotential Φ, such that

$$\vec{g} = -\vec{\nabla}\Phi \tag{2.20}$$

and which contains both the effects of Newtonian gravity and of the centrifugal force. Noticing that

$$(\vec{\nabla} \times \vec{u}) \times \vec{u} = \vec{u}.\vec{\nabla}\vec{u} - \vec{\nabla}\frac{\vec{u}^2}{2} \tag{2.21}$$

Eq. (2.18) writes

$$\frac{\partial \vec{u}}{\partial t} + (\vec{\omega} + 2\vec{\Omega}) \times \vec{u} = -\frac{1}{\rho}\vec{\nabla}p - \vec{\nabla}\left(\Phi + \frac{\vec{u}^2}{2}\right) + \nu\left[\nabla^2\vec{u} + \frac{1}{3}\vec{\nabla}(\vec{\nabla}.\vec{u})\right]. \tag{2.22}$$

We recall that $\vec{\omega}$ is the vorticity of the fluid (in the rotating frame):

$$\vec{\omega} = \vec{\nabla} \times \vec{u} \tag{2.23}$$

One notices also in Eq. (2.22) the appearance of the absolute vorticity

$$\vec{\omega}_a = \vec{\omega} + 2\ \vec{\Omega} \tag{2.24}$$

which is the vorticity of the fluid in an "absolute" reference frame, and will be seen to play an interesting role with respect to the relative flow $\vec{u}$ in the rotating reference frame.

With the mass conservation, we have two equations for three unknown variables $\vec{u}, \rho, p$. The last equation will come from thermodynamic principles developed in the following section.

2.3.4 First Bernoulli's theorem

A last remark concerns the 1st Bernoulli's theorem, due to Daniel Bernoulli [58] in 1738, which is anterior to Euler's equations, and was derived using the kinetic-energy theorem. It has very important applications in fluid dynamics.

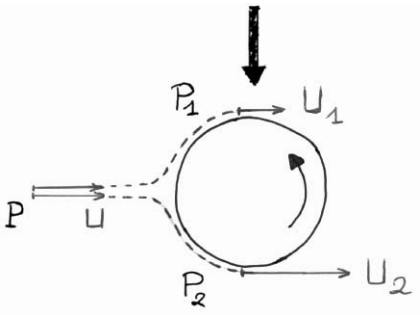

Figure 2.1. Applications of Bernoulli's theorem to a rotating object.

We are going to demonstrate it with the aid of Euler equations: assume that the flow is inviscid ($\nu = 0$), incompressible according to Eq. (2.7), and time-independent ($\partial/\partial t = 0$, which implies $D/Dt = \vec{u}.\vec{\nabla}$). Hence, taking the scalar product of Eq. (2.22) by $\vec{u}$, one obtains:

$$\frac{D}{Dt}\left(p + \rho\Phi + \rho\frac{\vec{u}^2}{2}\right) = 0 \ . \tag{2.25}$$

Therefore the quantity $(p + \rho\Phi + \rho u^2/2)$ is conserved following the motion. The consequences of the theorem are numerous. We give here three examples.

• Balls lift:

We consider a rotating object (see Figure 2.1). In the frame fixed to its centre (but not rotating), and taking into account viscous friction at the surface of the object, the flow above (velocity U_1) will be slowed down, and the flow underneath (velocity U_2) will be accelerated. We write

$$p + \frac{1}{2}\rho U^2 = p_1 + \frac{1}{2}\rho U_1^2 = p_2 + \frac{1}{2}\rho U_2^2 \ .$$

Since $U_2 > U_1, p_1 > p_2$, and the object will be submitted to a force from top to bottom. When applied to a rotating cylinder, this is called Magnus effect. Numerous applications exist in ball sports such as tennis, football,[3] ping-pong, etc.

• Airfoil lift:

In aeronautics, if a flow separates around an assymmetric airfoil and reforms behind, the velocity differences implied by the different paths followed by the

[3] Mainly soccer, where it allows to mark directly during corner kicks. In American football and rugby, the ball is rotated more to stabilize it as a rotating top.

fluid particles on each side of the airfoil will generate pressure differences between both sides, and hence lift (see Figure 2.2a).

• Atmospheric highs and lows:

In meteorology, let us consider two air masses initially very close (same pressure and velocity), which are entrained into respectively a cyclonic and an anticyclonic perturbation: the fluid particle trapped into the depression will acquire a higher velocity than the one going into the pressure high. This is one of the reasons why winds tend to be strong in the troughs and weak in the highs[4] (Figure 2.2b).

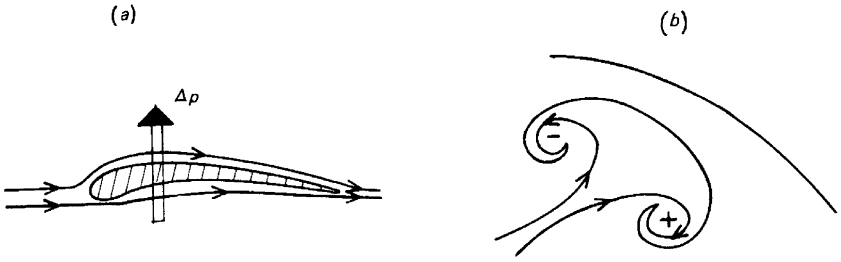

Figure 2.2. Applications of Bernoulli's theorem to (a) lift exerted on an airfoil; (b) winds generated in pressure highs and troughs.

2.4 The thermodynamic equation

Let us first take the scalar product of Eq. (2.13) by $\rho\vec{u}$, and integrate over δV. After some manipulations, and provided the geopotential Φ is time independent, one obtains:

$$\frac{D}{Dt}\int_{\delta V}\left(\frac{u^2}{2}+\Phi\right)\,\rho dV=\int_{\partial(\delta V)}u_i\sigma_{ij}n_j\;d\Sigma-\int_{\delta V}\sigma_{ij}\frac{\partial u_i}{\partial x_j}\;dV \qquad (2.26)$$

with summation over the repeated indices. This is nothing more than the kinetic-energy theorem for the fluid particle. Since the first term of the r.h.s., $P_e=\int_{\partial(\delta V)}u_i\sigma_{ij}n_j\;d\Sigma$, represents the rate of work done by the surface stresses per time unit, the second term

$$P_i=-\int_{\delta V}\sigma_{ij}(\partial u_i/\partial x_j)\;dV \qquad (2.27)$$

[4] But the major reason of this is due to baroclinic instability, see Chapter 9.

is the rate of work done by the forces internal to δV. Using Eq. (2.12), this term turns out to be equal to

$$P_i = \int_{\delta V} \left[p \, \vec{\nabla}.\vec{u} \; - 2\mu \left(S_{ij} S_{ij} - \frac{1}{3} S_{ii} S_{jj} \right) \right] \, dV \; , \tag{2.28}$$

where S_{ij} is defined in Eq. (2.11). P_i is thus decomposed into an internal pressure forces contribution, and a negative viscous contribution, corresponding to an internal dissipation of kinetic energy due to viscous stresses inside δV.

Now, let e_i be the internal energy per unit mass of the fluid particle. The first law of thermodynamics yields

$$\frac{D}{Dt} \int_{\delta V} \left(\frac{u^2}{2} + \Phi + e_i \right) \, \rho dV = \delta m \; \dot{Q} - [\text{molecular diffusion heat loss}] + P_e, \tag{2.29}$$

where $\dot{Q}$ is the rate of heat per mass unit supplied to the system, e.g. by radiative, chemical or nuclear processes. Let λ be the thermal diffusivity, such that the rate of heat transport across a small surface $d\Sigma$ oriented by the unit normal vector $\vec{n}$ is equal to, according to Fourier law:

$$-\lambda \, \frac{\partial T}{\partial n} \, d\Sigma = -\lambda \, (\vec{\nabla} T). \, \vec{n} \, d\Sigma \; , \tag{2.30}$$

where T is the temperature. The rate of heat loss of the fluid particle is then given by $-\vec{\nabla}.(\lambda \vec{\nabla} T) \; \delta V$. Using Eq. (2.26), one obtains

$$\frac{De_i}{Dt} = \dot{Q} + \frac{1}{\rho} \vec{\nabla}.(\lambda \vec{\nabla} T) - \frac{P_i}{\rho \; \delta V}, \tag{2.31}$$

or, using Eq. (2.27):

$$\frac{De_i}{Dt} = \dot{Q} + \frac{1}{\rho} \vec{\nabla}.(\lambda \vec{\nabla} T) - \frac{p}{\rho} \; \vec{\nabla}.\vec{u} + 2\nu \left(S_{ij} S_{ij} - \frac{1}{3} S_{ii} S_{jj} \right) \; . \tag{2.32}$$

In Eq. (2.32), $\lambda(T)$ is also a function of T, as $\nu = \mu(T)/\rho$. We will neglect the thermal forcing $\dot{Q}$ (which could nevertheless be introduced if necessary), and introduce the enthalpy of the fluid

$$h = e_i + \frac{p}{\rho} \; . \tag{2.33}$$

Thus one gets the exact enthalpy equation, valid even in the compressible cases or with strong heating effects:

$$\frac{Dh}{Dt} = \frac{1}{\rho} \frac{Dp}{Dt} + \frac{1}{\rho} \vec{\nabla}.(\lambda \vec{\nabla} T) + 2\nu \left(S_{ij} S_{ij} - \frac{1}{3} S_{ii} S_{jj} \right) \; . \tag{2.34}$$

2.4.1 Second Bernoulli's theorem

Notice also that, within the assumption of a time-independent perfect fluid,[5] it may easily be shown from Eqs. (2.22) and (2.34) that

$$\frac{D}{Dt}\left(h+\frac{1}{2}\vec{u}^2+\Phi\right)=0\ , \tag{2.35}$$

which is a generalized Bernoulli theorem. Let us mention finally that, for a perfect barotropic fluid[6], the momentum equation reduces to:

$$\frac{D\vec{u}}{Dt}=-\vec{\nabla}(h+\Phi)-2\vec{\Omega}\times\vec{u}\ . \tag{2.36}$$

Indeed, the internal energy e_i is in general function of p and ρ, so that for a barotropic fluid the enthalpy h depends also only of ρ. We denote by $d/d\rho$ the derivatives with respect to ρ. Then Eq. (2.34) yields

$$\left(\frac{dh}{d\rho}-\frac{1}{\rho}\frac{dp}{d\rho}\right)\frac{D\rho}{Dt} \tag{2.37}$$

which implies when the flow is compressible that $dh/d\rho=(1/\rho)dp/d\rho$, and hence $\vec{\nabla}h=(1/\rho)\vec{\nabla}p$.

Now, we consider successively the case of a liquid and of an ideal gas.

2.4.2 Liquid

For a liquid, one has approximately

$$e_i=C_p\ T\ , \tag{2.38}$$

where C_p is the specific heat at constant pressure, which will be considered as constant and T independent. Thus, Eq. (2.32) yields

$$\frac{DT}{Dt}=\frac{1}{\rho C_p}\vec{\nabla}.(\lambda\vec{\nabla}T)-\frac{p}{\rho C_p}\vec{\nabla}.\vec{u}+\frac{2\nu}{C_p}\left(S_{ij}S_{ij}-\frac{1}{3}S_{ii}S_{jj}\right)\ . \tag{2.39}$$

Finally, since liquids are very slightly compressible, the evaluation of the last two terms of the r.h.s. of Eq. (2.39) shows that they are negligible in comparison to the first. We will also assume that λ is T independent. To a very good approximation, the thermodynamic equation needed for a liquid is (in the absence of thermal forcing)

[5] We will define a perfect fluid as an approximation of the motion where molecular viscous and conductive effects are neglected, that is, $\nu=0$ and $\lambda=0$.

[6] Defined such as p is a function of ρ only.

$$\frac{DT}{Dt} = \kappa \nabla^2 T \ , \tag{2.40}$$

where

$$\kappa = \frac{\lambda}{\rho \ C_p} \tag{2.41}$$

is the molecular conductivity, already introduced in Chapter 1 to define the Peclet number. Since in a liquid temperature and density are approximately linearly related, this is equivalent to

$$\frac{D\rho}{Dt} = \kappa \nabla^2 \rho \ . \tag{2.42}$$

Eq. (2.42) provides then the third equation which was needed to close the system of equations of motion of the liquid. Notice finally in this case that if the motion is adiabatic ($\kappa = 0$), Eq. (2.42) reduces to $D\rho/Dt = 0$, which implies from the continuity equation that the velocity is non-divergent.

2.4.3 Ideal gas

For an ideal gas, things are somewhat more complicated because less terms can be neglected, the gas being more compressible than a liquid. To a good approximation, one now has

$$e_i = C_v T \ , \tag{2.43}$$

where C_v is the specific heat at constant volume, which will be assumed constant and T independent. Let C_p be the specific heat at constant pressure, related to C_v by

$$R = C_p - C_v \tag{2.44}$$

with the state equation

$$\frac{p}{\rho} = R \ T \ . \tag{2.45}$$

As C_v, C_p will be assumed T independent. We also introduce the coefficient

$$\gamma = \frac{C_p}{C_v} \ . \tag{2.46}$$

Therefore, the enthalpy is here equal to:

$$h = C_p T \ . \tag{2.47}$$

The enthalpy equation (2.34), together with the continuity equation and the momentum equation, close the problem, since $h = [\gamma/(\gamma-1)](p/\rho)$ is a function of p and ρ only. Notice that, for a barotropic ideal gas within the perfect flow

approximation, it may be shown that p/ρ^γ is constant and uniform throughout the fluid; the enthalpy is in this case $\sim \rho^{\gamma-1}$, and the motion is totally described by the momentum equation Eq. (2.36) and the continuity equation, which is then written

$$\frac{1}{h}\frac{Dh}{Dt} + (\gamma - 1)\ \vec{\nabla}.\vec{u} = 0\ . \tag{2.48}$$

Returning to the general case, one can also write the thermodynamic equation in the form:

$$\frac{D\Theta}{Dt} = \frac{\Theta}{C_p T}\ \left[\frac{1}{\rho}\vec{\nabla}.(\lambda\vec{\nabla}T) + 2\nu(S_{ij}S_{ij} - \frac{1}{3}S_{ii}S_{jj})\right]\ , \tag{2.49}$$

where Θ is the potential temperature:

$$\Theta = T\left(\frac{p_0}{p}\right)^{(\gamma-1)/\gamma} \tag{2.50}$$

which is the temperature of the gas if it was brought adiabatically to a reference level of pressure p_0. Θ is conserved following the motion[7] for a perfect fluid, and plays for the gas the role of the temperature in a liquid. The thermal diffusivity $\lambda(T)$ in Eq. (2.49) is related to the molecular Prandtl number by

$$Pr = \frac{\nu}{\kappa} = \frac{C_p\mu(T)}{\lambda(T)}\ . \tag{2.51}$$

where the molecular conductivity κ is still equal to $\lambda/\rho C_p$. In the air at ambient temperature, the Prandtl number is equal to 0.7. The entropy is defined (to an additive constant) by

$$s = s_0 + C_p \ln\frac{\Theta}{\Theta_0}\ . \tag{2.52}$$

For subsonic or non-strongly heated flows, one can approximate Eq. (2.49) as

$$\frac{T}{\Theta}\ \frac{D\Theta}{Dt} = \kappa\nabla^2 T\ , \tag{2.53}$$

where κ is assumed constant.

[7] This is equivalent to the conservation of p/ρ^γ and of the entropy (see definition below) following the motion.

2.5 Compressible Navier–Stokes equations in flux form

We are in Cartesian coordinates x_1, x_2, x_3, and assume that gravity is anti-parallel to $\vec{x}_3$, such that $\vec{g} = -g\vec{x}_3$. We give here a well-know conservative "flux form" of compressible Navier–Stokes equations for an ideal gas:

$$\frac{\partial U}{\partial t} + \frac{\partial F_1}{\partial x_1} + \frac{\partial F_2}{\partial x_2} + \frac{\partial F_3}{\partial x_3} = G \ , \tag{2.54}$$

with

$$U = {}^T(\rho, \rho u_1, \rho u_2, \rho u_3, \rho e) \ , \tag{2.55}$$

$$G = {}^T(0, 0, 0, -\rho g, 0) \ . \tag{2.56}$$

In this matrix identity, the various terms are respectively relative to mass, linear momentum, and energy balances. Total energy per unit mass is

$$e = C_v \ T + \tfrac{1}{2}(u_1^2 + u_2^2 + u_3^2) + g \ x_3 \ , \tag{2.57}$$

The fluxes are:

$$F_i = \begin{pmatrix} \rho u_i \\ \rho u_i u_1 - \sigma_{i1} \\ \rho u_i u_2 - \sigma_{i2} \\ \rho u_i u_3 - \sigma_{i3} \\ \rho e u_i - u_j \sigma_{ij} - \lambda \dfrac{\partial T}{\partial x_i} \end{pmatrix} \ , \tag{2.58}$$

Quantities σ_{ij}, and λ have been defined above. We have

$$F_i = \begin{pmatrix} \rho u_i \\ \rho u_i u_1 + p \ \delta_{i1} - 2\mu A_{i1} \\ \rho u_i u_2 + p \ \delta_{i2} - 2\mu A_{i2} \\ \rho u_i u_3 + p \ \delta_{i3} - 2\mu A_{i3} \\ (\rho e + p) u_i - 2\mu u_j A_{ij} - \lambda \dfrac{\partial T}{\partial x_i} \end{pmatrix} \ . \tag{2.59}$$

where

$$A_{ij} = \frac{1}{2}\left[\frac{\partial u_j}{\partial x_i} + \frac{\partial u_i}{\partial x_j} - \frac{2}{3}(\boldsymbol{\nabla}.\boldsymbol{u})\delta_{ij}\right] \tag{2.60}$$

is the deviator of the deformation tensor.

2.6 The incompressibility assumption

Let ρ_0 be a basic density in the fluid, ρ' the characteristic value of the density fluctuation about ρ_0, and U and L a characteristic velocity and length. In

the continuity equation Eq. (2.6), the term $(1/\rho)(D\rho/Dt)$ is of the order of $(U/L)(\rho'/\rho_0)$, and $\vec{\nabla}.\vec{u}$ of the order of U/L. Hence, when

$$\epsilon_\rho = \frac{\rho'}{\rho_0} \ll 1 \ , \tag{2.61}$$

and to the lowest order with respect to this small parameter, the continuity equation reduces to

$$\vec{\nabla}.\vec{u} = 0 \ . \tag{2.62}$$

2.6.1 Liquid

The condition (2.61) is generally fulfilled in a liquid, unless it his submitted to an intense heating by some combustion process.

2.6.2 Ideal gas

We assume that the flow "locally barotropic", and expand locally in space Eqs. (2.36) and (2.34) to the first order in ϵ_ρ about a basic state defined by h_0, ρ_0 and p_0. Neglecting gravity, rotation and molecular diffusion, it is found for the fluctuations h', ρ' and $p' = c^2\rho'$ (where $c = (dp/d\rho)^{1/2}$ is the sound velocity)

$$\frac{D\vec{u}}{Dt} = -\vec{\nabla}h' \ ; \quad \frac{Dh'}{Dt} = \frac{c^2}{\rho_0}\frac{D\rho'}{Dt} \ . \tag{2.63}$$

This shows that $h' \sim U^2$, and $\rho'/\rho_0 \sim p'/p_0 \sim M^2$, where $M = U/c$ is the Mach number. Therefore, the incompressibility assumption (2.62) is acceptable up to $\rho'/\rho_0 <\approx 0.1$, that is up to a Mach number of the order of 0.3. It fixes for gases the limit under which a gas and a liquid obey the same equations of motion. An advantage of the incompressibility assumption is the suppression of all the sound waves, which greatly reduces the computational times in numerical simulations. Such a simplification does not prevent variation of the density through the thermodynamic equation: density variations will in turn affect the velocity through the momentum equation. In that sense density is not a passive scalar.

It should be stressed that more elaborate low-Mach number expansions of the compressible gas motion equations in terms of γM^2 have been developed (see Riley [601] for a review). They still give rise to a non-divergent velocity field (so they discard acoustic waves), and are very efficient to treat at low cost flows involving high density differences such as in combustion. They have also been used successfully by Golanski et al. [260] to calculate by DNS the flow in a two-dimensional periodic mixing layer with density differences. From this solution, they compute satisfactorily the noise radiated away using the so-called Lighthill analogy [438].

Remark that at a Mach number of the order of one or higher, barotropy assumption does not hold anymore. However, one can write for a perfect ideal gas: $p' \sim c^2\rho',\ p_0 \sim \rho_0 U^2$. Therefore, we now have

$$\frac{p'}{p_0} \sim M^{-2}\frac{\rho'}{\rho_0}\ . \tag{2.64}$$

This shows that, in supersonic flows, the relative pressure fluctuations are small compared with the relative density fluctuations. Such an assumption is one of the several Morkovin's hypothesis, and is well verified experimentally. This shows that the barotropy assumption does not hold anymore if compressibility is high enough.

Returning to low Mach numbers and the related incompressibility approximation, the equations of motion will reduce to:

$$\frac{D\vec{u}}{Dt} = -\frac{1}{\rho}\vec{\nabla}p + \vec{g} - 2\vec{\Omega}\times\vec{u} + \nu\nabla^2\vec{u}\ , \tag{2.65}$$

$$\vec{\nabla}.\vec{u} = 0\ , \tag{2.66}$$

$$\frac{D\rho}{Dt} = \kappa\nabla^2\rho \quad \text{for a liquid}\ , \tag{2.67}$$

$$\frac{T}{\Theta}\ \frac{D\Theta}{Dt} = \kappa\nabla^2 T \quad \text{for a gas.} \tag{2.68}$$

These equations are extremely general, and describe very well the motion of neutral (not electrically-conducting) fluids at low Mach numbers in the majority of laboratory and environmental situations, even with heat exchange, provided the temperature fluctuations are not too strong (the incompressibility assumption is certainly not valid for combustion problems). We stress again that the incompressibility assumption is not in contradiction with the possibility of density or temperature variations offered by Eqs. (2.67) and (2.68). When density is close to a uniform value ρ_0, these equations (to the lowest order in ρ'/ρ_0) yield (for a liquid or a gas)

$$P = p + \rho_0\Phi\ , \tag{2.69}$$

$$\frac{D\vec{u}}{Dt} = -\frac{1}{\rho_0}\vec{\nabla}P - 2\vec{\Omega}\times\vec{u} + \nu\nabla^2\vec{u}\ , \tag{2.70}$$

$$\vec{\nabla}.\vec{u} = 0\ , \tag{2.71}$$

where the modified pressure built with the geopotential Φ is no longer proportional to the stress tensor trace, and now includes gravitational and possible centrifugal effects: it mainly acts to maintain the incompressibility of the velocity field. The density and temperature satisfies

$$\frac{D\rho}{Dt} = \kappa \nabla^2 \rho \ , \tag{2.72}$$

which is in this case a passive-scalar equation, since density variations have no effect on the dynamics.

A less drastic step of simplification than Eq. (2.70), still taking into account the effects of density stratification, is known as Boussinesq's approximation, and will be given later on. But beforehand it is of interest to study the dynamics of vorticity within the general framework of the Navier–Stokes equations.

2.7 The dynamics of vorticity

The results given in this section can be found in a more extensive form in Batchelor [50] and Pedlosky [567]. We consider Eq. (2.22), which is valid even for compressible fluids if temperature fluctuations are not too high. By taking its curl and neglecting the possible spatial variations[8] of ν, one obtains:

$$\frac{\partial \vec{\omega}}{\partial t} + \vec{\nabla} \times (\vec{\omega}_a \times \vec{u}) = \frac{1}{\rho^2} \ \vec{\nabla}\rho \times \vec{\nabla} p + \nu \nabla^2 \vec{\omega} \ , \tag{2.73}$$

or equivalently, since $\partial \vec{\omega}_a / \partial t = \partial \vec{\omega} / \partial t$:

$$\frac{\partial \vec{\omega}_a}{\partial t} + \vec{\nabla} \times (\vec{\omega}_a \times \vec{u}) = \frac{1}{\rho^2} \ \vec{\nabla}\rho \times \vec{\nabla} p + \nu \nabla^2 \vec{\omega} \ , \tag{2.74}$$

$$\frac{D\vec{\omega}_a}{Dt} = \vec{\omega}_a . \vec{\nabla} \vec{u} - (\vec{\nabla} . \vec{u}) \ \vec{\omega}_a + \frac{1}{\rho^2} \ \vec{\nabla}\rho \times \vec{\nabla} p + \nu \nabla^2 \vec{\omega} \ . \tag{2.75}$$

The term $(1/\rho^2)\vec{\nabla}\rho \times \vec{\nabla} p$ is called the *baroclinic vector*. It is zero when density is uniform or if the fluid is barotropic: in this case, the isopycnal surfaces [$\rho =$ constant] are also isobaric surfaces [$p =$ constant].

Multiplying Eq. (2.75) by ρ^{-1} and using the compressible continuity equation yields:

$$\frac{D}{Dt} \left(\frac{\vec{\omega}_a}{\rho} \right) = \frac{\vec{\omega}_a}{\rho} . \vec{\nabla} \vec{u} + \frac{1}{\rho^3} \ \vec{\nabla}\rho \times \vec{\nabla} p + \frac{\nu}{\rho} \nabla^2 \vec{\omega} \ . \tag{2.76}$$

Hence, for a perfect barotropic fluid, $\vec{\omega}_a / \rho$ satisfies the equation of evolution of a small vector $\delta \vec{M} = M \vec{M}'$ when M and M' follow the fluid motion: indeed

[8] This assumption is not very constraining at this point, and allows in particular the recovery (with $\nu = 0$) of the exact compressible Euler equation for a perfect fluid.

$$\frac{D}{Dt}M\vec{M}' = \vec{u}(M') - \vec{u}(M) = M\vec{M}'.\vec{\nabla}\vec{u} \tag{2.77}$$

characterizes the *passive vector equation*, valid to the lowest order in $M\vec{M}'$. This is an argument for the stretching of vorticity by turbulence, in the same way as a pair of Lagrangian tracers are dispersed. For *Magneto-Hydrodynamic turbulence* (M.H.D.), it can be shown that the magnetic field satisfies an equation similar to Eq. (2.77) (see e.g. Moffatt [510] and Moreau [519]).

2.7.1 Helmholtz–Kelvin theorems

In fact Eq. (2.77) provides a straightforward derivation of the Helmholtz–Kelvin theorems (without rotation). Indeed, considering a closed contour C moving with the flow, we have:

$$\frac{D}{Dt}\int_C \vec{u}.\vec{\delta l} = \int_C \vec{u}.\frac{D\vec{\delta l}}{Dt} + \int_C \frac{D\vec{u}}{Dt}.\vec{\delta l}\ . \tag{2.78}$$

The first term of the r.h.s. is zero because of the passive vector equation which applies to $\vec{\delta l}$. The second term will be zero if $D\vec{u}/Dt$ is a gradient. Considering a perfect fluid satisfying Euler equation, this is the case for $\rho = \rho_0$ due to Eq. (2.70) (Helmholtz theorem), and for a barotropic flow because of Eq. (2.36). Remark also that we have

$$\int_C \vec{u}.\vec{\delta l} = \iint_\Sigma \vec{\omega}.\vec{n}\ d\Sigma \tag{2.79}$$

where Σ is a surface closed by C (with differential surface area $d\Sigma$ oriented by a unit vector $\vec{n}$) and moving with the fluid. This relates the velocity circulation to the flux of vorticity. One consequence is that the vortex elements (lines and surfaces)[9] are *material* in the flow and move with the fluid particles they contain. Indeed, a small surface $d\Sigma$ oriented by $\vec{n}$ drawn at a given time on a vortex surface will be such that $\vec{\omega}.\vec{n}d\Sigma = 0$. Since this quantity is an invariant of motion, the vorticity will still be tangential to the material surface at later times. This demonstrates that a vortex surface is material. Since a vortex line is the intersection of two vortex surfaces, it is also material. Finally, a vortex tube, which is a cylinder made of vortex lines, is still material.

With rotation, it is better to work in a fixed frame: then the above results apply to the circulation of the absolute velocity $\vec{u}_a$, equal to $\iint_\Sigma \vec{\omega}_a.\vec{n}\ d\Sigma$. So, in the same conditions (perfect flow, uniform density or barotropy), absolute

[9] A vortex line (resp. vortex surface) is, at a given time, a line (resp. surface) whose points have their vorticity vector tangential to it. A vortex tube is a vortex surface composed of generating lines which are vortex lines.

vortex elements (that is, tangential to the absolute vorticity) are material in the flow. Indeed, we have now $\vec{\omega}_a.\vec{n}d\Sigma = 0$ on an absolute vortex surface.

One can give another derivation of these theorems, allowing to demonstrate some useful results. Indeed, one can check (see e.g. Germain [246]) that if $\vec{A}$ is a non-divergent vector field, then

$$\frac{D}{Dt}\iint_{\Sigma} \vec{A}.\vec{n}\ d\Sigma = \iint_{\Sigma} \left[\frac{\partial \vec{A}}{\partial t} + \vec{\nabla} \times (\vec{A} \times \vec{u})\right] .\vec{n}\ d\Sigma\ . \tag{2.80}$$

If we calculate the flux of the l.h.s. of Eq. (2.74) across Σ and apply Eq. (2.80), we obtain

$$\frac{D}{Dt}\iint_{\Sigma} \vec{\omega}_a.\vec{n}\ d\Sigma = \iint_{\Sigma} \left(\frac{1}{\rho^2}\vec{\nabla}\rho \times \vec{\nabla}p + \nu\nabla^2\vec{\omega}\right) .\vec{n}\ d\Sigma\ . \tag{2.81}$$

Let us consider first the case with no entrainment rotation ($\vec{\omega}_a = \vec{\omega}$). Eq. (2.81) shows that the vorticity flux across Σ, which is the intensity of the vortex tube on which C is drawn), is a constant of motion in the absence of viscosity and if the fluid is barotropic or of uniform density. We recover the Helmholtz–Kelvin theorems.

• Vortex tube stretching:

The consequence is that if the vortex tube is stretched in such a way that its cross section decreases, its mean vorticity across the section will increase. If one then considers a thin vortex tube embedded in turbulence in a real (i.e. slightly viscous) flow, it will be both stretched by turbulence, as would be a material line of dye injected into the fluid, and diffused by molecular viscosity due to the second term of the r.h.s. of Eq. (2.81). This point of view leads one finally to consider the turbulence as a collection of thin vortex tubes stretched by the induced velocity field. This vortex-tube stretching might lead to the formation of regions of space characterized by a high vorticity (and therefore, as will be seen later, by a high dissipation of kinetic energy), surrounded by nearly irrotational fluid with low vorticity. Such a state of the fluid, i.e. highly dissipative structures embedded into an irrotational flow, corresponds to what is called internal intermittency. Conjectures have been made as to the topology of these structures: Corrsin [145] proposed they would form elongated sheets, while Tennekes [683] advocated a tube form. It was also suggested by Mandelbrot [467, 469] that turbulent structures at small scales could be distributed on sets of fractal dimensions. Frisch [229] developed multi-fractal models in the lines of Mandelbrot's.

In fact, it is now clear from direct-numerical simulations that three-dimensional isotropic turbulence is composed of an ensemble of thin tubes of high vorticity (see Siggia [647], She et al. [643], Vincent and Meneguzzi

[704–706], Métais and Lesieur [496], Jimenez and Wray [317]. It will be seen in the rest of this book (see also Lesieur et al. [431]) that vortex tubes of various size are present in all shear flows, free or wall-bounded. Vortex sheets may exist upstream in free-shear and separated flows. They destabilize under the action of Kelvin–Helmhotz instability, and are eventually three-dimensionalized into big Λ-shaped vortices. The issue of fractality or multi-fractality is still posed at small scales for very high Reynolds numbers. Of course, this phenomenology of vortex stretching is totally invalid for two-dimensional flows, where there is no stretching of vortex tubes since the vorticity is conserved following the motion.

Let us conclude these considerations by mentioning that some numerical methods based on vortex dynamics and using Biot and Savart law have been developed in two (Zabusky and Deem [735], Chorin [122], and Ashurst [18]) and three dimensions (Leonard [407], Chorin [123, 124], Meiburg [483]). The reader will find in the book of Cottet and Koumoutsakos [148] advanced developments on these methods taking into account boundaries, for applications in particular to the three-dimensional instabilities of wakes of real obstacles.

The effects of stratification and compressibility will be mainly examined in Chapter 13. Some of them are nevertheless contained in the next section.

2.8 Potential vorticity and Rossby number

2.8.1 Absolute vortex elements

For a perfect barotropic rotating fluid, we stress here two consequences of Helmholtz–Kelvin theorems, relating to the fact that absolute vortex lines are material. In the case of a rapid rotation characterized by $|\omega|/2\Omega \ll 1$ (this parameter has already been associated with the Rossby number in Chapter 1), it is straightforward that the absolute vortex filaments are at any time very close to a set of straight lines parallel to Ω. It follows that material lines (marked with a dye for instance) following initially absolute vortex lines (and hence quasi two-dimensional), will evolve with time keeping their quasi two-dimensional character. On the contrary, the same material lines drawn in an initially identical non-rotating flow will lose very quickly their two-dimensionality if the initial relative flow is turbulent. A more precise argument associating strong rotation to quasi two-dimensionality will be given below, with the Proudman–Taylor theorem. We will see also in Chapters 3 and 13 the possible destabilizing effects of a moderate rotation on turbulence.

2.8.2 Ertel's theorem

Another consequence of Eq. (2.81), sometimes referred to as Ertel's theorem (see Pedlosky [567]), carries some important effects of rotation and stratification.

This theorem states that if $\sigma(\vec{x},t)$ is a scalar quantity conserved following the relative fluid motion, if the fluid is perfect and if one of the two following conditions is fulfilled:

i) the fluid is barotropic or of uniform density,

ii) σ is a function of p and ρ only,

then the *potential vorticity* associated with σ, defined as

$$\Pi_\sigma = \frac{\vec{\omega}_a.\vec{\nabla}\sigma}{\rho} \tag{2.82}$$

is conserved following the flow motion. The derivation is straightforward: we consider an iso-σ surface S_{σ_0}, corresponding to $\sigma = \sigma_0$ (see Figure 2.3). This surface is material, since σ is conserved following the motion. It may however move and deform with time. One considers a small closed contour δC drawn on S_{σ_0} and enclosing an area $d\Sigma$ oriented by $\vec{n}$. Eq. (2.81) implies that

$$\frac{D}{Dt}\ (\vec{\omega}_a.\vec{n}\ d\Sigma) = 0 \tag{2.83}$$

since the mixed product $(\vec{\nabla}p, \vec{\nabla}\rho, \vec{n})$, is zero in both cases i) and ii): indeed, the condition $\sigma(p,\rho)$ implies that $\vec{\nabla}\sigma = \partial\sigma/\partial p\vec{\nabla}p + \partial\sigma/\partial\rho\vec{\nabla}\rho$, and hence $\vec{n}$, parallel to $\vec{\nabla}\sigma$, is normal to the baroclinic vector. Therefore, $\vec{\omega}_a.\vec{n}\ d\Sigma$ is conserved on S_{σ_0}, following the motion. Let us consider another iso-σ surface $S_{\sigma_0 - d\sigma}$, where $d\sigma$ is a small fixed increment of σ_0. Let dn be the distance between the two iso-surfaces in the neighbourhood of $d\Sigma$. Let us consider at a given time a small fluid cylinder of section $d\Sigma$, contained between the two iso-surfaces (see Figure 2.3): since the latter are material, the conservation of mass for the cylinder writes

$$\frac{D}{Dt}\ (\rho\ d\Sigma\ dn) = 0\ , \quad d\Sigma \sim \frac{1}{\rho\ dn}\ , \tag{2.84}$$

and hence

$$\frac{D}{Dt}\ \left(\frac{\vec{\omega}_a.\ \vec{n}}{\rho\ dn}\right) = 0\ . \tag{2.85}$$

Multiplying this equation by $d\sigma$ (which is fixed), gives the desired result

$$\frac{D}{Dt}\ \left(\frac{\vec{\omega}_a.\vec{\nabla}\sigma}{\rho}\right) = 0\ . \tag{2.86}$$

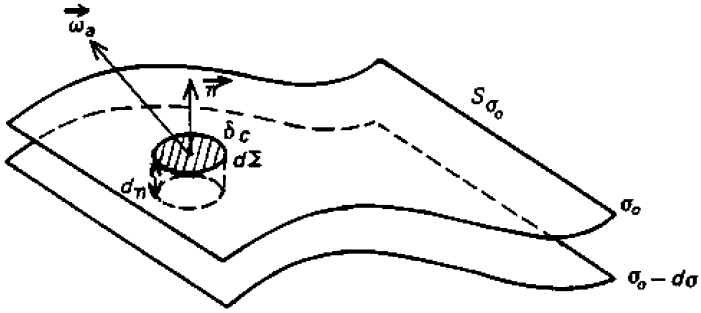

Figure 2.3. Sketch of iso-σ surfaces used in the derivation of Ertel's theorem.

The consequences of this theorem are numerous for geophysical flows: they imply in particular, for large-scale horizontal barotropic atmospheric and oceanic motions, the conservation of $\vec{\omega}_a.\vec{n}$, where $\vec{n}$ is the unit vector defining the local vertical on the Earth: indeed, one may take σ as the potential temperature for the atmosphere, and as the density for the ocean, and assume approximately that $\vec{\nabla}\sigma$ and $\vec{n}$ are parallel. Let f be the projection of the *planetary vorticity* $2\vec{\Omega}$ on $\vec{n}$, and equal to

$$f = 2\Omega \sin\varphi \ , \tag{2.87}$$

where φ is the local latitude which may vary with the motion. This parameter, already mentioned in Chapter 1, is the Coriolis parameter. The potential vorticity is proportional to $f + \vec{\omega}.\vec{n}$, which is conserved following the horizontal fluid motion. Ertel's theorem thus implies vorticity is exchanged between the relative motion and the horizontal planetary vorticity. These exchanges are in particular responsible for the propagation of waves called Rossby waves in the atmosphere and the oceans: indeed, the effective Coriolis force acting on the horizontal motion is equal to $-f\vec{n} \times \vec{u}$, and varies with the latitude, resulting in a restoring force causing a meridional oscillation of the fluid and the propagation of waves. How these waves interact with horizontal turbulent large-scale motions will be discussed in Chapter 9. Notice finally that $f/2$ is the frequency of rotation of the Foucault pendulum oscillation plane. As mentioned by Holton [294], the conservation of $f + \omega$ (where $\omega = \vec{\omega}.\vec{n}$) implies that uniform westerly zonal flows must remain zonal, otherwise they would violate the potential vorticity conservation. On the other hand, easterly flows may deviate either to the North or to the South while conserving their potential vorticity. Therefore, westerly zonal flows tend to be more stable than the easterly ones.

Another application of Ertel's theorem may be found in non-rotating shear flows. One considers a perfect barotropic fluid convecting a passive scalar Θ. From the theorem, $(\vec{\omega}.\vec{\nabla}\Theta)/\rho$ is an invariant of motion. It is assumed that at

some initial instant t_0 the velocity is not far from a parallel flow $\bar{u}(y)$, and the scalar from a distribution $\bar{\Theta}(y)$. Hence $\vec{\omega}_0.\vec{\nabla}\Theta_0 = \epsilon$ is close to zero, in the sense that the two vectors are quasi orthogonal. At later times, one has $\vec{\omega}.\vec{\nabla}\Theta = \epsilon\rho/\rho_0$, and these vectors will remain quasi orthogonal as soon as ρ does not depart too much from ρ_0. This implies that iso-Θ surfaces (normal to $\vec{\nabla}\Theta$) are quasi parallel to the vorticity, and are very close to vortex surfaces. Therefore, if the initial departure from $\bar{u}$ is responsible for the formation of coherent vortices of the spiral or hairpin type (see Chapters 3 and 4), a passive scalar initially distributed close to $\bar{\Theta}$ may serve to visualize the vortex surfaces. This is however wrong as soon as molecular viscous and diffusive effects become important. In practice, one may expect that, in a laboratory experiment, a passive scalar may visualize the vortex surfaces during the transitional stage to turbulence.

2.8.3 Molecular diffusion of potential vorticity

Let us consider now how Ertel's theorem may be generalized in a viscous fluid. We still define the potential vorticity with Eq. (2.82). Its conservation following the fluid motion is no more exact, since the vorticity, as well as quantities chosen for σ, diffuse molecularly. The exact potential vorticity evolution equation including molecular-diffusion effects can be derived in the following way: we suppose that σ is a function of p and ρ only, and diffuses as

$$\frac{D\sigma}{Dt} = \kappa_\sigma \ \nabla^2\sigma \ , \tag{2.88}$$

where κ_σ is a molecular diffusion coefficient relative to σ. As an exercise, the reader can show that, for any scalar σ,

$$\frac{D}{Dt} \ \vec{\nabla}\sigma = \vec{\nabla}\frac{D\sigma}{Dt} - \vec{\nabla}\vec{u}|^t \otimes \vec{\nabla}\sigma \ , \tag{2.89}$$

where we recall that $\vec{\nabla}\vec{u}|^t$ is the transposed velocity gradient tensor. Let us rewrite Eq. (2.76) as

$$\frac{D}{Dt}\left(\frac{\vec{\omega}_a}{\rho}\right) = \vec{\nabla}\vec{u} \otimes \frac{\vec{\omega}_a}{\rho} + \frac{1}{\rho^3} \ \vec{\nabla}\rho \times \vec{\nabla}p + \frac{\nu}{\rho}\nabla^2\vec{\omega} \ . \tag{2.90}$$

After forming the scalar product of respectively this equation with $\vec{\nabla}\sigma$ and Eq. (2.89) with $\vec{\omega}_a/\rho$ and adding, the potential vorticity satisfies

$$\frac{D}{Dt} \ \frac{\vec{\omega}_a.\vec{\nabla}\sigma}{\rho} = \left(\vec{\nabla}\vec{u} \otimes \frac{\vec{\omega}_a}{\rho}\right).\vec{\nabla}\sigma - (\vec{\nabla}\vec{u}|^t \otimes \vec{\nabla}\sigma).\frac{\vec{\omega}_a}{\rho}$$

$$+\frac{1}{\rho^3}(\vec{\nabla}\rho,\vec{\nabla}p,\vec{\nabla}\sigma)+\frac{\nu}{\rho}\nabla^2\vec{\omega}.\vec{\nabla}\sigma+\frac{\vec{\omega}_a}{\rho}.\vec{\nabla}(\kappa_\sigma\nabla^2\sigma)\ ,$$

where $(.,.,.)$ is a mixed product between three vectors. As an exercise, one can show that, for two arbitrary vector fields $\vec{a}$ and $\vec{b}$, we have

$$(\vec{\nabla}\vec{u}\otimes\vec{a}).\vec{b}-(\vec{\nabla}\vec{u}|^t\otimes\vec{b}).\vec{a}=0\ .$$

Indeed, and using the deformation tensor $\overline{\overline{S}}$, such an expression is equal to

$$(\overline{\overline{S}}\otimes\vec{a}).\vec{b}-(\overline{\overline{S}}\otimes\vec{b}).\vec{a}+\frac{1}{2}(\vec{\omega},\vec{a},\vec{b})+\frac{1}{2}(\vec{\omega},\vec{b},\vec{a})=(\overline{\overline{S}}\otimes\vec{a}).\vec{b}-(\overline{\overline{S}}\otimes\vec{b}).\vec{a}\ .$$

This term is zero, the easiest way to check it being to project it in the principal axis of deformation, in which the matrix of $\overline{\overline{S}}$ is diagonal. In the conditions of Ertel's theorem, the mixed product $(\vec{\nabla}\rho,\vec{\nabla}p,\vec{\nabla}\sigma)$ is zero, so that we have finally

$$\frac{D}{Dt}\frac{\vec{\omega}_a.\vec{\nabla}\sigma}{\rho}=\frac{\nu}{\rho}\nabla^2\vec{\omega}.\vec{\nabla}\sigma+\frac{\vec{\omega}_a}{\rho}.\vec{\nabla}(\kappa_\sigma\nabla^2\sigma)\ . \tag{2.91}$$

One recovers Ertel's theorem in the absence of molecular-diffusive effects. This result is valid even in the absence of rotation. It should be mentioned that molecular diffusion effects could be of significance in three-dimensional developed turbulence, and lead to a production of potential vorticity, as remarked by Staquet and Riley [670]. These diffusion effects may be much less important however in quasi two-dimensional situations, for example geostrophic turbulence, resulting from a strong rotation and stratification. Notice finally that for an ideal gas, the potential temperature Θ does not diffuse exactly according to Eq. (2.88), but to Eq. (2.49).

2.8.4 The Rossby number

One considers here a fluid of arbitrary depth, uniform density ρ_0, in a rotating frame of reference (angular-velocity vector $\vec{\Omega}$). The gravity $\vec{g}=-g\vec{z}$ and the rotation $\vec{\Omega}=\Omega\vec{z}$ are constant and antiparallel. Let U be a characteristic velocity of the fluid (with respect to the rotating frame) and D a length characterizing the fluid motions. U/D is a characteristic frequency of these motions. It is also characteristic of the vorticity of this "relative motion", while $2\vec{\Omega}$ is the vorticity of the solid-body rotation (entrainment vorticity). The Rossby number

$$R_o=\frac{(U/D)}{2\Omega}=\frac{U}{2\Omega D} \tag{2.92}$$

measures the relative importance of inertial forces to the forces due to rotation (Coriolis force). When $R_o\gg 1$, rotation effects are negligible and the fluid

will be fully turbulent if the Reynolds number is high. When $R_o \ll 1$, rotation effects will be dominant. We pose $f = 2\Omega$.

One takes U, D and D/U as units of velocity, length and time. We anticipate that the gradient of the corrected pressure $P = p + \rho_0 \Phi$ is $\rho_0 \approx fU$. Therefore, we will take $\rho_0 fUD$ as pressure unit. In non-dimensional variables, Navier–Stokes equation writes

$$R_o \frac{D\vec{u}}{Dt} = -\vec{\nabla} P - \vec{z} \times \vec{u} + \frac{R_o}{R_e} \nabla^2 \vec{u} \ . \tag{2.93}$$

$R_e = UD/\nu$ is the Reynolds number, assumed to be large enough in front of the Rossby number in order to neglect the viscous term and work on the basis of Euler equation

$$R_o \frac{D\vec{u}}{Dt} = -\vec{\nabla} P - \vec{z} \times \vec{u} \ . \tag{2.94}$$

We now focus on the case $R_o \ll 1$, and assume that the velocity and pressure can be expanded into series of the small parameter R_o, in the form:

$$\vec{u}(x, y, z, t) = \vec{u}^{(0)}(x, y, z, t) + R_o \ \vec{u}^{(1)}(x, y, z, t) + \cdots \ . \tag{2.95}$$

$$P = P^{(0)} + R_o \ P^{(1)} + {R_o}^2 P^{(2)} + \cdots \ . \tag{2.96}$$

Substituting these expansions into Eq. (2.94), and identifying the terms corresponding to the same power of the Rossby number, one obtains to the leading order

$$\vec{\nabla} P^{(0)} = -\vec{z} \times \vec{u}^{(0)} \ . \tag{2.97}$$

Since the gravity is assumed vertical, it is found after projecting in the horizontal and vertical directions

$$\vec{\nabla}_H p^{(0)} = -\vec{z} \times \vec{u}^{(0)} \ , \tag{2.98}$$

which expresses the geostrophic balance, and

$$\frac{\partial p^{(0)}}{\partial z} = -\frac{g}{fU} \ , \tag{2.99}$$

which expresses hydrostatic balance in non-dimensional variables.[10] Since the horizontal pressure gradient balances Coriolis force, cyclonic and anticyclonic vortices of axis parallel to the axis of rotation will correspond respectively to pressure troughs and highs.[11]

[10] The equivalent relation in dimensional variables is

$$\frac{\partial p^{(0)}}{\partial z} = -\rho_0 g \ . \tag{2.100}$$

[11] Contrary to non-rotating flows, where vortices always correspond to low pressure (see below).

2.8.5 Proudman–Taylor theorem

This theorem (see e.g. Pedlosky [567]) states that, in the limit of R_o decreasing to zero, a flow of uniform density tends to become two-dimensional, independent of the direction parallel to the rotation vector. This may be shown by taking the curl of Eq. (2.97), which yields

$$\frac{\partial}{\partial z}\vec{u}^{(0)} = \vec{0} \ . \tag{2.101}$$

Another way of obtaining this result is to write the inviscid vorticity equation corresponding to Eq. (2.94),

$$R_o \left(\frac{\partial \vec{\omega}}{\partial t} + \vec{u}.\vec{\nabla}\vec{\omega} \right) = R_o \ \vec{\omega}.\vec{\nabla}\vec{u} + \frac{\partial \vec{u}}{\partial z} \ , \tag{2.102}$$

and Eq. (2.101) is obtained at the lowest order of the expansion in powers of R_o. Then, the field $\vec{u}^{(0)}$ is two-dimensional, so that the actual flow is quasi two-dimensional at high rotation rates. Let us consider the vertical vorticity of the basic flow (component parallel to $\vec{\Omega}$), $\omega^{(0)}(x, y, t)$. To the first order, one gets

$$\frac{\partial}{\partial t}\omega^{(0)} + \vec{u}_{2D}^{(0)}.\vec{\nabla}\omega^{(0)} = \frac{\partial w^{(1)}}{\partial z} \ , \tag{2.103}$$

where $\vec{u}_{2D}^{(0)}$ is the projection of $\vec{u}^{(0)}(x, y, t)$ onto the plane perpendicular to $\vec{\Omega}$, and $w^{(1)}$ the vertical component of $\vec{u}^{(1)}$. Let us assume that the vertical velocity w is zero on a horizontal plane (for instance the bottom of the tank, taken as $z = 0$, in case of free-slip boundary conditions). Then the vertical components of all the terms in the expansion (2.95) will be zero on this plane, in particular $w^{(0)}$ and $w^{(1)}$. Due to Eq. (2.101), $w^{(0)} \equiv 0$ everywhere. Eq. (2.103) implies that $\partial w^{(1)}/\partial z = A(x, y, t)$ is independent of z, and thus $w^{(1)} = Az$. If one further assumes the existence of an upper plane at $z = H$ with the same free-slip boundary conditions (rigid lid), then $w^{(1)} \equiv 0$ everywhere, since it is a linear function of z which must be zero for two different values of z. Consequently $\partial w^{(1)}/\partial z \equiv 0$ everywhere, and Eq. (2.103) implies that the vertical vorticity of the basic flow satisfies a two-dimensional Navier–Stokes equation in the (x, y) plane. To summarize, high rotation in a perfect fluid of uniform density and arbitrary depth in a rotating tank implies geostrophic balance, hydrostatic balance, and quasi two-dimensionality. But the flow will satisfy the two-dimensional Euler equation only with a rigid lid. For such solutions, the rotation has no more effect on the motion and the "horizontal"(i.e. in planes perpendicular to the rotation axis) motions may give rise to inertial effects much larger than the molecular viscous effects, with a horizontal Reynolds number far greater than one. In that sense, one can speak of two-dimensional turbulence. Intense rotation has profoundly reorganized the structure of turbulence, but has no more effect on it once it is two-dimensional.

2.8.6 Taylor column

If we go back to Eq. (2.101) without any particular upper and lower boundary conditions, we can explain the phenomenon called Taylor column, displayed by Taylor [680] in a laboratory experiment: if some body is displaced horizontally within the flow, and if one assumes that, due to viscosity, the fluid in the immediate neighbourhood of the obstacle will follow it, the whole column of fluid above and below will move with the body. This is illustrated in Figure 2.4.

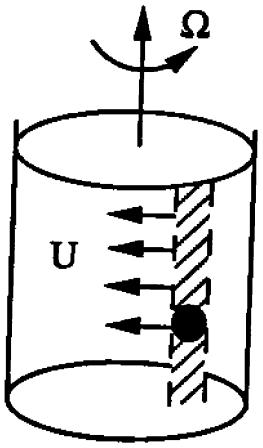

Figure 2.4. Sketch of the Taylor column created by a moving obstacle.

When applied to a shallow layer of stratified flow on a rotating sphere (the Earth for instance),[12] it is, as stressed above, the modulus of the Coriolis parameter f and the horizontal characteristic length L and velocity U which are generally employed to construct the local Rossby number $U/|f|L$. Thus planetary-scale atmospheric or oceanic motions in medium or high latitudes are characterized by a local Rossby number small with respect to one (see the discussion in Chapter 1), and the geostrophic analysis (see Chapter 9) will show that rotation reinforces the tendency to two-dimensionality[13] due to the fact that these flows are in shallow layers. The combined effects of rotation and stratification will be considered in Chapters 9 and 13.

[12] *Shallow*, with respect to Earth radius, as already discussed in Chapter 1.
[13] On a sphere.

2.9 Boussinesq approximation

These equations are an abridgement of Navier–Stokes equations which enables one to take into account variations of density when the pressure and the density are not too far from a hydrostatic state. We start with Eqs. (2.65) and (2.66) and define $\bar{p}(\vec{x})$ and $\bar{\rho}(\vec{x})$ as a basic hydrostatic pressure and density distribution obtained by setting $\vec{u} = \vec{0}$ in the equation of motion and thus satisfying

$$-\frac{1}{\bar{\rho}}\vec{\nabla}\bar{p} + \vec{g} = \vec{0} \; . \tag{2.104}$$

Therefore, the gravity $\vec{g}$ is normal to the isobaric surfaces of the basic state. Notice also that, by taking the curl of Eq. (2.104), $\vec{\nabla}\bar{p} \times \vec{\nabla}\bar{\rho} = \vec{0}$ since $\vec{g}$ is irrotational. Thus, the isobaric and isopycnal surfaces of the basic state coincide[14] and are normal to $\vec{g}$; the vectors $\vec{\nabla}\bar{p}$, $\vec{\nabla}\bar{\rho}$ and $\vec{g}$ are parallel.

The essence of the Boussinesq approximation is to assume that the actual pressures, densities and potential temperatures (for a gas) are close to the basic profiles:

$$\begin{aligned} p(\vec{x},t) &= \bar{p}(\vec{x}) + p'(\vec{x},t) \\ \rho(\vec{x},t) &= \bar{\rho}(\vec{x}) + \rho'(\vec{x},t) \\ \Theta(\vec{x},t) &= \bar{\Theta}(\vec{x}) + \Theta'(\vec{x},t) \end{aligned} \tag{2.105}$$

with $|p'| \ll \bar{p}, |\rho'| \ll \bar{\rho}$ and $|\Theta'| \ll \bar{\Theta}$. Let us define an "average level" in the layer, of density ρ_0, temperature T_0 and pressure p_0. For the gas, the reference pressure which allows the definition of potential temperature in Eq. (2.50) will be taken equal to the same p_0, in such a way that the potential temperature of this average level will be $\Theta_0 = T_0$. Now, we perform a first order expansion of Eq. (2.65) with respect to the small parameters $p'/\bar{p}$ and $\rho'/\bar{\rho}$, and obtain the momentum equation

$$\frac{D\vec{u}}{Dt} = -\frac{1}{\bar{\rho}}\vec{\nabla}p' + \frac{\rho'}{\bar{\rho}}\vec{g} - 2\vec{\Omega} \times \vec{u} + \nu\nabla^2\vec{u} \tag{2.106}$$

to which one will associate the zero-divergence condition. Assuming that the thickness D of the layer is small with respect to the total depth of the fluid H (see Figure 2.5), $\bar{\rho}$ is close to ρ_0). We have:

$$\frac{D\vec{u}}{Dt} = -\frac{1}{\rho_0}\vec{\nabla}p' + \frac{\rho'}{\rho_0}\vec{g} - 2\vec{\Omega} \times \vec{u} + \nu\nabla^2\vec{u} \; , \tag{2.107}$$

where we recall that ρ' is the density fluctuation with respect to $\bar{\rho}$ (and not ρ_0). Notice that an equation equivalent to Eq. (2.107) is:

[14] In other words, the hydrostatic basic state is barotropic.

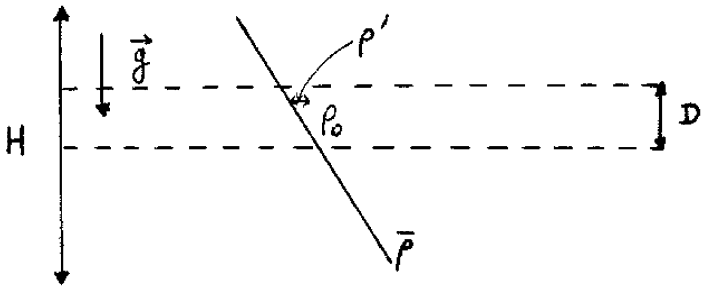

Figure 2.5. Schematic view of the vertical section of the fluid within Boussinesq approximation.

$$\frac{D\vec{u}}{Dt} = -\frac{1}{\rho_0}\vec{\nabla}p + \frac{\rho}{\rho_0}\vec{g} - 2\vec{\Omega}\times\vec{u} + \nu\nabla^2\vec{u}\ , \tag{2.108}$$

which may be useful for direct-numerical simulations and large-eddy simulations where ρ may have important spatio-temporal variations.

The momentum equation Eq. (2.107) is valid both for a liquid and an ideal gas.

2.9.1 Liquid

For a liquid, the thermodynamic equation will be Eq. (2.67), which can be written as:

$$\frac{D\rho'}{Dt} + \vec{u}.\vec{\nabla}\bar{\rho} = \kappa\nabla^2\rho' \tag{2.109}$$

(we have neglected the contribution coming from $\bar{\rho}$ in the Laplacian, which is usually very small, if not zero).

2.9.2 Ideal gas

For an ideal gas, the thermodynamic equation is given by Eq. (2.68). Here, the relative dynamic pressure fluctuations (due to velocity differences) are, from Section 2.6, of the order of M^2. This justifies the use of a non-divergent velocity field. On the other hand, the relative pressure fluctuations due to gravity are of the order of $(\rho'/\rho_0)(D/H)$. Hence, at low Mach number, the hydrostatic pressure dominates, and $p'/p_0 \ll \rho'/\rho_0$ since $D/H \ll 1$. It can easily be checked in this case that

$$\frac{T'}{\bar{T}} = \frac{\Theta'}{\bar{\Theta}} = -\frac{\rho'}{\bar{\rho}} \tag{2.110}$$

which implies $\Theta' = T'$ (to the lowest order), since $\Theta_0 = T_0$. Hence, the thermodynamic equation Eq. (2.68) gives, if one neglects the $\nabla^2 \bar{T}$ term in the r.h.s., and to the lowest order:

$$\frac{D\Theta'}{Dt} + \vec{u}.\vec{\nabla}\bar{\Theta} = \frac{\Theta}{T}\ (\kappa\nabla^2 T') \approx \kappa\nabla^2\Theta' \ . \tag{2.111}$$

It turns out that the Boussinesq approximation yields the same equations for the liquid and the gas: indeed, setting $\tilde{p} = p'/\rho_0$, these equations are:

$$\begin{gathered} \frac{D\vec{u}}{Dt} = -\vec{\nabla}\tilde{p} + \tilde{\rho}\ \vec{g} - 2\vec{\Omega} \times \vec{u} + \nu\nabla^2\vec{u} \\ \vec{\nabla}.\vec{u} = 0 \\ \frac{D\tilde{\rho}}{dt} + \vec{u}.\vec{\nabla}\bar{\rho}_* = \kappa\nabla^2\tilde{\rho} \\ \tilde{\rho} = \frac{\rho'}{\rho_0},\ \bar{\rho}_* = \frac{\bar{\rho}}{\rho_0} \quad \text{for a liquid,} \\ \tilde{\rho} = -\frac{\Theta'}{\Theta_0},\ \bar{\rho}_* = -\frac{\bar{\Theta}}{\Theta_0} \quad \text{for a gas.} \end{gathered} \tag{2.112}$$

Here the density is not a passive scalar, since it influences the velocity through the buoyancy force.

When the buoyancy force is neglected in the Boussinesq approximation, and the mean profile $\bar{\rho}_*$ assumed to be uniform, one obtains the Navier–Stokes equations with *constant* density in the momentum equation, and with fluctuations of density (or temperature, or potential temperature) satisfying the diffusion equation Eq. (2.42): density behaves as a passive scalar, and is decoupled from the velocity which now satisfies Eqs. (2.70). The latter equations describe very well non-heated (or slightly-heated) flows. They are independent of gravity including centrifugal effects, and the temperature is only a passive quantity which marks the flow, as would a dye. An appreciable part of this monograph will be devoted to such flows.

2.9.3 Vorticity dynamics within Boussinesq

One may wonder about the vorticity dynamics within the Boussinesq approximation on the basis of Eq. (2.112): neglecting the molecular diffusion, the analogue of the vorticity equation (2.74) is now

$$\frac{\partial\vec{\omega}_a}{\partial t} + \vec{\nabla} \times (\vec{\omega}_a \times \vec{u}) = \vec{\nabla}\tilde{\rho} \times \vec{g} \tag{2.113}$$

to which one has to associate the density[15] transport equation

[15] For a gas, "density" means here the opposite of the potential temperature.

$$\frac{D\rho_*}{Dt} = 0 \tag{2.114}$$

with $\rho_* = \bar{\rho}_* + \tilde{\rho}$. We first remark that

$$\vec{\nabla}\rho_* \times \vec{g} = \vec{\nabla}\tilde{\rho} \times \vec{g} \ . \tag{2.115}$$

This is obvious for a liquid since, because of the remark following Eq. (2.104), $\vec{\nabla}\bar{\rho}_* \times \vec{g} = \vec{0}$. For an ideal gas, $\bar{\Theta}$ is a function of $\bar{p}$ and $\bar{\rho}$ only, and hence $\vec{\nabla}\bar{\Theta} = (\partial\bar{\Theta}/\partial\bar{p})\vec{\nabla}\bar{p} + (\partial\bar{\Theta}/\partial\bar{\rho})\vec{\nabla}\bar{\rho}$ is parallel to $\vec{\nabla}\bar{p}, \vec{\nabla}\bar{\rho}$ and $\vec{g}$. It is then easy to check that Ertel's theorem derived above is no longer valid for any conserved quantity σ, except if σ is taken equal to ρ_*: indeed, in this latter case, the flux of the r.h.s. of Eq. (2.113) across a small surface $\delta\Sigma$ drawn on an isopycnal surface (surface of constant total density ρ_*) is zero since $\vec{\nabla}\rho_* \times \vec{g}$ is tangential to the isopycnal surface. Thus Ertel's theorem is valid within the Boussinesq equations only with a potential vorticity

$$(\vec{\omega} + 2\vec{\Omega}).\vec{\nabla}\rho_* \ , \tag{2.116}$$

where we recall that $\rho_* = \rho/\rho_0$ for the liquid, and $\rho_* = -\Theta/\Theta_0$ for the ideal gas.

One can recover this result, writing the absolute vorticity and "density" gradient equations as

$$\frac{D\vec{\omega}_a}{Dt} = \vec{\nabla}\vec{u} \otimes \vec{\omega}_a + \vec{\nabla}\rho_* \times \vec{g} \ , \tag{2.117}$$

$$\frac{D}{Dt}\ \vec{\nabla}\rho_* = -\vec{\nabla}\vec{u}|^t \otimes \vec{\nabla}\rho_* \ , \tag{2.118}$$

the latter equation being just an application of Eqs. (2.89) and (2.114). Taking the scalar product of Eqs. (2.117) and (2.118) by respectively $\vec{\nabla}\rho_*$ and $\vec{\omega}_a$, then adding, yields the invariance of $\vec{\omega}_a.\vec{\nabla}\rho_*$ with the motion.

2.10 Internal-inertial gravity waves

Another interesting application of the Boussinesq approximation is the possibility of obtaining inertial-gravity waves after a linearization about a rest state. These waves are internal in the sense that they propagate within the fluid. Surface waves presenting analogies with the internal waves can be found on the free surface of a rotating fluid. For the internal waves, one obtains to the lowest order in $\vec{u}, \vec{\omega}$ and $\tilde{\rho}$, neglecting molecular diffusion:

$$\frac{\partial\vec{\omega}}{\partial t} + \vec{\nabla} \times (2\vec{\Omega} \times \vec{u}) = \vec{\nabla}\tilde{\rho} \times \vec{g} \tag{2.119}$$

$$\frac{\partial \tilde{\rho}}{\partial t} + w \frac{d\bar{\rho}_*}{dz} = 0 \ . \tag{2.120}$$

We also assume that $\vec{\Omega}$ is parallel to $\vec{g}$, which defines the vertical coordinate z:

$$\vec{\Omega} = \Omega \ \vec{z} \ . \tag{2.121}$$

This latter hypothesis does not apply *a-priori* to a flow on a rotating sphere already considered above (and where gravity is normal to the sphere), nor to a rotating flow in a laboratory experiment when centrifugal effects are significant and produce a non-negligible spatial variation of the effective gravity field. We will show later on that the following analysis can nevertheless be approximately generalized to geophysical flows.

With the assumption Eq. (2.121), and using the zero velocity divergence condition, Eq. (2.119) reduces to

$$\frac{\partial \vec{\omega}}{\partial t} = 2\Omega \ \frac{\partial \vec{u}}{\partial z} + \vec{\nabla} \tilde{\rho} \times \vec{g} \ . \tag{2.122}$$

Notice that Eq. (2.122) shows in particular that, when Ω is zero, the vertical component of $\partial \vec{\omega} / \partial t$ is zero. The gravity waves, which will be shown below to propagate, are vertically irrotational: indeed the time-independent vertical component of the vorticity corresponds to a permanent motion which has no direct influence on the propagation of the wave and can be eliminated. This property that the gravity waves induce irrotational horizontal motions has to be related to the wave-vortex decomposition of the flow, which will be derived in Chapter 5.

Taking now the curl of Eq. (2.122), and noticing that, since $\vec{u}$ is non-divergent,

$$\vec{\nabla} \times \vec{\omega} = -\nabla^2 \vec{u} \ , \tag{2.123}$$

one finally obtains

$$\frac{\partial \nabla^2 \vec{u}}{\partial t} + 2\Omega \ \frac{\partial \vec{\omega}}{\partial z} = g \ \frac{\partial \vec{\nabla} \tilde{\rho}}{\partial z} + (\nabla^2 \tilde{\rho}) \ \vec{g} \ . \tag{2.124}$$

Differentiating Eq. (2.124) with respect to time, projecting it onto the z axis, and making use of Eq. (2.122), one finds for the vertical velocity component w (see Gill [258]):

$$\frac{\partial^2}{\partial t^2} \nabla^2 w + 4\Omega^2 \frac{\partial^2 w}{\partial z^2} = -g \ \frac{\partial}{\partial t} \left(\frac{\partial^2 \tilde{\rho}}{\partial x^2} + \frac{\partial^2 \tilde{\rho}}{\partial y^2} \right) \ . \tag{2.125}$$

Then, using Eq. (2.120), one finds finally

$$\frac{\partial^2 \nabla^2 w}{\partial t^2} + 4\Omega^2 \ \frac{\partial^2 w}{\partial z^2} + N^2 \left(\frac{\partial^2 w}{\partial x^2} + \frac{\partial^2 w}{\partial y^2} \right) = 0 \tag{2.126}$$

with

$$N^2 = -g\ \frac{d\bar{\rho}_*}{dz}\ . \tag{2.127}$$

Thus, for a liquid, we find $N^2 = -(g/\rho_0)(d\bar{\rho}/dz)$, while for an ideal gas $N^2 = (g/\Theta_0)(d\bar{\Theta}/dz)$.

2.10.1 Internal gravity waves

Let us first consider the case of the non-rotating fluid: if $N^2 < 0$, the solutions of Eq. (2.126) amplify exponentially, and the system is unstable (unstable stratification). This corresponds to the onset of thermal convection in the absence of conductivity (that is the infinite Rayleigh number case, as will be seen in the next chapter). Notice that a neutral atmosphere such that $N^2 = 0$ will be in adiabatic equilibrium ($d\bar{\Theta}/dz = 0$), which may easily be shown to correspond to $d\bar{T}/dz = -g/C_p$: this represents the dry adiabatic lapse rate of the atmosphere (see e.g. Holton [294]). If N^2 is positive (stable stratification), N is called the Brunt–Vaisala frequency,[16] and the system admits gravity waves. When N is independent of z , the dispersion relation of these waves is, from Eq. (2.126)

$$\varpi = \pm N \frac{\sqrt{k_1^2 + k_2^2}}{\sqrt{k_1^2 + k_2^2 + k_3^2}}\ , \tag{2.128}$$

where ϖ is the frequency and k_1, k_2, k_3 the components of the wave-vector. Let $k_H = \sqrt{k_1^2 + k_2^2}$ and $k = \sqrt{k_1^2 + k_2^2 + k_3^2}$ be respectively the horizontal and total wavenumber. The phase velocity is $\varpi/k = Nk_H/k^2$, and the group velocity $\vec{\nabla}\vec{\omega}$ has for components (noticing that $\partial\varpi/\partial k_H = \pm N\ (k_3^2/k^3)$)

$$\frac{\partial \varpi}{\partial k_1} = \frac{\partial \varpi}{\partial k_H}\frac{\partial k_H}{\partial k_1} = \pm N\ \frac{k_3^2}{k^3}\frac{k_1}{k_H}\ , \tag{2.129}$$

$$\frac{\partial \varpi}{\partial k_2} = \frac{\partial \varpi}{\partial k_H}\frac{\partial k_H}{\partial k_2} = \pm N\ \frac{k_3^2}{k^3}\frac{k_2}{k_H}\ , \tag{2.130}$$

$$\frac{\partial \varpi}{\partial k_3} = \mp N\ \frac{k_3 k_H}{k^3}\ . \tag{2.131}$$

These waves are dispersive. An example corresponds to *lee waves*, which are a particular internal gravity waves field in the wake of a mountain (see Wurtele et al. [724] for a review). They can propagate vertically to high altitudes. For instance, their break up into small-scale turbulence gives rise to the so-called *clear-air turbulence* encountered by planes while flying at altitudes of 10,000 m above mountains of height 3,000 m. The vertical propagation of these waves

[16] Or the *buoyancy frequency*.

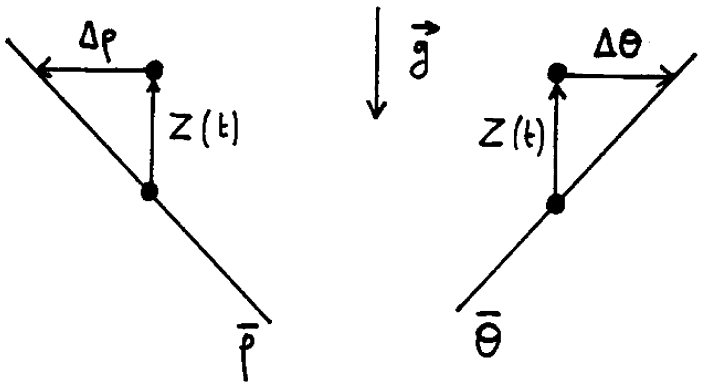

Figure 2.6. Harmonic oscillator model in a stratified fluid.

may also be an important source of energy to the stratosphere. Lee waves may be stationary with respect to the obstacle which created them, as shows the very simple example of taking $k_3 = 0$ and waves propagating upwind with $k_H = N/U$. In this case, they are usually marked by regularly spaced stationary clouds, and may be of great help to the flight of gliders. It is also possible that they interact with large-scale quasi horizontal motions.

• Exercise on internal stratification:

The second term of the r.h.s. of Eq. (2.107) can be interpreted as a buoyancy force, difference between the weight of the fluid parcel and Archimedeus thrust. It is possible to understand the role of this term by considering a simple physical model of fictitious fluid parcel isolated by mind from the rest of the fluid (see Figure 2.6). One assumes that the parcel is vertically displaced along z from its equilibrium position z_0 to $z = z_0 + Z(t)$, corresponding to a density difference $\Delta\rho = \rho(z) - \bar{\rho}(z)$ with the ambiant fluid. Newton's first principle of dynamics permits to write

$$\rho \Delta V \, \frac{d^2 Z}{dt^2} = -g \, \Delta\rho \, \Delta V \ ,$$

that is

$$\frac{d^2 Z}{dt^2} = -\frac{g}{\rho} \, \Delta\rho \approx -\frac{g}{\rho_0} \, \Delta\rho \ .$$

For a liquid, we assume incompressibility, so that the fluid parcel keeps its density ρ_0. We obtain to the first order

$$\Delta\rho = \rho - \bar{\rho}(z) = \rho_0 - \bar{\rho}(z) = -\frac{d\bar{\rho}}{dz} Z \ ,$$

that is,

$$\frac{d^2Z}{dt^2} + N^2\ Z = 0\ , \tag{2.132}$$

with the same definition for N^2 as above.

For a gas, we apply also Eq. (2.110), which yields

$$\frac{\Delta\rho}{\rho_0} \approx -\frac{\Delta\Theta}{\Theta_0}\ .$$

If we suppose that Θ is now conserved during the motion, we have:

$$\Delta\Theta = \Theta - \bar{\Theta} = \Theta_0 - \bar{\Theta} = -\frac{d\bar{\Theta}}{dz}Z\ ,$$

and Eq. (2.132) is still valid.

If $N^2 > 0$, the fluid parcel is an harmonic oscillator, corresponding to stable-stratification. The so-called available potential energy of the parcel is the potential energy of the oscillator:

$$E_p = \frac{1}{2}\ N^2\ Z^2\ ,$$

proportional to $\Delta\rho^2$ for the liquid and $\Delta\Theta^2$ for the gas.

If $N^2 < 0$, N is imaginary, and certain solutions will increase exponentially in $e^{|N|t}$. For $N = 0$, we have a neutral situation (marginal stability).

In the ocean, the stability condition $d\bar{\rho}/dz < 0$ corresponds to $d\bar{T}/dz > 0$: heavy cold layers are at the bottom, and light hot ones at the top. Neutral situation corresponds to uniform density and temperature along the vertical (see Figure 2.7). In the atmosphere, neutral situation $d\bar{\Theta}/dz = 0$ corresponds, as already stressed, to $d\bar{T}/dz = -g/C_p$, yielding to a temperature decrease of about 1°K per 100 m in mountains. Figure 2.7 precises the stability conditions for a dry atmosphere. When $d\bar{T}/dz > 0$, there is a stable inversion situation, where cold layers are at the bottom.[17] The unstable situation $d\bar{\Theta}/dz < 0$ implies $d\bar{T}/dz < 0$ (hot layers at the bottom and cold ones at the top). But there is an intermerdiate buffer zone ($-g/C_p < d\bar{T}/dz < 0$), stable although the hot layers are at the bottom. This is what happens in the lower atmosphere during the transition from night inversion to day thermal convection after sunrise. Let us stress also that basin situations within mountains favour atmospheric inversion, and hence pollution for cities located there: indeed, inversion tends to inhibate vertical motions, and the induced pollutant transport towards superior layers, which reinforces clouds formation. The latter filter out the incoming solar radiation, contributing to enhance inversion. Finally, the permanent stratospheric inversion allows a quasi two-dimensional diffusion on

[17] It is what happens in general during the night in medium latitudes.

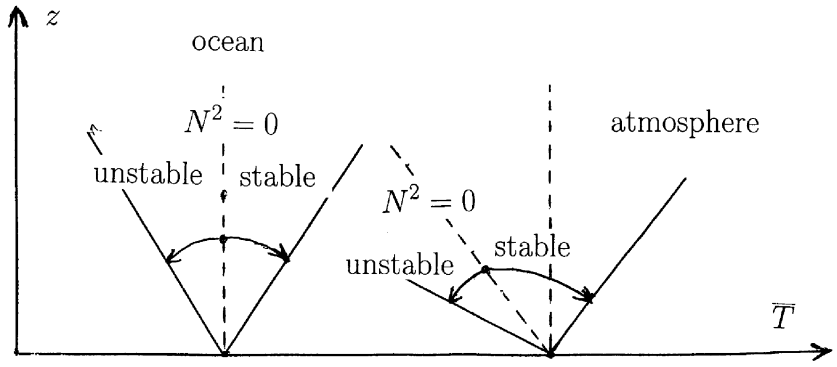

Figure 2.7. Sketch presenting the stability of a stratified layer of liquid and gas in a perfect fluid.

a sphere of pollutants, which can be transported up to the two poles: it is in this manner that chemical reactants contributing to ozone destruction are transported, and finally are at the origin of ozone holes.

2.10.2 Role of rotation

When Ω is non-zero, waves are inertial-gravity waves, and the dispersion relation becomes

$$\varpi^2 = \frac{N^2(k_1^2 + k_2^2) + 4\Omega^2 k_3^2}{k_1^2 + k_2^2 + k_3^2} \ . \tag{2.133}$$

In the case of a uniform density fluid ($N = 0$), the waves are purely inertial. The reader is referred to Lighthill [439], Holton [294] or Gill [258] for further details on these waves, which play a particularly important role in the dynamics of the meso-scale and middle atmosphere.

An important characteristic length in regard to the ocean or planetary atmospheres dynamics is the internal Rossby radius of deformation, which can be defined in the following way: let

$$H = 2\pi k_3^{-1} \ , \quad L = 2\pi (k_1^2 + k_2^2)^{-1/2} \ , \tag{2.134}$$

be respectively a characteristic vertical and horizontal length scale of the motion. Thus, the relative importance of the "inertial" to the "gravity" contribution in the r.h.s. of Eq. (2.133) is equal to $(L/r_I)^2$ where the internal Rossby radius of deformation r_I is given by

$$r_I = \frac{NH}{f} \tag{2.135}$$

f being here equal to 2Ω.

Eq. (2.135) can be generalized to Earth atmosphere or ocean dynamics in the medium or high latitudes. One has to replace f by $|f|$, f now being given by Eq. (2.87): indeed, let u, v, w, be the components of the velocity in a local frame of reference with axes directed respectively along a parallel, a meridian and the local vertical defined with the gravity field, the latter taking into account centrifugal effects.[18] The Boussinesq approximation Eq. (2.112) projected in this frame yields, if one neglects some sphericity corrections

$$\begin{aligned} \frac{Du}{Dt} &= -\frac{\partial \tilde{p}}{\partial x} + fv - 2\Omega w \cos\varphi + \nu \nabla^2 u \ , \\ \frac{Dv}{Dt} &= -\frac{\partial \tilde{p}}{\partial y} - fu + \nu \nabla^2 v \ , \\ \frac{Dw}{Dt} &= -\frac{\partial \tilde{p}}{\partial z} - \tilde{\rho} g + 2\Omega u \cos\varphi + \nu \nabla^2 w \ , \end{aligned} \tag{2.136}$$

We consider a shallow layer of fluid of depth H much smaller than the horizontal amplitude of motions L. Due to continuity, the vertical velocity w is at most of the order of UH/L, where U is a characteristic horizontal velocity. Thus, in medium or high latitudes, one can neglect the $\Omega w \cos\varphi$ term in the Du/Dt equation. Let us consider now in the Dw/Dt equation the ratio of the vertical component of the Coriolis force over the buoyancy force, of the order of

$$\frac{2\Omega u}{g\tilde{\rho}} \sim \frac{|f|U}{N^2 H} \sim \frac{|f|}{N} F \ ,$$

where $F = U/NH$ is the Froude number. If $R_o = U/|f|L$ is the Rossby number, this ratio is $\sim (H/L)(F^2/R_o)$. Usually, in atmospheric large or mesoscales, F and R_o are of same order, and never exceed values of the order of one. This permits us to replace Eq. (2.136) by

$$\frac{D\vec{u}}{Dt} = -\vec{\nabla}\tilde{p} + \tilde{\rho}\vec{g} - f\vec{z} \times \vec{u} + \nu \nabla^2 \vec{u} \tag{2.137}$$

where the actual solid-body vorticity $2\vec{\Omega}$ has been replaced by its projection on the local vertical on the sphere. The analysis of the inertial-gravity waves arising from Eq. (2.137) is the same as that done previously in this section, provided the parameter 2Ω should be replaced by $|2\Omega \sin\varphi|$. Notice also that the approximation which has led us to replace the Coriolis force by $-f\vec{z} \times \vec{u}$

[18] Because of the centrifugal force due to its rotation, the Earth has evolved towards an ellipsoidal shape such that the gravity field (gravitation + centrifugal effects) is, in the mean, normal to the surface. In fact, the geoid presents deviations from this shape due to the non-homogeneous distribution of masses, caused in particular by the motions in Earth mantle.

in Eq. (2.137) could also be done usefully on the Navier–Stokes equations themselves.[19]

As already stressed, the length r_I characterizes the horizontal scales of motion over which internal waves are mainly inertial, and under which they are gravity dominated. It will be seen in Chapter 9 that this length is also characteristic of the baroclinic instability due to the combined effects of rotation and stratification. It is difficult to determine r_I precisely, mainly because the Brunt–Vaisala frequency N may vary appreciably with stratification profiles. Average values of r_I are of 50 km in the oceans and 1000 km in Earth atmosphere. In the latter case and at this scale, $R_o \sim 0.3$. The reader is warned that rotation may have an important effect on motions of wavelength smaller than r_I and which are not of the inertial-gravity wave type: in the mesoscale atmosphere (scales of a few tenths of kilometers) for instance, the Rossby numbers are larger than one, and we will see later on (Chapters 3 and 13) that there is in this case a strong assymmetry between cyclones and anticyclones, the latter being prevented to grow by entrainment rotation.

The above considerations have shown that the Navier–Stokes equations within the Boussinesq approximation are quite satisfactory to study rotating stably-stratified flows, in particular in situations related to geophysical fluid dynamics. The Boussinesq approximation is simpler mathematically. Its incompressibility character (suppressing the acoustic waves) greatly simplifies the numerical simulations done using pseudo-spectral methods (see Chapter 5), and also allows us to apply the stochastic models of turbulence (see Chapter 7) in the stably-stratified case. The Boussinesq approximation is, on the contrary, certainly not valid in situations with strong heat release such as in combustion or reacting flows, and more generally, with sharp density gradients. In these cases, the low-Mach number expansions presented above (see Riley [601]) should be preferred if the Mach number is small.

2.11 Barré de Saint-Venant equations

2.11.1 Derivation of the equations

These equations are also known as the *shallow-water equations*. We consider the Navier–Stokes equations locally on a sphere for a fluid of constant uniform density ρ_0, with the same approximation as in Eq. (2.137) for the Coriolis force, that is

$$\frac{D\vec{u}}{Dt} = -\frac{1}{\rho_0}\vec{\nabla}p + \vec{g} - f\vec{z}\times\vec{u} + \nu\nabla^2\vec{u} \tag{2.138}$$

[19] However, this analysis is valid only for a shallow layer in medium or high latitudes. For a fluid of arbitrary depth or close to the equator, the complete Coriolis force $-2\vec{\Omega}\times\vec{u}$ must be considered.

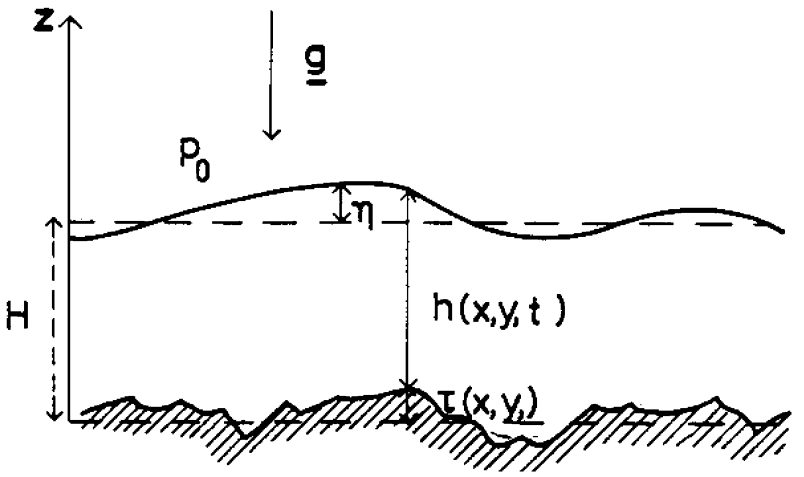

Figure 2.8. Schematic vertical cross-section of the shallow layer: $\tau(x, y)$ is the height of the topography, $h(x, y, t)$ the depth of the fluid, H the average height of the free surface, and $\eta(x, y, t)$ the elevation of the free surface.

$$\vec{\nabla}.\vec{u} = 0 \ , \tag{2.139}$$

$\vec{g}$ and $\vec{z}$ being parallel. The fluid is assumed to have a free surface of mean elevation H and to lie above a topography of height $\tau(x, y)$. $h(x, y, t)$ is the depth of the fluid layer[20] and $\eta(x, y, t)$ the elevation of the free surface with respect to H (see Figure 2.8). Hence we have

$$h(x, y, t) + \tau(x, y) = H + \eta(x, y, t) \ . \tag{2.140}$$

The pressure at the free surface is uniform and equal to p_0. The assumption of shallowness actually means that one assumes the pressure is hydrostatically distributed along the vertical, that is,

$$p(x, y, z, t) = p_0 + \rho_0 \ g \ (h + \tau - z) \ , \tag{2.141}$$

and that the horizontal velocity field $\vec{u}_H = (u, v, 0)$ depends only on the horizontal space variables x and y and on the time. The vertical velocity $w(x, y, z, t)$ still depends on the vertical coordinate, in order to allow vertical variations of the free surface. With these assumptions, and integrating the continuity equation (2.139) along the vertical, one obtains Barré de Saint-Venant equations

[20] This depth h is not to be confused with the enthalpy considered above, although analogies exist, as stressed below.

$$\frac{D_H u}{Dt} = -g\frac{\partial \eta}{\partial x} + fv + \nu \nabla_H^2 u \tag{2.142}$$

$$\frac{D_H v}{Dt} = -g\frac{\partial \eta}{\partial y} - fu + \nu \nabla_H^2 v \tag{2.143}$$

$$\frac{D_H h}{Dt} = -h\ \vec{\nabla}_H . \vec{u} \tag{2.144}$$

where

$$\frac{D_H}{Dt} = \frac{\partial}{\partial t} + u\frac{\partial}{\partial x} + v\frac{\partial}{\partial y} \tag{2.145}$$

is the derivative following the horizontal motion, and ∇_H^2 and $(\vec{\nabla}_H .)$ stand respectively for the horizontal Laplacian and divergence operators.

2.11.2 The potential vorticity

Now, let us write in this case an analogous potential vorticity conservation result: let

$$\vec{\omega} = \omega\ \vec{z} = \vec{\nabla} \times \vec{u}_H \tag{2.146}$$

be the vorticity of the horizontal velocity, with

$$\omega = \frac{\partial v}{\partial x} - \frac{\partial u}{\partial y}\ . \tag{2.147}$$

Paralleling Eq. (2.22), Barré de Saint-Venant equations may be written in the form:

$$\frac{\partial \vec{u}_H}{\partial t}\ +\ (f+\omega)\ \vec{z} \times \vec{u}_H\ =\ -g\vec{\nabla}_H \eta - \vec{\nabla}_H\ \frac{u_H^2}{2} + \nu \nabla_H^2 \vec{u}_H . \tag{2.148}$$

Taking the three-dimensional curl of Eq. (2.148), one obtains, after projection onto the z axis:

$$\frac{\partial \omega}{\partial t} + u\frac{\partial}{\partial x}(\omega + f) + v\frac{\partial}{\partial y}(\omega + f) + (\omega + f)\ \vec{\nabla}_H . \vec{u}_H = \nu \nabla_H^2 \omega\ , \tag{2.149}$$

that is,

$$\frac{D_H}{Dt}(\omega + f) + (\omega + f)\ \vec{\nabla}_H . \vec{u}_H = \nu \nabla_H^2 \omega\ . \tag{2.150}$$

Finally, making use of the continuity equation (2.144), we obtain

$$\frac{D_H}{Dt}\ \frac{\omega + f}{h} = \frac{\nu}{h}\nabla_H^2 \omega\ . \tag{2.151}$$

As an exercise, let us give another derivation of this result: we take the momentum equations as

$$\frac{\partial u}{\partial t} + u\frac{\partial u}{\partial x} + v\frac{\partial u}{\partial y} = -g\frac{\partial \eta}{\partial x} + fv + \nu\nabla_H^2 u \quad (a)$$

$$\frac{\partial v}{\partial t} + u\frac{\partial v}{\partial x} + v\frac{\partial v}{\partial y} = -g\frac{\partial \eta}{\partial y} - fu + \nu\nabla_H^2 v \quad (b)$$

and form $\partial(b)/\partial x) - \partial(a)/\partial y)$. Using partial-derivatives commutativity, we get

$$\frac{\partial \omega}{\partial t} + u\frac{\partial \omega}{\partial x} + v\frac{\partial \omega}{\partial y} + \omega\vec{\nabla}_H.\vec{u}_H = -\frac{\partial}{\partial x}(fu) - \frac{\partial}{\partial y}(fv) + \nu\nabla_H^2\omega$$

yielding

$$\frac{\partial}{\partial t}(\omega + f) + u\frac{\partial}{\partial x}(\omega + f) + v\frac{\partial}{\partial y}(\omega + f) + (\omega + f)\vec{\nabla}_H.\vec{u}_H = \nu\nabla_H^2\omega \ ,$$

which is Eq. (2.149).

When the viscous effects are neglected, we find that

$$\frac{\omega + f}{h} = \frac{(\vec{\omega} + 2\vec{\Omega}).\vec{z}}{h} \tag{2.152}$$

is conserved following the horizontal motion $\vec{u}_H$. In fact, this is a result which could also have been obtained directly from Ertel's theorem, assuming a shallow fluid layer, and taking $\sigma = p = p_0$ on the free surface: assuming quasi two-dimensionality, Eq. (2.83) leads to

$$\frac{D_H}{Dt}\ [(\vec{\omega} + 2\vec{\Omega}).\vec{z}\ d\Sigma] = 0 \ , \tag{2.153}$$

and the mass conservation written for a fluid cylinder of depth h and section $d\Sigma$ yields

$$\frac{D_H}{Dt}(h\ d\Sigma) = 0 \ , \tag{2.154}$$

which proves the result and justifies calling $(\omega + f)/h$ the potential vorticity. Such a result allows the recovery of the relative vorticity changes due to the variation of f (differential rotation) and of h (by stretching or compression of the relative vortex tubes). In this case, a "positive" topography (mountain) will tend to create anticyclonic eddies which may lock on it, while cyclonic vortices may be trapped in a trough.

2.11.3 Surface inertial-gravity waves

A surface-wave analysis, analogous to what has been done previously for the case of internal waves, can be performed on the Barré de Saint-Venant equations. One assumes that f is a constant (f-plane approximation), that there is

no topography, and neglects viscosity. After linearizing about rest the vorticity and continuity equations, we obtain

$$\frac{\partial \omega}{\partial t} + f\lambda = 0$$

$$\frac{\partial \eta}{\partial t} + H\lambda = 0$$

with

$$\lambda = \vec{\nabla}_H . \vec{u} = -\frac{1}{f}\ \frac{\partial \omega}{\partial t} = -\frac{1}{H}\ \frac{\partial \eta}{\partial t}\ . \tag{2.155}$$

Linearization of the momentum equation yields

$$\frac{\partial u}{\partial t} = -g\frac{\partial \eta}{\partial x} + fv$$

$$\frac{\partial v}{\partial t} = -g\frac{\partial \eta}{\partial y} - fu\ .$$

Taking the divergence of this system, one gets

$$\frac{\partial \lambda}{\partial t} = -g\nabla_H^2 \eta + f\omega$$

and finally

$$\left(\frac{\partial^2}{\partial t^2} + f^2\right)\lambda = gH\ \nabla_H^2 \lambda\ . \tag{2.156}$$

One seeks for solutions in the form of horizontally-propagating plane waves:

$$\lambda(\vec{x}, t) = \hat{A}\ e^{i(\vec{k}.\vec{x} - \varpi t)} \tag{2.157}$$

where $\vec{k}$ is a real wave number, of components $[k_1, k_2]$, ϖ the pulsation, here real, and $\hat{A}$ a constant complex amplitude. It yields the following dispersion relation

$$\varpi^2 = f^2 + (k_1^2 + k_2^2)\ gH\ . \tag{2.158}$$

This allows definition of a horizontal scale r_E, called the external Rossby radius of deformation:

$$r_E = \frac{1}{f}\sqrt{gH}\ , \tag{2.159}$$

such that Eq. (2.158) writes

$$\varpi^2 = f^2(1 + k_H^2\ r_E^2)\ . \tag{2.160}$$

• Gravity waves:

For motions of horizontal length scale L smaller than r_E, surface gravity waves are predominant, and Eq. (2.158) yields

$$\varpi = k\,\sqrt{gH}\ , \tag{2.161}$$

an expression originally due to Lagrange, and which corresponds to non-dispersive waves propagating at the constant phase velocity $\sqrt{gH}$. This has important applications in seas and oceans: if one takes $H = 1000$ m (assuming a submarine earthquake underneath), we obtain ≈ 100 m/s, which is of the order of the velocity of a tsunami.

• Inertial waves:

For L much larger than r_E, surface inertial waves of frequency f dominate.

Let us take for instance Earth atmosphere, and consider it as a homogeneous shallow layer with a free surface: taking $H \approx 10{,}000$ m and $f = 10^{-4}$ rd s^{-1} (which corresponds to medium latitudes), the external Rossby radius of deformation is of the order of 3000 km. The velocity of external gravity waves (of wavelenght smaller than r_E) is ≈ 300 m/s. This is of the order of the sound velocity in the air, and much higher than the typical values ≈ 30 m/s for the synoptic perturbations.

Let us finally try to evaluate the ratio r_I/r_E in a thin layer where a stable vertical stratification exists. It is found

$$\left(\frac{r_I}{r_E}\right)^2 = \frac{N^2H^2}{gH} \approx \frac{|\Delta\rho|}{\rho}\ , \tag{2.162}$$

where $|\Delta\rho|/\rho$ is a typical vertical relative density (or potential temperature) variation across the layer. This shows that the external radius of deformation is larger than the internal one.

Analogy with a compressible gas

We recall at this point the barotropic equations of motion (2.36) for a barotropic perfect fluid in the case of an ideal gas, for which we neglect the entrainment rotation. If one considers a two-dimensional flow, the momentum equation for u and v reduces to inviscid Barré de Saint-Venant momentum equations (without topography), provided the enthalpy h_e of the gas be replaced by $gh(x, y, t)$ in the shallow-water equations. Since, as already stressed, the enthalpy of the gas is proportional to $\rho^{\gamma-1}$, the gas continuity equation

(2.48) reduces to Eq. (2.144) only if $\gamma = 2$. Therefore, Barré-de Saint-Venant equations may be considered as a special case of two-dimensional compressible turbulence, but with a not very realistic value of γ (equal to 1.4 in the air). However, the analogy (called the shallow-water analogy) is interesting, since the gravity-waves velocity $\sqrt{gH}$ may be interpreted as the sound velocity $\sqrt{(\gamma-1)\ h_e}$ for the associated barotropic gas (see below). Let us remark also that for atmospheric synoptic motions of length scale smaller than the external Rossby radius of deformation considered above, the equivalent Mach number is of the order of 0.1, and the equivalent gas motion may be considered as incompressible, with no effect of the waves upon the dynamics. Thus, Barré de Saint-Venant equations reduce in this case to two-dimensional Navier–Stokes equations in a layer of constant depth, and gravity waves have no influence on the horizontal motion.

• Sound waves in a gas:

As an exercise, we consider an ideal barotropic gas (perfect fluid) of arbitrary γ and space dimension. We are going to linearize the equations of motion about rest, posing $h_e = h_0 + h'$. We have

$$\frac{\partial \vec{u}}{\partial t} = -\vec{\nabla} h' \ , \quad \frac{\partial h'}{\partial t} + h_0(\gamma-1)\vec{\nabla}.\vec{u} = 0 \ ,$$

from which one can derive $(\partial/\partial t)\vec{\nabla}.\vec{u} = -\nabla^2 h'$, and

$$\frac{\partial^2}{\partial t^2} h' - h_0(\gamma-1)\nabla^2 h' = 0 \ . \tag{2.163}$$

This is an equation similar to Eq. (2.156)) without rotation. We find sound waves propagating at a speed

$$c_s = \sqrt{(\gamma-1)\ h_o} = \sqrt{\gamma RT} = \sqrt{dp/d\rho} \ . \tag{2.164}$$

Kelvin waves

Another application of Barré de Saint-Venant equations concerns Kelvin waves, which have important applications in tides.[21] The flow is still in a shallow layer as in Figure 2.8 with no topography, but it is now constrained between two vertical parallel planes. The first plane is chosen to define the frame xOz, and the second plane is located at a distance $y = L_1 > 0$. We still use the above surface inertial-gravity waves equations in the inviscid case, which yields:

$$\left(\frac{\partial^2}{\partial t^2} + f^2\right) \frac{\partial \eta}{\partial t} = gH\ \nabla_H^2\ \frac{\partial \eta}{\partial t} \ . \tag{2.165}$$

[21] The source of this exercise was communicated to me by O. Métais.

Boundary conditions are $v = 0$ on the two vertical planes. This leads to

$$\frac{\partial^2 \eta}{\partial y \partial t} - f \frac{\partial \eta}{\partial x} = 0$$

on the two vertical walls ($y = 0$ and $y = L_1$). One looks for solutions which are longitudinal waves in the x direction of amplitude $A(y)$:

$$\eta(x, y, t) = A(y)\ e^{i(k.x - \varpi t)} \tag{2.166}$$

where k is a positive real number. Posing $c_0 = \sqrt{gH}$, one can show that v is zero everywhere and $\varpi = \pm k c_0$. The final solution writes

$$\eta(x, y, t) = \eta_0\ e^{\mp f y / c_0} \cos[k(x \mp c_0 t) + \Phi]\ , \tag{2.167}$$

where Φ is a phase, corresponding to two family of waves travelling at a phase velocity c_0, respectively in the directions $x > 0$ and $x < 0$. It is interesting to note that $A(y)$ decreases from its maximum (located on the plane which is to the right of the wave propagation) to its minimum on the opposite plane, the difference between the extrema being $\eta_0(1 - e^{-f L_1 / c_0})$.

Let us apply this result to tides in the channel sea ("Manche" in French) separating France from Britain. Here, the source of waves is the tides within the Atlantic located to the west, so that we will consider only waves propagating in the direction $x > 0$. The tidal range ("marnage" in French) is then $M_{ar} = 2\eta_0$ in France and $2\eta_0 e^{-f L_1 / c_0}$ in Britain, so that the relative variation of this tidal range with respect to France is

$$1 - e^{-f L_1 / c_0} = 1 - e^{-L_1 / r_E}\ ,$$

where r_E is the external Rossby radius of deformation already introduced. Taking $f = 10^{-4}, H = 70$ m and $L_1 = 150$ km, we have $r_E = 260$ km and $(\delta M_{ar}/M_{ar}) \approx 0.44$. This is very important: indeed, if one takes $M_{ar} = 10$ m in France, it is reduced of about 4 m in Britain. The velocity of the waves is 26 m/s (93 km/h), to be compared with the velocity of a galloping horse (60 km/h), as tidal waves are supposed to travel in the Mount Saint-Michel bay in Normandy.

2.12 Gravity waves in a fluid of arbitrary depth

The calculation of surface-gravity waves can be made for a fluid of arbitrary depth H (see e.g. Lighthill [439]). We ignore rotation, consider a perfect flow and assume a uniform density ρ_0 and a vertical constant gravity g. If p_0 is the pressure at the free surface, we define a modified pressure

$$\tilde{P} = p + \rho_0 g z - p_0\ , \tag{2.168}$$

choosing the rest state of the free surface as $z = 0$. $\tilde{P}$ is the pressure fluctuation with respect to the hydrostatic rest state. Eq. (2.70), after linearization with respect to the velocity fluctuations, becomes

$$\frac{\partial \vec{u}}{\partial t} = -\frac{1}{\rho_0}\vec{\nabla}\tilde{P} \ , \tag{2.169}$$

and the linearized vorticity equation is

$$\frac{\partial \vec{\omega}}{\partial t} = 0 \ . \tag{2.170}$$

In fact, we will assume that initially the flow is irrotational, and hence it will remain irrotational for any time. The velocity is such that $\vec{u} = \vec{\nabla}\Phi$, and is non-divergent. Therefore the potential $\Phi(x, y, z, t)$ satisfies a Laplace equation

$$\nabla^2\Phi = 0 \ , \tag{2.171}$$

to which the equation of motion reduces. From Eq. (2.169), Φ may be chosen such that

$$\tilde{P} = -\rho_0 \frac{\partial \Phi}{\partial t} \ . \tag{2.172}$$

The boundary condition at the free surface for the linearized problem is

$$\frac{\partial \eta}{\partial t} = \frac{\partial \Phi}{\partial z}(x, y, 0, t) \ , \tag{2.173}$$

where $\eta(x, y, t)$ (defined as in Barré de Saint-Venant equations), is the elevation of the free suface with respect to its rest level. Furthermore, we assume that the flow is hydrostatic close to the free surface, which yields

$$\tilde{P}(x, y, 0, t) = \rho_0 \ g \ \eta(x, y, t) \ . \tag{2.174}$$

Hence, using Eq. (2.173), it is found that

$$g \ \eta(x, y, t) = -\frac{\partial \Phi}{\partial t}(x, y, 0, t) \ ,$$

which when differentiated with respect to t yields, with the aid of Eq. (2.173):

$$\frac{\partial^2 \Phi}{\partial t^2}(x, y, 0, t) + g\frac{\partial \Phi}{\partial z}(x, y, 0, t) = 0 \ . \tag{2.175}$$

Eq. (2.171) can then be solved with the boundary condition (2.175) using a normal-mode approach: one looks for solutions of the type

$$\Phi(x, y, z, t) = A(z) \ \exp i(\vec{k}.\vec{x} - \varpi t) \ , \tag{2.176}$$

where $\vec{k}$ is here a horizontal wave vector which corresponds to horizontally-propagating waves. One obtains:

$$A''(z) - k^2 A(z) = 0 \ , \tag{2.177}$$

$$-\varpi^2 \ A(0) + g \ A'(0) = 0 \ . \tag{2.178}$$

For a fluid of depth H with a zero vertical velocity $\partial\Phi/\partial z$ at the bottom $z = -H$, the solution of Eq. (2.177) is

$$A(z) = A_0 \ \cosh[k(z + H)] \ , \tag{2.179}$$

and hence it is found, from Eq. (2.178):

$$\varpi^2 = gk \ \tanh(kH) \ . \tag{2.180}$$

The phase velocity $c = \varpi/k$ is given by

$$c = \sqrt{gH} \ \left[\frac{\tanh(kH)}{kH}\right]^{1/2} \ . \tag{2.181}$$

In the limit $kH \to 0$ (long-wave approximation), which corresponds to horizontal wavelengths large in comparison to the depth of the layer, one recovers the shallow-layer result $\sqrt{gH}$. On the contrary, and in the limit $kH \to \infty$ (fluid of infinite depth),

$$c = \sqrt{\frac{g}{k}} \ . \tag{2.182}$$

2.12.1 Supersonic shocks and wakes of floating bodies

Let us consider a small body moving three-dimensionally through a gas at a constant velocity U. If the Mach number M is smaller than 1, the body will go slower than its sound waves. If, on the other hand, $M > 1$, then it will go past the waves. It is well known that in this case, a shock cone forms in front of the body. It is the envelope of all the wave surfaces (which are spheres) emitted by the body at anterior times. Its half-angle sine is M^{-1}. For a supersonic plane, the bang due to the shock cone will be heard when the aircraft passes over our heads.

Let me recall what is stressed by Lesieur [424, p. 165] on this topic:

> We underline a very interesting analogy between the shock cone of a supersonic plane and the wake of a boat on the sea or a duck travelling on the surface of a pond: if c is the speed of gravity waves at the pond surface, the duck will at each instant (through his legs flapping)

excite waves which will form circles whose radius increases proportionally to time and the speed c. If the duck's speed U is smaller than c ("subsonic" duck), it will be caught up by the waves it has created, and will bathe into them. If U is larger than c ("supersonic" duck), it will never be caught up by the various wave circles: the envelope of these circles will no more be a cone (as for the supersonic plane sound waves), but a diedre whose half angle is given by the same expression as the supersonic plane. The pond surface is agitated by he duck waves inside the diedre, where it therefore knows about the animal presence. Outside of the diedre on the contrary, nothing indicates (from an hydrodynamical point of view) the presence of the poultry. If the duck accelerates, one sees the diedre closing.[22] It is certainly more relaxing, in order to understand the planes supersonic bangs, to observe ducks, swans or boats on water.

[22] If it accelerates furthermore, the wake will become turbulent, and the diedre will transform into a parabole.

3

Transition to Turbulence

3.1 Introduction

As already stressed in Chapter 1, turbulence can only develop in rotational flows: it is due to the existence of shear in a basic flow that small perturbations will develop, through various instabilities, and eventually degenerate into turbulence. Some of these instabilities, at least during the initial stage of their development, may be understood within the framework of linear-instability theory, the main results of which will be recalled in this chapter. The nonlinear instability studies may prove to be useful in the future in understanding transition to turbulence, but, to date, they are still in progress and have not led to a unified theory of transition. Extremely useful tools to understand the transition, and assess the various theories proposed to describe it, are direct-numerical simulations of Navier–Stokes equations: numerous examples of these calculations will be given here.

Among the basic shear flows which will be considered, we will make a distinction between the free-shear flows, such as mixing layers, jets or wakes on the one hand, and wall-bounded flows such as boundary layers, pipe flows or channel flows on the other hand. In free-shear flows, primary instabilities leading to the formation of coherent vortices are *inviscid*, in the sense that they are not affected by molecular viscosity, if it is small enough. In wall-bounded flows, on the contrary, the linear instabilities depend critically upon the viscosity (*viscous instabilities*), and vanish in the Euler case. Inviscid instabilities are much more vigorous than viscous ones. The present chapter will consider transition to turbulence both from the point of view of linear-instability theory of parallel flows, and experimental or numerical data. We will look also at transition in rotating shear layers and thermal convection.

It has to be emphasized that the concept of *transition to turbulence* is not very well defined: generally, what experimentalists call transition corresponds

to the development of small-scale three-dimensional turbulence within the fluid. Actually, we will see that the whole process of transition to turbulence may involve several successive stages: in the plane mixing layer behind a splitter plate for instance, these stages observed experimentally are:

(A) The growth of two-dimensional coherent vortices.
(B) The merging of these vortices together (pairing).
(C) A catastrophic breakdown into three-dimensional turbulence.

But, as already discussed in Chapter 1 and will be justified later on in the book, the two-dimensional coherent vortices, which appear before the transition to three-dimensional turbulence, may have some features of two-dimensional turbulence.

3.2 The Reynolds number

The most famous experiment on the transition to turbulence is the Reynolds experiment of a flow in a circular pipe (circular Poiseuille flow). Let U be an average velocity of the flow across the tube section (bulk velocity), D the diameter of the tube, and ν the molecular viscosity. Reynolds [592] introduced in 1883 the non -dimensional parameter

$$R = \frac{U\ D}{\nu} \tag{3.1}$$

and showed experimentally that there was a critical value of R above which the flow inside the tube became turbulent. This was done by varying independently the velocity U, the diameter D of the pipe, or considering fluids of various viscosities. The critical value R_c found by Reynolds was of the order of 2000. For $R < R_c$, the flow remained regular (*laminar*), and for $R > R_c$ it became turbulent. It is interesting to go back to Reynolds's article concerning one experiment where he introduced a fine line of dye upstream at the centre of the pipe inlet (which has a trumpet shape):

The general results were as follows:

(1) When the velocities are sufficiently low, the streak of colour extended in a beautiful straight line through the tube.

(2) If the water in the tank had not quite settled to rest, at sufficiently low velocities, the streak would shift about the tube, but there was no appearance of sinusoity.

(3) As the velocity was increased by small stages, at some point in the tube, always at considerable distance from the trumpet or intake, the colour band would all at once mix up with the surrounding water, and fill the rest of the tube with a mass of coloured water (...).

Any increase in the velocity caused the point of break down to approach the trumpet, but with no velocities that were tried did it reach this.

On viewing the tube by the light of an electric spark, the mass of colour resolved itself into a mass of more ore less distinct curls, showing eddies (. . .).

These observations are corroborated by the measurements of the mean[1] skin-friction coefficient at the wall $2\mu(d\bar{u}/dy)/\rho U^2$, done later on. Below R_c, it decreases as R^{-1}, as predicted theoretically with the laminar Poiseuille parabolic profile. At R_c it undergoes an abrupt jump. Above R_c its decrease is much more gentle than in the laminar case, and follows first a $R^{-1/4}$ law, as shown experimentally by Blasius [67]. Though, as we shall see, the notion of a critical Reynolds number is extremely ambiguous, this parameter can nevertheless be shown to characterize the relative importance of nonlinear interactions developing in the fluid: indeed, let us consider a fluid particle of transverse velocity v in a the pipe. The time which is necessary for crossing is the "inertial" time

$$T_{in} = \frac{D}{v} \tag{3.2}$$

provided the fluid particle is not prevented from moving by viscous effects: the latter will act on the distance D in a time of the order of

$$T_\nu = \frac{D^2}{\nu} \tag{3.3}$$

as can be seen by considering the simple diffusion equation

$$\frac{\partial v}{\partial t} = \nu \, \nabla^2 v \ . \tag{3.4}$$

Thus the particle will be able to cross the tube only if the ratio of the inertial frequency over the viscous frequency is greater than 1. This condition corresponds to:

$$\frac{T_\nu}{T_{in}} = \frac{v \ D}{\nu} > 1 \ . \tag{3.5}$$

If one assumes that the order of magnitude of v is small with respect to U, it can be concluded that the velocity fluctuations will be able to develop in the flow only if the Reynolds number UD/ν based on the basic flow is much greater than 1.

From this oversimplified phenomenological analysis, we retain the idea that the Reynolds number characterizes the relative importance of nonlinear effects over viscous effects in the Navier–Stokes equation.

The same experiment repeated in a plane Poiseuille flow (plane channel) shows, as in Reynolds experiment, a transition to turbulence at a critical

[1] In a sense defined later.

Reynolds[2] number of the order of 2000. For a plane Couette flow, the critical Reynolds number[3] is of the order of 1000. We will discuss below in detail the case of the plane boundary layer.

It is, nevertheless, difficult to give a firm basis to this notion of critical Reynolds number: in fact, experiments show that the transitional Reynolds number to turbulence depends on the intensity of turbulence existing in the incoming flow (residual turbulence). Furthermore, no theory (including instability analysis[4]) has, up to now, predicted satisfactorily the critical Reynolds number for transition to turbulence in the above-quoted flows.

In spite of the limitations of this approach, it is of interest to go back to the hydrodynamic instability theory, in order to understand some basic mechanisms of the transition to turbulence in free-shear or wall-bounded flows. This theory also permits us to understand the mechanisms of generation of primary coherent vortices in some free-shear flows such as mixing layers, wakes or jets.

To conclude this section, let us stress that, in order to accurately define the Reynolds number, one has to choose a characteristic velocity and length. According to these choices, various Reynolds numbers can be associated to a given flow. Note also that the Reynolds number can evolve following the motion of the fluid particle if the characteristic scale and velocity depend upon space or time: in the spatially-growing mixing layer or boundary layer, for instance, the Reynolds number based on the layer thickness increases with this scale in the downstream direction. In the round jet on the other hand, the Reynolds number is constant and fixed by its upstream value (see Chapter 4).

3.3 Linear-instability theory

We recall here some important results of linear-hydrodynamic instability theory which are of interest in understanding the transition to turbulence. For a more complete presentation of the theory, the reader is referred to Drazin and Reid [173]. We consider a fluid of uniform density ρ, and work in a Cartesian frame $Oxyz$. We will restrict our attention to the stability of a parallel flow of components $\bar{u}(y), 0, 0$ to which a small perturbation is superposed. Let us write the velocity-field components and pressure as

$$u(x,y,z,t) = \bar{u}(y) + \tilde{u}(x,y,z,t) \ , \quad v(x,y,z,t) = \tilde{v}(x,y,z,t) \ ,$$

$$w(x,y,z,t) = \tilde{w}(x,y,z,t) \ , \quad p(x,y,z,t) = \bar{p}(x,y,z) + p'(x,y,z,t) \ .$$

[2] Based on the width of the channel and the average velocity across its section.
[3] Based on the relative velocity between the two plates and their distance.
[4] Linear or nonlinear.

We write Navier–Stokes equations as

$$\frac{\partial \vec{u}}{\partial t} + (\vec{u}.\vec{\nabla})\vec{u} = -\frac{1}{\rho}\vec{\nabla}p + \nu\nabla^2\vec{u}$$

and linearize, assuming that the components $\tilde{u}, \tilde{v}, \tilde{w}$ of the perturbed velocity $\vec{\tilde{u}}$ are small (in modulus) in front of $\bar{u}$, and that $|p'| \ll \bar{p}$. It is obtained

$$\frac{\partial \vec{\tilde{u}}}{\partial t} + (\vec{\bar{u}}.\vec{\nabla})\vec{\tilde{u}} + \frac{\partial \vec{\tilde{u}}}{\partial t} + (\vec{\tilde{u}}.\vec{\nabla})\vec{\tilde{u}} + (\vec{\tilde{u}}.\vec{\nabla})\vec{\bar{u}} = -\frac{1}{\rho}\vec{\nabla}\bar{p} - \frac{1}{\rho}\vec{\nabla}\tilde{p} + \nu\nabla^2\vec{\bar{u}} + \nu\nabla^2\vec{\tilde{u}} \ .$$

The basic flow is assumed to satisfy Navier–Stokes equations. One can check that the parallel basic flow assumption implies $\bar{p}(x, y, z) = \bar{p}(x)$, with a constant longitudinal basic pressure gradient (which may be zero). This implies respectively parabolic (plane Poiseuille) or linear (plane Couette) profiles for $\bar{u}$. In fact people chose $\bar{u}(y)$ quite arbitrarily. This may be justified assuming that the error due to the parallel-flow assumption is negligible within the linear-instability approach. One can also assume the existence of a forcing term in the equations of motion, whose role is to maintain the basic flow stationary.

Since the basic flow satisfies Navier–Stokes equations, one gets

$$\frac{\partial \vec{\tilde{u}}}{\partial t} + (\vec{\bar{u}}.\vec{\nabla})\vec{\tilde{u}} + (\vec{\tilde{u}}.\vec{\nabla})\vec{\bar{u}} = -\frac{1}{\rho}\vec{\nabla}p' + \nu\nabla^2\vec{\tilde{u}} \ , \tag{3.6}$$

with the continuity equation $\vec{\nabla}.\vec{\tilde{u}} = 0$. One can work also on the basis of the vorticity equation, as will be done below in two dimensions.

Notice that a parallel flow is solution of Euler equation for any function $\bar{u}(y)$ (with a uniform pressure).

3.3.1 Two-dimensional temporal analysis

It will be seen later that in many cases (free-shear flows at high Reynolds number in particular), small three-dimensional perturbations amplify slower than two-dimensional ones within the framework of linear-instability theory. This is a reason to study first the two-dimensional problem.

We assume the reference frame is not rotating, and that the total velocity field (basic flow + perturbation) is two-dimensional (no z-dependence) with $w = 0$. Incompressibility permits to use a stream function $\psi(x, y, t)$ such that

$$u = \frac{\partial \psi}{\partial y} \ , \quad v = -\frac{\partial \psi}{\partial x} \ . \tag{3.7}$$

The vorticity $\vec{\omega} = \omega\vec{z}$ is spanwise, of intensity

$$\omega = \partial v/\partial x - \partial u/\partial y = -\nabla_H^2 \psi \ , \tag{3.8}$$

with $\nabla_H^2 = \partial^2/\partial x^2 + \partial^2/\partial y^2$. We introduce the perturbations such that

$$\psi = \bar{\psi} + \tilde{\psi} \ , \quad \omega = \bar{\omega} + \tilde{\omega} \ ,$$

$$\bar{\omega} = -\frac{d\bar{u}}{dy} \ , \quad \tilde{\omega} = -\nabla_H^2 \tilde{\psi} \ . \tag{3.9}$$

The vorticity equation in this two-dimensional case reduces, from Eq. (2.75), to

$$\frac{D_H}{Dt}\omega = \nu \nabla_H^2 \omega \ , \tag{3.10}$$

since the flow is incompressible ($\vec{\nabla}.\vec{u} = 0$), and $(\vec{z}.\vec{\nabla})\vec{u} = \vec{0}$. In Eq. (3.10), $D_H/Dt = \partial/\partial t + u\partial/\partial x + v\partial/\partial y$ stands for the derivative following the horizontal motion.

Notice that, when studying the stability of a two-dimensional geophysical flow on a rotating sphere, one can make use of Barré de Saint-Venant equations with constant depth, which yields

$$\frac{D_H}{Dt} \ (\omega + f) = \nu \nabla_H^2 \omega \ . \tag{3.11}$$

This equation will be used later on in order to obtain the so-called Kuo equation, allowing one to study the influence of differential rotation upon the stability of parallel flows.

The linearized vorticity equation writes

$$\frac{\partial \tilde{\omega}}{\partial t} + \bar{u}(y)\frac{\partial \tilde{\omega}}{\partial x} + \tilde{v}\frac{d\bar{\omega}}{dy} = \nu \nabla_H^2 \tilde{\omega} \ . \tag{3.12}$$

This is a *linear* partial differential equation $L(\tilde{\psi}) = 0$ for the unknown function $\tilde{\psi}$, which is, up to now, real. Let us first show that the problem may be solved as well by looking for complex solutions of real and imaginary parts $\tilde{\psi}_r$ and $\tilde{\psi}_i$. Indeed,

$$L(\tilde{\psi}_r + i\tilde{\psi}_i) = 0 = L(\tilde{\psi}_r) + iL(\tilde{\psi}_i)$$

implies both $L(\tilde{\psi}_r) = 0$ and $L(\tilde{\psi}_i) = 0$. In other words, two real solutions can be associated to a complex solution. This leads to the so-called normal-mode analysis, where the perturbed stream function is sought in the form

$$\tilde{\psi} = \Phi(y) \ e^{i \ \alpha(x-ct)} \ , \tag{3.13}$$

where $\Phi(y)$ is complex. It corresponds to a "complex perturbed velocity field" of components $\tilde{u} = \partial\tilde{\psi}/\partial y$ and $\tilde{v} = -\partial\tilde{\psi}/\partial x$, i.e.,

$$\tilde{u} = \frac{d\Phi}{dy}\ e^{i\ \alpha(x-ct)}\ , \quad \tilde{v} = -\ i\alpha\Phi(y)\ e^{i\ \alpha(x-ct)} = -i\alpha\tilde{\psi}\ . \tag{3.14}$$

α is real, and is the spatial longitudinal wave number of the perturbation: this is a temporal analysis (where we have periodicity in the basic flow direction), as opposed to a spatial analysis where α is complex. In this temporal study, c is complex, of real and imaginary parts c_r and c_i. The phase-speed of the perturbation is c_r, while αc_i is its temporal-growth rate.

3.3.2 The two-dimensional Orr–Sommerfeld equation

The following remark allows to simplify the calculation: if a function is of the form $f(y)e^{i\ \alpha(x-ct)}$, its horizontal Laplacian is $D_{\alpha,0}f(y)e^{i\ \alpha(x-ct)}$ with

$$D_{\alpha,0} = \frac{d^2}{dy^2} - \alpha^2\ .$$

We have

$$\tilde{\omega} = -D_{\alpha,0}\Phi e^{i\ \alpha(x-ct)}\ , \quad \frac{\partial}{\partial t}\tilde{\omega} = -i\alpha c\ \tilde{\omega}\ , \quad \frac{\partial}{\partial x}\tilde{\omega} = i\alpha\ \tilde{\omega}\ .$$

Then Eq. (3.12) writes

$$i\alpha(\bar{u}-c)\tilde{\omega} + i\alpha\tilde{\psi}\frac{d^2\bar{u}}{\partial y^2} = -\nu D^2_{\alpha,0}\Phi e^{i\ \alpha(x-ct)}\ .$$

Multiplying by $e^{-i\ \alpha(x-ct)}$ gives

$$-i\alpha(\bar{u}-c)D_{\alpha,0}\Phi + i\alpha\Phi\frac{d^2\bar{u}}{\partial y^2} = -\nu D^2_{\alpha,0}\Phi\ .$$

Assuming that $\alpha \neq 0$, we have finally:

$$[\bar{u}(y)-c]\ \left(\frac{d^2\Phi}{dy^2} - \alpha^2\Phi\right) - \frac{d^2\bar{u}}{dy^2}\ \Phi = -\frac{i\nu}{\alpha}\ \left(\frac{d^2}{dy^2} - \alpha^2\right)^2\ \Phi\ , \tag{3.15}$$

which is the traditional form of the two-dimensional Orr–Sommerfeld equation. The boundary conditions at the two boundaries $y = y_A,\ y = y_B$ (which may also be rejected to infinity) are of the no-slip type for the perturbed velocity (since we are working with a non-zero viscosity), and hence, from Eq. (3.14): $\Phi = 0;\ d\Phi/dy = 0$. Orr–Sommergeld equation may be written in a non-dimensional form: we take a characteristic length and velocity, and obtain for the non-dimensional variables

$$[\bar{u}(y)-c]\ \left(\frac{d^2\Phi}{dy^2} - \alpha^2\Phi\right) - \frac{d^2\bar{u}}{dy^2}\ \Phi = -\frac{i}{\alpha R}\ \left(\frac{d^2}{dy^2} - \alpha^2\right)^2\ \Phi\ , \tag{3.16}$$

R being the Reynolds number built on the chosen units. Before studying the stability of viscous flows using Eq. (3.15), we will look at what can be said from the point of view of a perfect flow.

3.3.3 The Rayleigh equation

When viscous effects have a negligible influence in the evolution of the perturbed flow described by $\tilde{\psi}$, the above Orr–Sommerfeld equation simplifies to the Rayleigh equation:

$$[\bar{u}(y) - c] \left(\frac{d^2\Phi}{dy^2} - \alpha^2 \Phi \right) - \frac{d^2\bar{u}}{dy^2} \Phi = 0 \ , \tag{3.17}$$

with free-slip boundary counditions $\Phi = 0$ at $y = y_A,\ y = y_B$.

The problem to be solved is the following: for a given $\bar{u}$, we have to determine the values of α (real) and c (complex) for which Eq. (3.17) admits complex solutions, which will be noted $\Phi_{\alpha,c}$. A first and important remark concerning the possible solutions is that, if $\Phi_{\alpha,c}$ is a solution, then $\Phi^*_{\alpha,c}$ is also a solution corresponding to α (real) and c^* (here $*$ denotes the complex conjugate). In other words

$$\Phi_{\alpha,c^*} = \Phi^*_{\alpha,c} \ .$$

This is easily derived by taking the complex conjugate of Eq. (3.17). Since without loss of generality we may restrict ourselves to positive values of α, it turns out that, for any damped solution (such that $\alpha c_i < 0$), one may associate an amplified solution such that $\alpha(-c_i) > 0$. Therefore, the research of unstable modes is reduced to the research of non-neutral modes ($c_i \neq 0$). This is of course not valid for the Orr–Sommerfeld equation. A second remark concerns the critical points y (see e.g. Maslowe [474]), such that $\bar{u}(y) = c$. These points can exist only in the case of a neutral mode, since $\bar{u}(y)$ is evidently real. Therefore, eigen solutions corresponding to amplified modes[5] do satisfy Eq. (3.17) divided by $[\bar{u}(y) - c]$:

$$\Phi'' = \left[\frac{\bar{u}''}{\bar{u} - c} + \alpha^2 \right] \Phi \ , \tag{3.18}$$

where the suffix $'$ stands for the operator d/dy. In order to look for necessary conditions of instability, we assume hence that $c_i \neq 0$, and multiply Eq. (3.18) by Φ^*. Integrating from y_A to y_B, we obtain after an integration by parts and making use of the boundary conditions $\Phi = 0$:

$$\int_{y_A}^{y_B} \Phi''\Phi^* dy = [\Phi'\Phi^*]_A^B - \int_{y_A}^{y_B} \Phi'\Phi'^* dy = - \int_{y_A}^{y_B} |\Phi'|^2 dy$$

and

$$- \int_{y_A}^{y_B} \left(|\Phi'|^2 + \alpha^2 |\Phi|^2 \right) dy = \int_{y_A}^{y_B} |\Phi|^2 \, \frac{\bar{u}''(\bar{u} - c^*)}{|\bar{u} - c|^2} \, dy \ . \tag{3.19}$$

[5] If they exist.

The imaginary part of the r.h.s. must be zero, which yields

$$\int_{y_A}^{y_B} |\Phi|^2 \, \frac{\bar{u}''}{|\bar{u}-c|^2} \, dy = 0 \ , \tag{3.20}$$

since $c_i \neq 0$. Taking into account the fact that $|\Phi|$ cannot be zero everywhere, it implies that $\bar{u}''$ must change sign at least once on the $[y_A, y_B]$ interval, or, equivalently, that $\bar{u}$ admits at least one inflection point:[6] this necessary criterion of instability, known as the *Rayleigh inflection-point inviscid-instability criterion*, shows that basic velocity profiles such as the Blasius boundary-layer velocity profile on a flat plane, or the parabolic plane Poiseuille flow in a channel, are unconditionally stable from an inviscid point of view. In fact, it will be seen below that they are subject to viscous instabilities.

This criterion can be improved in the following manner: one still considers an unstable solution ($c_i \neq 0$), and looks at the real part of Eq. (3.19), which is written:

$$-\int_{y_A}^{y_B} (|\Phi'|^2 + \alpha^2 |\Phi|^2) \, dy = \int_{y_A}^{y_B} |\Phi|^2 \, \frac{\bar{u}''(\bar{u}-c_r)}{|\bar{u}-c|^2} \, dy \ . \tag{3.21}$$

We notice that the constant c_r arising in the r.h.s. may be replaced by any other constant, due to Eq. (3.20). This is true in particular if this constant is set equal to $\bar{u}(y_s)$, where y_s is any of the inflection points of $\bar{u}$. The result is that

$$\int_{y_A}^{y_B} |\Phi|^2 \, \frac{\bar{u}''[\bar{u}-\bar{u}(y_s)]}{|\bar{u}-c|^2} \, dy < 0 \ , \tag{3.22}$$

and $\bar{u}''[\bar{u}-\bar{u}(y_s)]$ must be negative somewhere, in order for the flow to be unstable. This is the *Fjortoft criterion*, which implies that $|d\bar{u}/dy|$, the absolute value of the basic vorticity, must have a local maximum at y_s (see Drazin and Reid [173] for details).

We consider first a temporal mixing layer of basic profile given by

$$\bar{u}(y) = U \ \tanh \frac{y}{\delta_0} \ , \tag{3.23}$$

(see Figure 3.1a).[7] It has an inflection point, and thus satisfies the Rayleigh criterion. Since $\bar{u}.\bar{u}''$ is negative everywhere, it satisfies also Fjortoft criterion. It is therefore expected to be unstable from an inviscid point of view. It

[6] The case $\bar{u}'' = 0$ everywhere, corresponding to a plane Couette flow, leads from Eq. (3.19) to $\Phi = 0$ on $[y_A, y_B]$. Therefore, there is in this case no amplified mode within the Rayleigh analysis.

[7] Notice, however, that the laminar or mean turbulent velocity profile of the temporal mixing layer is an error function. In fact, this is very close to a hyperbolic-tangent velocity profile.

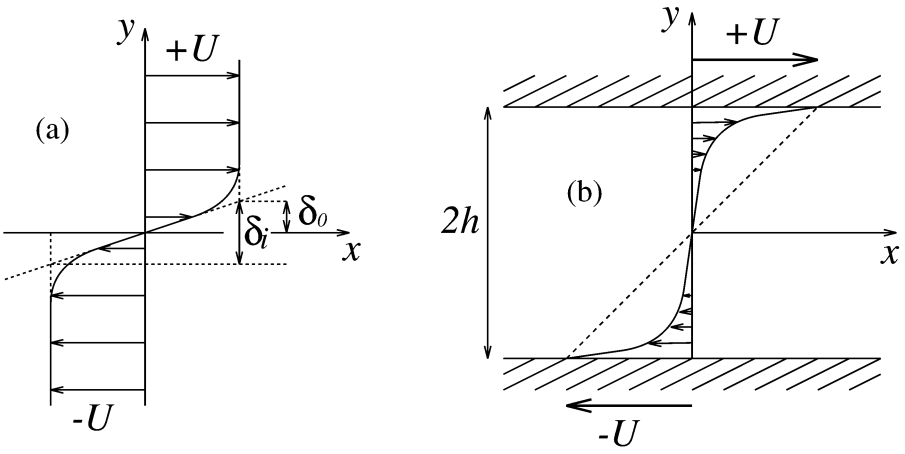

Figure 3.1. Basic velocity profiles in (a) the temporal mixing layer; (b) the turbulent plane Couette flow. For the latter, the dashed line indicates the linear laminar profile.

is indeed violently unstable (Kelvin–Helmholtz instability). The same holds for a plane jet or a wake. On the other hand, the basic velocity profile of the turbulent plane Couette flow (shown in Figure 3.1b) satisfies Rayleigh criterion (since it has an inflection point), but not Fjortoft ($\bar{u}.\bar{u}''$ is positive). Notice also that the two above criteria give only *necessary conditions* for the instability. These conditions are not always *sufficient*: for instance, the basic velocity profile $\sin y$ is stable.

Kuo equation

Let us consider Eq. (3.11), describing the two-dimensional horizontal motion of a flow on a rotating sphere. The Coriolis parameter f is given by Eq. (2.87). Let us consider a reference parallel of latitude φ_0, serving as an origin for the meridional coordinate y. The β-plane approximation consists in expanding f about φ_0 as

$$f = f_0 + \beta y \ , \tag{3.24}$$

$\beta = df/dy$ being assumed to be constant. If we perform a linear-instability analysis about a parallel flow $\bar{u}(y)$, the term $\tilde{v}\ d\bar{\omega}/dy$ in Eq. (3.12) has to be replaced by $\tilde{v}(\beta + d\bar{\omega}/dy)$, and the analogous Rayleigh equation for this problem, the Kuo equation, is (see Howard and Drazin [299])

$$[\bar{u}(y) - c]\ \left(\frac{d^2\Phi}{dy^2} - \alpha^2\Phi\right) + \left(\beta - \frac{d^2\bar{u}}{dy^2}\right)\ \Phi = 0 \ . \tag{3.25}$$

It is easy to check that Eq. (3.19) is now transformed into

$$-\int_{y_A}^{y_B} (|\Phi'|^2 + \alpha^2|\Phi|^2)\, dy = \int_{y_A}^{y_B} |\Phi|^2\, \frac{(\bar{u}'' - \beta)(\bar{u} - c^*)}{|\bar{u} - c|^2}\, dy\ . \qquad (3.26)$$

Therefore, the necessary criterion of instability is now that $(\bar{u}'' - \beta)$ must change sign. For a hyperbolic-tangent velocity profile of the form Eq. (3.23), this is not possible if

$$\beta > \frac{4}{3\sqrt{3}}\, \frac{U}{\delta_0^2} = 0.77 \frac{U}{\delta_0^2}\ , \qquad (3.27)$$

which is a critical value above which the instability cannot exist.

A two-dimensional DNS of the temporal mixing-layer submitted to differential rotation has been carried out by Laroche [381]. These calculations show that no rollup occurs for $\beta > 0.2$, although, from Eq. (3.27), the linear instability may develop.[8] For $0.05 < \beta < 0.2$, the roll up occurs, but the pairing is suppressed. As will be shown in Chapter 9, differential rotation is responsible for the propagation of Rossby waves, which limit the meridional extent of motions: the inhibition of the pairing is thus one of the aspects of this limitation. This range might correspond to realistic values of β for Earth atmosphere,[9] and also for Jupiter. This might explain why cyclonic depressions above the northern Atlantic rarely pair (André [8]), and could question the theories interpreting Jupiter's great red spot as the result of pairings of smaller-size eddies created in the shear between two neighbouring jets (Somméria et al. [661]).

3.3.4 Three-dimensional temporal normal-mode analysis

Non-rotating case

We go back to the non-rotating flow with a parallel basic profile, with notations of Eq. (3.6). We recall that the perturbed velocity field has for components $(\tilde{u}, \tilde{v}, \tilde{w})$. Let $\tilde{p} = p'/\rho$. The linearized equations write

$$\left(\frac{\partial}{\partial t} + \bar{u}\frac{\partial}{\partial x}\right)\tilde{u} + \tilde{v}\bar{u}' = -\frac{\partial \tilde{p}}{\partial x} + \nu\nabla^2\tilde{u}$$

$$\left(\frac{\partial}{\partial t} + \bar{u}\frac{\partial}{\partial x}\right)\tilde{v} = -\frac{\partial \tilde{p}}{\partial y} + \nu\nabla^2\tilde{v}$$

$$\left(\frac{\partial}{\partial t} + \bar{u}\frac{\partial}{\partial x}\right)\tilde{w} = -\frac{\partial \tilde{p}}{\partial z} + \nu\nabla^2\tilde{w}\ .$$

[8] β is here non-dimensionalized with U/δ_0^2.

[9] δ_0 and U being properly chosen with respect to the coherent eddies.

One carries out a normal-mode analysis, where the fluctuations take the form

$$(\tilde{u},\tilde{v},\tilde{w},\tilde{p}) = [\hat{u}(y),\hat{v}(y),\hat{w}(y),\hat{p}(y)]\; e^{i\;(\alpha x+\beta z-\varpi t)}\;, \tag{3.28}$$

where β (real) is the spanwise wave number of the perturbation, and ϖ is complex.[10] When substituted into the linearized equations, one obtains

$$i(\alpha\bar{u}-\varpi)\hat{u}+\bar{u}'\hat{v} = -i\alpha\hat{p}+\nu D_{\alpha,\beta}\hat{u}\;, \tag{3.29}$$

$$i(\alpha\bar{u}-\varpi)\hat{v} = -\hat{p}'+\nu D_{\alpha,\beta}\hat{v}\;, \tag{3.30}$$

$$i(\alpha\bar{u}-\varpi)\hat{w} = -i\beta\hat{p}+\nu D_{\alpha,\beta}\hat{w}\;, \tag{3.31}$$

with

$$D_{\alpha,\beta} = \frac{d^2}{dy^2}-(\alpha^2+\beta^2)\;.$$

The continuity equation yields

$$\alpha\hat{u}+\beta\hat{w} = i\hat{v}'\;. \tag{3.32}$$

Multiplying Eq. (3.29) by α and Eq. (3.31) by β and adding permits, with the use of Eq. (3.32), to express the pressure in terms of $\hat{v}$:

$$-(\alpha^2+\beta^2)\hat{p} = i(\alpha\bar{u}-\varpi)\hat{v}'-i\alpha\bar{u}'\hat{v}-\nu D_{\alpha,\beta}\hat{v}'\;.$$

Substituting into Eq. (3.30) gives

$$i(\alpha\bar{u}-\varpi)\hat{v} = \frac{i}{\alpha^2+\beta^2}[(\alpha\bar{u}-\varpi)\hat{v}''-\alpha\bar{u}''\hat{v}]-\frac{\nu}{\alpha^2+\beta^2}D_{\alpha,\beta}\hat{v}''+\nu D_{\alpha,\beta}\hat{v}\;, \tag{3.33}$$

or equivalently

$$i(\alpha\bar{u}-\varpi)\left[\hat{v}-\frac{\hat{v}''}{\alpha^2+\beta^2}\right]+\frac{i\alpha}{\alpha^2+\beta^2}\bar{u}''\hat{v} = \nu D_{\alpha,\beta}\left[\hat{v}-\frac{\hat{v}''}{\alpha^2+\beta^2}\right]\;,$$

which writes finally

$$(\alpha\bar{u}-\varpi)D_{\alpha,\beta}\hat{v}-\alpha\bar{u}''\hat{v} = -i\nu D^2_{\alpha,\beta}\hat{v}\;. \tag{3.34}$$

This is for $\hat{v}(y)$ an equation having similarities with Eq. (3.15) multiplied by α, where α^2 has been replaced by $\alpha^2+\beta^2$, and αc by ϖ. In non-dimensional variables, this three-dimensional Orr–Sommerfeld equation reads:

$$[\alpha\bar{u}(y)-\varpi]\;\left[\frac{d^2\hat{v}}{dy^2}-(\alpha^2+\beta^2)\hat{v}\right]-\alpha\frac{d^2\bar{u}}{dy^2}\;\hat{v} = -\frac{i}{R}\;\left[\frac{d^2}{dy^2}-(\alpha^2+\beta^2)\right]^2\;\hat{v}\;. \tag{3.35}$$

The boundary conditions are $\hat{v}=0$ and $\hat{v}'=0$ at y_A and y_B in the no-slip case, and $\hat{v}=0$ in the free-slip case.

[10] Remark that a possible contibution $e^{i\gamma y}$ in the exponential has been included in the amplitudes $\hat{u},\hat{v},\hat{w},\hat{p}$.

Squire's theorem

We consider first the case $\alpha \neq 0$. We pose

$$\alpha_{2D}^2 = \alpha^2 + \beta^2 \ , \quad R_{2D} = \frac{\alpha}{\alpha_{2D}} \ R \ . \tag{3.36}$$

Eq. (3.35) is identical to Eq. (3.16) with the following changes of variables. Let us consider a solution of three-dimensional Orr–Sommerfeld equation characterized by $\alpha \neq 0$ (longitudinal wave number), β (spanwise wave number), ϖ_i (imaginary part of ϖ, amplification rate), and R (Reynolds number). Then it is solution of two-dimensional Orr–Sommerfeld equation characterized by a wave number α_{2D}, an amplification rate $(\alpha_{2D}/\alpha)\varpi_i$, and a Reynolds number R_{2D}. If for instance the three-dimensional solution is unstable ($\varpi_i > 0$), then the dual two-dimensional solution will more amplified, with smaller wavelength and Reynolds number. It turns out that if one looks for critical Reynolds numbers of linear instability, a two-dimensional analysis is sufficient: indeed, an unstable three-dimensional mode will correspond to a two-dimensional unstable mode with a smaller Reynolds. If one considers an inviscid instability at infinite Reynolds number, and vary the wavevector (α, β) of the perturbation, the mode with the highest amplification rate (most amplified mode) will be two-dimensional. But Squire's theorem does not imply that, for a given finite Reynolds number, the most amplified mode will be two-dimensional. This was discussed by Casalis [101] for the Blasius boundary layer.

In principle, Squire's theorem does not apply directly to purely longitudinal modes ($\alpha = 0$). Orr–Sommerfeld equation Eq. (3.35) yields in this case

$$\left(\frac{d^2}{dy^2} - \beta^2\right)^2 \hat{v} = sR \left(\frac{d^2}{dy^2} - \beta^2\right) \hat{v} \tag{3.37}$$

with $s = -i\varpi$. Here s has to be real, in order to have standing waves which do not propagate in the spanwise direction. One can show that there are no non-zero solutions for $s > 0$, which means stability (in the sense of the normal-mode approach where a solution proportional to e^{st} is sought for).

Solid-body rotation

As an exercise, we perform now the three-dimensional linear-instability analysis of a basic parallel flow submitted to a solid-body rotation of entrainment vorticity $2\vec{\Omega} = f\vec{z}$. The parameter f may here be positive or negative, according to the sense of rotation. The linearized equations are now

$$\left(\frac{\partial}{\partial t} + \bar{u}\frac{\partial}{\partial x}\right) \tilde{u} + \tilde{v}(\bar{u}' - f) = -\frac{\partial \tilde{p}}{\partial x} + \nu \nabla^2 \tilde{u} \ ,$$

$$\left(\frac{\partial}{\partial t}+\bar{u}\frac{\partial}{\partial x}\right)\tilde{v}=-\frac{\partial\tilde{p}}{\partial y}-f\tilde{u}+\nu\nabla^2\tilde{v}\ ,$$

$$\left(\frac{\partial}{\partial t}+\bar{u}\frac{\partial}{\partial x}\right)\tilde{w}=-\frac{\partial\tilde{p}}{\partial z}+\nu\nabla^2\tilde{w}\ .$$

With a fluctuation of the form (3.28), we just look for longitudinal inviscid modes ($\alpha=0,\nu=0$). One gets (with $s=-i\varpi$)

$$s\hat{u}+(\bar{u}'-f)\hat{v}=0$$

$$s\hat{v}=-\hat{p}'-f\hat{u}$$

$$s\hat{w}=-i\beta\hat{p}\ ,\quad \beta\hat{w}=i\hat{v}'\ .$$

It yields

$$\hat{p}=-\frac{s}{\beta^2}\hat{v}'\ ,\quad s\hat{v}=\frac{s}{\beta^2}\hat{v}''-f\hat{u}\ ,$$

and finally

$$\left(\frac{d^2}{dy^2}-\beta^2\right)\hat{v}=\frac{\beta^2}{s^2}f(f-\bar{u}')\hat{v}\quad ,$$

or equivalently

$$\left(\frac{d^2}{dy^2}-\beta^2\right)\hat{v}=\frac{\beta^2 f^2}{s^2}[1+R_o(y)]\hat{v}\quad , \tag{3.38}$$

where

$$R_o(y)=-\frac{\bar{u}'}{f} \tag{3.39}$$

is a local Rossby number. When it is positive, the flow is locally cyclonic (vorticity of same sign as the entrainment rotation), while a negative sign implies local anticyclonicity. Eq. (3.38) was studied by Pedley [566] (see also Yanase et al. [730]). As stressed by Drazin and Reid [173, p. 78], it corresponds to a classical eigenvalue problem of the Stürm–Liouville type, and a necessary and sufficient condition for instability is (with $\hat{v}=0$ on y_A and y_B) that

$$R_o(y)<-1 \tag{3.40}$$

somewhere in the flow.[11] The corresponding instability was called *shear-Coriolis instability* by Yanase et al. We will see in Chapter 12 how to interpret this result physically in terms of appearance of longitudinal vortices, as far as absolute vorticity is concerned. We just mention that DNS starting with the basic laminar profiles perturbed by weak random perturbations do confirm the above instability condition in the case of periodic mixing layers

[11] This condition was also derived by Bradshaw [78] from an analogy with stratified flows.

and wakes (Métais et al. [498]) and of a plane Poiseuille flow (Lamballais et al. [366–369]).

Remark that inviscid linear centrifugal instabilities are, for axisymmetric modes, governed by an equation very close to Eq. (3.38):

$$\left[\frac{d}{dr}\left(\frac{d}{dr}+\frac{1}{r}\right)-\beta^2\right]\hat{v}=\frac{\beta^2}{s^2}\Phi\hat{v} \quad , \tag{3.41}$$

where r is the distance to the axis, and $\Phi(r) = (1/r^3)(d/dr)(r^2\Omega)^2$ is the Rayleigh discriminant based on the local angular velocity $\Omega(r)$. We recover the famous Rayleigh criterion for centrifugal instability, stating that a necessary and sufficient condition for instability is that $\Phi < 0$ somewhere in the flow.

3.3.5 Non-normal analysis

A linearized approach

We go back to the non-rotating case. We have seen with Eq. (3.37) that no longitudinal mode is unstable with a perturbation proportional to $e^{-i\varpi t}$. Here, and still in the framework or a linear analysis, we are going to look for different solutions. We consider the vorticity equation (2.75), and linearize it. We take first a quite general basic flow $\vec{u}_{2D}(x,y,t)$, two-dimensional in the x,y plane, of zero spanwise component, and of vorticity $\vec{\omega}_{2D} = \omega_{2D}\vec{z}$. We superimpose a three-dimensional velocity $\vec{u}^{(1)}(x,y,z,t)$ of small amplitude with respect to the basic flow,[12] and of components $\tilde{u},\tilde{v},\tilde{w}$. Let

$$\vec{\omega}^{(1)}(x,y,z,t)=\vec{\nabla}\times\vec{u}^{(1)}$$

be the perturbed vorticity, of components $\tilde{\omega}_x,\tilde{\omega}_y,\tilde{\omega}_z$. An expansion of the vorticity equation with respect to the small parameters $|u^{(1)}/u_{2D}|$ and $|\omega^{(1)}/\omega_{2D}|$ (assumed to be of the same order) yields to the first order

$$\frac{D_{2D}}{Dt}\vec{\omega}^{(1)}=\vec{\omega}^{(1)}.\vec{\nabla}\vec{u}_{2D}+\omega_{2D}\,\frac{\partial}{\partial z}\vec{u}^{(1)}-\vec{u}^{(1)}.\vec{\nabla}\vec{\omega}_{2D}+\nu\nabla^2\vec{\omega}^{(1)} \ . \tag{3.42}$$

We suppose now that the basic flow is a parallel flow $\bar{u}(y)$. The linearized vorticity equation yields then:

$$\frac{D_{2D}}{Dt}\tilde{\omega}_x-\nu\nabla^2\tilde{\omega}_x=\bar{u}'\left(\tilde{\omega}_y-\frac{\partial\tilde{u}}{\partial z}\right)=-\bar{u}'\frac{\partial\tilde{w}}{\partial x} \ , \tag{3.43}$$

[12] The latter may not be parallel, and the following analysis may serve for secondary-instability studies.

$$\frac{D_{2D}}{Dt}\tilde{\omega}_y - \nu\nabla^2\tilde{\omega}_y = -\bar{u}'\frac{\partial\tilde{v}}{\partial z} \ , \tag{3.44}$$

$$\frac{D_{2D}}{Dt}\tilde{\omega}_z - \nu\nabla^2\tilde{\omega}_z = -\bar{u}'\frac{\partial\tilde{w}}{\partial z} + \bar{u}''\tilde{v} \ . \tag{3.45}$$

This set of equations expresses the rate of change of the perturbed vorticity following the basic flow. The first one shows that there cannot be production of longitudinal vorticity in a longitudinal mode.[13] On the other hand, Eq. (3.44) shows that the vertical vorticity ω_y may increase approximately linearly (if viscous effects are neglected and $\partial\tilde{v}/\partial z$ is treated as a constant). This provides in particular an amplified longitudinal solution, where longitudinal vorticity is conserved following the basic flow, while $\tilde{\omega}_y = \partial\tilde{u}/\partial z$ will grow linearly. In other words, weak vertical oscillations of the flow in planes parallel to (x, y) (responsible for the creation of $\partial\tilde{v}/\partial z$) will produce alternate longitudinal velocity oscillations whose amplitude has a linear (and not exponential) growth. This is reminiscent of longitudinal velocity streaks (which produce vorticity oriented in the y direction) found in developed turbulent boundary layers. Algebraic instabilities of this type, which are not accounted for within the linear normal-mode analysis, have been proposed by Landhal (see e.g. Landhal and Mollo-Christensen [372, pp. 115–122]) to explain the growth of low and high-speed streaks in these flows close to the wall. This is also commented in the book of Schmidt and Henningson [637]. We will discuss Eq. (3.45) in Chapter 4.

Recent results concerning these approaches may be found in the stimulating book of Schmidt and Henningson [637].

The velocity-sheets model

As an exercise, we propose an exact solution (without any linearization) of Navier–Stokes equation in a constant shear within an infinite domain, having some of the features of the amplified longitudinal solution we have just considered. We assume a basic parallel flow of constant shear $\lambda = \bar{u}'(y)$, which has to be obtained by some type of forcing. We look for a perturbed real velocity (with respect to the basic flow) of the form

$$\underline{\tilde{u}} = U(z)\ [X(t)\ \vec{x} + Y(t)\ \vec{y}]\,, \tag{3.46}$$

and assume a zero spanwise velocity w and a uniform pressure. The vorticity of the perturbed field

[13] This result is valid even in the fully nonlinear regime: indeed, in case of independance with respect to x, the spanwise and transverse velocity components satisfy a two-dimensional Navier–Stokes equation, in which the vorticity $\tilde{\omega}_x$ cannot increase (see Chapter 8).

$$\underline{\tilde{\omega}} = \frac{dU}{dz}(-Y\ \vec{x} + X\ \vec{y})$$

is perpendicular to the perturbed velocity. Substituting into Navier–Stokes equations, it is obtained

$$U(z)\left(\frac{dX}{dt} + \lambda Y\right) = \nu U''(z)X\ , \quad U(z)\frac{dY}{dt} = \nu\ U''(z)Y\ . \tag{3.47}$$

This is possible only if $U(z)$ and its second derivative are proportional, which implies that $U(z)$ is a sine function:

$$U(z) = \sin \beta z\ ,$$

where β is the spanwise wave number of the perturbation. Therefore Navier–Stokes is satisfied if

$$\frac{dY}{\partial t} = -\nu\beta^2 Y\ , \quad \frac{dX}{\partial t} + \lambda\ Y = -\nu\beta^2 X\ ,$$

whose solutions are

$$Y = Y_0\ e^{-\nu\beta^2 t}\ , \quad X = (X_0 - \lambda\ Y_0 t)\ e^{-\nu\beta^2 t}\ ,$$

which gives

$$\tilde{u} = (\tilde{u}_0 - \lambda\tilde{v}_0 t)e^{-\nu\beta^2 t}\ , \quad \tilde{v} = \tilde{v}_0 e^{-\nu\beta^2 t}\ , \tag{3.48}$$

where the suffix $_0$ stands for the initial instant. Thus, the vertical velocities and longitudinal vorticities are damped with time. There is no vortex stretching in the longitudinal direction within this model. To simplify, one supposes $\tilde{u}_0 = 0$. This provides a streaky pattern where:

- fluid sheets parallel to the x, y plane rise or sink (with a vertical velocity damped with time),
- the rising sheets are of the low-speed type ($\tilde{u} < 0$), while the sinking sheets correspond to high speed ($\tilde{u} > 0$).

The longitudinal velocity amplitude (and the vorticity ω_y) is proportional to $\lambda t e^{-\nu\beta^2 t}$: it increases up to

$$t_\nu = \frac{1}{\nu\beta^2}\ , \tag{3.49}$$

then decreases. For $t \ll t_\nu$, one recovers an inviscid linear growth. The flow is schematically shown in Figure 3.2: vertical oscillations (damped viscously) produce longitudinal oscillations which grow first linearly with time and then dissipate. The angle formed by the perturbed vorticity and the horizontal plane is characterized by its tangent, equal to λt. Thus, at large times, the

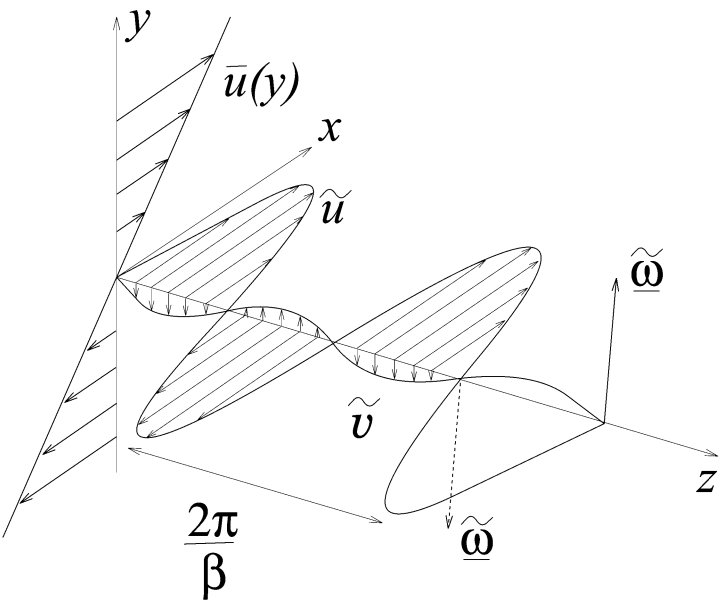

Figure 3.2. Schematic view of velocity and vorticity fluctuations in the velocity-sheets model.

perturbed vorticity tends to be vertical.[14] The maximum longitudinal fluctuating velocity is (in modulus)

$$\tilde{u}_m = \frac{\lambda \tilde{v}_m}{\nu \beta^2} = R_e^{(\beta)}\ \tilde{v}_0\ , \tag{3.50}$$

where

$$R_e^{(\beta)} = \frac{\lambda}{e\nu\beta^2} \approx 10^{-2} \left(\frac{l_z}{l_\nu}\right)^2 \tag{3.51}$$

is a sort of Reynolds number characteristic of the efficiency of the streaking mechanism. $l_z = 2\pi/\beta$ is the spanwise wavelength of the instability, and

$$l_\nu = \left(\frac{\nu}{\lambda}\right)^{1/2} \tag{3.52}$$

[14] As noticed by Métais et al. [497], the total local helicity of the flow is

$$\frac{1}{2}\vec{u}.\vec{\omega} = \frac{1}{2}\bar{u}(y)\frac{dU}{dz}Y(t)\ ,$$

which tends to zero at large times with Y.

is a viscous length associated to the shear. If $R_e^{(\beta)}$ is high enough, the longitudinal velocity attained will be much larger than the initial vertical velocity. Eqs. (3.51) and (3.52) show also that this instability will be all the more active than the spanwise wavelength $2\pi/\beta$ is large.

In the following, such a model will be called the "velocity-sheets model". We will discuss later to which extent it may represent the low and high-speed streaks observed at the wall in turbulent-boundary layers. One defect is that, due to the uniform-pressure assumption done, it is unable to reproduce pressure troughs induced by Λ-shaped vortices which form in reality.

The influence of rotation upon this model will be looked upon in Chapter 13.

3.4 Transition in free-shear flows

3.4.1 Mixing layers

We start by considering the temporal mixing layer, which is, periodic in the x direction, of basic velocity profile given by Eq. (3.23). This velocity profile is shown in Figure 3.1a. Let $\delta_i = 2\delta_0$ be the initial vorticity thickness. This is an approximation of the more realistic spatial mixing layer, where the two parallel flows which mix have two different velocities $U_1 > U_2$ of same sign: if one takes a reference frame moving with the average velocity $(U_1 + U_2)/2$ and neglects locally the lateral spreading of the layer in the y direction, one recovers a temporal mixing layer such that $U_1 - U_2 = 2U$; therefore, the distance x downstream of the splitter plate behind which the flows are in contact in the spatial mixing layer will correspond to $t = 2x/(U_1 + U_2)$ in the temporal mixing layer.

Two-dimensional structure

The two-dimensional stability diagram of the temporal mixing layer, obtained from a numerical solution of the Orr–Sommerfeld equation, is shown in Figure 3.3 (taken from Betchov and Szewczyk [61]). Here, U_0 and L correspond to U and δ_0 in Eq. (3.23). On the figure, the neutral curve separates the region with negative amplification rates αc_i (stable) from the region with positive αc_i (unstable). In two dimensions and for a given Reynolds number, there exists a range of unstable modes α. It may be shown that their amplification rate αc_i is maximum for a wave number α_a, called the most-amplified wave number. It is this mode which is expected to be selected if a two-dimensional initial perturbation, superposed upon the basic hyperbolic-tangent velocity profile, contains an equal amount of energy in all the unstable modes: indeed, the perturbations grow exponentially with time, and the one with the

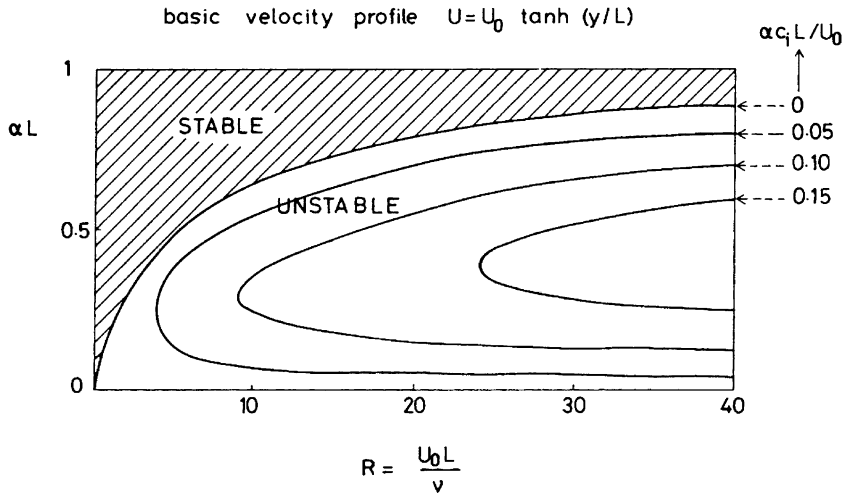

Figure 3.3. Two-dimensional linear-stability diagram of the mixing-layer instability in the (α, R) domain (non-stratified case). The different curves correspond to various rates of amplification αc_i. Under the neutral curve ($c_i = 0$), the flow is unstable (from Betchov and Szewczyk [61], courtesy of *The Physics of Fluids*).

highest amplification rate will grow to finite amplitude before the other unstable modes will have time to develop. This has been verified for instance in the case of a two-dimensional white-noise perturbation by Lesieur et al. [420].

When the Reynolds number exceeds values of the order of $30 \sim 40$, the amplification rates are no longer affected by viscosity, and the instability becomes inviscid, in the sense that it is well described by the Rayleigh equation. The most amplified wave number, calculated by Michalke [503], is given by

$$\alpha_a = 0.44\ \delta_0^{-1}\ , \tag{3.53}$$

corresponding to a spatial wave length

$$\lambda_a = 14\ \delta_0\ . \tag{3.54}$$

The mechanism of instability may be described in the following manner (see Batchelor [50] and Drazin and Reid [173]): let us consider a longitudinal stripe of rotational fluid (approximately of width $2\delta_0$) in the x, y plane, separating the two irrotational regions corresponding to the uniform flows of respective velocity U and $-U$ (see Figure 3.4). Suppose that this rotational zone is perturbed and undulates in a sine wave about the line $y = 0$ with a longitudinal wavelength λ_a (Figure 3.4a). First, pressure differences between the two layers, analogous to those induced on both sides of an airfoil, will be responsible for

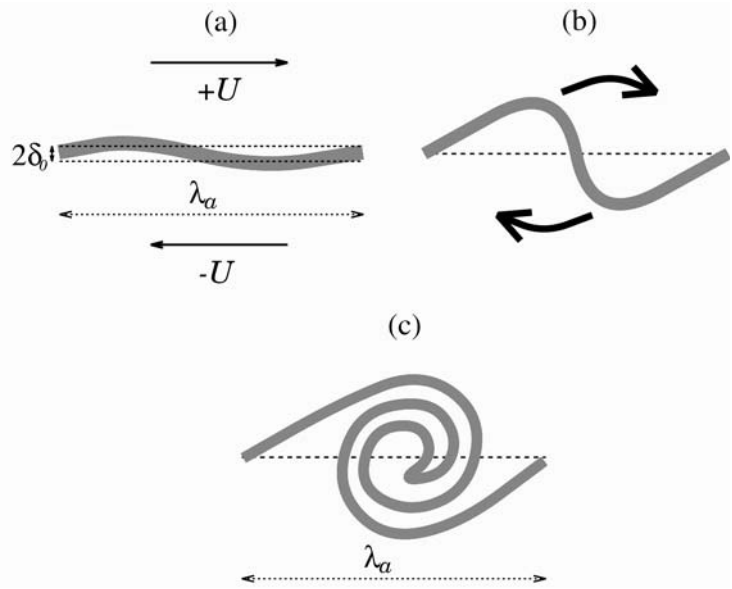

Figure 3.4. Schematic illustration showing the formation of spiralling Kelvin–Helmholtz vortices in a mixing layer.

the growth of the perturbation amplitude. Second, and since $d^2\bar{u}/dy^2 \approx 0$ in the neighbourhood of the inflection point, the inviscid equation (3.12) implies that the total vorticity is convected by the basic flow $\bar{u}(y)$. Hence, the crests of disturbance (in the region $y > 0$) and the troughs of disturbance ($y < 0$) will travel in opposite directions. This will steepen the vortex sheet (Figure 3.4b), and velocity-induction will transform the sheet into a spiral (Figure 3.4c). The vortices have initially a longitudinal wave length λ_a. This instability will be called here the Kelvin–Helmholtz instability, the resulting vortices being Kelvin–Helmholtz vortices. Vortex roll up may also be understood using the so-called displaced fluid particle arguments: a fluid particle located initially at $y = 0$ (where the vorticity is maximum) and moved towards the regions $y > 0$ or $y < 0$ will keep its vorticity,[15] and therefore will be surrounded by fluid of weaker vorticity, which will induce the roll up by velocity induction.

Afterwards, the two-dimensional evolution of the layer can be investigated by means of direct-numerical simulations: Plates 7 and 8, taken from Comte [134], present the time evolution of a temporal mixing layer in a square domain of size equal to 8 fundamental wave lengths: the vorticity (left) shows how the fundamental eddies form, then undergo successive pairings. A passive scalar

[15] We recall that, in two dimensions (without viscosity), vorticity is transported following the velocity field.

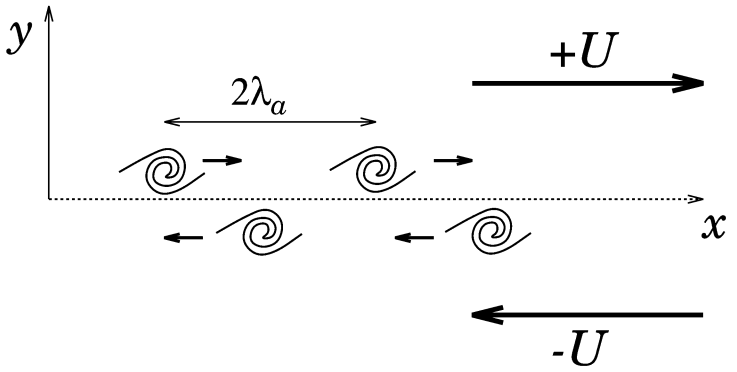

Figure 3.5. Initial stage of the two-dimensional subharmonic instability leading to a pairing.

(right) plays the role of a numerical dye marking the two streams, and shows how the coherent vortices mix the two flows. The first pairing occurring in coherent vortex the row of primary vortices may be understood in terms of a two-dimenional subharmonic instability of wave length $2\lambda_a$, as is shown in Figure 3.5. Indeed, suppose that the phase of this subharmonic perturbation is such that vortices are either lifted into the upper region ($y > 0$) or pushed down in the region $y < 0$. If one remembers that, within linear-instability analysis, the vorticity is transported by the basic flow, vortices in the upper region will be pushed against vortices in the lower region. Then, velocity induction mechanisms will act: each vortex will tend to entrain the other in the irrotational motion it induces outside, so that the vortices will roll up about each other. Since the irrotational motion induced a distant r apart from each vortex centre has an angular velocity $v/r \propto r^{-2}$, the outer part of both vortices will turn slower than the inner part, and they will develop a tail. Such tails are clear in Plate 2. During the pairing, the tails will mix into spirals.

These pairings present striking similarities with van Gogh's starry night (see Figure 3.6), where one can see an astonishing representation of pairing vortices, which are going to pair with a third vortex. From the title, the painter seems to have reprensented ensemble of stars in galaxies. He did not know that many galaxies are composed of black holes, which are huge vortices which may pair also. In fact it is probable that van Gogh met in France japonese painters of the famous Utagawa school, who painted vortices in currents similar to those due to Hiroshige shown in Lesieur [424, p. 63]. It is also of interest to remark that instabilities corresponding to roll up and pairing and referred to as

Figure 3.6. Vincent van Gogh (1889): *Starry night.* Courtesy DIGITAL IMAGE ©2007, The Museum of Modern Art/Scala, Florence.

"starry" by reference to van Gogh's painting have been found by neurologists to explain the cell structure in the brain.

Notice also that the features of the passive-scalar field in Plates 7 and 8 are reminiscent of the experimental visualizations of a spatially-growing mixing layer between two reacting flows carried out by Koochesfahani and Dimotakis [342]. More generally, these types of mixing layers are very important for their application to non-premixed combustion..

Temporal mixing-layer experiments are difficult to realize experimentally, although they may be much more relevant to geophysical situations. However, there is a less known aspect of Reynolds' [592] historical paper on transition, where he remarked that the pipe flow was difficult to destabilize. He then performed a second experiment involving two fluids of different densities ρ_1 and ρ_2 in a slightly inclined tube (with the lighter fluid on the top), and stressed that such a flow could be destabilized much more easily. Let us quote him:

> A glass tube (...) having its ends slightly bent up (...) was half filled with bisulphide of carbon, and then filled up with water and both ends corked. The bisulphide was chosen as (...) little heavier than water and completely insoluble, the surface between the two liquids being clearly distinguishable (...). On one end of the tube being slightly raised the water would flow to the upper end and the bisulphide fall to the lower, causing opposite currents along the upper and lower halves of the tube (...). When one end was raised quickly (...), (and) at a certain definite inclination, waves (nearly stationary) showed themselves, presenting all the appearance of wind waves (...), (and) of length being comparable to the diameter of the tube. (...) When the rise was sufficient, the waves would curl and break, the one fluid winding itself into the other in regular eddies.

This is obviously a very thorough description of Kelvin–Helmholtz vortices forming in a temporal mixing layer. This experiment was redone later on in greater details by Thorpe [688], who shows the formation of a row of Kelvin–Helmholtz vortices very much resembling the passive-scalar distribution of the calculation presented in Plate 7, when the primary vortices form. In such an experiment, the density difference is essential to create the mixing layer and hence the instability. On the other hand, it is well known (see Miles [505], Howard [298], and Drazin and Reid [173]) that the instability saturates if the density difference exceeds the value corresponding to a local Richardson number of 0.25. This number is defined as

$$R_i = -g\Delta\bar{\rho}_* \frac{\delta}{U^2} \ ,$$

where $\Delta\bar{\rho}_*$ is the difference between the upper and lower layer of $\bar{\rho}/\rho_0$ (for a liquid) and $-\bar{\Theta}/\Theta_0$ (for a gas), while δ is the local vorticity thickness.[16] A schematic picture of this second Reynolds experiment in a tilted pipe is shown in Figure 3.7. Rows of Kelvin–Helmholtz vortices thus frozen by stratification are often encountered in the atmosphere in the wake of mountains. We have already presented in Plate 1 a two-dimensional numerical simulation of a spatially-growing mixing layer, performed by Normand et al. [536]. This calculation is forced by a small random perturbation at the inflow, superposed upon the incoming hyperbolic-tangent velocity profile. This is done in order to model the turbulent fluctuations brought by the boundary layers developing along the splitter plate in the experiment. In this calculation,

[16] With no shear, a negative value of the Richardson number (properly defined) will correspond to thermal convection, provided the Rayleigh number (see below) is high enough. For positive high values of the Richardson number, the stratification is preponderant. For positive small values, on the other hand, inertial forces dominate. In the stably-stratified case, one may introduce a Froude number $F = U/(N\delta)$, with $N^2 = -g\Delta\bar{\rho}_*/\delta$, and equal to $R_i^{-1/2}$.

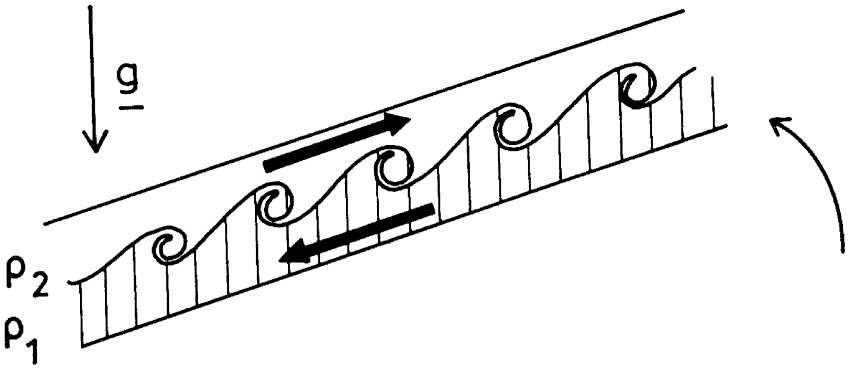

Figure 3.7. Formation of Kelvin–Helmholtz billows and transition to turbulence in Reynolds' stratified tilted pipe.

Kelvin–Helmholtz instability develops following the mean flow: as in the temporal case, Kelvin–Helmholtz vortices form by roll up, pair, and are finally carried away downstream, out of the computational domain. Analogous calculations, where the inflow is forced at the fundamental with a random phase, were made by Lowery and Reynolds [455].

Three-dimensional structure

Although, as already stressed in Chapter 1, the two-dimensional simulation seems to represent quite well the large-scale coherent-vortex dynamics of the experiments, it cannot of course simulate the transition to small-scale fully-developed turbulence. Experiments (see e.g. the review by Ho and Huerre [286]) do show that this transition occurs after the first pairing. Thin longitudinal vortex tubes of opposite sign interconnecting the Kelvin–Helmholtz billows, (see e.g. Konrad [341], Breidenthal [80], Bernal and Roshko [56], Jimenez [314], Lasheras et al. [383], and Lasheras and Choi [384]) seem to play a role in this transition: they are highly distorted during the pairing, and give rise to small-scale three-dimensional turbulence. The topology of secondary vortex filaments stretched between the primary vortices was recovered numerically in temporal mixing layers by Meiburg [481] (see also Ashurst and Meiburg [19]) using vortex-filament methods, and by Metcalfe et al. [501] (see also Rogers and Moser [615]) with three-dimensional direct-numerical simulations using pseudo-spectral methods.

The origin of these filaments is still subject to discussions: In Breidenthal's [80] experiment, this author notes a *wiggle disturbance* in the outer edge of the billows, from which the longitudinal vortices originate, due to *the global*

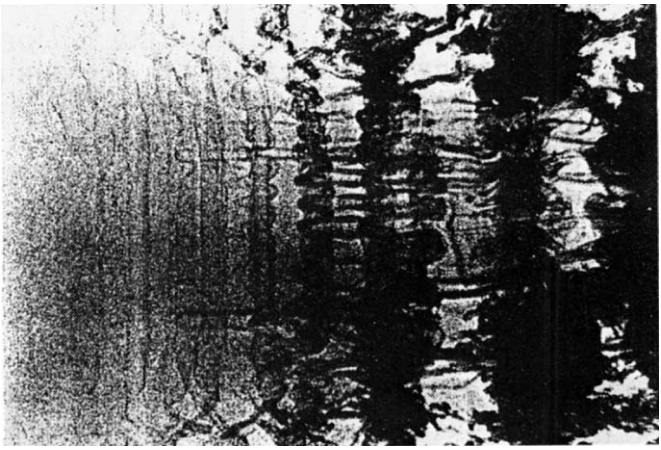

Figure 3.8. Plan view of Breidenthal's [80] mixing-layer experiment, showing the development of a sinuous spanwise instability of the Kelvin–Helmholtz billows. Simultaneously, longitudinal vortices form downstream (courtesy of Cambridge University Press).

strain field of the flow (*sic*). This is shown in Figure 3.8, taken from this reference. In this experiment, the spanwise wave length of the oscillation is 1.1 λ, where λ is the longitudinal wave length of the local Kelvin–Helmholtz billows. The topology of these hairpin vortices in the mixing layer downstream, when small-scale turbulence has developed, has been experimentally reconstructed by Bernal and Roshko [56], who propose a hairpin-shaped vortex filament, *which loops back and forth between adjacent primary vortices* (*sic*, see Figure 3.9) with an average spanwise wave length of $\approx (2/3)\lambda$. This spanwise spacing scales downstream with λ. A cross section view of these longitudinal vortices in Bernal and Roshko's experiment is shown in Figure 3.10. In fact, Huang and Ho [302] showed in their experiment that the spanwise spacing of the longitudinal vortices doubled at each pairing of the primary vortices.

Some people interpret these longitudinal filaments as a consequence of the *translative instability*, discovered by Pierrehumbert and Widnall [573], on the basis of a three-dimensional linear secondary-instability analysis (Floquet analysis) performed on a row of two-dimensional Stuart vortices: this instability consists of a global sinuous spanwise oscillation of the primary billows. The most-amplified spanwise wave length λ_s of the instability is found to be

$$\lambda_s \approx \frac{2}{3}\lambda \,, \tag{3.55}$$

where λ is the longitudinal wavelength of the two-dimensional vortices. This accords well with Bernal and Roshko's [56] experiments. However experiments

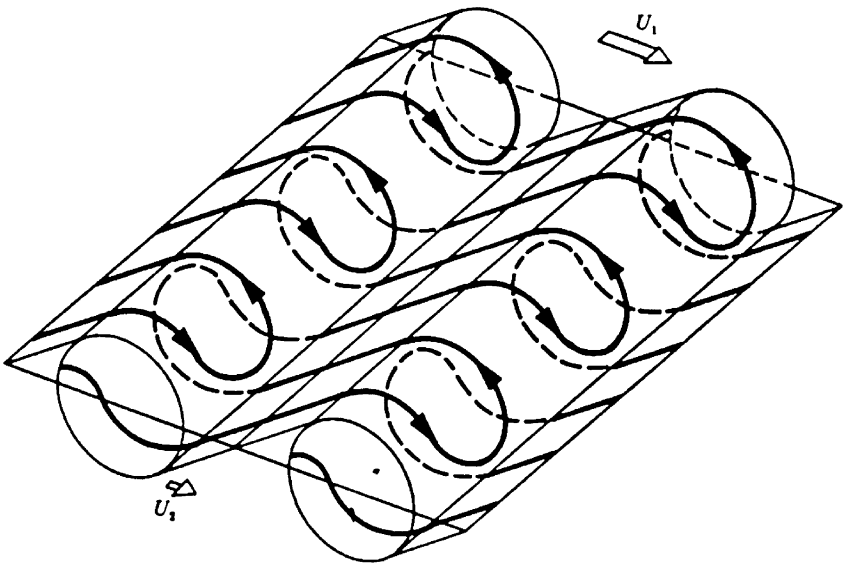

Figure 3.9. Topology of streamwise vortex lines in the mixing layer, as proposed by Bernal and Roshko [56] from their experiments (courtesy of Cambridge University Press).

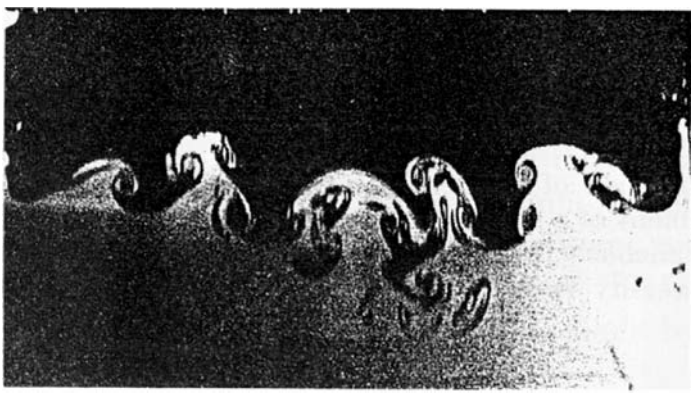

Figure 3.10. Cross-section of the longitudinal vortices in the experiments of Bernal and Roshko [56]; the flow direction is normal to the figure (courtesy of Cambridge University Press).

and numerical simulations show clearly that the hairpin vortices are much thinner than the primary billows. It is therefore difficult to consider the hairpin vortices as the eventual evolution of a sinuous oscillation of the billows.

There is another explanation of the hairpins, which may be found in Corcos and Lin [144] (see also Neu [531]). It can be explained as follows. Weak vorticity existing initially in the stagnation region between the spiral vortices will be stretched longitudinally in the following way: let us consider the vorticity equation, written for a perfect fluid of uniform density as

$$\frac{D\vec{\omega}}{Dt} = \vec{\nabla}\vec{u} \otimes \vec{\omega} = \overline{\overline{S}} \otimes \vec{\omega} + \frac{1}{2}\vec{\omega} \times \vec{\omega} = \overline{\overline{S}} \otimes \vec{\omega} \quad , \tag{3.56}$$

where $\overline{\overline{S}}$ is the deformation tensor introduced in Eq. (2.11). If one supposes that the vorticity in the stagnation region between the vortices is weak (in some sense) in front of the deformation, one can assume (at least initially) that the deformation tensor will not vary while the vorticity is stretched. Since the deformation tensor is real and symmetric, it admits eigenvectors (principal axes of deformation) which are orthogonal and can form a basis. Let s_1, s_2, s_3 be the three eigenvalues. Due to incompressibility, their sum is zero, so that one is positive (called here s_1) and another one at least is negative. Let s_2 be the smallest eigenvalue, always negative. Working in the orthonormal frame formed by the eigenvectors respectively associated to s_1, s_2, s_3, the vorticity components $\omega_1, \omega_2, \omega_3$ satisfy the following equations

$$\frac{D\omega_1}{Dt} = s_1\omega_1 \ , \quad \frac{D\omega_2}{Dt} = s_2\omega_2 \ , \quad \frac{D\omega_3}{Dt} = s_3\omega_3 \ ,$$

and the vorticity will be stretched in the direction of the first principal axis, and compressed in the direction of the second. It is not a bad approximation to assume $s_3 \approx 0$ in the stagnation region, so that there will be no vortex stretching or compression along the third principal axis.[17] There is here no preferred spanwise wave length, but it could be imposed by the above-described translative instability of the billows, and as proposed by Sandham and Reynolds [629].

Comte and Lesieur [134] and Silvestrini et al. [651] found intense longitudinal hairpins stretched in the LES of a temporal mixing layer forced by a weak random quasi two-dimensional perturbation. These LES are of the Euler type, since carried out at zero molecular viscosity. The former of these calculations is shown in Plate 9, presenting the passive-scalar interface of the layer, as well as positive longitudinal vorticity in red. The longitudinal vorticity can here reach values of the order of $\approx 2\omega_i$, where ω_i is the maximum initial spanwise vorticity modulus. An interesting feature of Plate 9 is to show that longitudinal

[17] Which is approximately spanwise.

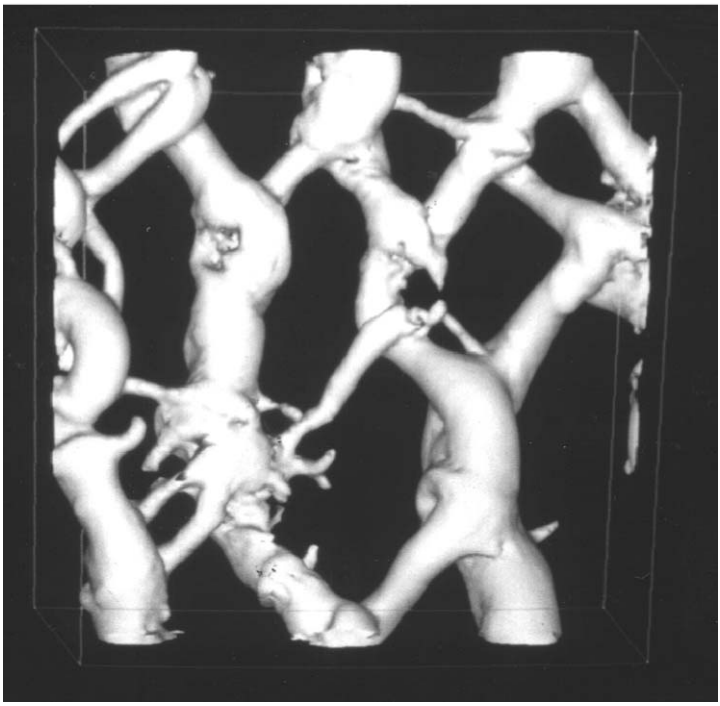

Figure 3.11. Low-pressure field obtained in the inviscid LES of a temporal mixing layer undergoing helical pairing (courtesy J. Silvestrini, Grenoble).

vorticity stretched between the primary Kelvin–Helmholtz vortices is rolled up within the cores of the big vortices, thus producing intense longitudinal vorticity fluctuations in the cores themselves. Silvestrini et al.'s LES were carried out with the same subgrid model (spectral eddy-viscosity, see Chapter 12), but in a cubic box at a higher resolution (96^3 Fourier modes) and with four initial fundamental wavelenghts. Plate 10a presents in this simulation an isosurface of the vorticity modulus corresponding to a threshold $(2/3)\omega_i$. Here, the maximum longitudinal vorticity stretched is of the order of $4\omega_i$, which might be larger than the effective values reached experimentally. Actually, the efficiency of the longitudinal stretching in reality depends also upon the amplitude of the initial perturbation and the Reynolds number. In fact Squire's theorem (at infinite Reynolds number) and the numerical resolution of the three-dimensional Orr–Sommerfeld equation at large Reynolds show that the most amplified mode in the three-dimensional temporal mixing layer is indeed two-dimensional. By a naive application of this result, one might have believed that two-dimensional Kelvin–Helmholtz vortices would emerge from

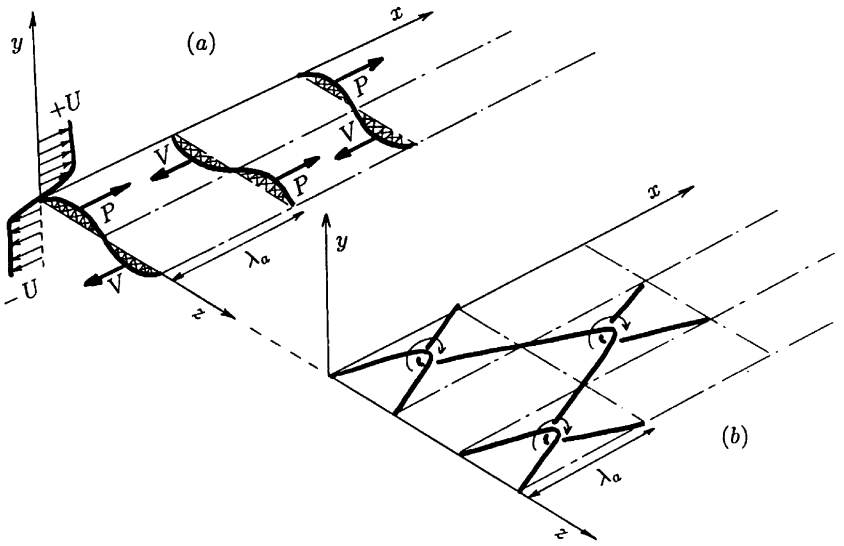

Figure 3.12. Schematic view of helical pairing, where vortex filaments oscillating out of phase vertically (a) are stretched by the basic flow and reconnect (b).

a weak three-dimensional isotropic perturbation superposed upon the basic shear. But this is not at all what happens. Instead, Comte et al. [137, 138], using DNS with pseudo-spectral methods at a resolution of 128^3 Fourier wave vectors and a Reynolds number $U\delta_i/\nu = 100$, displayed the evidence for *helical pairing*. This is shown in Plate 11, which represents a top view of respectively the vorticity components, vortex filaments and passive-scalar interface. The same dislocated pattern was recovered by Silvestrini et al. [651] in inviscid LES with the same forcing (see Plate 10b). Figure 3.11 presents the low-pressure field obtained in the calculation of Plate 10b. It confirms that low pressure and high vorticity modulus are well correlated in large structures, indicating that low pressure is a good indicator of big or intense vortices. A schematic view of the helical-pairing interaction is shown in Figure 3.12: one assumes that the fundamental Kelvin–Helmholtz billows oscillate vertically out of phase (three-dimensional subharmonic perturbation), and are in the meanwhile transported by the basic flow. A staggered pattern will develop, and the pairing will occur locally, yielding a vortex lattice.[18] Remark also in Plates 10b and 11 the existence of thinner longitudinal hairpin vortices

[18] Let us mention also the kinematic model of three-dimensional vortex lattice proposed by Chorin [123] in order to describe Kolmogorov's inertial range of turbulence.

strained by the flow in the stagnation like zone between two local-pairing regions. Notice that one leg of this hairpin is much stronger than the other one. This will in fact be the case for most of hairpin vortices found in shear flows, in particular in turbulent boundary layers (see Chapter 4). Plate 12 shows a side view (in the $x-y$ plane) of the passive-scalar interface. It indicates apparently regular Kelvin–Helmholtz vortices. It is possible that some mixing-layer experiments, showing coherent structures when visualizing cross sections of the flow, could correspond to a high degree of three-dimensionalization.

The expression "helical pairing" was used in the secondary-instability analysis of Pierrehumbert and Widnall [573] to characterize a three-dimensional subharmonic instability (staggered mode). As remarked by Comte [141], its amplification rate in terms of this theory is of the same order as that of the translative instability already mentioned. This shows that the use of instability theories requires great care, since most experimentalists only retained from Pierrehumbert and Widnall's work the concept of translative instability. Another remark is that when looking at DNS or LES of helical-pairing, it turns out that this is not exactly a "secondary instability": one does not observe first the roll up of primary billows followed by a staggered deformation. Instead, oblique waves are seen to grow quickly, yielding directly the lattice structure of dislocated billows. In fact, the terminology helical pairing was first proposed by Chandrsuda et al. [107] in a mixing layer experiment (behind a backstep) where the coherent vortices were highly three-dimensional. Let us finally mention that the helical-pairing configuration had been simulated, previously to Comte et al. [137, 138], by Meiburg [481], in a calculation using vortex-filament methods, when the forcing consisted in an initial subharmonic perturbation. Further details on helical pairing in spatial mixing layers will be given in Chapter 4.

To summarize on this problem of structures geometry in plane mixing layers (experimental and numerical), it seems that they may have two organization types:

(A) a quasi two-dimensional topology, where Kelvin–Helmholtz billows are submitted to translative instability, and oscillate in phase. The preferred mode of this spanwise oscillation imposes its wavelength to intense thin longitudinal hairpins stretched in the stagnation regions between the big billows.

(B) a vortex-lattice topology, consisting in a helical-pairing reconnection of Kelvin–Helmholtz billows, with the stretching of thinner longitudinal vortices.

As will be seen below, this is close to what we can obtain in round jets.

3.4.2 Round jets

It is of interest, from a two-dimensional point of view, to consider also the axisymmetric jets or wakes. They are an axisymmetric version of spatial mixing layers, and the Orr–Sommerfeld and Rayleigh stability analysis can be generalized in this case. The primary unstable modes will give rise to vortex rings, which are the axisymmetric analogues of Kelvin–Helmholtz vortices.

Numerous experiments on round jets have been carried out (see e.g. Crow and Champagne [154], Hussain and Zaman [309], and Van Dyke [698, pp. 34, 60]. Possibilities of pairing between vortex rings of same sign exist, as shown by Yamada and Matsui [729] (quoted by Van Dyke [698, p. 46]): in the same way as Kelvin–Helmholtz vortices rotate about each other before merging, vortex rings *leapfrog* during the pairing. Such a pairing might also be visible in the round jet, shown in Figure 1.2 before its breakdown into three-dimensional turbulence. As quoted by Winant and Browand [721], *Laufer, Kaplan and Chu [387] have made indirect observations of vortex-ring pairing in an axisymmetric jet at Reynolds numbers of order 160,000 (...). It is, in fact, proposed that pairing of the vortex rings is the primary mechanism responsible for the production of jet noise.*

In fact, Michalke and Hermann [504] have carried out analyses showing the important role of various upstream parameters on the jet development as far as instabilities are concerned. We mention also the pioneering work of Widnall et al. [716] about the preferred mode obtained in the inviscid secondary instability of the rings. In fact, the latter is subject to an azimuthal instability and oscillates in a wavy manner.

Numerous experimental and numerical-simulation works carried out since then have confirmed that the turbulent round jet topology is very close to the two possible structures A) and B) just mentioned above for the plane mixing layer. In case A, the stretching of longitudinal hairpin vortices gives rise to *side jets* due to velocity induction by the primary rings. In case B, helical pairing is replaced by alternate pairing: this interaction (see below in Chapter 4) is a subharmonic oscillation of primary vortex rings. More details on the jets dynamics and its numerical control by upstream velocity perturbations can be found in the book of Lesieur et al. [431], as well as in da Silva and Métais [158] and Balarac [27].

3.4.3 Plane jets and wakes

It is well known from the Prandtl viscous boundary-layer equations (see e.g. Schlichting [635]) that a laminar plane jet issuing from point source will have, at a certain distance downstream x, a longitudinal velocity given by

$$u = \frac{U}{\cosh^2 y/\delta_0} \ , \tag{3.57}$$

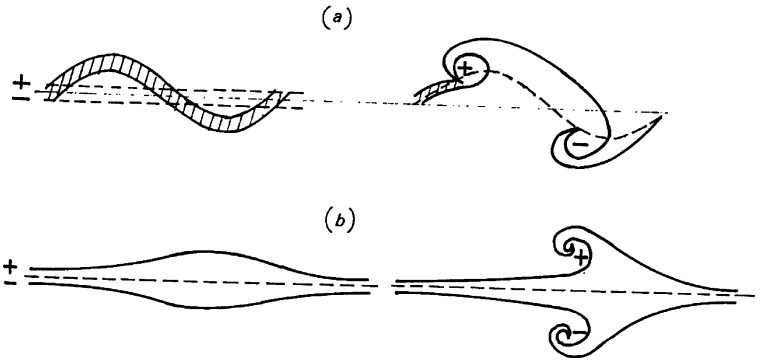

Figure 3.13. Growth in a Bickley jet of (a) the sinuous mode, leading to the formation of a Karman street; (b) the varicose mode.

where $U(x)$ is the velocity at the centre of the jet, and $\delta_0(x)$ a characteristic width. The same expression holds approximately for a turbulent plane jet, as can be demonstrated using Prandtl's mixing-length theory [587] (see also Chapter 4), and is well verified experimentally. This plane-jet velocity profile is sometimes referred to as the Bickley jet.

The two-dimensional linear-instability analysis of the velocity profile given by Eq. (3.57) has been investigated by Drazin and Howard [172] on the basis of the Rayleigh equation. It was found that two classes of unstable solutions exist, corresponding respectively to the *even modes* (called also *sinuous modes*), where the amplitude $\Phi(y)$ in Eq. (3.13) is even, and the *odd modes* (called *varicose modes*), where it is odd. The schematic evolution of the jet in both cases is shown in Figure 3.13: in the sinuous mode, vorticity of alternatively positive and negative signs is transported into the upper and lower irrotational regions, tending, by velocity-induction effects, to form a Karman-like vortex street. On the contrary, the varicose mode will form a pattern symmetric with respect to the x axis. The stability analysis shows that the most-amplified sinuous mode grows three times faster than the varicose one.

In the viscous case, and if the Reynolds number is high enough, it may be shown that the instability is of the inviscid type (see Drazin and Reid [173]). Therefore, it is natural that the two-dimensional direct-numerical simulations of the Bickley jet, submitted initially to a random white-noise perturbation of small amplitude, show the formation of only the sinuous mode, at the most-amplified wave length predicted by the linear-stability theory, that is

$$\lambda_a = 6.54\ \delta_0\ . \tag{3.58}$$

This is shown on Plate 13, taken from Comte et al. [133]. It represents the vorticity during respectively the initial stage, the growth of the sinuous in-

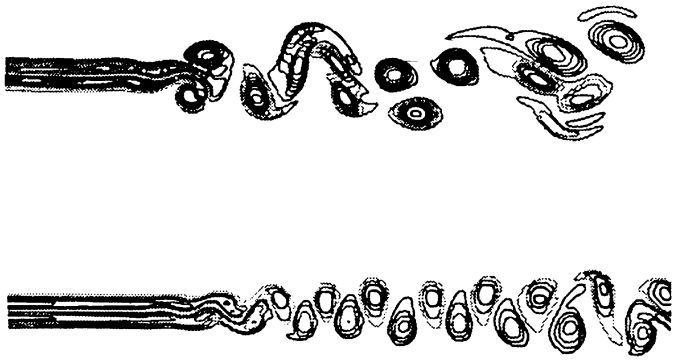

Figure 3.14. Direct-numerical simulations of a two-dimensional spatially growing (a) Bickley jet; (b) Gaussian wake. Both are submitted to a white-noise upstream forcing of small amplitude (courtesy P. Alexandre, I.M.G.).

stability, and the formation of the Karman street. The red colour corresponds to positive vorticity, and blue colour to negative vorticity. This calculation also shows the tendency for eddies of same sign to pair, thus increasing the wave length of the coherent structures.

A plane wake is characterized by a Gaussian deficit velocity profile, both in the viscous laminar and the turbulent cases. Its linear-stability analysis in the temporal case has been carried out by Sato and Kuriki [632]. The results are qualitatively similar to the Bickley jet case, with dominant sinuous modes resulting in a Karman street. This is to be expected, since, within the temporal approximation, a wake and a jet differ only in the form of respectively the basic velocity and the basic deficit velocity.[19]

How do these temporal calculations apply to spatially-growing situations: for a wake of external velocity U_e, and whose deficit velocity is small compared to U_e, a Galilean transformation of velocity U_e allows one to associate a temporal problem to the spatial evolution. On the contrary, there is no global transport velocity in a jet, whose velocity on the axis decays downstream. Two-dimensional spatially-growing calculations of both a Bickley jet and a Gaussian wake, presented in Figure 3.14, confirm the experimental fact that the jet is more unstable than the wake, but still displays pairing interactions between eddies of same sign. In this calculation, the jet grows proportionally to x, while the wake expands only like $\sqrt{x}$, as predicted by both theory (see Chapter 4) and experiments for the turbulent jet and wake. As a comparison, Plate 14, taken from Werlé [715], presents the experimental Karman

[19] Indeed, the temporal approximation allows both a Galilean transformation and the reversal of the velocity.

street obtained in a wake behind a splitter plate. A last remark to be made is that the formation of a Karman street behind an obstacle seems to be qualitatively independent of the shape of the obstacle: for instance, a cylinder, a splitter plate or a wedge give rise to the same type of wake. This is easily understandable if one interprets the Karman street as resulting from the development of a sinuous instability upon the doubly-inflectional basic velocity profile created downstream of the obstacle: the perturbations which trigger this instability come from the shear layers existing in the close vicinity of the obstacle. Behind a cylinder for instance, experiments show immediately downstream a pair of symmetric (with respect to the x axis) small vortices (see e.g. Kourta et al. [344]), before the appearance further downstream of the Karman street. Let us mention also the two-dimensional DNS of a spatial wake done by Maekawa et al. [463], where they study the influence of various two-dimensional upstream perturbations.

Let us mention finally that there are numerous three-dimensional instabilities associated with the transition of plane wakes or jets into developed turbulence. For the plane wake for instance, experiments (see Breidenthal [80], Lasheras and Meiburg [385], Williamson [720]) and calculations (see Meiburg and Lasheras [482], Lasheras and Meiburg [385], Chen et al. [114], Gonze [261], and Meiburg [483]) show the formation of longitudinal hairpins, which resemble those encountered in the mixing layer. They are visible on Plate 15, taken from Gonze [261], which represents various vorticity components in the DNS of a temporal plane wake, starting from a Gaussian basic velocity profile destabilized by a quasi two-dimensional random perturbation of small amplitude. In fact, the alternate longitudinal vortices are stretched between Karman vortices of opposite sign, on which they reconnect to form closed loops. Plate 16 presents the scalar field obtained eventually in the same calculation as Plate 15. It still displays longitudinal vortices, whereas Karman vortices have become much thinner, due to viscous effects. The evolution of the same wake in an "inviscid" LES is displayed in Chapter 4. It has still a quasi two-dimensional structure, with straight Karman vortices stretching intense longitudinal vortices.

3.4.4 Convective and absolute instabilities

This approach, developed by Huerre and Monkewitz [303] (see also Chomaz [121]), poses interesting questions about the character of the instabilities arising in a spatially-developing flow with large-scale inhomogeneities. From this analysis, a plane mixing layer of uniform density developing behind a splitter plate with a thin edge is *convectively unstable*, in the sense that it requires perturbations close the upstream splitter plate to develop. The latter grow following the average flow. If these upstream perturbations are cancelled, the flow returns to laminarity. However, such a mixing layer will become *absolutely*

unstable if the splitter plate has a blunt edge (see Huerre and Monkewitz [303], Wallace and Redekopp [710]).

The absolute-instability character of a flow means that a perturbation existing anywhere in the fluid domain (and not only upstream) is sufficient for the development of instabilities. Recent three-dimensional DNS by Laizet and Lamballais [364] of the mixing layer using the immersed boundary method with compact schemes have confirmed the bifurcation from a convectively to an absolutely unstable character when one goes from a thin edge to a blunt edge. Monkewitz et al. [516] have studied the heated jet, and determined for which density differences it could become absolutely unstable. Finally, there are also arguments in favour of the absolute instability character of a uniform-density wake. If this is true, one should reconsider the arguments developed above analysing the spatial wake by looking at the development with the mean flow of perturbations generated upstream.

3.5 Wall flows

3.5.1 The boundary layer

• Linear stability analysis

Let us start with the Blasius velocity profile, corresponding to a laminar boundary layer without pressure gradient over a semi-infinite flat plate. We define the displacement thickness as

$$\delta_1(x) = \frac{1}{U} \int_0^{+\infty} [U - \bar{u}(x, y)] \, dy \tag{3.59}$$

which is such that

$$\delta_1(x) = 1.73 \, \left(\frac{\nu x}{U} \right)^{1/2} \tag{3.60}$$

(see e.g. Schlichting [635]), x being the distance downstream of the leading edge, and U the free-stream velocity. In the two-dimensional temporal case, the Orr–Sommerfeld equation exhibits an unstable region in the [perturbation wave number-Reynolds number] domain, and a critical Reynolds number below which the flow is always linearly stable (see e.g. Drazin and Reid [173]). The stability diagram of such a flow is shown schematically in Figure 3.15. With the Reynolds number defined as $U\delta_1/\nu$, its critical value is equal to 520 (see Schlichting [635]). In the downstream direction, the laminar boundary-layer thickness and the Reynolds number will grow like $\sqrt{x}$: when

$$R_e^{(x)} = \frac{Ux}{\nu} \geq \left(\frac{520}{1.73} \right)^2 = 90347 \, ,$$

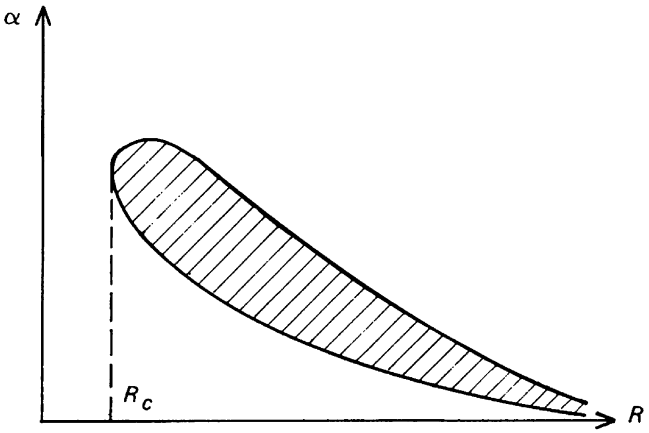

Figure 3.15. Schematic linear-stability diagram for the Blasius boundary-layer velocity profile, in the [α (longitudinal wave number of the perturbation) – R (Reynolds number of the basic flow)] domain. Inside the dashed area, the perturbations will amplify exponentially. When R goes to infinity, the unstable region will collapse onto the $\alpha = 0$ axis.

the flow will become unstable to small perturbations, and unstable waves will begin to grow. These waves are called Tollmien–Schlichting waves,[20] from the work of Tollmien and Schlichting,[21] who solved in the early thirties the Orr–Sommerfeld equation for the boundary layer. The waves give rise to periodic oscillations in the boundary layer.

• Forced transition

The experimental existence of T.S. waves was subsequently established experimentally by Schubauer and Skramstad [638]. The experimental critical Reynolds number for the growth of the waves is in good agreement with the theoretical value given above. In practice, the transition to turbulence above a semi-infinite flat plate proceeds as follows (see Klebanoff et al. [334], Hinze [285], and Herbert [271]). In Klebanoff et al. [334] the boundary layer is forced upstream with a thin metal ribbon parallel to the wall and stretched in the spanwise direction, which vibrates two-dimensionally close to the wall; further downstream, cellophane tape is fixed to the wall, regularly spaced in the spanwise direction. Parameters are chosen in such a way that T.S. waves begin growing. One observes downstream the development of a spanwise oscillation in the wave, with formation of longitudinal streaks of respectively slow

[20] Hereafter called T.S. waves.
[21] See Schlichting [635] for a review.

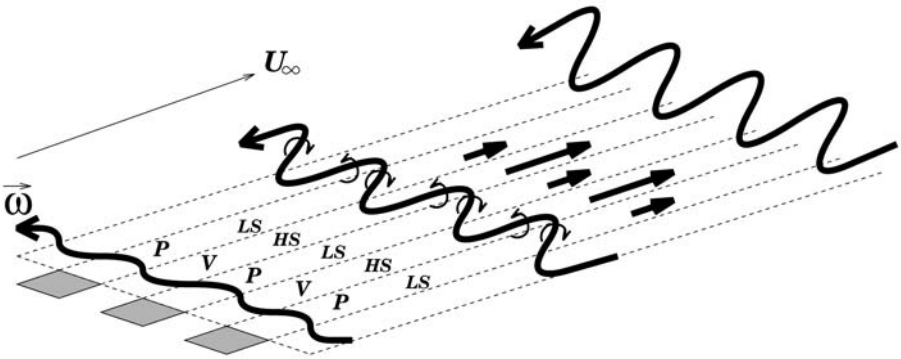

Figure 3.16. Schematic view of haipin vortices stretched in the forced-transition experiment of Klebanoff et al. [334].

and fast fluid, as far as the longitudinal velocity is concerned. The low-speed streaks are located downstream of the tape peaks, while the high-speed streaks are downstream of the tape valleys. Klebanoff interpreted this system of low- and high-speed streaks as the evidence for a hairpin-shaped vortex structure stretched in the boundary layer. These hairpins correspond to spanwise vortex filaments passing regularly with the T.S. wave upstream and deformed in the spanwise direction by the tape, which are strained longitudinally downstream by the ambient shear (see Figure 3.16). With this interpretation, the longitudinal legs of the hairpins will pump slow fluid up from the wall, and fast fluid down to the wall. Experiments of Hama et al. [268], where vortex structures are visualized by injection of hydrogen bubbles in the flow, do confirm the existence of hairpins stretched by the flow. Experiments show also that the longitudinal velocity profile (measured in terms of y) becomes inflectional in the low-speed streaks, with a local formation of Kelvin–Helmholtz like vortices (called spikes) which are shed and degenerate into three-dimensional turbulence (see Hinze [285, pp. 600ff.], for a review). DNS in the temporal case where a Blasius velocity profile is forced by a T.S. wave and a small spanwise perturbation confirm the above experimental findings (see e.g. Kleiser and Zang [336], and Normand and Lesieur [538]). The hairpin stretched are inclined approximately 40° with respect to the horizontal. In the spatially-developing case Ducros et al. [180] consider an upstream forcing consisting in the superposition of a laminar velocity profile, T.S. waves and a three-dimensional random noise (see Chapter 4). They show that, during the transition process, low-pressure regions resulting from T.S. waves propagation do organize into big two-dimensional billows of higher vorticity, which distort downstream in a hairpin manner.

Most of the numerical simulations show also under the hairpins the formation of a weaker secondary hairpin system close to the wall, which rotate in the opposite direction. This is due to the adherence condition which implies that a vortex approaching the wall will generate antivorticity at the wall.

More recent LES results of this type (with animations of vorticity, velocity and pressure maps on a web site), based on the work of Briand [82], are presented in Lesieur et al. [431].

• Natural transition and turbulent spots

Now we look at the case of natural transition, where there is no forcing in the upstream flow except for residual turbulence. Experiments show that the layer is first laminar, up to $R_e^{(x)} = Ux/\nu \approx 10^5$. As stressed above, this accords well with the critical Reynolds number predicted by the linear-instability theory. An interesting phenomenon which occurs in the range $10^5 < R_e^{(x)} < 10^6$ is the formation of turbulent spots (Emmons and Bryson [187], Schubauer and Klebanoff [639]) which are spatially localized in the form of large Λ's, and where turbulence has already developed. They are some sort of big packets of breaking three-dimensional T.S. waves which travel downstream, and give the transition an intermittent character. In fact, this collective behaviour of the transitional boundary layer may be an aspect in physical space of some backscatter effects considered later in this monograph for isotropic turbulence, and where resonant interactions between energetic modes provide energy to very large scales: in the boundary layer, resonance between two distorted T.S. waves might thus be responsible of spots formation.

For $R_e^{(x)} > 10^6$ the boundary layer has become turbulent everywhere. Up to now, no theory has been able to predict this last Reynolds number characterizing the transition to fully-developed turbulence in a boundary layer.

Secondary-instability analysis

As already stressed, transition in the boundary layer on a flat plate depends upon the type of perturbations exerted upstream on the flow. In Klebanoff's afore-mentioned experiment, the three-dimensional forcing was harmonic in the sense that the crests of the T.S. waves were oscillating in phase in the spanwise direction. This corresponds to what is generally referred to as the K-mode, where vortex filaments are aligned. On the other hand, if the perturbation is subharmonic, the crests oscillate out of phase. This is called H-mode, from Herbert [272], and corresponds to a staggered organization of vortex filaments. For the temporal problem, Herbert [272] showed, with the aid of a secondary-instability analysis where a perturbation is superposed upon a two-dimensional T.S. wave of finite amplitude, that the staggered mode was more amplified than the aligned mode. This should favour the emergence

of H-mode during transition in natural situations (see, however, discussions about that for Poiseuille flows). Let us mention also the work of Kachanov and Levchenko [325] on these subjects.

Remark that in a lot of cases, where the level of perturbation is higher, transition does not occur through these various routes, and the flow goes directly to developed turbulence. This is called *by-pass transition*. Remark finally that common life offers a lot of manifestations of T.S. waves: those travelling in the air boundary layer above water will force the wavelength of water waves. The ripples left in the sand after the tide are the footprints of transition in the boundary layer within the water. As for the structure of dunes in deserts, it might rather result of the presence of big haipin vortices ejected from the ground in the turbulent atmospheric boundary-layer (see next chapter).

3.5.2 Poiseuille flow

For the plane Poiseuille flow in a channel of width $H = 2h$, the situation is even more frustrating than in a boundary layer upon a flat plate: the two-dimensional Orr–Sommerfeld equation leads to a stability diagram which resembles the boundary-layer one, with a critical Reynolds number (based on H and the bulk velocity across the channel)[22] of $R_C = 7696$. On the other hand, experiments show a transition to fully-developed turbulence at a Reynolds number of 2000, as already mentioned above. They show also waves, analogous to T.S. waves, which propagate at lower Reynolds numbers (see e.g. Nishioka et al. [535]). The instabilities developing below R_C are called subcritical instabilities. A two-dimensional nonlinear instability theory has been developed by Orszag and Patera [554] for this case, predicting a lower critical Reynolds number, but still not enough to agree with the experiments.

It is now possible to investigate with the aid of three-dimensional DNS the transition in the channel flow. They show phenomena qualitatively analogous to what has been observed in the boundary-layer (see e.g. the calculations of Biringen [64], Zang and Krist [736] and Sandham and Kleiser [631]). There is however an issue opened about the type of mode which emerges when a small three-dimensional random perturbation is superposed upon a parabolic laminar velocity profile, at a supercritical Reynolds number: if the perturbation is isotropic, one should expect first the growth of two-dimensional T.S. waves to finite amplitudes. Then, if one applies the secondary-instability analysis of Herbert, one should have emergence of the staggered H-mode, since the white noise is supposed to bring as much energy in the subharmonic than in the harmonic. In fact, numerical simulations of Kim and Moser [331] and

[22] The critical Reynolds based on h and the maximal velocity is $U_m h/\nu = 7696 \times (3/4) = 5772$.

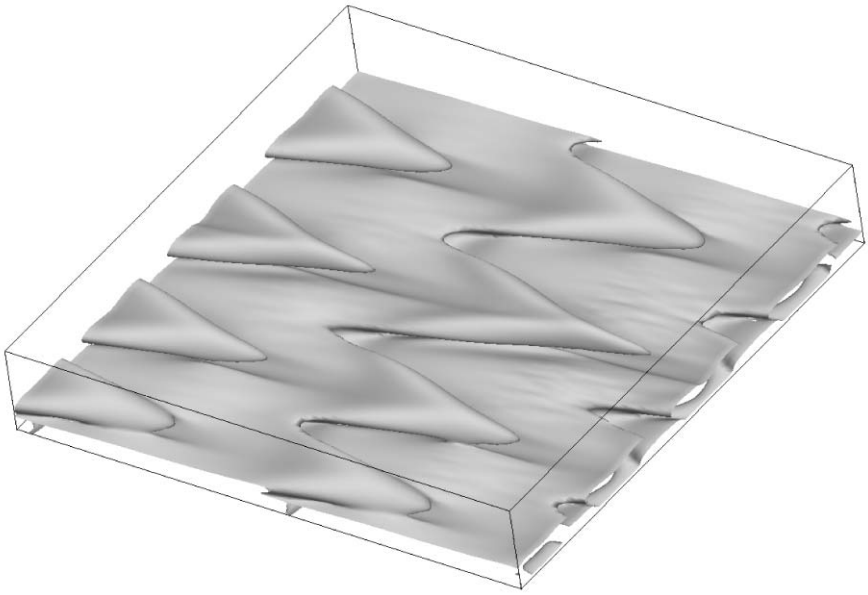

Figure 3.17. Vorticity modulus (threshold 1.5 U_m/h) obtained in the DNS (using mixed spectral-compact methods) of a periodic channel forced by a small three-dimensional isotropic white noise superposed to the parabolic Poiseuille profile; it shows the formation of aligned hairpins at the wall (courtesy E. Lamballais, Grenoble).

Lamballais [366] show instead the emergence of the aligned K mode. Kim and Moser [331] explain it as due to an initial growth of the longitudinal velocity coming from the white noise, which can be justified if one drops the pressure gradient out of the linearized equation for $\tilde{u}$. With the same reasoning, $\tilde{v}$ is going to have essentially a viscous decay. Thus, the initial white noise will become strongly anisotropic and will pick up a longitudinal component characterized by the wavevectors $(\alpha = 0, \beta \neq 0)$. At the same time, the two-dimensional fundamental mode $(\alpha_a, 0)$ will grow. Kim and Moser [331] observe eventually the growth of oblique harmonic modes $(\alpha_a, \pm\beta)$ which overwhelm the subharmonic modes, yielding the aligned configuration. They interpret the emergence of the three-dimensional harmonic mode as a nonlinear resonance between the weak longitudinal mode (resulting from the white noise) and the two-dimensional fundamental.[23] Indeed, we anticipate from Chapter 5 that nonlinear interactions proceed by triads of wavevectors whose sum is zero. Figure 3.17, taken from Lamballais [366], shows the aligned hairpins resulting

[23] One could also envisage a resonance between two subharmonics.

from the same calculation where a Poiseuille flow at Reynolds $U_m h/\nu = 8000$ is forced by a small isotropic white-noise.

We finally mention the two-dimensional direct-numerical simulations of the periodic channel flow done by Jimenez [315,316], which show the formation of a street of eddies of opposite sign.[24] These two-dimensional calculations give valuable information on the growth of two-dimensional nonlinear instabilities. In fact, it will be seen in Chapter 13 that such a solution does arise in the case of a channel submitted to a rapid solid-body rotation of axis parallel to the spanwise direction (see also Lamballais [366]).

For a circular Poiseuille flow (pipe flow), as well as for the plane Couette flow, the classical linear-instability analysis leads to stability, whatever the Reynolds number and the wavenumber of the perturbation. Experimentally, one observes also turbulent spots[25] in these flows.

3.6 Thermal convection

3.6.1 Rayleigh–Bénard convection

We will give here some very simple basic notions on the transition to turbulence in a fluid heated from below and confined between two planes (Rayleigh–Bénard convection). To analyze this problem, we come back to the Boussinesq approximation derived in the previous chapter, even if their conditions of applicability (vertical scale of motions small compared with the height of the apparatus) are not generally fulfilled in the experiment. One takes $\Omega = 0$. It has already been seen in the previous chapter that, in the stable case, gravity produces waves characterized by a frequency N given by Eq. (2.127). Here we consider the unstable case, but the previous analysis has shown that the characteristic time of the exponential amplification of the perturbation is given by

$$T_b = \left[g \frac{d\bar{\rho}_*}{dz} \right]^{-1/2} \tag{3.61}$$

with an associated frequency N_b given by

$$N_b^2 = g \, \frac{d\bar{\rho}_*}{dz} \approx \, \frac{g}{H} \, \Delta\bar{\rho}_* \, , \tag{3.62}$$

where $\Delta\bar{\rho}_*$ corresponds to the variation of $\bar{\rho}/\rho_0$ for a liquid and $-\bar{\Theta}/\Theta_0$ for a gas on the height H. In this case the upward motion of the fluid particle, of

[24] Each sign corresponding to one of the boundaries.

[25] In the pipe, they were called "flashes" by Reynolds [592] and "slugs" by Tritton [691].

characteristic frequency N_b, may be slowed down and possibly annihilated by viscosity (whose characteristic frequency has been seen to be of the order of ν/H^2) and thermal-diffusive effects (whose characteristic frequency may be easily shown to be of the order of κ/H^2). Therefore, the Rayleigh number is defined as

$$Ra = \frac{N_b^2}{(\nu/H^2)(\kappa/H^2)} \tag{3.63}$$

and measures the relative importance of buoyant effects compared to viscous and diffusive effects. A more quantitative study may be done using the Boussinesq approximation in the form (2.112) without rotation, performing a linearization with respect to the rest state. The vorticity equation becomes:

$$\frac{\partial \vec{\omega}}{\partial t} = \vec{\nabla}\tilde{\rho} \times \vec{g} + \nu \nabla^2 \vec{\omega} \tag{3.64}$$

with

$$\frac{\partial \tilde{\rho}}{\partial t} + w \frac{d\bar{\rho}_*}{dz} = \kappa \nabla^2 \tilde{\rho} \ . \tag{3.65}$$

Taking the curl of Eq. (3.64), one gets

$$-\frac{\partial \nabla^2 \vec{u}}{\partial t} = -g \ \frac{\partial \vec{\nabla}\tilde{\rho}}{\partial z} - (\nabla^2 \tilde{\rho}) \ \vec{g} - \nu (\nabla^2)^2 \vec{u} \ \ . \tag{3.66}$$

Projecting this equation on the z axis, it is found that

$$\frac{\partial}{\partial t} \nabla^2 w = -g \ \left(\frac{\partial^2 \tilde{\rho}}{\partial x^2} + \frac{\partial^2 \tilde{\rho}}{\partial y^2} \right) + \nu (\nabla^2)^2 w \ . \tag{3.67}$$

Eqs. (3.67) and (3.65) may be written as:

$$\left(\frac{\partial}{\partial t} - \nu \nabla^2 \right) \ \nabla^2 w = -g {\nabla_H}^2 \tilde{\rho} \ ; \ \left(\frac{\partial}{\partial t} - \kappa \nabla^2 \right) \ \tilde{\rho} = -w \frac{d\bar{\rho}_*}{dz} \ , \tag{3.68}$$

which yields

$$\left(\frac{\partial}{\partial t} - \nu \nabla^2 \right) \left(\frac{\partial}{\partial t} - \kappa \nabla^2 \right) \nabla^2 w = g \frac{d\bar{\rho}_*}{dz} {\nabla_H}^2 w \ , \tag{3.69}$$

since $d\bar{\rho}_*/dz$ does not depend upon x and y. Taking H^2/κ and H as units of time and space, Eqs. (3.69) becomes

$$\left(\frac{\partial}{\partial t} - \nabla^2 \right) \left(P_r^{-1} \frac{\partial}{\partial t} - \nabla^2 \right) \nabla^2 w = R_a \ {\nabla_H}^2 w \ , \tag{3.70}$$

where R_a is the Rayleigh number and

$$P_r = \frac{\nu}{\kappa} \tag{3.71}$$

the Prandtl number. Eq. (3.70) may be found in Busse [89], or in Drazin and Reid [173]. It is straightforward to show that $\tilde{\rho}$ satisfies the same equation. The problem can be solved by a normal-mode approach, where solutions of the form

$$w = W(z)\ e^{i(\vec{k}.\vec{x}-\varpi t)}, \quad \tilde{\rho} = R(z)\ e^{i(\vec{k}.\vec{x}-\varpi t)} \tag{3.72}$$

are sought, $\vec{k}$ being here a real horizontal wave vector of modulus k, and ϖ an imaginary frequency.

The solution of the problem depends upon the boundary conditions, which may be of the free-slip or no-slip type, with R, arising in Eq. (3.72), being equal to zero at the boundaries in both cases. Thus, the above equations impose at the boundaries the following conditions:

free-slip:

$$W = 0\ ; \quad \frac{d^2W}{dz^2} = 0\ ; \quad \frac{d^4W}{dz^4} = 0, \tag{3.73}$$

no-slip:

$$W = 0;\ \frac{dW}{dz} = 0\ ; \quad \frac{d^4W}{dz^4} + \left(i\frac{\varpi}{P_r} - 2k^2\right)\frac{d^2W}{dz^2} = 0\ , \tag{3.74}$$

the equation to be solved inside the fluid being

$$\left(\frac{d^2}{dz^2} - k^2\right)\left(\frac{d^2}{dz^2} - k^2 + i\varpi\right)\left(\frac{d^2}{dz^2} - k^2 + i\frac{\varpi}{P_r}\right)\ W = -k^2 R_a W\ . \tag{3.75}$$

This problem was solved analytically in 1916 by Rayleigh (see Drazin and Reid [173] for details) in the rather unrealistic case of two free-slip boundary conditions. In this case, solutions of the form

$$W(z) = \sin j\pi z \tag{3.76}$$

may be sought for, j being an integer. Let $s = -i\varpi$ be the time-amplification rate in Eq. (3.72). Eq. (3.75) reduces then to the following second-order equation for s:

$$\left(j^2\pi^2 + k^2\right)\left(j^2\pi^2 + k^2 + s\right)\left(j^2\pi^2 + k^2 + \frac{s}{P_r}\right) = k^2 R_a, \tag{3.77}$$

which may be easily solved. It admits real roots, one of them being negative. The second root (corresponding to an exponential growth of the perturbation, and hence to instability) is positive if

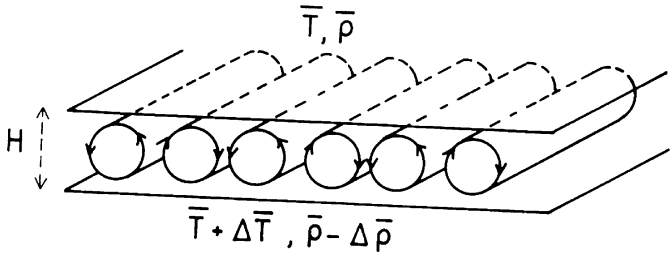

Figure 3.18. Schematic representation of Rayleigh–Bénard experiment of a fluid heated from below.

$$R_a > \frac{(\pi^2 j^2 + k^2)^3}{k^2} \ , \tag{3.78}$$

a condition which is independent of the Prandtl number. The minimum of these Rayleigh numbers is obtained for $j = 1$ and $k = \pi/\sqrt{2}$, and is equal to

$$R_a^{(c)} = \frac{27\pi^4}{4} = 657.5 \ . \tag{3.79}$$

This is the critical Rayleigh number of the problem, under which no instability can develop.[26] Note also that the amplification rate will depend upon the Prandtl number. In the case of two no-slip boundaries, a numerical resolution of Eq. (3.75) shows that the critical Rayleigh number is equal to

$$R_a^{(c)} = 1708 \ , \tag{3.80}$$

which agrees well with the experiments. For $Ra < Ra^{(c)}$, no motion can exist. For $Ra > Ra^{(c)}$, convective rolls appear in the case of large aspect-ratio apparatus (see Figure 3.18). If the domain is not constrained horizontally, convective cells will rather be of hexagonal shape, with warm fluid ascending in the centre, and cold fluid descending along the edges. When the Rayleigh number is increased, the system becomes turbulent via successive bifurcations. But the instability is still present and creates coherent structures, as can be seen for instance at the surface of the sun, where the Rayleigh number is huge ($\approx 10^{20}$), with the existence of solar granulation. It consists of hexagonal cells (size ≈ 1000 km), which are extremely unpredictable, since they have a life-time of the order of ten minutes. This is an exemple of turbulent system where an instability (here Rayleigh–Bénard convection) drives the creation of coherent structures, which are unstable and blow-up due to nonlinear interactions, and finally reform through the instability. We will encounter this cycle of *creation-destruction-recreation* in many turbulent flows. Other aspects of

[26] From a linear point of view.

the transition to turbulence in the Rayleigh–Bénard convection can be found in Busse [89] and Bergé et al. [55].

3.6.2 Other types of thermal convection

Bénard–Marangoni

We mention first *Bénard–Marangoni convection*, where the fluid is in a thin layer with a free surface, the convection being here controlled by surface-tension effects. It yields also the formation of hexagonal cells whose size is of the order of the layer thickness (see e.g. Guyon et al. [267]).

Double-diffusive convection

Let us finally look at thermal convection (in a deep layer) in the presence of a transported scalar of concentration c whose molecular diffusivity is much smaller than thermal conductivity. In this case, the direction of convection may be reversed. Let us consider for instance a temperature distribution with warm fluid of high c above cold fluid of low c: a fluid particle diplaced towards the top (for instance) will have time to adjust to the ambiant temperature before its scalar concentration changes. Its mass will thus be lower than the displaced fluid mass, and it will feel a positive buoyancy and keep on rising. This is called a *double-diffusive instability*, yielding the formation of hexagonal convective cells with cold fluid of low c rising in the centre, and warm fluid of high c descending along the edges (see e.g. Tritton [691]). One can thus explain thermohaline convection in an ocean strongly heated on its surface by the sun, with as a result an increased evaporation and thus a higher salt concentration: cold fresh water rises, and warm salty water sinks and forms salt fingers.

Oceanic conveyor belt

This essential part of oceanic circulation in northern Atlantic has already been mentioned in Chapter 1. Here, deep-water formation is due to ice formation at the surface which increases the salinity (and hence density). This is a key point in the presently observed worrying melting of ice and water warming in this region.

3.7 Transition, coherent structures and Kolmogorov spectra

It is not the aim of the present book to discuss at length all the stability problems involved in the transition to turbulence. How in practice will a real

flow of high Reynolds number degenerate into turbulence? It has already been stressed that turbulence is due to diffusion and stretching of vorticity, which could be created in the flow by various means, such as a boundary for instance. In fact, the transition to turbulence greatly depends on the manner in which this vorticity is created: if the basic velocity profile is inflectional, the inflection-point instability (also called barotropic instability), which is "inviscid" (i.e. nearly unaffected by viscosity if small enough) and linear, will give rise to the formation of large quasi two-dimensional vortices provided the small perturbations present in the flow contain energy in the unstable wave numbers range. Examples of such vortices have already been given for the Kelvin–Helmholtz waves of the mixing layer. Other examples are given by jets or wakes. These large vortices can be, as already pointed out, unpredictable and we will not refuse to assign the denomination of turbulence to them. Sometimes the large vortices can amalgamate and lead to the formation of larger vortices. This is due to the vorticity conservation constraint characteristic of two-dimensional turbulence (see Chapter 8). Simultaneously, these vortices degenerate into smaller and smaller structures, through some successive instabilities which are not always very clearly understood, but which seem to agree very well in the small three-dimensional scales with the statistical phenomenological predictions made by Kolmogorov in 1941 (see Chapter 6). The reason for such good experimental correspondance with the theory certainly remains one of the great mysteries of modern fluid dynamics. These small scales "cascade" down to a dissipative scale where they are damped and die under the action of molecular viscosity. They are, as already emphasized in Chapter 1, what can be called fully-developed turbulence. But it would be erroneous to think that the large transitional vortices disappear at a sufficiently high Reynolds number once small-scale turbulence has developed: modern methods of investigation and visualization of turbulent flows have contributed to a radical change in this former classical point of view, and it is, for instance, now widely recognized that they reform intermittently in the case of the mixing layer (Brown and Roshko [88]) and of the jet (Crow and Champagne [154]). This is also true for the vortex streets in the wake of a cylinder for instance. This will be widely discussed in the next chapter.

We will discuss in details in Chapter 4 what happens if the velocity profile is not inflectional.

4

Shear Flow Turbulence

4.1 Introduction

We will consider here developed turbulence submitted to a shear, both from a very simple statistical point of view (mixing-length theory) and from the coherent-vortex point of view. Concerning the latter, one will recall how to visualize vortices. We will be interested in flows such as free-shear flows (mixing layers, jets and wakes) and wall flows. Notice that coherent vortices in isotropic turbulence will be considered in three and two dimensions (Chapters 6 and 8, respectively).

4.1.1 Use of random functions

From a mathematical viewpoint, we use random functions. The averaging is taken in the sense of an ensemble average, that is a statistical average upon a large collection of independent realizations. The average of f will be denoted as $\langle f \rangle$. By definition, this averaging operator is linear, in such a way that, if α and β are two numbers (not random), we have

$$\langle \alpha f + \beta g \rangle = \alpha \langle f \rangle + \beta \langle g \rangle.$$

We have also $\langle \langle f \rangle \rangle = \langle f \rangle$. Let $f = \langle f \rangle + f'$ and $g = \langle g \rangle + g'$. It is easy to show that $\langle f' \rangle = 0$ and

$$\langle fg \rangle = \langle f \rangle \langle g \rangle + \langle f' g' \rangle \ . \tag{4.1}$$

4.2 Reynolds equations

When one is interested in predicting the ensemble-average quantities associated with a turbulent flow, the main difficulty comes from what is called the

closure problem, which arises from the nonlinearity of Navier–Stokes equations: for instance, when averaging these equations, one obtains using Eq. (4.1) for the averaged velocity field (in the case of uniform density) the so-called Reynolds equations:

$$\frac{\partial}{\partial t}\langle u_i\rangle + \frac{\partial}{\partial x_j}\langle u_i\rangle\langle u_j\rangle = -\frac{1}{\rho}\frac{\partial}{\partial x_i}\langle p\rangle$$
$$+\frac{1}{\rho}\frac{\partial}{\partial x_j}\left[\mu\left(\frac{\partial\langle u_i\rangle}{\partial x_j}+\frac{\partial\langle u_j\rangle}{\partial x_i}\right)+\sigma_{ij}^t\right] \tag{4.2}$$

with

$$\sigma_{ij}^t = -\rho\langle u_i' u_j'\rangle, \tag{4.3}$$

where the u_i' are the velocity fluctuations with respect to the mean velocity. These equations are analogous to Navier–Stokes equations for the mean velocity and pressure, but with the supplementary turbulent Reynolds stresses σ_{ij}^t. The latter are generally responsible for a loss of momentum in the mean motion. Physically, these Reynolds stresses can be understood as fictitious stresses which allow one to consider the mean motion as a real flow motion, submitted to the mean pressure gradients, the mean molecular stresses and the turbulent Reynolds stresses. But the Reynolds equation is not closed, in the sense that the Reynolds stresses are unknown.

Now, and if one substracts Reynolds equations from Navier–Stokes, an evolution equation for u_i' is obtained. Writing the same for u_j', multiplying respectively by u_j' and u_i' and adding, yields after averaging an equation for the Reynolds stresses. However, it involves third-order correlations. In the same way, an evolution equation for these correlations will involve fourth-order correlations, and so on: we are still in front of the closure problem, where a system describing the coupled evolution of the statistical moments will always contain one more unknown moment than equations. The statistical theories of turbulence need therefore a closure hypothesis, which is a supplementary equation between the moments, generally quite arbitrary. For inhomogeneous turbulence, and when the average quantities involve only one point $\vec{x}$ of the physical space, one talks of "one-point closure modelling". "Two-point closure" models will be considered in Chapter 7.

4.2.1 The mixing-length theory

The simplest way of determining the Reynolds stresses for inhomogeneous turbulence is to make an eddy-viscosity assumption, that is, assume that the deviator of the corresponding tensor can be written as:

$$\sigma_{ij}^t + \frac{\rho}{3}\langle u_s' u_s'\rangle\delta_{ij} = \mu_t\left(\frac{\partial\langle u_i\rangle}{\partial x_j}+\frac{\partial\langle u_j\rangle}{\partial x_i}\right). \tag{4.4}$$

μ_t is an eddy-viscosity, given by a mixing-length argument

$$\frac{\mu_t}{\rho} = l_m v, \tag{4.5}$$

where the mixing length l_m is a turbulent analogue of the mean free path of molecules in the kinetic theory of gases, and the velocity v characterizes the turbulent fluctuations. In turbulent free-shear flows for instance, it is assumed that l scales on the layer thickness δ, and v on the typical mean-velocity difference across the layer U (Prandtl [587]). Another Prandtl hypothesis concerns turbulent boundary layers: here one assumes that l is proportional to the distance from the wall. This assumption is valid in the so-called logarithmic layer (see below).

4.2.2 Application of mixing length to turbulent-shear flows

The plane jet

Let $\langle u \rangle$ and $\langle v \rangle$ be the components of the mean velocity $\langle \vec{u}(\vec{x}, t) \rangle$ respectively in the streamwise x and transverse y direction. The spanwise component $\langle w \rangle$ is zero. Reynolds equations write for the first two components of the velocity

$$\begin{aligned}
\langle u \rangle \frac{\partial}{\partial x}\langle u \rangle + \langle v \rangle \frac{\partial}{\partial y}\langle u \rangle &= -\frac{1}{\rho}\frac{\partial}{\partial x}\langle p \rangle - \frac{\partial}{\partial x}\langle {u'}^2 \rangle - \frac{\partial}{\partial y}\langle u'v' \rangle \\
\langle u \rangle \frac{\partial}{\partial x}\langle v \rangle + \langle v \rangle \frac{\partial}{\partial y}\langle v \rangle &= -\frac{1}{\rho}\frac{\partial}{\partial y}\langle p \rangle - \frac{\partial}{\partial x}\langle u'v' \rangle - \frac{\partial}{\partial y}\langle {v'}^2 \rangle,
\end{aligned} \tag{4.6}$$

where the $\partial/\partial z$ terms have been discarded, for we assume spanwise homogeneity.[1] Let $u_0(x)$ be the velocity at the centre of the jet, and $\delta(x)$ a properly defined jet width: in the second equation of Eq. (4.6), and due to continuity, the two terms of the l.h.s. are of same order $u_o \bar{v}/\delta$, $\bar{v}$ being a typical transverse mean velocity. Let $v_*(x)$ be a typical turbulent velocity such that $\langle {u'}^2 \rangle \sim |\langle u'v' \rangle| \sim \langle {v'}^2 \rangle \sim {v_*}^2$. Since the average parameters of the jet vary much faster in the transverse than in the streamwise direction, the r.h.s. of the $\langle v \rangle$ momentum equation reduces to $-(1/\rho)(\partial/\partial y)\langle p + \rho {v'}^2 \rangle$, where the pressure gradient dominates: indeed, the transverse pressure gradient term is of the order of ${u_0}^2/\delta$, large in front of ${v_*}^2/\delta$, since v_* will be assumed to be of the form $v_*(x) = a u_0(x)$, where $a \ll 1$ is a constant. Finally, and since $\bar{v} \ll u_0$, the $\langle v \rangle$ equation reduces to

[1] We neglect also the molecular viscous terms, which are small in front of their eddy-viscous counterparts. However, this will not be valid for wall flows close to the boundary.

$$\frac{\partial}{\partial y}\langle p\rangle = 0,$$

which shows that the mean pressure in the jet is uniform and equal to the pressure p_0 at infinity. Finally, Reynolds equations for the plane jet yield:

$$\langle u\rangle\frac{\partial}{\partial x}\langle u\rangle + \langle v\rangle\frac{\partial}{\partial y}\langle u\rangle = -\frac{\partial}{\partial y}\langle u'v'\rangle,$$

or equivalently (because of the incompressibility of the mean flow)

$$\frac{\partial}{\partial x}\langle u\rangle^2 + \frac{\partial}{\partial y}\langle u\rangle\langle v\rangle = -\frac{\partial}{\partial y}\langle u'v'\rangle\ . \tag{4.7}$$

This equation, integrated from $y = -\infty$ to $y = +\infty$, yields (assuming the Reynolds stresses are zero for y going to infinity)

$$\frac{d}{dx}\int_{-\infty}^{+\infty}\langle u\rangle^2(x)dy = 0, \tag{4.8}$$

which expresses the conservation downstream of the mean momentum flux across the jet.[2] Following Prandtl [587] and Schlichting [635], we introduce an eddy viscosity $\nu_t(x) \sim lv_* = b\delta(x)u_0(x)$, where $b \ll 1$ is a constant and l the integral scale of turbulence. Since

$$\left|\frac{\partial}{\partial y}\langle u\rangle\right| \gg \left|\frac{\partial}{\partial x}\langle v\rangle\right|,$$

the momentum equation is written:

$$\langle u\rangle\frac{\partial}{\partial x}\langle u\rangle + \langle v\rangle\frac{\partial}{\partial y}\langle u\rangle = \nu_t(x)\frac{\partial^2}{\partial y^2}\langle u\rangle. \tag{4.9}$$

We look for self-similar solutions of the form

$$\langle u\rangle(x,y) = u_0(x)f(\eta); \quad \eta = \frac{y}{\delta(x)}. \tag{4.10}$$

Notice first that this implies, from Eq. (4.8),

$$\frac{d}{dx}{u_0}^2\delta = 0. \tag{4.11}$$

Since the mean flow is non-divergent, one may introduce a stream function which is necessarily of the form

[2] It is well known that, due to the continuous turbulent entrainment of outer fluid by the jet, the mass is not conserved across the jet downstream. Such a conservation would correspond to the constancy with x of $\int_{-\infty}^{+\infty}\langle u\rangle(x)dy$.

$$\langle\psi\rangle(x,y) = u_0\delta F(\eta), \tag{4.12}$$

with $f(\eta) = dF/d\eta = F'$. Substituting into Eq. (4.9) yields finally:

$$F'^2 - \frac{(u_0\delta)'}{u_0'\delta}FF'' = b\frac{u_0}{u_0'\delta}F''', \tag{4.13}$$

(where the prime refers to a derivative with respect to x or η) with the boundary conditions

$$\langle u\rangle(x,0) = u_0(x), \langle u\rangle(x,\infty) = 0,$$
$$\frac{\partial}{\partial y}\langle u\rangle(x,0) = 0, \frac{\partial}{\partial y}\langle u\rangle(x,\infty) = 0,$$

which write:

$$F'(0) = 1, F'(\infty) = 0, F''(0) = 0, F''(\infty) = 0. \tag{4.14}$$

For $\eta = 0$, it is found that $u_0/u_0'\delta$ is a constant, which is negative since $u_0' < 0$. Using Eq. (4.11) in order to eliminate δ, we finally obtain

$$\frac{d}{dx}\left(\frac{1}{{u_0}^2}\right) = \text{constant}, \tag{4.15}$$

which proves that

$$u_0(x) \propto x^{-1/2}; \quad \delta(x) \sim x. \tag{4.16}$$

This allows to write Eq. (4.13) as

$$F'^2 + FF'' + \nu_t^+ F''' = 0, \tag{4.17}$$

where ν_t^+ is a positive number, which will be chosen equal to $1/2$. This fixes the choice of δ. Integrating twice leads finally to

$$F\left(\frac{y}{\delta}\right) = \tanh\frac{y}{\delta}, \tag{4.18}$$

and

$$\langle u\rangle(x,y) \propto x^{-1/2}\frac{1}{\cosh^2(y/\delta)}, \tag{4.19}$$

which is the velocity profile of the turbulent Bickley jet. Notice also that the $\langle v\rangle$ component is not zero for $y \to \infty$. Remark finally from Eq. (4.16) that the local Reynolds number grows downstream like $\sqrt{x}$.

The round jet

With the same assumptions as above, the mean pressure is uniform, and the $\langle u\rangle$ equation writes:

$$\langle u\rangle\frac{\partial}{\partial x}\langle u\rangle + \langle v\rangle\frac{\partial}{\partial y}\langle u\rangle + \langle w\rangle\frac{\partial}{\partial z}\langle u\rangle =$$

$$-\frac{\partial}{\partial y}\langle u'v'\rangle - \frac{\partial}{\partial z}\langle u'w'\rangle.$$

Again, the momentum flux is an invariant:

$$\frac{d}{dx}\int\!\!\int \langle u\rangle^2 dydz = 0. \tag{4.20}$$

One assumes that the longitudinal velocity is of the form

$$\langle u\rangle(x,y,z) = u_0(x)f(\eta); \quad \eta = \frac{r}{\delta(x)}; \quad r = \sqrt{y^2+z^2}. \tag{4.21}$$

Hence, Eq. (4.20) yields

$$\frac{d}{dx}(u_0\delta) = 0, \tag{4.22}$$

which shows that the eddy viscosity is now a constant ν_t. Finally, the momentum equation reduces to:

$$\langle u\rangle\frac{\partial}{\partial x}\langle u\rangle + \langle v\rangle\frac{\partial}{\partial y}\langle u\rangle + \langle w\rangle\frac{\partial}{\partial z}\langle u\rangle$$

$$= \nu_t\left(\frac{\partial^2}{\partial y^2}\langle u\rangle + \frac{\partial^2}{\partial z^2}\langle u\rangle\right). \tag{4.23}$$

We now assume that the jet is statistically axisymmetric, and work using cylindrical coordinates x and r. Let $u(x,r) = \langle u\rangle$ and $v(x,r) = \langle v\rangle$ be respectively the longitudinal and radial mean velocity. We assume that the jet is not swirling, and take the mean azimuthal velocity equal to zero. The momentum and continuity equations write:

$$u\frac{\partial u}{\partial x} + v\frac{\partial u}{\partial r} = \nu_t\frac{1}{r}\frac{\partial}{\partial r}\left(r\frac{\partial u}{\partial r}\right); \quad \frac{\partial ru}{\partial x} + \frac{\partial rv}{\partial r} = 0. \tag{4.24}$$

The complete calculation may be done by introducing a generalized stream function $\psi(x,r)$ such that

$$u = \frac{1}{r}\frac{\partial\psi}{\partial r}, \quad v = -\frac{1}{r}\frac{\partial\psi}{\partial x}.$$

Taking into account the boundary conditions, it is finally found that $u_0(x) \propto x^{-1}, \delta(x) \sim x$, and

$$\langle u\rangle(x,r) = u_0(x)\,\frac{1}{[1+(\eta^2/8)]^2}; \quad \langle v\rangle(x,r) = \frac{1}{2}u_0(x)\delta'\,\frac{\eta[1-(\eta^2/8)]}{[1+(\eta^2/8)]^2}\ . \tag{4.25}$$

The local Reynolds number is now constant downstream.

The plane wake

In the far region of the wake, one assumes that

$$\langle u(x,y)\rangle = U - u_d(x,y),$$

where $u_d(x,y)$ is the deficit-velocity profile, assumed to be much smaller than the velocity at infinity U. Estimates of the orders of magnitude in the Reynolds equations allow one to show that $\langle p\rangle$ is uniform. The momentum equation reduces to

$$U\frac{\partial u_d}{\partial x} = \frac{\partial}{\partial y}\langle u'v'\rangle, \tag{4.26}$$

whose integration across the wake yields

$$\frac{d}{dx}\int_{-\infty}^{+\infty} u_d(x,y)dy = 0. \tag{4.27}$$

Assuming that the deficit velocity is of the form

$$u_d(x,y) = u_0(x) f\left(\frac{y}{\delta}\right), \tag{4.28}$$

Eq. (4.27) yields

$$\frac{d}{dx}u_0\delta = 0, \tag{4.29}$$

which expresses the conservation of the mass in the wake. Again, we suppose that $\nu_t = bu_0\delta$, where b is a constant number. It is obtained

$$U\frac{\partial u_d}{\partial x} = \nu_t\frac{\partial^2 u_d}{\partial y^2}, \tag{4.30}$$

or equivalently,

$$f - \frac{u_0}{u_0'}\frac{\delta'}{\delta}\eta f' = b\frac{u_0^2}{Uu_0'\delta}f'', \tag{4.31}$$

with the boundary conditions

$$f(0) = 1, \quad f'(0) = 0, \quad f(\infty) = 0, \quad f'(\infty) = 0. \tag{4.32}$$

For $\eta = 0$, the coefficient of f'' in the r.h.s. of Eq. (4.31) must be x independent: this, together with Eq. (4.30), yields

$$u_0(x) \propto x^{-1/2}; \quad \delta(x) \propto x^{1/2}, \tag{4.33}$$

and Eq. (4.31) leads, with a proper definition of δ, to

$$f + \eta f' + f'' = 0,$$

which is also valid in the laminar-viscous case. It may easily be solved to give $f = \exp -(\eta^2/2)$, and the deficit velocity is:

$$u_d(x, y) \propto x^{-1/2} \exp -\frac{y^2}{2\delta^2}. \tag{4.34}$$

As in the round jet, the local Reynolds number is constant.

The round wake

We will just summarize the results. In cylindrical coordinates, we take

$$\langle u \rangle = U - u_0(x) f\left(\frac{r}{\delta}\right). \tag{4.35}$$

the mass conservation now implies that

$$\frac{d}{dx} u_0 \delta^2 = 0. \tag{4.36}$$

The Reynolds equation is written

$$U \frac{\partial u_d}{\partial x} = \nu_t \left(\frac{\partial^2 u_d}{\partial r^2} + \frac{1}{r} \frac{\partial u_d}{\partial r} \right), \tag{4.37}$$

whose solution is:

$$u_0(x) \propto x^{-2/3}; \quad \delta(x) \propto x^{1/3}; \quad f = \exp -\frac{\eta^2}{2}. \tag{4.38}$$

The local Reynolds number decreases like $x^{-1/3}$.

The plane mixing layer

The analysis is more difficult here in the spatially-growing case, since no analytic solution is found: if U_1 and U_2 are the respective velocities of the two streams ($U_1 > U_2$), with

$$\bar{U} = \frac{U_1 + U_2}{2}, U = \frac{U_1 - U_2}{2},$$

one looks for self-similar solutions of the form

$$\langle u \rangle(x, y) = \bar{U} + UF'(\eta); \quad \eta = \frac{y}{\delta}, \tag{4.39}$$

$\delta(x)$ being a properly-defined thickness of the layer. The stream function of the mean flow is

$$\langle \psi \rangle(x, y) = U\delta F(\eta) + \bar{U}y,$$

and the transverse mean velocity

$$\langle v \rangle(x, y) = U\delta'(\eta F' - F).$$

The boundary conditions for F' are $F'(+\infty) = 1, F'(-\infty) = -1$. As for the above flows, the mean pressure is found to be uniform. The Reynolds equation for $\langle u \rangle$ is the same as for the plane jet, but the eddy-viscosity is now $\nu_t(x) = bU\delta(x)$. One obtains:

$$bF''' + \delta' F'' \left(F + \eta \frac{\bar{U}}{U} \right) = 0. \tag{4.40}$$

This shows that δ' is a constant, and hence $\delta(x) \sim x$. A numerical solution of this differential equation is shown in Schlichting [635]. It differs from the hyperbolic-tangent velocity profile which, however, is not far from the experimental results. In the case $U/\bar{U} \ll 1$ (or in the temporally-growing case) the equation reduces to

$$bF''' + \delta' \frac{\bar{U}}{U} \eta F'' = 0,$$

and admits for solution an error function, with

$$F''(0) = \frac{2\sqrt{C}}{\sqrt{2\pi}}; \quad C = \frac{\delta' \bar{U}}{bU}.$$

Notice that, if the layer thickness is defined as the mean vorticity thickness:

$$\delta(x) = 2U / \frac{\partial}{\partial y} \langle u \rangle(x, 0) = \frac{2\delta}{F''(0)},$$

this yields $F''(0) = 2$, and implies

$$\frac{\bar{U}}{U} \delta' = 2\pi b.$$

Experiments where the Reynolds stresses can be measured and the eddy-viscosity determined (see e.g. Wygnanski and Fiedler [725], Dziomba and

Fiedler [183]), show that $b \approx 0.02$. This leads to a non-dimensional vorticity spreading rate of 0.126, to be compared with the more commonly accepted experimental value of 0.17 for a *natural mixing layer* without external forcing.[3] This proves the inadequacy of the temporal approximation in this case. Experimental bounds for the velocity components variances normalized by U^2 in the central region of the incompressible turbulent spatial mixing layer are: $[0.11 \sim 0.14], [0.07 \sim 0.12], [0.09 \sim 0.11]$ respectively in the streamwise, transverse and spanwise directions. Hence, typical velocity fluctuations are of the order of $0.3U$.

It has to be stressed finally that the statistical self-similarity found in the turbulent shear layers do in no way contradict the existence of coherent vortices or vortices in turbulence: the latter have a self-similar evolution which is part of the global self-similarity of the flow.

As already stressed, the local Reynolds number of the plane mixing layer increases like x.

The boundary layer

In the turbulent boundary layer without pressure gradient above a flat plate, we assume for simplicity a statistical invariance in the x and z directions, and a parallel mean flow. The Reynolds equation writes now:

$$0 = \frac{1}{\rho}\frac{d}{dy}\left(\mu\frac{d\langle u\rangle}{dy} - \rho\langle u'v'\rangle\right) \ .$$

Thus the total (turbulent and viscous) stress

$$\sigma = \mu\frac{d\langle u\rangle}{dy} - \rho\langle u'v'\rangle \tag{4.41}$$

is independent of y (the distance to the boundary). The friction velocity v_* is thus defined by

$$\sigma = \rho v_*^2.$$

It satisfies the relation

$$\rho v_*^2 = \mu\left[\frac{d\langle u\rangle}{dy}\right]_{y=0} \tag{4.42}$$

since at the wall the velocity fluctuations and Reynolds stresses are zero. In fact, v_* characterizes the turbulent velocity fluctuations away from the wall. Indeed, one can there neglect the molecular stresses in Eq. (4.41), which reduces to

[3] In fact, experiments give for $(\bar{U}/U)(d\delta/dx)$ values ranging from 0.15 (Browand and Lattigo [85]) to 0.27 (Huang and Ho [302]).

$$v_*^2 = -\langle u'v' \rangle. \tag{4.43}$$

Sufficiently close to the wall, a linearization of the mean velocity with respect to y yields, thanks to Eq. (4.42)

$$\langle u \rangle = \frac{v_*^2}{\nu} y. \tag{4.44}$$

Assuming such a form, one defines a distance δ_v, called the viscous thickness, such that

$$\langle u \rangle (\delta_v) = v_*,$$

which gives

$$\delta_v = \frac{\nu}{v_*}. \tag{4.45}$$

In fact, it can be shown experimentally and by numerical simulations that Eq. (4.44) holds up to $y \approx 5\delta_v$. In this range, the mean velocity gradient is thus constant and equal to v_*^2/ν.

Usually, one defines wall units (index "+"), where the velocities and lengths are normalized by v_* and δ_v. Eq. (4.41) writes

$$\frac{d\langle u^+ \rangle}{dy^+} = 1 + \langle u'^+ v'^+ \rangle, \tag{4.46}$$

with close to the wall

$$\langle u^+ \rangle = y^+. \tag{4.47}$$

Away from the wall, Eq. (4.43) is equivalent to neglecting the l.h.s. of Eq. (4.46). One assumes also that

$$\nu_t(y) = Ay v_*, \tag{4.48}$$

A being called the Karman constant. This yields

$$-\langle u'^+ v'^+ \rangle = Ay^+ \frac{d\langle u^+ \rangle}{dy^+} \ .$$

Hence, the Reynolds equation reduces in this range to

$$\frac{d\langle u^+ \rangle}{dy^+} = A^{-1} (y^+)^{-1},$$

which leads to the famous mean logarithmic mean velocity profile:

$$\langle u^+ \rangle = A^{-1} \ln y^+ + B. \tag{4.49}$$

This has been very well verified experimentally for $y^+ > 30$, since the observations of Nikuradse [534]). The values found from the experiments for the

constants are $A \approx 0.4$ and $B \approx 5.5$. The extent of the logarithmic layer in the upper direction depends on the Reynolds number. Typical values of δ_v in water and air will be calculated below.

Notice also that, for a turbulent boundary layer spatially developing above a flat plate, arguments based on continuity imply for the boundary-layer thickness $\delta(x)$

$$\frac{\delta(x)}{x} \sim \frac{v_*}{U_\infty}, \tag{4.50}$$

which is very close to a linear spreading rate if one assumes that v_*/U_∞ is not far from a constant (see below).

• Evaluation of wall units

It is easy to show as an exercise that the mean friction coefficient at the wall satisfies

$$C_f = \frac{2\mu}{\rho U_\infty^2} \left[\frac{d\langle u\rangle}{dy}\right]_{y=0} = 2\left(\frac{v_*}{U_\infty}\right)^2. \tag{4.51}$$

In his book, Cousteix [151] proposes the following relation

$$C_f \approx 0.05 R_\delta^{-1/4}, \tag{4.52}$$

where R_δ is the Reynolds number based on the velocity at infinity U_∞ and the 99% boundary-layer thickness. We will take $R_\delta = 2000$, which is comparable to values found in Spalart's DNS [663]. With such a value, we have $v_* \approx 0.06 U_\infty$.

• Olympic swimmer in water

We have $U_\infty = 2$ m/s, $\nu = 10^{-6}$ m^2/s, which gives $\delta_v = 0.83 \times 10^{-5} \approx 10^{-5}$ m.

• Subsonic plane

For a plane in air ($U_\infty = 200$ m/s, $\nu = 1.4 \times 10^{-5}$ m^2/s), we have $\delta_v = 1.16 \times 10^{-6} \approx 10^{-6}$ m.

Channel flow

We consider a plane channel of width $2h$, the origin of the y axis corresponding to the bottom plate. Statistical homogeneity is assumed in the streamwise and spanwise directions. Due to the existence of a pressure gradient $d\langle p\rangle/dx$ in the streamwise direction, the total stress is a function of y. Reynolds equations yield in this case

$$\mu \frac{d\langle u\rangle}{dy} - \rho\langle u'v'\rangle = \rho v_*^2 \left(1 - \frac{y}{h}\right), \tag{4.53}$$

where v_* is defined by Eq. (4.42) with the aid of the mean velocity gradient at one of the walls. So the same wall units as in the boundary layer, v_* and ν/v_*, may be introduced. This yields

$$\frac{d\langle u^+\rangle}{dy^+} - \langle u'^+ v'^+\rangle = 1 - \frac{y^+}{h^+}, \tag{4.54}$$

which differs from Eq. (4.46) by the last term of the right-hand side. The logarithmic range may also be recovered if one assumes there is a region where the Reynolds stress is approximately constant, and makes for the eddy-viscosity the same assumptions as for the boundary layer. Although this derivation is not very satisfactory, the logarithmic layer is indeed observed at both sides of the channel, with approximately the same constants[4] as for the boundary layer.[5] This is clear from Figure 4.1a, corresponding to a comparison of DNS carried out by Kuroda [362] using spectral methods at a Reynolds $h^+ = v_* h/\nu = 150$) and by Lamballais [366] using mixed spectral and finite-difference methods at a Reynolds number based on the friction velocity $h^+ = 162$). These DNS, which use precise numerical methods, turn out to be in very good agreement with the experiments. We see that the logarithmic range begins at $y^+ = 30$. We show in Figure 4.1b the r.m.s. velocity-fluctuations profile in terms of y. It is clear that there is a strong production of u' at the wall, with a peak at $y^+ = 12$. This corresponds in fact to the low- and high-speed streaks, discussed below. Figure 4.1e shows the Reynolds stresses, whose peak is higher (at the bottom of the logarithmic layer), which is the signature of bursting events (ejections). The same peak is observed for the pressure fluctuations (Figure 4.1d), which is certainly due to low pressure associated to high vorticity at the tip of the ejected hairpin (see below). Finally Figure 4.1f shows the r.m.s. vorticity fluctuations (a quantity very difficult to measure precisely experimentally). It indicates that the maximum vorticity produced is spanwise and at the wall. The vorticity perpendicular to the wall is about 40% higher than the longitudinal vorticity in the region $5 < y^+ < 30$, which shows only a weak longitudinal vorticity stretching by the ambient shear.

We mentioned already in Chapter 3 Blasius law of skin friction in a pipe flow, which writes

$$2\left(\frac{v_*}{U}\right)^2 \approx 0.054 R_e^{-1/4}, \tag{4.55}$$

where R_e is built on the mean velocity U across the pipe and its diameter. An analogous result exists for the plane channel, but with a different constant, as

[4] The same is obtained in a pipe.

[5] This logarithmic layer may also be obtained by dimensional arguments, assuming just that the mean velocity gradient is function of v_* and y only, which yields $d\bar{u}/dy \sim v_*/y$ (see e.g. Landau and Lifchitz [371, p. 201]).

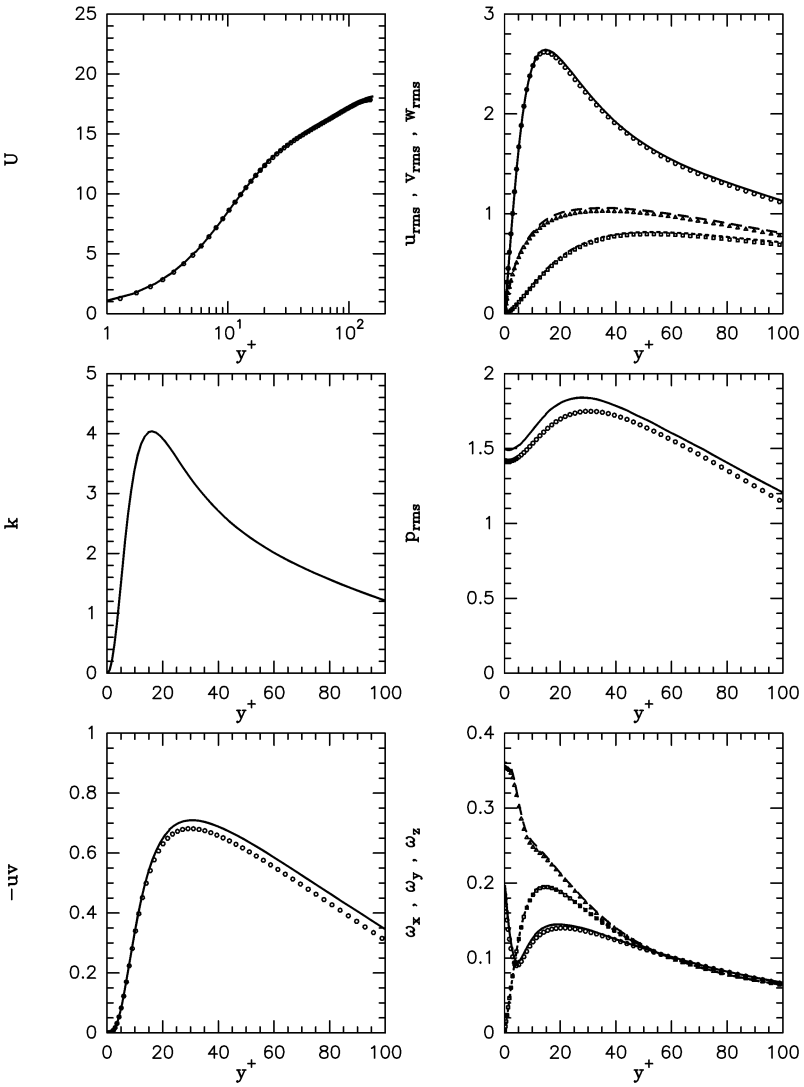

Figure 4.1. Statistical data obtained in DNS of a turbulent channel flow by Lamballais (straight line) and Kuroda (symbols); from left to right and top to bottom, (a) mean velocity, (b) r.m.s. velocity fluctuations (respectively from top to bottom, longitudinal, spanwise, vertical), (c) kinetic energy, (d) r.m.s. pressure fluctuation, (e) Reynolds stresses, (f) r.m.s. vorticity (from top to bottom, spanwise, vertical, longitudinal).

remarked by Dean [161], who proposes

$$2\left(\frac{v_*}{U}\right)^2 \approx 0.073 R_e^{-1/4}, \tag{4.56}$$

whith $R_e = 2Uh/\nu$ (still built on the mean velocity across the channel). It yields

$$h^+ = 0.095 R_e^{7/8}. \tag{4.57}$$

This relation is a good test to assess the validity of DNS or LES carried out for a channel. Remark finally that the above $R_e^{-1/4}$ law for the friction coefficient is the same as for the boundary layer above a flat plate.

Plane Couette flow

In a plane Couette flow, where for instance the upper and lower plates (distance of $2h$) are moved respectively at opposite velocities U and $-U$, laboratory experiments show, when turbulence has developed, a mean velocity profile of the type shown in Figure 3.1b (see e.g. Schlichting [635, chapter 19]). In fact, the profile in not far from uniform in the central region of the channel, and much steeper than the laminar profile close to the walls. As in the turbulent boundary layer, the mean longitudinal pressure gradient is zero, and the stress σ is constant, so that the same analysis as for the boundary layer applies. This provides a nice example allowing to understand why turbulence steepens the velocity gradients at the wall, with respect to the laminar case. Indeed, in the laminar case, the laminar velocity gradient is U/h, and the longitudinal stress which has to be applied on the walls so that they move at a velocity difference $2U$ is $\mu U/h$. In the turbulent case, the mean stress at the wall is $\mu d\langle u\rangle/dy$. In order to move the walls at the same velocity, and to compensate for the increased viscous kinetic-energy dissipation due to turbulence, the mean stress has to be larger than in the laminar regime. It implies $v_* > (\nu U/h)^{1/2}$.

4.3 Characterization of coherent vortices

We have already defined coherent vortices in Chapter 1. We recall that they are regions which have a vorticity concentration strong enough to induce a local roll-up of the flow, and keep a characteristic shape during a time T_c large enough in front of the local turnover time. Now we are going to see how to characterize them. We just summarize here the main conclusions of Lesieur et al. [431].

A good manner to capture them is to look at iso-surfaces of high-vorticity modulus, or vorticity components, or low pressure. A very efficient way is the Q criterion, defined below.

4.3.1 The Q criterion

We recall that S_{ij} and Ω_{ij} are respectively the symmetric and antisymmetric parts of the velocity-gradient tensor $\partial u_i/\partial x_j$. Numerous analyses done on various flows (isotropic turbulence, free-shear layers, separated flows, wall flows, etc.) show that coherent vortices are very well characterized by positive isosurfaces of

$$Q = \frac{1}{2}(\Omega_{ij}\Omega_{ij} - S_{ij}S_{ij}) = \frac{1}{4}(\vec{\omega}^2 - 2S_{ij}S_{ij}) = \frac{\nabla^2 p}{2\rho}. \tag{4.58}$$

This criterion was introduced by Hunt et al. [306] for incompressible flows, but it works also in compressible or heated cases (see the review of Lesieur et al. [431]).

4.4 Coherent vortices in free-shear layers

4.4.1 Spatial mixing layer

In the spatial mixing layer, we have already mentioned that once small-scale turbulence has developed, coherent vortices of the Kelvin–Helmholtz type are still present and undergo various pairings (Brown and Roshko [88]). Their average local longitudinal wavelength λ is of the order of 3.5 times the local vorticity thickness δ (as in the temporal mixing layer when fundamental vortices have developed). We have also pointed out the appearance of secondary coherent vortices in the form of strong longitudinal hairpins stretched between the primary vortices (Bernal and Roshko [56]). As stressed in Chapter 3, the spanwise spacing of these vortices doubles at each pairing (Huang and Ho [302]). In the average, the spanwise wavelength is $\approx (2/3)\lambda$. It is clear that the primary Kelvin–Helmholtz vortices result from a Kelvin–Helmholtz instability of the basic shear, to which are superposed 3D perturbations resulting from the turbulent field. Indeed, if one takes a simple model where the molecular viscosity in Navier–Stokes is replaced by an eddy-viscosity of the order of $0.02U\delta$ (as determined above), the equivalent Reynolds number $U\delta/(2\nu_t)$ will be of the order of 25, which is not far from the inviscid instability regime. Then one should expect the emergence of either straight 2D billows, or possibly the helical-pairing configuration. In the first case, the billows will stretch the secondary longitudinal vortices, by mechanisms already looked at in Chapter 3 (Configuration A). This is the most-commonly accepted view of coherent-vortex topology in a spatially-growing mixing layer. However, and as discussed in the previous chapter, helical pairing has been obtained in DNS and LES of temporal mixing layers (Configuration B). It was also clearly identified by Nygaard and Glezer [541] in experiments with a

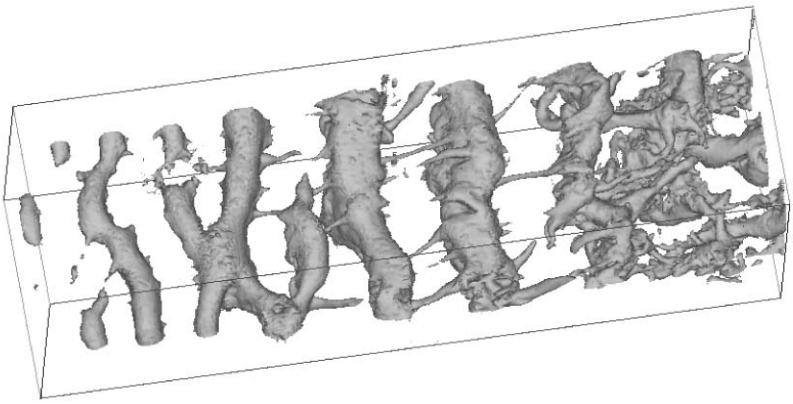

Figure 4.2. LES of an incompressible spatial mixing layer at infinite molecular Reynolds number, forced upstream by a 3D white noise; low-pressure isosurfaces are shown (courtesy G. Silvestrini, Grenoble).

subharmonic forcing at the splitter plate (see also Husain and Hussain [308]). In unforced mixing layers, Browand and Troutt [86] and Nassef and Browand [529] display evidence for dislocations of weak amplitude. They stress that the spanwise longitudinal velocity correlation falls below 20% at spanwise separations of $6\delta \approx 1.7\lambda$, which gives an order of magnitude for the spanwise wavelength of the process. Silvestrini et al. [651] have also carried out LES of spatially-growing mixing layers. With an upstream forcing consisting in a quasi two-dimensional random perturbation, intense longitudinal hairpins stretched between quasi two-dimensional Kelvin–Helmholtz vortices are found again (Plate 17). When the forcing is a three-dimensional random white noise, helical pairing occurs, as indicated by the low-pressure maps of Figure 4.2. But none of these simulations has reached self-similarity, since the kinetic-energy spectra in the downstream region are steeper than $k^{-5/3}$, and rms velocity fluctuations have a departure of about 20% with respect to the experiments. Thus calculations in longer domains are necessary, in order in particular to know in the helical-pairing case whether two-dimensionality might not be restaured further downstream. Complementary numerical results may be found in Comte et al. [140] and Lesieur et al. [431]. Mixing-layer experiments carried out in Poitiers by Bonnet and co-workers [175] display also helical-pairing interactions.

As already proposed in Chapter 3 for turbulent thermal convection at high Rayleigh numbers, one can envisage for coherent vortices in developed mixing layers a cyclic evolution of *creation-destruction-recreation*. Creation comes

from the linear instability of the mean vortex sheet. Afterwards the resulting vortices will three-dimensionalize. This will occur in a first stage either by stretching of longitudinal hairpins or through helical pairing.[6] Then nonlinear interactions of all the modes thus produced may yield the explosive disruption of the coherent vortex, with formation of an ultraviolet Kolmogorov cascade. Recreation would again be due to the linear instability of the mean shear, making the coherent vortices emerge from the smaller-scale turbulence. Such a cyclic evolution had been proposed by Lesieur et al. [420].[7] This corresponds to the phenomenon of large-scale intermittency, well known by experimentalists. It is also possible that some of the conclusions relating to the three-dimensionality growth and the recreation of coherent vortices could be applied to other large Reynolds number shear flows, even if the shear is not inflexional (see Hamilton et al. [269] for a plane Couette flow).

4.4.2 Plane spatial wake

We have seen in Chapter 3 the emergence of quasi two-dimensional Karman vortices as well as longitudinal vortices in a plane wake during the transition to turbulence. This structure had in fact been discovered in experiments at high Reynolds number (2×10^5) done in cavitating wakes by Franc et al. [216]. A picture of the experiment is shown in Figure 4.3a. Here, vortices do correspond to low pressure, and will be marked by cavitating bubbles. One sees very clearly both the shedding of the Karman vortices and the stretching of longitudinal hairpins reconnecting the latter. The pressure in the hairpins is lower than in the Karman billows, as can be shown by increasing progressively the pressure of the facility: Karman vortices will disappear before the longitudinal ones. Figures 4.3b and 4.3c show the LES (at zero molecular viscosity) of an incompressible spatially-growing wake carried out by Gonze [261]. The upstream velocity profile is close to a top hat (in order to simulate the near wake), plus a small 3D isotropic white noise which is regenerated at each time step. In the simulation (Figure 4.3b side view, Figure 4.3c perspective view) is shown an isosurface of the vorticity modulus at a threshold equal to the maximum upstream spanwise vorticity. Resemblance between the experiment and the LES is striking.

As far as the helical pairing is concerned, Cimbala, Nagib and Roshko [127] observe in a far wake a three-dimensional vortex structure resembling very much the above-discussed one, and attribute it to *a secondary instability in the form of a parametric subharmonic resonance similar to that analysed by*

[6] It is in fact possible to have simultaneously longitudinal stretching of thin vortices and helical pairing of the large ones.

[7] They use the analogy between three-dimensionality growth and two-dimensional statistical unpredictability, which will be studied in Chapter 9.

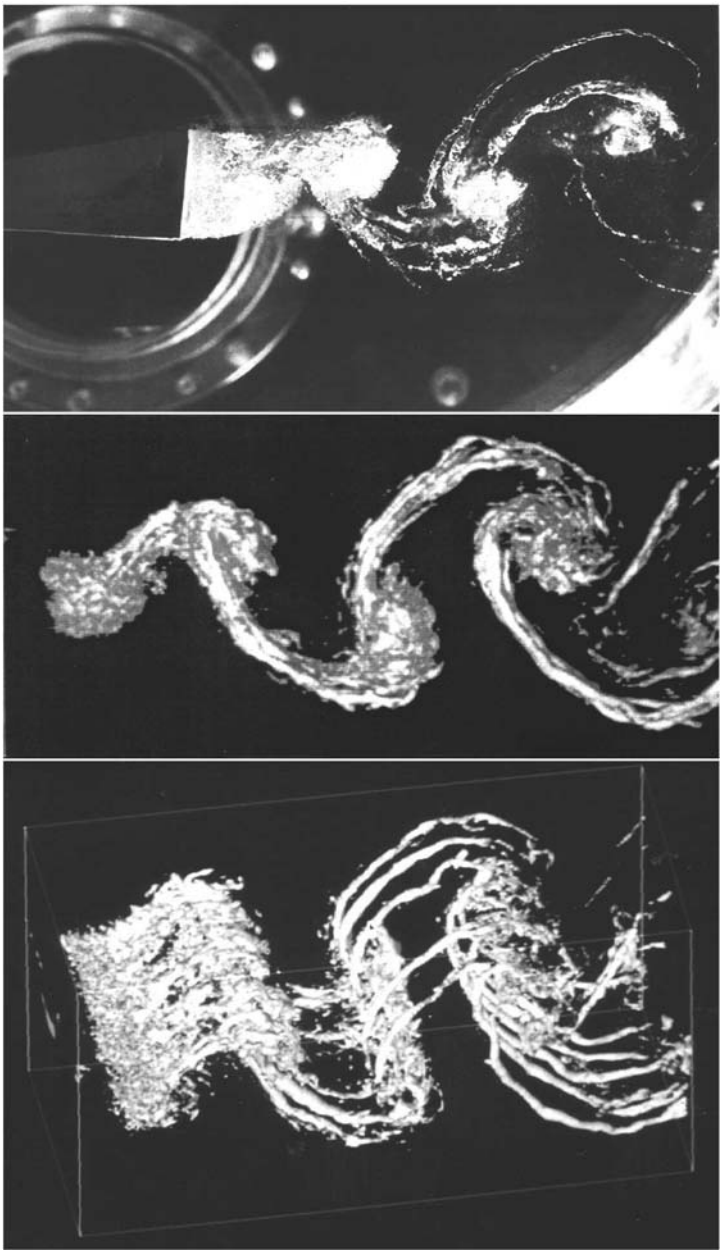

Figure 4.3. (a) Visualization of coherent vortices in a cavitating wake at very high Reynolds number (courtesy J.P. Franc and J.M. Michel, Grenoble); (b) and (c) side and perspective view of the vorticity modulus in the inviscid LES of a spatial wake (courtesy M.A. Gonze, Grenoble).

Pierrehumbert and Widnall [573] in free shear layers, and more extensively for boundary layers and channel flows by Herbert [272]. This question was revisited later on by Williamson and Prasad [719] (see also Williamson [720]) who explain such a dislocated pattern as due to a resonance between oblique shedding in the near wake and 2D Karman modes in the far wake.

4.4.3 Round jets

We first recall the DNS of a weakly incompressible periodic (in the flow direction) round jet done by Fouillet [211]. The jet is initiated from a top-hat profile characteristic of the potential cone immediately downstream of the orifice. The initial Mach number based on the maximum velocity is 0.6, so that, from a mixing-layer point of view (see Chapter 13), the convective Mach number is approximately 0.3 and the flow is quasi-incompressible. A weak 3D random white-noise perturbation is superposed to the initial velocity. The computational grid is a rectangular mesh of resolution $64 \times 32 \times 32$. The initial Reynolds number based on the maximum velocity at the centre U_1 and the half-velocity radius R is of 2000.

The evolution of the simulation at various times is shown in Figure 4.4. One sees iso-surfaces of density[8] (core of the vortex) and low-pressure. At $t = 15R/U_1$, the instability is still not visible on the isopycnic surface. The isobaric surfaces are made of portions of tori of axis slightly inclined with respect to the streamwise direction. They reveal the emergence of an axisymmetric mode of vortex rings. This is compatible with the linear-instability theory which predicts that the axisymmetric mode is the most amplified in the potential cone (Michalke and Hermann [504]), in good agreement with experiments (Tso and Hussain [695]). As time proceeds, the jet spreads out, and its shape factor decreases, the velocity profile becoming quasi-Gaussian. Then the low-pressure tori (or vortex rings) incline each other with respect to the axis in an alternate way, corresponding to the growth of oblique (or helical) modes in the linear-stability theory (Michalke and Hermann [504]). Afterwards the tori reconnect (see Figure 4.4), giving rise to a structure of vortex rings undergoing alternate pairing which has already been encountered in Chapter 3. This is particularly the case at $t = 35R/U_1$. This is obviously the equivalent of helical pairings observed in the plane mixing layer. Then the jet breaks down very abruptly into turbulence, and one can check that the longitudinal kinetic-energy spectrum is close to the $k^{-5/3}$ Kolmogorov's law. However, the double-helix shaped coherent vortices persist. As in the mixing layer, this scenario of transition is reminiscent of the Ruelle–Takens route to turbulence, with emergence of a fundamental mode and growth of a subharmonic.

[8] Here, density is not a passive scalar, since the flow is compressible.

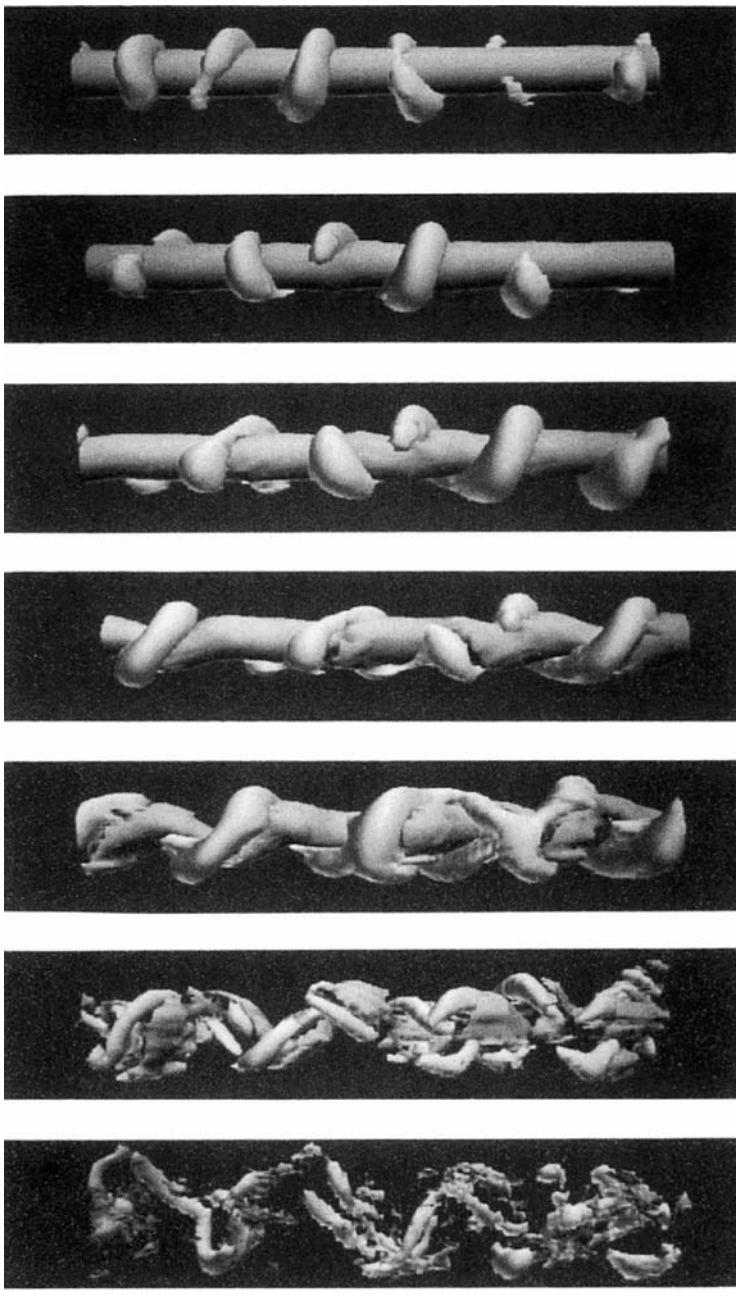

Figure 4.4. DNS of transition to turbulence in a weakly-compressible temporal round jet; time evolution at 15, 20, 25, 30, 35, 40 and 45 initial characteristic times R/U_1 (courtesy Y. Fouillet, 1991).

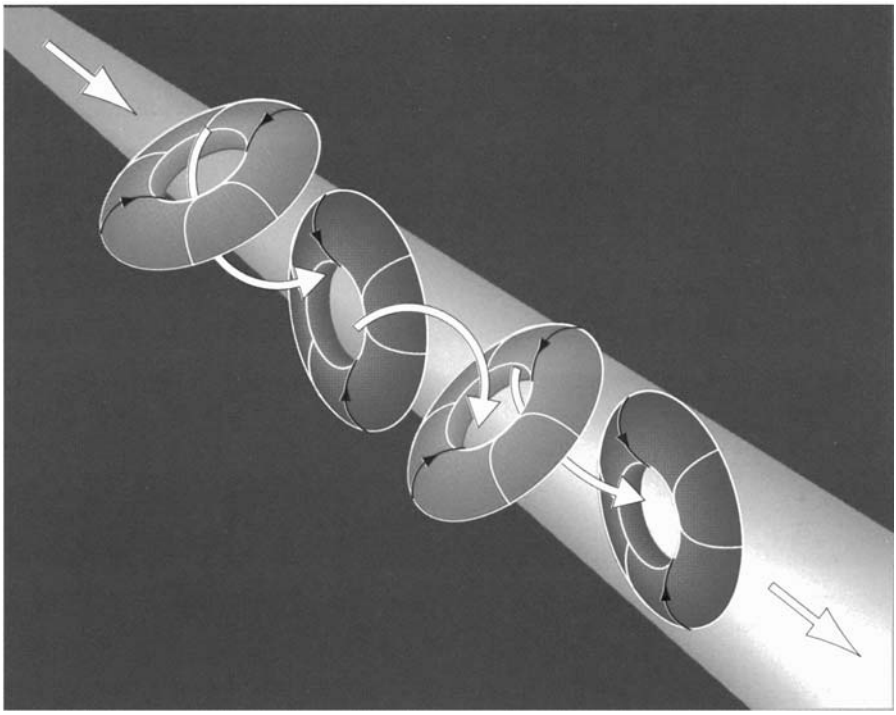

Figure 4.5. Alternate pairing of vortex rings in a round jet. (From Lesieur [424], courtesy EDP-Springer).

Alternate pairing of vortex rings is also discussed in more details in Lesieur et al. [431]. Figure 4.5, reproduced from Lesieur [424], displays a scheme of this phenomenon.

Other DNS of the temporal round jet, where the white-noise perturbation is replaced by a deterministic sine oscillation in the azimuthal direction, show the formation of vortex rings, which stretch longitudinal hairpin vortex filaments between them.[9] These filaments have been very nicely visualized in laboratory experiments performed by Lasheras and Meiburg [386]. Let us mention also the numerical simulations using vortex-filament methods done by Martin and Meiburg [472, 473], both in the case of azimuthal and helical perturbations.

Three-dimensional LES of the incompressible spatially-growing round jet have been carried out by Urbin [696]. The jet is forced upstream by a top-hat profile to which is superposed a weak 3D white noise ("natural forcing"). The

[9] As stressed in Chapter 3, this is exactly like in a plane mixing layer forced by a quasi two-dimensional perturbation.

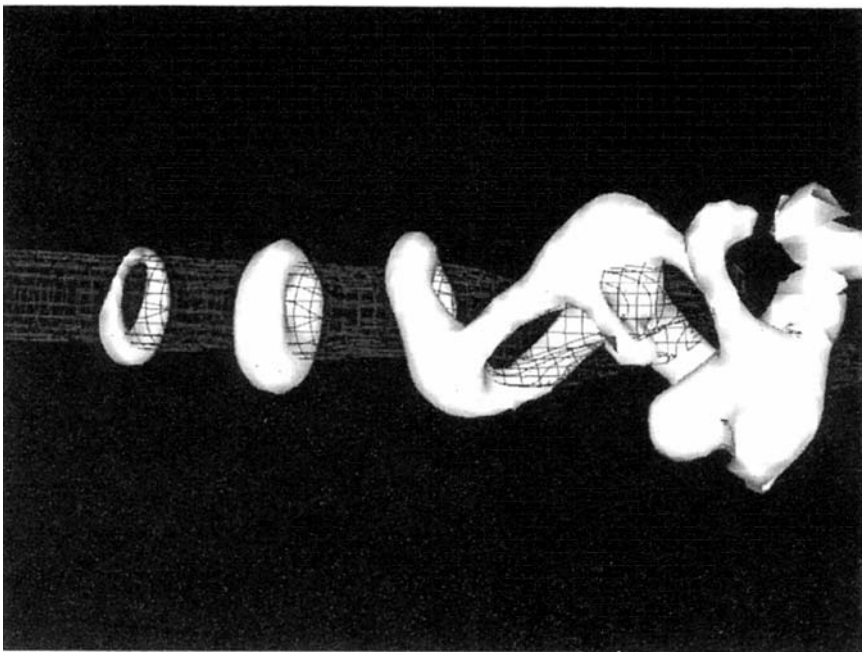

Figure 4.6. LES of a spatially-developing round jet forced naturally; low-pressure field (courtesy G. Urbin, Grenoble).

Reynolds number based on the upstream maximum velocity and diameter is 2000. Figure 4.6 presents a low-pressure wired isosurface. It indicates again the development of the alternate-pairing organization of vortex rings. It seems then that this is the preferred topology of the turbulent round jet forced "naturally" upstream. Similar instabilities might occur in round wakes. As stressed in Lesieur et al [431], numerical methods used by Urbin [696], which are of finite-volume type on a structured mesh, are numerically diffusive. In [431] are presented DNS and LES of the same type of jet at higher Reynolds (25000), with less-diffusive numerical methods (combination of pseudo-spectral and finite-differences of sixth order). One can see on animations of low-pressure and Q the shedding of vortex rings undergoing intermittently alternate pairing, and stretching also thin longitudinal vortices.

We present now a LES of a free[10] spatial compressible round jet at Mach 0.7 and Reynolds number 36000 carried out by Maidi and Lesieur [464]. The convective Mach number is ≈ 0.35, so that compressibility effects are low. As

[10] Initiated upstream by a close to top-hat velocity profile to which a weak white-noise perturbation is superposed.

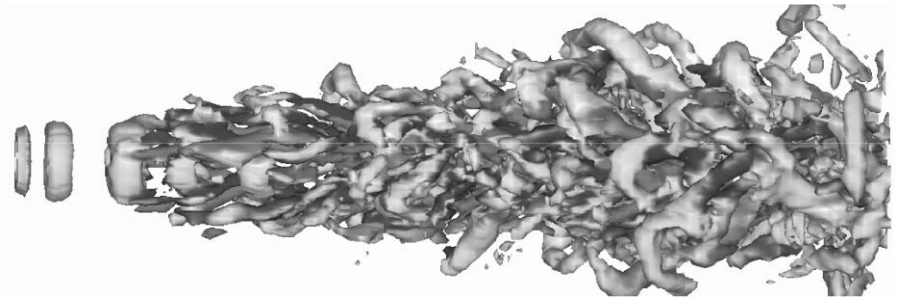

Figure 4.7. LES of a compressible free round jet at Mach 0.7; positive Q isosurfaces coloured by longitudinal vorticity (courtesy M. Maidi, Grenoble).

stressed in Lesieur et al. [431], the code uses MacCormack's [460] predictor-corrector scheme of fourth order in space for the nonlinear terms, modified by Gottlieb and Turkel [262]. The code is second-order accurate in time. It uses characteristic methods for the outflow boundary conditions (see Poinsot and Lele [580]), and a sponge zone downstream. It has been carefully validated against DNS and experiments. A view of Q isosurfaces coloured by longitudinal vorticity is presented in Figure 4.7. One can see very neatly upstream the shedding of quasi axisymmetric vortex rings, which seem to undulate as in Widnall's instability [716]. It is clear that a pairing of the tori has taken place at the level of the third ring. At this point, longitudinal hairpins are stretched. It is well recognized that they bring three-dimensionality to the jet development downstream. One can see also that large vortices take the alternate-pairing organization.

More of these jet simulations in the free and forced cases may be found in Lesieur et al. [431]. Here, the forcings consist in additional perturbations to the upstream velocity. Of particular importance are the varicose (forcing the axisymmetric vortex rings) and flapping (forcing the alternate-pairing mode in these rings) excitations. Da Silva and Métais [158] have shown that the combination of both forcings at respectively harmonic and subharmonic frequencies have a dramatic effect upon the jet structure, with an important spreading in the bifurcating plane. Maidi et al. [465] have considered the effect of the same type of forcing upon a compressible jet (subsonic and supersonic). They recover the incompressible results at Mach 0.7.

This enhanced jet spreading leads to a reduction of the aerodynamic jet noise, as was shown by Maidi [466] using Lighthill's analogy in the forced Mach 0.7 jet case. Complete aeroacoustic applications of DNS and LES may be found in the works of Freund [217, 218], Bogey and Bailly [70], and Wang et al. [711].

4.4.4 Coaxial jets

We consider now coaxial jets in the same fluid, consisting in an interior round jet of velocity U_1 surrounded by an annular jet (axisymmetric layer of flow) going at a different velocity U_2. With a low external velocity, the system is used to reduce the noise emitted by aircraft turbojets. With a high external velocity, this is a configuration close to rocket engines.[11] A complete review of this problem can be found in Balarac [27]. The key parameter is the velocity ratio $r_u = U_2/U_1$. For jets of different densities ρ_1 and ρ_2, it was shown by Favre-Marinet et al. [203, 204] that r_u should be replaced by the momentum flux ratio $\rho_2 U_2^2/\rho_1 U_1^2$. With uniform densities, we have a double inflection point in the upstream velocity profile, leading to the interaction of an inner and outer mixing layer generating vortex rings which are going to interact. We mention the experiments at high velocity ratio carried out by Rehab, Villermaux et al. [591, 702]. DNS in the same conditions have been done by da Silva et al. [159] and Balarac et al. [26, 27]. These computations show that the outer vortex rings impose their frequency to the inner ones. An illustration of a coaxial jet LES at Reynolds 30,000, taken from Balarac [27], is given on the front page, presenting the vorticity norm coloured by tangential vorticity, with four transverse sections of passive-scalar isolines allowing to characterize mixing.

4.5 Coherent vortices in wall flows

As already stressed before, it is well known since the experiments of Kline et al. [337] in the turbulent boundary layer, that streaks of respectively low and high longitudinal velocity (with respect to the local mean velocity profile) exist close to the wall, between approximately $y^+ = 5$ and $y^+ = 40 \sim 50$. The same low and high-speed streaks were found in the turbulent channel, since the LES of Moin and Kim [513] (see also the DNS of Kim et al. [330]). Figure 4.8 shows an illustration of these streaks, in a DNS done by Lamballais and corresponding when turbulence has developed to the same simulation[12] as the transitional calculation of Figure 4.1. The streaks have a spanwise wavelength of about 100 (in wall units), and an average length of ≈ 500. Numerical simulations have confirmed the experimental findings that vorticity patches located just above the low-speed streaks may be ejected away from the wall. This is associated with quasi-longitudinal vortices apparently stretched

[11] But in this real case we have a two-phase flow.

[12] Carried out with pseudo-spectral methods in the streamwise and spanwise directions, and using finite-differences of sixth-order (compact schemes) in the transverse direction.

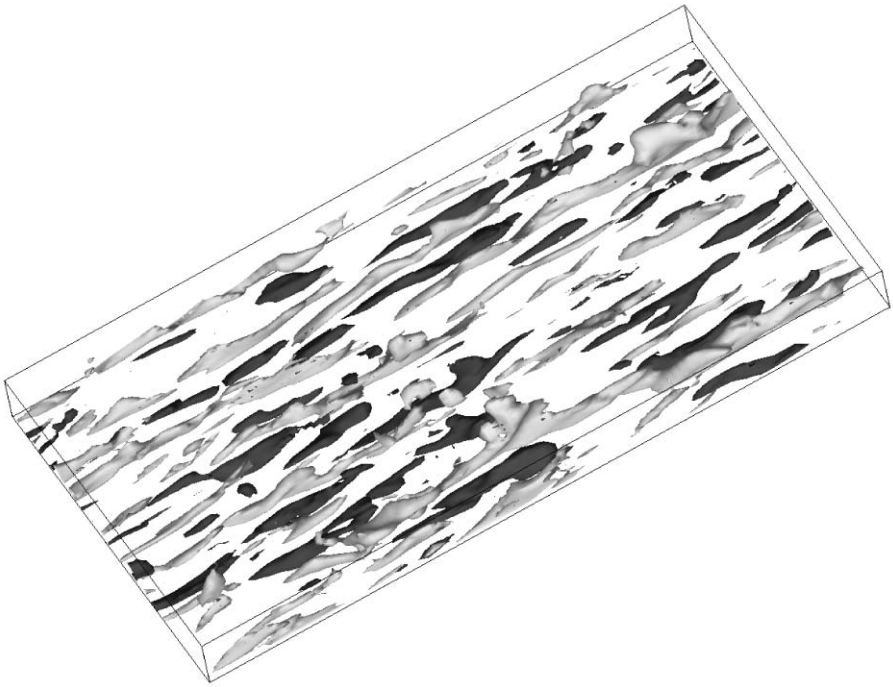

Figure 4.8. Iso-contours of positive (dark) and negative (grey) longitudinal fluctuating velocity in the DNS of a turbulent channel ($h^+ = 162$) close to one wall (courtesy E. Lamballais, Grenoble).

by the ambient shear. It is by this ejection mechanism that vorticity at the wall is transported into the boundary layer, making it turbulent.

In fact, Lesieur et al. [431] display animations of these longitudinal vortices (seen with positive Q isosurfaces) in a periodic channel having a flat wall and a wall equipped with two fine spanwise grooves. The two boundaries are independent. The LES calculation is weakly compressible (Mach 0.3), and uses the same numerical methods as described above for the compressible jet. Let us quote Lesieur et al. [431]:

> Animations of Q presented as well in Dubief and Delcayre [176] permit to follow numerous semi-hairpins traveling downstream. Their legs form quasi-longitudinal vortices close to the wall of approximate length 300 wall units, and many of them have a self-induced, raised-arch-form tip. The animation gives more detailed informations on Q isosurfaces and ω_z isolines at the walls with perspective and top view (...). We recall that for the spatial boundary layers previously presen-

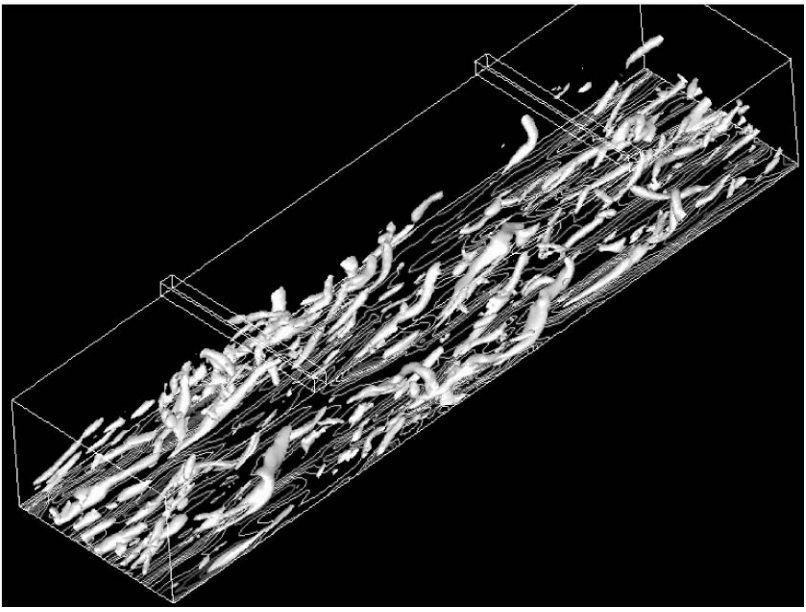

Figure 4.9. Quasi longitudinal vortices (seen by positive Q isosurfaces) traveling close to a flat wall in a weakly-compressible channel (courtesy Y. Dubief, Grenoble).

ted, high values of ω_z at the wall (...) correspond to regions of high friction and should be correlated with the high-speed streaks.

In Figure 4.9 we present a picture taken from the animation.

There are still a lot of controversies about the interpretation of the low- and high-speed streaks, and how they relate to the generation of longitudinal vortices. We will present first fundamental mechanisms involving streaks/vortices interaction. Figure 4.10 is a schematic view of a cross-section of longitudinal vortices and streaks in a plane perpendicular to the mean flow direction. This figure may be interpreted with the aid of the linearized spanwise vorticity equation (3.45) written as

$$\left(\frac{\partial}{\partial t} + \langle u \rangle\right) \omega'_z - \nu \nabla^2 \omega'_z = v' \frac{d^2\langle u \rangle}{dy^2} - \frac{\partial w'}{\partial z} \frac{d\langle u \rangle}{dy}, \tag{4.59}$$

where the "prime" refers now to fluctuations with respect to the mean flow. Close to the wall (e.g. at $y^+ < 5$), $d^2\langle u \rangle/dy^2$ is zero, so that the growth or decay of spanwise vorticity will be characterized by the second term in the r.h.s. of Eq. (4.59). Under the high-speed regions, $\partial w'/\partial z$ is positive, and hence there is production[13] of spanwise vorticity by vortex stretching.

[13] We recall that the basic spanwise vorticity $-d\langle u \rangle/dy$ is negative.

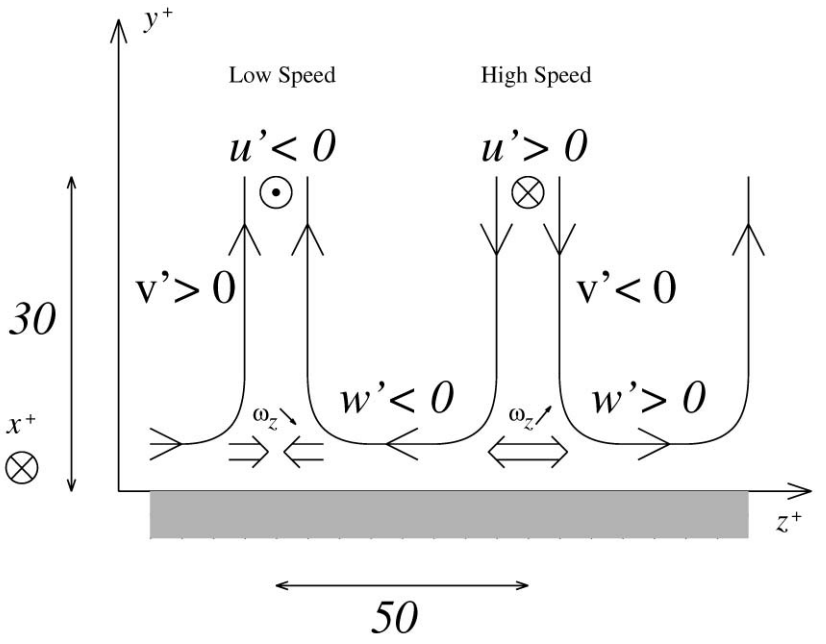

Figure 4.10. Behaviour of the fluid in the streaks close to the wall in the turbulent boundary layer.

This can be interpreted also by saying that sinking fluid in the high-speed streak will reduce locally the boundary-layer thickness and increase the velocity gradient at the wall and the drag. Within this interpretation, and as already stressed, increased drag comes from the friction of high-speed streaks upon the wall. On the other hand, low-speed regions will correspond to a sink of spanwise vorticity by vortex-tube compression. Above, the rising fluid will render inflectional the longitudinal velocity profile: as already mentioned, a local Kelvin–Helmholtz instability will develop, with spanwise vorticity shed downstream (see Figure 4.11). The vortex lines thus formed will reconnect to the wall via vortex filaments, and will form a coherent hairpin of low vorticity, except at the wall.

Plate 18 shows a hairpin in the LES of a spatially-developing boundary layer carried out by Ducros et al. [180]. As it is the case in most of shear flows, and has been mentioned in the previous chapter, this hairpin is very assymmetric, with a much larger concentration of vortex filaments in the right leg than in the left one.

There are still a lot of controversies about the interpretation of the low- and high-speed streaks, and how they relate to the generation of hairpins.

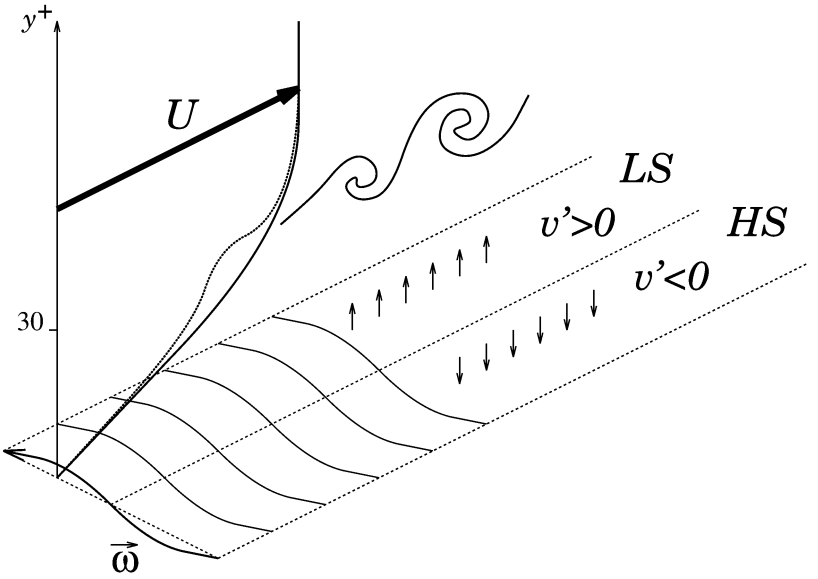

Figure 4.11. Behaviour of the fluid in the streaks close to the wall in the turbulent boundary layer.

The more classical explanation was to invoke a sort of aligned K mode where hairpins generated by some instability of the basic flow would pump up low-speed fluid from the wall, and down high speed fluid from the upper boundary layer. But there is no clear linear or nonlinear theory for such an instability, and one does not understand why it should create aligned hairpins having enough coherence downstream to generate streaks so elongated. Furthermore, the mechanism where spanwise vortex filaments close to the boundary, and hence of spanwise vorticity $\approx v_*^2/\nu$, are stretched longitudinally by the basic shear, should produce a longitudinal vorticity at least of the same order (even though viscosity is active). In fact, numerical experiments indicate rather that the rms longitudinal vorticity is upper bounded by $0.14 v_*^2/\nu$ for $y^+ > 5$ (see the statistics of Figure 4.1).

We remark also that the longitudinal vortices were predicted by Townsend [689] for turbulence submitted to a constant mean velocity gradient, using rapid-distorsion theory. The latter consists in solving in spectral space the linearized equation of motion (see an example of this technique in the next chapter).[14] The longitudinal vortices would pump between them low and high-speed fluid, producing the streaks, as displayed in Figure 4.10.

[14] Townsend's conclusions are based on the sign and behaviour of various velocity correlations. It is however difficult from this to extract a definite information

Among the numerous authors having contributed to this difficult problem of *hen and chicken*, we discuss some works: Blackwelder [65] proposed that the longitudinal vortices, of approximate length 500 wall units, existed, by analogy with Görtler vortices in curved boundary layers (which happen also to be weak). But it is difficult to consider a flat wall as a limiting case of curvature. In Smith and Walker [654], it is proposed that a hairpin travelling downstream is going to pump the fluid it crosses, and induce a trailing low-speed streak region.

Another explanation is to assume that everything is governed by the development close to the wall of a longitudinal mode, as mentioned in Chapter 3. This was first proposed by Landhal and Mollo-Christensen [372], and further discussed by Schmidt and Henningson [637]. We stress that the mean velocity gradient (expressed in wall units) goes from 1 at the wall to a very weak value at $y^+ = 40$ (≈ 0.06, as given by the logarithmic law). This implies that the shear has no direct effect above. The streaks might originate from a weak vertical oscillation of the fluid layers in planes parallel to (x, y), yielding strong longitudinal oscillations of the flow (high speed in the downward motion, low-speed in the upward motion), according to Eqs. (3.43) and (3.44), or to the velocity-sheets model proposed in Chapter 3 (taking in account for the latter case the fluctuations with respect to the mean velocity gradient v_*^2/ν at the wall). Such a longitudinal mode corresponds in fact to writing that the fluid parcel keeps its velocity with the motion, a sort of "Taylor hypothesis", as noted by Landhal and Mollo Christensen [372]. Within this interpretation, the streaks are responsible for the production of vorticity ω_y (see Chapter 3). The longitudinal vorticity is weaker, and cannot increase following the motion in the longitudinal mode. This explanation does not suppose the existence of a wall in order to produce the streaks. This point was confirmed by the DNS of homogeneous turbulence submitted to a constant high shear rate carried out by Lee et al. [395]. They introduce a shear-rate parameter $S_* = \lambda l/q$, where λ is the mean velocity gradient, and l and $q = \langle u_i' u_i' \rangle^{1/2}$ are respectively the integral scale and characteristic velocity fluctuation of the initial isotropic turbulence upon which the shear is exerted.[15] Low and high-speed streaks very similar to those of a turbulent boundary layer or channel are observed for S_* larger than ≈ 30 (which corresponds to values obtained in a channel at $y^+ \approx 10$). Longitudinal vorticity in this calculation is low. They show also a very good agreement with rapid-distorsion theory, applied starting initially with an instantaneous turbulent field taken from the DNS.

about the flow topology, and longitudinal streaks of finite extent without longitudinal vortices at the wall would certainly produce the same type of correlations.

[15] S_* is the ratio of the inertial time of turbulence l/q divided by the shear characteristic time S^{-1}. High values of S_* mean that the effects of the shear may take place before nonlinear interactions of turbulence start acting.

Let us comment the DNS of Hamilton et al. [269] in a plane Couette flow, where they observe a quasi-cyclic process of regeneration of near-wall structures, composed of three stages: formation of streaks by streamwise vortices, breakdown of the streaks, and regeneration of the streamwise vortices.

From an experimental point of view, the work of Christensen and Adrian [126] displays nicely the small-scale vortex structure in a boundary layer.

4.5.1 Vortex control

Mathematical optimal-control strategies have been developed for the plane channel (see e. g. Bewley et al. [62]). They yield interesting results on systems with modified flow dynamics. But they have not lead to applications in real boundary layers.

From a more practical viewpoint, Choi et al. [115] have shown with the aid of DNS which role do the longitudinal vortices play in the presence of longitudinal riblets. They studied a channel whose lower wall was equipped with riblets, while the upper was flat. Two different calculations were carried out, one with a spanwise spacing of riblets of 40 wall units, the second with 20. In the first case, the longitudinal structures (whose diameter is ≈ 25) can stay in the riblet valleys, and the drag is increased with respect to the non-equipped wall. In the second case, the longitudinal vortices have no place to stand in the valleys, and sit above the peaks, so that their contact surface with the boundary is reduced. In this case the drag decreases of $\approx 8\%$. The reader will find in Lesieur et al. [431] new LES (with animations) of flows above riblets in the compressible case. They are carried out in a channel (same type of configuration as Choi et al. [115] with immersed-boundary techniques (see Hauët [270]). In the latter work, a LES at low Mach is validated against [115]. LES in supersonic regimes (without changing the physical size of riblets) do confirm the anterior experimental findings of Coustols and Cousteix [152] that riblets efficiency is not affected by compressibility.

Notice that Nature has provided the skin of some fast sharks with riblets. Let us mention also that the so-called shark-skin swimming costumes are equipped with riblets. With the evaluation $\delta_v \approx 10^{-5}$ m given above, they should have a size of 2×10^{-4} m for the olympic swimmer. For the subsonic aircraft, the size is 2×10^{-5} m.

4.6 Turbulence, order and chaos

This discussion, in fact, belongs more to Chapter 1 than the present chapter, but since it requires some of the instability results which have just been presented, we have preferred to postpone it to the present chapter. This section

will contain some historical and philosophical developments about turbulence, which are not really needed for an understanding of the rest of the book, but which could, nevertheless, be of some interest to the reader.

Actually, the concepts of "order", "disorder" and "chaos" are ill-defined when applied to fluid turbulence: in statistical thermodynamics for instance, "disorder" can be associated to the entropy of the system, and it is generally believed that the second principle of thermodynamics (that is the tendency for an isolated system to increase its entropy) implies a maximization of the disorder, and hence an evolution of the system from order to disorder. Valid or not, this last statement at any rate has proven useless for fluid turbulence, where no analogous entropy function has been defined.[16] As for the word "coherence", it is, as already stressed, generally used for vortices or structures having some kind of spatial organization, such as the mixing-layer large eddies, the boundary layer streaks, or the "dissipative structures" of the internal intermittency envisaged in Chapter 2 for instance. Some people are puzzled by the existence of such structures in turbulent flows, and tend either to reject their existence or to consider them separately from the rest of the flow, denying then the appellation of turbulence to them. Actually, it seems more reasonable to consider these vortices, when they exist, as part of the turbulence itself: we have already seen that such structures are generally unpredictable, though they have a spatial coherence. It is erroneous to associate the concept of unpredictability to a spatial disorganization where no well-defined spatial structures would appear: in actual fact, when looking at a particular realization of a turbulent flow, one sometimes sees mainly a set of "coherent" vortices, which nevertheless are unpredictable in phase (that is position in space), but which may conserve their geometrical shape for times much longer than the characteristic time of loss of predictability. Even in such situations a statistical analysis of turbulence using the statistical tools presented below can be performed, as will be seen in the following chapters.

With that in mind, it is not difficult to understand the points of view which associate "turbulence" to "order", if we interpret this latter word as meaning the existence of spatially organized "coherent" vortices. This interpretation of turbulence was for instance contained in the Latin poet Lucretius' ideas, which were very aptly commented upon by Serres [642]: Lucretius interpreted the universe as a "turbulent order" which had emerged from an initial "Brownian-like chaos" through the development of what he called the "declination",[17] and which is exactly the infinitesimal perturbation in the instability theory.

[16] It has to be stressed however that in the case of the truncated Euler equations (Euler equations where only a finite number of modes has been retained), statistical thermodynamics apply, and the entropy of the system can be defined (see Chapter 10 and also Carnevale [98]).

[17] From the Latin "clinamen".

This initial "chaos" was assimilated to what we call a "laminar state", so that the usual scheme

"laminar yields turbulence"

was thus transformed into the provocative statement

"order (i.e. turbulence) emerges from chaos" (4.60)

which could also be used to explain the appearance of life, the formation of the universe, and even the evolution of human societies.

Actually, there is not such a great gap between Lucretius' statement Eq. (4.60) and the general ideas on transition to turbulence which have been presented in section 1: Lucretius' philosophy contains both the idea of the development of a perturbation due to an instability, and perhaps also the idea of intermittency, where an initial random state distributed homogeneously in space would evolve towards spatially organized structures like the dissipative structures of turbulence. The appearance of dissipative structures as the result of the development of an instability was also emphasized by Prigogine [589].

In the reality of fluid dynamics, it seems nevertheless difficult to accept blindly statements like Eq. (4.60) in order to explain turbulence. But perhaps this concept of order emerging from chaos can be adapted in the following way: let us start with the example of the mixing layer, where we superpose upon an inflectional velocity profile a small white-noise random perturbation, which possesses energy on all wave lengths and in particular in the unstable modes (see Plate 7): these latter modes will then grow, and the most unstable mode (that is with the highest amplification rate) will appear the first, corresponding to the coherent vortices which are initially observed on Plate 7. In that sense, one can say that an "ordered structure" (the coherent eddy) has emerged from the chaos represented by the random perturbation. But the entire process was completely dependent on the existence of the linearly-unstable basic inflectional velocity profile, which in particular imposes the vorticity sign of all the large eddies which will successively appear. The same kind of analysis can be made for wakes or jets. In fact, Eq. (4.60) could be more correctly restated as

coherent vortices emerge from chaos,

under the action of an external constraint. (4.61)

In the preceding examples, the external constraint was the instability of the inflectional basic velocity profile. In stratified turbulence, the constraint is the buoyancy which creates convective structures in the unstable case, and could tend to create quasi two-dimensional turbulence in the stable case (see Chapter 13). In the experiment of rotating turbulence of Hopfinger et al. [296] presented in Plate 4, the coherent structures are the high-vorticity eddies

whose axes are parallel to the axis of rotation, the "chaos" consists of the three-dimensional turbulence created at the bottom of the tank, and the external constraint might be the shear-Coriolis instability described in Chapter 3.

5

Fourier Analysis of Homogeneous Turbulence

5.1 Introduction

When turbulence is homogeneous, i.e. statistically invariant under translations, it is extremely useful to work in Fourier space. In this chapter various Fourier representations of a statistically homogeneous turbulent flow will be presented, as well as Navier–Stokes or Boussinesq equations projected in that space. We will discuss more the utilization of random functions for turbulence study, and describe the properties of isotropic turbulence (statistically invariant under rotations). Helical turbulence will be considered, with the helical-wave decomposition of the velocity field. This corresponds to fully-developed turbulence. We will look also briefly at axisymmetric turbulence. Finally, we will see how rapid-distorsion theory applies to homogeneous turbulence submitted to a plane strain.

5.2 Fourier representation of a flow

5.2.1 Flow "within a box"

The simplest mathematical way of introducing the Fourier representation of a homogeneous turbulent flow is to consider a fictitious ideal flow – the flow within a box – defined in the following way: given a particular turbulent flow (which may not even be homogeneous), we consider in the physical space a cubic box of size L, chosen in such a way that it contains all the spatial features of the flow one wants to study. It is also assumed that the boundary conditions on the sides of the box are cyclic: this of course may pose some problems and will make this ideal flow differ from the actual flow. Once the cyclic flow within the box is constructed, we fill the whole space with an infinite number

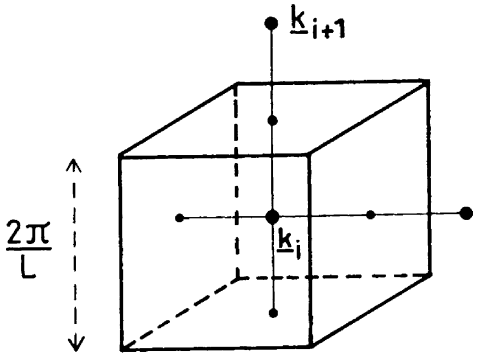

Figure 5.1. The discrete Fourier transform of a "flow within a box of size L" at the mode $\vec{k}_i$ is the average of the integral Fourier transform of the flow on an elementary cube B_i of side $2\pi/L$ surrounding $\vec{k}_i$.

of identical boxes, so that one obtains a periodic flow of period L in the three directions of space. Thus this "flow within a box" is a periodic flow filling the whole space and whose features for scales smaller than L are close to the features of the real flow. Let $\vec{u}(\vec{x},t)$ be the periodic velocity field. Since it is periodic of period L, it can be expanded as an infinite series

$$\vec{u}(\vec{x},t) = \left(\frac{2\pi}{L}\right)^3 \sum_{n_1,n_2,n_3=-\infty}^{+\infty} e^{(2i\pi/L)(n_1x_1+n_2x_2+n_3x_3)} \underline{\hat{u}}_B(n_1,n_2,n_3,t), \quad (5.1)$$

where $n_1 n_2 n_3$ are positive or negative integers. The coefficient in front of the r.h.s. of Eq. (5.1) has been chosen for reasons of normalization. Introducing the wave-vector $\vec{k}$ of components

$$\vec{k} = \left[\frac{2\pi}{L}n_1, \frac{2\pi}{L}n_2, \frac{2\pi}{L}n_3\right],$$

Eq. (5.1) can be written as

$$\vec{u}(\vec{x},t) = (\delta k)^3 \sum_{n_1,n_2,n_3=-\infty}^{+\infty} e^{i\vec{k}.\vec{x}} \underline{\hat{u}}_B(\vec{k},t), \quad (5.2)$$

with $\delta k = 2\pi/L$.

The Fourier transform $\underline{\hat{u}}_B(\vec{k},t)$ of the periodic velocity $\vec{u}(\vec{x},t)$ is only defined for wave vectors whose components are multiples of the elementary wave number δk. The next section will show how $\underline{\hat{u}}_B(\vec{k},t)$ can be determined in terms of $\vec{u}(\vec{x},t)$.

5.2.2 Integral Fourier representation

Let us now consider a flow $\vec{u}(\vec{x},t)$ defined in the whole physical space R^3 and not necessarily periodic. The integral Fourier transform of $\vec{u}(\vec{x},t)$ is defined as

$$\underline{\hat{u}}(\vec{k},t) = \left(\frac{1}{2\pi}\right)^3 \int e^{-i\vec{k}.\vec{x}} \vec{u}(\vec{x},t) d\vec{x}, \tag{5.3}$$

with $d\vec{x} = dx_1 dx_2 dx_3 = d^3x$. Generally, in homogeneous turbulence, $\vec{u}(\vec{x},t)$ does not decrease rapidly to infinity, and $\underline{\hat{u}}(\vec{k},t)$ has to be defined by referral to the theory of distributions[1] (see Schwartz [641]). We use the inverse Fourier transform relation

$$\vec{u}(\vec{x},t) = \int e^{i\vec{k}.\vec{x}} \underline{\hat{u}}(\vec{k},t).d\vec{k} \tag{5.4}$$

In fact Eqs. (5.3) and (5.4) hold also for a scalar function. Replacing in Eq. (5.4) $\hat{u}(\vec{k},t)$ by the three-dimensional Dirac function $\delta(\vec{k})$, such that $\int \delta(\vec{k}) d\vec{k} = 1$ yields with the aid of Eq. (5.3):

$$\delta(\vec{k}) = \left(\frac{1}{2\pi}\right)^3 \int e^{-i\vec{k}.\vec{x}} d\vec{x} = \left(\frac{1}{2\pi}\right)^3 \int e^{i\vec{k}.\vec{x}} d\vec{x}. \tag{5.5}$$

So a flow within a box possesses two different Fourier transforms, the integral one and the discrete one, and it is of interest to determine a relation between these Fourier transforms. The following calculation is not essential for the understanding of the present chapter, but has been given here as an exercise allowing the reader to become accustomed to these notions: using Eqs. (5.2) and (5.3), we obtain:

$$\underline{\hat{u}}(\vec{k},t) = \left(\frac{1}{2\pi}\right)^3 \int e^{-i\vec{k}.\vec{x}} \left(\frac{2\pi}{L}\right)^3 \sum_{\vec{k}'} e^{i\vec{k}'.\vec{x}} \underline{\hat{u}}_B(\vec{k}',t) d\vec{x}. \tag{5.6}$$

In Eq. (5.6), $\vec{k}$ is not necessarily of components multiple of δk; $\vec{k}'$, on the contrary, must satisfy this condition. Then Eq. (5.6) is written, using Eq. (5.5)

$$\underline{\hat{u}}(\vec{k},t) = \left(\frac{2\pi}{L}\right)^3 \sum_{\vec{k}'} \delta(\vec{k}-\vec{k}') \underline{\hat{u}}_B(\vec{k}',t), \tag{5.7}$$

and $\underline{\hat{u}}(\vec{k},t)$ is a three-dimensional Dirac comb of "intensities"

$$(2\pi/L)^3 \underline{\hat{u}}_B(\vec{k}',t).$$

[1] Also called generalized functions.

Let us consider now an average in Fourier space of $\underline{\hat{u}}(\vec{k},t)$ on a cubic box B_i of centre $\vec{k}_i$ (where $\vec{k}_i$ is one of the discrete wave vectors for which $\underline{\hat{u}}_B$ is defined) and of sides $2\pi/L$:

$$\bar{\underline{\hat{u}}}(\vec{k}_i) = \frac{1}{\mathrm{Vol}(B_i)} \int_{B_i} \underline{\hat{u}}(\vec{k}) d\vec{k}. \tag{5.8}$$

We have

$$\bar{\underline{\hat{u}}}(\vec{k}_i) = \frac{1}{\mathrm{Vol}\ (B_i)} \int_{B_i} \left(\frac{2\pi}{L}\right)^3 \sum_{\vec{k}'} \delta(\vec{k}-\vec{k}') \underline{\hat{u}}_B(\vec{k}') d\vec{k}, \tag{5.9}$$

where $\mathrm{Vol}(B_i) = (2\pi/L)^3$ is the volume of box B_i. In Eq. (5.9), $\vec{k}'$ must belong to B_i, otherwise $\delta(\vec{k}-\vec{k}')$ is always zero. Thus, using the identity

$$\int \delta(\vec{k}-\vec{k}_i) d\vec{k} = 1,$$

we finally obtain

$$\bar{\underline{\hat{u}}}(\vec{k}_i,t) = \underline{\hat{u}}_B(\vec{k}_i,t). * * \tag{5.10}$$

Eq. (5.10) shows that the discrete Fourier transform of a flow within a box is the integral Fourier transform of the flow averaged on the cubic box B_i, that is:

$$\underline{\hat{u}}_B(\vec{k}_i,t) = \frac{1}{\mathrm{Vol}(B_i)} \int_{B_i} \left(\frac{1}{2\pi}\right)^3 d\vec{k} \int e^{-i\vec{k}.\vec{x}} \vec{u}(\vec{x},t) d\vec{x}. \tag{5.11}$$

Therefore, Eq. (5.11) enables us to calculate $\underline{\hat{u}}_B(\vec{k},t)$ in terms of $\vec{u}(\vec{x},t)$. In this book, we will mainly use the integral Fourier representation of the flow, but all the derivations could be given using the discrete representation. The latter is employed in numerical simulations using pseudo-spectral methods. Notice also that, in two dimensions, the factors $(2\pi/L)^3$ and $(1/2\pi)^3$ have to be replaced by $(2\pi/L)^2$ and $(1/2\pi)^2$.

5.3 Navier–Stokes equations in Fourier space

This section will consider the case of a fluid of constant and uniform mean density ρ_0, without buoyancy or rotation Ω, which satisfies, from Chapter 2:

$$\frac{\partial \vec{u}}{\partial t} + \vec{u}.\vec{\nabla}\vec{u} = -\frac{1}{\rho_0}\vec{\nabla}p + \nu\nabla^2\vec{u},$$

$$\frac{\partial \rho'}{\partial t} + \vec{u}.\vec{\nabla}\rho' = \kappa\nabla^2\rho', \tag{5.12}$$

$$\vec{\nabla}.\vec{u} = 0.$$

ρ' is the density (resp. temperature, potential temperature, or any passive scalar) fluctuation.

Let us consider any function $f(x_1, x_2, x_3, t)$, of Fourier transform $\hat{f}$. Then the Fourier transform of $\partial f/\partial x_i$ is $ik_i\hat{f}(k_1, k_2, k_3, t)$, where k_i is the i-component of the wave vector $\vec{k}$. This is easily obtained by taking the derivative of Eq. (5.4) with respect to x_i. Thus, calling "F.T." the Fourier transform operator, one has:

$$f(\vec{x}, t) \text{F.T. } \hat{f}(\vec{k}, t)$$

$$\frac{\partial f}{\partial x_i} \text{ F.T. } ik_i\hat{f}(\vec{k}, t)$$

$$\vec{\nabla} f \text{ F.T. } i\hat{f}(\vec{k}, t)\vec{k}$$

$$\nabla^2 f = \frac{\partial^2 f}{\partial x_1^2} + \frac{\partial^2 f}{\partial x_2^2} + \frac{\partial^2 f}{\partial x_3^2} \text{ F.T. } -(k_1^2 + k_2^2 + k_3^2)\hat{f} = -k^2\hat{f}$$

$$\vec{\nabla}.\vec{u} \text{ F.T. } i\vec{k}.\underline{\hat{u}}(\vec{k}, t)$$

$$\vec{\nabla} \times \vec{u} \text{ F.T. } i\vec{k} \times \underline{\hat{u}}(\vec{k}, t)$$

$$f(\vec{x}, t)g(\vec{x}, t) \text{ F.T. } [\hat{f} * \hat{g}](\vec{k}, t) \tag{5.13}$$

where * is the convolution product $\int_{\vec{p}+\vec{q}=\vec{k}} \hat{f}(\vec{p}, t)\hat{g}(\vec{q}, t)d\vec{p}$. The incompressibility condition $\vec{\nabla}.\vec{u} = 0$ implies

$$\vec{k}.\underline{\hat{u}}(\vec{k}, t) = 0, \tag{5.14}$$

and the velocity $\underline{\hat{u}}(\vec{k}, t)$ is in a plane Π perpendicular to $\vec{k}$.

Now let us write Navier–Stokes equations in Fourier space: since $\underline{\hat{u}}(\vec{k}, t)$ is in the plane perpendicular to $\vec{k}$, $\partial\underline{\hat{u}}(\vec{k}, t)/\partial t$ and $\nu k^2\underline{\hat{u}}$ also belong to that plane. On the contrary the pressure gradient $i\hat{p}\vec{k}$ is parallel to $\vec{k}$. The consequence is that the Fourier transform of

$$\vec{u}.\vec{\nabla}\vec{u} + (1/\rho_0)\vec{\nabla}p$$

is the projection on Π of the Fourier transform of $\vec{u}.\vec{\nabla}\vec{u}$. Let us introduce the tensor

$$P_{ij}(\vec{k}) = \delta_{ij} - \frac{k_i k_j}{k^2} \tag{5.15}$$

which allows a vector $\vec{a}$ to be projected on a plane perpendicular to $\vec{k}$:

$$a_j P_{ij}(\vec{k}) = i\text{-component of the projection of } \vec{a} \text{ upon } \Pi \tag{5.16}$$

with the Einstein convention of summation upon repeated indices. Then, noticing that, due to incompressibility

$$\text{F.T.}\ \left[u_j\frac{\partial u_i}{\partial x_j}\right] = \text{F.T.}\ \left[\frac{\partial (u_iu_j)}{\partial x_j}\right] = ik_j\int_{\vec{p}+\vec{q}=\vec{k}}\hat{u}_i(\vec{p},t)\hat{u}_j(\vec{q},t)d\vec{p}, \qquad (5.17)$$

the i-component of $\vec{u}.\vec{\nabla}\vec{u} + (1/\rho_0)\vec{\nabla}p$ in Fourier space is equal to

$$ik_mP_{ij}(\vec{k})\int_{\vec{p}+\vec{q}=\vec{k}}\hat{u}_j(\vec{p},t)\hat{u}_m(\vec{q},t)d\vec{p}.$$

Finally the Navier–Stokes equation in Fourier space is written

$$\left(\frac{\partial}{\partial t}+\nu k^2\right)\hat{u}_i(\vec{k},t) = -ik_mP_{ij}(\vec{k})\int_{\vec{p}+\vec{q}=\vec{k}}\hat{u}_j(\vec{p},t)\hat{u}_m(\vec{q},t)d\vec{p}. \qquad (5.18)$$

The pressure has thus been eliminated by projection on the "incompressibility plane". The evolution equation for the density fluctuation $\hat{\rho}'(\vec{k},t)$ is straightforward:

$$\left(\frac{\partial}{\partial t}+\kappa k^2\right)\hat{\rho}'(\vec{k},t) = -ik_j\int_{\vec{p}+\vec{q}=\vec{k}}\hat{u}_j(\vec{p},t)\hat{\rho}'(\vec{q},t)d\vec{p}. \qquad (5.19)$$

One can already notice that the nonlinear interactions involve triad interactions between wave vectors such that $\vec{k}=\vec{p}+\vec{q}$. A structure of wave length $2\pi/k$ will also often be associated with a wave number k.

In the pseudo-spectral methods used for direct-numerical simulations of turbulence (Orszag and Patterson [552]), Navier–Stokes equation for an incompressible non-rotating fluid in Fourier space is, from Eq. (2.22), written as:

$$\frac{\partial}{dt}\underline{\hat{u}}(\vec{k},t) = \Pi(\vec{k})\circ F[F^{-1}(\underline{\hat{u}})\times F^{-1}(\underline{\hat{\omega}})] - \nu k^2\underline{\hat{u}}(\vec{k},t), \qquad (5.20)$$

where $\Pi(\vec{k})\circ$ stands for projection on the plane perpendicular to $\vec{k}$. F is the Fast Fourier transform operator. This procedure is much faster than a direct evaluation in Fourier space of the generalized convolution product in the r.h.s. of Eq. (5.18). With these notations, the passive scalar equation writes

$$\frac{\partial}{dt}\hat{\rho}'(\vec{k},t) = -i\vec{k}.F[F^{-1}(\hat{\rho}')F^{-1}(\underline{\hat{u}})] - \kappa k^2\hat{\rho}'(\vec{k},t). \qquad (5.21)$$

5.4 Boussinesq equations in Fourier space

One can also write in Fourier space the Boussinesq equations in a rotating frame of rotation $\vec{\Omega}$. This will be useful when studying stably-stratified turbulence in Chapter 13. We recall them in physical space (see Eqs. (2.112)):

$$\frac{\partial \vec{u}}{\partial t} + \vec{u}.\vec{\nabla}\vec{u} = -\vec{\nabla}\tilde{p} - \tilde{\rho} g\vec{\beta} - 2\vec{\Omega} \times \vec{u} + \nu\nabla^2\vec{u},$$

$$\frac{\partial \tilde{\rho}}{\partial t} + \vec{u}.\vec{\nabla}\tilde{\rho} - \frac{N^2}{g} w = \kappa\nabla^2\tilde{\rho}, \tag{5.22}$$

$$\vec{\nabla}.\vec{u} = 0,$$

where, according to the discussion of Chapter 2, the vertical axis of coordinate $\vec{z}$ has been taken parallel to $\vec{g}$ and $\vec{\Omega}$, $\vec{\beta}$ being a vertical unit vector such that $\vec{g} = -g\vec{\beta}$ and $\vec{\Omega} = \Omega\vec{\beta}$. In the r.h.s. of the thermal equation, the contribution of the mean stratification has been neglected. N is the Brunt–Vaisala frequency. In Fourier space, the nonlinear (advection and pressure), gravity and Coriolis terms have now to be projected on the plane Π (since incompressibility $\vec{\nabla}.\vec{u} = 0$ still holds). One obtains:

$$\left(\frac{\partial}{\partial t} + \nu k^2\right) \hat{u}_i(\vec{k}, t) = -ik_m P_{ij}(\vec{k}) \int_{\vec{p}+\vec{q}=\vec{k}} \hat{u}_j(\vec{p}, t)\hat{u}_m(\vec{q}, t)d\vec{p},$$

$$-g\beta_j P_{ij}(\vec{k})\hat{\rho}'_*(\vec{k}, t) - 2\Omega P_{ij}(\vec{k})\epsilon_{jab}\beta_a\hat{u}_b(\vec{k}, t), \tag{5.23}$$

$$\left(\frac{\partial}{\partial t} + \kappa k^2\right) \hat{\rho}'_*(\vec{k}, t) = -ik_j \int_{\vec{p}+\vec{q}=\vec{k}} \hat{u}_j(\vec{p}, t)\hat{\rho}'_*(\vec{q}, t)d\vec{p} + \frac{N^2}{g}\hat{u}_3(\vec{k}, t), \tag{5.24}$$

where ϵ_{ijl} is the antisymmetric tensor of order 3, not equal to zero only if i, j and l are different, equal to 1 if the permutation i, j, l is even, and to -1 if the permutation is odd.

5.5 Craya decomposition

The particular property that the velocity field is orthogonal to the wave vector $\vec{k}$ allows one to find other decompositions of the velocity field in Fourier space: the most common, often called the Craya decomposition (Craya [153]), involves associating to $\vec{k}$ an orthonormal frame constructed in the following way: let $\vec{\alpha}$ be an arbitrary (but fixed) unit vector, and let us consider the reference frame

$$Z_{\vec{k}} \equiv \vec{i}(\vec{k}) = \frac{\vec{k} \times \vec{\alpha}}{\|\vec{k} \times \vec{\alpha}\|}, \quad \vec{j}(\vec{k}) = \frac{\vec{k} \times \vec{i}}{k}, \quad \frac{\vec{k}}{k}.$$

The velocity field $\underline{\hat{u}}(\vec{k})$ is characterized by two components on[2] $\vec{i}(\vec{k})$ and $\vec{j}(\vec{k})$, for which it is possible to write evolution equations. This representation has

[2] The complex number i such that $i^2 = -1$ has evidently no relation with the unit vector $\vec{i}$.

been extensively used to study homogeneous strained or sheared turbulence (see Cambon et al. [94]). The same representation has also been called the triad-interaction representation (Lee [393]).

Let us now project $\hat{\underline{u}}(\vec{k},t)$ upon $\vec{i}$ and $\vec{j}$:

$$\hat{\underline{u}}(\vec{k},t) = u_V(\vec{k},t)\vec{i}(\vec{k}) + u_W(\vec{k},t)\vec{j}(\vec{k}). \tag{5.25}$$

Back to physical space, we have

$$\vec{u}(\vec{x},t) = \vec{u}_V(\vec{x},t) + \vec{u}_W(\vec{x},t), \tag{5.26}$$

where $\vec{u}_V(\vec{x},t)$ and $\vec{u}_W(\vec{x},t)$ are respectively the inverse Fourier transforms of $u_V(\vec{k},t)\vec{i}(\vec{k})$ and $u_W(\vec{k},t)\vec{j}(\vec{k})$. Let us choose the "vertical" axis of coordinate $\vec{z}$ oriented in the direction of $\vec{\alpha}$. $\vec{u}_V(\vec{x},t)$ is a horizontal (since it is perpendicular to $\vec{\alpha}$) non-divergent (since its Fourier transform is normal to $\vec{k}$) velocity field, which can be put under the form:

$$\vec{u}_V(\vec{x},t) = -\vec{\alpha} \times \vec{\nabla}_H \psi(\vec{x},t), \tag{5.27}$$

where ψ is an unknown function of $\vec{x}$ and t, $\vec{\nabla}_H$ being the gradient taken in the direction perpendicular to $\vec{\alpha}$. Notice also that $(\vec{\nabla} \times \vec{u}_V).\vec{\alpha}$ is generally non-zero, since its Fourier transform is $iku_V(\vec{k},t)[j(\vec{k}).\vec{\alpha}]$. Therefore, $\vec{u}_V(\vec{x},t)$ is vertically rotational, of stream function (for a given z) ψ. On the contrary, $\vec{u}_W(\vec{x},t)$ is vertically irrotational, since the Fourier transform of $\vec{\nabla} \times \vec{u}_W(\vec{x},t)$ is $-iku_W(\vec{k},t)i(\vec{k})$. Since $\vec{k} \times \vec{i} = k\vec{j}$, $\vec{u}_W(\vec{x},t)$ is the curl of a vector whose Fourier transform is parallel to $\vec{i}(\vec{k})$. Hence, it may be put under the form:

$$\vec{u}_W(\vec{x},t) = -\vec{\nabla} \times [\vec{\alpha} \times \vec{\nabla}_H \zeta(\vec{x},t)], \tag{5.28}$$

where ζ is another unknown function of $\vec{x}$ and t. This decomposition was proposed, in a slightly different form than Eqs. (5.27) and (5.28), by Riley et al. [600]. $\vec{u}_W$ can also be written as

$$\vec{u}_W(\vec{x},t) = \vec{\nabla}_H(\phi) - (\nabla_H^2 \zeta)\vec{\alpha}, \tag{5.29}$$

with $\phi = \partial\zeta/\partial z$.

The indices V and W stand respectively for *vortex* and *wave* component. This terminology makes sense in the case of homogeneous stably-stratified turbulence: indeed, taking $\vec{\alpha}$ equal to the vertical unit vector $\vec{\beta}$, it was shown by Riley et al. [600] that the field $\vec{u}_W$ satisfies, for small amplitudes and when $\vec{\Omega} = \vec{0}$, the equation of propagation of internal-gravity waves. The field $\vec{u}_V$ may in certain conditions, and for a given z, satisfy a two-dimensional Navier–Stokes equation in the limit of low Froude numbers: this accords with

the ideas of collapse to quasi two-dimensional turbulence under stratification which will be looked at in Chapter 13. Notice finally that the "vortex-wave" decomposition still holds in the case of unstratified non-rotating fluid, but with no physical significance attached to the words "wave" and "vortex".

Such a decomposition is a-priori different from Helmholtz's decomposition of a divergent field into a non-divergent part and an irrotational part. Both decompositions coincide from a three-dimensional point of view when the horizontal velocity field is two-dimensional (i.e. independent of z) and horizontally divergent. This is in particular the case for the Barré de Saint-Venant equations for a shallow fluid layer with a free surface introduced in Chapter 2: when a solid-body rotation $\vec{\Omega}$ is present, the "vortex" field is then essentially a horizontal two-dimensional turbulent field which interacts with a surface inertial-gravity waves field (Farge and Sadourny [195]).

5.6 Complex helical-waves decomposition

Helicity in a flow is the scalar product of the velocity and the vorticity. It will be considered physically in detail in the following sections. Here we will introduce a particular decomposition of the velocity field that will be called the *complex helical-wave decomposition*, proposed by Lesieur [411].

Flows we will call *helical waves* have been introduced by Moffatt [509]: let $\vec{k}$ be a given vector, and $\vec{i}$ and $\vec{j}$ two orthogonal unit vectors perpendicular to $\vec{k}$ such that the frame formed by $\vec{i}, \vec{j}$ and $\vec{k}$ should be direct. One considers in physical space, within an infinite domain, the velocity field

$$\vec{V}_1^+(\vec{k}, \vec{x}) = (\cos \vec{k}.\vec{x})\vec{j} + (\sin \vec{k}.\vec{x})\vec{i} \tag{5.30}$$

which is such that

$$\vec{\nabla} \times \vec{V}_1^+ = k\vec{V}_1^+. \tag{5.31}$$

This flow is an eigenmode of the curl operator (Beltrami flow). Its vectorial product with its curl is zero, thus satisfying the vorticity equation

$$\frac{\partial \vec{\omega}}{\partial t} + \vec{\nabla} \times (\vec{\omega} \times \vec{u}) = 0$$

associated with the Euler equation, in an infinite domain, with constant density and no rotation. Its helicity $\vec{V}_1^+.(\vec{\nabla} \times \vec{V}_1^+)$ is positive and equal to k. In the same way, one will consider the following flows

$$\vec{V}_2^+(\vec{k}, \vec{x}) = (\sin \vec{k}.\vec{x})\vec{j} - (\cos \vec{k}.\vec{x})\vec{i} \tag{5.32}$$

$$\vec{V}_1^-(\vec{k}, \vec{x}) = (\cos \vec{k}.\vec{x})\vec{j} - (\sin \vec{k}.\vec{x})\vec{i} \tag{5.33}$$

$$\vec{V}_2^-(\vec{k},\vec{x}) = (\vec{k}.\vec{x})\vec{j} + (\cos\vec{k}.\vec{x})\vec{i} \tag{5.34}$$

with

$$\vec{\nabla}\times\vec{V}_2^+ = k\vec{V}_2^+, \vec{\nabla}\times\vec{V}_1^- = -k\vec{V}_1^-, \vec{\nabla}\times\vec{V}_2^- = -k\vec{V}_2^-,$$

and of respective helicity $k, -k, -k$. They too are Beltrami flows and solutions of the Euler equation. We will now introduce (still in physical space) complex helical waves

$$\vec{V}^+(\vec{k},\vec{x}) = \vec{V}_1^+(\vec{k},\vec{x}) + i\vec{V}_2^+(\vec{k},\vec{x}) = (\vec{j} - i\vec{i})e^{i\vec{k}.\vec{x}} \tag{5.35}$$

$$\vec{V}^-(\vec{k},\vec{x}) = \vec{V}_1^-(\vec{k},\vec{x}) + i\vec{V}_2^-(\vec{k},\vec{x}) = (\vec{j} + i\vec{i})e^{i\vec{k}.\vec{x}} \tag{5.36}$$

which are still Beltrami flows and have a respective helicity k and $-k$. They are complex solutions of Euler equations in physical space.

Now, we assume that $\vec{k}$ is one of the wave vectors of the Fourier decomposition of $\vec{u}(\vec{x},t)$, and that $\vec{i}(\vec{k})$ and $\vec{j}(\vec{k})$ are the same as in Craya decomposition, associated to $\vec{k}$ with the aid of the fixed arbitrary unit vector $\vec{\alpha}$. It is easy to show that

$$\frac{1}{2}\left[\underline{\hat{u}}(\vec{k},t) + i\frac{\vec{k}\times\underline{\hat{u}}(k,t)}{k}\right]e^{i\vec{k}.\vec{x}} = u^+(\vec{k},t)\vec{V}^+(\vec{k},\vec{x}) \tag{5.37}$$

$$\frac{1}{2}\left[\underline{\hat{u}}(\vec{k},t) - i\frac{\vec{k}\times\underline{\hat{u}}(k,t)}{k}\right]e^{i\vec{k}.\vec{x}} = u^-(\vec{k},t)\vec{V}^-(\vec{k},\vec{x}) \tag{5.38}$$

where $u^+(\vec{k},t)$ and $u^-(\vec{k},t)$ are two complex numbers. Eqs. (5.4), (5.37) and (5.38) thus permit one to write the following decomposition of any non-divergent field $\vec{u}(\vec{x},t)$ into positive and negative complex helical waves:

$$\vec{u}(\vec{x},t) = \int [u^+(\vec{k},t)\vec{V}^+(\vec{k},\vec{x}) + u^-(\vec{k},t)\vec{V}^-(\vec{k},\vec{x})]d\vec{k}. \tag{5.39}$$

The orthogonality relations existing between the $\vec{V}^+$ and $\vec{V}^-$ allow one to invert Eqs. (5.39), showing that the decomposition of $\vec{u}(\vec{x},t)$ is unique once the fixed vector $\vec{\alpha}$ determining the vectors $\vec{i}(\vec{k})$ and $\vec{j}(\vec{k})$ has been chosen. One obtains

$$2u^+(\vec{k},t) = \left(\frac{1}{2\pi}\right)^3 \int \vec{u}(\vec{x},t).\vec{V}^+(\vec{k},\vec{x})^* d\vec{x} \tag{5.40}$$

$$2u^-(\vec{k},t) = \left(\frac{1}{2\pi}\right)^3 \int \vec{u}(\vec{x},t).\vec{V}^-(\vec{k},\vec{x})^* d\vec{x}, \tag{5.41}$$

where the symbol "*" refers to the complex conjugate. We have therefore obtained an orthogonal decomposition of the velocity field along complex helical waves, which could prove to be useful for the study of isotropic helical or non-helical turbulence. Similar decompositions have been

introduced by Moses [526] and Cambon [93]. Let us mention that Lesieur was not aware of Moses' work. One can also note that the coordinates of $\vec{\nabla} \times \vec{u}(\vec{x},t)$ in this "helical space" are ku^+ and $-ku^-$, while those of $\nabla^2\vec{u}(\vec{x},t)$ are k^2u^+ and $-k^2u^-$. Notice finally that the change of $\vec{k}$ into $-\vec{k}$ in $\vec{V}^+(\vec{k},\vec{x}), \vec{V}^-(\vec{k},\vec{x}), u^+(\vec{k},t), u^-(\vec{k},t)$ is equivalent to taking their complex conjugate.

Eq. (5.18) can also be projected in this helical space: if $u_a(\vec{k},t)$ stands for u^+ or u^- according to the value $+1$ or -1 of the parameter a, one obtains (Lesieur [411]):

$$\left(\frac{\partial}{\partial t} + \nu k^2\right) u_a(\vec{k},t) = -\frac{1}{2}\int_{\vec{p}+\vec{q}=\vec{k}} Q_{abc}(\vec{k},\vec{p},\vec{q}) u_b(\vec{p},t) u_c(\vec{q},t) d\vec{p} \qquad (5.42)$$

with

$$Q_{abc}(\vec{k},\vec{p},\vec{q}) = -bp[\vec{j}(\vec{k}) + ia\vec{i}(\vec{k}), \vec{j}(\vec{p}) - ib\vec{i}(\vec{p}), \vec{j}(\vec{q}) - ic\vec{i}(\vec{q})], \qquad (5.43)$$

where [.,.,.] holds for a mixed product of three vectors, and the "indices" b and c take the values $+1$ or -1 , with summation upon the repeated indices. Further studies upon these lines have been carried out by Waleffe [709], Melander and Hussain [484] and Virk et al. [707].

Finally, it is easy to relate the latter complex helical decomposition to Craya decomposition: with the aid of Eqs. (5.25), (5.40) and (5.41), the following is obtained (Lesieur [411], Cambon [93]):

$$\begin{aligned} 2u^+(\vec{k},t) &= \underline{\hat{u}}(\vec{k},t).(\vec{j} + i\vec{i}) = u_W(\vec{k},t) + iu_V(\vec{k},t) \\ 2u^-(\vec{k},t) &= \underline{\hat{u}}(\vec{k},t).(\vec{j} - i\vec{i}) = u_W(\vec{k},t) - iu_V(\vec{k},t) \end{aligned} \qquad (5.44)$$

or equivalently

$$u_V(\vec{k},t) = i[u^-(\vec{k},t) - u^+(\vec{k},t)], \quad u_W(\vec{k},t) = [u^-(\vec{k},t) + u^+(\vec{k},t)]. \qquad (5.45)$$

Notice finally that $\vec{i}(-\vec{k}) = -\vec{i}(\vec{k})$ and $\vec{j}(-\vec{k}) = \vec{j}(\vec{k})$. Hence, using Eqs. (5.25) and the relation

$$\underline{\hat{u}}(-\vec{k},t) = \underline{\hat{u}}(\vec{k},t)^*, \qquad (5.46)$$

due to the fact that $\vec{u}(\vec{x},t)$ is real, it is found:

$$u_V(-\vec{k},t) = -u_V(\vec{k},t)^*; \quad u_W(-\vec{k},t) = u_W(\vec{k},t)^*. \qquad (5.47)$$

We will see in Chapter 9 how Lilly [448] uses helical waves for a model of tornado generation to perform a secondary linear-unstability analysis upon an helical wave rotating along the vertical as the Ekman boundary-layer mean velocity profile. A last remark about the complex helical waves decomposition: it is an attractive projection of the turbulent velocity field, but was never applied to simulations of real flows.

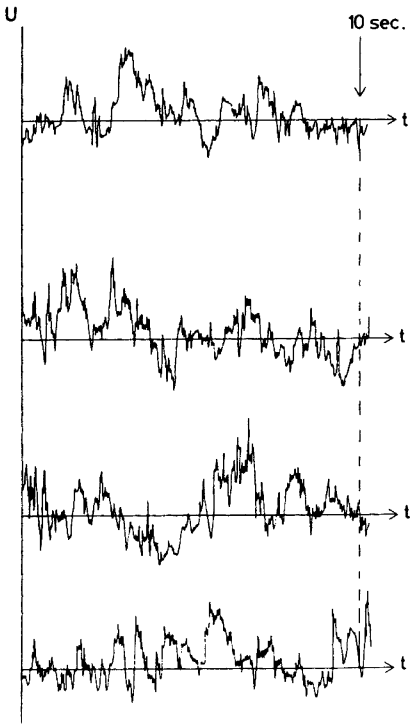

Figure 5.2. Four independent samples of the longitudinal velocity fluctuations recorded in the turbulent channel of the Institut de Mécanique de Grenoble (courtesy Y. Gagne).

5.7 Utilization of random functions

From a mathematical standpoint, and as already mentioned, the velocity field $\vec{u}(\vec{x},t)$ will be assumed to be a random function defined on a sample space (see e.g. Papoulis [563]). One can imagine for instance that we record the longitudinal air velocity at a given location in a wind tunnel: if the experiment is repeated N times in the same conditions, one obtains N realizations of the velocity evolution, each of them corresponding to a point in the sample space. For instance Figure 5.2 represents four recordings of the u' velocity fluctuations obtained in such an experiment. In a statistical description of the flow, we consider an "ensemble average", i.e. a statistical average performed on an infinite number of independent realizations, already noted as $\langle . \rangle$ in Chapter 4: let for example in the above experiment $u^{(i)}(\vec{x},t)$ be any component of the velocity at location $\vec{x}$ and time t measured during the experiment "i" ("i"realization). The ensemble average of the product of n of these components

at n locations $\vec{x}_1, \vec{x}_2, \dots \ \vec{x}_n$ and n times $t_1, t_2, \dots, t_n$ will be given by

$$\langle u(\vec{x}_1, t_1) u(\vec{x}_2, t_2) \dots \ u(\vec{x}_n, t_n) \rangle = \lim_{N \to \infty} \frac{1}{N} \sum_{i=1}^{N}$$

$$u^{(i)}(\vec{x}_1, t_1) u^{(i)}(\vec{x}_2, t_2) \dots \ u^{(i)}(\vec{x}_n, t_n). \tag{5.48}$$

This ensemble average operator is analogous to the one used in statistical thermodynamics. It is not to be confused with temporal or spatial averages, except in certain conditions which will be specified below.

In the following, the various functions characterizing the turbulent flow will be considered as random functions: this will in particular be the case for the velocity $\vec{u}(\vec{x}, t)$, the vorticity, the pressure, the temperature or the density fluctuations, etc. Notice also that these random functions are defined on the four-dimensional space $(\vec{x}, t)$.

5.8 Moments of the velocity field, homogeneity and stationarity

Definition: The "n"th order moment of the velocity field is the ensemble average of any tensorial product of n components of the velocity field: $\langle \vec{u}(\vec{x}, t) \rangle$ is the mean velocity at time t.$\langle u_i(\vec{x}_1, t_1) u_j(\vec{x}_2, t_2) \rangle$ is the velocity correlation tensor at points $\vec{x}_1$ and $\vec{x}_2$ and at times t_1 and t_2. In the same way it is possible to define the moments of order $3, 4, \dots, n$.

• Homogeneity

Turbulence is called *homogeneous* if all the mean quantities built with a set of n points $\vec{x}_1, \vec{x}_2, \dots \ \vec{x}_n$ (at times $t_1, t_2, .., t_n$) are invariant under any translation of the set $(\vec{x}_1, \vec{x}_2, \dots \ \vec{x}_n)$. One has in particular

$$\langle u_{\alpha_1}(\vec{x}_1, t_1) \dots \ u_{\alpha_n}(\vec{x}_n, t_n) \rangle = \langle u_{\alpha_1}(\vec{x}_1 + \vec{y}, t_1) \dots \ u_{\alpha_n}(\vec{x}_n + \vec{y}, t_n) \rangle. \tag{5.49}$$

For instance the second order velocity correlation tensor writes

$$U_{ij}(\vec{r}, t_1, t_2) = \langle u_i(\vec{x}_1, t_1) u_j(\vec{x}_1 + \vec{r}, t_2) \rangle \tag{5.50}$$

Notice also that

$$U_{ij}(-\vec{r}, t_1, t_2) = U_{ji}(\vec{r}, t_2, t_1). \tag{5.51}$$

For homogeneous turbulence, the mean velocity field $\langle \vec{u}(\vec{x}, t) \rangle$ is independent of $\vec{x}$. It must be stressed, however, that it is possible to consider a turbulence homogeneous with respect to the fluctuations of velocity with a non-constant mean velocity, provided the mean velocity gradients are constant (Craya [153],

Townsend [689], Maréchal [471], Cambon et al. [92], Rogallo [611], Rogers and Moin [613]). This question has already been addressed in Chapter 4. It will be considered using rapid-distorsion theory at the end of this chapter. At low shear rate, the DNS carried out by Rogers and Moin [613] show hairpin vortices strained by the mean shear.

If there is no mean shear, the mean velocity is constant, and one will generally work in a frame moving with the mean flow, so that $\langle \vec{u} \rangle = \vec{0}$. When turbulence is homogeneous, an *ergodic hypothesis* allows one to calculate an ensemble average as a spatial average: for instance

$$U_{ij}(\vec{r}, t_1, t_2) = \lim_{V \to \infty} \frac{1}{V} \int_V u_i(\vec{x}_1, t_1) u_j(\vec{x}_1 + \vec{r}, t_2) d\vec{x}_1. \tag{5.52}$$

No proof of the ergodic theorem is known for Navier–Stokes equations. There is however some numerical evidence that it is valid for the truncated Euler equations (that is where only a finite number of degrees of freedom are retained) both in two dimensions (Fox and Orszag [215], Basdevant and Sadourny [36]) and in three dimensions (Lee [394]).

• Stationarity

Turbulence is *stationary* if all the mean quantities involving n times $t_1 t_2 \dots t_n$ are invariant under any translation of $(t_1 t_2 \dots t_n)$. In particular

$$\langle u_{\alpha_1}(\vec{x}_1, t_1) \dots u_{\alpha_n}(\vec{x}_n, t_n) \rangle = \langle u_{\alpha_1}(\vec{x}_1, t_1 + \tau) \dots u_{\alpha_n}(\vec{x}_n, t_n + \tau) \rangle. \tag{5.53}$$

If one assumes a zero mean velocity, $(1/2)U_{ii}(\vec{0}, t, t)$ is the mean kinetic energy per unit mass. So in a stationary turbulence this quantity will be independent of time. This implies that a stationary turbulence needs to be sustained by external forces, otherwise the kinetic energy would decay with time, due to viscous dissipation. For a stationary turbulence, an ergodic hypothesis allows one to calculate an ensemble average as a time average. A large part of this monograph will be devoted to homogeneous turbulence, but stationarity will not necessarily be assumed: indeed the latter assumption requires, as just seen above, the use of external forces which are generally only a mathematical trick to sustain the turbulence and can strongly modify its structure, specially in the scales where the energy is injected. On the contrary, the freely-evolving turbulence (also called decaying turbulence), as can be obtained for instance in a wind tunnel downstream of a grid, reorganizes according to its own dynamics, and might give more information about the nonlinear interactions between the various scales of motion.

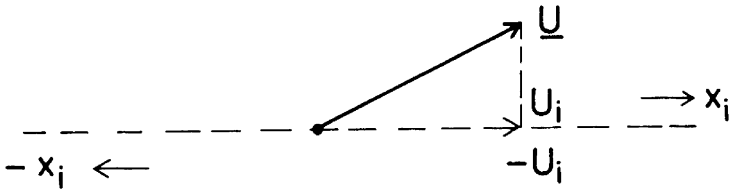

Figure 5.3. The mean velocity of isotropic turbulence is zero, since a rotation of angle π about an axis of origin $\vec{x}$ perpendicular to $x\vec{x}_i$ can change u_i into $-u_i$.

5.9 Isotropy

5.9.1 Definition

Homogeneous turbulence is statistically "isotropic" if all the mean quantities concerning a set of n points $\vec{x}_1\vec{x}_2 \dots \vec{x}_n$ (at times $t_1t_2 \dots t_n$) are invariant under any simultaneous arbitrary rotation of the set of the n points and of the axis of coordinates. The first immediate consequences are

$$\langle \vec{u}(\vec{x},t) \rangle = \vec{0} \tag{5.54}$$

as can be seen in Figure 5.3: indeed, a rotation of angle π about an axis perpendicular to xx_i implies

$$\langle \vec{u}(\vec{x},t) \rangle = -\langle \vec{u}(\vec{x},t) \rangle = \vec{0}, \tag{5.55}$$

and for any scalar quantity $\vartheta(\vec{x},t)$:

$$\langle \vartheta(\vec{x},t)\vec{u}(\vec{x},t) \rangle = 0. \tag{5.56}$$

In fact, it will be shown later that the scalar-velocity correlation between two distinct points $\vec{x}$ and $\vec{y}$ is also zero. An important remark is that an isotropic turbulence is homogeneous, since a translation can be decomposed as the product of two rotations. In this respect, the expression *homogeneous isotropic turbulence (HIT)* is irrelevant.

5.9.2 Longitudinal velocity correlation

We consider two points $\vec{x}$ and $\vec{y}$ separated by $\vec{r}$. Let u be the projection of the velocity on $\vec{r}$ (see Figure 5.4). The longitudinal correlation is defined by (Batchelor [47], Hinze [285])

$$F(r,t,t') = \langle u(\vec{x},t)u(\vec{x}+\vec{r},t') \rangle. \tag{5.57}$$

It is independent of the direction of $\vec{r}$ because of the isotropy assumption.

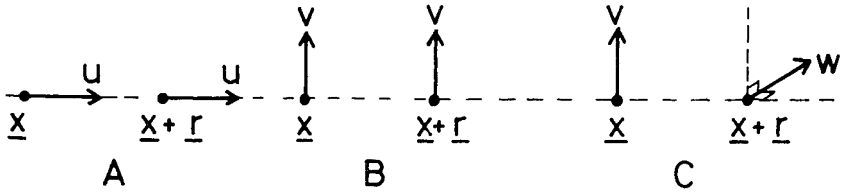

Figure 5.4. Schematic representation of longitudinal, transverse and cross velocity correlations.

5.9.3 Transverse velocity correlation

Let v be the projection of the velocity on an axis v normal to $\vec{r}$. The transverse velocity correlation is defined as

$$G(r,t,t') = \langle v(\vec{x},t)v(\vec{x}+\vec{r},t')\rangle. \tag{5.58}$$

Due to isotropy it is also independent of the direction of $\vec{r}$. Notice that a correlation like $\langle u(\vec{x},t)v(\vec{x}+\vec{r},t')\rangle$ is always zero, as can be easily seen with a rotation of angle π around the axis xu (see Figure 5.4).

5.9.4 Cross velocity correlation

Let w be the projection of the velocity on an axis $\vec{w}$ normal to the $(\vec{r},\vec{v})$ plane. The cross velocity correlation is defined as:

$$H(r,t,t') = \langle v(\vec{x},t)w(\vec{x}+\vec{r},t')\rangle. \tag{5.59}$$

One can notice in particular that $H(0,t,t') = 0$.

In the present monograph, isotropic turbulence has been defined as statistically invariant under any rotation. Such a turbulence can possess or not the property of also being statistically invariant under any plane symmetry ("mirror symmetry"). If it is the case, the cross velocity correlation $H(r,t,t')$ is zero, and there is no preferred helical tendency in the flow. We will say that the turbulence possesses no helicity. The reader is warned that our definition of isotropy is different from Batchelor's [47], which includes the mirror symmetry property in the isotropy definition.

5.9.5 Helicity

The quantity

$$H_e = \frac{1}{2}\langle \vec{u}(\vec{x},t).[\vec{\nabla}\times\vec{u}(\vec{x},t)]\rangle, \tag{5.60}$$

is called the mean helicity of the flow.[3] It is evidently zero if the turbulence possesses the mirror symmetry property. Like the mean kinetic energy and passive-scalar variance, it is conserved by the nonlinear terms of statistically homogeneous Navier–Stokes equations (see next chapter). Helicity seems to play an important role in some magneto-hydrodynamic flows of electrically conducting fluids (M.H.D flows): indeed it can be shown on some models that helicity enhances the so-called "dynamo effect", corresponding to the generation of a magnetic field by a flow. A review of this problem can be found in Moffatt [510] and Moreau [519]. Let us consider Earth turbulent outer core, which is electrically-conducting and strongly heated from the interior. It is well recognized (Cardin [97]) that it is composed of quasi two-dimensional vortices of axis parallel to Earth axis of rotation. With velocities of 10^{-3} m/s, and scales of 1000 km, the Rossby number is $\approx 10^{-5}$. This is very small, and explains why the vortices are quasi geostrophic. Schaeffer and Cardin [633] have shown by numerical simulations that quasi geostrophic MHD turbulence may produce a dynamo effect. Le Mouël [406] stresses that helicity is present here, even though the structures are quasi two-dimensional.

Let us mention new experimental results obtained in a strongly-turbulent swirling flow of liquid sodium between two counter-rotating turbines by Monchaux, Daviaud, Fauve, Pinton et al. [514]: above a magnetic Reynolds number of approximately 30, an important mean magnetic field is obtained. There are here a lot of big vortices in this experiment which produce mean helicity. But this situation is highly three-dimensional, and it is not obvious that it represents correctly Earth outer core.

5.9.6 Velocity correlation tensor in physical space

At this point we recall how in the case of isotropic turbulence (with or without helicity), the second-order velocity correlation tensor written in the physical space may be expressed only in terms of the quantities $F(r,t,t')$, $G(r,t,t')$, and $H(r,t,t')$. The derivation is not simple[4] and can be partially found in Batchelor [47]: let $\vec{a}$ and $\vec{b}$ be two arbitrary fixed vectors. The contracted tensorial product

$$a_i U_{ij}(\vec{r},t,t')b_j$$

is a scalar, and consequently must be invariant under rotation of the three vectors $(\vec{r},\vec{a},\vec{b})$, without worrying about rotation of the axis of coordinates. It can thus be shown (Robertson [608]) that this scalar is only a function of

[3] The local instantaneous helicity at a given point is $\vec{u}.\vec{\omega}/2$. In a longitudinal hairpin shed in a shear flow for instance, the right leg of the hairpin will have positive helicity, and the left leg a negative helicity.

[4] A simpler derivation in Fourier space will be given below.

$\vec{r}.\vec{r}$ $\vec{r}.\vec{a}$ $\vec{r}.\vec{b}$ $\vec{a}.\vec{a}$ $\vec{b}.\vec{b}$ $\vec{a}.\vec{b}$ and $\vec{r}.(\vec{a}\times\vec{b})$, i.e. of the lengths, relative angles and orientation of this set of three vectors. Furthermore, it is linear with respect to the coordinates of $\vec{a}$ and $\vec{b}$. The only possible combination is then

$$a_i U_{ij}(\vec{r},t,t')b_j = A(r,t,t')\vec{a}.\vec{b} + B(r,t,t')(\vec{r}.\vec{a})(\vec{r}.\vec{b}) + C(r,t,t')\epsilon_{ijs}a_i b_j r_s. \tag{5.61}$$

If we choose the vectors $\vec{a}$ and $\vec{b}$ corresponding respectively to the unit vectors of axis x_i and x_j, we obtain:

$$U_{ij}(\vec{r},t,t') = A(r,t,t')\delta_{ij} + B(r,t,t')r_i r_j + C(r,t,t')\epsilon_{ijs}r_s. \tag{5.62}$$

In fact, such an expression can be obtained much more easily, by projecting the spectral tensor in the local Craya space (see below).

In a reference frame such that $\vec{r}$ has components $(r,0,0)$, the velocity correlation tensor is diagonal, of components

$$F(r,t,t') = A(r,t,t') + r^2 B(r,t,t')$$

$$G(r,t,t') = A(r,t,t')$$

$$H(r,t,t') = rC(r,t,t'),$$

and $U_{ij}(\vec{r},t,t')$ writes

$$U_{ij}(\vec{r},t,t') = G(r,t,t')\delta_{ij} + \frac{[F(r,t,t') - G(r,t,t')]}{r^2} r_i r_j$$

$$+ H(r,t,t')\epsilon_{ijs}\frac{r_s}{r}. \tag{5.63}$$

The incompressibility condition

$$\frac{\partial u_i}{\partial x_i} = 0 \tag{5.64}$$

allows one to obtain a relationship between $F(r,t,t')$ and $G(r,t,t')$. Writing Eq. (5.64) as

$$\frac{\partial}{\partial r_i} U_{ij}(\vec{r},t,t') = 0 \tag{5.65}$$

and replacing $U_{ij}(\vec{r},t,t')$ by its expression Eq. (5.63), it can be shown after some simple algebra (see Batchelor [47]) that

$$G(r,t,t') = F(r,t,t') + \frac{r}{2}\frac{\partial F}{\partial r}. \tag{5.66}$$

Let us now, as an exercise, calculate the helicity of the flow in terms of these correlations: the following calculation is not a simple one, but enables one

to become familiar with these tensorial calculations. From the definition of helicity, one has:

$$\begin{aligned} 2H_e &= \lim_{\vec{y}\to\vec{x}} \langle \vec{u}(\vec{x},t).[\vec{\nabla}\times\vec{u}(\vec{y},t)]\rangle \\ &= \lim_{\vec{y}\to\vec{x}} \epsilon_{ijl}\langle u_i(\vec{x},t)\frac{\partial u_l(\vec{y},t)}{\partial y_j}\rangle \\ &= \lim_{\vec{r}\to\vec{0}} \epsilon_{ijl}\frac{\partial U_{il}(\vec{r},t,t)}{\partial r_j} \\ &= \lim_{\vec{r}\to\vec{0}} \left(\frac{\partial}{\partial r_j}\right)\epsilon_{ijl}U_{il}(\vec{r},t,t) \end{aligned}$$

and, using Eq. (5.63)

$$\begin{aligned} \frac{\partial}{\partial r_j}\epsilon_{ijl}U_{il}(\vec{r},t,t) &= -\epsilon_{ijl}\epsilon_{ial}\frac{\partial}{\partial r_j}\left[H(r,t,t)\frac{r_a}{r}\right] \\ &= -\epsilon_{ijl}\epsilon_{ial}\left(\frac{r_a r_j}{r^2}\frac{\partial H}{\partial r}+\frac{H}{r}\delta_{ja}-\frac{H}{r^3}r_a r_j\right) \\ &= -2\frac{\partial H}{\partial r}-4\frac{H}{r}\,. \end{aligned}$$

When $\vec{r}$ goes to zero, $\partial H/\partial r$ is equivalent to H/r, since $H(0)=0$, and the mean helicity is equal to

$$H_e = -3\lim_{r\to 0}\frac{H(r,t,t)}{r} = -3C(0,t,t). \tag{5.67}$$

5.9.7 Scalar-velocity correlation

Another interesting result is to show that the scalar-velocity correlation in two different points $\vec{x}$ and $\vec{x}+\vec{r}$ is always zero in isotropic three-dimensional turbulence (Hinze [285]): let

$$S_i(\vec{r},t,t') = \langle \vartheta(\vec{x},t)u_i(\vec{x}+\vec{r},t')\rangle \tag{5.68}$$

be the correlation of any scalar ϑ(for instance the pressure or the temperature) with the velocity field. Let a_i be an arbitrary vector. The scalar $a_i S_i$ must be invariant under any rotation. It must therefore depend upon r, a, and $\vec{a}.\vec{r}$; due to the linearity with respect to a_i, we must have

$$a_i S_i(\vec{r},t,t') = S(r,t,t')r_i a_i \tag{5.69}$$

which yields

$$S_i(\vec{r},t,t') = S(r,t,t')r_i. \tag{5.70}$$

The incompressibility condition $\partial S_i/\partial r_i = 0$ implies

$$3S(r,t,t') + r\frac{\partial S}{\partial r} = 0. \tag{5.71}$$

Thus, $S_i(\vec{r},t,t')$ is proportional to $r^{-3}r_i$. On the other hand it cannot diverge at $\vec{r}=0$ since $S_i(\vec{0},t,t')$ is zero, as already seen above. Consequently, $S_i(\vec{r},t,t')$ must be equal to zero for arbitrary $\vec{r}$. For instance, the pressure-velocity correlation is always zero in isotropic turbulence. This is also true for the temperature-velocity correlation, or the density-velocity correlation. Another consequence is that the scalar-vorticity correlation is also zero. As will be seen later, this is not automatically ensured in two-dimensional isotropic turbulence.

This zero scalar-velocity correlation property is valid only when the velocity and the scalar satisfy the isotropy conditions: indeed it might happen that an inhomogeneous scalar field is diffused by homogeneous isotropic turbulence, as for instance in a "thermal mixing layer" where two regions of a grid turbulence are initially at a different temperature (La Rue and Libby [382], Warhaft [713]). The particular case of scalar-velocity correlation in two-dimensional isotropic turbulence will be considered later, as a special case of three-dimensional axisymmetric turbulence.

5.9.8 Velocity spectral tensor of isotropic turbulence

The velocity spectral tensor of a homogeneous turbulence is the Fourier transform of the second order velocity correlation tensor

$$\hat{U}_{ij}(\vec{k},t,t') = \left(\frac{1}{2\pi}\right)^3 \int e^{-i\vec{k}.\vec{r}} U_{ij}(\vec{r},t,t')d\vec{r}. \tag{5.72}$$

Here, the velocity spectral tensor decreases to infinity fast enough in general, so that $\hat{U}_{ij}(\vec{k},t,t')$ is an ordinary function. We also have a relation equivalent to Eq. (5.4)

$$U_{ij}(\vec{r},t,t') = \int e^{i\vec{k}.\vec{x}} \hat{U}_{ij}(\vec{k},t,t').d\vec{k}. \tag{5.73}$$

The spectral tensor can also be viewed as the velocity correlation tensor in Fourier space: indeed, let us calculate

$$\langle \hat{u}_i(\vec{k}',t)\hat{u}_j(\vec{k},t')\rangle$$

$$= \left(\frac{1}{2\pi}\right)^6 \int e^{-i(\vec{k}'.\vec{x}+\vec{k}.\vec{x}')} \langle u_i(\vec{x},t)u_j(\vec{x}',t')\rangle d\vec{x}d\vec{x}'$$

$$= \left(\frac{1}{2\pi}\right)^6 \int e^{-i\vec{k}.\vec{r}} e^{-i(\vec{k}+\vec{k}').\vec{x}} U_{ij}(\vec{r},t,t')d\vec{r}d\vec{x}.$$

Then one obtains, using Eq. (5.5):

$$\langle \hat{u}_i(\vec{k}',t)\hat{u}_j(\vec{k},t')\rangle = \left(\frac{1}{2\pi}\right)^3 \delta(\vec{k}+\vec{k}') \int e^{-i\vec{k}.\vec{r}} U_{ij}(\vec{r},t,t')d\vec{r}$$

which yields, with the aid of Eq. (5.46)

$$\langle \hat{u}_i(\vec{k}',t)\hat{u}_j(\vec{k},t')\rangle = \hat{U}_{ij}(\vec{k},t,t')\ \delta(\vec{k}+\vec{k}'). \tag{5.74}$$

We notice also from Eqs. (5.4) and (5.51) that the tensor $\hat{U}_{ij}(\vec{k},t,t)$ is Hermitian, that is

$$\hat{U}_{ji}(\vec{k},t,t) = \hat{U}^*_{ij}(\vec{k},t,t)$$

where the symbol $*$ stands for the complex conjugate. Eq. (5.74) shows that, for homogeneous turbulence, there is no correlation in Fourier space between two wave vectors whose sum is different from zero. This result can be generalized to a set of N vectors, which must satisfy this zero-sum condition in order to allow a non-zero velocity correlation between them. Eq. (5.51) shows also that $\hat{U}_{ii}(\vec{k},t,t)$ is real and positive since it is "proportional" (modulo a Dirac distribution) to $\langle \hat{u}^*_i(\vec{k},t)\hat{u}_i(\vec{k},t)\rangle$. In fact, it may be easier to consider these quantities from the point of view of the turbulence within a box already introduced, since the Dirac distributions disappear, and $\hat{U}_{ii}(\vec{k},t,t)$ then becomes exactly equal to $\langle \hat{u}^*_i(\vec{k},t)\hat{u}_i(\vec{k},t)\rangle$(the symbol "B" has been omitted, and δk has been set equal to 1).

In the case of isotropic turbulence, with or without helicity, the spectral tensor takes a simple form which can be obtained either by taking the Fourier transform of Eq. (5.62) or by working directly in Fourier space: indeed the isotropy hypothesis which leads to Eq. (5.62) is also valid in Fourier space, and the isotropic spectral tensor can then be written as

$$\hat{U}_{ij}(\vec{k},t,t') = \hat{A}(k,t,t')\delta_{ij} + \hat{B}(k,t,t')k_ik_j + \hat{C}(k,t,t')\epsilon_{ijl}k_l. \tag{5.75}$$

Therefore, the incompressibility condition in Fourier space implies

$$k_j\hat{U}_{ij}(\vec{k},t,t') = 0$$

and

$$\hat{B}(k,t,t') = -\frac{\hat{A}(k,t,t')}{k^2}$$

$$\hat{U}_{ij}(\vec{k},t,t') = \hat{A}(k,t,t')P_{ij}(\vec{k}) + \hat{C}(k,t,t')\epsilon_{ijs}k_s, \tag{5.76}$$

where $P_{ij}(\vec{k})$ has been defined in Eq. (5.15). A simpler derivation of this result will be given below, when working in the local Craya frame.

5.10 Kinetic-energy, helicity, enstrophy and scalar spectra

5.10.1 Kinetic energy spectrum

Considering the case $t = t'$, one obtains

$$\hat{U}_{ii}(\vec{k}, t, t) = \hat{U}(k, t) = 2\hat{A}(k, t) \tag{5.77}$$

where $\hat{U}(k, t)$ is the trace (real and positive) of the tensor $\hat{U}_{ij}(\vec{k}, t, t)$. Eq. (5.76) can then be written as

$$\hat{U}_{ij}(\vec{k}, t, t) = \frac{1}{2}[\hat{U}(k, t)P_{ij}(\vec{k}) + i\tilde{U}(k, t)\epsilon_{ijs}k_s]. \tag{5.78}$$

In two-dimensional isotropic turbulence, Eq. (5.78) has to be replaced by

$$\hat{U}_{ij}(\vec{k}, t, t) = \hat{U}(k, t)P_{ij}(\vec{k}). \tag{5.79}$$

(see Chapter 8). It will be shown later that $\tilde{U}(k, t)$ is real. We first calculate the mean kinetic energy per unit mass

$$\frac{1}{2}\langle \vec{u}(\vec{x}, t)^2 \rangle = \frac{1}{2}U_{ii}(\vec{0}, t) = \frac{1}{2}\int \hat{U}(k, t)d\vec{k}$$

$$= \int_0^{+\infty} 2\pi k^2 \hat{U}(k, t)dk \text{ (in three dimensions)}$$

$$= \int_0^{+\infty} \pi k \hat{U}(k, t)dk \text{ (in two dimensions).}$$

This determines the kinetic-energy spectrum, density of kinetic energy at wave number k, and such that

$$E(k, t) = 2\pi k^2 \hat{U}(k, t) \text{ in three dimensions,} \tag{5.80}$$

$$E(k, t) = \pi k \hat{U}(k, t) \text{ in two dimensions.} \tag{5.81}$$

$E(k, t)$ corresponds to the kinetic-energy density in Fourier space integrated on a sphere (or a circle in two dimensions) of radius k. It is always real and positive.

5.10.2 Helicity spectrum

It can be shown to be equal to

$$H_e = \frac{1}{2}\langle \vec{u}.\vec{\omega}\rangle = -\frac{i}{2}\epsilon_{ijl}\int k_j \hat{U}_{il}(-\vec{k},t,t)d\vec{k}$$

which yields, using Eq. (5.78)

$$H_e = \int_0^{+\infty} 2\pi k^4 \tilde{U}(k,t)dk. \tag{5.82}$$

This determines the helicity spectrum,

$$H(k) = 2\pi k^4 \tilde{U}(k), \tag{5.83}$$

density of helicity at wave number k. This quantity can only be defined in three dimensions, since it is zero in two dimensions. Finally, the spectral tensor Eq. (5.78) writes

$$\hat{U}_{ij}(\vec{k},t,t) = \frac{1}{2}\left[\frac{E(k,t)}{2\pi k^2}P_{ij}(\vec{k}) + i\epsilon_{ijs}k_s\frac{H(k,t)}{2\pi k^4}\right] \tag{5.84}$$

in three dimensions and

$$\hat{U}_{ij}(\vec{k},t,t) = \frac{E(k,t)}{\pi k}P_{ij}(\vec{k}) \tag{5.85}$$

in two dimensions.

5.10.3 Enstrophy

It is the variance of the vorticity

$$D(t) = \frac{1}{2}\langle \vec{\omega}^2\rangle. \tag{5.86}$$

One can show that for homogeneous turbulence the enstrophy is equal to

$$D(t) = -\frac{1}{2}\langle \vec{u}(\vec{x},t).\nabla^2\vec{u}(\vec{x},t)\rangle. \tag{5.87}$$

Indeed, let $\vec{A}(\vec{x},t)$ and $\vec{B}(\vec{x},t)$ be two vector fields depending on the velocity field. Since, because of homogeneity,

$$\left\langle a_i\epsilon_{ijs}\frac{\partial b_s}{\partial x_j}\right\rangle = -\left\langle \frac{\partial a_i}{\partial x_j}\epsilon_{ijs}b_s\right\rangle$$

one has

$$\langle \vec{A}.(\vec{\nabla} \times \vec{B})\rangle = \langle \vec{B}.(\vec{\nabla} \times \vec{A})\rangle. \tag{5.88}$$

Now we use the property of a non-divergent flow that

$$\vec{\nabla} \times (\vec{\nabla} \times \vec{u}) = -\nabla^2 \vec{u}, \tag{5.89}$$

which shows Eq. (5.87). This allows calculation of the enstrophy spectrum: since the Fourier transform of $\nabla^2 \vec{u}(\vec{x}, t)$ is $-k^2 \underline{\hat{u}}(\vec{k}, t)$, we have

$$\begin{aligned} D(t) &= \frac{1}{2} \int d\vec{k} d\vec{k}' \; e^{i(\vec{k}+\vec{k}').\vec{x}} k^2 \langle \hat{u}_i(\vec{k}', t) u_i(\vec{k}, t)\rangle \\ &= \frac{1}{2} \int k^2 \hat{U}_{ii}(\vec{k}, t) d\vec{k} = \int_0^{+\infty} k^2 E(k, t) dk. \end{aligned} \tag{5.90}$$

It turns out that the enstrophy spectrum $k^2 E(k, t)$ is completely determined by the kinetic-energy spectrum. This is not the case for the helicity spectrum.

5.10.4 Scalar spectrum

Let $\vartheta(\vec{x}, t)$ be a scalar satisfying the isotropy conditions and $\hat{\vartheta}(\vec{k}, t)$ its Fourier transform. A calculation analogous to that leading to Eq. (5.74) gives now

$$\begin{aligned} &\langle \hat{\vartheta}(\vec{k}', t) \hat{\vartheta}(\vec{k}, t)\rangle \\ &= \left(\frac{1}{2\pi}\right)^6 \int e^{-i(\vec{k}'.\vec{x}+\vec{k}.\vec{x}')} \langle \vartheta(\vec{x}, t) \vartheta(\vec{x}', t)\rangle d\vec{x} d\vec{x}' \\ &= \left(\frac{1}{2\pi}\right)^6 \int e^{-i\vec{k}.\vec{r}} e^{-i(\vec{k}+\vec{k}').\vec{x}} U_\vartheta(\vec{r}, t, t') d\vec{r} d\vec{x} \end{aligned}$$

which gives

$$\langle \hat{\vartheta}(\vec{k}', t) \hat{\vartheta}(\vec{k}, t)\rangle = \frac{E_\Theta(k, t)}{2\pi k^2} \delta(\vec{k} + \vec{k}'), \tag{5.91}$$

where $E_\Theta(k, t)/2\pi k^2$ is the Fourier transform of the spatial scalar correlation $U_\theta = \langle \vartheta(\vec{x}, t) \vartheta(\vec{x}+\vec{r}, t)\rangle$. The scalar spectrum $E_\Theta(k, t)$ is in fact half the scalar variance density, such that

$$\frac{1}{2} \langle \vartheta^2(\vec{x}, t)\rangle = \int_0^{+\infty} E_\Theta(k, t) dk. \tag{5.92}$$

Of particular interest will be the study of a passive-scalar spectrum in isotropic turbulence, considered in Chapters 6 and 7. Relations equivalent to Eqs. (5.91) and (5.92) exist in two dimensions (see Chapter 8).

5.11 Alternative expressions of the spectral tensor

For sake of simplicity, we work here from the point of view of turbulence within a box. We will write the spectral expansion as

$$\vec{u}(\vec{x},t) = \sum_{\vec{k}} e^{i\vec{k}.\vec{x}} \underline{\hat{u}}(\vec{k},t), \tag{5.93}$$

where the extremity of $\vec{k}$ follows the nodes of a regular grid of mesh $\delta k = 2\pi/L$. Then the kinetic energy is

$$\frac{1}{2}\langle \vec{u}^*.\vec{u}\rangle = \frac{1}{2}\sum_{\vec{k}} \langle \underline{\hat{u}}^*(\vec{k},t).\underline{\hat{u}}(\vec{k},t)\rangle. \tag{5.94}$$

In computations by pseudo-spectral methods, one calculates the energy spectrum by summing up all the modal energies in shells of radius comprised between $k - \delta k/2$ and $k + \delta k/2$. If $\delta k \ll k$, and if turbulence is isotropic, the number of points in a shell is of the order of

$$\frac{4}{3\pi\delta k^3}\frac{dk^3}{dk}\delta k = 4\pi\frac{k^2}{\delta k^2}.$$

Then the energy of the shell is

$$(\delta k)E(k) = 2\pi\frac{k^2}{\delta k^2}\langle \underline{\hat{u}}^*(\vec{k},t).\underline{\hat{u}}(\vec{k},t)\rangle. \tag{5.95}$$

Here, $E(k)$ is such that

$$\frac{1}{2}\langle \vec{u}^*.\vec{u}\rangle = \frac{1}{2}\sum_k E(k)\delta k \approx \int_0^{+\infty} E(k)dk.$$

In two dimensions, one has to sum over a ring, and the equivalent above expressions are

$$\frac{\pi}{\delta k^2}\frac{dk^2}{dk}\delta k = 2\pi\frac{k}{\delta k},$$

$$(\delta k)E(k) = \pi\frac{k}{\delta k}\langle \underline{\hat{u}}^*(\vec{k},t).\underline{\hat{u}}(\vec{k},t)\rangle. \tag{5.96}$$

The spectral tensor is now

$$\bar{\bar{U}}(\vec{k},t) = \langle \underline{\hat{u}}^*(\vec{k},t) \otimes \underline{\hat{u}}(\vec{k},t)\rangle. \tag{5.97}$$

When projected in the local Craya space associated to the wave vector $\vec{k}$ its coordinates become

$$\bar{\bar{U}}(\vec{k},t) = \begin{pmatrix} A(\vec{k},t) & C(\vec{k},t) \\ C^*(\vec{k},t) & B(\vec{k},t) \end{pmatrix} \tag{5.98}$$

with

$$\begin{aligned} \langle u_V^*(\vec{k},t) u_V(\vec{k},t)\rangle &= A(\vec{k},t), \\ \langle u_V^*(\vec{k},t) u_W(\vec{k},t)\rangle &= C(\vec{k},t), \\ \langle u_W^*(\vec{k},t) u_V(\vec{k},t)\rangle &= C^*(\vec{k},t), \\ \langle u_W^*(\vec{k},t) u_W(\vec{k},t)\rangle &= B(\vec{k},t), \end{aligned} \tag{5.99}$$

where u_V and u_W are defined by Eq. (5.25) and where the functions $A(\vec{k},t)$ and $B(\vec{k},t)$ are real.[5] Such expressions are valid as soon as the turbulence is homogeneous, and isotropy is not required. One can now calculate easily from Eq. (5.99) the mean kinetic energy

$$\frac{1}{2}\sum_{\vec{k}} \langle \underline{\hat{u}}^*(\vec{k},t).\underline{\hat{u}}(\vec{k},t)\rangle = \frac{1}{2}\sum_{\vec{k}} A(\vec{k},t) + B(\vec{k},t), \tag{5.100}$$

the mean helicity

$$\begin{aligned} \frac{1}{2}\sum_{\vec{k}} \langle \underline{\hat{u}}^*(\vec{k},t).[i\vec{k}\times\underline{\hat{u}}(\vec{k},t)]\rangle &= \frac{1}{2}\sum_{\vec{k}} ik(C^* - C) \\ &= \sum_{\vec{k}} k\Im[C(\vec{k},t)], \end{aligned} \tag{5.101}$$

where $\Im(C)$ stands for the imaginary part of $C(\vec{k},t)$, and the mean enstrophy

$$\frac{1}{2}\sum_{\vec{k}} \langle [\vec{k}\times\underline{\hat{u}}^*(\vec{k},t)].[\vec{k}\times\underline{\hat{u}}(\vec{k},t)]\rangle = \frac{1}{2}\sum_{\vec{k}} k^2(A+B). \tag{5.102}$$

The advantage of working in this local frame is that the isotropy consequences can be implemented extremely easily, since any rotation acting simultaneously on $\vec{k}$ and $\vec{\alpha}$ will rotate also the local frame $(\vec{i},\vec{j},\vec{k}/k)$. Let us for example envisage a rotation of angle $\pi/2$ about $\vec{k}$, which leaves $\underline{\hat{u}}(\vec{k},t)$ unchanged, but transforms $\vec{i}$ into $\vec{j}$ and $\vec{j}$ into $-\vec{i}$. The coordinates of the spectral tensor in the new local frame are

$$\begin{pmatrix} B(\vec{k},t) & -C^*(\vec{k},t) \\ -C(\vec{k},t) & A(\vec{k},t) \end{pmatrix}$$

[5] These functions $A(\vec{k},t)$, $B(\vec{k},t)$ and $C(\vec{k},t)$ have no evident relation with other functions $\hat{A}$, $\hat{B}$, $\hat{C}$ introduced above.

and isotropy immediately implies that $A = B$ and C is imaginary. Since any simultaneous rotation of $\vec{k}$ and $\vec{\alpha}$ leaves the coordinates of the tensor unchanged, it follows that A, B, and C depend on k and t only.

We return to the integral Fourier representation, and express Eq. (5.88) under the form

$$\frac{1}{4\pi k^2}\begin{pmatrix} E(k,t) & iH(k,t)/k \\ -iH(k,t)/k & E(k,t) \end{pmatrix}, \tag{5.103}$$

where, because of Eqs. (5.100) and (5.101), $E(k,t)$ and $H(k,t)$ are exactly the energy and helicity spectra already defined. Such an expression has been proposed by Cambon [93]. It allows the recovery of $\hat{U}_{ij}(\vec{k},t)$ given by Eq. (5.84) with the proper change of coordinates: indeed the spectral tensor can, from Eq. (5.103), be written three-dimensionally in the local frame as

$$\frac{E(k,t)}{4\pi k^2}\begin{pmatrix} 1 & 0 & 0 \\ 0 & 1 & 0 \\ 0 & 0 & 0 \end{pmatrix} + i\frac{H(k,t)}{4\pi k^3}\begin{pmatrix} 0 & 1 & 0 \\ -1 & 0 & 0 \\ 0 & 0 & 0 \end{pmatrix},$$

where the first matrix, contracted with any three-dimensional vector, projects it in the plane perpendicular to $\vec{k}$, while the second multiplies it vectorially by $\vec{k}/k$. In the original reference frame, the projection in the plane perpendicular to $\vec{k}$ is represented by the tensor $P_{ij}(\vec{k})$, while the vectorial multiplication by $\vec{k}/k$ is $\epsilon_{ijs}k_s/k$. Such an expression, when transformed back into the physical space, yields a velocity correlation tensor of the form Eq. (5.62).

As for the spectral tensor in the complex helical wave decomposition, it is given by, using Eqs. (5.44), (5.99) and (5.103)

$$\langle u^+(\vec{k}',t)u^+(\vec{k},t)\rangle = \frac{E^{++}(k,t)}{4\pi k^2}\delta(\vec{k}+\vec{k}'), \tag{5.104}$$

$$\langle u^+(\vec{k}',t)u^-(\vec{k},t)\rangle = \langle u^-(\vec{k}',t)u^+(\vec{k},t)\rangle = 0, \tag{5.105}$$

$$\langle u^-(\vec{k}',t)u^-(\vec{k},t)\rangle = \frac{E^{--}(k,t)}{4\pi k^2}\delta(\vec{k}+\vec{k}'), \tag{5.106}$$

with (Lesieur [411])

$$E^{++}(k,t) = \frac{1}{2}\left[E(k,t) + \frac{H(k,t)}{k}\right], \tag{5.107}$$

$$E^{--}(k,t) = \frac{1}{2}\left[E(k,t) - \frac{H(k,t)}{k}\right]. \tag{5.108}$$

We remark that E^{++} and E^{--} must by definition be positive, since they are respectively proportional to $\langle u^{+*}(\vec{k},t)u^+(\vec{k},t)\rangle$ and $\langle u^{-*}(\vec{k},t)u^-(\vec{k},t)\rangle$ (modulo a Dirac distribution). It implies the inequality

$$\frac{|H(k,t)|}{k} < E(k,t). \tag{5.109}$$

Finally the mean kinetic energy, helicity and enstrophy are given, using these complex helical coordinates, by

$$\frac{1}{2}\langle \vec{u}^2 \rangle = \int_0^{+\infty} [E^{++}(k) + E^{--}(k)]dk, \tag{5.110}$$

$$\frac{1}{2}\langle \vec{u}.(\vec{\nabla} \times \vec{u}) \rangle = \int_0^{+\infty} k[E^{++}(k) - E^{--}(k)]dk, \tag{5.111}$$

$$\frac{1}{2}\langle \vec{\omega}^2 \rangle = \int_0^{+\infty} k^2[E^{++}(k) + E^{--}(k)]dk. \tag{5.112}$$

The scalar-velocity correlation in three-dimensional isotropic turbulence can also be considered in spectral space: let $\hat{\vartheta}(\vec{k},t)$ be the Fourier transform of the scalar, any rotation of angle π about the vector $\vec{k}$ will change $\vec{i}$ into $-\vec{i}$ and $\vec{j}$ into $-\vec{j}$, with for consequence the nullifying of $\langle \hat{\vartheta}(\vec{k},t)\hat{u}_V(\vec{k},t) \rangle$ and $\langle \hat{\vartheta}(\vec{k},t)\hat{u}_W(\vec{k},t) \rangle$, and hence of $\langle \hat{\vartheta}(\vec{k},t)\underline{\hat{u}}(\vec{k},t) \rangle$. We recover the fact that the scalar-velocity correlation is zero, as already shown in the physical space.

5.12 Axisymmetric turbulence

An important class of homogeneous non-isotropic turbulent flows possesses the property of axisymmetry, that is statistical invariance under rotations about one particular axis $\vec{\alpha}$. This type of turbulence may correspond for instance to rotating or stratified turbulence. The same kind of analysis as in the isotropic case can be performed, namely projecting the spectral tensor in the local Craya frame (defined with the same $\vec{\alpha}$), in which it still has the form Eq. (5.98): A and B are real, but C is no more a pure imaginary. The three quantities depend now on k and $\cos\theta$, as can be easily checked by writing the invariance of the coordinates of the tensor under any rotation about $\vec{\alpha}$ (θ is the angle between $\vec{\alpha}$ and $\vec{k}$). The spectral tensor is thus of the form

$$\begin{pmatrix} e - Z_1 & Z_2 + ih/k \\ Z_2 - ih/k & e + Z_1 \end{pmatrix} \tag{5.113}$$

already proposed in Cambon [93], where the real functions e, Z_1, Z_2 and h depend only on k, $\cos\theta$ and t. The mean kinetic energy and helicity are, from Eqs. (5.100) and (5.101), equal to $\int e d\vec{k}$ and $\int h d\vec{k}$. In the complex helical waves frame, the coordinates of the tensor are

$$\begin{pmatrix} e^{++} & Z^*/2 \\ Z/2 & e^{--} \end{pmatrix}, \tag{5.114}$$

where $Z = Z_1 + iZ_2$, e^{++} and e^{--} being related to e and h in the same way as E^{++} and E^{--} are related to E and H through Eqs. (5.107) and (5.108).

As remarked by Cambon [93], the statistical invariance with respect to a plane containing $\vec{\alpha}$ implies that h is zero and Z is real ($Z_2 = 0$). This axisymmetric turbulence "without helicity" exists if initial and boundary conditions contain no helicity. Z_1 characterizes thus the degree of anisotropy of the flow. In the latter case, the spectral tensor is diagonal in the local Craya frame, and is characterized by the two scalar functions

$$\Phi_1(k, \cos\theta, t) = e - Z_1; \Phi_2(k, \cos\theta, t) = e + Z_1$$

as was noticed by several authors (Chandrasekhar [106], Batchelor [47], Herring [275,277] and Capéran [96]). We recall that Φ_1 characterizes the "vortex" spectrum, and Φ_2 the "wave" spectrum, in the terminology of Riley et al. [600]. In that case the spectral tensor can be written in this local frame as

$$\Phi_2 \begin{pmatrix} 1 & 0 & 0 \\ 0 & 1 & 0 \\ 0 & 0 & 0 \end{pmatrix} + (\Phi_1 - \Phi_2) \begin{pmatrix} 1 & 0 & 0 \\ 0 & 0 & 0 \\ 0 & 0 & 0 \end{pmatrix},$$

or equivalently

$$\hat{U}_{ij}(\vec{k}, t) = \Phi_2 P_{ij}(\vec{k}) + (\Phi_1 - \Phi_2) Q_{ij}(\vec{k}) \tag{5.115}$$

in the original frame. $Q_{ij}(\vec{k})$ is the tensor which projects on $\vec{i}$, the first unit vector of the local frame (the vortex mode): it is the equivalent of $P_{ij}(\vec{k})$ for isotropic two-dimensional turbulence. Eq. (5.115) might be useful for the study of rotating homogeneous stably-stratified turbulence.

Finally, let us write the scalar velocity correlation of axisymmetric turbulence, which we need for instance when considering the stratified turbulence problem on the basis of Boussinesq equations. The same reasoning as above shows that, if $\hat{\vartheta}(\vec{k}, t)$ is the Fourier transform of the scalar $\vartheta(\vec{x}, t)$

$$\langle \hat{\vartheta}(\vec{k}', t) u_V(\vec{k}, t) \rangle = F_1(k, \cos\theta, t) \delta(\vec{k} + \vec{k}'), \tag{5.116}$$

$$\langle \hat{\vartheta}(\vec{k}', t) u_W(\vec{k}, t) \rangle = F_2(k, \cos\theta, t) \delta(\vec{k} + \vec{k}'). \tag{5.117}$$

F_1 is zero if the turbulence has the mirror symmetry just mentioned above.

In the particular case of two-dimensional isotropic turbulence, where $\vec{k}$ lies in a plane perpendicular to $\vec{\alpha}$, $u_W(\vec{k}, t)$ is evidently zero. A rotation of π about $\vec{\alpha}$ transforms $F_2(k, t)$ into $-F_2^*(\vec{k}, t)$, and F_2 is then a pure imaginary. If this turbulence possesses the mirror symmetry property (with respect to planes containing $\vec{\alpha}$), the scalar-velocity correlation will thus become zero. This result shows why isotropic two-dimensional turbulence may differ from isotropic

three-dimensional turbulence, and has not automatically zero scalar-velocity or zero scalar-vorticity correlations. As remarked in Lesieur and Herring [418], the one-point scalar-vorticity correlation in two-dimensional turbulence, if not zero, is conserved by the nonlinear terms of the equations.

5.13 Rapid-distorsion theory

As an exercise, we show how this theory can be developed for a homogeneous shear flow (see Townsend [689]). Let $\vec{U}$ be the mean velocity, of constant shear $\partial U_i/\partial x_j$. The linearized momentum equation for the perturbed flow (u_i, p) writes

$$\frac{\partial u_i}{\partial t} + U_j \frac{\partial u_i}{\partial x_j} + u_j \frac{\partial U_i}{\partial x_j} = -\frac{\partial p}{\partial x_i} + \nu \nabla^2 u_i. \tag{5.118}$$

Here, we work with a wave vector $\vec{k}(t)$ varying in Fourier space.[6] We still consider for a given function $f(\vec{x}, t)$ a Fourier expansion of the type

$$f(\vec{x}, t) = \int e^{i\vec{k}(t).\vec{x}} \hat{f}[\vec{k}(t)] d\vec{k} \ . \tag{5.119}$$

This does not pose problems as far as the motion of $\vec{k}(t)$ is incompressible. It yields

$$\frac{\partial f}{\partial t}(\vec{x}, t) = \int e^{i\vec{k}(t).\vec{x}} \frac{d\hat{f}}{dt}(\vec{k}) d\vec{k} + i \int \vec{x}.\frac{d\vec{k}}{dt} e^{i\vec{k}(t).\vec{x}} \hat{f}(\vec{k}) d\vec{k},$$

where $d\hat{f}/dt$ is the derivative of $\hat{f}$ following the motion of $\vec{k}$. We notice also that there exists some Galilean frame in which we have $U_j = x_l \partial U_j/\partial x_l$. Hence

$$\frac{\partial u_i}{\partial t} + U_j \frac{\partial u_i}{\partial x_j} = \int e^{i\vec{k}(t).\vec{x}} \left[\frac{d\hat{u}_i}{dt} + i x_l \left(\frac{dk_l}{dt} + k_j \frac{\partial U_j}{\partial x_l} \right) \hat{u}_i \right] d\vec{k},$$

and the "moving Fourier expansion" makes sense only if

$$\frac{dk_l}{dt} = -k_j \frac{\partial U_j}{\partial x_l}. \tag{5.120}$$

This shows that the motion of $\vec{k}$ is non-divergent, since

$$\frac{\partial}{\partial k_l} \left(\frac{dk_l}{\partial t} \right) = -\frac{\partial U_l}{\partial x_l} = 0.$$

[6] This is equivalent to considering a system of coordinates moving with the mean flow.

Thus, the equation of motion in Fourier space is

$$\frac{d\hat{u}_i}{dt} + \frac{\partial U_i}{\partial x_j}\hat{u}_j = -ik_i\hat{p} - \nu k^2\hat{u}_i. \tag{5.121}$$

To eliminate the pressure, we take the divergence of Eq. (5.113), and obtain the following Poisson equation

$$-\nabla^2 p = \frac{\partial U_l}{\partial x_j}\frac{\partial u_j}{\partial x_l} + \frac{\partial U_j}{\partial x_l}\frac{\partial u_l}{\partial x_j} = 2\frac{\partial U_l}{\partial x_j}\frac{\partial u_j}{\partial x_l},$$

which gives in Fourier space

$$\hat{p} = 2i\frac{k_l}{k^2}\frac{\partial U_l}{\partial x_j}\hat{u}_j \tag{5.122}$$

and finally

$$\frac{d\hat{u}_i}{dt} = -\frac{\partial U_i}{\partial x_l}\hat{u}_l + 2\frac{k_i k_l}{k^2}\frac{\partial U_l}{\partial x_m}\hat{u}_m - \nu k^2\hat{u}_i, \tag{5.123}$$

which is Eq. (3.2.7) of Townsend [689].

When applied to a plane shear $U_1 = \lambda y, U_2 = U_3 = 0$, we have

$$\frac{dk_1}{dt} = 0, \frac{dk_2}{dt} = -\lambda k_1, \frac{dk_3}{dt} = 0, \tag{5.124}$$

$$\frac{d\hat{u}_1}{dt} + \nu k^2\hat{u}_1 = \lambda\left(2\frac{k_1^2}{k^2} - 1\right)\hat{u}_2, \tag{5.125}$$

$$\frac{d\hat{u}_2}{dt} + \nu k^2\hat{u}_2 = 2\lambda\frac{k_1 k_2}{k^2}\hat{u}_2, \tag{5.126}$$

$$\frac{d\hat{u}_3}{dt} + \nu k^2\hat{u}_3 = 2\lambda\frac{k_1 k_3}{k^2}\hat{u}_2. \tag{5.127}$$

This shows that k_1 and k_3 are constant, while $k_2 = k_2(0) - \lambda t$ goes to infinity, indicating some sort of cascade to small scales in the transverse direction. The general solution is given in Townsend [689, p. 83] in terms of a modified time $\beta = \lambda t$. He can then evaluate the spectral tensor $\hat{U}_{ij}[\vec{k}(t)]$, and the time-evolution of the velocity fluctuation variances and Reynolds stresses.

6

Isotropic Turbulence: Phenomenology and Simulations

6.1 Introduction

Here, we will consider fully-developed isotropic turbulence both from a phenomenological point of view, using basically dimensional arguments (for instance to derive Kolmogorov's theory or Richardson's law) or DNS and LES. We will be interested in small-scale transfers of kinetic energy, and diffusion of passive scalars. Numerical simulations will allow us to study the coherent vortices of isotropic turbulence. We will give finally some informations on small-scale intermittency.

6.2 Triad interactions and detailed conservation

When considering homogeneous turbulence, whith zero mean velocity,[1] our interest lies in correlations between *different* points of the space: indeed these quantities give access to energy transfers between different scales of motion. Even in this case the closure problem arises, and the closures we will try to develop are sometimes referred to as *two-point closures*. They involve in particular the velocity correlations between two wave vectors in Fourier space, namely the spectral tensor.

The simplest of these spectral theories are obtained via phenomenological or dimensional arguments which will be presented in this chapter. Some of them are based on conservation properties of Navier–Stokes equations, and on particular behaviour due to the triadic character of the energy exchanges.

Let us first consider the exact evolution equation of the energy spectrum in terms of the triple-velocity moments: for homogeneous isotropic turbulence, it

[1] Provided one works in a frame moving with the mean velocity (assumed to be constant).

is possible to obtain from Navier–Stokes equations an exact equation relating the longitudinal second-order velocity correlation to the third-order velocity correlations which result from the "advection" term $u_j \partial u_i / \partial x_j$ (we recall that the pressure-velocity correlation, as already mentioned, is then zero). The resulting equation is known as the Karman-Howarth equation, and its derivation can be found (for instance) in Hinze [285]. An equivalent equation for the trace of the spectral tensor of homogeneous turbulence (with constant uniform density) can be found by working in Fourier-space (see Rose and Sulem [617]): one writes the time evolution equations of $\hat{u}_i(\vec{k}', t)$ and $\hat{u}_j(\vec{k}, t)$, multiplies respectively by $\hat{u}_j(\vec{k}, t)$ and $\hat{u}_i(\vec{k}', t)$, adds the two equations, averages, and obtains the time derivative of $\langle \hat{u}_i(\vec{k}', t) \hat{u}_j(\vec{k}, t) \rangle$. When integrating on $\vec{k}'$ and taking the trace of the tensor, one finally obtains after some algebra

$$\left(\frac{\partial}{\partial t} + 2\nu k^2 \right) \hat{U}_{ii}(\vec{k}, t) = -P_{ijm}(\vec{k}) \int \Im[\langle \hat{u}_i(\vec{k}) \hat{u}_j(\vec{p}) \hat{u}_m(\vec{q}) \rangle] d\vec{p} d\vec{q} \tag{6.1}$$

with

$$P_{ijm}(\vec{k}) = k_m P_{ij}(\vec{k}) + k_j P_{im}(\vec{k}) \tag{6.2}$$

and where $\Im$ stands for the imaginary part. In the integrand of Eq. (6.1), the $\langle uuu \rangle$ term is proportional to a $\delta(\vec{k} + \vec{p} + \vec{q})$ Dirac function, so that only the triads $\vec{k} + \vec{p} + \vec{q} = \vec{0}$ are involved in the integration. It allows one to show a theorem of

- Detailed conservation of kinetic energy:
  Let Eq. (6.1) be written under a symmetrized form

$$\left(\frac{\partial}{\partial t} + 2\nu k^2 \right) \hat{U}_{ii}(\vec{k}, t) = \int s(\vec{k}, \vec{p}, \vec{q}) \delta(\vec{k} + \vec{p} + \vec{q}) d\vec{p} d\vec{q} \tag{6.3}$$

with

$$s(\vec{k}, \vec{p}, \vec{q}) = s(\vec{k}, \vec{q}, \vec{p}). \tag{6.4}$$

From Eq. (6.1) one obtains:

$$\begin{aligned} & s(\vec{k}, \vec{p}, \vec{q}) \delta(\vec{k} + \vec{p} + \vec{q}) \\ & = -\Im[\langle (\vec{k}.\vec{\hat{u}}(\vec{q}))(\vec{\hat{u}}(\vec{k}).\vec{\hat{u}}(\vec{p})) \rangle + \langle (\vec{k}.\vec{\hat{u}}(\vec{p}))(\vec{\hat{u}}(\vec{k}).\vec{\hat{u}}(\vec{q})) \rangle]. \end{aligned} \tag{6.5}$$

In fact, using the incompressibility condition $\vec{k}.\underline{\hat{u}}(\hat{k}) = 0$, we remark that

$$\begin{aligned} & \langle (\vec{k}.\vec{\hat{u}}(\vec{q}))(\vec{\hat{u}}(\vec{k}).\vec{\hat{u}}(\vec{p})) \rangle + \langle (\vec{k}.\vec{\hat{u}}(\vec{p}))(\vec{\hat{u}}(\vec{k}).\vec{\hat{u}}(\vec{q})) \rangle \\ & + \langle (\vec{p}.\vec{\hat{u}}(\vec{k}))(\vec{\hat{u}}(\vec{p}).\vec{\hat{u}}(\vec{q})) \rangle + \langle (\vec{p}.\vec{\hat{u}}(\vec{q}))(\vec{\hat{u}}(\vec{p}).\vec{\hat{u}}(\vec{k})) \rangle \\ & + \langle (\vec{q}.\vec{\hat{u}}(\vec{p}))(\vec{\hat{u}}(\vec{q}).\vec{\hat{u}}(\vec{k})) \rangle + \langle (\vec{q}.\vec{\hat{u}}(\vec{k}))(\vec{\hat{u}}(\vec{q}).\vec{\hat{u}}(\vec{p})) \rangle \end{aligned}$$

is zero for $\vec{k}+\vec{p}+\vec{q}=\vec{0}$. So the function

$$G(\vec{k},\vec{p},\vec{q}) = [s(\vec{k},\vec{p},\vec{q}) + s(\vec{p},\vec{q},\vec{k}) + s(\vec{q},\vec{k},\vec{p})]\delta(\vec{k}+\vec{p}+\vec{q})$$

is zero for such triads. Forming

$$\int G(\vec{k},\vec{p},\vec{q})d\vec{q} = G(\vec{k},\vec{p},-\vec{k}-\vec{p}) = 0$$

$$= s(\vec{k},\vec{p},-\vec{k}-\vec{p}) + s(\vec{p},-\vec{k}-\vec{p},\vec{k}) + s(-\vec{k}-\vec{p},\vec{k},\vec{p})$$

yields

$$s(\vec{k},\vec{p},\vec{q}) + s(\vec{p},\vec{q},\vec{k}) + s(\vec{q},\vec{k},\vec{p}) = 0 \tag{6.6}$$

for triads such that $\vec{k}+\vec{p}+\vec{q}=\vec{0}$.

The interpretation of this result is that, if only three modes (such that $\vec{k}+\vec{p}+\vec{q}=0$) were interacting, nonlinear exchanges of kinetic energy between these modes would conserve the energy. Also, one can derive a mean kinetic energy conservation result: by integrating Eq. (6.3) on wave vector $\vec{k}$, one obtains

$$\frac{1}{2}\int\left(\frac{\partial}{\partial t}+2\nu k^2\right)\hat{U}_{ii}(\vec{k},t)d\vec{k} = \frac{1}{6}\int[s(\vec{k},\vec{p},\vec{q}) + s(\vec{p},\vec{q},\vec{k})$$

$$+s(\vec{q},\vec{k},\vec{p})]\delta(\vec{k}+\vec{p}+\vec{q})d\vec{k}d\vec{p}d\vec{q} = 0. \tag{6.7}$$

If turbulence is isotropic, Eq. (6.7) is equivalent to

$$\frac{d}{dt}\int_0^{+\infty} E(k,t)dk + 2\nu\int_0^{+\infty} k^2 E(k,t)dk = 0. \tag{6.8}$$

This result shows that the mean kinetic energy is conserved by nonlinear terms of Navier–Stokes equations, and dissipated by molecular viscosity at a rate $2\nu\int_0^{+\infty} k^2E(k,t)dk$. Eq. (6.8) may of course be shown much more easily in physical space, as will be seen below. But the detailed conservation property gives significant information about the way nonlinear interactions redistribute the energy between the modes.

This theorem of detailed conservation can actually be generalized to any quadratic quantity conserved by nonlinear terms of Navier–Stokes equations, i.e. the mean kinetic energy, the helicity (in three dimensions), the enstrophy (in two dimensions) and the passive-scalar variance: Let $\hat{U}_c(\vec{k},t)$ be the density of this conserved quantity at the wave vector $\vec{k}$, satisfying the evolution equation

$$\left(\frac{\partial}{\partial t}+2\kappa_c k^2\right)\hat{U}_c(\vec{k},t) = \int s_c(\vec{k},\vec{p},\vec{q})\delta(\vec{k}+\vec{p}+\vec{q})d\vec{p}d\vec{q} \tag{6.9}$$

with

$$s_c(\vec{k},\vec{p},\vec{q}) = s_c(\vec{k},\vec{q},\vec{p}) \tag{6.10}$$

where κ_c arising in the l.h.s. of Eq. (6.9) is the molecular diffusivity of the quantity, which will be either the molecular viscosity or the conductivity. A result from Kraichnan [356] states that $s_c(\vec{k},\vec{p},\vec{q})$ satisfies a detailed conservation relation analogous to Eq. (6.6). This will have profound consequences for the dynamics of two-dimensional isotropic turbulence, since the enstrophy transfer density at wave vector $\vec{k}$ is $k^2 s(\vec{k},\vec{p},\vec{q})$, thus implying both the detailed energy and enstrophy conservation:

$$k^2 s(\vec{k},\vec{p},\vec{q}) + p^2 s(\vec{p},\vec{q},\vec{k}) + q^2 s(\vec{q},\vec{k},\vec{p}) = 0. \tag{6.11}$$

6.2.1 Quadratic invariants in physical space

Let us write directly in physical space the evolution equations for homogeneous turbulence of the following quadratic quantities: kinetic energy, helicity and passive scalar variance.

• Kinetic energy:

We start with an incompressible Navier–Stokes equation (with constant density) under the form

$$\frac{\partial u_i}{\partial t} + u_j \frac{\partial u_i}{\partial x_j} = -\frac{\partial p}{\partial x_i} + \nu \nabla^2 u_i, \tag{6.12}$$

that we multiply by u_i, for fixed i. It yields

$$\frac{1}{2}\frac{\partial}{\partial t} u_i^2 + \frac{1}{2} u_j \frac{\partial}{\partial x_j} u_i^2 = -u_i \frac{\partial p}{\partial x_i} + \nu u_i \nabla^2 u_i, \tag{6.13}$$

or equivalently, because of incompressibility:

$$\frac{1}{2}\frac{\partial}{\partial t} u_i^2 + \frac{1}{2}\frac{\partial}{\partial x_j} u_j u_i^2 = -u_i \frac{\partial p}{\partial x_i} + \nu u_i \nabla^2 u_i.$$

After summation upon the i, one obtains

$$\frac{1}{2}\frac{\partial}{\partial t}\vec{u}^2 + \frac{1}{2}\frac{\partial}{\partial x_j} u_j \vec{u}^2 = -\frac{\partial p u_i}{\partial x_i} + \nu \vec{u}.\nabla^2 \vec{u}.$$

Making use of the homogeneity property and averaging, one has:

$$\frac{d}{dt}\frac{1}{2}\langle \vec{u}^2 \rangle = \nu \langle \vec{u}.\nabla^2 \vec{u} \rangle.$$

Because of Eq. (5.87), the mean kinetic energy evolution equation is:

$$\frac{d}{dt}\frac{1}{2}\langle \vec{u}^2 \rangle = -2\nu D(t), \tag{6.14}$$

which allows to recover Eq. (6.8) when turbulence is isotropic.

• Helicity:

We consider both Eq. (6.12) as well as the corresponding vorticity equation:

$$\frac{\partial \omega_i}{\partial t} + u_j \frac{\partial \omega_i}{\partial x_j} = \omega_j \frac{\partial u_i}{\partial x_j} + \nu \nabla^2 \omega_i, \tag{6.15}$$

multiply them respectively by $\omega_i/2$ and $u_i/2$, add and average. It is found that

$$\frac{dH_e}{dt} + \frac{1}{2}\left\langle u_j \frac{\partial}{\partial x_j}(\omega_i u_i) \right\rangle = -\frac{1}{2}\left\langle \omega_i \frac{\partial p}{\partial x_i} \right\rangle + \frac{1}{2}\left\langle \omega_j u_i \frac{\partial u_i}{\partial x_j} \right\rangle$$
$$-\nu \langle \vec{\omega}.(\vec{\nabla} \times \vec{\omega}) \rangle,$$

where we recall that $H_e = (1/2)\langle \vec{u}.\vec{\omega} \rangle$. Making use of the incompressibility and homogeneity conditions, nonlinear terms vanish. With the aid of Eqs. (5.88) and (5.89), the mean helicity evolution equation is

$$\frac{dH_e}{dt} = \frac{\nu}{2}(\langle \vec{\omega}.\nabla^2 \vec{u} \rangle + \langle \vec{u}.\nabla^2 \vec{\omega} \rangle).$$

Remarking that the operators ∇^2 and $\vec{\nabla}\times$ commute, the latter term is equal to

$$\langle \vec{u}.(\vec{\nabla} \times \nabla^2 \vec{u}) \rangle = \langle \vec{\omega}.\nabla^2 \vec{u} \rangle,$$

which gives

$$\frac{dH_e}{dt} = \nu \langle \vec{\omega}.\nabla^2 \vec{u} \rangle. \tag{6.16}$$

In a similar way as was done for Eq. (5.90), we can write

$$\langle \vec{\omega}.\nabla^2 \vec{u} \rangle = -\int d\vec{k} d\vec{k}' \; e^{i(\vec{k}+\vec{k}').\vec{x}} k^2 \langle \hat{\omega}_i(\vec{k}', t)\hat{u}_i(\vec{k}, t) \rangle \; .$$

We introduce the helical spectral tensor $\hat{H}_{ij}(\vec{k}, t)$, Fourier transform of the correlation $\langle \omega_i(\vec{x}, t)u_j(\vec{x} + \vec{r}, t) \rangle$. It is such that

$$\langle \hat{\omega}_i(\vec{k}', t)\hat{u}_i(\vec{k}, t) \rangle = \hat{H}_{ii}(\vec{k}, t)\delta(\vec{k} + \vec{k}')$$

with, for isotropic turbulence

$$H_e = \frac{1}{2}\int \hat{H}_{ii}(\vec{k},t)d\vec{k} = \int_0^{+\infty} H(k,t)dk.$$

The helicity dissipation rate is then

$$\nu\langle\vec{\omega}.\nabla^2\vec{u}\rangle = -\nu\int k^2\hat{H}_{ii}(\vec{k},t)d\vec{k} = \nu\int_0^{+\infty} k^2H(k,t)dk,$$

and the final helicity dissipation equation is

$$\frac{d}{dt}\int_0^{+\infty} H(k,t)dk + 2\nu\int_0^{+\infty} k^2H(k,t)dk = 0. \tag{6.17}$$

• Passive scalar:

We consider a passive scalar $\vartheta(\vec{x},t)$ satisfying the equation

$$\frac{\partial\vartheta}{\partial t} + u_j\frac{\partial\vartheta}{\partial x_j} = \kappa\nabla^2\vartheta. \tag{6.18}$$

Multiplying by ϑ and averaging yields, for homogeneous turbulence

$$\frac{1}{2}\frac{d}{dt}\langle\vartheta^2\rangle = \kappa\langle\vartheta\nabla^2\vartheta\rangle = -\kappa\langle(\vec{\nabla}\vartheta)^2\rangle, \tag{6.19}$$

since for a given i and due to homogeneity

$$\frac{\partial}{\partial x_i}\left\langle\vartheta\frac{\partial\vartheta}{\partial x_i}\right\rangle = 0 = \left\langle\left(\frac{\partial\vartheta}{\partial x_i}\right)^2\right\rangle + \left\langle\vartheta\frac{\partial^2\vartheta}{\partial x_i^2}\right\rangle.$$

Again we can write, using Eq. (5.91)

$$\langle\vartheta\nabla^2\vartheta\rangle = -\int d\vec{k}d\vec{k}'\ e^{i(\vec{k}+\vec{k}').\vec{x}}k^2\langle\hat{\vartheta}(\vec{k}',t)\hat{\vartheta}(\vec{k},t)\rangle$$

$$= -\int k^2\frac{E_\Theta(k,t)}{2\pi k^2}d\vec{k} = -2\int_0^{+\infty} k^2E_\Theta(k,t)dk,$$

that is

$$\frac{d}{dt}\int_0^{+\infty} E_\Theta(k,t)dk + 2\kappa\int_0^{+\infty} k^2E_\Theta(k,t)dk = 0. \tag{6.20}$$

Therefore, the above three quantities are conserved by nonlinear terms of the equations. We will call them *quadratic invariants of turbulence*, although they are not invariant, since the viscous dissipation will be seen to be of prior importance in three-dimensional turbulence.

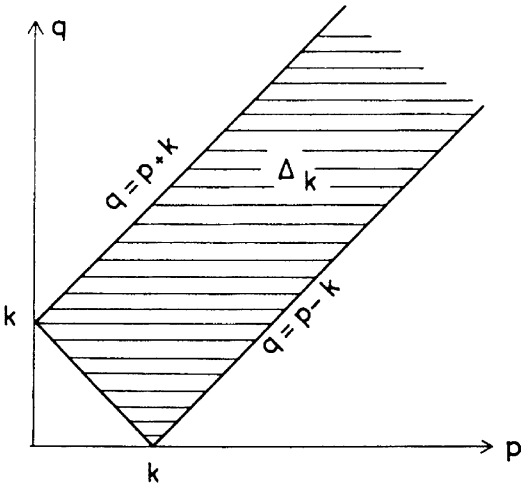

Figure 6.1. Domain in the (p, q) plane such that (k, p, q) should be the sides of a triangle, and allowing triad interactions with the wave number k.

6.3 Transfer and flux

For isotropic turbulence, and after multiplication of Eq. (6.3) by $2\pi k^2$ (or πk in two-dimensional turbulence), one obtains

$$\left(\frac{\partial}{\partial t} + 2\nu k^2\right) E(k,t) = T(k,t) \tag{6.21}$$

where $T(k,t)$ corresponds to the triple-velocity correlations coming from nonlinear interactions of Navier–Stokes equations:

$$T(k,t) = \int_{\vec{k}+\vec{p}+\vec{q}=\vec{0}} 2\pi k^2 s(k,p,q) d\vec{p} = \iint_{\Delta_k} dp\ dq S(k,p,q) \tag{6.22}$$

with

$$S(k,p,q) = 4\pi^2 kpqs(k,p,q) \tag{6.23}$$

$s(k,p,q)$ being introduced in Eqs. (6.2)–(6.4). We precise that the double integral in Eq. (6.22) is performed on a domain Δ_k of the plane (p, q) such that the positive numbers $p = |\vec{p}|$ and $q = |\vec{q}|$ should be the sides of a triangle of a third side $k = |\vec{k}|$. This domain is shown in Figure 6.1. $S(k,p,q)$ is symmetric in p and q, and possesses the detailed conservation property (6.6). When considering forced turbulence, one needs to add a forcing term $F_o(k)$ to the r.h.s. of Eq. (6.21). This forcing term is a mathematical expedient which allows

the supplying of the viscous loss of kinetic energy and convergence towards a stationary energy spectrum $E(k)$. It has generally no physical reality, since the forces acting on real flows induce anisotropy and inhomogeneity in the large scales. $T(k,t)$ will be called the kinetic-energy transfer. The kinetic-energy flux through wave number k is defined as

$$\Pi(k,t) = \int_k^{+\infty} T(k',t)dk' \tag{6.24}$$

which is equivalent to

$$T(k,t) = -\frac{\partial \Pi(k,t)}{\partial k}. \tag{6.25}$$

The kinetic energy dissipation result (6.8) implies that

$$\int_0^{+\infty} T(k,t)dk = 0. \tag{6.26}$$

This result can also be deduced from Eq. (6.22), given that $S(k,p,q)$ satisfies the detailed conservation property and that the domain of the $[k,p,q]$ space, such that (k,p,q) are the sides of a triangle, is invariant by circular permutation of (k,p,q). Thus, Eq. (6.26) is also valid for forced turbulence. One also has

$$\Pi(k,t) = -\int_0^{k} T(k',t)dk'. \tag{6.27}$$

A transfer function $T(k,t)$ calculated in a direct-numerical simulation of isotropic turbulence is shown in Figure 6.2: it is negative in the large energy-containing eddies, and positive at high wave numbers, indicating a tendency for the energy to cascade from large to small scales. At higher Reynolds numbers, we will see later on that the transfer function presents a plateau at zero value, indicating a constant flux of kinetic energy.

Kraichnan [354] has shown, using the symmetry and detailed conservation properties of $S(k,p,q)$, that the energy flux through a wave number k could be written as

$$\Pi(k,t) = \Pi^+(k,t) - \Pi^-(k,t) \tag{6.28}$$

$$\Pi^+(k,t) = \int_k^{\infty} dk' \int_0^k \int_0^k S(k',p,q)dpdq \tag{6.29}$$

$$\Pi^-(k,t) = \int_0^{k} dk' \int_k^{\infty} \int_k^{\infty} S(k',p,q)dpdq. \tag{6.30}$$

This formalism will be useful when considering the notion of enstrophy cascade in two-dimensional turbulence (see Chapter 8), and the eddy-viscosity concept in spectral space for three-dimensional isotropic turbulence with a

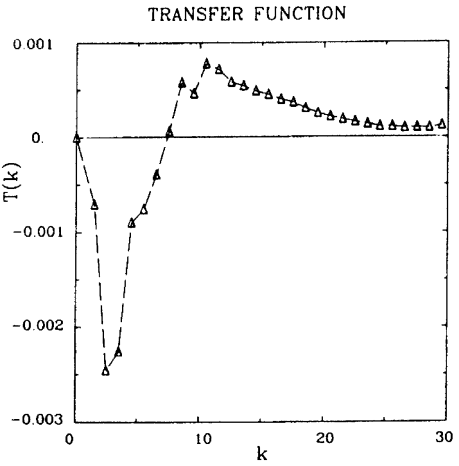

Figure 6.2. Transfer function of three-dimensional isotropic turbulence, computed in a direct numerical simulation (courtesy O. Métais, Institut de Mécanique de Grenoble).

separation of scales (turbulence with a "spectral gap", see e.g. Pouquet et al. [586]). In this last case, $-\Pi^-$ is the flux of kinetic energy from the "large" scales (low wave numbers) to the "small" scales (large wave numbers), and the corresponding energy transfer $\partial\Pi^-/\partial k$ can be approximated (via the stochastic models discussed in the next chapter) as $-2\nu_t k^2 E(k), \nu_t$ depending on the kinetic energy in the small scales. Since the molecular viscous energy transfer is $-2\nu k^2 E(k), \nu_t$ can be interpreted as an eddy-viscosity.

Then an exact result can be obtained directly on Navier–Stokes equations without any approximation: let us assume that there exists a forcing $F_o(k)$ concentrated on a narrow spectral band in the vicinity of a wave number k_i, which will thus be characteristic of the "large energy-containing eddies". We assume also that the turbulence is stationary, so that the energy spectrum and the transfer are independent of t (see Figure 6.3). Eq. (6.21) with the forcing term writes

$$2\nu k^2 E(k) = T(k) + F_o(k). \tag{6.31}$$

For $k \neq k_i$, it yields

$$T(k) = 2\nu k^2 E(k) \tag{6.32}$$

and for k fixed

$$\lim_{\nu \to 0} T(k) = 0. \tag{6.33}$$

Now let

$$\epsilon = \int_0^{+\infty} F_o(k) dk \tag{6.34}$$

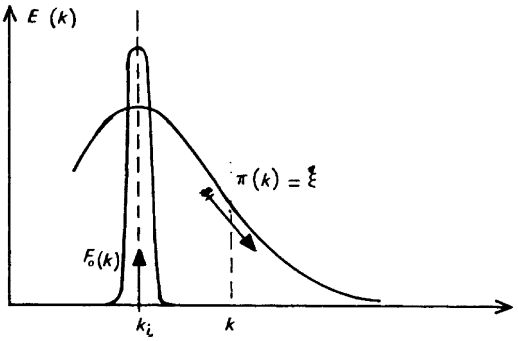

Figure 6.3. Schematic stationary kinetic energy spectrum forced, within Navier–Stokes equation in the limit of zero viscosity, by a narrow forcing spectrum $F_o(k)$ concentrated at k_i. The kinetic energy flux $\Pi(k)$ is, for $k > k_i$, equal to the injection rate ϵ.

be the rate of injection of kinetic energy. Integrating Eq. (6.31) from 0 to ∞, and using Eq. (6.26), leads to

$$\epsilon = 2\nu \int_0^{+\infty} k^2 E(k) dk, \tag{6.35}$$

and the injection of kinetic energy is balanced by molecular viscous dissipation, which is quite obvious intuitively. If in Eq. (6.35) one lets ν go to zero (ϵ being imposed by the stationary injection), the enstrophy will go to infinity. Finally integration of Eq. (6.31) from 0 to $k \neq k_i$ yields

$$\lim_{\nu \to 0} \Pi(k) = 0, k < k_i \tag{6.36}$$

$$\lim_{\nu \to 0} \Pi(k) = \epsilon, k > k_i \tag{6.37}$$

(for a fixed k). The conclusion of this very simple discussion is that there exists a spectral range extending beyond the injection wave number k_i where, at vanishing viscosity, the kinetic energy transfer is identically zero, the energy flux is constant and equal to the injection rate. We anticipate that these results are the major ingredients of Kolmogorov's 1941 theory, which will be looked at in the next section.

6.4 Kolmogorov's 1941 theory

This is certainly the most famous theory of isotropic turbulence. What people call Kolmogorov's 1941 theory corresponds in fact to dimensional predictions

concerning either the second-order velocity structure-function (defined below) done by Kolmogorov [338], or the kinetic-energy spectrum (Oboukhov [542, 543]). There is another important paper by Kolmogorov [339] the same year, where he predicts the so-called $-4/5$ law, which will be discussed later. We stress also that Kolmogorov [340] was led to revise his 1941 point of view, in order to account for intermittency (see below). For all the historical aspects related to these laws, the reader is referred to the book of Frisch [229].

6.4.1 Kolmogorov 1941 in spectral space

We have just seen that for stationary isotropic turbulence forced at a rate ϵ in a narrow spectral range around k_i, and in the limit of an infinite Reynolds number (or equivalently zero viscosity), the energy flux $\Pi(k)$ is independent of k and equal to ϵ for $k > k_i, \epsilon$ being also the viscous dissipation rate. This shows that ϵ is an extremely important parameter which controls the energy flux from the large scales where it is injected to the small scales where it will be dissipated by viscosity: this scheme of progressive energy cascade from large to smaller-size eddies has been immortalized by Richardson [595][2] with his parody of Jonathan Swift's *fleas sonnet*,[3] and this infinite hierarchy of eddies/fleas sucking the energy/blood of the bigger ones on which they ride, while they are being sucked by smaller eddies/fleas riding on them. So Kolmogorov's 1941 theory assumes that the energy spectrum at wave numbers greater than k_i depends only on ϵ and k. A dimensional analysis, based on the Vaschy–Buckingham π-theorem, yields

$$E(k) = C_K \epsilon^{2/3} k^{-5/3} \tag{6.38}$$

where C_K is a universal constant called Kolmogorov constant.

• Exercise: show Eq. (6.38).

One seeks for an expansion of the spectrum of the form

$$E(k) = G(\epsilon, k) = \sum_{\alpha,\beta} \epsilon^{\alpha}\ k^{\beta},$$

and looks for exponents α and β such that $\epsilon^{\alpha} k^{\beta}$ has the dimension of a kinetic energy spectrum. If $[L]$ and $[T]$ are dimensions of space and time respectively, we have:

$$k = [L]^{-1}; E(k) = [L]^3[T]^{-2}; \epsilon = [L]^2[T]^{-3}$$

[2] *Big whirls have little whirls, which feed on their velocity, and little whirls have lesser whirls, and so on to viscosity.*

[3] *A flea hath smaller fleas that on him prey; and these have smaller yet to bite'em, and so proceed ad infinitum*, quoted from Frisch and Orszag [228].

$$[L]^{2\alpha-\beta}[T]^{-3\alpha} = [L]^3[T]^{-2}.$$

There is only one possible couple (α, β), such that

$$\alpha = \frac{2}{3}, \beta = -\frac{5}{3}.$$

Text
When the turbulence is freely decaying, Eq. (6.38) can be generalized taking

$$\epsilon(t) = -\frac{d}{dt}\int_0^{+\infty} E(k,t)dk,$$

the dissipation rate of kinetic energy, given by Eq. (6.8) and formally identical to Eq. (6.35). k_i is now a function of t, and will later on be seen to decrease with time.

The Richardson-Kolmogorov cascade scheme is certainly questionable since it does not correspond physically to well identified instabilities arising in the fluid. But, and for whatever may be the reason, the law equation (6.38) is remarkably well verified experimentally in the small scales of a flow when the Reynolds number is sufficiently high: this is, for instance the case in the ocean (Grant et al. [264], Gargett et al. [240]), the atmosphere (Champagne et al. [105]), or in wind tunnels (Dumas [181], Gagne [239]),[4] mixing layers (Browand and Ho [87]), or jets (Gibson [255], Giger et al. [256]). As an example, the spectrum measured in the ocean in a tidal channel in British Columbia (the "Knight Inlet", see Gargett et al. [240]) displays a Kolmogorov law extending to nearly three decades. This spectrum is presented in Figure 6.4. The value of the universal Kolmogorov constant C_K, found experimentally, is of the order of 1.5. It is, however, not certain that the constant is the same in stationary-forced or decaying situations.

In fact, there are former experimental checkings of Kolmogorov's $-5/3$ law: Betchov [60] found it upon two decades in a box where 80 jets interacted.[5] He quotes also Laufer in a channel and a pipe, and Corrsin in a jet [145]).

Many recent numerical simulations (DNS and LES) of jets or coaxial round jets display interesting $k^{-5/3}$ laws on about one decade (see Balarac [27, 28]). This, together with the fact that these flows are close to isotropy in the small scales, makes them much better candidates than grid turbulence to reach high Reynolds numbers at low cost.

Kolmogorov's law is not, of course, valid for any scale of motion: under k_i, the spectrum will be influenced by forcing (if any) and by long-range (*non-local*) interactions which will be studied in the following chapter.

[4] These two experiments were carried out in the Modane ONERA facility, where the Reynolds numbers are huge.
[5] This facility was called the "porcupine" by his students.

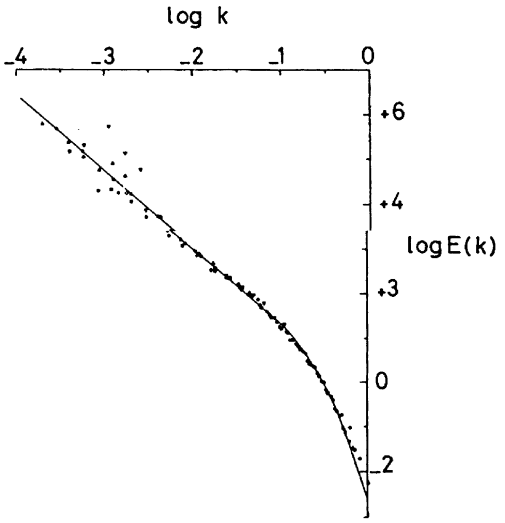

Figure 6.4. Longitudinal kinetic energy spectrum measured in the three-dimensional turbulence generated in a tidal channel in the ocean (Knight inlet, British Columbia): turbulence is decaying with time, and the spectra at various stages of the evolution are normalized by the Kolmogorov dissipative scale (see below). They display the self-similar behaviour proposed in Eq. (6.70). The spectra exhibit a three-decade Kolmogorov $k^{-5/3}$ inertial range (from Gargett et al. [240], courtesy *J. Fluid Mech.*)

6.4.2 Kolmogorov wave number

Above a sufficiently high wave number k_d, called the Kolmogorov wave number, the viscous dissipation will damp the velocity perturbations. The order of magnitude of this wave number can for instance be obtained by taking a schematic energy spectrum equal to zero for $k < k_i$ and $k > k_d$ and given by Eq. (6.38) in between, and by calculating ϵ with the aid of Eq. (6.35). One finds

$$k_d = \left(\frac{\epsilon}{\nu^3}\right)^{1/4} . \tag{6.39}$$

For $k > k_d$, the energy spectrum will rapidly (possibly exponentially) drop to negligible values. This range is called the dissipation range. The inverse of k_d is the Kolmogorov dissipative scale l_d.

6.4.3 Integral scale

The inverse of k_i is of the order of the integral scale l. This scale is exactly defined as

$$l = \int_0^{+\infty} f(r)dr. \tag{6.40}$$

Here,

$$f(r) = \frac{F(r,t,t)}{u'^2}$$

is the longitudinal velocity correlation coefficient, where $F(r,t,t)$ is defined in Eq. (5.57), and corresponds to the correlation of u, the velocity component in the $\vec{r}$ direction, of rms u'. The associated Reynolds number is defined as

$$R_l = \frac{u'l}{\nu}. \tag{6.41}$$

One finds experimentally (see Tennekes and Lumley [684]) that

$$\epsilon = Au'^3/l, \tag{6.42}$$

with $A \approx 1$.

Notice that, in the forced case where ϵ is imposed by the forcing spectrum, k_d goes to infinity and the enstrophy diverges as $k_d^{4/3}$ when the molecular viscosity goes to zero. In the decaying case, and if one assumes that half the kinetic energy is contained in wave numbers $k \geq k_i$, one finds with the aid of Eq. (6.38)

$$\epsilon = (6C_K)^{-3/2} v^3 k_i.$$

Here v is the r.m.s. velocity such that $v^2 = \langle \vec{u}^2 \rangle$. This is close to Eq. (6.42). Whatever the exact value of the constant, there is ample evidence that, at high Reynolds number, the rate of dissipation ϵ is finite and independent of viscosity. This is, as stressed by Orszag [553], one of the main properties characterizing three-dimensional isotropic turbulence, namely a *finite* viscous dissipation of energy when the viscosity goes to zero. As already seen above, one of the physical mechanisms is the vortex-filaments stretching by turbulence, which dramatically increases the enstrophy, thus compensating the low molecular viscosity in the energy-dissipation rate.

6.4.4 Oboukhov's theory

In 1941, the $k^{-5/3}$ law was proposed by Oboukhov [542] with the aid of the following theory: one introduces a constant flux of kinetic energy ϵ proportional to the "available cascading kinetic energy" in the vicinity of k, divided by a characteristic local time of the cascade $\tau(k)$, assumed to depend only on k and $E(k)$, and thus equal to

$$\tau(k) = [k^3 E(k)]^{-1/2}. \tag{6.43}$$

It will be seen in Chapter 7 that $\tau(k)$ is a nonlinear time characteristic of the relaxation of triple-velocity correlations towards a quasi equilibrium state. The available kinetic energy in the vicinity of k can be obtained by integration of $E(k)$ on a logarithmic spectral vicinity of k, and is of the order of $kE(k)$. This again yields Kolmogorov's law equation (6.38). We recall that this law is valid in the so-called "inertial-range", when molecular-viscous and external-forcing effects can be neglected.

6.4.5 Kolmogorov 1941 in physical space

In his first 1941 paper, Kolmogorov [338] makes in fact predictions relating to S_p, the longitudinal velocity structure functions of order p. Let

$$\delta v_r = [\vec{u}(\vec{x},t) - \vec{u}(\vec{x}+\vec{r},t)].\frac{\vec{r}}{r}, \tag{6.44}$$

be the velocity difference between two points a distance $\vec{r}$ apart, projected upon $\vec{r}$, and

$$S_p(r,t) = \langle(\delta v_r)^p\rangle \tag{6.45}$$

be the longitudinal velocity structure function of order p. If one carries out the same dimensional analysis as the one done in order to obtain Eq. (6.38), and supposes that S_p is a function of ϵ and r, one finds

$$S_p(r,t) = C_p(\epsilon r)^{p/3}, \tag{6.46}$$

where C_p is a "universal" constant depending only on p. In fact this can be recovered more physically (see Landau and Lifchitz [371] and also Rose and Sulem [617]), by considering an eddy (the word "eddy" is not associated here with a particular structure of the flow) with typical rotational velocity δv_r and radius r. The inertial time (or "local turnover time") of this eddy is $r/\delta v_r$. If one assumes that this eddy loses an appreciable part of its energy during a turnover time, the energy dissipation rate ϵ is proportional to $\delta v_r^2/(r/\delta v_r)$. We obtain

$$\delta v_r \approx (\epsilon r)^{1/3}, \tag{6.47}$$

which yields Eq. (6.46) if one assumes that $S_p \sim (\delta v_r)^p$. Let us associate to r a wave number $k = r^{-1}$. At this point, δv_r has to be considered in some average sense. The kinetic energy of eddies in a spectral vicinity of k is proportional e.g. to $\int_{k/10}^{k} E(p)dp$, and therefore (as already stressed) to $kE(k)$, if $E(k)$ decreases following a power law of k. Thus δv_r^2 has to be associated to $kE(k)$, and Eq. (6.47) is equivalent to the $k^{-5/3}$ Kolmogorov spectrum.

Now, let us consider another second-order velocity structure function, defined in the following way:

$$F_2(r,t) = \langle [\vec{u}(\vec{x},t) - \vec{u}(\vec{x}+\vec{r},t)]^2 \rangle. \tag{6.48}$$

Within the same approximation, it should still be proportional to $\delta v_r^2 \sim (\epsilon r)^{2/3}$ in the inertial range (for $l_d < r < l$). This can be checked directly in the following manner, as shown by Orszag [553]: an exact expression of F_2 in terms of $E(k)$ is (Batchelor [47]):

$$\begin{aligned} F_2(r,t) &= 2 \int \hat{U}_{ii}(\vec{k},t)(1 - e^{i\vec{k}.\vec{r}})\, d\vec{k} \\ &= 4 \int_0^{+\infty} E(k,t) \left(1 - \frac{\sin kr}{kr}\right) dk, \end{aligned} \tag{6.49}$$

and the replacement of $E(k)$ in Eq. (6.49) by an infinite inertial range extending from 0 to ∞ yields

$$F_2(r,t) = 4.82 C_K (\epsilon r)^{2/3}. \tag{6.50}$$

However, such an inertial range will exist in physical space only if the extension of the Kolmogorov range in spectral space is wide enough. Otherwise, side effects coming from both the dissipative range and the energy-containing range will contaminate the law equation (6.50).

Notice also that, within this presentation of the Kolmogorov law in physical space, one may build with δv_r and r a local Reynolds number

$$R(r) = \frac{r \delta v_r}{\nu}, \tag{6.51}$$

which is proportional to $\epsilon^{1/3} r^{4/3}/\nu$ when using Eq. (6.47). Hence, for

$$r < l_d = \left(\frac{\nu^3}{\epsilon}\right)^{1/4}, \tag{6.52}$$

this local Reynolds number falls under 1, and viscous effects become preponderant. This allows us to understand why motions are damped by viscosity in the dissipation range, under the Kolmogorov dissipative scale.

We go back to Eq. (6.46) with $p = 3$, which yields $S_3 = C_3 \epsilon\, r$. In fact, it turns out that this is an exact result, with $C_3 = -4/5$. This law was proposed by Kolmogorov in his second 1941 paper for decaying turbulence. It can be demonstrated rigorously in the case of high Reynolds number stationary turbulence forced around k_i, using Eq. (6.37) (see Frisch [229]).

6.5 Richardson law

Let us now consider an ensemble of pairs of Lagrangian tracers which separate in isotropic turbulence. One assumes they are released initially from the

same distance r_0, the vector $\vec{r}_0$ being isotropically distributed. Let $\vec{r}(t)$ be the separation vector at time t. It is clear that $\langle \vec{r}(t) \rangle = 0$. We define $R(t)$ as the r.m.s. separation of the tracers ($R^2(t) = \langle \vec{r}^2(t) \rangle$), and assume that it lies in the inertial range (l_d, l). Now, we introduce a dispersion coefficient, given by

$$\sigma = \frac{1}{2}\frac{d}{dt}R^2(t) = R\frac{dR}{dt} = \langle \vec{r}.\frac{d\vec{r}}{dt} \rangle. \tag{6.53}$$

Furthermore, one will assume that dR/dt, the mean dispersion velocity, is given by Eq. (6.47) with $r = R(t)$. It yields

$$\sigma = C_R \epsilon^{1/3} R^{4/3}, \tag{6.54}$$

where C_R is a constant. This yields also

$$\frac{dR}{dt} = C_R \epsilon^{1/3} R^{1/3}. \tag{6.55}$$

Thus a $k^{-5/3}$ isotropic energy spectrum is equivalent to a $R^{4/3}$ turbulent dispersion coefficient. The latter law will be called here Richardson law, and C_R the Richardson's constant.

If one considers for instance isotropic turbulence forced in the large scales in order to get a stationary kinetic-energy spectrum, and if the pairs diffuse in the Kolmogorov range, then ϵ in Eq. (6.54) is time-independent, and one finds

$$R^2 = \left(\frac{2}{3}C_R\right)^3 \epsilon t^3, \tag{6.56}$$

(see also Oboukhov [543]). This diffusion law is sometimes called "anomalous" with respect to the "coherent diffusion", where $R^2 \propto t^2$, or the "incoherent diffusion" in a random walk (Brownian motion), where $R^2 \propto t$.

Let us look in more details what Richardson [596] did exactly in his original 1926 paper. He considers marked particles of concentration he calls $\nu(x,t)$ which diffuse along one space direction x in the atmosphere. He defines at a given time the p.d.f. $Q(l,t)$ that particles are separated of l, and $q(l,t)$ as the mean correlation coefficient between the concentrations $\nu(x,t)$ and $\nu(x+l,t)$, the average being taken in the direction x. He does propose that the r.m.s. separation of particles σ_m is proportional to $t^{3/2}$ (his Eq. (732-9). It is interesting to quote Richardson's conclusion (numbering of equations corresponds to the present book):

If the movement of concentration ν is described by Fick's equation,

$$\frac{\partial \nu}{\partial t} + \bar{u}\frac{\partial \nu}{\partial x} = K\frac{\partial^2 \nu}{\partial x^2} \tag{6.57}$$

where t is time, x is distance, $\bar{u}$ is mean velocity, and K is diffusivity. Then it is proved that

$$\frac{\partial q}{\partial t} = 2K \frac{\partial^2 q}{\partial l^2}. \tag{6.58}$$

If, however, the diffusion is "non-Fickian", as in the atmosphere, then the former of these equations cannot be generalised, but the latter can, taking the form

$$\frac{\partial q}{\partial t} = \frac{\partial}{\partial l}\left[F(l)\frac{\partial q}{\partial l}\right]. \tag{6.59}$$

A discussion of existing observations shows that a rough average value is $F(l) = 0.6 l^{4/3}$ cm.^{2}sec.$^{-1}$ for the atmosphere, when l lies between one metre and 10 km.

The only problem with Richardson's 1926 analysis is that the dispersion coefficient he introduces in his Eq. (733-10) is

$$K = \frac{\sigma_m^2}{2t}. \tag{6.60}$$

Then he can easily derive $K \propto \sigma_m^{4/3}$, assuming $\sigma_m \propto t^{3/2}$. But this applies only to Brownian motion. In 1948 he reintroduces the correct dispersion coefficient $(1/2)d\sigma_m^2/dt$ (Richardson and Stommel [597], Hunt [307]).

As stressed above, Richardson considered the spatial correlation of tracers and the p.d.f. that two tracers are separated by a distance l. We will discuss in Chapter 7 the relation between both quantities. All these $l^{4/3}$ laws for diffusion and dispersion coefficients proposed by Richardson in 1926 are certainly a first step before Kolmogorov's 1941 prediction concerning the second-order velocity structure function [338], as mentioned by Leith [401].

A very interesting presentation of Richardson's scientific papers can be found in the compilation carried out by Drazin et al. [598]. Yaglom [727], a close collaborator of Kolmogorov, mentions that Kolmogorov was not aware of Richardson's law, and aknowledged the anteriority of the latter when he could read Richardson's work.

There have been several attempts to determine C_R. Fung et al. [234] propose a value of 0.1 for the constant arising in Eq. (6.56), which yields $C_R \approx 0.7$. They use a kinematic simulation, where a Gaussian velocity field following Kolmogrov law on several decades is prescribed by some sort of Monte-Carlo method, and in which the pair-dispersion equation is solved numerically. The same type of calculation with a longer inertial range was done by Elliott and Majda [186]. On the other hand, stochastic models of the E.D.Q.N.M. type considered in Chapter 7 give $C_R \approx 2.14$. It is feasible that the E.D.Q.N.M.

prediction is too high, due to the fact that such a model ignores coherent vortices, which prevent the particles to disperse when they are trapped within a vortex.

Let us mention the reviews of Falkovich et al. [192] on dispersion in laminar and turbulent flows, and of Hunt [305] on various aspects of diffusion of heat and matter applied to industrial situations. Remark finally that, within the classical phenomenology of three-dimensional isotropic turbulence, Richardson law equation (6.54) will be shown to govern the evolution of the velocity and temperature integral scales in various situations (stationary or freely-decaying turbulence, different velocity and scalar integral scales). In the decaying case, Eq. (6.56) is of course no more valid.

6.6 Characteristic scales of turbulence

We have already introduced the integral scale and the dissipative scale, between which the inertial-range eddies see their kinetic energy organize along the Kolmogorov energy cascade. As shown above, the dissipative scale can be understood with the aid of Eq. (6.47). This is also the case for the integral scale, if one assumes that the second-order structure function at a separation of l is proportional to $v^2 = 3u'^2$. This leads to $l \sim u'^3/\epsilon$, as already seen above. The value of the dissipative scale l_d measured in the atmosphere is about $10^{-3}m$, while it is $10^{-4}m$ in a laboratory grid turbulence in the air. The reason being that, in the latter case, the Reynolds numbers are moderate, and the viscous dissipative rates of energy are stronger than their asymptotic value at high Reynolds numbers.

6.6.1 Degrees of freedom of turbulence

Preceeding relations allow one to write

$$\frac{l}{l_d} = \frac{k_d}{k_i} \sim \left(\frac{u'l}{\nu}\right)^{3/4}, \tag{6.61}$$

which shows that the extension of the inertial range in Fourier space goes to infinity with the three-fourth power of the large-scale turbulent Reynolds number $R_l = u'l/\nu$. This result is extremely important, for it gives an upper bound for the number of degrees of freedom which are needed to describe the motion (from dissipative scales under which the motion is quickly damped by viscosity, to large-scale energy-containing eddies) in each direction of the space. Indeed, let us work for instance within the discreet Fourier representation of a periodic flow in a box of size l. As stressed in Chapter 5, The velocity field may be expanded as an infinite series

$$\vec{u}(\vec{x},t) \propto \sum_{n_1,n_2,n_3} \underline{\hat{u}_B}(\vec{k},t)\ e^{i\vec{k}.\vec{x}}, \tag{6.62}$$

where the components k_i of $\vec{k}$ are

$$k_1 = \frac{2\pi}{l} n_1, k_2 = \frac{2\pi}{l} n_2, k_3 = \frac{2\pi}{l} n_3, \tag{6.63}$$

n_1, n_2 and n_3 being relative integers. It is clear that this expansion may be truncated for $|k_i| > Ak_d$, where A is a constant of the order of unity. This gives an upper bound for n_i of the order of $k_d l = k_d/k_i$. Hence, one expects that the total number of degrees of freedom of the flow is *a-priori* of the order of k_d/k_i in each direction of space. This yields a maximum total number for the degrees of freedom equal to $(k_d/k_i)^3$ in three-dimensional turbulence, and $(k_d/k_i)^2$ in two-dimensional turbulence.[6] This number has been interpreted by Constantin et al. [143] as an upper bound on the dimension of the Navier–Stokes attractor. It follows from Eq. (6.61) that the total number of degrees of freedom is of the order of $R_l^{9/4}$ in three dimensions. Notice that in two-dimensional turbulence, the phenomenology of the enstrophy cascade (see Chapter 8) leads to a total number of degrees of freedom equal to R_l.

Dimension of the attractor

Several experimental or numerical attempts, still based on the concept of dimension of the attractor, have been carried out in order to determine whether the *actual* number of degrees of freedom of the flow could not be smaller than the upper bounds presented above. These attempts have not, up to now, improved significantly these bounds (see Sreenivasan and Strykowski [666], Atten et al. [20], Lafon [363]). The question is still open to know whether, in flows where spatially organized large structures exist (such as atmospheric planetary scale motions, mixing layers, wakes, jets, boundary layers, thermal convective turbulence, rotating flows, etc), the dynamics of these large scales may be modelled, with a proper parameterization of the exchanges with smaller scales, by a dynamical system involving a relatively low number of degrees of freedom, and possibly displaying a chaotic behaviour and strange-attractor solutions. Such an approach has been proposed by Lumley [456] and, as already mentioned, applied to the boundary layer by Aubry et al. [21], assuming longitudinal vortices at the wall. This could be a way of bridging the *chaos* and statistical fully-developed points of view of turbulence, the latter being used to understand and model the energy exchanges between the small-scale turbulence and the large organized scales analysed by the former. But a serious

[6] In two-dimensional turbulence, it will be shown in Chapter 9 that the equivalent Kolmogorov wave number k_d characterizes the enstrophy dissipation.

obstacle to such an analysis lies in the fact that, in developed turbulence, there is no spectral separation of scales between the coherent vortices and the rest of turbulence. We do not think that a terminology such as "incoherent" turbulence helps to describe the latter motions, because of the perpetual reorganisation of small scales by large scales.

To end this discussion, the Kolmogorov viewpoint of energy cascade from large to small scales has often been opposed to the experimental evidence that large scales could pair and amalgamate, leading to the formation of larger structures. In fact, as already mentioned in this book, there does not seem to be any contradiction at all between both mechanisms, which certainly occur simultaneously: the large scales of the flows may be quasi two-dimensional (in the free-shear layers for instance) and obey the two-dimensional vorticity conservation constraint which implies strong inverse transfers of energy. On the other hand, they will simultaneously degenerate quite explosively, through successive instabilities due to the three-dimensional perturbations they are submitted to, towards small-scale Kolmogorov fully-developed three-dimensional turbulence which will dissipate the kinetic energy of the large scales or of the mean flow.

6.6.2 Taylor microscale

A third characteristic length scale is often used in turbulence, mainly by experimentalists. It is the Taylor microscale, characteristic of the mean spatial extension of the velocity gradients, and defined by (see Tennekes and Lumley [684], for details)

$$\lambda^2 = \frac{u'^2}{\langle (\partial u_1/\partial x_1)^2 \rangle}, \tag{6.64}$$

where u_1 is the velocity component in any direction x_1. We know already that $\epsilon = \nu \langle (\vec{\nabla} \times \vec{u})^2 \rangle$. One can also show in isotropic turbulence that $\langle (\vec{\nabla} \times \vec{u})^2 \rangle = 15 \langle (\partial u_1/\partial x_1)^2 \rangle$, so that Eqs. (6.64) and (6.42) yield

$$\lambda^2 = 15 \frac{u'^2 \nu}{\epsilon} = \frac{15 \nu l}{A u'}. \tag{6.65}$$

We define $R_\lambda = u' \lambda / \nu$, and Eq. (6.65) gives

$$R_\lambda = \sqrt{\frac{15}{A}} \sqrt{R_l} \sim \frac{l}{\lambda}. \tag{6.66}$$

In a typical grid turbulence laboratory experiment, the integral scale l is of the order of 4 cm (the grid mesh), the Kolmogorov scale is 0.1 mm, and the Taylor microscale is 2 mm. The above law is very well verified experimentally, even at moderate Reynolds numbers. The proportionality constant in Eq. (6.66)

is such that $R_\lambda \approx 4R_l^{1/2}$ (which shows that the constant A is very close to one), and an experimental value of R_l equal to 300 corresponds to $R_\lambda \approx 70$ (see Hinze [285]). Let us mention also from Eqs. (6.61) and (6.66) that the total number of degrees of freedom of turbulence is $\sim R_\lambda^{9/2}$. This is a lot if one remarks as Jimenez [318] that $R_\lambda = 3000$ in a plane wing and 10.000 in the atmospheric boundary layer.

6.6.3 Self-similar spectra

The integral and dissipative scales allow one to propose self-similar expressions for the energy spectrum equivalent to Karman–Howarth [326] solutions for the spatial velocity correlations in the physical space, i.e.

$$E(k,t) = ELF(kL), \tag{6.67}$$

where E and L are respectively a typical kinetic energy and a typical scale, and $F(x)$ is a dimensionless function of the dimensionless argument x. If E and L are chosen as v^2 (twice the kinetic energy) and l, one obtains a self-similar solution

$$E(k,t) = v^2(t)l(t)F[kl(t)] \tag{6.68}$$

which can be shown to be valid in describing the energy-containing and inertial ranges. In particular, the assumption that F is a power law of kl and $E(k,t)$ is independent of v leads to the Kolmogorov law. If E and L are chosen to characterize the dissipation range, the self-similar solution is

$$E(k,t) = \frac{\nu^2}{l_d}G(kl_d) = \epsilon^{2/3}l_d^{5/3}G(kl_d), \tag{6.69}$$

where G is another dimensionless function. Eq. (6.69) effectively predicts the behaviour of the energy spectrum in the inertial and dissipative ranges. The assumption that G is a power law of kl_d and $E(k,t)$ does not depend on ν yields again the Kolmogorov law. As remarked in particular in Lesieur et al. [431], experiments (see the review of Coantic and Lasserre [129]) show that the Kolmogorov compensated spectrum

$$\epsilon^{-2/3}k^{5/3}E(k,t) = (kl_d)^{5/3}G(kl_d) \tag{6.70}$$

has a "Mammoth" shape, and renormalizes well the data at high k. In the mammoth, the back (flat) is the $k^{-5/3}$ plateau, the neck is a pre-dissipative "bump", and the trump the dissipative range. It will be shown in Chapter 7 that the E.D.Q.N.M. approximation gives rise to the same shape.

6.7 Skewness factor and enstrophy divergence

6.7.1 Skewness factor

Let $X(\omega)$ be a random variable of zero mean. Its skewness factor is defined as $\langle X^3\rangle/\langle X^2\rangle^{3/2}$. The skewness factor of isotropic turbulence will be defined in the present monograph as the skewness factor of $-\partial u_1/\partial x_1$, u_1 being any component of the velocity:

$$s = -\left\langle \left(\frac{\partial u_1}{\partial x_1}\right)^3 \right\rangle \Big/ \left\langle \left(\frac{\partial u_1}{\partial x_1}\right)^2 \right\rangle^{3/2}. \tag{6.71}$$

This factor would is zero if the random function $\vec{u}$ is Gaussian. Experimental values of s found in grid turbulence (Batchelor and Townsend [43]) are of the order of 0.4, and direct numerical simulations at moderate Reynolds numbers done by Orszag and Patterson [552] give a value of 0.5. This shows that turbulence cannot certainly be considered as Gaussian. Actually the skewness characterizes the rate at which the enstrophy increases by vortex stretching: indeed, one obtains from Eq. (6.15), after multiplication by ω_i, averaging, and making use of the incompressibility condition:

$$\frac{d}{dt}D(t) = \left\langle \omega_i\omega_j \frac{\partial u_i}{\partial x_j} \right\rangle + \nu\langle \vec{\omega}.\nabla^2\vec{\omega}\rangle,$$

where the enstrophy $D(t)$ is given by Eqs. (5.86) and (5.90). It writes

$$\frac{d}{dt}D(t) = \langle \omega_i\omega_j \frac{\partial u_i}{\partial x_j}\rangle - 2\nu P(t), \tag{6.72}$$

where $P(t)$ is the "palinstrophy",[7] such that

$$P(t) = \frac{1}{2}\langle(\vec{\nabla}\times\vec{\omega})^2\rangle = -\frac{1}{2}\langle\vec{\omega}.\nabla^2\vec{\omega}\rangle = \int_0^{+\infty} k^4 E(k,t)dk. \tag{6.73}$$

• Exercise: show Eq. (6.73)

We notice, due to Eq. (5.88), that

$$\langle(\vec{\nabla}\times\vec{\omega})^2\rangle = \langle\vec{\omega}.\vec{\nabla}\times(\vec{\nabla}\times\vec{\omega})\rangle = -\langle\vec{\omega}.\nabla^2\vec{\omega}\rangle$$

$$= -\langle\vec{u}.\nabla^2(\vec{\nabla}\times\vec{\omega})\rangle = \langle\vec{u}.(\nabla^2)^2\vec{u}\rangle.$$

Then, in the same way as in Eq. (5.90), we have

[7] See footnote 3 in Chapter 8.

$$P(t) = \frac{1}{2}\int d\vec{k}d\vec{k}'\ e^{i(\vec{k}+\vec{k}').\vec{x}}k^4\langle\hat{u}_i(\vec{k}',t)u_i(\vec{k},t)\rangle$$

$$= \frac{1}{2}\int k^4\hat{U}_{ii}(\vec{k},t)d\vec{k} = \int_0^{+\infty} k^4E(k,t)dk,$$

which demonstrates the result.

Text
It has been shown by Batchelor and Townsend [42] that, for isotropic three-dimensional turbulence, the skewness factor s is equal to

$$s(t) = \left(\frac{135}{98}\right)^{1/2}\left\langle\omega_i\omega_j\frac{\partial u_i}{\partial x_j}\right\rangle\Big/D(t)^{3/2}. \tag{6.74}$$

Therefore Eq. (6.72) is written

$$\frac{d}{dt}D(t) = \left(\frac{98}{135}\right)^{1/2}s(t)D^{3/2} - 2\nu P(t). \tag{6.75}$$

As noticed by Orszag [550], who wrote this equation, a positive skewness factor is needed in order to increase the enstrophy by vortex-filaments stretching. We notice also that the first term of the r.h.s. of Eq. (6.75) is, from Eq. (6.21), equal to $\int_0^{+\infty} k^2T(k,t)dk$: therefore, the skewness factor is also equal to (Orszag [550])

$$s(t) = \left(\frac{135}{98}\right)^{1/2}D(t)^{-3/2}\int_0^{+\infty} k^2T(k,t)dk. \tag{6.76}$$

Hence it will certainly be positive, since the k^2 factor will enhance the high wave number positive contribution of $T(k,t)$. We recall that $T(k,t)$ satisfies Eq. (6.26) in the Navier–Stokes case, and has, at least at moderate Reynolds numbers, the shape shown in Figure 6.2. At high times, and if turbulence is unforced and decays self-similarly, it has been noticed by Orszag [553] that the term dD/dt in Eq. (6.75) is now much smaller than the two terms of the r.h.s., so that we have approximately:

$$s(t) = 2.35\frac{\nu P(t)}{D(t)^{3/2}}. \tag{6.77}$$

Then the use of Eq. (6.69) to calculate $P(t)$ and $D(t)$, which are dominated by viscous-range contributions, yields the constancy of $s(t)$ with time.

• Exercise: show this result.

$$P(t) = \frac{\nu^2}{l_d} \int_0^{+\infty} k^4 V(kl_d) dk = \frac{\nu^2}{l_d^6} \int_0^{+\infty} \lambda^4 V(\lambda) d\lambda$$

$$D(t) = \frac{\nu^2}{l_d} \int_0^{+\infty} k^2 V(kl_d) dk = \frac{\nu^2}{l_d^4} \int_0^{+\infty} \lambda^2 V(\lambda) d\lambda$$

$$s(t) \sim \frac{\int_0^{+\infty} \lambda^4 V(\lambda) d\lambda}{(\int_0^{+\infty} \lambda^2 V(\lambda) d\lambda)^{3/2}} = \text{cte},$$

provided the integrals converge.

Text
This property of constant skewness seems to be characteristic of decaying three-dimensional isotropic turbulence, as well as the finiteness of the kinetic energy dissipation.

Now we are going to consider the question of the enstrophy and skewness factor time evolution, for an unforced initial-value problem, where we assume an initial energy spectrum sharply peaked at $k_i(0)$, with a finite enstrophy $D(0)$ (hereafter called *type S* initial conditions). The problem will be looked at both in the case of Euler and Navier–Stokes equations.

6.7.2 Does enstrophy blow up at a finite time in a perfect fluid?

We will display in Chapter 7 stochastic models of the Euler equations predicting the blow up of the enstrophy at a finite time. As will be seen below, this is an extremely controversial question which we are going to examine here on the basis of the phenomenology. If one accepts the idea that a Kolmogorov spectrum extending to infinity[8] will eventually form, yielding an infinite enstrophy, the questions which arise are: "will the enstrophy-divergence time be finite or not"? Or, "will it take a finite time to build up a Kolmogorov spectrum extending to infinity"? To answer these questions, several phenomenological models will be considered. We will use the Euler counterpart of Eq. (6.75)

$$\frac{d}{dt} D(t) = \left(\frac{98}{135}\right)^{1/2} s(t) D^{3/2}. \tag{6.78}$$

Constant skewness model

Let us suppose a skewness factor $s \equiv s_0$ constant with time. The enstrophy will thus be equal to

$$D(t) = \frac{D(0)}{[1 - (t/t_c)]^2} \tag{6.79}$$

[8] Since $k_D \to \infty$ when $\nu \to 0$ if ϵ is finite.

with

$$t_c = \frac{1}{0.425 s_0} D(0)^{-1/2}. \tag{6.80}$$

Therefore the enstrophy blows up at the critical time t_c (equal to $5.9 D(0)^{-1/2}$ for $s_0 = 0.4$).

But the skewness factor certainly does not fulfill this assumption: direct-numerical simulations of Euler equations carried out with Gaussian[9] *type S* initial conditions[10] show that the skewness factor grows initially from zero to finite positive values[11] (Wray [723]). In fact, one can show the following results, which are valid for Euler equations as long as the enstrophy remains finite:

Positiveness of the skewness

• Theorem 1: for solutions[12] of Euler equations which are limits of Navier–Stokes solutions when $\nu \to 0$, the skewness factor is positive.

The derivation proceeds as follows: due to Eq. (6.14), the kinetic energy of the Euler solutions we consider will be conserved with time as long as the enstrophy remains finite. Therefore, the transfer $T(k,t)$ will satisfy Eq. (6.26). The same argument as used above in the case of a viscous fluid shows then that $\int_0^{+\infty} k^2 T(k,t) dk$ will be positive if the transfer has the form displayed in Figure 6.2, which all the numerical simulations show: the transfer is negative in the vivinity of k_i and positive in the vicinity of k_E. Hence the skewness factor will be, from Eq. (6.76), positive and the enstrophy will grow, due to Eq. (6.78).

For instance, if the initial velocity is Gaussian, the skewness factor will grow from zero, and either keep on growing, or reach a maximum and decay. Then, another theorem can be shown:

[9] See details on Gaussian functions in Chapter 7.

[10] These simulations are valid as soon as the characteristic maximum wave number $k_E(t)$ of the kinetic-energy spectrum does not exceed the computation cutoff wave number k_m.

[11] These calculations, using pseudo-spectral methods, were carried out with the same initial velocity field, and a maximum cutoff wave number k_m respectively equal to 32, 64 and 128. The skewness factor evolution consisted in two stages: a growth up to a maximum corresponding to the time when the ultra-violet kinetic-energy cascade starts being affected by the cutoff k_m, then a decay afterwards, due to the build up of Gaussian absolute-equilibrium ensemble solutions whith a kinetic-energy spectrum proportional to k^2 (see Chapter 10). The calculation seems to indicate that the maximum of the skewness grows with k_m.

[12] We work in Fourier space, and these solutions will be characterized by their kinetic energy spectrum.

Enstrophy blow up theorems

• Theorem 2: if the skewness $s(t)$ has a strictly positive lower bound s_0, the enstrophy will blow up at a finite time

$$t_* < \frac{1}{0.425 s_0} D(0)^{-1/2}. \tag{6.81}$$

The derivation of this result is staighforward: one considers Eq. (6.75), which writes

$$\frac{d}{dt} D(t)^{-1/2} = -0.425 s(t). \tag{6.82}$$

In the same way, the function $D_{s_0}(t)$, solution of

$$\frac{d}{dt} D_{s_0}(t) = \left(\frac{98}{135}\right)^{1/2} s_0 D_{s_0}^{3/2},$$

with $D_{s_0}(0) = D(0)$ satisfies

$$\frac{d}{dt} D_{s_0}(t)^{-1/2} = -0.425 s_0. \tag{6.83}$$

Since $s \geq s_0$, Eqs. (6.82) and (6.83) yield

$$\frac{d}{dt} D_{s_0}(t)^{-1/2} \geq \frac{d}{dt} D(t)^{-1/2},$$

and the function $D_{s_0}(t)^{-1/2} - D(t)^{-1/2}$, initially zero, is increasing with time and will remain positive. Hence $D(t) \geq D_{s_0}(t)$. Since $D_{s_0}(t)$ blows up at t_c given by Eq. (6.80), this demonstrates the theorem.

In the above example where the velocity is initially Gaussian, for instance, a continuous growth of the skewness (which might possibly be extrapolated from Wray's [723] calculations) implies the enstrophy blow up. Even a subsequent decay of the skewness from a maximum to a strictly positive value leads also to the enstrophy divergence at a finite time.[13]

• Theorem 3: if the skewness $s(t)$ evolves like $t^{-\alpha_S}$, with $\alpha_S < 1$, the enstrophy will blow up at a finite time.

This result may easily be shown by solving Eq. (6.82) under the form

$$D(t) = \frac{D(0)}{[1 - 0.425 D(0)^{1/2} \int_0^t s(\tau) d\tau]^2}. \tag{6.84}$$

It yields a blow up at a finite time. The latter is proportional to

$$[(1 - \alpha_S) D(0)^{-1/2}]^{1/(1-\alpha_S)}.$$

[13] Indeed, just take as initial time the time where the skewness is maximum.

Oboukhov's enstrophy blow up model

To finish with these inviscid enstrophy blow up models, we recall a calculation done by Brissaud et al. [83] showing an exact result of enstrophy blow up in the case of a modified time-dependent Oboukhov theory proposed by Panchev [559]: this model is written in the inviscid case

$$\frac{\partial}{\partial t}\int_0^k E(p,t)dp = -\frac{1}{\tau(k)}\int_k^\infty E(p,t)dp \tag{6.85}$$

with $\tau(k) = [\int_0^k p^2 E(p,t)dp]^{-1/2}$. The time $\tau(k)$, which will also be used in the next chapter, characterizes the shearing action of the "large scales" $< k$ upon the "small scales" $> k$. The l.h.s. of Eq. (6.85) is the loss of kinetic energy of the large scales, equal to the "available" cascading kinetic energy $\int_k^\infty E(p)dp$ divided by the time $\tau(k)$. Starting with an initially rapidly decreasing spectrum with a finite initial enstrophy $D(0)$, and by differentiation of Eq. (6.85) with respect to k, multiplication by k^2 and integration over k, one obtains

$$\frac{dD(t)}{dt} = \int_0^{+\infty} k^2 E(k)\tau(k)dk \left[\int_0^k p^2 E(p)dp - \frac{k^2}{2}\int_k^\infty E(p)dp\right].$$

By successive majorations and minorations of the integrals, described in Brissaud et al. [83] , one obtains the following inequality

$$\frac{dD(t)}{dt} > \frac{1}{4}D(t)^{3/2}$$

showing that the enstrophy blows up before the time $8D(0)^{-1/2}$.

Discussion

Up to now, and since the pioneering work of Leray [409] on Navier–Stokes equations,[14] only regularity results for finite times of the order of $D(0)^{-1/2}$ have been rigorously demonstrated for Navier–Stokes or Euler equations (see for a review Temam [682] and Lions [450, 451]). Direct numerical simulations of Euler equations, starting with the Taylor–Green [681] vortex

$$u(\vec{x}) = \cos x_1 \sin x_2 \sin x_3$$

$$v(\vec{x}) = -\sin x_1 \cos x_2 \sin x_3$$

$$w(\vec{x}) = 0 \tag{6.86}$$

[14] Where solutions are meant in a "weak sense".

have been performed, using both the original perturbation expansion of Taylor and Green in powers of time (Orszag [553], Morf et al. [522]), and a truncated spectral method (Brachet et al. [74]). But the results concerning the appearance of a possible singularity at a finite time are difficult to interpret: indeed conclusions of Morf et al. [522] are at variance with those of Brachet et al. [74], depending upon the numerical method chosen. The more recent opinions expressed by the majority of the authors of these references are that there is no singularity. This statement concerns nevertheless only the inviscid Taylor–Green vortex. About this singularity-related issue, we also mention the works of Kerr [327], Boratav and Pelz [71], and Pelz [569] .

Let us stress finally that the existence or not of a singularity at a finite time within unforced Euler equations may depend also upon the existence and the nature of a perturbation of small amplitude superposed on the initial velocity field. Let us consider for instance at some initial time t_0 a two-dimensional temporal mixing layer, in an infinite domain, consisting in a row of rolling up Kelvin–Helmholtz vortices. If no perturbation is brought, the further evolution of the flow will certainly not lead to any enstrophy blow up, since the vorticity cannot in two dimensions exceed its initial value. On the contrary, a three-dimensional perturbation responsible for the stretching of hairpin vortex filaments between the Kelvin–Helmholtz billows, or vortex rings in a jet, might lead during the pairing (in the Euler case) to a vorticity blow up in certain regions of the flow. Finite-time singularity in free shear flows might be associated to the experimental observations of "mixing transition" done by Dimotakis [168,169], where one observes above a certain Reynolds number an abrupt breakup of turbulent structures into tiny three-dimensional scales close to isotropy..

6.7.3 The viscous case

Eq. (6.78) is valid for a viscous flow, when the viscosity is small enough, during the early period of the evolution when the kinetic-energy spectrum $E(k,t)$ decreases faster than k^{-5} for $k \to \infty$.[15] Meanwhile the kinetic energy, which is dissipated at the rate $2\nu D(t)$, is conserved with time in the limit of zero viscosity as long as the inviscid enstrophy remains finite, that is, for $t < t_c$ if one accepts the above ideas that the inviscid enstrophy blows up at a finite time.

For $t > t_c$, the dissipative term in Eq. (6.75) cannot be neglected anymore. One now uses the fact that the kinetic energy is, due to viscous dissipation, going to decay as

$$\frac{1}{2}\langle \vec{u}^2 \rangle \propto t^{-\alpha_E} \tag{6.87}$$

[15] This assumption allows the palinstrophy $P(t)$ to remain finite, so that the viscous term $\nu P(t)$ in Eq. (6.75) goes to zero with ν.

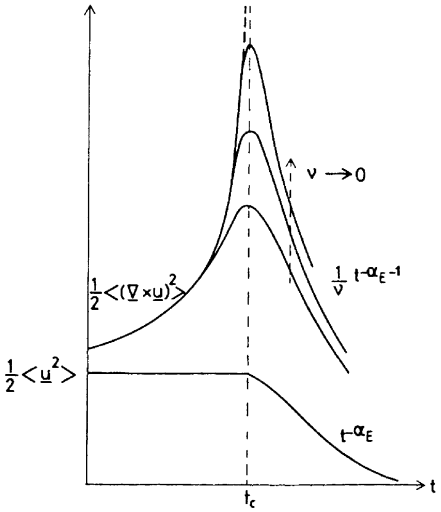

Figure 6.5. Schematic evolution with time of kinetic energy and enstrophy in a freely-decaying three-dimensional isotropic turbulence when viscosity goes to zero.

α_E being an exponent of the order of $1 \sim 1.5$, as will be seen in Chapter 7. Therefore, the enstrophy $\epsilon/2\nu$ will decay as

$$D(t) \propto \frac{t^{-\alpha_E-1}}{\nu} \tag{6.88}$$

as indicated in Figure 6.5. Due to the finiteness of ϵ in the limit of zero viscosity, the enstrophy will thus be infinite in this limit for $t > t_c$. Statistical models of Navier–Stokes equations displaying the same catastrophic behaviour will be introduced in Chapter 7. We recall finally that, up to now, there is no rigorous proof that enstrophy blows up at a finite time within Euler equations, or Navier–Stokes in the limit of zero viscosity.

6.8 Coherent vortices in 3D isotropic turbulence

The first DNS of 3D isotropic turbulence were done by Orszag and Patterson [552] by pseudo-spectral methods, at an equivalent resolution of 32^3 collocation points. In the seventies, people working in 3D isotropic turbulence were mainly interested by statistical quantities. Nobody in this community thought seriously of the possibility for vorticity to concentrate in coherent vortices, such as those encountered in free-shear flows. In 1981, Siggia [647] was the first to point out the existence of thin tubes of high vorticity, whose

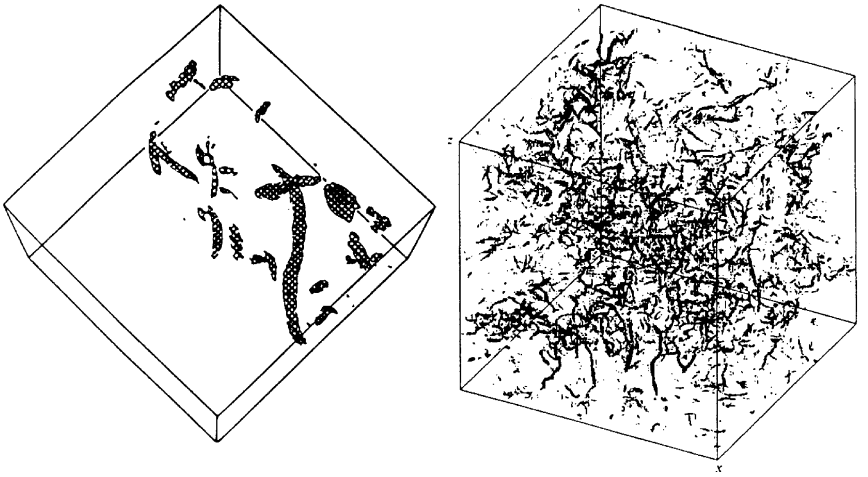

Figure 6.6. DNS of forced isotropic 3D turbulence. Evidence for coherent vortices displayed by vorticity-modulus isosurfaces; (a) Siggia [647], (b) Vincent and Meneguzzi [704] (courtesy *J. Fluid Mech.* and Kluwer).

existence was confirmed by numerous authors at higher resolution (see e.g. She et al. [643], Vincent and Ménéguzzi [704, 705], and Jimenez and Wray [317]). These tubes have a diameter of a few Kolmogorov dissipative scales, and a length of the order of the integral scale.[16] We present in Figure 6.6 vorticity isosurfaces obtained respectively in the simulations of Siggia [647] and Vincent and Meneguzzi [704]. Brachet [77] showed for turbulence with symmetries developing from a Taylor–Green vortex (see above) that these vortex tubes did correspond to pressure lows, with pressure probability distribution functions (referred to as p.d.f.) exponential in the lows and Gaussian in the highs. The same was found independently by Métais (see Métais and Lesieur [496]) for decaying isotropic turbulence. We present on Figure 6.7 a close-up visualization of the low-pressure tubes in this DNS, using pseudo-spectral methods at a resolution of 128^3 collocation points.

All DNS found also that the velocity gradients and vorticity components p.d.f.'s have wings of exponential type, that is, proportional to $e^{-|X|}$ instead of the Gaussian distribution e^{-X^2}. Remark that this was known experimentally for a long time as far as the velocity gradients are concerned, but explained more by a small-scale intermittency behaviour than by the formation of coherent vortices. Figure 6.8 shows such p.d.f. for one vorticity component and

[16] This of course does not mean that vortex filaments are not connected: Siggia's "bananas" (as he calls them) correspond to portions of closed vortex tubes where the vorticity is stronger.

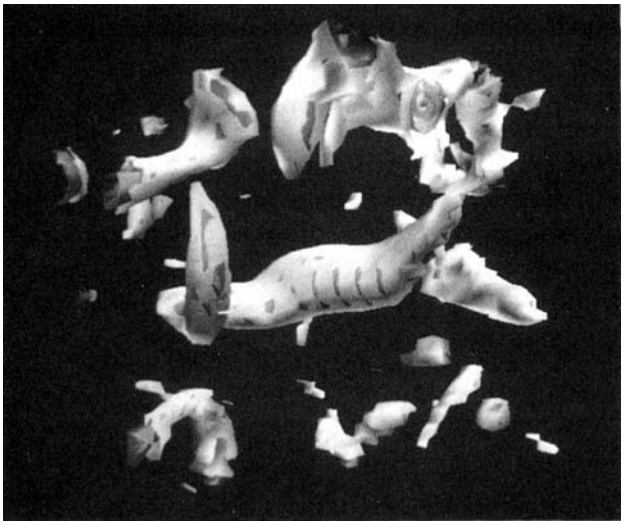

Figure 6.7. Low-pressure tubes in DNS of decaying isotropic turbulence (courtesy O. Métais, Institut de Mécanique de Grenoble).

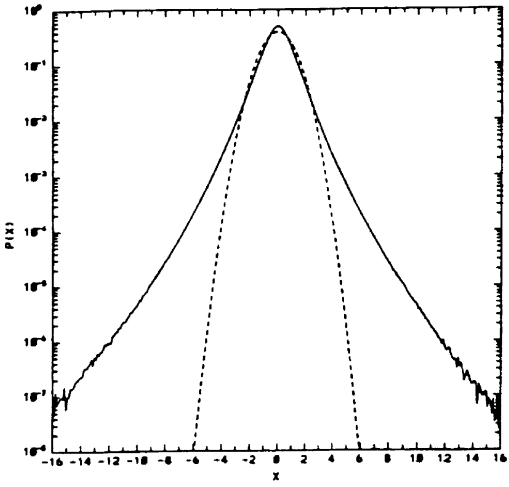

Figure 6.8. P.d.f. of one vorticity component in the DNS of Vincent and Meneguzzi [704]. The dashed line indicates a Gaussian distribution (courtesy Kluwer).

Figure 6.9a for the pressure. The fact that low pressure correlate with high vorticity seem to indicate that a non-Gaussian behaviour of the high vorti-

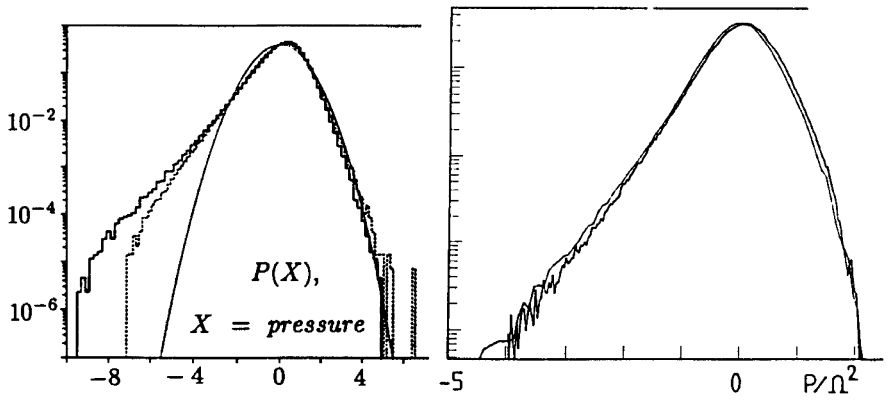

Figure 6.9. Pressure p.d.f.'s obtained in the DNS of Métais (a) and the experiment of Fauve et al. (b) [197]. In (a), the dots correspond to a Gaussian distribution, and the dashed line to a kinematic pressure computed from a fictitious Gaussian velocity (courtesy *J. Fluid Mech.* and *J. Physique*).

cities will imply the same in the low pressures,[17] as indicated by Figure 6.9a. Laboratory experiments concerning turbulence between two counter-rotating disks (Fauve et al. [197], Cadot et al. [91]) confirm that low pressures are associated with the passage of vortices, and the existence of skewed pressure p.d.f.'s (see Figure 6.9b).[18] In Vincent and Ménéguzzi's [706] calculations, it seems that these coherent vortices result from the roll up of vortex sheets formed during the initial stage of the evolution, after a scenario proposed by Moffatt [512]. However, recent LES discussed in Lesieur et al. [431] have looked at the generation of isotropic-turbulence vortices with animations of pressure, vorticity and Q isosurfaces. In these simulations, big structures of low pressure first form, followed by the condensation of vorticity into thin tubes, without vortex-sheet formation.

[17] However, one can check that a pressure field derived kinematically (with the aid of a Poisson equation) from a fictitious Gaussian velocity field, shows the same assymmetry, although less marked (Métais, private communication).

[18] Analogous results for the pressure p.d.f. have been obtained in the mixing-layer DNS of Comte et al. [138], and also in round-jet experiments (Gagne, private communication).

6.9 Pressure spectrum

6.9.1 Noise in turbulence

The pressure spectrum in turbulence is a very important quantity, since it allows to characterize the noise generated at a given point in terms of acoustic intensity. Indeed, Mankbadi [470] recalls thata relevant quantity for that is the sound pressure level (SPL, expressed in decibels) given by

$$\mathrm{SPL} = 20 \log_{10} \sqrt{\langle {p_a}'^2 \rangle} + 94. \tag{6.89}$$

Here, p'_a is the acoustic pressure. In the case of the sound emitted by a turbojet engine, one can show that away from the jet, $p'_a \approx p'$ (see Bogey and Bailly [70]), and the pressure spectrum allows to determine the noise thanks to the relation

$$\frac{1}{2}\langle p'^2 \rangle = \int_0^{+\infty} E_{pp}(k) dk. \tag{6.90}$$

Within the jet, however, the acoustic pressure is much smaller than the total pressure. But the latter is a signature of coherent vortices which are important for noise production.

6.9.2 Ultraviolet pressure

We recall here a law proposed by Oboukhov [544] and Batchelor [45] for the the pressure spectrum in isotropic turbulence at high wave numbers:

$$E_{pp}(k) = C_P \epsilon^{4/3} k^{-7/3}, \tag{6.91}$$

where C_P is a non-dimensional constant. This law can be obtained from Poisson's equation satisfied by the pressure (divided by density)

$$\nabla^2 p = -\frac{\partial^2}{\partial x_i \partial x_j} u_i u_j, \tag{6.92}$$

which writes in Fourier space as

$$\hat{p}(\vec{k}, t) = -\frac{k_i k_j}{k^2} \int \hat{u}_i(\vec{p}, t) \hat{u}_j(\vec{q}, t) \delta(\vec{k} - \vec{p} - \vec{q}) d\vec{p} d\vec{q}. \tag{6.93}$$

One can form now the second-order moment

$$\langle \hat{p}(\vec{k}) \hat{p}(\vec{k'}) \rangle = \frac{k_i k_j k'_{i'} k'_{j'}}{k^2 {k'}^2}$$

$$\int \langle \hat{u}_i(\vec{p})\hat{u}_j(\vec{q})\hat{u}_{i'}(\vec{p}')\hat{u}_{j'}(\vec{q}')\rangle \delta(\vec{k}-\vec{p}-\vec{q})\delta(\vec{k}'-\vec{p}'-\vec{q}')d\vec{p}d\vec{q}d\vec{p}'d\vec{q}',$$

which involves fourth-order velocity correlations. If we express the latter in terms of second-order velocity correlations using the quasi normal approximation, where the fourth-order cumulants are discarded (see next chapter for details), it is obtained

$$\langle \hat{u}_i(\vec{p})\hat{u}_j(\vec{q})\hat{u}_{i'}(\vec{p}')\hat{u}_{j'}(\vec{q}')\rangle = \langle \hat{u}_i(\vec{p})\hat{u}_j(\vec{q})\rangle\langle \hat{u}_{i'}(\vec{p}')\hat{u}_{j'}(\vec{q}')\rangle$$

$$+\langle \hat{u}_i(\vec{p})\hat{u}_{i'}(\vec{p}')\rangle\langle \hat{u}_j(\vec{q})\hat{u}_{j'}(\vec{q}')\rangle + \langle \hat{u}_i(\vec{p})\hat{u}_{j'}(\vec{q}')\rangle\langle \hat{u}_j(\vec{q})\hat{u}_{i'}(\vec{p}')\rangle.$$

As recalled in Lesieur et al. [427], an integration over $\vec{k}'$ may be carried out. Making use of isotropy and "localizing" the integrals yields

$$E_{pp}(k) \sim k[E(k)]^2 \tag{6.94}$$

From which one gets Eq. (6.91) assuming a $k^{-5/3}$ kinetic-energy spectrum.[19] The constant C_P was calculated by Monin and Yaglom [515]. They found

$$C_P \approx 1.33 C_K^2. \tag{6.95}$$

One might argue about the validity of the quasi normal approximation. However, Larchevêque [380] has shown that it is equivalent to the eddy-damped quasi normal Markovian approximations as far as pressure is concerned. Such a spectrum is difficult to measure experimentally, and presently, the DNS or LES have not a resolution high enough to conclude about this law. Therefore, the nature of the ultraviolet pressure spectrum is still an open question in three-dimensional isotropic incompressible turbulence. More on the pressure infrared behaviour will be said later in Chapter 7.

6.10 Phenomenology of passive scalar diffusion

We have already seen that under certain approximations, the temperature $T(\vec{x},t)$ satisfies a passive-scalar type diffusion equation

$$\frac{\partial T}{\partial t} + \vec{u}.\vec{\nabla}T = \kappa \nabla^2 T \tag{6.96}$$

and is simply transported by the fluid particle (and diffused by molecular effects) without any action on the flow dynamics. More generally, one can consider any passive quantity which diffuses according to Eq. (6.96), such

[19] The same result can be found by dimensional arguments, assuming that the pressure spectrum is a function of ϵ and k only.

as a dye which marks the flow. The Schmidt number of the passive scalar is ν/κ, where κ is the molecular diffusivity of the scalar. It corresponds to the Prandtl number when the passive scalar is the temperature. Since we will consider only one diffusing quantity here, we will associate it with the temperature, and speak of the Prandtl number of the passive scalar.

When a passive scalar diffuses in homogeneous turbulence, one is interested mainly in two problems: the first concerns the small-scale statistics of the scalar, and will be studied by assuming that the scalar fluctuations are also homogeneous. This is, for instance, the case of a grid turbulence, where a slight statistically homogeneous heating in the fluid close to the grid will produce a random temperature fluctuation field whose intensity will decay downstream of the grid, due to the molecular-conductive effects that will tend to homogenize the temperature within the fluid. The second problem concerns the dispersion of a localized scalar cloud (or a heated spot) by turbulence: this is an inhomogeneous problem as far as the temperature is concerned, which requires to look both at the absolute diffusion of the cloud gravity centre, and the particle pair relative dispersion: the latter question gives information on the spreading rate of the cloud, and can be studied within a homogeneous formalism. It will be looked at in Chapter 7. The present section will deal essentially with three-dimensional isotropic turbulence. Here, we will mainly recall the phenomenology of the passive scalar turbulent diffusion problem, as described for instance by Tennekes and Lumley [684] and Leslie [432].

Assuming that the temperature $T(\vec{x},t)$ is statistically homogeneous and isotropic, of zero mean, we first introduce the conductive wave number, in a similar way we have earlier introduced the Kolmogorov dissipative wave number: let $r_c = k_c^{-1}$ be the scale at which the molecular diffusive effects in Eq. (6.96) are of the same order as the convective term $\vec{u}.\vec{\nabla}T$, that is such that the local Peclet number

$$P_e(r_c) = \frac{r_c(\delta v_{r_c})}{\kappa} \tag{6.97}$$

should be about one. Then two cases have to be considered: if r_c^{-1} lies in the $k^{-5/3}$ Kolmogorov energy inertial range, we have from Eq. (6.47):

$$\delta v_{r_c} \sim (\epsilon r_c)^{1/3} \tag{6.98}$$

which yields

$$k_c \sim \left(\frac{\epsilon}{\kappa^3}\right)^{1/4} \sim \left(\frac{\nu}{\kappa}\right)^{3/4} k_d. \tag{6.99}$$

But Eq. (6.99) is only valid when the Prandtl number ν/κ is smaller than one, since this analysis has been done assuming that r_c^{-1} lies in the kinetic energy inertial-range, or equivalently that $k_c < k_d$.

If the Prandtl number is greater than one, k_c is greater than k_d and is in the dissipative range (otherwise the preceding analysis should still hold, and Eq. (6.99) would yield $k_c > k_d$, in contradiction with the hypothesis): one can imagine that a small blob of temperature of diameter r_c is submitted to a velocity shear of characteristic scale and velocity k_d^{-1} and δv_d corresponding to a local Reynolds number equal to one and such that

$$(\delta v_d) k_d^{-1} = \nu. \tag{6.100}$$

This scalar blob will therefore be elongated in the direction of the shear, and develop smaller transverse scales satisfying $P_e(r_c) = 1$, $P_e(r_c)$ being defined according to Eq. (6.97), with δv_{r_c} equal to δv_d . It yields in this case

$$k_c \sim \frac{\nu}{\kappa} k_d. \tag{6.101}$$

Thus Eqs. (6.99) and (6.101) allow us to determine the conductive wave number, according to the respective value of the Prandtl number compared to one. When the Prandtl number goes to infinity, the scalar transported by turbulence is thus expected to develop infinitely small structures.

6.10.1 Inertial-convective range

We recall that the temperature spectrum satisfies

$$\frac{1}{2}\langle T(\vec{x},t)^2 \rangle = \int_0^{+\infty} E_T(k,t) dk. \tag{6.102}$$

Let

$$\epsilon_T = 2\kappa \int_0^{+\infty} k^2 E_T(k,t) dk \tag{6.103}$$

be the scalar dissipative rate. When the scalar is decaying, it is equal to

$$\epsilon_T = -\frac{1}{2}\frac{d}{dt}\langle T(\vec{x},t)^2 \rangle, \tag{6.104}$$

as shown in Eq. (6.20). This allows one to define the temperature enstrophy

$$D_T(t) = \frac{1}{2}\langle (\vec{\nabla} T)^2 \rangle = \int_0^{+\infty} k^2 E_T(k,t) dk, \tag{6.105}$$

characteristic of the mean temperature gradients fluctuations. Let k_i and k_i^T be the wave numbers characteristic of the peaks of respectively the energy and the temperature spectra: these wave numbers could be imposed by an external stationary forcing of kinetic energy and temperature at rates ϵ and

ϵ_T, or correspond to freely-evolving situations, where we will see that $k_i(t)$ and $k_i^T(t)$ decrease with time. We assume that

$$\sup(k_i, k_i^T) \ll \inf(k_d, k_c). \tag{6.106}$$

Oboukhov [545] and Corrsin [145] have independently proposed that for k lying in the range defined by Eq. (6.106), the temperature spectrum should be proportional to $(\epsilon_T/\epsilon)E(k)$. Such an hypothesis is due to the linear character of the diffusion equation Eq. (6.96). It leads to

$$E_T(k) = C_{CO}\epsilon_T\epsilon^{-1/3}k^{-5/3}, \tag{6.107}$$

where C_{CO} is a universal constant (Corrsin–Oboukhov's constant). Measurements in the atmospheric boundary layer indicate $C_{CO} \approx 0.64$ (Champagne et al. [105]). In fact, the easiest way to obtain Eq. (6.107) is to apply an Oboukhov-type theory, that is

$$\epsilon_T \sim \frac{kE_T(k)}{\tau(k)}, \tag{6.108}$$

where $\tau(k)$ is a nonlinear characteristic time, defined by either Eq. (6.43) or (6.85), proportional to $\epsilon^{-1/3}k^{-2/3}$ when k lies in the Kolmogorov inertial range. The linear-cascade assumption actually assumes that the rate at which the scalar cascade proceeds is governed by the local velocity gradients at k. An alternative way of obtaining this result is to write that a typical temperature fluctuation δT_r at a scale $r \approx k^{-1}$ is such that

$$\epsilon_T \sim \frac{\delta T_r^2}{r/\delta v_r}. \tag{6.109}$$

Remembering that $\delta v_r \sim (\epsilon r)^{1/3}$, this yields

$$\delta T_r^2 \approx \langle [T(\vec{x}+\vec{r},t) - T(\vec{x},t)]^2 \rangle \sim \epsilon_T\epsilon^{-1/3}r^{2/3} = \frac{\epsilon_T}{\epsilon}(\epsilon r)^{2/3} \tag{6.110}$$

which is the equivalent Kolmogorov law for the second-order structure function of the temperature. Eqs. (6.107) and (6.110) characterize the inertial-convective range, where the velocity is *inertial* (no influence of viscosity) and the scalar is *convective* (that is, simply transported by the velocity field). A very impressive experimental confirmation of the inertial-convective range was provided by Gagne [239]. Eq. (6.109) provides also a generalization of Eq. (6.46) under the form

$$\langle [T(\vec{x}+\vec{r},t) - T(\vec{x},t)]^p \rangle \sim \left(\frac{\epsilon_T}{\epsilon}\right)^{p/2} (\epsilon r)^{p/3}. \tag{6.111}$$

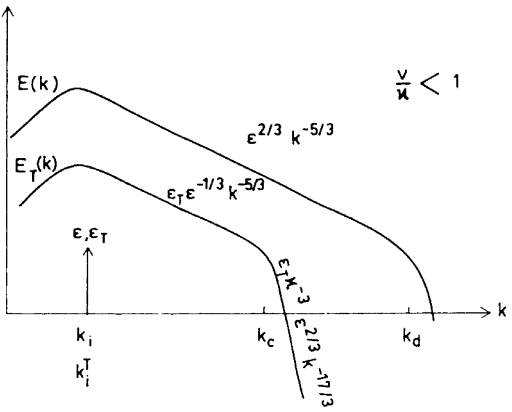

Figure 6.10. Schematic inertial-convective and inertial-conductive ranges of the temperature spectrum in the Kolmogorov inertial range of the kinetic energy spectrum (low Prandtl number).

6.10.2 Inertial-conductive range

We assume that the Prandtl number is smaller than one, so that the conductive wave number k_c is smaller than k_d and given by Eq. (6.99). For $k < k_c$, the temperature spectrum displays an inertial-convective range described above. For $k_c < k < k_d$, we are still in the Kolmogorov energy cascade (that is, "inertial"), but the molecular-conductive effects are predominant for the scalar (see Figure 6.10). This allows us in Eq. (6.96) to neglect the time-derivative term $\partial T/\partial t$. It has been proposed by Batchelor et al. [49], that the Quasi-Normal theory (see next chapter) should be valid in this case. This makes it easy to calculate the temperature spectrum. This calculation, already developed by Leslie [432], is recalled here: let $\hat{T}(\vec{k}, t)$ be the Fourier transform of the temperature. Eq. 6.96 is then written for two wave vectors $\vec{k}$ and $\vec{k}'$:

$$-\kappa k^2 \hat{T}(\vec{k}, t) = i \int \hat{u}_j(\vec{p}, t) q_j \hat{T}(\vec{q}, t) \delta(\vec{k} - \vec{p} - \vec{q}) d\vec{p} d\vec{q};$$

$$-\kappa k'^2 \hat{T}(\vec{k}', t) = i \int \hat{u}_l(\vec{p}', t) q'_l \hat{T}(\vec{q}', t) \delta(\vec{k}' - \vec{p}' - \vec{q}') d\vec{p}' d\vec{q}',$$

and hence, after multiplication of both equations and ensemble averaging

$$\kappa^2 k^2 k'^2 \langle \hat{T}(\vec{k}', t) \hat{T}(\vec{k}, t) \rangle = - \int \langle \hat{u}_j(\vec{p}) \hat{u}_l(\vec{p}') \hat{T}(\vec{q}) \hat{T}(\vec{q}') \rangle q_j q'_l$$

$$\delta(\vec{k} - \vec{p} - \vec{q}) \delta(\vec{k}' - \vec{p}' - \vec{q}') d\vec{p} d\vec{q} d\vec{p}' d\vec{q}'. \qquad (6.112)$$

The Quasi-Normal approximation gives

$$\langle \hat{u}_j(\vec{p})\hat{u}_l(\vec{p}')\hat{T}(\vec{q})\hat{T}(\vec{q}')\rangle = \langle \hat{u}_j(\vec{p})\hat{u}_l(\vec{p}')\rangle\langle \hat{T}(\vec{q})\hat{T}(\vec{q}')\rangle \tag{6.113}$$

since the two other terms are of the type $\langle \hat{u}\hat{T}\rangle\langle \hat{u}\hat{T}\rangle$ are zero: indeed we recall that in three-dimensional isotropic turbulence, and if the isotropy assumptions are done both on the velocity and the scalar, the scalar-velocity correlations are zero. Using the homogeneity and isotropy relations seen above yields for Eq. (6.112), after integration on $\vec{p}'$ and $\vec{q}'$

$$\kappa^2 k^2 k'^2 \langle \hat{T}(\vec{k}')\hat{T}(\vec{k})\rangle = \int \hat{U}_{jl}(\hat{p})\frac{E_T(q)}{2\pi q^2}q_j q_l$$

$$\delta(\vec{k}-\vec{p}-\vec{q})\delta(\vec{k}'+\vec{p}+\vec{q})d\vec{p}d\vec{q}.$$

Further integrations on $\vec{p}$ and $\vec{k}'$ lead to

$$\kappa^2 k^4 \frac{E_T(k)}{2\pi k^2} = \int \hat{U}_{jl}(\vec{k}-\vec{q})\frac{E_T(q)}{2\pi q^2}q_j q_l d\vec{q}. \tag{6.114}$$

As will be shown soon, the temperature spectrum decreases very rapidly to infinity, and the essential part of the integral arising in Eq. (6.114) comes from the triads such that $q \ll k$. Once this non-local approximation has been made, Eq. (6.114) reduces to

$$\kappa^2 k^4 \frac{E_T(k)}{2\pi k^2} = \frac{E(k)}{4\pi k^2}\int \frac{E_T(q)}{2\pi q^2}q^2 \sin^2\beta d\S q$$

where $q^2\sin^2\beta$ stands for $q_j q_l P_{jl}(\vec{k})$, and the angle β is the interior angle opposite to the side p in the triangle (k,p,q). The integration on $\vec{q}$ is then carried out using the polar coordinates β, q, and ϕ, where ϕ is the angle defining the rotation about the vector $\vec{k}$. One obtains

$$\kappa^2 k^2 E_T(k) = \frac{E(k)}{4\pi k^2}2\pi\int_0^{+\infty} q^2 E_T(q)dq\int_0^{\pi}\sin^3\beta d\beta, \tag{6.115}$$

and finally

$$E_T(k) = \frac{2}{3}\kappa^{-2}\int_0^{+\infty} q^2 E_T(q)dq k^{-4}E(k) \tag{6.116}$$

or, using Eq. (6.103)

$$E_T(k) = \frac{1}{3}\epsilon_T\kappa^{-3}k^{-4}E(k). \tag{6.117}$$

Then the assumption of a $k^{-5/3}$ kinetic energy spectrum yields

$$E_T(k) \sim \epsilon_T\kappa^{-3}\epsilon^{2/3}k^{-17/3}, \tag{6.118}$$

which is the inertial-conductive range predicted by Batchelor et al. [49]. Both kinetic energy and temperature spectra are schematically shown in Figure 6.10: the inertial-convective range extending up to k_c is then followed by the $k^{-17/3}$ inertial-conductive range extending from k_c to k_d. Experimentally, such a range could be expected to exist for turbulence in liquid metals, but the $-17/3$ slope is too steep to allow such a verification. A numerical simulation of a passive scalar convected by a frozen velocity field (that is, with an infinite correlation time) done by Chasnov et al. [111] confirms the $-17/3$ exponent. We also anticipate that in two-dimensional turbulence the preceding calculation leading to Eq. (6.117) is still valid, except for the factor 2π of the integration on the angle ϕ (see Lesieur et al. [414]).

6.10.3 Viscous-convective range

We will now consider the case of a fluid with a Prandtl number larger than one. The conductive wave number k_c is given by Eq. (6.101). For $k_d < k < k_c$, we have seen that the scalar is strained by a uniform shear of vorticity $\delta v_d k_d$. This vorticity can easily be shown to be of the order of $(\epsilon/\nu)^{1/2}$, that is the square root of the enstrophy. Therefore, we assume that there is a scalar cascade of constant rate ϵ_T (recalling that the scalar is "convective" and not affected by molecular diffusive effects) such that

$$\epsilon_T \sim k E_T(k) \left(\frac{\epsilon}{\nu}\right)^{1/2} \tag{6.119}$$

which yields

$$E_T(k) = C_B \epsilon_T \left(\frac{\nu}{\epsilon}\right)^{1/2} k^{-1}. \tag{6.120}$$

This is the k^{-1} viscous-convective range proposed by Batchelor [48]. The constant C_B is called Batchelor's constant. Actually this range cannot, as stressed in this reference (see also Leslie [432]), extend up to k_c: indeed, if k_{vc} is the maximum wave number for which the k^{-1} range is valid, we must have from Eq. (6.120)

$$\epsilon_T \sim 2\kappa \int_0^{k_{vc}} \epsilon_T \left(\frac{\nu}{\epsilon}\right)^{1/2} k dk,$$

which gives

$$\frac{k_{vc}}{k_d} = \left(\frac{\nu}{\kappa}\right)^{1/2}, \tag{6.121}$$

to be compared with Eq. (6.101). Thus, this wave number k_{vc} is smaller than k_c. It has been shown by Batchelor [48] that the temperature spectrum decreases exponentially for $k_{vc} < k < k_c$. Figure 6.11 shows the kinetic energy and temperature spectra in the case of the viscous-convective range.

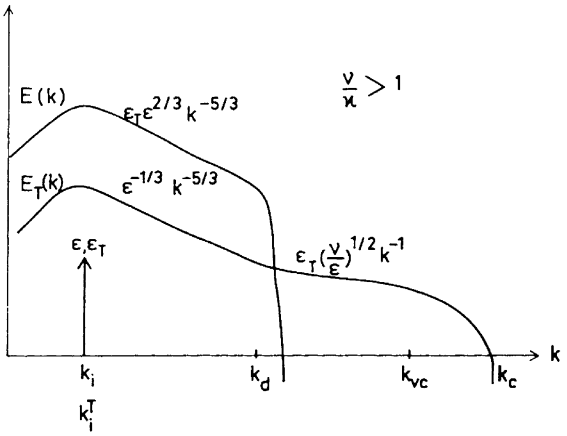

Figure 6.11. Schematic inertial-convective and viscous-convective ranges of the temperature spectrum at high Prandtl number. Remark two errors in the expression of the kinetic-energy spectrum and the temperature spectrum in the inertial-convective range.

6.11 Internal intermittency

We have already emphasized the intermittent character of the small scales of isotropic turbulence, as a result of the process of stretching of vortex filaments. This leads in particular to the formation of the long thin coherent vortices which have been shown above to exist. Thus, in a homogeneous three-dimensional isotropic turbulent flow, the intensity of the velocity fluctuations is not distributed in a uniform manner in space, and presents what is called "internal intermittency". This intermittency is of a different nature from the "external intermittency" which characterizes the large coherent vortices of a turbulent flow at the frontier with the outer irrotational flow, in turbulent boundary layers or jets for instance. The existence of internal intermittency is not in contradiction with the assumption of homogeneity, which is an average property of the flow. So the "local" kinetic-energy dissipation rate $\epsilon = \nu(\vec{\nabla} \times \vec{u})^2$ displays important fluctuations about its mean value[20] $\langle \epsilon \rangle$. A consequence is Kolmogorov's 1941 [338] theory, which does not involve these fluctuations of ϵ, must certainly be corrected in order to take into account this intermittent character. This has been noticed by Kolmogorov himself, who proposed a theory in 1962, based on a lognormality assumption, which corrected his original theory (Kolmogorov [340]). The same ideas were simultaneously expressed by Oboukhov [546], and developed by Yaglom [726].

[20] In the rest of the book, the notation ϵ is generally used for the quantity called $\langle \epsilon \rangle$ in this section only.

A different class of models was proposed by Novikov and Stewart [540], and worked out by Frisch et al. [223]. Mandelbrot [468] proposed a very interesting unifying synthesis of these various theories, based on a weighted or absolute "curdling" principle (see also Mandelbrot [467]).

In this section, we will summarize the main results of both Kolmogorov–Oboukhov–Yaglom and Novikov–Stewart theories. A useful reference for this purpose is Gagne [239].

6.11.1 Kolmogorov–Oboukhov–Yaglom theory

This theory is developed in detail in Monin and Yaglom's [515] textbook of turbulence. It assumes that the local kinetic-energy dissipation ϵ possesses a log-normal distribution (i.e. that the random function $\ln \epsilon$ is Gaussian): as shown by Yaglom [726], such a result comes from a model called "self-similar breakdown of turbulent eddies". More specifically, this theory introduces another local kinetic energy dissipation rate, $\epsilon_r(\vec{x}, t)$, which is the average of ϵ on a sphere of center $\vec{x}$ and radius $r/2$. Within the model, the variance σ_r^2 of $\ln \epsilon_r$ is of the form

$$\sigma_r^2 = Q(\vec{x}, t) + \chi \ln \frac{l}{r} \tag{6.122}$$

where l is the integral scale of turbulence, $Q(\vec{x}, t)$ a function depending on the large scales, and χ a universal constant. Eq. (6.122) is only valid for $r \ll l$. From these assumptions it can be shown that the order q moments of ϵ are given by

$$\langle \epsilon_r^q \rangle = \langle \epsilon \rangle^q e^{q(q-1)\sigma_r^2/2} \tag{6.123}$$

which yields, using Eq. (6.122)

$$\langle \epsilon_r^q \rangle = D_q \langle \epsilon \rangle^q \left(\frac{l}{r} \right)^{\chi q(q-1)/2} \tag{6.124}$$

where $D_q(\vec{x}, t)$ is a coefficient which depends on the large scales of the flow. In the particular case $q = 2$, and using the statistical homogeneity condition, one has (see Monin and Yaglom [515])

$$\langle \epsilon(\vec{x}, t)\epsilon(\vec{x} + \vec{r}, t) \rangle = \frac{1}{2} \left(\frac{\partial^2}{\partial r^2} \right) [r^2 \langle \epsilon_r(\vec{x}, t)^2 \rangle] = D_2 \langle \epsilon \rangle^2 \left(\frac{l}{r} \right)^{\chi} \tag{6.125}$$

which shows that the parameter χ characterizes the spatial correlation of ϵ. At this point the classical Kolmogorov 1941 theory can be shown again locally, assuming that the crucial parameter is ϵ_r. This yields for the local second-order velocity structure function the proportionality to $\epsilon_r^{2/3} r^{2/3}$. After an ensemble averaging and use of Eq. (6.124) for $q = 2/3$, we obtain

$$S_2(r,t) \sim \langle\epsilon\rangle^{2/3} r^{2/3} \left(\frac{r}{l}\right)^{\chi/9} \tag{6.126}$$

which, translated in Fourier space, yields

$$E(k) \sim \langle\epsilon\rangle^{2/3} k^{-5/3} (kl)^{-\chi/9}. \tag{6.127}$$

The same analysis for a structure function of order n would give with the aid of Eq. (6.124) with $q = n/3$

$$S_n \sim \langle\epsilon_r^{n/3}\rangle r^{n/3} \sim \langle\epsilon\rangle^{n/3} r^{n/3} \left(\frac{l}{r}\right)^{\chi n(n-3)/18} \tag{6.128}$$

to be compared with Eq. (6.46), as recalled in Anselmet et al. [9]. Eqs. (6.126), (6.127) and (6.128) show the departure from the Kolmogorov 1941 theory due to the intermittency in the framework of the lognormal theory. In particular Eq. (6.128) shows that the structure function of order 6 is proportional to $r^2(l/r)^{\chi}$.

6.11.2 Novikov–Stewart (1964) model

This model, or a dynamical equivalent one known as the β-model (Frisch et al. [223]), assumes that during the cascade process only a fraction β of the volume occupied by the cascading eddies will be filled by turbulence: more specifically, let us consider an "eddy" of size l_p and volume l_p^3 which gives rise to N eddies of size $l_p/2$: the fraction β of the volume occupied by turbulence is

$$\beta = \frac{N}{2^3}. \tag{6.129}$$

N can be defined with the aid of the concept of fractal dimension of Hausdorff (see Mandelbrot [467, 468]): the turbulent structures are assumed to be self-similar, and to lie on a fractal set of dimension D such as $N = 2^D$, and

$$\beta = 2^{D-3}. \tag{6.130}$$

The essence of the theory is to assume that the standard Kolmogorov phenomenology is valid only in the active regions: at step p of the cascade corresponding to eddies of size l_p of typical velocity δv_{l_p}, the kinetic energy dissipation rate will be equal to $\delta v_{l_p}^3/l_p$ in the active regions and to zero in the "non-turbulent" regions: thus the mean kinetic energy dissipation rate $\langle\epsilon\rangle$ on the whole volume will be

$$\langle\epsilon\rangle \sim \beta^p \delta v_{lp}^3/l_p \tag{6.131}$$

since the eddies l_p occupy a fraction β^p of the initial volume. Hence the assumption of a constant mean kinetic energy flux along the cascade yields

$$\delta v_{l_p} \sim (\langle\epsilon\rangle l_p)^{1/3}\beta^{-p/3}. \tag{6.132}$$

The kinetic energy spectrum associated to the wave number $k = l_p^{-1}$ is $\delta v_{l_p}^2 k^{-1}$ in the active regions and zero elsewhere. Therefore the energy spectrum of the mean kinetic energy is

$$E(k) \sim \beta^p \delta v_{l_p}^2 k^{-1} \sim \beta^{p/3}\langle\epsilon\rangle^{2/3}k^{-5/3} \tag{6.133}$$

which, with the aid of Eq. (6.130), can be written as

$$E(k) \sim (kl)^{-(3-D)/3}\langle\epsilon\rangle^{2/3}k^{-5/3} \tag{6.134}$$

since $kl = l/l_p = 2^p$. Eq. (6.134) shows the departure from the 1941 Kolmogorov law within the Novikov–Stewart theory.

The structure functions of order n of the velocity can then be evaluated in the same way, assuming the velocity differences to be zero in the non-active regions:

$$\langle\delta v_r^n\rangle \sim \beta^s(\langle\epsilon\rangle r)^{n/3}\beta^{-ns/3} \tag{6.135}$$

with $(l/r) = 2^s$. This yields

$$\langle\delta v_r^n\rangle \sim \langle\epsilon\rangle^{n/3} r^{n/3}\left(\frac{l}{r}\right)^{\chi(n-3)/3} \tag{6.136}$$

as has been recalled by Anselmet et al. [9]. In Eq. (6.136) the coefficient χ is now defined as

$$\chi = 3 - D. \tag{6.137}$$

Finally the kinetic energy dissipation product between two points separated by r is equal to $\delta v_r^6/r^2$ if $r < l_s$ and zero if $r > l_s$. The spatial ϵ-correlation is thus

$$\langle\epsilon(\vec{x},t)\epsilon(\vec{x}+\vec{r},t)\rangle \sim \frac{\beta^s\delta v_r^6}{r^2} \sim \langle\epsilon\rangle^2\left(\frac{l}{r}\right)^{\chi}. \tag{6.138}$$

6.11.3 Experimental and numerical results

Eqs. (6.125), (6.128), (6.136) and (6.138) show that the coefficients χ introduced in both lognormal and β-model theories characterize the behaviour of the ϵ-correlation or of $\langle\delta v_r^6\rangle/r^2$, which decay as $(l/r)^\chi$ when r goes to zero (and in the limit of zero viscosity). This allows experimental determinations of χ, by measuring either the ϵ-correlation (or equivalently their Fourier spectrum) or the sixth-order velocity structure function. Values of the order of 0.5, using the ϵ-correlation method in a wind tunnel (Gagne [238]), the ϵ-spectrum method in a jet (Friehe et al. [219]), or the structure function method in the atmosphere (Van Atta and Chen [697], were thus determined. A numerical

simulation done by Brachet [73] tends to confirm this value. It seems however, as shown by Anselmet et al. [9] in a turbulent jet, that a more reliable value of χ (determined with the aid of the sixth-order structure function) is of 0.20. The same work shows that, with this value of χ, the velocity structure functions up to the order 12 follow the quadratic dependence in n of the lognormal theory displayed in Eq. (6.128), and not the linear dependence of Eq. (6.126). So the lognormal theory seems to be valid for $n \leq 12$. For $12 < n \leq 18$ however, departures from the lognormal distribution have been observed by Anselmet et al. [9]. These departures could possibly be explained by what is called a multifractal approach (see Schertzer and Lovejoy [634], Argoul et al. [14][21] and Frisch [229]). Recent theoretical results on turbulence multifractal analysis can be found in Frisch et al. [231, 232].

Another point to mention is that, at the level of the kinetic-energy spectrum, the intermittency corrections which steepen the $k^{-5/3}$ Kolmogorov law are (with this value of χ) respectively in both theories of $\chi/9 \simeq 0.02$ (from Eq. (6.127) and $\chi/3 \simeq 0.06$ (from Eqs. (6.134) and (6.137)). This is too small to allow an experimental verification at that level. This could suggest that the closure theories envisaged in the next chapter, and which concern energy spectra, could give satisfactory results, even if they cannot deal with the spatial intermittency envisaged here. Notice also that the experimentaly observed high-k departure from the $k^{-5/3}$ spectrum corresponds to the already mentioned bump. This diminishes the spectral exponent modulus, contrary to internal intermittency.

The same experimental study as that carried out for the velocity by Anselmet et al. [9], was done by Antonia et al. [10] for a passive temperature. In these two studies (see also Gagne [239]), the p.d.f. of respectively the velocity and temperature difference between two points a given distance apart were found to have an exponential tail. This is obviously related to the velocity-gradient p.d.f.'s mentioned above, and indicates exponential-tail temperature gradients. But the departure from Gaussianity is much more marked for the temperature than for the velocity. On the other hand, Métais and Lesieur [493, 496] have found in DNS of decaying isotropic turbulence that not only the temperature derivatives, but also the temperature itself, display an exponential distribution. On the contrary, the velocity is very close to Gaussian. Measurements in grid turbulence done by Jayesh and Warhaft [313] confirm the exponential temperature p.d.f. in the case of a non-zero mean temperature gradient, but find a close to Gaussian behaviour without mean gradient.

Figure 6.12 shows the decay of respectively the kinetic-energy and temperature spectra in LES (using pseudo-spectral methods and a spectral eddy

[21] This work analyzes the turbulent signal coming from Gagne's [239] data with the aid of the *wavelet analysis* technique.

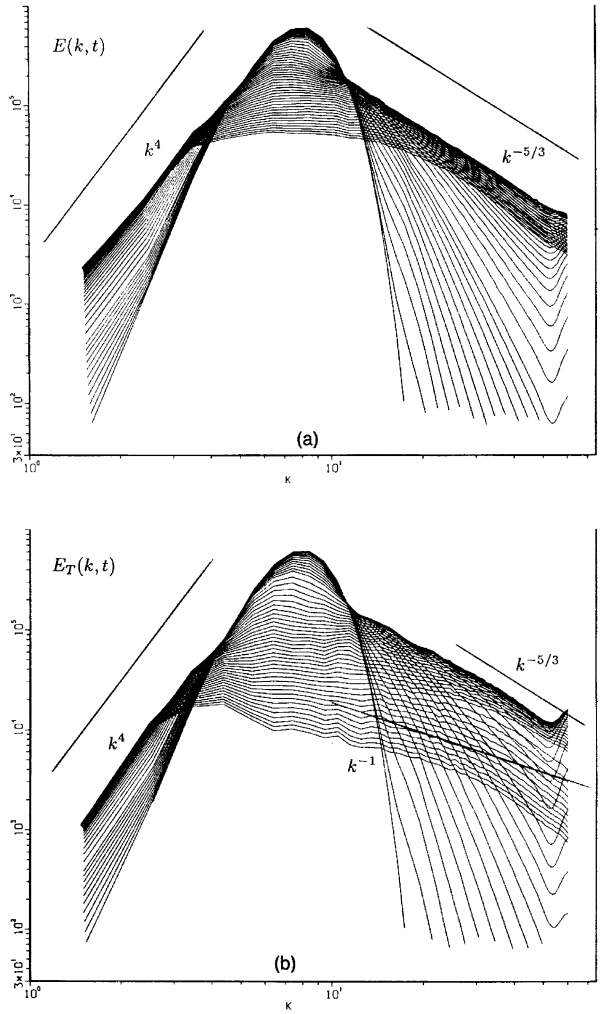

Figure 6.12. Time-evolution of the kinetic-energy spectrum (a) and the temperature spectrum (b) in a pseudo-spectral large-eddy simulation done by Lesieur and Rogallo [421], starting initially with k^8 spectra at low k. The resolution is 128^3 modes (courtesy *Physics of Fluids*).

viscosity, see Chapter 12 for details), done by Lesieur and Rogallo [421]. These simulations, on which more details will be given in the following chapter, start with identical energy and temperature spectra sharply peaked in the large scales. They show first the establishment of a $\propto k^4$ backscatter spectrum in the very large scales, which will be explained next chapter. In the small scales, both spectra cascade towards high wave numbers. The kinetic energy follows approximately a Kolmogorov law.[22] On the other hand, the temperature exhibits in the large scales a long range of slope shallower than k^{-1}. Such an *anomalous*[23] law has been explained by Lesieur and Rogallo [421] with the same type of arguments as those leading to the viscous-convective range (but here the molecular Prandtl number is assumed to be ~ 1): one assumes that, due to the lack of pressure gradient in the scalar equation, the scalar is going to react very quickly in a quasi linear manner to the large-scale shears, before nonlinear effects start acting. We write:

$$\epsilon_T \sim \frac{kE_T(k,t)}{\tau(k_I)}, \tag{6.139}$$

where $\tau(k_I)$ is the large-eddy turnover time at k_I, which can be evaluated as the decay time scale $\langle \vec{u}^2 \rangle / \epsilon$. It yields

$$E_T(k,t) = C_T \eta \frac{\langle \vec{u}^2 \rangle}{\epsilon} k^{-1}. \tag{6.140}$$

Lesieur and Rogallo [421] do collapse their temperature data of Figure 6.12b on the law equation (6.140 in the large scales (with $C_T = 0.1$), and on the inertial-convective law[24] Eq. (6.107) in the small scales.

This scalar k^{-1} range has been also found in DNS done by Métais and Lesieur [493, 496]. A visualization of the temperature distribution in a cross section of such a calculation is shown on Plate 19. It confirms the strong intermittency of the scalar, with a few "hot spots". The latter are in fact located on braids between the coherent longitudinal vortices. The scalar $\sim k^{-1}$ spectrum resembles the inertial-convective range of two-dimensional turbulence (see Lesieur and Herring [418] and Chapter 8), instead of the classical $k^{-5/3}$ Corrsin– Oboukhov's inertial-convective range of three-dimensional turbulence. This reorganization of the scalar distribution around the vortices explains also why, when the scalar is injected at scales much smaller than the energy, it cascades rapidly back to larger scales.

[22] It is in fact closer to k^{-2} with the spectral eddy viscosity used in this LES.

[23] With respect to the $k^{-5/3}$ inertial-convective range.

[24] With a Corrsin–Oboukhov constant C_{CO} comprised between 0.8 and 1, value which has to be compared with the experimental value of 0.64 mentioned above found by Champagne et al. [105].

Remark however that the law equation (6.140) poses a problem of random Galilean invariance. Indeed, since Navier–Stokes equations are invariant under any arbitrary translation of constant velocity (Galilean invariance), homogeneous turbulence (without mean shear) should be unchanged if for instance a random velocity $\vec{U}_0$ of constant modulus and arbitrary orientation is added to each realization of the flow. This is the concept of random Galilean transformation, where the kinetic energy of the flow increases of $U_0^2/2$. The same is true for the passive scalar. Therefore Eq. (6.140) is inconsistent with this concept, since such a law is changed with the kinetic energy. One should find a modification of the large-scale diffusing time involved in Eq. (6.140) which is compatible with random Galilean invariance. One could for instance try to define a "slow turbulence", associated to the large-scale quasi two-dimensional motions, which would fix the parameters of the scalar quasi two-dimensional cascade.

Let us stress that a k^{-1} passive scalar spectrum has been found in coaxial jets experimentally by Villermaux et al. [702, 703] and numerically (DNS and LES) by Balarac et al. [27, 28].

Métais and Lesieur [496] show that the scalar becomes Gaussian again and looses its k^{-1} spectrum when coupled with the velocity (through Boussinesq approximation) in stably-stratified turbulence.[25] This behaviour could be associated with the regimes of respectively *hard* and *soft* turbulence found for the temperature by Castaing et al. [102] in an experiment involving a heated boundary layer: in this work, hard turbulence corresponds to an exponential temperature p.d.f., while soft turbulence refers to a Gaussian temperature.

Finally, it has to be stressed that the evolution towards an intermittent state is a natural tendency for a turbulent flow. When applied to the universe, assumed to be fluid, this concept allows one to understand how the initially quasi homogeneous universe of the "big bang" has lost its homogeneity, and has now developed such an intermittent distribution of galaxies. We mention in this respect the simulations of Frisch [230] based on a multi-dimensional Burgers equation. More generally, intermittency seems to characterize any dissipative nonlinear system.

[25] More about these calculations (in the isotropic or stratified cases) will be given throughout the following chapters.

7

Analytical Theories and Stochastic Models

7.1 Introduction

Our objective in this chapter is to provide the reader with a good understanding of the analytical statistical theories and stochastic models of turbulence sometimes referred to as *two-point closures* since, as will be seen, they deal with correlations in two different points of the space (or two different wave numbers $\vec{k}$ and $\vec{k}'$ such that $\vec{k}+\vec{k}'=\vec{0}$ in Fourier space). A whole book would not be sufficient to contain all the details of the algebra which is involved, and the reader will be referred to the quoted references for further details: of particular interest for that purpose are Orszag [550, 553], Leslie[1] [432], and Rose and Sulem [617]. Here, we will mainly focus on the so-called E.D.Q.N.M. approximation (Eddy-Damped Quasi-Normal Markovian approximation), and will situate it among other theories of the same type. These theories can generally be presented from two different points of view, the stochastic-model point of view, and the closure point of view. Some of these theories, as will be seen, do not exactly correspond to these points of view, but they lead to spectral equations of the same family, which can be solved with the same methods. We will not use too much energy deriving the "best" analytical theory, for it seems that they all have qualitatively the same defects and qualities, and differ essentially in the values of the inertial-range exponents. We will concentrate principally on the E.D.Q.N.M., because in the case of isotropy it can be solved numerically at a much cheaper cost than the direct simulations, and allows one to reach extremely high Reynolds numbers.[2] We will discuss to what extent the results can be relied upon for "real" turbulence (that is turbulence governed by Navier–Stokes equation). The confidence we can have in these

[1] Leslie's work reviews in detail Kraichnan's *Direct-Interaction Approximation*, see below.

[2] With several-decade Kolmogorov inertial-range spectra.

theories is based on some of the results of the numerical large-eddy simulations of turbulence which will be discussed in Chapter 12. We will show also in the same chapter how these theories apply to passive-scalar diffusion. Results on diffusion in two-dimensional turbulence will be given in Chapter 8, and those on the predictability problem in Chapter 11. These closures will also, through the concept of non-local interactions (the equivalent of long-range interactions in physics), allow us to propose statistical parameterizations of the "subgrid-scales" useful for the large eddy simulations, as will be seen in Chapter 12. Our feeling about these closures is that, notwithstanding their inability to deal with spatial intermittency or situations with strong departures from Gaussianity, they are a unique tool for the study of strong nonlinearities in small-scale developed turbulence, and allow to handle situations inaccessible to the nonlinear stability analysis or to the so-called Renormalization Group techniques (see Forster et. al. [210], Fournier [212], Yakhot and Orszag [728] and Dannevik et al. [156]). Some details on these techniques will be given in this chapter). Coupled with large-eddy-simulations to represent the large anisotropic and inhomogeneous scales, the two-point closures have contributed to a decisive advance of our understanding of "real-world" turbulence. Finally, they give a good description of the inverse cascading tendency of two-dimensional turbulence, and provide valuable qualitative information on diffusion and dispersion of transported species in isotropic turbulence.

The closure problem inherent to a statistical description of turbulence has already been discussed in Chapter 6. Here we reformulate it for homogeneous turbulence in Fourier space: the following formal analysis can be found in a lot of works, for instance in Sulem et al. [673] (see also Lesieur [412]): let $\hat{u}(\vec{k})$ represent the velocity field, and let the Navier–Stokes equation be written formally as

$$\frac{\partial \hat{u}(\vec{k})}{\partial t} = \hat{u}\hat{u} - \nu k^2 \hat{u}(\vec{k}), \tag{7.1}$$

which states for Eq. (5.18), $\hat{u}\hat{u}$ representing the nonlinear convolution term. Since $\langle \vec{u} \rangle = \vec{0}$, the averaging of Eq. (7.1) yields the trivial identity $\vec{0} = \vec{0}$. To obtain an evolution equation for the spectral tensor $\hat{U}_{ij}(\vec{k}, t)$, one has to write the evolution equation for $\hat{u}(\vec{k}')$,

$$\frac{\partial \hat{u}(\vec{k}')}{\partial t} = \hat{u}\hat{u} - \nu k'^2 \hat{u}(\vec{k}') \tag{7.2}$$

multiply it tensorially by $\hat{u}(\vec{k})$, multiply Eq. (7.1) by $\hat{u}(\vec{k}')$, add the resulting equations, and average. We obtain

$$\left[\frac{\partial}{\partial t} + \nu(k'^2 + k^2)\right] \langle \hat{u}(\vec{k}')\hat{u}(\vec{k}) \rangle = \langle \hat{u}\hat{u}\hat{u} \rangle \tag{7.3}$$

which, after a further integration on $\vec{k}'$ and because of Eq. (5.74), gives the desired equation for $\hat{U}_{ij}(\vec{k})$. This procedure is similar to the one followed to obtain Eq. (6.3). The formal term $\langle \hat{u}\hat{u}\hat{u} \rangle$, which is a linear combination of third-order moments of the velocity components, involves integrations on triads of wave numbers, and corresponds to the nonlinear transfer between various scales of motion. The problem is evidently not closed, since the triple-velocity correlations are unknown. Then the use of a third evolution equation for $\hat{u}(\vec{k}'')$ analogous to Eqs. (7.1) and (7.2) allows us to write

$$\left[\frac{\partial}{\partial t} + \nu(k^2 + p^2 + q^2) \right] \langle \hat{u}(\vec{k}) \hat{u}(\vec{p}) \hat{u}(\vec{q}) \rangle = \langle \hat{u}\hat{u}\hat{u}\hat{u} \rangle. \tag{7.4}$$

One could go to higher orders, and still have one more unknown moment than equations. The hierarchy of the moments is for instance written in André [6] and Tatsumi [677], but this hierarchy is not closed, and the only way of solving the problem using this method is to introduce an arbitrary further relation between the velocity moments, called a closure hypothesis. We notice however that here there is no closure needed at the level of the pressure (which has been eliminated) or of the viscous dissipation, contrary to what happens in the "one-point closure modelling". In this monograph, we will focus on closures which assume that turbulence is close to Gaussianity, which is not totally unphysical if we consider turbulence as the result of a superposition of independent Brownian-like chaotic motions to which the central limit theorem could apply. But we have already seen examples of strong departures from Gaussianity in turbulence, for instance when considering the p.d.f.'s in Chapter 6. However, kinetic-energy spectra and energy transfers do not seem to be much affected by these departures.

This chapter will be divided into two parts: the method and the results.

PART A: THE METHOD

7.2 Quasi-Normal approximation

The most known of the closure hypotheses is the famous Quasi-Normal approximation (Q.N.), proposed by Millionshtchikov [507] and independently by Chou [125], as emphasized in Tatsumi [677]. The resulting spectral equations for isotropic turbulence were obtained independently by Proudman and Reid [590] and Tatsumi [675].

7.2.1 Gaussian random functions

Before developing this analysis, it is useful to recall the main results concerning the Gaussian random functions (see e.g. Blanc-Lapierre and Picinbono [66]):

Let X be a four-dimensional variable (three dimensions of space and one of time), and let $g(X)$ be a random function of X (g might also be a vector) of zero mean. We recall that $g(X)$ is a *Gaussian random function* if, given N arbitrary numbers α_i and N values X_i of X, the linear combination $\sum \alpha_i g(Xi)$ is a *Gaussian random variable*. The consequences of this definition are in particular that

- for any $X, g(X)$ is a random Gaussian variable
- the odd moments of g are zero
- the even moments can be expressed in terms of the second-order moments.

In particular, fourth-order moments in four points $X_1 \dots X_4$ satisfy

$$\begin{aligned}\langle g(X_1)g(X_2)g(X_3)g(X_4)\rangle = &\langle g(X_1)g(X_2)\rangle\langle g(X_3)g(X_4)\rangle \\ &+\langle g(X_1)g(X_3)\rangle\langle g(X_2)g(X_4)\rangle \\ &+\langle g(X_1)g(X_4)\rangle\langle g(X_2)g(X_3)\rangle. \end{aligned} \tag{7.5}$$

Given any (non-Gaussian) random function whose second-order moments are known, it is then possible to calculate the fictitious moments of order n that this function would have if it were a Gaussian function: the difference between the actual n-th order moment of the function and the corresponding Gaussian value is called the n-th order *cumulant*. In particular the odd cumulants are equal to the moments. For a Gaussian function, all the cumulants are zero by definition.

7.2.2 Formalism of the Q.N. approximation

As already seen in the previous chapter, and although the velocity probability densities measured experimentally in turbulence are not far from a normal distribution, the velocity derivatives p.d.f.'s display an assymmetry about the mean value which is more and more marked as the order is increased (Gagne [238]). The non-zero value of the velocity-derivative skewness factor introduced in Chapter 6 is a manifestation of this fact. Also, as already seen in Chapter 6, the velocity derivatives p.d.f.'s are closer to an exponential than to a Gaussian. It is therefore irrealistic to approximate the velocity field of turbulence by a Gaussian random function, since such a turbulence would have no energy transfer between wave numbers (we recall from Eq. (7.3) that the transfer is proportional to third-order moments in Fourier space). The idea of the Quasi-Normal approximation (Q.N.) is to simply assume that the fourth-order cumulants are zero, without any assumption on the third-order moments. This allows one to close the problem at the level of Eq. (7.4), by replacing the fourth-order moment by the Gaussian value obtained from Eq. (7.5). It leads to

$$\left[\frac{\partial}{\partial t}+\nu(k^2+p^2+q^2)\right]\langle\hat{u}(\vec{k})\hat{u}(\vec{p})\hat{u}(\vec{q})\rangle=\sum\langle\hat{u}\hat{u}\rangle\langle\hat{u}\hat{u}\rangle \tag{7.6}$$

where the sum $\sum$ corresponds to three terms coming from Eq. (7.5), and to the various terms included in the $\langle\hat{u}\hat{u}\hat{u}\rangle$ transfer of the r.h.s. of Eq. (7.3). Again the terms $\langle\hat{u}\hat{u}\rangle\langle\hat{u}\hat{u}\rangle$ are a complicated integral involving various wave numbers and components of the velocity. Then integration of Eq. (7.3) upon $\vec{k}'$ yields with the aid of Eq. (7.6) and because of homogeneity

$$\left(\frac{\partial}{\partial t}+2\nu k^2\right)\hat{U}_{ij}(\vec{k},t)=\int_0^t d\tau\int_{\vec{p}+\vec{q}=\vec{k}}e^{-\nu(k^2+p^2+q^2)(t-\tau)}$$

$$\sum\langle\hat{u}\hat{u}\rangle\langle\hat{u}\hat{u}\rangle d\vec{p} \tag{7.7}$$

with τ as time argument in the products $\langle\hat{u}\hat{u}\rangle\langle\hat{u}\hat{u}\rangle$. The calculation of these products involves a lengthy algebra which will not be given in this book, but is at hand for any reader who wants to use these theories. The exact set of Eqs. (7.3) and (7.6) can be found for instance in Tatsumi [677].

The calculation is simpler for isotropic turbulence without helicity: taking the trace of $\hat{U}_{ij}(\vec{k},t)$ in Eq. (7.7) and replacing the spectral tensors by their isotropic values Eq. (5.84) leads to

$$\left(\frac{\partial}{\partial t}+2\nu k^2\right)E(k,t)=\int_0^t d\tau\iint_{\Delta_k}dp\;dq$$

$$e^{-\nu(k^2+p^2+q^2)(t-\tau)}S(k,p,q,\tau) \tag{7.8}$$

where S has been defined in Eq. (6.23). We have

$$S(k,p,q,\tau)=\frac{k^3}{pq}a(k,p,q)E(p,\tau)E(q,\tau)$$

$$-\frac{1}{2}\frac{k}{pq}E(k,\tau)[p^2b(k,p,q)E(q,\tau)+q^2b(k,q,p)E(p,\tau)]. \tag{7.9}$$

The integration in Eq. (7.8) is done on the domain Δ_k in the (p,q) plane such that (k,p,q) should be the sides of a triangle, already defined in Chapter 6. The geometrical coefficients $a(k,p,q)$ and $b(k,p,q)$ are evaluated in Leslie [432]. They are equal to, using Leslie's and Kraichnan's [345] notations

$$a(k,p,q)=\frac{1}{4k^2}P_{ijm}(\vec{k})P_{ibc}(\vec{k})P_{jb}(\vec{p})P_{mc}(\vec{q})$$

$$=\frac{1}{2}(1-xyz-2y^2z^2) \tag{7.10}$$

$$b(k,p,q) = \frac{1}{2}k^2 P_{cjm}(\vec{k})P_{jbc}(\vec{p})P_{mb}(\vec{q})$$
$$= \frac{p}{k}(xy + z^3) \tag{7.11}$$

with summation on the repeated indices, $P_{ijm}(\vec{k})$ having been defined previously in Eq. (6.2). x, y, and z are the cosines of the interior angles of the triangle (k,p,q) facing respectively the sides k,p,q. Actually $a(k,p,q)$ can be obtained by symmetrization of $b(k,p,q)$

$$a(k,p,q) = \frac{b(k,p,q) + b(k,q,p)}{2} \tag{7.12}$$

and Eqs. (7.8)–(7.9) can be simplified using the above symmetry properties to

$$\left(\frac{\partial}{\partial t} + 2\nu k^2\right) E(k,t) = \int_0^t d\tau \iint_{\Delta_k} dpdq e^{-\nu(k^2+p^2+q^2)(t-\tau)}$$
$$\frac{k}{pq} b(k,p,q)[k^2 E(p,\tau) - p^2 E(k,\tau)]E(q,\tau). \tag{7.13}$$

7.2.3 Solution of the Q.N. approximation

It was only in the early sixties that the development of computers allowed a numerical resolution of the isotropic Q.N. equation (7.8). This was done by Ogura [548] who showed that this approximation eventually led to the appearance of negative energy spectra in the energy-containing eddies range, and checked that this phenomenon was not a numerical artefact. Such a behaviour is of course unacceptable, since the energy spectrum, proportional to $\langle|\underline{\hat{u}}(\vec{k})|^2\rangle$, is a positive quantity by nature. It shows that the Q.N. approximation is incompatible with the dynamics of Navier–Stokes. The same result was independently obtained by O'Brien and Francis [547] who used the Q.N. approximation to study the evolution of a passive scalar in isotropic turbulence: it was thus the passive scalar spectrum which developed negative values. The reason for this anomalous behaviour of the Q.N. theory was identified by Orszag [551, 553] who showed that the r.h.s. of Eq. (7.6) was responsible for the build-up of too high third-order moments. These moments saturate in reality, as is shown for instance experimentally by the not excessive values of the skewness factor. Then the role of the fourth-order cumulants (discarded in the Q.N. theory) is to provide a damping action leading to a saturation of the third-order moments. This is the motivation of the E.D.Q.N. and E.D.Q.N.M. theories:

7.3 Eddy-Damped Quasi-Normal type theories

7.3.1 Eddy damping

Orszag [551, 553] proposed then to approximate the fourth-order cumulants neglected in Eq. (7.6) by a linear damping term, and to replace Eq. (7.6) by

$$\left[\frac{\partial}{\partial t} + \nu(k^2+p^2+q^2) + \mu_{kpq}\right] \langle \hat{u}(\vec{k})\hat{u}(\vec{p})\hat{u}(\vec{q})\rangle = \sum \langle \hat{u}\hat{u}\rangle\langle \hat{u}\hat{u}\rangle \tag{7.14}$$

where μ_{kpq}, which has the dimension of the inverse of a time, is a characteristic "eddy-damping rate" of the third-order moments associated to the triad (k,p,q). This parameter is arbitrary in the theory, and its choice is essential, at least if one wants to use the theory for quantitative predictions. For isotropic turbulence, the following expression

$$\mu_{kpq} = \mu_k + \mu_p + \mu_q \tag{7.15}$$

where

$$\mu_k \sim [k^3 E(k)]^{1/2} \tag{7.16}$$

is the inverse of the local nonlinear time defined in Eq. (6.43), has been proposed by Orszag [550]. The value of the numerical constant in front of the r.h.s. of Eq. (7.16) can be shown to be proportional to $C_K^{3/2}$, where C_K is the Kolmogorov constant (we anticipate here that these Eddy-Damped theories will lead to a Kolmogorov $k^{-5/3}$ inertial-range spectrum for isotropic three-dimensional turbulence). Actually the choice Eq. (7.16) is less satisfactory for a rapidly decreasing spectrum at high k (in the initial stage of evolution of decaying turbulence for instance), where μ_k, given by Eq. (7.16), becomes a decreasing function of k: this is fairly irrealistic, since μ_k is a kind of characteristic time-frequency of turbulence, and one might expect an increase of the frequencies with k. It was thus proposed by Frisch [221] (see also Pouquet et al. [584]) to modify μ_k as:

$$\mu_k = a_1 \left[\int_0^k p^2 E(p,t)dp\right]^{1/2}, \tag{7.17}$$

which is growing with k in any situation, and represents the average deformation rate of eddies of size $\sim k^{-1}$ by larger eddies.[3] The choice of the numerical

[3] We have already encountered this frequency in the previous chapter, for the time-dependent Oboukhov theory.

constant a_1 will be specified later on. As a matter of fact, both expressions collapse in the inertial-range with a proper choice of the numerical constants involved in the r.h.s. of Eqs. (7.16) and (7.17).

The choice of μ_k is more difficult in non-isotropic situations, for instance for problems where waves (Rossby waves, inertial or gravity waves) interact with turbulence (see Legras [396], Cambon et al. [94]), and this is still an open question.

This approximation is known as the Eddy-Damped Quasi-Normal approximation (E.D.Q.N.). It has to be stressed that the eddy-damping procedure concerns the third-order moments, and that there is no eddy damping of the energy in the theory, where the kinetic energy is still conserved by nonlinear interactions. The resulting evolution equation for the spectral tensor is formally identical to Eq. (7.7), provided the viscous damping term arising in the exponential term of the r.h.s. be modified to take into account the eddy damping. One obtains

$$\left(\frac{\partial}{\partial t}+2\nu k^2\right)\hat{U}_{ij}(\vec{k},t)=\int_0^t d\tau\int_{\vec{p}+\vec{q}=\vec{k}} e^{-[\mu_{kpq}+\nu(k^2+p^2+q^2)](t-\tau)} \sum\langle\hat{u}\hat{u}\rangle\langle\hat{u}\hat{u}\rangle(\tau)d\vec{p}. \tag{7.18}$$

7.3.2 Markovianization

This E.D.Q.N. approximation, though physically more acceptable, does not nevertheless guarantee the *realizability* (positiveness of the energy spectrum) in all the situations. As shown by Orszag [553], this can be ensured with a minor modification, called the *Markovianization*: this consists in assuming that the exponential term in the integrand of Eq. (7.18) varies with a characteristic time $[\mu_{kpq}+\nu(k^2+p^2+q^2)]^{-1}$ much smaller than the characteristic evolution time of $\sum\langle\hat{u}\hat{u}\rangle\langle\hat{u}\hat{u}\rangle$; the latter is of the order of the large-eddy turnover time of the turbulence. This assumption is valid in the inertial and dissipative range, but questionable in the energy-containing range where both times are of the same order. Nevertheless the Markovianization allows a considerable simplification of the resulting spectral equations, while ensuring the realizability. Eq. (7.18) is therefore changed into

$$\left(\frac{\partial}{\partial t}+2\nu k^2\right)\hat{U}_{ij}(\vec{k},t)=\int_{\vec{p}+\vec{q}=\vec{k}}\theta_{kpq}\sum\langle\hat{u}\hat{u}\rangle\langle\hat{u}\hat{u}\rangle(t)d\vec{p} \tag{7.19}$$

with

$$\theta_{kpq}=\int_0^t e^{-[\mu_{kpq}+\nu(k^2+p^2+q^2)](t-\tau)}d\tau.$$

A last assumption consists in neglecting the time variation of μ_{kpq} in the above determination of θ. This yields for θ_{kpq} an expression proposed by Leith [399]

$$\theta_{kpq} = \frac{1 - e^{-[\mu_{kpq}+\nu(k^2+p^2+q^2)]t}}{\mu_{kpq} + \nu(k^2+p^2+q^2)}. \tag{7.20}$$

One can also notice that when t goes to infinity, θ_{kpq} is equivalent to $1/[\mu_{kpq} + \nu(k^2+p^2+q^2)]$.

This approximation is the Eddy-Damped Quasi-Normal Markovian approximation (E.D.Q.N.M). The time θ_{kpq} is characteristic of the relaxation (towards a quasi-equilibrium) by nonlinear transfers and molecular viscosity of $\langle \hat{u}(\vec{k})\hat{u}(\vec{p})\hat{u}(\vec{q})\rangle$. The final E.D.Q.N.M. equation for the spectral tensor is for homogeneous turbulence without mean velocity (Lesieur [412])

$$\left(\frac{\partial}{\partial t} + 2\nu k^2\right)\hat{U}_{in}(\vec{k},t) = \int_{\vec{p}+\vec{q}=\vec{k}} d\vec{p}\theta_{kpq}(t)P_{ijm}(\vec{k})$$

$$[P_{nab}(\vec{k})\hat{U}_{jb}(\vec{p},t)\hat{U}_{ma}(\vec{q},t) - 2P_{mab}(\vec{p})\hat{U}_{ja}(\vec{q},t)\hat{U}_{bn}(\vec{k},t)]. \tag{7.21}$$

Let us write for instance the spectral E.D.Q.N.M. equation in the case of three-dimensional isotropic turbulence without helicity: taking the trace of Eq. (7.21), using Eqs. (5.84), (7.10) and (7.11), and noticing that

$$P_{ijm}(\vec{k})P_{bi}(\vec{k}) = P_{bjm}(\vec{k}),$$

one obtains

$$\left(\frac{\partial}{\partial t} + 2\nu k^2\right)E(k,t) =$$

$$\iint_{\Delta_k} dp\ dq\theta_{kpq}(t)\frac{k}{pq}b(k,p,q)E(q,t)[k^2E(p,t) - p^2E(k,t)]. \tag{7.22}$$

This is, as expected, the equation obtained from Eq. (7.13) after the eddy-damping and Markovianization procedures. The realizability of Eq. (7.22) can be easily obtained by noticing that the coefficient $a(k,p,q)$ is positive (see Orszag [553]).

7.4 Stochastic models

This is another point of view, due to Kraichnan [346] (see also Herring and Kraichnan [273]), which consists in replacing the Navier–Stokes equation (for which we cannot solve exactly the closure problem), by a set of modified equations having the same basic structural properties as Navier–Stokes (quadratic nonlinearity, nonlinear quadratic invariants, existence of truncated inviscid

equipartition solutions[4]), and for which the closure problem can be solved. Thus, instead of considering Navier–Stokes equation, one replaces it by a set of N equations coupling N fictitious random velocity fields $\underline{\hat{u}}^{\alpha}(\vec{k},t)$, in the following way[5]

$$\left(\frac{\partial}{\partial t}+\nu k^2\right)\hat{u}_i^{\alpha}(\vec{k},t)=-\frac{i}{N}k_m P_{ij}(\vec{k})\int_{\vec{p}+\vec{q}=\vec{k}}\Phi_{\alpha\beta\sigma}\hat{u}_j^{\beta}(\vec{p},t)\hat{u}_m^{\sigma}(\vec{q},t)d\vec{p} \quad (7.23)$$

where the $\Phi_{\alpha\beta\sigma}$ are N^3 Gaussian random functions of time, symmetric with respect to the permutations of α,β,σ, of zero mean, having the same statistical properties, and which may also depend on the wave numbers triad $\vec{k},\vec{p},\vec{q}$. It may be shown (Frisch et al. [220]) that in the limit $N\to\infty$, the various $\underline{\hat{u}}^{\alpha}$ become independent and Gaussian, and that their energy spectrum satisfies a closed integro-differential equation which depends on the choice of $\Phi_{\alpha\beta\sigma}$: if $\Phi_{\alpha\beta\sigma}(t)$ is a white-noise Gaussian function of temporal correlation given by

$$\langle\Phi_{\alpha\beta\sigma}(t)\Phi_{\alpha\beta\sigma}(t')\rangle=2\theta_{kpq}(t)\delta(t-t'), \quad (7.24)$$

one recovers the same spectral equation as Eq. (7.21). Thus, though the "closure" and the "stochastic model" philosophies are different, they finally correspond to the same spectral evolution equations: the first method insists more on the physics of the departures from Gaussianity, while the second permits to keep the model along the same structural parapets as the Navier–Stokes equation. Both philosophies are complementary, and allow an understanding of which kind of performances can be expected (and which cannot) from the theory. It is evident for instance that small-scale intermittency will certainly be badly treated by the spatial stirring due to the random phases $\Phi_{\alpha\beta\sigma}$, and that the small-scale departures from the Kolmogorov law which can be predicted with the aid of intermittency theories (see Chapter 6) escape to the E.D.Q.N.M. On the other hand, this theory is able to make non-trivial predictions when applied to the important mathematical questions (on the existence of singularities for instance) or physical problems (helicity cascades, turbulent diffusion, backscatter, unpredictability, two-dimensional turbulence for instance) envisaged below.

When θ_{kpq} is taken equal to a constant θ_0, the particular E.D.Q.N.M. equation obtained is called the Markovian Random Coupling Model (M.R.C.M., proposed by Frisch et al. [221] for it corresponds to a *Markovian* version of an earlier model due to Kraichnan [346], the Random Coupling Model (R.C.M.),

[4] See Chapter 10.

[5] An alternative stochastic-model philosophy, based on a stochastic Langevin equation for the velocity, has also been introduced (see Leith [399] and Herring and Kraichnan [273]). It yields the same final spectral equations than the theories presented here.

obtained by taking $\Phi_{\alpha\beta\sigma}$ constant (that is independent of time and wave number, but random) in the stochastic model Eq. (7.23). The R.C.M. gives the same resulting equations as the Direct-Interaction Approximation (D.I.A., see Kraichnan [345]), introduced earlier by Kraichnan through formal diagrammatic expansions of the velocity field.[6] It is not a Markovian theory, and its spectral equations have a "time-memory", contrary to the E.D.Q.N.M. which has forgotten the past and is unable to give information on two-times velocity covariances. The R.C.M. (resp D.I.A.) introduces a Green's function formalism, in the following way: assume that Navier–Stokes equation possesses a forcing term $\hat{f}(\vec{k})$, and writes:

$$\left(\frac{\partial}{\partial t} + \nu k^2\right) \hat{u}(\vec{k}, t) = l(\hat{u}, \hat{u}) + \hat{f}(\vec{k}, t), \tag{7.25}$$

where l is a bilinear operator of $\hat{u}$. The Green's function operator g represents the linearized response $\delta\hat{u}$ of $\hat{u}$ to a perturbation $\delta\hat{f}$ of the force $\hat{f}$, and is solution of the linearized equation:

$$\left(\frac{\partial}{\partial t} + \nu k^2\right) g = l(g, \hat{u}) + l(\hat{u}, g) + I, \tag{7.26}$$

where I is the identity operator, with

$$\delta\hat{u}_i(\vec{k}, t) = \int_{-\infty}^{t} g_{ij}(\vec{k}, t, t')\delta\hat{f}_j(\vec{k}, t')dt'. \tag{7.27}$$

We will assume furthermore that the stirring force is a white noise in time. Hence, for homogeneous turbulence, the correlation of the forcing writes:

$$\langle\hat{f}_i(\vec{k}', t)\hat{f}_j(\vec{k}, t')\rangle = F_{ij}(\vec{k}, t)\delta(\vec{k} + \vec{k}')\delta(t - t'). \tag{7.28}$$

Therefore the D.I.A. spectral equations involve two tensors, the two-time spectral tensor and the average Green's function. They write (see Lesieur et al. [410], Leslie [432]):[7]

$$\left(\frac{\partial}{\partial t} + \nu k^2\right) \hat{U}_{in}(\vec{k}, t, t') =$$

$$\frac{1}{2}\int_{\vec{p}+\vec{q}=\vec{k}} d\vec{p} \int d\tau P_{ijm}(\vec{k})P_{lab}(\vec{k})\langle g_{nl}\rangle(\vec{k}, t', \tau)\hat{U}_{jb}(\vec{p}, t, \tau)\hat{U}_{ma}(\vec{q}, t, \tau)$$

[6] Leslie [432, p. 51] summarizes the various steps of the D.I.A.

[7] In these two references, the two-time velocity spectral tensor is defined in such a way that it corresponds to the complex conjugate $\hat{U}^*_{ij}(\vec{k}, t, t') = \hat{U}_{ij}(-\vec{k}, t, t')$ of the spectral tensor $\hat{U}_{ij}(\vec{k}, t, t')$ used here.

$$-\int_{\vec{p}+\vec{q}=\vec{k}} d\vec{p} \int d\tau P_{ijm}(\vec{k}) P_{lab}(\vec{p}) \langle g_{lm} \rangle (\vec{p}, t, \tau) \hat{U}_{ja}(\vec{q}, t, \tau) \hat{U}_{bn}(\vec{k}, t, \tau)$$

$$+\langle g_{nl} \rangle (\vec{k}, t', t) F_{il}(\vec{k}, t). \tag{7.29}$$

$$\left(\frac{\partial}{\partial t} + \nu k^2 \right) \langle g_{in} \rangle (\vec{k}, t, t') =$$

$$-\int_{\vec{p}+\vec{q}=\vec{k}} d\vec{p} \int d\tau P_{ijm}(\vec{k}) P_{lab}(\vec{p}) \langle g_{ml} \rangle (\vec{p}, t, \tau) \langle g_{bn} \rangle (\vec{k}, \tau), t')$$

$$\hat{U}_{aj}(\vec{q}, t, \tau) + P_{in}(\vec{k}) \delta(t - t'). \tag{7.30}$$

Now, the following operations are performed: (a) "Markovianize" the above D.I.A. equations in the sense that the average Green's function $\langle g_{in}(\vec{k}, t, \tau \rangle$ is replaced by $\theta_0 P_{in}(\vec{k}) \delta(t - \tau)$; (b) remark that

$$\frac{\partial}{\partial t} U_{in}(\vec{k}, t, t) = \frac{\partial}{\partial t} [U_{in}(\vec{k}, t, t') + U_{ni}(-\vec{k}, t, t')]_{t'=t}.$$

One recovers the M.R.C.M. spectral evolution equation Eq. (7.21) (with $\theta_{kpq} = \theta_0$), with a forcing term $P_{nl}(\vec{k}) F_{il}(\vec{k}, t)$.

As we will see below, the D.I.A. does not yield a Kolmogorov $k^{-5/3}$ inertial range, but a $k^{-3/2}$ range instead. One of the reasons for that is the non-invariance of the theory under random Galilean transformations. Kraichnan [347] proposed a heuristic Lagrangian modification of D.I.A., which restores Galilean invariance, known as Lagrangian History Direct Interaction Approximation (L.H.D.I.A.). These theories are not widely utilized presently, and it is not certain that they improve other theories like the E.D.Q.N.M. for instance. More details on that can be found in Leslie [432]. A last model we will briefly present is Kraichnan's Test-Field Model (T.F.M.), see Kraichnan [353]. It is a Markovian model of the E.D.Q.N.M. type, that is satisfying Eq. (7.22), but with a relaxation time θ_{kpq} determined in a more sophisticated way than the simple relation Eq. (7.20): the T.F.M. evaluates θ_{kpq} by studying the triple correlations of an auxiliary velocity field, the "test-field", transported by the turbulence itself. Such an analysis poses difficulties due to the loss of incompressibility of the test-field, which has to be separated into a solenoidal and compressible component. After various "ad hoc" approximations, one finally obtains coupled equations for the evolution of θ_{kpq}. As shown by Herring et al. [280], the TFM time reduces to the simple E.D.Q.N.M. time Eq. (7.20) in the inertial range. Moderate Reynolds number direct-numerical simulations of turbulence seem to indicate a very good agreement with the T.F.M. calculations (Herring et al. [274]). It is nevertheless not evident that the further "price" paid for the use of the T.F.M. instead of the E.D.Q.N.M. is really worthwhile.

Figure 7.1 is an attempt to draw a map of this complicated closure world and of the routes which link the various theories: the double arrows indicate an exact result, while the simple lines correspond to an approximation or a modification. We will propose three possible trips starting from the Navier–Stokes equation, trips employing circuits which will be shown to communicate:

• trip A
The hiker takes the "moments equations" way, and from there goes either to the Q.N. approximation (by discarding the fourth-order cumulants $\langle uuuu \rangle_c$), or to the E.D.Q.N. approximation (by setting these cumulants equal to $-\mu\langle uuu \rangle$). In any case he can commute easily from the Q.N. to the E.D.Q.N., by changing νk^2 into $\mu_k + \nu k^2$. With the aid of a "Markovianization", he will go from the E.D.Q.N. to the E.D.Q.N.M. The same operation would have led him from the Q.N. to the Q.N.M. (Quasi-Normal Markovian approximation), that he could also have reached from the E.D.Q.N.M., by simply setting $\mu_k = 0$. Notice that the Q.N.M. was extensively studied by Tatsumi and colleagues [676, 677]. We will discuss it by comparison with the E.D.Q.N.M. later on. Notice also that attached to the E.D.Q.N.M. is the T.F.M., which has a special status for the time θ_{kpq}.

• trip B
The hiker takes the difficult path of the Feynman formal diagrammatic expansions: then he has the choice between the already mentioned Renormalization-Group Techniques (R.N.G.) (see below), or the D.I.A. From there he can go to the L.H.D.I.A., by restoring the random Galilean invariance.

• trip C
The hiker modifies the nonlinear terms of the Navier–Stokes equation with the aid of Gaussian random phases $\Phi_{\alpha\beta\sigma}$, and goes to the Stochastic Models. Then he has several choices: taking the coupling phases satisfying Eq. (7.24) enables him to go to the E.D.Q.N.M. (and then rejoin the trip A). Taking the phases as random *variables* (and not *functions*) will permit him to go to the R.C.M. which, as already stressed, is identical to the D.I.A. This indicates a communication with the circuit B. A "Markovianization" of the R.C.M. at the level of the Green's function leads to the M.R.C.M., which could also have been reached from the E.D.Q.N.M. by letting $\theta_{kpq} \equiv \theta_0$. This provides a bridge to trip A. Finally, as already mentioned, the M.R.C.M. can also be obtained from the stochastic models by letting the random phases be a white noise with respect to time, but independent of the wave numbers.

It is of course difficult to give a definitive answer to the question of what is the "best" analytical theory to use. From a personal experience of these tools, which will be developed in the following sections and chapters, I

would suggest that if the turbulence is isotropic (in three- or two-dimensions), the E.D.Q.N.M. is certainly an excellent tool to predict the energy transfers between various modes and the high Reynolds number behaviours, at low numerical cost (compared with the numerical direct or large-eddy-simulations). The M.R.C.M. will be its faithful ally, allowing qualitative analytical predictions about the existence of inertial ranges, and the possible loss of regularity for vanishing viscosity or diffusivity. Some problems where we need information on two-point correlations will require the use of the D.I.A. (which is not good at high Reynolds number). In non-isotropic situations such as the collapse of stably-stratified turbulence, the anisotropic E.D.Q.N.M. with the isotropic form of the time θ_{kpq} could also allow a first step towards the understanding of the problem. This is nevertheless not true for rotating turbulence, where, as shown in Cambon et al. [94], the only effect of the rotation within the E.D.Q.N.M. is to modify θ in a non-trivial way. Such modifications require looking to higher-order moments in the hierarchy, following methods developed e.g. by André [6] and Legras [396].

However, it seems now that the increased computing possibilities offered by the present super-computers will render possible a direct calculation of the large scales of the flows and of the inhomogeneities and anisotropies they contain, the small isotropic scales being modelled with the aid of the closures, for instance the E.D.Q.N.M. This corresponds to a certain type of LES which will be presented below in the book. For these reasons there does not seem to be an urgency to find a new closure of the type presented above, since it would behave essentially in the same way as its predecessors. In the so-called "shell models", approximate isotropic spectral equations are written involving a given mode k_n and its neighbours, the coefficients being chosen so as to conserve quadratic invariants. But these models are too rough with respect to the rich possibilities offered by the E.D.Q.N.M., in particular as far as scale separation and non-local effects are concerned.

The rest of this Chapter will be devoted to analytical and numerical results concerning the closure spectral equations in the case of isotropic three-dimensional turbulence. Other situations will be envisaged in the following chapters.

PART B: THE RESULTS

7.5 Closures phenomenology

It is possible to derive a simple phenomenological analysis allowing one to predict the inertial-range exponents obtained in the frame of the closures. These predictions will of course be checked numerically later on, but they

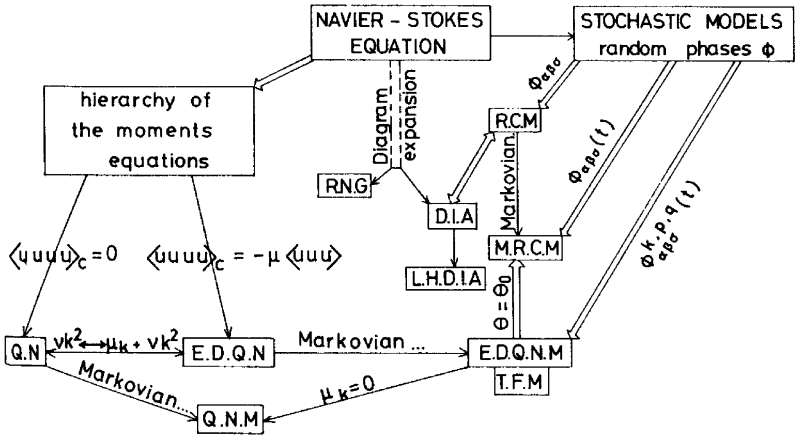

Figure 7.1. Map of the analytical statistical theories and stochastic models land (see text for comments).

constitute a first step towards an analytical understanding of these theories, which in turn will enable us to understand more deeply the phenomenological analysis of turbulence presented in Chapter 6 . We will concentrate on isotropic turbulence without helicity. In this case, Eq. (7.22) permits to calculate the E.D.Q.N.M. energy flux

$$\Pi(K) = \int_K^\infty dk \iint_{\Delta_k} dp\ dq \theta_{kpq}(t)$$

$$\frac{k}{pq} b(k,p,q) E(q,t)[k^2 E(p,t) - p^2 E(k,t)]. \tag{7.31}$$

We are looking for an inertial range, where viscous effects can be neglected, and where $\Pi(K)$ will be independent of K and equal to ϵ. It has been shown by Kraichnan [354] (see also André and Lesieur [7]) that, within the E.D.Q.N.M. or the T.F.M. theories, and in the Kolmogorov inertial range, wave numbers in a spectral vicinity of one decade about K participate in more than 80% of the energy flux across K. This allows us to assume that, to a first approximation, the integral (7.31) is dominated by wave numbers k, p, q, of order K (i.e. comprised for instance between $K/10$ and $10K$). Assuming also that the quantities under the integral vary as powers of k, p, q, and remembering a remark already made in Chapter 6 that $\int_{K/10}^{K} E(k)dk$ is of the order of $KE(K)$, we finally obtain

$$\Pi(k) \sim \theta(k) k^4 E(k)^2 \tag{7.32}$$

where $\theta(k)$ is the value taken by θ_{kpq} for $k = p = q$. We notice also that if k is smaller than the Kolmogorov dissipative wave number, and for large

times, $\theta(k)$ is of the order of $a_1[k^3E(k)]^{-1/2}$, where a_1 is defined in Eq. (7.17). Inserting this value in Eq. (7.32) and looking for solutions such that $\Pi(k) \equiv \epsilon$ yields

$$E(k) \sim (a_1\epsilon)^{2/3}k^{-5/3}.$$

This shows that the E.D.Q.N.M. leads to a Kolmogorov $k^{-5/3}$ energy cascade,[8] and that the Kolmogorov constant is proportional to $a_1^{2/3}$. More precisely, one can show that

$$C_K \approx 2.76a_1^{2/3} \tag{7.33}$$

(see e.g. Métais and Lesieur [496]). Taking $a_1 = 0.36$ yields $C_K = 1.40$.

In the case of the M.R.C.M., the time $\theta(k)$ is equal to θ_0, and the above analysis gives

$$E(k) \sim \left(\frac{\epsilon}{\theta_0}\right)^{1/2} k^{-2}. \tag{7.34}$$

It is not the Kolmogorov law, which is not surprising since θ_0 enters now as an independent parameter. The -2 power is here equivalent to the actual $-5/3$ power of Kolmogorov's theory. It will be seen later on that the M.R.C.M. is nevertheless a very good tool which permits analytical calculations and predicts the existence and direction of the cascades.

For the R.C.M. (resp. D.I.A.), and though Eq. (7.31) is not exact, Eq. (7.32) can still be shown to be valid, $\theta(k)$ being now the relaxation time of the Green's function. In the inertial range, this time is of order $1/(v_0k)$, where v_0 is the r.m.s. velocity (Kraichnan [345], Lesieur et al. [410]). This is different from the E.D.Q.N.M. where the time $\theta(k)$ can also be written as $(1/kv_k)$, v_k being the local velocity $[kE(k)]^{1/2}$. Therefore the *D.I.A.* inertial range is

$$E(k) \sim (\epsilon v_0)^{1/2}k^{-3/2}. \tag{7.35}$$

It has been shown by Kraichnan [348] that the existence of a D.I.A. inertial-range exponent differing from $-5/3$ was related to the non-invariance of the model by random Galilean transformations: indeed this non-invariance implies that the large eddies have a direct action on the small eddies, which is in contradiction with the locality assumption implicitly contained in the Kolmogorov theory. So a necessary condition for obtaining the $k^{-5/3}$ law is to satisfy the random Galilean invariance principle. This is *not* a sufficient condition, as shown by the example of the M.R.C.M., which is random Galilean invariant (at the level of the final spectral equation, not of the stochastic model itself, cf. Lesieur [412]) but does not admit the $-5/3$ inertial range.

The case of the Q.N.M. is different: this theory seems to be quite far from the actual physics of turbulence, since only molecular viscosity damps the third-order moments. Nevertheless the Markovianization guarantees the

[8] Which was to be expected as soon as $\theta(k)$ is a function of k and $E(k)$ only.

realizability, though the skewness factor (calculated from Eq. (6.76)) reaches values far superior to the experimental values (cf. Tatsumi et al. [676], Frisch et al. [225]). Actually, the latter authors have shown that, in the limit of zero viscosity (with the *type S* initial conditions defined in Chapter VI), the skewness factor of the Q.N.M. blows up with the enstrophy, while for the E.D.Q.N.M. it remains bounded. The other interesting particularity of the Q.N.M. is to exhibit two inertial ranges: indeed the time θ_{kpq} can then be obtained from Eq. (7.20) by setting μ_{kpq} equal to zero. For a given time t, one can therefore introduce a wave number

$$k_t = \frac{1}{(\nu t)^{1/2}} \tag{7.36}$$

which is such that

$$\theta_{kpq} = \begin{cases} t, for & k \ll k_t \\ 1/\nu(k^2+p^2+q^2), & \text{for } k \gg k_t \end{cases}$$

and Eq. (7.32) leads to

$$\Pi(k) \sim tk^4 E(k)^2; \quad E(k) \sim \left(\frac{\epsilon}{t}\right)^{1/2} k^{-2} (k \ll k_t), \tag{7.37}$$

$$\Pi(k) \sim \frac{1}{\nu} k^2 E(k)^2; \quad E(k) \sim (\epsilon\nu)^{1/2} k^{-1} (k \gg k_t). \tag{7.38}$$

These two inertial ranges separated by k_t are actually well recovered in the numerical resolution of the Q.N.M. spectral equation done by Frisch et al. [225], as is shown in Figure 7.2. The same inertial ranges exist in the Q.N. approximation, as recalled in Tatsumi [677]. In this reference, are also presented high Reynolds number Q.N.M. calculations (independent of the above quoted calculations done by Frisch et al. [225]) which display without ambiguity both k^{-2} and k^{-1} ranges. Notice finally that the k^4 infrared ($k \to 0$) behaviour of the spectrum appearing in Figure 7.2 will be explained below.

7.6 Decaying isotropic non-helical turbulence

The closure equations of the Markovian type can be solved numerically in the isotropic case, even at very high Reynolds numbers $R = v_0/\nu k_i(0)$ (v_0 and $k_i(0)$ are the initial values of the r.m.s. velocity and of the wave number where the energy spectrum peaks. The relative simplicity of the numerical resolution, as compared to the direct simulations of the Navier- Stokes equation itself, comes from the existence of one spatial variable (the wave number k), and from the fact that the energy spectrum varies smoothly with k. This allows us to take a logarithmic discretization for k

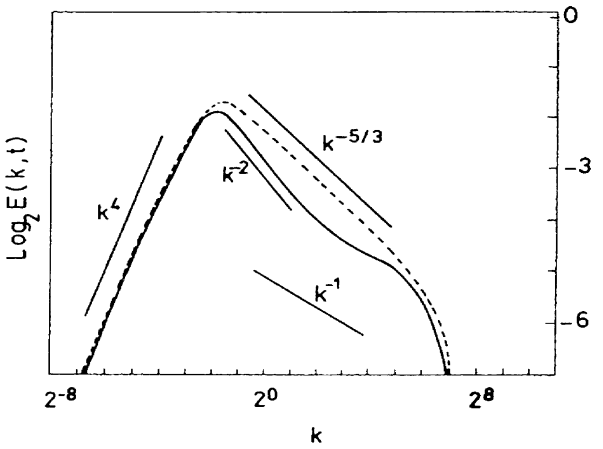

Figure 7.2. Decaying energy spectra in (a) an E.D.Q.N.M. calculation (dashed line); (b) a Q.N.M. calculation (straight line). In the latter case, the two k^{-2} and k^{-1} inertial ranges are clearly displayed (from Frisch et al. [225], courtesy *J. Fluid Mech.*).

$$k_L = \delta k 2^{L/F} \tag{7.39}$$

where δk is the minimum wave number, and F the number of wave numbers per octave. In the following results (due to André and Lesieur [7], and Lesieur and Schertzer [413]), the third-order velocity correlations relaxation rate μ_k is chosen according to Eq. (7.17), with $a_1 = 0.36$, which corresponds to a Kolmogorov constant of 1.4. These calculations take $F = 4$, and a maximum wave number k_c related to $k_i(0)$ by

$$\frac{k_c}{k_i(0)} = 8R^{3/4} \tag{7.40}$$

following the law equation (6.61). The numerical factor 8 has been adjusted in the calculation, so as to take into account the dissipative range in the wave-number span. For instance, a calculation with 65 points taking $\delta k = 1/4$ and $k_i(0) = 1$ has a maximum wave number $k_c = 2^{14}$ and an initial Reynolds number of 26000. The nonlinear transfer of Eq. (7.22) can be calculated with a numerical scheme developed by Leith [399] which conserves exactly the quadratic invariants (kinetic energy, helicity, enstrophy in two-dimensions) when applied to the E.D.Q.N.M. spectral equations. The time-differencing in Eq. (7.22) is approximated by a forward scheme, with a stability condition

$$\nu k_{\max}^2 \delta t \leq 1. \tag{7.41}$$

7.6.1 Non-local interactions

Due to the logarithmic discretization, a problem arises nevertheless when evaluating the kinetic-energy transfer: indeed the "elongated" triads (k, p, q) whose ratio of the minimum to the maximum wave number is lower than $2^{1/F} - 1$ or $1 - 2^{-1/F}$ are not taken into account in the discretization (except for the isosceless interactions $k = p$ or $k = q$). This may be at the origin of non-negligible errors, especially for two-dimensional turbulence where, as will be seen in Chapter 8, the non-local interactions play a major role in the enstrophy cascade. One possible way of getting rid of this difficulty is to discard all the remaining non-local interactions in the transfer computed numerically, calculate analytically the transfers corresponding to the non-local interactions, and reintroduce them in the calculation. Details on this method are given in Lesieur and Schertzer [413]. It applies also to two-dimensional turbulence (Pouquet et al. [584], Basdevant et al. [37]). We will only give here the general approach of the method: to simplify, we assume that the two numbers $2^{1/F} - 1$ and $1 - 2^{-1/F}$ are equal (for $F = 4$, they are respectively 0.19 and 0.16) to a, and that a is small compared with 1. Therefore, as shown in Lesieur and Schertzer [413], the non-local transfers $T_{NL}(k, t)$ due to triad-interactions in Eq. (7.22) such that

$$\inf(k, p, q)/\sup(k, p, q) \leq a \tag{7.42}$$

can be written as

$$T_{NL}(k, t) = -\frac{\partial \Pi_{NL}(k, t)}{\partial k} \tag{7.43}$$

with

$$\Pi_{NL}(k, t) = \Pi^{+}_{NL}(k, t) - \Pi^{-}_{NL}(k, t) \tag{7.44}$$

$$\Pi^{+}_{NL}(k, t) = 2 \int_0^{ak} dq \int_k^{k+q} dk' \int_{k'-q}^{k} S(k', p, q) dp \tag{7.45}$$

$$\Pi^{-}_{NL}(k, t) = 2 \int_0^{k} dk' \int_{\sup(k,k'/a)}^{\infty} dp \int_{p-k'}^{p} S(k', p, q) dq. \tag{7.46}$$

$S(k, p, q)$ is the integrand in the r.h.s. of Eq. (7.22), symmetrized with respect to p and q. The non-local flux $\Pi^{+}_{NL}(k, t)$ corresponds to a "semi-local" flux through k in the sense that the triads involved are such that $q \ll p \approx k < k'$. Then expansions with respect to the small parameters q/k' in Eq. (7.45) and k'/p in Eq. (7.46) can be performed (cf. Kraichnan [348, 354], Lesieur and Schertzer [413], and Métais [490]). These expansions are somewhat tedious, but can be appreciably simplified, using the two following results derived in Lesieur and Schertzer [413] and concerning the calculation of Π^{+}_{NL} and Π^{-}_{NL}:

– First result ($q \ll k$): if, for $q \ll k$, $(kq/p)S(k, p, q)$ is expanded in (q/k) as $S_1[E(k), E(q)]g_1(y)$, then

$$\Pi_{NL}^{+}(k,t) = 2\int_0^{ak} qdqS_1[E(k),E(q)]\int_0^1 d\phi\int_\phi^1 g_1(y)dy$$

– Second result ($k \ll p$): if, for $k \ll p$, $(kp/q)S(k,p,q)$ is expanded in (k/p) as $S_2[E(p),E(k)]g_2(z)$, then

$$\Pi_{NL}^{-}(k,t) = 2\int_0^{k} dk'\int_{\sup(k,k'/a)}^{\infty} S_2[E(p),E(k')]dp\int_0^1 g_2(z)dz$$

Actually, these results are valid also for the non-local fluxes of other quantities such as the helicity or a passive scalar (see below). Notice also that generally the time θ_{kpq} is not expanded. In the three-dimensional isotropic case without helicity for instance, we have[9]

$$\Pi_{NL}^{+}(k,t) = \frac{2}{15}\int_0^{ak}\theta_{kkq}q^2E(q)dq\left[kE(k)-k^2\frac{\partial E}{\partial k}\right] + \frac{2}{15}\int_0^{ak}\theta_{kkq}q^4dq\frac{E^2(k)}{k} \tag{7.47}$$

$$\Pi_{NL}^{-}(k,t) = -\frac{2}{15}\int_0^{k}k'^2E(k')dk'\int_{\sup(k,k'/a)}^{\infty}\theta_{k'pp}\left[5E(p)+p\frac{\partial E}{\partial p}\right]dp + \frac{14}{15}\int_0^{k}k'^4dk'\int_{\sup(k,k'/a)}^{\infty}\theta_{k'pp}\frac{E(p)^2}{p^2}dp \tag{7.48}$$

The physics of these terms will be interpreted later. The non-local transfer is then calculated from Eqs. (7.47) and (7.48). Notice that with this "flux form", these non-local transfers are energy conservative provided $\Pi_{NL}(0,t) = 0$.

The non-local energy transfers derived from Eqs. (7.47) and (7.48) are then[10]

$$T_{NL}(k,t) = \frac{2}{15}\left[4E(k)+2k\frac{\partial E}{\partial k}+k^2\frac{\partial^2 E}{\partial k^2}\right]\int_0^{ak}\theta_{kkq}q^2E(q)dq$$

[9] The non-local fluxes given below have been carefully checked by Métais [490], and correspond to the notations of the present book for the energy spectrum (density of $(1/2)\langle\vec{u}^2\rangle$). The reader is warned that an error of a factor 2 is contained in one of the terms of the analogous expressions given in Lesieur and Schertzer [413].

[10] These non-local energy transfers can also be obtained directly from non-local expansions of the transfer term $T(k,t)$ integrated on the domain satisfying the condition Eq. (7.42). The calculation is equivalent, as noticed in Lesieur and Schertzer [413], but is longer since a second-order expansion in a is then needed. In fact, it has been verified by Métais [490] that the two methods give the same result.

$$-\frac{4}{15}\left[3E(k)+k\frac{\partial E}{\partial k}\right]\frac{E(k)}{k^2}\int_0^{ak}\theta_{kkq}q^4dq$$
$$-\frac{2}{15}\theta_{k,k,ak}a^5k^3E(k)^2$$
$$-\frac{2}{15}\theta_{k,k,ak}a^3k^3E(ak)\left[E(k)-k\frac{\partial E}{\partial k}\right]$$
$$-\frac{2}{15}k^2E(k)\int_{k/a}^{\infty}\theta_{kpp}\left[5E(p)+p\frac{\partial E}{\partial p}\right]dp$$
$$+\frac{14}{15}k^4\int_{k/a}^{\infty}\theta_{kpp}\frac{E(p)^2}{p^2}dp. \tag{7.49}$$

7.6.2 Energy spectrum and skewness

The numerical resolution of Eq. (7.22) consists then in solving the equation

$$\left(\frac{\partial}{\partial t}+2\nu k^2\right)E(k,t)=T_{NL}(k,t)+T_L(k,t) \tag{7.50}$$

where $T_L(k,t)$ is the local transfer calculated numerically with Leith's numerical scheme mentioned above. In fact, calculations which neglect the non-local transfers do not, for $F>4$, depart very much from the complete calculation. The non-local expansions are anyhow extremely useful to understand the infrared dynamics, and also to provide subgrid-scale parameterizations, as will be seen in Chapter 12.

Figure 7.3 (taken from André and Lesieur [7]) shows on a log-log plot the time-evolving kinetic-energy spectra, initially peaked in the vicinity of $k=k_i(0)$. The large-scale Reynolds number $R_{k_i(0)}$ (see definition below) is 40,000: one can clearly see the spreading of the spectrum towards large wave numbers, due to nonlinear interactions; a $k^{-5/3}$ spectrum establishes after a time of about $t_*=5/v_0k_i(0)$. Since the initial energy spectrum is strongly peaked at $k_i(0)$, the time t_* is also of the order of $5D(0)^{-1/2}$ (it is actually of $5.6D(0)^{-1/2}$ in this calculation). For $t>t_*$, the spectrum decays self-similarly following what can be checked to be the law equation (6.68). Figure 7.4 (also taken from André and Lesieur [7]) shows the asymptotic tendency of the kinetic-energy time evolution: when the Reynolds number exceeds a few thousands, the kinetic energy reaches an asymptotic state where it is conserved for $t<t_*$ and then dissipated at a finite rate for $t>t_*$. Finally, Figure 7.5 shows, in the same calculation as that of Figure 7.4, the time-evolution of the velocity-derivative skewness factor (calculated from Eq. (6.76)), which also reaches at high Reynolds number an asymptotic evolution where it is conserved for $t>t_*$, as predicted in Chapter 6. The value of the skewness for

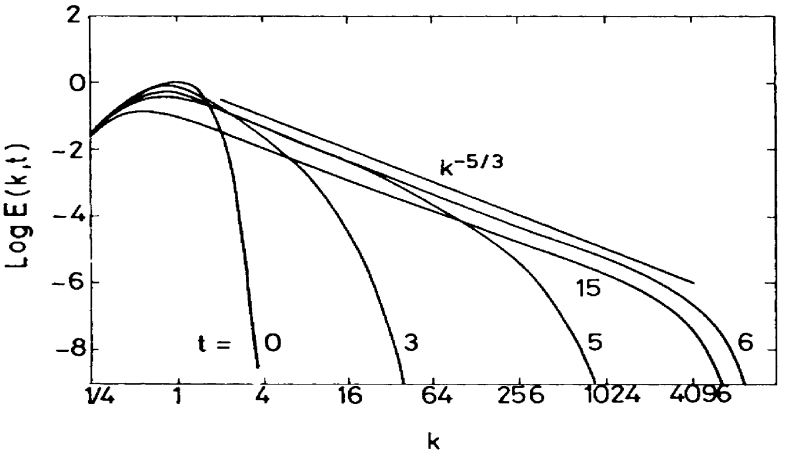

Figure 7.3. Time evolution at initial large-scale Reynolds number 40,000 of a freely-evolving three-dimensional kinetic energy spectrum, within the E.D.Q.N.M. theory (from André and Lesieur [7], courtesy *J. Fluid Mech.*).

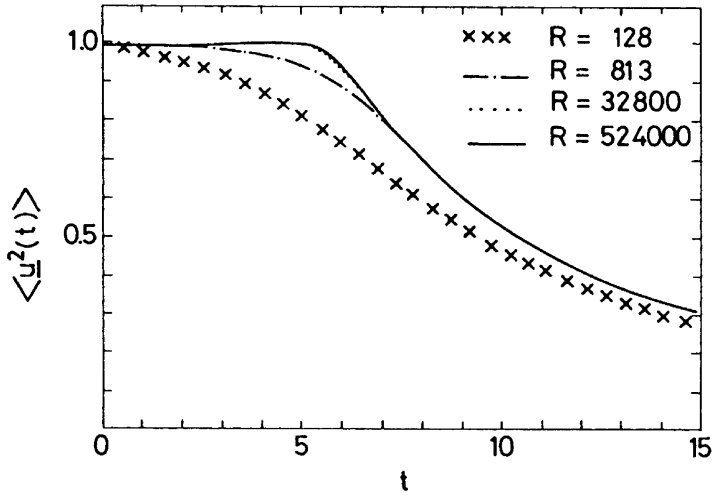

Figure 7.4. Time evolution of the kinetic energy at different initial Reynolds numbers, in decaying E.D.Q.N.M. calculations performed by André and Lesieur [7] (courtesy *J. Fluid Mech.*).

$t > t_*$ is equal to 0.5, close to the value found in previously-reported DNS, and not far from the 0.4 value found experimentally. This is a further argument in favor of the E.D.Q.N.M. theory which, once its adjustable constant a_1 arising in Eq. (7.17) has been chosen to fit the Kolmogorov constant, predicts the velocity-derivative skewness factor satisfactorily. It will be shown analytically below that the E.D.Q.N.M. skewness remains finite for $t < t_*$ when the viscosity goes to zero. The abrupt decrease of the skewness for $t > t_*$ may, from Chapter 6, be explained in the following manner: before t_*, still in the limit of zero viscosity, one may assume that the skewness obeys Euler equation, with a kinetic-energy spectrum decreasing rapidly at infinity. At $t = t_*$, the "Euler skewness" would fall to 0, corresponding to the formation of a $k^{-5/3}$ spectrum extending to infinity. In fact, the skewness for $t > t_*$ is now determined by the viscous balance Eq. (6.77) and the shape of the spectrum in the dissipation range, and has no reason to be equal to the Euler value just before t_*. In André and Lesieur's [7] calculation, the skewness peak value is 0.75.

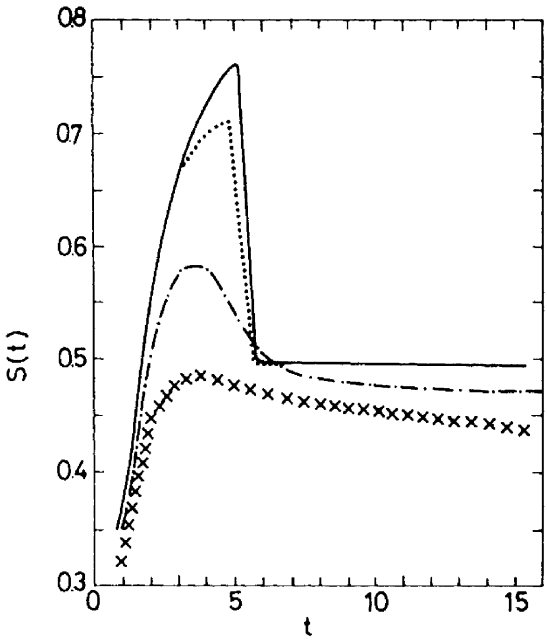

Figure 7.5. Time evolution of the skewness factor at different Reynolds numbers (same conditions as in Figure 7.4, from André and Lesieur [7], courtesy *J. Fluid Mech.*).

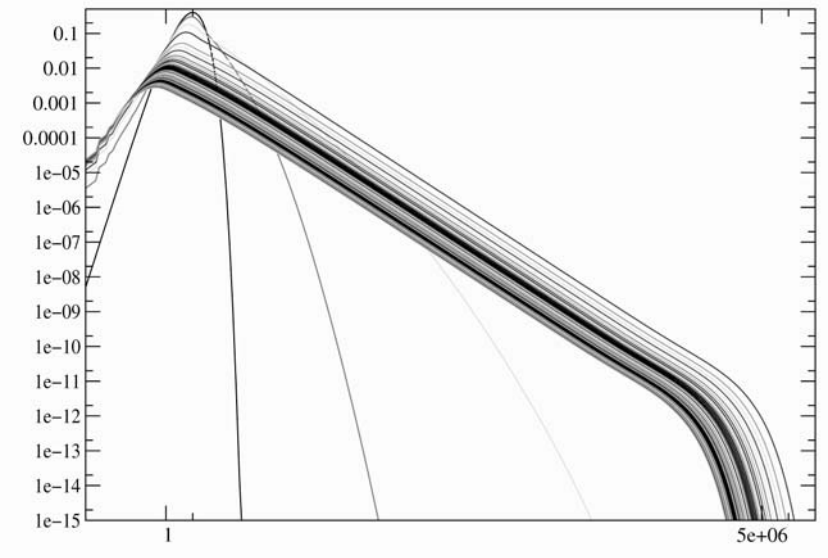

Figure 7.6. Decaying E.D.Q.N.M. calculation at very high Reynolds number($R_{k_i(0)} \approx 1.70 \times 10^9$).

More recent E.D.Q.N.M. calculations at higher Reynolds number carried out by Lesieur and Ossia [428] (see also Lesieur et al. [431]) indicate a maximum skewness value of 1.132 followed by a plateau of 0.547. In these calculations (done with $F = 8$ on a PC Linux machine) the coefficient 8 arising in Eq. (7.40) has been replaced without problems by 1, which permits to increase substancially the Reynolds number. The initial kinetic-energy spectrum is

$$E(k,0) = A_s k^s \exp\left[-\frac{s}{2}\frac{k^2}{k_i(0)^2}\right], \tag{7.51}$$

A_s being a normalization constant such that $\int_0^{k_{\max}} E(k,0)dk = \frac{1}{2}v_0^2 = \frac{1}{2}$. The large-scale Reynolds number is $R_{k_i(0)} = v_0/\nu k_i(0)$. Figure 7.6 shows on a log-log plot the kinetic-energy spectrum evolution (25 curves) in one of these simulations at $R_{k_i(0)} \approx 1.70 \times 10^9$. The initial infrared slope of the energy spectrum is $s = 8$. One sees an infrared backscatter with a spectral slope close to k^4 (see below). In the ultraviolet range, the spectrum develops a slope which is close to $-5/3$ along about five decades. As remarked in Lesieur and Ossia [428], the Taylor-microscale based Reynolds number at the end of the run (100 initial turnover times $[v_0 k_i(0)]^{-1}$) is 72600, which is huge! It is of interest to look on a semi-log plot at the corresponding compensated energy spectrum defined by Eq. (6.70) (Figure 7.7). In the figure, $K_* = kl_d$. Except for

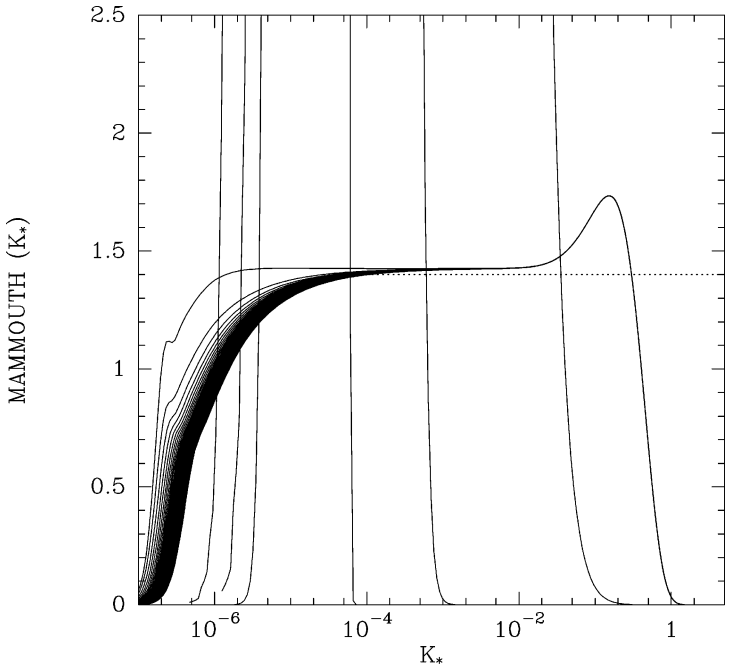

Figure 7.7. Same run as Figure 7.6: Kolmogorov compensated kinetic-energy spectrum evolution (in dissipative units).

the initial times (vertical lines), the curves do take a mammoth shape, whose rear advances gradually. The plateau is equal to the Kolmogorov constant C_K. At the end of the evolution, the exact $k^{-5/3}$ inertial range extends on less than two decades. On the other hand, there is a very well-marked pre-dissipative bump. The high k part of the spectrum (composed of the inertial range, the bump and the dissipative range) exhibits a very good self-similarity, with a perfect superposition of the compensated spectra.

Let us mention that forced E.D.Q.N.M. calculations are presented in Chapter 11 in the context of predictability studies.

7.6.3 Enstrophy divergence and energy catastrophe

All the numerical three-dimensional isotropic evolving E.D.Q.N.M. calculations show after the critical time t_* a behaviour characterized by a finite dissipation of energy and a constancy of the skewness factor, agreeing well with the phenomenology of Chapter 6.

The last consequence which can be drawn from Figure 7.4 is that at vanishing viscosity the enstrophy blows up at t_*: indeed, we recall from Eq. (6.8)

that in freely-evolving turbulence (without external forces), the kinetic-energy dissipation rate is equal to

$$\epsilon = -\frac{1}{2}\frac{d}{dt}\langle \vec{u}^2 \rangle = 2\nu D(t) \tag{7.52}$$

where $D(t)$ is the enstrophy. So the fact that kinetic energy is conserved at vanishing viscosity for $t < t_*$, and dissipated at a finite rate afterwards, implies that the enstrophy diverges at t_* in the limit of zero viscosity: this is not surprising, since we have already seen that a Kolmogorov $k^{-5/3}$ spectrum appears at $t = t_*$; for vanishing viscosity the Kolmogorov wave number k_d defined in Eq. (6.39) goes to infinity, and the total enstrophy diverges with $\int^{k_d} k^{1/3} dk$. The divergence of the enstrophy at t_* cannot be proved exactly analytically in the frame of the E.D.Q.N.M., but an exact result can be derived with the M.R.C.M., as demonstrated in Lesieur [412] and André and Lesieur [7]: by multiplication of Eq. (7.22) by k^2, integration over k from zero to infinity, and the exchange of the (k, p) variables in the $E(q)E(k)$ term, one obtains

$$\frac{dD}{dt} = \int \frac{k^2}{q}(k^2 - p^2)(xy + z^3)\theta_{kpq} E(p)E(q) dp dq dk - 2\nu \int_0^\infty k^4 E(k) dk. \tag{7.53}$$

We start initially with *type S* conditions (see Chapter 6) in the Euler case. A symmetrization with respect to p and q, and the change of variable $k \to x, dk = -(pq/k)dx$, yields

$$\frac{dD}{dt} = \frac{1}{2}\int_0^{+\infty}\int_0^{+\infty} p^2 q^2 E(p)E(q) \int_{-1}^{+1} \theta_{kpq}(1 - x^2) dx dp dq$$

$$-\{\text{a term which would be zero if } \theta_{kpq} \text{ were an even function of}$$

$$x \text{ for } p \text{ and } q \text{ fixed}\}. \tag{7.54}$$

Thus, if $\theta_{kpq} \equiv \theta_0$, Eq. (7.54) becomes

$$\frac{dD}{dt} = \frac{2}{3}\theta_0 D^2 \tag{7.55}$$

whose solution is

$$D(t) = \frac{3}{2\theta_0}\frac{1}{t_* - t} \tag{7.56}$$

$$t_* = \frac{3}{2D(0)\theta_0}. \tag{7.57}$$

This result shows analytically that whithin the M.R.C.M. the enstrophy also diverges at a critical time t_* (of course different from the critical time found

numerically in the E.D.Q.N.M.). Note that the replacement of θ_{kpq} by θ_{00q} in Eq. (7.53) (which is extremely arbitrary here, but will be shown to be physically plausible when studying the passive scalar diffusion) will give an enstrophy evolution equation of the type

$$\frac{dD}{dt} \sim D^{3/2} - 2\nu P(t) \tag{7.58}$$

which, when $\nu \to 0$, will blow up at a time t_* proportional to $D(0)^{-1/2}$. Notice also, as stressed by Orszag [553], that a calculation similar to the analysis leading to Eq. (7.55) was performed by Proudman and Reid [590] in the Quasi-Normal case. The resulting equation for the enstrophy is

$$\frac{d^2D}{dt^2} = \frac{2}{3}D^2,$$

as the reader may easily check using Eq. (7.13).

All these results go in favour of the same singular behaviour for the decaying Navier–Stokes equation in the limit of zero viscosity: this divergence of the enstrophy, due to the stretching of vortex filaments by turbulence, would be accompanied by the abrupt formation of the Kolmogorov $k^{-5/3}$ spectrum. The further evolution would be characterized by a finite dissipation of kinetic energy and a constancy of the skewness factor. The rigourous derivation of these conjectures, if correct, would certainly constitute a major breakthrough in the theory of isotropic turbulence. Notice finally that the value of $5.6D(0)^{-1/2}$ predicted for t_* by the E.D.Q.N.M. calculation of André and Lesieur [7] is not far from the value predicted in Eq. (6.80) assuming a constant skewness factor of 0.4.

A last remark concerning these enstrophy equations refers to the Q.N.M. approximation and is developed in Frisch et al. [225]: from Eq. (7.55), the enstrophy equation of this latter theory is (when $\nu \to 0$)

$$\frac{dD}{dt} = \frac{2}{3}tD^2 \tag{7.59}$$

since the Q.N.M. θ_{kpq} time is then equal to t (for a fixed t, the wave number k_t introduced in Eq. (7.36) goes to infinity at vanishing viscosity). Therefore the enstrophy blows up at $t_* = [3/D(0)]^{1/2}$, as can be shown easily by replacing in Eq. (7.59) the variable t by t^2. Since in the early stage of evolution (that is for $t < t_*$) the skewness factor is, from Eq. (6.77), proportional to $D^{-3/2}(dD/dt)$, it will grow like $tD^{1/2}$ and become infinite with the enstrophy. In the E.D.Q.N.M. on the contrary, it can be shown (see André and Lesieur [7]) that $D^{-3/2}(dD/dt) \leq 1.51$: hence the skewness will be upper bounded by 1.77 before t_*. This is in agreement with the maximal value of 1.132 found by Lesieur and Ossia [428].

7.7 Burgers-M.R.C.M. model

The Burgers equation

$$\frac{\partial}{\partial t}u(x,t) + u\frac{\partial u}{\partial x} = \nu\frac{\partial^2 u}{\partial x^2} \tag{7.60}$$

has been widely studied as a unidimensional model of turbulence (see e.g. Tatsumi [677]), Fournier and Frisch [213]). Actually it has been shown to develop randomly distributed shocks (*sawtooth profile*) in the inviscid case and starting with random initial conditions). These shocks correspond to a k^{-2} energy spectrum extending to infinity. When the viscosity is finite, but small, the k^{-2} inertial range is terminated at high wave numbers by a dissipation range.

It is very easy to apply the M.R.C.M. procedure to Burgers equation. The simplest way is to take the stochastic model point of view, and to work in the $\vec{x}$ physical space. The resulting equation, proposed in Lesieur [412] and Brissaud et al. [83], is

$$\frac{\partial}{\partial t}U(r,t) = -\theta_0\frac{\partial^2}{\partial r^2}[U(r,t) - U(0,t)]^2 + 2\nu\frac{\partial^2 U}{\partial r^2} \tag{7.61}$$

where $U(r,t) = \langle u(x,t)u(x+r,t)\rangle$ is the spatial simultaneous velocity covariance (homogeneity is assumed). U is an even function of the real variable r . The kinetic-energy dissipation rate is

$$\epsilon = -\frac{1}{2}\frac{d}{dt}U(0,t) = \nu\left\langle\left(\frac{\partial u}{\partial x}\right)^2\right\rangle = 2\nu D(t) \tag{7.62}$$

where the enstrophy is

$$D(t) = \frac{1}{2}\left\langle\left(\frac{\partial u}{\partial x}\right)^2\right\rangle = -\frac{1}{2}\left\langle u\frac{\partial^2 u}{\partial x^2}\right\rangle = -\frac{1}{2}\frac{\partial^2}{\partial r^2}U(r,t)|_{r=0}.$$

An equation very close to Eq. (7.61) (t replacing θ_0) had been obtained before by Kraichnan [351] with the aid of L.H.D.I.A. techniques applied to Burgers equation. When assuming an additional forcing spectrum in the r.h.s. of Eq. (7.61), it can be shown analytically (Lesieur [412]) that stationary solutions displaying a k^{-2} inertial range exist. They are limited by viscosity at high wave numbers. In the r space, it corresponds to a $U(r) \propto |r|$ range, smoothed by viscosity in the small scales. This k^{-2} range is exactly the equivalent of the k^{-2} M.R.C.M. three-dimensional turbulence inertial range, as can be checked by writing Eq. (7.62) in Fourier space and applying the analysis leading to Eq. (7.34).

In the freely-evolving case (no forcing) and for the inviscid problem, the occurrence of enstrophy divergence at a finite time t_* has been demonstrated analytically by Brissaud et al. [83]: let us expand the velocity covariance $U(r,t)$ as

$$U(r,t) = 2E(t) - D(t)r^2 + O(r^4) \tag{7.63}$$

where $E(t)$ is the kinetic energy, and substitute this expansion into the inviscid Eq. (7.61). By identification of the r expansion coefficients, one obtains

$$\frac{d}{dt}E(t) = 0 \tag{7.64}$$

which expresses the conservation of kinetic energy during this initial period, and

$$\frac{dD(t)}{dt} = 12\theta_0 D^2 \tag{7.65}$$

which is analogous to Eq. (7.63) and shows a divergence of the enstrophy at a critical time t_*. For $t > t_*$, a numerical resolution of the inviscid Eq. (7.61) performed by Brissaud et al. [83]) shows the appearance of a $U(r,t) \propto |r|$ behaviour for $r \to 0$ (that is a k^{-2} spectrum for $k \to \infty$), and a finite dissipation of kinetic energy: indeed, the following expansion

$$U(r,t) = 2E(t) - A|r| + O(r^2) \tag{7.66}$$

yields

$$\frac{dE(t)}{dt} = -A^2\theta_o \tag{7.67}$$

and the kinetic energy is dissipated at a finite rate if $A \neq 0$. Let us mention finally that exact mathematical theorems for this problem have been derived by Foias and Penel [208].

The Burgers M.R.C.M. model is therefore a very good model for three-dimensional "M.R.C.M. isotropic turbulence", since it displays an inviscid dissipation of kinetic energy occurring after a critical time t_*, where the enstrophy has become infinite and a k^{-2} inertial-range spectrum has appeared. This k^{-2} spectrum does not seem to be related to any shocks statistics, as in the actual Burgers turbulence. Therefore, and quite surprisingly, the "Burgers M.R.C.M. turbulence" is closer to three-dimensional isotropic turbulence than to the "Burgers turbulence". As far as the latter problem is concerned, let us mention the DNS work of Gurbatov et al. [266] in the decaying case.

7.8 Decaying isotropic helical turbulence

In this section we will study decaying isotropic turbulence with helicity, using the E.D.Q.N.M. approximation equations (7.21) and the spectral tensor form

Eq. (5.84). Separating the symmetrical and antisymmetrical parts of the r.h.s. of Eq. (7.21) leads, after a lengthy calculation, to the following set of coupled equations for the energy and helicity spectra (cf. Lesieur [412], André and Lesieur [7])[11]

$$\left(\frac{\partial}{\partial t}+2\nu k^2\right)E(k,t)=\iint_{\Delta_k} dp\ dq\theta_{kpq}$$
$$\frac{k}{pq}b(k,p,q)E(q,t)[k^2E(p,t)-p^2E(k,t)]$$
$$-\frac{1}{p^2q}z(1-y^2)H(q,t)[k^2H(p,t)-p^2H(k,t)], \tag{7.68}$$
$$\left(\frac{\partial}{\partial t}+2\nu k^2\right)H(k,t)=\iint_{\Delta_k} dp\ dq\theta_{kpq}$$
$$\frac{k}{pq}b(k,p,q)E(q,t)[k^2H(p,t)-p^2H(k,t)]$$
$$-\frac{k^2}{q}z(1-y^2)H(q,t)[E(p,t)-E(k,t)]. \tag{7.69}$$

Here the time θ_{kpq} has not been modified by the presence of helicity, and this remains an open question. Again it can be checked that the nonlinear terms of these equations conserve in a detailed fashion the kinetic energy and the helicity, and that the kinetic-energy and helicity dissipation rates are respectively given by

$$\epsilon=2\nu\int_0^{+\infty}k^2E(k,t)dk$$
$$\epsilon_H=2\nu\int_0^{+\infty}k^2H(k,t)dk. \tag{7.70}$$

We have mentioned in Chapter 5 the role of helicity for the generation of magnetic fields in M.H.D. flows (see also Frisch et al. [222], and Pouquet et al. [585]). As already stressed, helicity is not required in order to have a dynamo effect, as shown by Léorat et al. [408], but it enhances it. The latter have made an E.D.Q.N.M. study of isotropic M.H.D. turbulence, and shown that the critical magnetic Reynolds number was considerably decreased with helicity.

For neutral flows, helicity seems to be characterized by a strong inhibition of energy transfers towards small scales. This point could have implications in meteorology, where it has been suggested by Lilly [444,445] that tornadoes remained coherent because of their helicity, and that helicity contained in

[11] Equivalent helical D.I.A. spectral evolution equations were obtained from Eqs.(7.29) and (7.30) by Lesieur et al. [410] (see also André and Lesieur [7]).

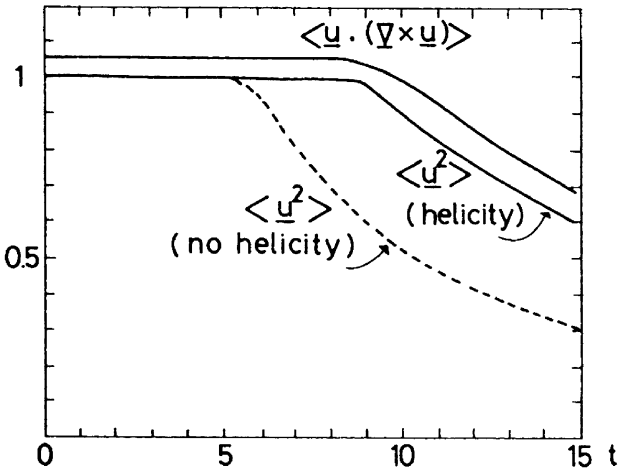

Figure 7.8. E.D.Q.N.M. helical calculation showing the kinetic energy and helicity time evolutions in the inviscid limit (straight lines). The dashed line shows the kinetic energy in the non-helical case. This demonstrates the delay of the enstrophy blow up, due to the presence of helicity (from André and Lesieur [7], courtesy *J. Fluid Mech.*).

small-scale atmospheric motions could increase the large-scale atmospheric predictability. Such an inhibition of the transfers can be justified in various ways: a very simple argument on the basis of the vorticity equation

$$\frac{\partial \vec{\omega}}{\partial t} + \vec{\nabla} \times (\vec{\omega} \times \vec{u}) = \nu \nabla^2 \vec{\omega} \tag{7.71}$$

says that in the non-helical case, and since $\langle \vec{\omega}.\vec{u} \rangle = 0$, the vorticity is perpendicular "in the mean" to the velocity, and therefore the vectorial product $\langle \vec{\omega} \times \vec{u} \rangle$ and the energy transfers are maximum.

This tendency can also be quantified with the aid of a freely-evolving E.D.Q.N.M. calculation, starting with the same energy conditions as in Section 7.6 (energy spectrum sharply peaked in the vicinity of k_i), with the maximum helicity

$$H(k,0) = kE(k,0) \tag{7.72}$$

permitted by the inequality (5.109): these calculations, presented in André and Lesieur [7], show without ambiguity the following results:

• (i) the critical time t_* at which the enstrophy blows up (in the inviscid limit) is increased by nearly a factor of 2, and is now of the order of $9/v_0 k_i(0)$. The *helicity enstrophy* $\int_0^{+\infty} k^2 H(k,t)dk$ blows up at the same time. The kinetic energy starts being dissipated at a finite rate at this time, and so does

the helicity, as can be expected from Eq. (7.70). The energy and helicity dissipation curves are shown in Figure 7.8. It must be noted that an analytical calculation analogous to Eq. (7.55) and showing in the M.R.C.M. helical case the enstrophy blow-up delay has not yet been done and seems to pose some difficulties.

• (ii) at t_* appear simultaneously $k^{-5/3}$ inertial ranges for the energy spectrum and the helicity spectrum. The helicity spectrum follows a "linear" cascade

$$H(k) \sim \frac{\epsilon_H}{\epsilon} E(k) = 2.25 \epsilon_H \epsilon^{-1/3} k^{-5/3} \tag{7.73}$$

which can be easily obtained (except for the value of the constant) from Eq. (7.69) by writing

$$\epsilon_H \sim \theta(k) k^4 E(k) H(k) \tag{7.74}$$

in analogy with Eq. (7.32). The numerical constant 2.25 was obtained with the same θ_{kpq} as in the non-helical calculation, adjusted in order to have a Kolmogorov constant of 1.4 in the energy cascade. We have employed the term "linear" for the cascade, because of the analogies with the passive scalar inertial-convective range envisaged in the previous chapter. These energy and helicity spectra are shown in Figure 7.9.

• (iii) the *relative helicity* $H(k)/kE(k)$ is, in the inertial range, proportional to k^{-1}, and decreases rapidly with k. Thus the helicity has no real influence on the energy flux, expressed in terms of the energy dissipation rate ϵ. It follows that the Kolmogorov constant in the energy cascade is not modified by the presence of helicity.

In fact these double cascades had been conjectured dimensionally by Brissaud et al. [84], using phenomenological arguments. They propose also, by analogy with two-dimensional turbulence (see Chapter 8), the possibility of a pure helicity cascade towards large wave numbers, with a zero energy flux, together with an inverse energy cascade towards low wave numbers, with no helicity flux. The latter inverse cascade is such that

$$E(k) \sim \epsilon^{2/3} k^{-5/3}; \quad H(k) \sim \epsilon^{2/3} k^{-2/3}. \tag{7.75}$$

These cascades did not appear in the calculations of André and Lesieur [7] which, however, were unforced calculations. Nevertheless, it was checked in the same reference that the E.D.Q.N.M. energy flux through stationary energy and helicity spectra given by Eq. (7.75) was positive, which eliminates the possibility of such inverse cascading spectra. This result was corroborated by the study of the absolute equilibrium ensemble solutions of the truncated Euler equations (see Chapter 10) with helicity, made by Kraichnan [355], which did not show any inverse energy transfer tendency. So the possibility of strong inverse energy transfers in the presence of maximal helicity seems to be ruled out.

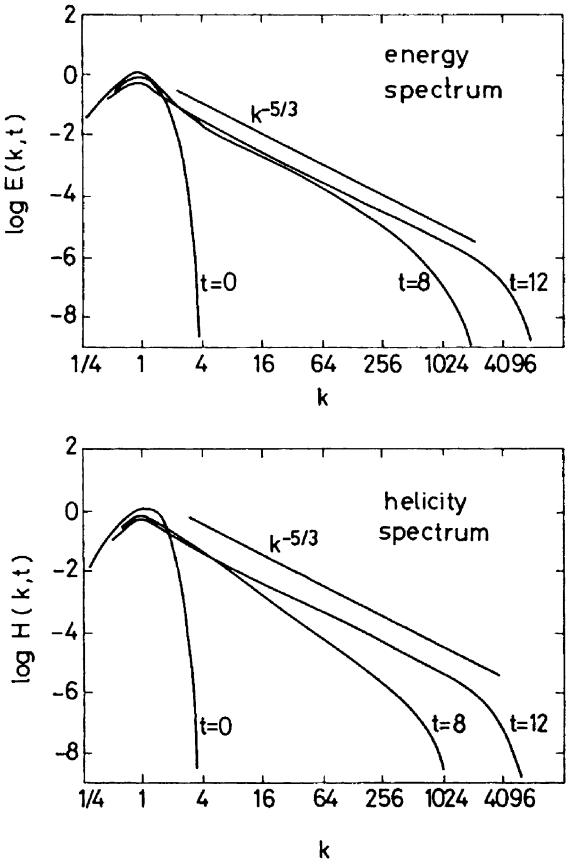

Figure 7.9. Time evolution of the energy and helicity spectra (time unit is $1/v_0 k_i(0)$), in the same calculation as in Figure 7.8. Now the inertial ranges establish at about $t_* = 9$ (from André and Lesieur [7], courtesy *J. Fluid Mech.*).

We stress that the existence of the double cascade of kinetic energy and helicity has been validated by Borue and Orszag [72] with the aid of LES This is a remarkable proof of validity for the E.D.Q.N.M. theory.

Let us mention the conjectures of Tsinober and Levich [693] and Moffatt [512], where there would exist in a flow with zero mean helicity local regions (in the $\vec{x}$ space) with non-zero helicity (positive or negative) where the kinetic energy dissipation would be less active than in the non-helical regions, because of the preceding results concerning the inhibition of kinetic energy dissipation by helicity. The flow would then evolve towards a set of "coherent" helical structures separated by non-helical dissipative structures

(maybe fractal). The coherent structures of same sign could possibly pair. Up to now this is nothing more than a conjecture. This tendency has been found in DNS of the Taylor–Green vortex (Shtilman et al. [645]). However, other simulations of isotropic or inhomogeneous turbulence done by Rogers and Moin [614] do not exhibit a correlation between the local relative helicity and the kinetic energy dissipation.

7.9 Decay of kinetic energy and backscatter

Section 7.6 has shown that after a critical time the kinetic energy of freely-evolving three-dimensional isotropic turbulence would decay at a finite rate. The asymptotic laws of decay pose an interesting question, and such information can be very useful for the one-point closure modelling of turbulence for instance. Experimentally these problems are studied in grid-turbulence facilities, where turbulence observed at a distance x downstream of the grid has decayed during a time $t = x/U$ since it was formed behind the grid (U is the mean velocity of the flow in the apparatus): for instance Comte-Bellot and Corrsin [142] found a decay exponent of the kinetic energy equal to -1.26

$$\frac{1}{2}\langle \vec{u}^2 \rangle \propto t^{-1.26}$$

while Warhaft and Lumley [712] found -1.34. The latter law was valid up to about 60 initial large-eddy-turnover times. We will see in this section that the E.D.Q.N.M. closures give valuable information about the possible decay laws, according to the shape of the initial energy spectrum. It must also be stressed that if it could be shown experimentally that this finite decay of kinetic energy occurs at a finite time when the viscosity goes to zero, it would be a further argument in favour of an inviscid enstrophy blow up at a finite time.

7.9.1 Eddy viscosity and spectral backscatter

Let us first return to the concept of non-local interactions introduced in Section 7.6, and utilized here to calculate the energy transfer when $k \to 0[k \ll k_i$ and $E(k) < E(k_i)]$: the "non-local parameter" a will be taken equal here to k/k_i. The predominant terms in Eq. (7.49) are the last two terms, which correspond to non-local interactions $k \ll p \approx q \approx k_i$. We have to the lowest order in k/k_i

$$T(k,t) = -\frac{2}{15}k^2 E(k) \int_{k_i}^{\infty} \theta_{0pp} \left[5E(p) + p\frac{\partial E}{\partial p} \right] dp$$
$$+\frac{14}{15}k^4 \int_{k_i}^{\infty} \theta_{0pp} \frac{E(p)^2}{p^2} dp + O[kE(k)]^{3/2} \tag{7.76}$$

where the $O[kE(k)]^{3/2}$ term corresponds to the local interactions, which will turn out to be negligible in this spectral region. The first term in the r.h.s. of Eq. (7.76) is an "eddy-viscous" term of the form

$$-2\nu_t k^2 E(k)$$

with

$$\nu_t = \frac{1}{15}\int_{k_i}^{\infty} \theta_{0pp}\left[5E(p) + p\frac{\partial E}{\partial p}\right] dp \tag{7.77}$$

which represents the damping action of the turbulence on the low frequency modes. Throughout this book we will widely discuss this eddy-viscosity concept in spectral space, introduced by Kraichnan [358]. The second term is positive and injects a k^4 transfer in low wave numbers, through some kind of resonant interaction between two modes $\approx k_i$. We will call this transfer spectral backscatter. It is this term which is responsible for the sudden appearance of a k^4 spectrum at $k < k_i$ when the initial energy spectrum is sharply peaked at k_i (or simply $\propto k^s$ with $s > 4$). Eq. (7.76), derived from the E.D.Q.N.M., is important, for it contains the two leading terms which govern the dynamics of three-dimensional isotropic turbulence at low wave numbers: if turbulence is stationary and sustained by a forcing spectrum concentrated at $k_i (k_i$ fixed), the balance between eddy-viscosity and backscatter yields a k^2 energy spectrum for $k \to 0$. It is called an energy equipartition spectrum, for it corresponds to the same amount of energy at each wave vector $\vec{k}$. Such a behaviour will be verified in Chapter 11.

Infrared exponent in unforced turbulence

If turbulence is unforced and decays freely, the behaviour of the "infrared" energy spectrum (that is at low wave numbers) depends on the infrared spectral exponent s of the initial conditions such that

$$E(k, 0) \propto k^s. \tag{7.78}$$

We reproduce a discussion from Lesieur et al. [431] about the choice of s:

> The question of permissible values for s is a controversial one. There are arguments in favour of $s = 4$ (see the review of Davidson [160]), others in favour of $s = 2$ (Saffman [621]). Taking even values of s is compulsory if certain regularity conditions for the velocity-correlation tensor between two points when the distance goes to infinity are fulfilled. Mathematically, one may take initially odd values of s (such as 1 or 3), and even non-integer ones, as was proposed by Eyink and Thomson [190]. The latter, working on the basis of an analogy with Burgers turbulence studied by Gurbatov et al. [266] with direct-numerical

simulations, propose the existence of a crossover dimension $s \approx 3.45$, above which a k^4 backscatter should appear.

The first complete theoretical analysis (using the E.D.Q.N.M. theory) of relations between the infrared spectral exponent and kinetic-energy decay was carried out in Lesieur and Schertzer [413]. They considered integer values of s. Here we present these results trying to get rid as much as possible of the statistical closure used. The important phenomenon is due the k^4 backscatter. We first assume that s is integer:

• $1 \leq s < 4$: then the k^4 and eddy-viscous non-local transfers will modify negligibly the initial spectrum, which will keep its original shape in the low k, that is

$$E(k,t) = C_s k^s \tag{7.79}$$

C_s being a constant.

Exercise: Show Eq. (7.79).
One considers the spectral-evolution equation with the transfer given by Eq. (7.76). Assuming that $E(k,t) = C_s(t)k^s$ at low k, we have

$$\frac{dC_s}{dt}k^s = Ak^4 - 2C_s\nu_t k^{s+2} + O[k^{3(s+1)/2}], \tag{7.80}$$

where A and ν_t vary weakly with time. One considers only integer values of s. For $1 < s < 4$, the backscatter dominates the two other terms in the r.h.s., and to the lowest order we have $dC_s/dt = 0$. For $s = 1$, the local transfer is of order k^3, as the eddy-viscous transfer, so that the l.h.s. still dominates with again $dC_s/dt = 0$.

Text
Eq. (7.79) is a situation of perfect "permanence of big eddies".

• $s > 4$: now the above expansion Eq. (7.80) is inconsistent, so that the spectrum will immediately pick up the k^4 backscatter component. We are then lead to the $s = 4$ case, where we have

$$E(k,t) = C_4(t)k^4 \tag{7.81}$$

with, from Eq. (7.76)

$$\frac{dC_4}{dt} = \frac{14}{15}\int_{k_i}^{\infty} \theta_{0pp}\frac{E(p)^2}{p^2}dp. \tag{7.82}$$

As mentioned in Lesieur and Schertzer [413], this expresses the non-invariance with time of the Loitzianskii integral $I(t)$ (see Orszag [553]). As recalled in Lesieur et al. [431]:

the multiplying coefficient (C_4) is equal to $I(t)/24\pi^2$, were (...) $I(t) = \int r^2 U_{ii}(r,t)d\vec{r}$, $U_{ii}(r,t)$ being the trace of the second-order velocity correlation tensor. This proves that the latter quantity is not *stricto-sensu* a time-invariant, although it does not vary very much in the late stages of the computation. Remark that time-invariance of Loitzianskii's integral (was) related by Landau and Lifchitz [371] to angular-momentum conservation of the flow. In fact, such a principle does not hold exactly due to viscous-dissipation and boundary-conditions effects.

We will show later in this chapter recent E.D.Q.N.M. and LES simulations of the infrared dynamics.

7.9.2 Decay laws

In order to now solve the kinetic-energy decay problem, it suffices to simply assume a self-similar decaying energy spectrum already considered in Eq. (6.68)

$$E(k,t) = v^2 l F(kl), \quad l = \frac{v^3}{\epsilon}, \quad \epsilon = -\frac{1}{2}\frac{dv^2}{dt}, \tag{7.83}$$

where F is a dimensionless function. This form is not exact in the dissipative range, but the error thus introduced in the kinetic-energy decay exponent is very small, as the closures will show. Eq. (7.83) developed for $k \to 0$ allows us to obtain

$$v^2 l^{s+1} = \text{constant}, \quad s < 4, \tag{7.84}$$

$$v^2 l^{s+1} \propto t^{\gamma}, \quad s = 4; \quad \gamma = \frac{1}{C_4}\frac{dC_4}{d\ln t}, \tag{7.85}$$

where dC_4/dt is given by Eq. (7.82) if one trusts the closures. It is now very easy to solve the problem (see Lesieur and Schertzer [413]). Assuming that the kinetic energy and the integral scale follow time power laws such that

$$v^2 \propto t^{-\alpha_E}, \quad l \propto t^{\alpha_l}, \tag{7.86}$$

one finds

$$\alpha_E = 2\frac{s+1-\gamma}{s+3}, \tag{7.87}$$

$$\alpha_l = \frac{2+\gamma}{s+3}. \tag{7.88}$$

Here γ is zero for $s < 4$. For $s = 4$, E.D.Q.N.M. calculations of Lesieur and Schertzer [413] give $\gamma = 0.16$. We recall that s cannot exceed 4, in the sense that if it is greater, it will very quickly become equal to 4.

Exercise: Show the above decay laws.
Using Eq. (7.83), we have $\epsilon \propto t^{-(\alpha_E+1)}$, and $l = v^3/\epsilon \propto t^{1+\alpha_E-(3\alpha_E/2)}$, which yields

$$\alpha_l = 1 - \frac{\alpha_E}{2}. \tag{7.89}$$

Then Eq. (7.85) gives

$$-\alpha_E + (s+1)\alpha_l = \gamma. \tag{7.90}$$

Solving this system gives the correct answer.

Text
For $s = 2$, the energy follows Saffman's [622] $t^{-6/5}$ law. For $s = 4$, it follows a $t^{-1.38}$ law instead of the $t^{-10/7}$ (i.e. $t^{-1.43}$) Kolmogorov's law [339] obtained in this case when discarding γ. In any case $v/l = \epsilon/v^2$ decays as t^{-1}, and the integral scale grows as $t^{2/5}$ for $s = 2$ and $t^{0.31}$ for $s = 4$. The large-eddy turn-over time l/v grows like t, and the Reynolds number vl/ν evolves like $t^{(2\gamma+1-s)/(s+3)}$. To confirm the existence of self-similar evolving energy spectra, at least in the frame of the E.D.Q.N.M. closure, Figure 7.10 (taken from Lesieur and Schertzer [413]) shows the function $F(kl)$ introduced in Eq. (7.83) at various times of the evolution, for two different initial conditions corresponding to $s = 2$ and $s = 4$: it indicates a perfect self-similarity in the energy-containing and inertial ranges, and only a very slight departure from self-similarity in the dissipation range. The law equations (7.87) and (7.88) can also be derived, as in Comte-Bellot and Corrsin [142], by assuming a crude energy spectrum model of the form

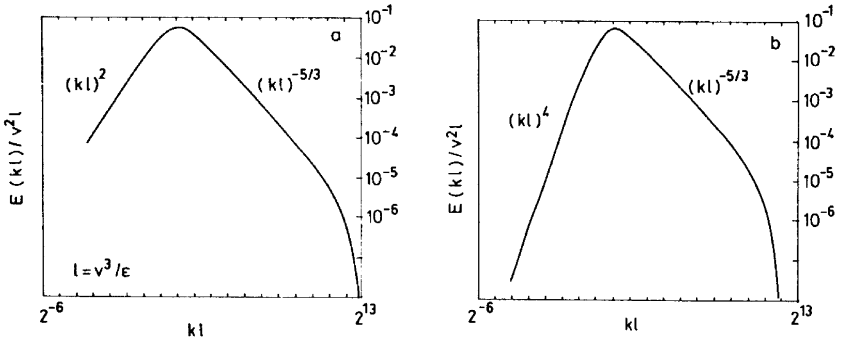

Figure 7.10. E.D.Q.N.M. calculation of the normalized kinetic energy spectra $E(kl)/v^2l$ at times 125, 150, 175 and 200, for two initial conditions corresponding to (a) $s = 2$ and (b) $s = 4$. The figure, where the spectra have been superposed, shows that they evolve self-similarly, according to Eq. (7.83) (from Lesieur and Schertzer [413], courtesy *Journal de Mécanique*).

$$E(k,t) = C_s k^s, \quad k < k_i(t)$$

$$E(k,t) = C_K \epsilon^{2/3} k^{-5/3}, \quad k > k_i(t)$$

with $k_i(t) \approx l(t)^{-1}$. In fact, the latter authors consider only the case $s = 4$. Notice finally that Eqs. (7.87) and (7.88) lead to a Richardson-type law equation (6.55)

$$\frac{1}{2}\frac{dl^2}{dt} \sim \epsilon^{1/3} l^{4/3}. \tag{7.91}$$

Discussion of these results

For $s < 4$ (still integer), these decay results are not dependent on the closure used, provided the latter gives a non-local transfer of the form Eq. (7.76) and a self-similar evolving spectrum Eq. (7.83). For $s = 4$, the results obtained by Tatsumi et al. [676] with the aid of the Q.N.M. theory are very close to the E.D.Q.N.M. ones. It is more difficult to interpret the experimental grid turbulence results: indeed, a grid of mesh M (distance between two bars) will produce immediately downstream a turbulence of integral scale M, turbulence due to the interaction of the wakes of neighbouring bars. Such a turbulence will not have, at $t = 0$, much energy at wave numbers different from M^{-1}. Therefore one might conjecture an energy spectrum that adjusts quickly on k^4 for $k \to 0$. Hence the kinetic energy would decay as $t^{-1.38}$. This is close to Warhaft and Lumley's [712] $t^{-1.34}$ result, but at variance with Comte-Bellot and Corrsin's [142] $t^{-1.26}$ measurements. The reason for the discrepancy is not obvious, and since it does not seem possible to measure experimentally the $k \to 0$ part of the energy spectrum, we can only propose various possible reasons such as the relatively low Reynolds number of the experiments, the lack of isotropy in the large scales, the problem of the determination of the origin of time, the insufficient length of the apparatus, etc.

Numerically, the unforced direct or large-eddy simulations having enough resolution in the small k and taking an initial kinetic-energy spectrum $\propto k^s$ with $s > 4$ (s integer), do show the appearance of the spectral backscatter corresponding to a k^4 energy spectrum (see Figure 6.12a, taken from Lesieur and Rogallo [421] where $s = 8$ initially). These simulations (see also Lesieur et al. [421]) give a kinetic-energy decay exponent of the order of 1.4, in not too bad agreement with the above theory. It is however difficult in these simulations to have reliable data on the infrared spectrum, due both to the shift of $k_i(t)$ towards the lower modes, and to the lack of statistical reliability of the spectra in these modes.[12] In Métais and Lesieur [496], the peak k_i is

[12] In these isotropic calculations, the spectra are calculated by an average on a sphere of radius k, and very few modes will contribute in the statistics at low k.

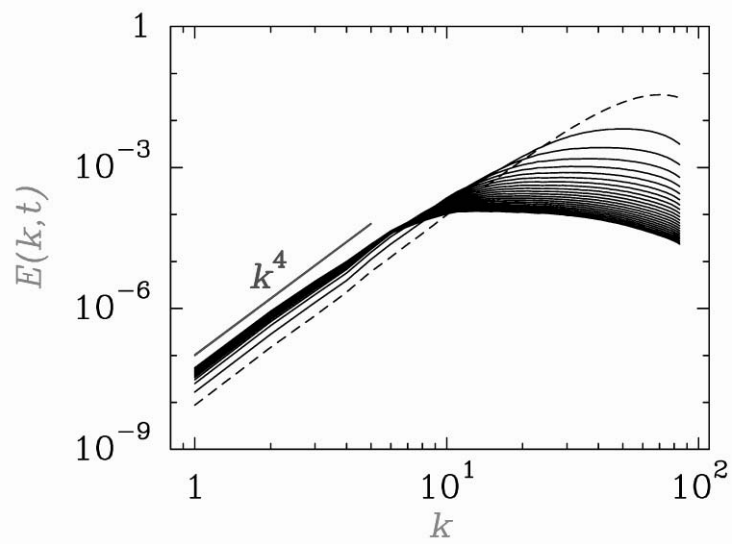

Figure 7.11. Kinetic-energy spectrum evolution in a 256^3 decaying LES starting initially with an infrared k^4 infrared energy spectrum. The dashed line is the initial spectrum (from Ossia and Lesieur [556]).

closer to $k_{\min}$ (which further diminishes the resolution), and the spectrum evolves towards k^2 at low k, with a $t^{-1.2}$ kinetic-energy decay law.

More recent E.D.Q.N.M. calculations are presented in Lesieur et al. [431]: the case $s = 1$ is very interesting since it yields a t^{-1} kinetic-energy decay law predicted by Batchelor [47], and a perfectly self-similar compensated kinetic-energy spectrum at all wave numbers. A very complete exploration of *s non-integer values* is also carried out, and no crossover slope, separating a regime of permanence of big eddies from a k^4 backscatter, may be found.

The LES of Ossia and Lesieur [556] does confirm the permanence of large eddies with $s = 2$, yielding $\alpha_E = 1.22$. With $s = 4$ one gets asymptotically $\alpha_E = 1.40$ in a LES with 256^3 points using pseudo-spectral methods, whose kinetic-energy spectra are presented in Figure 7.11. Here, the Loitzianskii integral $I(t)$ still increases slightly at the end of the computation. It is worth mentioning that the very high resolution DNS (1024^3 points, same pseudo-spectral methods) done by Ishida et al. [311] starting with a k^4 infrared spectrum shows eventually the saturation of $I(t)$ to a constant, with $\alpha_E = -10/7$. But this is a DNS (hence of low Reynolds number, with just a dissipative range), whereas our predictions on decay laws are based on self-similar arguments of Eq. (7.83) which assume a high Reynolds number. This is why LES' are more appropriate than DNS' for such studies.

7.9.3 Infrared pressure

New results on this topic are given in Lesieur et al. [427, 431, 556], and we summarize them. A k^2 pressure spectrum was predicted by Batchelor [45] with certain regularity assumptions on fourth-order velocity derivatives correlations (see also Hill [284]). Concerning closures, we recall that Larchevêque [380] has shown in three and two dimensions that the E.D.Q.N.M. and the Q.N. approximations yield the same results for pressure. In Lesieur et al. [427], non-local expansions of the closures yield

$$E_{pp}(k) = \frac{8}{15}\left(\int_0^{+\infty} \frac{E^2(q)}{q^2} dq\right) k^2. \tag{7.92}$$

In the LES of Ossia and Lesieur [556], this equation is recovered with a different constant 0.3 instead of $0.55 = 8/15$, which is not bad. In fact there is no pressure backscatter, since LES show that the coefficient in front of k^2 in the pressure spectrum decreases, due to the important time-decay of $E(k_I)$. In the LES, the pressure-variance decays approximately as $\langle p'^2 \rangle \propto t^{-2\alpha_E}$, law found by Batchelor [45] using the Q.N. approximation. So the sound pressure level of unforced three-dimensional isotropic turbulence (defined in Eq. (6.89)) decays rapidly.

7.10 Renormalization-Group techniques

The Renormalization-Group techniques (R.N.G.) were first developed with great success in the Physics of *critical phenomena*, in for instance, studies relating to nonlinear spin dynamics in ferromagnetic systems. These analysis consider generally the dimension of space d as a variable parameter, and it turns out that the problem can be solved for $d = 4$. The solutions for $d = 4-\epsilon$, where ϵ is a small parameter, are then expanded in powers of ϵ, and ϵ is taken equal to 1 in order to recover the solution for $d = 3$.

Noticing certain similarities between these nonlinear spin dynamics and Navier–Stokes equations with random forcing, Forster, Nelson and Stephen [210] applied the R.N.G. to the latter equations. In this analysis, the dimension of space was still a variable parameter. The formalism has been adapted by Fournier [212] to Navier–Stokes equations for a fixed dimension d, the variable parameter becoming the exponent of the forcing spectrum in Fourier space. It is this analysis (taken from Frisch and Fournier [223]), which will be summarized now.

7.10.1 R.N.G. algebra

One considers Navier–Stokes equation with a Gaussian random forcing of zero mean, Fourier expanded both with respect to space and time.[13] The velocity field

$$V_i(\vec{k},\omega) = \frac{1}{2\pi}\int \hat{u}_i(\vec{k},t)e^{i\omega t}dt$$

satisfies

$$(-i\omega + \nu k^2)V_i(\vec{k},\omega) = f_i(\vec{k},\omega)$$

$$-\frac{i}{2}\lambda P_{ijm}(\vec{k})\int_{\vec{p}+\vec{q}=\vec{k}}\int d\vec{p}d\Omega V_j(\vec{p},\Omega)V_m(\vec{p},\omega-\Omega). \tag{7.93}$$

λ is a parameter equal to 1 for Navier–Stokes equations, but which will be considered as small at certain stages of the R.N.G. theory.[14] The forcing spectrum, statistically stationary, is still defined by Eq. (7.28), hence

$$\langle f_i(\vec{k}',\omega)f_n(\vec{k},\omega')\rangle = \left(\frac{1}{2\pi}\right)^2\iint\langle f_i(\vec{k}',\tau)f_n(\vec{k},\tau')\rangle$$

$$e^{i(\omega\tau+\omega'\tau'}d\tau d\tau' = \frac{1}{2\pi}F_{in}(\vec{k})\delta(\vec{k}+\vec{k}')\delta(\omega+\omega'). \tag{7.94}$$

The following analysis will be carried out for three-dimensional isotropic turbulence, where it is assumed that

$$F_{in}(\vec{k}) = 2DP_{ij}(\vec{k})\frac{F(k)}{4\pi k^2}\,, \tag{7.95}$$

(the forces have no helicity), with

$$F(k) = k^{-r}. \tag{7.96}$$

D is a dimensional parameter which allows to vary the intensity of the forcing.

If $\lambda = 0$ in Eq. (7.93), the solution of this Langevin equation is

$$V_i^{(0)}(\vec{k},\omega) = G_0(\vec{k},\omega)f_i(\vec{k},\omega)$$

$$G_0 = \frac{1}{-i\omega+\nu k^2}\ . \tag{7.97}$$

Eq. (7.93) (with $\lambda \neq 0$) may be written as

[13] Which requires that the velocity field should be statistically stationary. This is one of the limitations of the theory, which cannot handle freely-decaying turbulence.

[14] In fact, the R.N.G. theory resembles the D.I.A. in this respect (see Leslie [432]), and both theories can be considered in this sense as weakly nonlinear.

$$V = G_0 f + \lambda G_0 \gamma(V, V). \tag{7.98}$$

Now, one looks for solutions where V is expanded in series of the small parameter λ:

$$V = V^{(0)} + \lambda V^{(1)} + \lambda^2 V^{(2)} + \cdots. \tag{7.99}$$

An easy way to generate this expansion is to substitute V given by Eq. (7.99) into Eq. (7.98) itself. It is found

$$V = G_0 f + \lambda G_0 \gamma(G_0 f, G_0 f) + 2\lambda^2 G_0 \gamma[\gamma(G_0 f, G_0 f), G_0 f] + O(\lambda^3).$$

In fact, the solution may be written formally up to any order, using diagrams built with the *propagator* $G_0(k, \omega)$ and the *vertex* $\lambda\gamma(V, V)$.

The above technique is used in the following way: one considers now Eq. (7.93) on a wave-number span extending from 0 to Λ (*Problem A*). Let Λe^{-l} be a "cutoff wave number" $(0 < l \ll 1)$, $V^<$ and $V^>$ the velocity corresponding to the modes below and above the cutoff. Eq. (7.98) written for $V^>$ and $V^<$ yield

$$V^> = G_0^> f^> + \lambda G_0^> \gamma(V^>, V^>) + \lambda G_0^> \gamma(V^<, V^<) + 2\lambda G_0^> \gamma(V^<, V^>), \tag{7.100}$$

$$V^< = G_0^< f^< + \lambda G_0^< \gamma(V^<, V^<) + \lambda G_0^< \gamma(V^>, V^>) + 2\lambda G_0^< \gamma(V^<, V^>), \tag{7.101}$$

where the symbols $<$ and $>$ refer to modes (or interaction with modes) below or above the cutoff. Afterwards, Eq. (7.100) is solved up to order 2 by the same perturbation techniques as above for the Langevin equation, and the result is substituted into Eq. (7.101) for $V^<$. A last step is, in this equation, to average on the terms $f^>$, assuming that they vary on a much smaller time scale than $V^<$ (which is in fact an assumption of separation of spatial scales at the cutoff). The resulting equation for $V^<$ is

$$[-i\omega + \nu(l)k^2]V_i^<(\vec{k}, \omega) = \hat{f}_i(\vec{k}, \omega) - \frac{i}{2}\lambda P_{ijm}(\vec{k}) \int_{\vec{p}+\vec{q}=\vec{k}} \int d\vec{p} d\Omega V_j^<(\vec{p}, \Omega)\ V_m^<(\vec{p}, \omega - \Omega), \tag{7.102}$$

with

$$\nu(l) = \nu \left[1 + \bar{\lambda}^2 H(r) \frac{1 - e^{-(3+r)l}}{3 + r}\right]$$

$$\bar{\lambda} = \lambda D^{1/2} \nu^{-3/2} \Lambda^{-(r+3)/2} \tag{7.103}$$

$$H(r) = \frac{1}{60\pi^2}(3 - r).$$

The forcing has not been modified, which may be shown to be valid for $r \geq -4$. Notice that the non-dimensional parameter $\bar{\lambda}$ (called by Fournier and Frisch [214] *reduced coupling constant*) characterizes the relative importance of nonlinear and viscous terms (equivalent Reynolds number).[15] Thus, the wave-number range $[\Lambda e^{-l}, \lambda]$ has been eliminated. This operation is called a *decimation*. Notice that, in Eq. (7.102), terms called *non-pertinent* have been discarded, not that they are negligible at this stage, but because they vanish after an infinite number of decimations, when the cutoff wave number has tended to 0. Hence, Eq. (7.102) is questionable for subgrid-scale modelling purposes if the cutoff wave number Λe^{-l} remains fixed.

Afterwards, expansions are done with respect to the small parameter $\epsilon = 3 + r$. Eq. (7.103) writes

$$\frac{d\nu}{dl} = \nu\bar{\lambda}^2 H, \tag{7.104}$$

equivalent to

$$\frac{\delta\nu}{\nu} = \bar{\lambda}^2 H \frac{\delta\Lambda}{\Lambda}, \tag{7.105}$$

and showing the increase of viscosity on modes $[0, \Lambda - \delta\Lambda]$ due to modes $[\Lambda - \delta\Lambda, \Lambda]$. Now, the following changes of variable are done in Eq. (7.102):

$$\tilde{k} = e^l k, \tilde{\omega} = e^l Z\omega, \tilde{V}(\tilde{k}, \tilde{\omega}) = e^{-lX} V^<(k, \omega).$$

The wave-number span is again $[0, \Lambda]$, and the coefficients $\nu(l), D, \lambda$ are changed into:

$$\nu_N(l) = \nu(l)e^{Z-2}l; \quad \lambda_N(l) = \lambda e^{X-4},$$
$$D_N(l) = De^{3Z-2X+r+5}l.$$

Supposing that $\nu_N(l)$ and D_N will remain unchanged (equal respectively to ν and D), it is found:

$$Z - 2 + \bar{\lambda}^2 H = 0; \quad 3Z - 2X + r + 5 = 0,$$

$$\lambda(l) = \lambda \exp \frac{1}{2}(r + 3 - 3H\bar{\lambda}^2).$$

[15] Indeed, let Eq. (7.93) be written in physical space: the velocity will be evaluated by assuming a balance between the forcing and the viscous damping, which yields $V \sim f/\nu\Lambda^2$. Therefore, the equivalent Reynolds number $R = \lambda V/\nu\Lambda$ is equal to $\lambda f/\nu^2\Lambda^3$. In order to evaluate f, one writes from Eqs. (7.95) and (7.96): $f^2 \sim DT_\nu \int_0^\Lambda k^{-r} dk$, where $T_\nu = 1/\nu\Lambda^2$ is the shortest time correlation time permitted by the viscous forces. This yields $R = \bar{\lambda}$.

Hence we are back to the initial problem (Problem A), with the same ν, D and Λ but with a new parameter $\lambda(l)$ which satisfies

$$\frac{1}{\lambda}\frac{d\lambda}{dl} = \frac{1}{\bar{\lambda}}\frac{d\bar{\lambda}}{dl} = \frac{1}{2}[r + 3 - 3H(r)\bar{\lambda}^2]. \tag{7.106}$$

The process can now be iterated, letting k go to zero. Then, two cases have to be considered: if $\epsilon = r+3$ is negative,[16] $\bar{\lambda}(l)$ will tend to zero when $l \to \infty$, and the eventual solution for $V^<$ will be given by the Langevin equation Eq. (7.97): the stationary spatial simultaneous spectral tensor may thus be easily determined as

$$\langle \hat{U}_{ij}(\vec{k}, t)\rangle = \frac{F_{ij}(\vec{k})}{2\nu k^2},$$

and the kinetic-energy spectrum will thus be equal to, from Eq. (7.95)

$$E(k) = 2DF(k)/2\nu k^2 \propto k^{-r-2}. \tag{7.107}$$

If $\epsilon > 0$, there will be a fixed point given by

$$\bar{\lambda}_* = \sqrt{\frac{\epsilon}{3H}}. \tag{7.108}$$

At the fixed point, the kinetic energy spectrum $E(k) \propto k^{-m}$ does not vary during one iteration. This allows us to show, taking into account the changes of variable done, that

$$m = Z + r = 2 - \bar{\lambda_*}^2 H + r = 1 + \frac{2r}{3}.$$

In this case Eq. (7.93) may be easily integrated, yielding an exact expression for the renormalized viscosity, as shown by Fournier and Frisch [214]:

$$\nu(\Lambda) = (3H)^{1/3} D^{1/3} \epsilon^{-1/3}\ \Lambda^{-\epsilon/3}. \tag{7.109}$$

The corresponding asymptotic kinetic energy spectrum may be calculated by perturbative methods from the above ($\bar{\lambda} = 0$) Langevin equation, since the fixed-point value for $\bar{\lambda}$ is $O(\epsilon)$, and we get (Fournier and Frisch [214]):

$$E(k) = \frac{2DF(k)}{2\nu(k)k^2} = D^{2/3}(3H)^{-1/3}\ \epsilon^{1/3} k^{1-2\epsilon/3}\ . \tag{7.110}$$

Eq. (7.109) writes:

[16] The parameter ϵ employed here has of course nothing to do with the kinetic-energy dissipation rate considered above.

$$\nu(\Lambda) = (3H)^{1/2}\epsilon^{-1/2}\sqrt{\frac{E(\Lambda)}{\Lambda}}\ , \tag{7.111}$$

which is independent of the forcing parameter D. This yields in particular $E(k) \propto k^{-5/3}$ for $F(k) \propto k^{-1}$, although the convergence of the method may be questioned, since $\epsilon = r + 3 = 4$, which by no means may be a small parameter. This last result has been used by Yakhot and Orszag [728] in order to implement the R.N.G. techniques for subgrid-scale modelling purposes (see Chapter 12). Eqs. (7.110) and (7.111) yield in this case (with, from Eq. (7.103), $H = 1/30\pi^2$)):

$$E(k) = 7.336 D^{2/3} k^{-5/3}$$

$$\nu(\Lambda) = 0.050\sqrt{\frac{E(\Lambda)}{\Lambda}}. \tag{7.112}$$

Other details on R.N.G. applied to turbulence theory can be found in Frisch [229].

7.10.2 Two-point closure and R.N.G. techniques

The $k^{-5/3}$ range

We will introduce in Chapter 12 an E.D.Q.N.M. spectral eddy viscosity of the form Eq. (7.112), but with a higher value of the numerical constant (0.267 instead of 0.050). Here the small parameters remain smaller than 1, but there is an adjustable constant a_1 which has to be tuned on the Kolmogorov constant.

In R.N.G. analysis as developed by Yakhot and Orszag [728] (see also Dannevik et al. [156]), certain expansions about the fixed point show that the kinetic energy spectrum must annul a transfer whose form is similar to the E.D.Q.N.M. transfer given by Eqs. (7.22) and (7.20) (μ_k being set equal to $\nu(k)\ k^2$, where $\nu(k)$ is the eddy-viscosity of the R.N.G. theory. This yields a Kolmogorov spectrum, with

$$\nu(k) = 0.388\sqrt{\frac{E(k)}{k}}, \tag{7.113}$$

result which is strongly at variance with the prediction of the original R.N.G. theory given in Eq. (7.112). Therefore there seems to be some inconsistency in using an E.D.Q.N.M.-type spectral equation within the R.N.G. formalism. Afterwards, the parameter D characterizing the forcing is adjusted in such a way that the energy flux is, for the Kolmogorov spectrum, constant and equal to $\bar{\epsilon}$. This yields a constant value for $D/\bar{\epsilon}$, and a Kolmogorov constant equal to 1.617. It is however questionable to use D, fixing the intensity of the forcing, as an adjustable parameter: indeed, D should satisfy, from the original equations,

$$\bar{\epsilon} = 2D \int_0^{\Lambda} k^{-r} dk,$$

where $\bar{\epsilon}$ is the kinetic-energy injection rate. When $r \geq 1$, a lower cutoff wave number $k_{\min}$ is required in order to prevent the divergence of $\bar{\epsilon}$. For $r = 1$, $\bar{\epsilon}/D = 2\ln(\Lambda/k_{\min})$ depends logarithmically on Λ and $k_{\min}$, and this is certainly not a constant.

Infrared spectrum

Returning to the case of the infrared spectrum, it may be of interest to compare the R.N.G. results obtained in the above case (turbulence forced up to a cutoff Λ by a forcing k^{-r} with $r \approx -3$, where the theory has good chances to converge) with the two-point closure predictions. We use Eq. (7.76) to write in the stationary case

$$2(\nu + \nu_t)k^2 E(k) = Ak^4 + F(k) + O[kE(k)]^{\frac{3}{2}} \tag{7.114}$$

where A is the coefficient of the k^4 transfer in Eq. (7.76). As already noticed, a k^1 infrared kinetic-energy spectrum gives a "crossover" exponent over which non-local transfers dominate, and under which the local transfers are preponderant. Contrary to the R.N.G., two-point closures may consider wide variations of r. They yield:

- (i) for $r \leq -4, E(k) = (A/\nu_t)k^2$ (which justifies discarding the local transfer), result already mentioned above.
- (ii) for $-4 < r \leq -3$, the non-local eddy-viscous term is still greater than the local transfer, and is balanced by the forcing: one has $E(k) \propto k^{-r-2}$.
- (iii) for $r > -3$, the local term balances the forcing, which yields $E(k) \propto k^{-1-(2r/3)}$. These two results are in agreement with the R.N.G. predictions.

It turns out that the R.N.G. method seems to handle correctly the isotropic forced turbulence in the infrared limit $k \to 0$, with a forcing exponent $r \geq -4$. However, there are severe convergence problems if one wants to describe the dynamics of the Kolmogorov inertial range. Furthermore, the method is unable to capture both the infrared and ultraviolet dynamics, and cannot be implemented if there is no forcing, unless an E.D.Q.N.M.-type equation is associated to the theory. Remarking also that it seems difficult to apply it to inhomogeneous problems, we will conclude that two-point closure are tools which are much more controllable, and offer a much wider range of possibilities than the R.N.G., even for subgrid-scale modelling purposes.

7.11 E.D.Q.N.M. isotropic passive scalar

In this section we show how to apply the E.D.Q.N.M. closure to the statistically homogeneous scalar, and will look on singular behaviour accompanying the catastrophic stretching of vortex filaments described above.

The E.D.Q.N.M. approximation can easily be derived for the passive scalar (Herring et al. [280], Larchevêque et al. [377], Larchevêque [378], Larchevêque and Lesieur [379]). With the same symbolic notation as Section 7.1, one can write:

$$\frac{\partial \hat{T}(\vec{k})}{\partial t} = \hat{T}\hat{u} - \kappa k^2 \hat{T}(\vec{k});$$

$$\frac{\partial}{\partial t}\langle \hat{T}(\vec{k},t)\hat{T}(\vec{k}',t)\rangle = \langle \hat{T}\hat{T}\hat{u}\rangle - \kappa(k^2+k'^2)\langle \hat{T}(\vec{k},t)\hat{T}(\vec{k}',t)\rangle;$$

$$\frac{\partial}{\partial t}\langle \hat{T}(\vec{k})\hat{T}(\vec{p})\hat{u}(\vec{q})\rangle = \langle \hat{T}\hat{T}\hat{u}\hat{u}\rangle$$

$$-[\kappa(k^2+p^2)+\nu q^2]\langle \hat{T}(\vec{k})\hat{T}(\vec{p})\hat{u}(\vec{q})\rangle,$$

and the same Quasi-Normal type approximations as for the velocity moments hierarchy can be made. Since the calculation is simpler than for the kinetic energy spectrum equation, we will derive it in detail: let us write the temperature equation in Fourier space for two wave vectors $\vec{k}$ and $\vec{k}'$

$$\left(\frac{\partial}{\partial t} + \kappa k^2\right)\hat{T}(\vec{k},t) = -i\int \hat{u}_j(\vec{p},t) q_j \hat{T}(\vec{q},t)\delta(\vec{k}-\vec{p}-\vec{q})d\vec{p}d\vec{q}, \qquad (7.115)$$

$$\left(\frac{\partial}{\partial t} + \kappa k'^2\right)\hat{T}(\vec{k}',t) = -i\int \hat{u}_l(\vec{p}',t) q'_l \hat{T}(\vec{q}',t)\delta(\vec{k}'-\vec{p}'-\vec{q}')d\vec{p}'d\vec{q}'. \qquad (7.116)$$

Multiplying Eq. (7.115) by $\hat{T}(\vec{k}',t)$ and Eq. (7.116) by $\hat{T}(\vec{k},t)$, adding and averaging yields

$$\left[\frac{\partial}{\partial t} + \kappa(k^2+k'^2)\right]\langle \hat{T}(\vec{k}',t)\hat{T}(\vec{k},t)\rangle =$$

$$-i\int q_j \langle \hat{T}(\vec{k}')\hat{T}(\vec{q})\hat{u}_j(p)\rangle \delta(\vec{k}-\vec{p}-\vec{q})d\vec{p}d\vec{q}$$

$$-i\int q'_l \langle \hat{T}(\vec{k})\hat{T}(\vec{q}')\hat{u}_l(\vec{p}')\rangle \delta(\vec{k}'-\vec{p}'-\vec{q}')d\vec{p}'d\vec{q}'. \qquad (7.117)$$

We also need the time evolution equation for $\vec{\hat{u}}(\vec{k},t)$:

$$\left(\frac{\partial}{\partial t} + \nu k''^2\right)\hat{u}_m(\vec{k}'',t) = -ik_n'' P_{ma}(\vec{k}'')$$

$$\int \hat{u}_n(\vec{p}'',t)\hat{u}_a(\vec{q}'',t)\delta(\vec{k}''-\vec{p}''-\vec{q}'')d\vec{p}''d\vec{q}''. \tag{7.118}$$

From Eqs. (7.115), (7.116) and (7.118), one can form the equation for the triple correlation $\langle\hat{T}\hat{T}\hat{u}\rangle$:

$$\left[\frac{\partial}{\partial t}+\kappa(k^2+k'^2)+\nu k''^2\right]\langle\hat{T}(\vec{k}',t)\hat{T}(\vec{k},t)\hat{u}_m(\vec{k}'',t)\rangle =$$

$$-i\int q_b\langle\hat{T}(\vec{k}')\hat{T}(\vec{q})\hat{u}_b(\vec{p})\hat{u}_m(\vec{k}'')\rangle\delta(\vec{k}-\vec{p}-\vec{q})d\vec{p}d\vec{q}$$

$$-i\int q'_c\langle\hat{T}(\vec{k})\hat{T}(\vec{q}')\hat{u}_c(\vec{p}')\hat{u}_m(\vec{k}'')\rangle\delta(\vec{k}'-\vec{p}'-\vec{q}')d\vec{p}'d\vec{q}'$$

$$-ik_n''P_{ma}(\vec{k}'')\int\langle\hat{T}(\vec{k})\hat{T}(\vec{k}')\hat{u}_n(\vec{p}'')\hat{u}_a(\vec{q}'')\rangle\delta(\vec{k}''-\vec{p}''-\vec{q}'')d\vec{p}''d\vec{q}''. \tag{7.119}$$

We are now in a situation to apply the Quasi-Normal approximation. As already emphasized, the temperature-velocity correlations are zero, and the Quasi-Normal expression of Eq. (7.119) becomes

$$\left[\frac{\partial}{\partial t}+\kappa(k^2+k'^2)+\nu k''^2\right]\langle\hat{T}(\vec{k}',t)\hat{T}(\vec{k},t)\hat{u}_m(\vec{k}'',t)\rangle$$

$$= ik'_b\frac{E_T(k',t)}{2\pi k'^2}\hat{U}_{bm}(\vec{k}'',t)\delta(\vec{k}+\vec{k}'+\vec{k}'')$$

$$+ik_c\frac{E_T(k,t)}{2\pi k^2}\hat{U}_{cm}(\vec{k}'',t)\delta(\vec{k}+\vec{k}'+\vec{k}''). \tag{7.120}$$

We solve Eq. (7.120) for the triple correlation $\langle\hat{T}\hat{T}\hat{u}\rangle$, substitute in Eq. (7.117), integrate on $\vec{k}'$, and obtain finally

$$\left(\frac{\partial}{\partial t}+2\kappa k^2\right)\hat{\Phi}(k,t) = 2\int_{\vec{p}+\vec{q}=\vec{k}}d\vec{p}\int_0^t d\tau k_b k_j$$

$$\hat{U}_{bj}(\vec{q},\tau)[\hat{\Phi}(\vec{p},\tau)-\hat{\Phi}(k,\tau)]e^{-[\kappa(k^2+p^2)+\nu q^2](t-\tau)} \tag{7.121}$$

where $\hat{\Phi}(k,t)=E_T(k,t)/2\pi k^2$ is the equivalent of the spectral tensor for the temperature (cf. Eq. (5.91)). As seen in Chapter 5, $\hat{\Phi}(\vec{k},t)$ is the spatial Fourier transform[17] of the temperature spatial correlation.

$$\Phi(\vec{r},t)=\langle T(\vec{x},t)T(\vec{x}+\vec{r},t)\rangle.$$

[17] Because of the isotropy assumption, $\hat{\Phi}(\vec{k},t)$ does not depend on the orientation of $\vec{k}$.

If linear damping rates had been introduced to model the action of discarded fourth-order cumulants, the E.D.Q.N. approximation for the temperature equation would be obtained from Eq. (7.121) by replacing the exponential term by

$$e^{-[\kappa(k^2+p^2)+\mu'(k)+\mu'(p)+\nu q^2+\mu''(q)](t-\tau)}, \tag{7.122}$$

where $\mu'(k)$ and $\mu''(k)$ are two functions of same structure as the triple-velocity correlation relaxation rate μ_k introduced in Eq. (7.17), but with possibly different constants, that is

$$\mu_k = a_1 \left(\int_0^k p^2 E(p,t) dp \right)^{1/2} \tag{7.123}$$

$$\mu'(k) = a_2 \left(\int_0^k p^2 E(p,t) dp \right)^{1/2} \tag{7.124}$$

$$\mu''(k) = a_3 \left(\int_0^k p^2 E(p,t) dp \right)^{1/2}. \tag{7.125}$$

Then the Markovianization yields the E.D.Q.N.M. equation for $\hat{\Phi}(k,t)$:

$$\left(\frac{\partial}{\partial t} + 2\kappa k^2 \right) \hat{\Phi}(k,t) = 2 \int_{\vec{p}+\vec{q}=\vec{k}} d\vec{p} k_b k_j \theta^T_{kpq} \hat{U}_{bj}(\vec{q},t)[\hat{\Phi}(\vec{p},t) - \hat{\Phi}(\vec{k},t)], \tag{7.126}$$

with

$$\theta^T_{kpq} = \frac{1 - e^{-[\kappa(k^2+p^2)+\mu'(k)+\mu'(p)+\nu q^2+\mu''(q)]t}}{\kappa(k^2+p^2)+\mu'(k)+\mu'(p)+\nu q^2+\mu''(q)}. \tag{7.127}$$

The choice of the new adjustable constants a_2 and a_3 in Eqs. (7.124) and (7.125) is not simple. We recall that $a_1 \approx 0.218 C_K^{3/2}$. It has been shown by Herring et al. [280] that a given value of the "Corrsin–Oboukhov constant" arising in the r.h.s. of Eq. (6.107) (here taken equal to 0.67 from experimental measurements of Champagne et al. [105]), imposes a certain one to one correspondence between a_2 and a_3. The last condition, allowing to determine a_2 and a_3, comes from considerations on the "turbulent Prandtl number", defined in the following way: it will be shown soon that an eddy conductivity κ_t of the same genre as the eddy viscosity ν_t defined in Eq. (7.77) can be introduced. For kinetic-energy spectra following Kolmogorov's law above k_i, the turbulent Prandtl number ν_t/κ_t is equal to $(a_2 + a_3)/6a_1$, as shown in Larchevêque and Lesieur [379] (see also Herring et al. [280], Chollet [118], and Section 7.12 of the present chapter). It is then possible to express this number

in function of a_2/a_3 only, in such a way that the Corrsin–Oboukhov constant should be fixed to the value given above. This leads to a turbulent Prandtl number decreasing continuously from 0.6 to 0.325 for a_2/a_3 going from zero to infinity. Since the values of turbulent Prandtl numbers found experimentally in the boundary layer are in the range $0.6 \approx 0.8$ (see e.g. Fulachier and Dumas [233]), this could lead to the choice $a_2 = 0$ (and hence $a_3 = 1.3$, from Herring et al. [280]). One could object that the analogy between both theoretical and experimental turbulent Prandtl numbers is not obvious. Nevertheless the choice $a_2 = 0$ has the further advantage of allowing analytical resolutions of the E.D.Q.N.M. temperature spectral equation. It has to be stressed that the simpler choice $a_2 = a_3 = a_1$ gives the same Corrsin–Oboukhov constant and a turbulent Prandtl number of 0.35. As shown by Herring et al. [280], both choices support a very good comparison with atmospheric kinetic energy and temperature spectra reported in Champagne et al. [105]. Eq. (7.126) can immediately be written for the temperature spectrum, if one remarks that

$$\int d\vec{p} = \iint_{\Delta_k} dp\ dq 2\pi \frac{pq}{k}$$

and, from Eq. (5.84)

$$k_b k_j \hat{U}_{bj}(\vec{q}, t) = k^2(1 - y^2)\frac{E(q,t)}{4\pi q^2}.$$

This shows that the helicity has no direct influence on the scalar spectrum. The resulting equation is

$$\frac{\partial}{\partial t}E_T(k,t) = \iint_{\Delta_k} dp\ dq \theta^T_{kpq}\frac{k}{pq}(1-y^2)E(q,t)[k^2 E_T(p) - p^2 E_T(k)]$$

$$-2\kappa k^2 E_T(k,t). \tag{7.128}$$

The generalization of this equation to a Test-Field Model study of the passive scalar may be found in Newman and Herring [532].

7.11.1 A simplified E.D.Q.N.M. model

With the choice $a_2 = 0, \theta^T$ is equal to a function θ^T_q, and Eq. (7.128) can be easily written in physical space with the aid of an inverse Fourier transform (Larchevêque and Lesieur [378]): indeed, the inverse Fourier transform of the convolution

$$\int \theta^T_q \hat{U}_{bj}(\vec{q})\hat{\Phi}(\vec{p})d\vec{p}$$

is

$$\int \theta_q^T \hat{U}_{bj}(\vec{q}) e^{i\vec{q}.\vec{r}} d\vec{q} \Phi(\vec{r}),$$

and the inverse Fourier transform of

$$\int \theta_q^T \hat{U}_{bj}(\vec{q}) \hat{\Phi}(\vec{k}) d\vec{p} = \int \theta_q^T \hat{U}_{bj}(\vec{q}) d\vec{q} \hat{\Phi}(\vec{k})$$

is

$$\int \theta_q^T \hat{U}_{bj}(\vec{q}) d\vec{q} \Phi(\vec{r}).$$

Then, by introducing the generalized turbulent diffusion tensor

$$K_{ij}(\vec{r},t) = 2 \int \theta_q^T \hat{U}_{ij}(\vec{q},t)(1 - e^{i\vec{q}.\vec{r}}) d\vec{q}, \tag{7.129}$$

it is possible to write Eq. (7.126) as a diffusion equation for the spatial temperature covariance $\Phi(r,t)$:

$$\frac{\partial}{\partial t}\Phi(r,t) = \frac{\partial^2}{\partial r_i \partial r_j}[K_{ij}(\vec{r},t)\Phi(r,t)] + 2\kappa\nabla^2\Phi(r,t) \ . \tag{7.130}$$

This equation has close analogies with an equation obtained by Kraichnan [349] using the Lagrangian History Direct Interation techniques, and widely discussed by Leslie [432]. It is also of interest for the determination of the p.d.f.'s in turbulent reacting flows (Eswaran and O'Brien [188]).

Then it is shown in Larchevêque and Lesieur [378], following Kraichnan [349], that the isotropy and zero-divergence of $K_{ij}(\vec{r},t)$ allow us to introduce a scalar $K_{//}(r,t)$ such that Eq. (7.130) reduces to

$$\frac{\partial}{\partial t}\Phi(r,t) = r^{-2}\frac{\partial}{\partial r}\left[r^2 K_{//}(r,t)\frac{\partial}{\partial r}\Phi(r,t)\right] + 2\kappa\nabla^2\Phi(r,t). \tag{7.131}$$

The turbulent diffusion coefficient $K_{//}(r,t)$, which is a function of θ_q^T and $E(q,t)$, is equal to

$$K_{//}(r,t) = 0.696 a_3^{-1} C_K^{1/2} \epsilon^{1/3} r^{4/3} \tag{7.132}$$

if one assumes that the wave number r^{-1} lies in an extended $k^{-5/3}$ kinetic energy inertial range, with $\theta_q^T = \mu''(q)^{-1}$. Without molecular conductivity, this has dimensional analogies with Richardson's equation Eq. (6.59), where the spatial correlation of a marker was considered.

Eqs. (7.131) and (7.132) can then be solved, using self-similarity arguments, giving in particular information on the decay law of temperature variance. This will be looked at in Section 7.13 when considering the dispersion of pairs of Lagrangian tracers.

7.11.2 E.D.Q.N.M. scalar-enstrophy blow up

We end this section with a study paralleling the enstrophy divergence study done above in this chapter, and showing how the E.D.Q.N.M. closure predicts that this enstrophy divergence at a finite time t_c (in the limit of zero viscosity) will imply a blow up of the scalar enstrophy appearing in Eq. (6.20): from Eq. (7.128), after multiplication by k^2 and integration from $k = 0$ to ∞, one obtains, using the same techniques as above

$$\frac{d}{dt}D_T(t) = \int_0^{+\infty}\int_0^{+\infty} \theta_q^T p^2 q^2 E(q) E_T(p) dp dq \int_{-1}^{+1} (1-x^2) dx$$

$$-2\kappa \int_0^{+\infty} k^4 E_T(k,t) dk, \tag{7.133}$$

where the time θ_{kpq}^T has again been approximated by θ_q^T, itself taken equal to $\mu''(q)^{-1}$. This yields

$$\frac{d}{dt}D_T(t) = \frac{8}{3} a_3 D_T(t) D(t)^{1/2} - 2\kappa \int_0^{+\infty} k^4 E_T(k,t) dk. \tag{7.134}$$

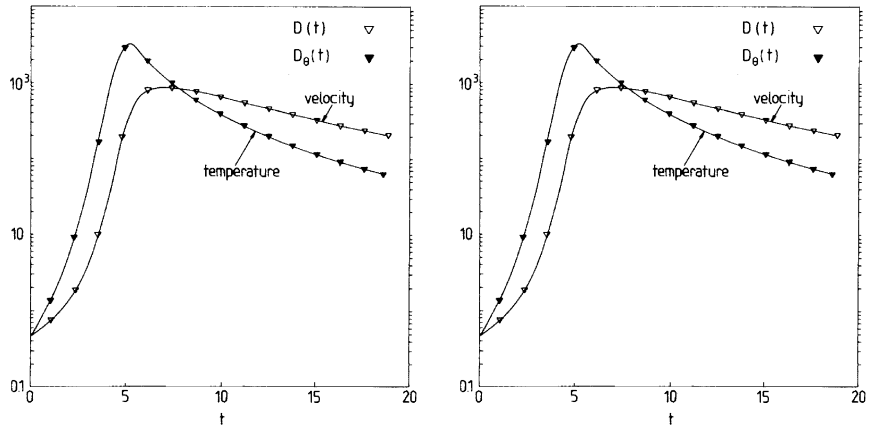

Figure 7.12. Time-evolution (at an initial Reynolds number of $R_{k_{i(0)}} = 40{,}000$ and a Prandtl number of one) of the velocity and temperature (called here Θ) enstrophies in an E.D.Q.N.M. initial-value problem where the initial temperature and velocity fluctuations are confined in the same large scales; (b) time-evolution of the velocity and temperature variances in the same calculation. (from Lesieur et al. [419], courtesy *Physics of Fluids*).

We assume first a perfect flow with no molecular diffusive effects (and hence $\nu = \kappa = 0$) and suppose that, initially, the energy spectrum and the temperature spectrum decrease rapidly (for instance exponentially) for $k > k_i \approx k_i^T$. Therefore the temperature enstrophy will diverge together with the enstrophy and at the same time t_c. The M.R.C.M. equation equivalent to Eq. (7.134) is

$$\frac{d}{dt} D_T(t) = \frac{4}{3} \theta_0 D_T(t) D(t), \tag{7.135}$$

and gives qualitatively the same result. Physically, one can say that the catastrophic stretching of vortex filaments by turbulence will at the same time steepen the temperature gradients in the fluid, leading to singularities which occur at the same time t_c at which the velocity gradients become singular.[18] More precisely, the M.R.C.M. enstrophies are, from Eqs. (7.56) and (7.135):

$$D(t) \propto (t_c - t)^{-1}; \quad D_T(t) \propto (t_c - t)^{-2}, \tag{7.136}$$

which shows that the scalar enstrophy diverges at t_c faster than the velocity enstrophy. The same tendency may be obtained with the E.D.Q.N.M. (non-diffusive) scalar equation 7.134, where the constant-skewness model prediction Eq. (6.79) has been used for the velocity. It is easily found

$$D_T(t) \propto (t_c - t)^{-(8/3) a_3 t_c \sqrt{D(0)}}, \tag{7.137}$$

and the critical exponent of the divergence is of the order of 19 (with $a_3 = 1.3$ and $t_c = 5.6 D(0)^{-1/2}$), which is huge compared with the $(t_c - t)^{-2}$ divergence of the velocity enstrophy. Therefore, it is expected that the temperature will cascade faster than the velocity towards small scales, due certainly to the fact that there is no pressure term in the scalar equation, and hence the scalar will directly react to the velocity gradients. The velocity, on the contrary will have to satisfy the incompressibility condition, and hence redistribute among its three components and throughout the fluid, with the aid of the pressure. Remark that we have mentioned in Chapter 6 the same physical arguments in order to explain the "anomalous" k^{-1} range found for the scalar.

A numerical resolution of the E.D.Q.N.M. temperature spectral equation (including viscous and conductive effects) is possible, using the same methods as for the kinetic-energy spectrum. Again the problem arises of the non-local interactions modelling, which will be developed in the next section. Figure 7.12a, taken from Lesieur et al. [419], shows the evolution in time of both enstrophies (velocity and temperature) for an unforced calculation done in the same conditions as in Figures 7.3 and 7.4, for an initial Reynolds number $R_{k_i(0)} = v(0)/\nu k_i(0) = 40{,}000$, a Prandtl number of 1, and $a_2 = 0$. One

[18] A similar result has been predicted by Falkovich and Shafarenko [191] in a study of weakly-interacting acoustic waves.

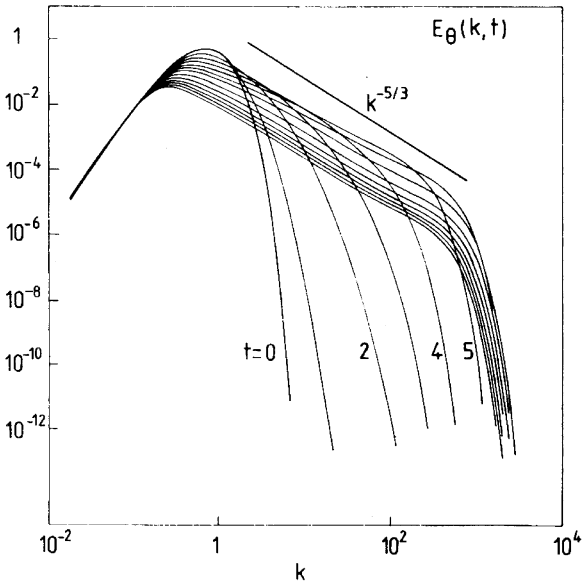

Figure 7.13. Time-evolution of the temperature spectra in the same calculation as in Figure 7.12, showing the appearance of the inertial-convective range. Temperature is called Θ (from Lesieur et al. [419]).

can see the overshoot of both quantities at $t_* \approx 5/v_0 k_i(0)$, with a faster divergence of the temperature enstrophy, in agreement with the above Euler flow considerations. Since ν and κ are small but not zero, D and D_T will saturate at values of the order of respectively ϵ/ν and ϵ_T/κ. The velocity and temperature variance decay is shown in Figure 7.12b: the passive scalar follows approximately the asymptotic tendency of the kinetic energy, that is no dissipation before t_* and a finite dissipation ϵ_T after t_*. We recall that $\epsilon_T = 2\kappa D_T(t)$, and hence the temperature enstrophy is finite (for $\kappa \to 0$) for $t < t_*$ and infinite for $t > t_*$, in good agreement with the analytical calculations already made. Notice however that the temperature-variance starts being dissipated appreciably sooner than the kinetic energy (4 instead of 5). This is due to the fact that the temperature enstrophy diverges faster than the velocity enstrophy at the critical time.

7.11.3 Inertial-convective and viscous-convective ranges

Figure 7.13 (from Lesieur et al. [419]) shows in this E.D.Q.N.M. calculation the evolution with time of the temperature spectrum, which is initially $\propto k^4$ at low k. One observes the following stages:

• for $t < t_*$, $E_T(k,t)$ is rapidly decreasing at large k

• at $t = t_*$ a $k^{-5/3}$ inertial-convective range establishes (in fact, the slope is closer to $k^{-3/2}$ than $k^{-5/3}$).

• for $t > t_*$, the spectrum will decay self-similarly, as will be explained in the next section.

In this calculation, the build up of the inertial-convective range is more rapid than the Kolmogorov cascade for the kinetic energy, since the latter establishes between 5 and 6 unit of time $1/v_0 k_i(0)$ (compare Figures 7.13 and 7.3). This specifies how temperature cascades faster than the velocity to high k. But, for a perfect fluid, this is not in contradiction with the possibility of forming simultaneously at t_* infinite ultra-violet $k^{-5/3}$ kinetic-energy and temperature spectra.

We remark that the scalar spectra of Figure 7.13 seem to display a bump at high k before the conductive range.

In fact, if the conductivity is increased with respect to the viscosity, this phenomenon of faster scalar cascade may be inhibited, as shown in the E.D.Q.N.M. calculation of Lesieur et al. [419] at a Prandtl number $P_r = 0.1$, where the velocity enstrophy now grows faster than the temperature enstrophy. This calculation shows also the appearance of a scalar spectrum close to the $k^{-17/3}$ inertial-conductive range. In the same reference, a calculation at $P_r = 10$ shows unambiguously the formation of both the $k^{-5/3}$ inertial-convective range and the k^{-1} viscous-convective range. The existence of the latter can be derived analytically, as shown in the next section.

At this point, we go back to the already quoted LES of isotropic decaying turbulence performed by Lesieur and Rogallo [421]. As stressed in Chapter 6, and when applied to the passive scalar, they show at Prandtl number one the establishment in the energy-containing eddies range of a scalar spectrum following approximately a k^{-1} law. In this calculation, the enstrophy reaches a maximum at about $t = 4/v_0 k_i(0)$, corresponding to the appearance of a Kolmogorov cascade at high wave numbers. Meanwhile, the temperature enstrophy reaches its maximum at $2.4/v_0 k_i(0)$, corresponding to a much faster ultra-violet cascade of scalar. This is qualitatively in agreement with what was observed above for the closures, except for the exponent of the scalar spectrum (-1 instead of -1.5).

7.12 Decay of temperature fluctuations

Once the temperature variance is dissipated at a finite rate, one can wonder about the existence of asymptotic (when ν and κ go to zero) temperature decay laws, and look for an exponent α_T such that

$$\frac{1}{2}\langle T(\vec{x},t)^2\rangle \propto t^{-\alpha_T}. \tag{7.138}$$

7.12.1 Phenomenology

The problem depends in fact on the relative initial location of the temperature and velocity integral scales, as was shown experimentally by Warhaft and Lumley [712].[19] An analytical study of this problem will be given here, based both on the phenomenology and on the E.D.Q.N.M. theory. It will try to explain some of the anomalous decay results found in the above quoted experiments: we will carry out the study in two cases: we assume first that both temperature and velocity scales are of the same order, and second, that the temperature is initially injected in scales much smaller than the velocity. Such a study has important practical applications, for its results are generally used to fix some of the adjustable coefficients in the so-called "one-point closure" modelling methods employed for engineering purposes.

Non-local interactions theory for the scalar

We first need to write down the non-local temperature fluxes and transfers, in the same way as for the kinetic energy above: the nonlinear temperature transfer term in the r.h.s. of Eq. (7.128) can be symmetrized with respect to p and q, under the form $\iint_{\Delta_k} dp\, dq S_T(k,p,q)$, with $S_T(k,p,q) = S_T(k,q,p)$. Then we expand $(kq/p)S_T(k,p,q)$ [or $(kp/q)S_T(k,p,q)$] with respect to the small parameter q/k (or k/p). To the first order with respect to the small parameter, we have without expanding θ:

(a) **For $q \ll k$**:

$$p = k - qy; \quad p^2 = k^2 - 2kqy;$$

$$E(p) = E(k) - qy\frac{\partial E}{\partial k}; \quad E_T(p) = E_T(k) - qy\frac{\partial E_T}{\partial k};$$

$$\frac{kq}{p} S_T(k,p,q) = \frac{1}{2}\theta^T_{kkq}(1-y^2)$$

$$\left[kqy\left\{2E_T(k) - k\frac{\partial E_T}{\partial k}\right\}E(q) + q^2 E_T(q)E(k) - \frac{q^4}{k^2}E_T(k)E(k)\right] \qquad (7.139)$$

and since

$$\int_0^1 d\phi \int_\phi^1 (1-y^2)dy = \frac{1}{4}; \quad \int_0^1 d\phi \int_\phi^1 y(1-y^2)dy = \frac{2}{15}$$

the non-local temperature flux π^{T+}_{NL} writes

[19] In these experiments, another important parameter is the grid heating intensity.

$$\pi_{NL}^{T+}(k,t) = \frac{2}{15}\int_0^{ak} \theta_{kkq}^T q^2 E(q)dq \left[2kE_T(k) - k^2\frac{\partial E_T}{\partial k}\right]$$
$$+\frac{1}{4}\int_0^{ak} \theta_{kkq}^T q^3 E_T(q)dqE(k)$$
$$-\frac{1}{4}\int_0^{ak} \theta_{kkq}^T q^5 dqE(k)\frac{E_T(k)}{k^2} \tag{7.140}$$

(b) **For $k \ll p$**:

$$q = p - kz; \quad q^2 = p^2 - 2kpz;$$
$$E(q) = E(p) - kz\frac{\partial E}{\partial p}; \quad E_T(q) = E_T(p) - kz\frac{\partial E_T}{\partial p};$$
$$\frac{kp}{q}S_T(k,p,q) = \theta_{kpp}^T\frac{k^2}{p^2}(1-z^2)[k^2E(p)E_T(p) - p^2E(p)E_T(k)] \tag{7.141}$$

and since $\int_0^1(1-z^2)dz = 2/3$, the non-local temperature flux π_{NL}^{T-} is

$$\pi_{NL}^{T-}(k,t) = -\frac{4}{3}\int_0^k k'^2 E_T(k')dk' \int_{\sup(k,k'/a)}^{\infty} \theta_{k'pp}^T E(p)dp$$
$$+\frac{4}{3}\int_0^k k'^4 dk' \int_{\sup(k,k'/a)}^{\infty} \theta_{k'pp}^T \frac{E(p)}{p^2}E_T(p)dp \tag{7.142}$$

The first term in the r.h.s. of Eq. (7.140) corresponds to interactions responsible for the k^{-1} viscous-convective range, since the corresponding flux is constant for such a spectrum. More precisely one may write in this range from this equation (see also Kraichnan [352], Newman and Herring [532], and Herring et al. [280]):

$$\epsilon_T \approx -\frac{2}{15}k^4\frac{\partial}{\partial k}\frac{E(k)}{k^2}P_1$$

with

$$P_1 = \frac{2}{15}\int_0^{+\infty} \frac{q^2E(q)dq}{a_3\sqrt{\int_0^q p^2E(p)dp} + \nu q^2},$$

calculated assuming $a_2 = 0$. This yields

$$E_T(k) = C_B\epsilon_T\left(\frac{\nu}{\epsilon}\right)^{1/2}k^{-1},$$

to be compared with Eq. (6.120). C_B is the Batchelor constant

$$C_B = \frac{1}{3P_1}\left(\frac{\epsilon}{\nu}\right)^{1/2},$$

which can be checked to be a constant by assuming a kinetic-energy spectrum of the form Eq. (6.69).

Otherwise, the interesting non-local temperature transfers as far as the infrared dynamics is concerned come from Eq. (7.142): when $k \ll k_i^T$, and taking $a = k/k_i^T$, it yields a non-local temperature transfer equal to (to the lowest order)

$$T_{NL}^T(k,t) = -\frac{4}{3}k^2 E_T(k) \int_{k_i^T}^{\infty} \theta_{0pp}^T E(p) dp$$
$$+\frac{4}{3}k^4 \int_{k_i^T}^{\infty} \theta_{0pp}^T \frac{E(p)}{p^2} E_T(p) dp. \tag{7.143}$$

This allows us to define an eddy diffusivity in spectral space, analogous to the eddy viscosity Eq. (7.77), and equal to

$$\kappa_t = \frac{2}{3} \int_{k_i^T}^{\infty} \theta_{0pp}^T E(p) dp. \tag{7.144}$$

If one takes $k_i = k_i^T$ and a schematic energy spectrum equal to zero for $k < k_i$ and to $k^{-5/3}$ for $k > k_i$, with the asymptotic values (neglecting the time exponential contribution) for θ and θ^T, it is easy to check that the turbulent Prandtl number ν_t/κ_t is equal to $(a_2 + a_3)/6a_1$, as mentioned above.

The second term of the r.h.s. of Eq. (7.143) is responsible for a positive k^4 temperature transfer. It is a temperature backscatter, and the same remarks as for the k^4 kinetic-energy backscatter can be applied: if in particular the temperature spectrum is stationary, due to an external thermal forcing acting at the fixed wave number k_i^T, the temperature spectrum will be (for $k \ll k_i^T$) a k^2 equipartition spectrum resulting from a balance between the temperature backscatter and the eddy diffusivity.

Self-similar decay

The study of the temperature decay will be made assuming that the kinetic-energy spectrum decays self-similarly according to the law equation (7.83), the kinetic energy and the integral scale following power laws of time given by Eqs. (7.87) and (7.88). We remind relations (7.86) to (7.89).

Firstly the temperature integral scale l_T is evaluated as shown below: we calculate the temperature dissipation rate ϵ_T as the ratio of the temperature variance $\langle T^2 \rangle$ divided by a characteristic dynamical time at scales of order l_T. This local time at l_T is l_T/v_T, where v_T is a velocity characteristic of the eddies of size l_T, that is $(\epsilon l_T)^{1/3}$. This yields[20]

[20] This assumes however that l_T is in the kinetic energy spectrum $k^{-5/3}$ inertial range, which will not be valid if $l_T \gg l$. The latter case has been looked at in Herring et al. [280].

$$\epsilon_T = \langle T^2 \rangle \epsilon^{1/3} l_T^{-2/3}. \tag{7.145}$$

In fact, Eqs. (7.83) and (7.145) should express only a proportionality as far as integral scales are concerned. We have chosen to consider them as equalities, which defines precisely here the velocity and temperature integral scales l and l_T. This scale is of the order of $(k_i^T)^{-1}$, wave number where the temperature spectrum peaks. Eq. (7.145) will be valid even in the case where $l_T \ll l$. As stressed above, it has no physical significance when $l < l_T$: indeed, the local dynamical time at l_T will be l_T/v, and Eq. (7.145) will have to be replaced by

$$\epsilon_T = \langle T^2 \rangle \epsilon^{1/3} l^{-2/3} \frac{l}{l_T}. \tag{7.146}$$

We also assume, however small l_T/l, that $E_T(k,t)$ is given by

$$E_T(k,t) = C_{CO} \epsilon_T \epsilon^{-1/3} k^{-5/3} \quad \text{for } k > k_i^T(t) \tag{7.147}$$

$$E_T(k,t) = C_{s'}(t) k^{s'} \quad \text{for } k < k_i^T(t). \tag{7.148}$$

The justification of Eq. (7.147) comes from an inertial-convective range assumption for the temperature spectrum.[21] Matching Eqs. (7.147) and (7.148) for $k = k_i^T \approx l_T^{-1}$ yields, using Eq. (7.145)

$$C_{s'}(t) \approx \langle T^2 \rangle l_T^{s'+1}. \tag{7.149}$$

The same reasoning as above for kinetic energy leads to, using Eq. (7.143)

$$\frac{dC_{s'}(t)}{dt} = 0 \quad \text{for } s' < 4 \tag{7.150}$$

$$\frac{dC_{s'}(t)}{dt} \sim \int_{k_i^T}^{\infty} [p^3 E(p)]^{-\frac{1}{2}} \frac{E(p)}{p^2} E_T(p) dp \quad \text{for } s' = 4 \tag{7.151}$$

and hence,[22] from Eq. (7.147)

$$\frac{dC_{s'}(t)}{dt} \sim \epsilon_T l_T^5 \quad \text{for } s' = 4. \tag{7.152}$$

All these relations are general for any $l_T/l \leq 1$. A last interesting relation can be easily derived (for $s' \leq 4$), i.e. (Lesieur et al. [419])

$$\frac{d}{dt} l_T \sim \epsilon^{1/3} l_T^{1/3} \tag{7.153}$$

[21] A similar analysis has been carried out by Métais and Lesieur [492] for the error spectrum in the predictability problem; it will be presented in Chapter 11.

[22] The constant of proportionality in Eq. (7.151) has not been expressed, but is not needed for the present analysis.

which shows that l_T satisfies a Richardson-type law analogous to Eq. (6.55), but with possibly a different numerical constant.

Looking then for time power law solutions $t^{-\alpha_T}$ and $t^{\alpha_{l_T}}$ respectively for the temperature variance and integral scale, Eq. (7.153) yields

$$\alpha_{l_T} = 1 - \frac{\alpha_E}{2} \tag{7.154}$$

which, from Eq. (7.89), indicates that α_l and α_{l_T} are equal. This, together with Eqs. (7.149), (7.150) and (7.152), gives

$$\alpha_T = (s'+1)\alpha_l - \gamma' = \frac{s'+1}{s+3}(2+\gamma) - \gamma' \tag{7.155}$$

with $C_{s'}(t) \propto t^{\gamma'}(\gamma' = 0 \text{ for } s' < 4)$, as predicted in Larchevêque et al. [377] and Herring et al. [280]. When $s = s' = 4, \gamma'$ has been found numerically with the aid of the E.D.Q.N.M. to be equal to 0.06 (Chollet [118]). Thus, in this case, $\alpha_T = 1.48$, in good agreement with the value of 1.5 found in Larchevêque et al. [377]. Chasnov [112] has reconsidered all these various laws using LES at very large times. The latter suffer however from a lack of infrared resolution due to backscatter effects.

In fact, these time power laws are not compatible with any value of the ratio l_T/l: indeed, let us write the equivalent expression of Eq. (7.145) for the velocity

$$\epsilon = v^2 \epsilon^{1/3} l^{-2/3} \tag{7.156}$$

which has been used as a definition of l as well. Eq. (7.156) shows that

$$\alpha_E = 2t\frac{\epsilon}{v^2} = 2t\epsilon^{1/3} l^{-2/3}.$$

In the same way Eq. (7.145) allows us to define an "instantaneous" temperature variance decay exponent α'_T, such that the temperature variance should locally be tangent to a $t^{-\alpha'_T}$ law, with

$$\alpha'_T = 2t\frac{\epsilon_T}{\langle T^2 \rangle} = 2t\epsilon^{1/3} l_T^{-2/3}. \tag{7.157}$$

Eqs. (7.156) and (7.157) show that

$$r = \frac{\alpha'_T}{\alpha_E} = \left(\frac{l}{l_T}\right)^{2/3}. \tag{7.158}$$

In Eq. (7.158), α'_T/α_E can also be interpreted as the velocity and scalar time scales ratio. This expression is from Corrsin [146]. With the particular definitions taken here for l_T and l, Eq. (7.158) is always valid (for $l \geq l_T$)

with a numerical constant equal to one, and even with a moderate Reynolds number. One may wonder how this relationship is modified with the classical definitions of the integral scales. It is claimed in Herring et al. [280], from a high Reynolds number E.D.Q.N.M. calculation ($l \geq l_T$), that a numerical constant of 1.63 has then to be introduced in front of the r.h.s. of Eq. (7.158). The same work stresses that, at a moderate Reynolds number, r is equal to l/l_T (even in the case $l \leq l_T$), a law which can immediately be derived from Eq. (7.146) in this latter case. This agrees well with the experiment carried out by Sreenivasan et al. [665].

When the temperature follows an actual time power law, α'_T is equal to α_T, and given by Eq. (7.155). This implies from Eq. (7.158) that one can have a time power law dependence only when l/l_T has the particular value predicted by Eqs. (7.155) and (7.85). This value depends on s and s', but in any case is very close to one. This demonstrates the point that the temperature variance decays as a power of time only if the temperature and velocity integral scales are of the same order.

Anomalous temperature decay

If l_T is initially much smaller than l, Eq. (7.158) shows that the apparent temperature time decay exponent α'_T is much greater than α_E, which might explain the anomalous temperature decay exponents found experimentally in this case by Warhaft and Lumley [712]. It has been shown in Lesieur et al. [419], using the above phenomenology, that the detailed time-evolution of the temperature variance and integral scales can be obtained analytically with these particular initial conditions. This analysis, which is an extension to an arbitrary $k^{s'}$ temperature spectrum (when $k \to 0$) of an analysis done by Nelkin and Kerr [530] in the case $s' = 2$, is based on the integration of the Richardson equation (7.153). It is found

$$l_T(t) = \left(\frac{\alpha_E}{\alpha_T}\right)^{3/2} l(t) \left[1 + B\left(\frac{t}{t_0}\right)^{-2\alpha_l/3}\right]^{3/2}, \tag{7.159}$$

where B is a negative constant, such that

$$B = -1 + \frac{\alpha_T}{\alpha_E}\left[\frac{l_T(t_0)}{l(t_0)}\right]^{3/2},$$

and initially ≈ -1. Therefore l_T/l increases with time. Hence $l_T(t)$ is going to grow and asymptotically (for t going to infinity) catch up with the time power law solution described above. Following Eq. (7.158) the instantaneous temperature decay exponent will decrease with time and eventually reach the

asymptotic value α_T given by Eq. (7.155). We again emphasize that these asymptotic values are fixed by the spectral exponents s and s' for $k \to 0$, and impose a particular ratio for l/l_T. If l/l_T is initially larger than this asymptotic ratio, it will decrease to it, and so will the temperature decay exponent. The temperature variance decays as (Lesieur et al. [419])

$$\langle T^2 \rangle \propto \left[B + \left(\frac{t}{t_0} \right)^{2\alpha_l)/3} \right]^{-3\alpha_T/2\alpha_l} . \tag{7.160}$$

This is equivalent to

$$\langle T^2 \rangle \propto l_T^{-\alpha_T/\alpha_l}. \tag{7.161}$$

In the case $s' = 2$ one recovers the above quoted results of Nelkin and Kerr [530]. Notice finally that expansions of Eqs. (7.160) and (7.161) for short times $(t - t_0)$ yield

$$l_T(t) \propto (t - t_0)^{3/2}.$$

Hence, the temperature integral scale will see its instantaneous growth exponent increase from 3/2 at short times to α_l at high times.[23] If one accepts to associate the mean thermal wake δ_T of a line source with l_T (see next section), this may be compared with the experimental findings of Warhaft [713] and Stapountzis et al. [667], who find a $\delta_T \propto (t - t_0)$ "turbulent-convective" range, and at higher times $\delta_T \propto (t - t_0)^{0.34}$ "turbulent-diffusive" range. To illustrate these results, Figure 7.14 (taken from Lesieur et al. [419]) shows the evolution of kinetic-energy and temperature spectra in a high Reynolds number E.D.Q.N.M. calculation where the initial ratio $l(0)/l_T(0) = 70$. Here $s = s' = 4$. One sees the rapid increase of l_T which tends to catch up with l. In this calculation the tangential temperature decay exponent goes from an initial value of 20 to a value of 3.5, after which the calculation is no longer significant since there remains a negligible amount of temperature variance. It is nevertheless to be expected that a calculation performed with $k^{-5/3}$ ranges extending to infinity would eventually yield a value of α'_T equal to α_T. In this calculation, as well as in Herring et al.'s [280] results, the temperature integral scale does satisfy the Richardson law when $l_T \leq l$. One may also notice in the calculation of Figure 7.14 that the temperature spectrum develops initially a range close to k^{-1}, as in Figure 6.12, and then eventually reorganizes towards a $k^{-5/3}$ inertial-convective range.

7.12.2 Experimental temperature decay data

The next results concern moderate Reynolds numbers: Figure 7.15, taken from Warhaft and Lumley [712], shows the time evolution of the kinetic energy and

[23] The same behaviour will be found for the "error-length" characterizing the decorrelation front in the predictability problem (see Chapter 11).

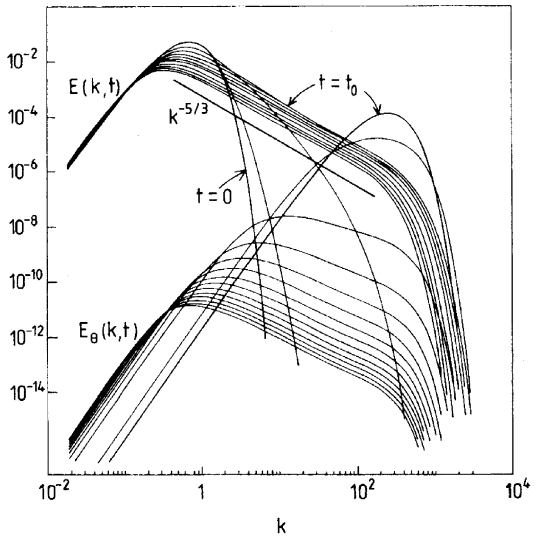

Figure 7.14. Same calculation as in Figure 7.12 for the kinetic-energy spectrum, but with an initial temperature integral scale 70 times smaller than the velocity integral scale. Temperature is called Θ (from Lesieur et al. [419]).

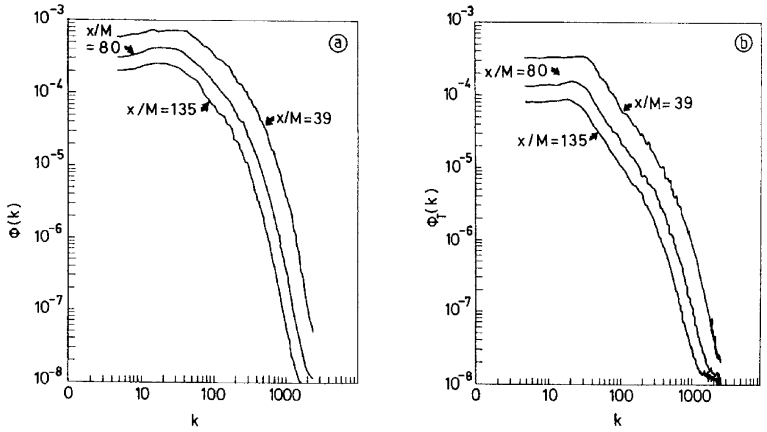

Figure 7.15. (a) Kinetic-energy and (b) temperature spectra at three locations dowstream of the grid in the experiment by Warhaft and Lumley [712], when $l_T \approx l$ initially. M is the grid mesh (courtesy *J. Fluid Mech.*).

temperature spectra in a heated-grid turbulence experiment at a Reynolds number $v_0 l/\nu$ of the order of 150. Here, and since the grid is heated, the temperature fluctuations are produced initially in the same scales as the velocity fluctuations. It is not surprising therefore, from the point of view of the above phenomenology, that the temperature decay exponent is found to be of same order ($\alpha_T = 1.41$) as the kinetic energy exponent[24] ($\alpha_E = 1.34$). At this moderate Reynolds number, a scalar range of slope $-3/2$ appears, although no inertial range is apparent for the corresponding kinetic energy spectrum. This point had already been noted by Yeh and Van Atta [732] from heated-grid turbulence experiments,[25] and could be due to the direct shearing of the scalar by the large-scale velocity gradients already mentioned in the theory leading to Eq. (6.140).

When the temperature is injected at scales such that initially $l_T/l = 1/2$, the experimental temperature decay exponent (averaged during the experiment) is found to be 3.2, in good agreement with another experiment of Sreenivasan et al. [665]. Figure 7.16, from Lesieur et al. [419], shows an E.D.Q.N.M. calculation under conditions close to these experiments: the kinetic energy decreases as $t^{-1.32}$, and the temperature variance as $t^{-3.45}$. One can also see the velocity enstrophy peak at the time when the kinetic energy starts being dissipated. It is quite remarkable to see how well the E.D.Q.N.M. theory fits the experiment in this "two-scale" (velocity and temperature) problem. It also seems that this moderate Reynolds number situation is widely influenced by the high Reynolds number theoretical predictions. As checked in the same reference, the spectra start building short $k^{-5/3}$ inertial ranges.

7.12.3 Discussion of LES results

In Lesieur and Rogallo's [421] LES starting with identical rapidly decreasing velocity and temperature spectra, the ratio k_i^T/k_i of the respective peaks of the temperature and kinetic energy spectra has shifted from 1 initially to 0.64 at the end of the run, with a temperature decay exponent $\alpha_T = 3$ of the order of twice the velocity decay exponent α_E. In the LES of Lesieur et al. [422], done with different initial conditions, one gets at the end of the run $k_i^T/k_i = 0.56, \alpha_E = 1.37$ and $\alpha_T = 1.85$. In these two cases however, where the temperature spectra are close to k^{-1} up to the cutoff wave number k_c, an appreciable part of the temperature variance may have shifted to the subgrid scales: hence, the calculated temperature variance decay rate (corresponding to the explicit scales) may just be the signature of the fast scalar transfer

[24] In a more recent experiment, Warhaft [713] shows some anisotropic effects in the kinetic-energy decay: the longitudinal velocity energy decays as $t^{-1.40}$, and the transverse velocity energy as $t^{-1.32}$.

[25] With $\alpha_T = 1.33$.

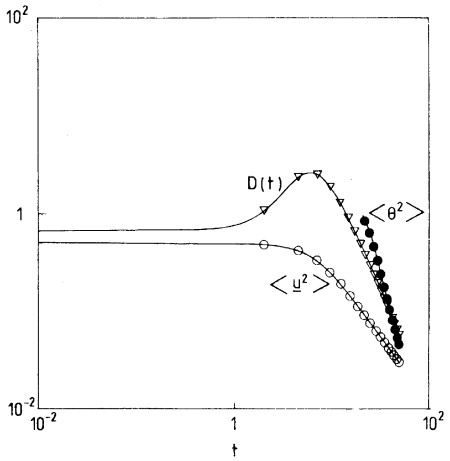

Figure 7.16. Time evolution of the kinetic energy, velocity enstrophy and temperature variance in an E.D.Q.N.M. moderate Reynolds number calculation ($R_{k_{i(0)}} = 140$), where $l_T(0)/l(0) = 0.4$ (from Lesieur et al. [419]).

towards subgrid scales, the total[26] temperature variance decaying at rates more comparable with the E.D.Q.N.M. and the experimental predictions.

How then can we reconcile the E.D.Q.N.M., L.E.S and experimental results? The faster temperature transfer towards small scales, due to the lack of pressure term in the passive scalar equation, seems to be well observed in both E.D.Q.N.M. and LES calculations, if the scalar is injected in the energy-containing range or in the inertial range. This may produce transient scalar spectra determined by the larger-scale eddies deformation. As already stressed, it is possible that these are transient effects, and that, at high Reynolds and Peclet numbers, the temperature will eventually cascade following the Corrsin–Oboukhov inertial-convective range.

7.12.4 Diffusion in stationary turbulence

Finally, it is of interest to look at the case where the kinetic energy spectrum is maintained stationary by external forces, while the temperature is decaying. We use the above phenomenological theory, where the Richardson law equation (7.153) is still valid, but things are simpler since ϵ is now a constant. For large times, l_T is proportional to $(\epsilon t^3)^{1/2}$. Eq. (7.149) is also valid, with the same distinction between the cases $s' < 4$ (where $dC_{s'}(t)/dt = 0$) and $s' = 4$. So for $s' < 4$ the temperature variance decays, for large times, proportionally

[26] Calculated on the whole temperature spectrum from $k = 0$ to $k = \infty$.

to $(\epsilon t^3)^{-3(s'+1)/2}$. If for instance $s' = 2$, the temperature decay exponent is $-9/2$, as will be retrieved in the next section using another method.

7.13 Lagrangian particle pair dispersion

Up to now we have mainly examined the statistics of a homogeneous passive scalar. But situations closer to reality are often the case when the scalar is locally injected in the homogeneous turbulent field, and then spreads out under the action of turbulent diffusion. It is, for instance, of interest to predict the evolution in time of the average size of a cloud of chemical or radioactive contaminant accidentally released in atmospheric turbulence.[27]

The formalism of the Lagrangian tracers pair relative dispersion problem allows us to give a first answer to these questions: let $R(t_0)$ be a properly defined average diameter of the cloud at a given time t_0, and consider an ensemble of pairs of particles a distance $R(t_0)$ apart, randomly distributed and oriented in space. It is reasonable to accept the idea that the subsequent mean dispersion in time of the Lagrangian tracers pairs will give information on the spreading of the cloud. More precisely, one arbitrarily associates the pair separation variance $R(t)$ to the diameter of the cloud. Such an analogy does not take into account the influence of molecular diffusion, and will be valid only for isotropic turbulence.

The homogeneous formulation of the pair dispersion problem has been given by Batchelor [46], and the problem has been studied with the aid of various statistical theories by Roberts [607] using D.I.A., Kraichnan [348] using L.H.D.I.A., Larchevêque and Lesieur [379] using E.D.Q.N.M., and Lundgren [459]. The p.d.f. $P(\vec{r}, t)$ that the two Lagrangian tracers of a pair are separated by the vector $\vec{r}$ can easily be shown to be equal to

$$P(\vec{r}, t) = \langle T(\vec{x} + \vec{r}, t) T(\vec{x}, t) \rangle - \delta(\vec{r}), \tag{7.162}$$

where $T(\vec{x}, t)$ is a homogeneous passive scalar field. It is easy to show that $P(\vec{r}, t)$ satisfies the same equation as $\Phi(\vec{r}, t)$, the spatial correlation of T. The normalization conditions satisfied by $P(\vec{r}, t)$ impose

$$\int P(\vec{r}, t) d\vec{r} = 1 \tag{7.163}$$

and the pair separation variance is

[27] When the pollutant has reached scales of several kilometers, atmospheric turbulence is no longer isotropic, and such a study is beyond the present chapter. Other practical applications of turbulent diffusion in complex flows may be found in Hunt [305]. Diffusion in two-dimensional turbulence will be looked at in Chapter 8.

$$R^2 = \int r^2 P(\vec{r}, t) d\vec{r}. \tag{7.164}$$

The problem has thus been reduced to the isotropic study carried out above, with the further condition (7.163), which corresponds to a passive scalar spectrum proportional to k^2 for $k \to 0$ (Larchevêque and Lesieur [379]). One could then simply apply the results of Section 7.11 with $s' = 2$, taking into account the difficulty that the relationship between $R(t)$ and $l_T(t)$ is not known.[28] When $R(t)^{-1}$ corresponds to Kolmogorov inertial-range eddies, it is possible to solve exactly Eqs. (7.131) and (7.132) for $P(r, t)$ (Larchevêque and Lesieur [379]), looking for self-similar solutions of the same genre as proposed by Kraichnan [348]: one seeks a solution of the form

$$P(r, t) = F[R(t)] f\left[\frac{r}{R(t)}\right], \tag{7.165}$$

and Eqs. (7.163) and (7.164) imply

$$F(R) = R^{-3},$$

with two normalization conditions for the non-dimensional function $f(x)$. The result is that $R(t)$ satisfies a Richardson law (with ϵ function of time in a decaying turbulence), and from Larchevêque and Lesieur [379],

$$P(r, t) \sim R^{-3} e^{-\left[5.44 (r/R)^{2/3}\right]}. \tag{7.166}$$

One recovers in particular the result that, for stationary forced turbulence, $P(0, t) \sim R^{-3}$ decays like $t^{-9/2}$ as shown in Section 7.12. More generally, an expansion of Eq. (7.166) for $r \ll R$ yields

$$P(0, t) - P(r, t) \sim \epsilon_T \epsilon^{-1/3} r^{2/3} \tag{7.167}$$

with

$$\epsilon_T = -\frac{1}{2} \frac{d}{dt} P(0, t) \sim R^{-4} \frac{dR}{dt} \sim \epsilon^{1/3} R^{-11/3}. \tag{7.168}$$

This is, in the particular case studied here, the derivation of the Corrsin–Oboukhov law equation (6.110) for the second-order scalar structure function, since, for any passive scalar

$$\langle [T(\vec{x} + \vec{r}, t) - T(\vec{x}, t)]^2 \rangle = 2[\Phi(\vec{r}, t) - \Phi(\vec{0}, t)].$$

[28] They turn out to be proportional.

7.14 Single-particle diffusion

7.14.1 Taylor's diffusion law

Let us first recall the classical Taylor's law [679] concerning the diffusion of a single particle in homogeneous stationary turbulence: let $\vec{X}(\vec{a},t)$ be the Lagrangian position of a tracer located in $\vec{a}$ at $t=0$. Let $\vec{v}(\vec{a},t)$ be the Lagrangian velocity, such that

$$\frac{D}{Dt}\vec{X}(\vec{a},t)=\vec{v}(\vec{a},t), \tag{7.169}$$

which yields

$$\vec{X}(\vec{a},t)=\vec{X}(\vec{a},0)+\int_0^t \vec{v}(\vec{a},\tau)d\tau\ . \tag{7.170}$$

Taking the average on an ensemble of velocity realizations ($\vec{a}$ is not random) leads to, if the turbulence is homogeneous with zero mean velocity, $\langle\vec{X}(\vec{a},t)\rangle=\vec{a}$. Now, let us consider the Lagrangian diffusion coefficient

$$K(t)=\frac{1}{2}\frac{D}{Dt}\langle[\vec{X}(\vec{a},t)-\vec{a}]^2\rangle=\langle\vec{X}(\vec{a},t).\vec{v}(\vec{a},t)\rangle,$$

which writes

$$K(t)=\left\langle\left[\vec{a}+\int_0^t\vec{v}(\vec{a},\tau)d\tau\right].\vec{v}(\vec{a},t)\right\rangle=\int_0^t\langle\vec{v}(\vec{a},\tau).\vec{v}(\vec{a},t)\rangle d\tau.$$

Since turbulence is stationary,

$$\langle\vec{v}(\vec{a},\tau).\vec{v}(\vec{a},t)\rangle=R_{ii}(t-\tau),$$

where $R_{ij}(t)$ is the Lagrangian two-time velocity correlation tensor. Hence it is found:

$$K(t)=\int_0^t R_{ii}(t-\tau)d\tau=\int_0^t R_{ii}(\tau)d\tau\ , \tag{7.171}$$

equation which is due to Taylor [679].

Now, we recall a result due to Batchelor [44]: assume that turbulence is isotropic, and that $X_i(\vec{a},t)$ is, at a given t, a Gaussian random variable (the X_i are assumed to be independent). The p.d.f. $P(x_i,t)$ that $X_i(\vec{a},t)$ is equal to x_i at time t is

$$P(x_i,t)=\frac{1}{\sqrt{2\pi\sigma_i^2}}e^{-(x_i-a_i)^2/2\sigma_i^2}\ ,$$

with

$$\sigma_i^2=\langle[X_i(\vec{a},t)-a_i]^2\rangle=\frac{1}{3}\langle[\vec{X}(\vec{a},t)-\vec{a}]^2\rangle=\frac{\sigma(t)^2}{3}.$$

This allows to show that

$$\frac{\partial}{\partial t}P(x_i,t) = \frac{1}{2}\frac{D\sigma_i^2}{Dt}\ \frac{\partial^2 P(x_i,t)}{\partial x_i^2}, \tag{7.172}$$

without summation upon the i. Now, let

$$Q(\vec{x},t) = P(x_1,t)P(x_2,t)P(x_3,t) \tag{7.173}$$

be the p.d.f. that the tracer is, at time t, located at $\vec{x}$. It satisfies the diffusion equation

$$\frac{\partial}{\partial t}Q(\vec{x},t) = \frac{K(t)}{3}\nabla^2 Q(\vec{x},t). \tag{7.174}$$

We have already seen that the Gaussianity assumption is questionable, particularly for the scalar. However, a subsequent E.D.Q.N.M. analysis will be shown to give a similar equation. Furthermore, Eq. (7.172) turns out to be valid at short and large times (see Batchelor [44]).

At short times, when the diffusion distance is short compared with the integral scale, it is obtained from Eq. (7.171):

$$K(t) \approx v_0^2 t, \sigma(t) \approx v_0 t, \tag{7.175}$$

with

$$v_0^2 = \langle \vec{v}(\vec{a},0)^2 \rangle.$$

The diffusion is *coherent*, in the sense that the r.m.s. displacement is proportional to the time. At high times, it is found, still from Eq. (7.171):

$$K(t) = \frac{1}{2}\frac{D\sigma^2}{Dt}\int_0^{+\infty} R_{ii}(\tau)d\tau = v_0^2 T_L,$$

relation which defines the Lagrangian correlation time T_L. Therefore:

$$\sigma(t)^2 = 2v_0^2 T_L t. \tag{7.176}$$

The r.m.s. displacement is now proportional to $t^{1/2}$, which characterizes an *incoherent* diffusion, as in the Brownian motion or the random walk.

7.14.2 E.D.Q.N.M. approach to single-particle diffusion

Let

$$\psi(\vec{x},t) = \delta[\vec{x} - \vec{X}(\vec{a},t)]. \tag{7.177}$$

This scalar quantity is obviously conserved following the motion. Let us calculate now the mean value of ψ. By definition of the p.d.f. $Q(\vec{x},t)$, it is obtained:

$$\langle\psi(\vec{x},t)\rangle = \int_{-\infty}^{+\infty} \delta(\vec{x}-\vec{y})Q(\vec{y})d\vec{y} = Q(\vec{x},t). \tag{7.178}$$

This allows to relate the preceding Lagrangian quantities to the Eulerian formalism of passive-scalar diffusion. We are now interested in the diffusion of an inhomogeneous scalar $\psi(\vec{x},t)$ in homogeneous isotropic turbulence (but we do not need to assume the stationarity here). We are going to write a diffusion equation satisfied by $Q = \langle\psi\rangle$, using E.D.Q.N.M.-type techniques. By averaging Eq. (5.19) with $\kappa = 0$, it is obtained

$$\frac{\partial}{\partial t}\langle\hat{\psi}(\vec{k},t)\rangle + ik_j \int \langle\hat{u}_j(\vec{p},t)\hat{\psi}(\vec{q},t)\rangle\delta(\vec{k}-\vec{p}-\vec{q})d\vec{p}d\vec{q} = 0. \tag{7.179}$$

This equation is not closed, since we need to determine the scalar-velocity correlation. For this, we use again Eq. (5.19) written for a wave vector $\vec{k}$ and Eq. (5.18) written for a wave vector $\vec{k}'$: multiplying the former by $\hat{u}_i(\vec{k}',t)$ and the latter by $\hat{\psi}(\vec{k},t)$ and adding yields, since $\langle\hat{f}\hat{\psi}\rangle = 0$:

$$\left(\frac{\partial}{\partial t} + \nu k'^2\right)\langle\hat{\psi}(\vec{k})\hat{u}_i(\vec{k}')\rangle + ik_j \int \langle\hat{u}_j(\vec{p})\hat{u}_i(\vec{k}')\hat{\psi}(\vec{q})\rangle\delta(\vec{k}-\vec{p}-\vec{q})d\vec{p}d\vec{q}$$

$$+ik'_m P_{in}(\vec{k}') \int \langle\hat{u}_n(\vec{p}')\hat{u}_m(\vec{q}')\hat{\psi}(\vec{k})\rangle\delta(\vec{k}'-\vec{p}'-\vec{q}')d\vec{p}'d\vec{q}' = 0. \tag{7.180}$$

Eqs. (7.179) and (7.180) are the two equations of the moments hierarchy with which we are going to work.

Let $\hat{\psi}'$ be the fluctuation of $\hat{\psi}$ with respect to its mean value. One can write

$$\langle\hat{\psi}(\vec{k})\hat{u}_i(\vec{p})\hat{u}_j(\vec{q})\rangle = \langle\hat{\psi}'(\vec{k})\hat{u}_i(\vec{p})\hat{u}_j(\vec{q})\rangle + \langle\hat{\psi}(\vec{k})\rangle\langle\hat{u}_i(\vec{p})\hat{u}_j(\vec{q})\rangle.$$

$\hat{\psi}'$ and $\hat{u}$ are random fonctions of zero mean. If they were Gaussian, the triple moment $\langle\hat{\psi}'(\vec{k})\hat{u}_i(\vec{p})\hat{u}_j(\vec{q})\rangle = 0$ would be zero, and hence

$$\langle\hat{\psi}(\vec{k})\hat{u}_i(\vec{p})\hat{u}_j(\vec{q})\rangle = \langle\hat{\psi}(\vec{k})\rangle\langle\hat{u}_i(\vec{p})\hat{u}_j(\vec{q})\rangle. \tag{7.181}$$

The corresponding "Quasi-Normal approximation" permits in Eq. (7.180) to write:

$$\langle\hat{u}_j(\vec{p})\hat{u}_i(\vec{k}')\hat{\psi}(\vec{q})\rangle = \hat{U}_{ji}(\vec{k}')\delta(\vec{p}+\vec{k}')\langle\hat{\psi}(\vec{q})\rangle$$

$$\langle\hat{u}_n(\vec{p}')\hat{u}_m(\vec{q}')\hat{\psi}(\vec{k})\rangle = \hat{U}_{nm}(\vec{q}')\delta(\vec{p}'+\vec{q}')\langle\hat{\psi}(\vec{k})\rangle,$$

and the second nonlinear term in Eq. (7.180) is zero (since interactions imply $\vec{k}' = \vec{0}$). Therefore, the following is obtained, within this quasi-normal assumption:

$$\left(\frac{\partial}{\partial t}+\nu k'^2\right)\langle\hat{\psi}(\vec{k})\hat{u}_i(\vec{k}')\rangle+ik_j\hat{U}_{ji}(\vec{k}')\langle\hat{\psi}(\vec{k}+\vec{k}')\rangle=0,$$

or, after a time integration:

$$\langle\hat{\psi}(\vec{k},t)\hat{u}_i(\vec{k}',t)\rangle=-ik_j\int_0^t e^{-\nu k'^2(t-\tau)}\hat{U}_{ji}(\vec{k}',\tau)\langle\hat{\psi}(\vec{k}+\vec{k}'),\tau)\rangle d\tau,$$

which is equivalent to

$$\langle\hat{\psi}(\vec{q},t)\hat{u}_i(\vec{p},t)\rangle=-iq_l\int_0^t e^{-\nu p^2(t-\tau)}\hat{U}_{lj}(\vec{p},\tau)\langle\hat{\psi}(\vec{p}+\vec{q}),\tau)\rangle d\tau.$$

Finally, the quasi-normal diffusion equation writes:

$$\frac{\partial}{\partial t}\langle\hat{\psi}(\vec{k},t)\rangle$$

$$+k_jq_l\int_{\vec{p}+\vec{q}=\vec{k}}\int_0^t e^{-\nu p^2(t-\tau)}\hat{U}_{lj}(\vec{p},\tau)\langle\hat{\psi}(\vec{p}+\vec{q}),\tau)\rangle d\tau d\vec{p}=0.$$

Noticing also, due to incompressibility, that

$$Q_l\hat{U}_{lj}(\vec{p},\tau)=k_l\hat{U}_{lj}(\vec{p},\tau),$$

the quasi-normal diffusion equation writes finally

$$\frac{\partial}{\partial t}\langle\hat{\psi}(\vec{k},t)\rangle=-k_ik_j\int_{\vec{p}+\vec{q}=\vec{k}}\int_0^t e^{-\nu p^2(t-\tau)}\hat{U}_{ij}(\vec{p},\tau)\langle\hat{\psi}(\vec{k},\tau)\rangle d\vec{p}d\tau. \quad (7.182)$$

Now, an "Eddy-Damped" procedure will consist in replacing νp^2 in Eq. (7.182) by $\nu p^2+\mu_1(p)+\mu_2(q)$, so that the E.D.Q.N. diffusion equation is

$$\frac{\partial}{\partial t}\langle\hat{\psi}(\vec{k},t)\rangle=-k_ik_j\int_{\vec{p}+\vec{q}=\vec{k}}\int_0^t e^{-[\nu p^2+\mu_1(p)+\mu_2(q)](t-\tau)}$$

$$\hat{U}_{ij}(\vec{p},\tau)\langle\hat{\psi}(\vec{k},\tau)\rangle d\vec{p}d\tau\ . \quad (7.183)$$

Finally, a "Markovianization" will consist in replacing Eq. (7.183) by:

$$\frac{\partial}{\partial t}\langle\hat{\psi}(\vec{k},t)\rangle=-k_ik_j\int_{\vec{p}+\vec{q}=\vec{k}}\Theta_{pq}^{(\psi u)}\hat{U}_{ij}(\vec{p},t)d\vec{p}\langle\hat{\psi}(\vec{k},t)\rangle \quad (7.184)$$

with

$$\Theta_{pq}^{(\psi u)}=\int_0^t e^{-[\nu p^2+\mu_1(p)+\mu_2(q)](t-\tau)}\,d\tau=\frac{1-e^{-[\nu p^2+\mu_1(p)+\mu_2(q)]t}}{[\nu p^2+\mu_1(p)+\mu_2(q)]}. \quad (7.185)$$

The choice of μ_1 and μ_2 will be made as for the E.D.Q.N.M. applied to the velocity field, that is

$$\mu_1(p) = \lambda_1 \left[\int_0^p y^2 E(y,t) dy \right]^{1/2}$$

$$\mu_2(q) = \lambda_2 \left[\int_0^q y^2 E(y,t) dy \right]^{1/2}, \tag{7.186}$$

where λ_1 and λ_2 are constants which have to be adjusted.

For diffusion times small in front of the turbulence large-eddy turn-over time, it is straightforward that

$$\Theta_{pq}^{(\psi u)} \approx t.$$

Noticing then that

$$\int \hat{U}_{ij}(\vec{p},t) d\vec{p} = \langle u_i(\vec{x},t) u_j(\vec{x},t) \rangle = \frac{\langle \vec{u}^2 \rangle}{3} \delta_{ij},$$

it is obtained:

$$\frac{\partial}{\partial t} \langle \hat{\psi}(\vec{k},t) \rangle = -k^2 t \frac{\langle \vec{u}^2 \rangle}{3} \langle \hat{\psi}(\vec{k},t) \rangle.$$

Coming back to the physical space, one recovers the diffusion equation Eq. (7.174) with the diffusion coefficient Eq. (7.175):

$$\frac{\partial}{\partial t} \langle Q(\vec{x},t) \rangle = t \frac{\langle \vec{u}^2 \rangle}{3} \nabla^2 \langle Q(\vec{x},t) \rangle. \tag{7.187}$$

For larger times, the knowledge of the two constants is required. By analogy with the isotropic problem, we will consider a simplified case where $\lambda_2 = 0$, which allows us to write Eq. (7.184) as

$$\frac{\partial}{\partial t} \langle \hat{\psi}(\vec{k},t) \rangle = -k_i k_j \left[\int \Theta_p^{(1)}(t) \hat{U}_{ij}(\vec{p},t) d\vec{p} \right] \langle \hat{\psi}(\vec{k},t) \rangle,$$

where $\Theta_p^{(1)}$ is given from Eq. (7.185) with $\lambda_2 = 0$. Using the isotropic form of the velocity spectral tensor, it is found:

$$k_i k_j P_{ij}(\vec{p}) = k^2 \sin^2 \gamma$$

where γ is the angle formed by $\vec{k}$ and $\vec{p}$. After an integration in spherical coordinates, one gets:

$$k_i k_j \int \Theta_p^{(1)} \hat{U}_{ij}(\vec{p},t) d\vec{p} = \frac{2}{3} k^2 \int_0^{+\infty} \Theta_p^{(1)}(t) E(p,t) dp,$$

which, by inverse Fourier transform, may be written as:

$$\frac{\partial}{\partial t}Q(\vec{x},t) = \frac{2}{3}\int_0^\infty \Theta_p^{(1)}(t)E(p,t)dp\nabla^2 Q(\vec{x},t). \tag{7.188}$$

It is again a diffusion equation, to be compared with Eq. (7.174), and we will associate to it the diffusion coefficient

$$K(t) = 2\int_0^\infty \Theta_p^{(1)}(t)E(p,t)dp, \tag{7.189}$$

which has the same structure as the eddy diffusivity equation (7.144).

We stress finally that many more aspects of turbulent diffusion with p.d.f. approaches applied to inhomogeneous turbulence can be found in Pope [583].

8

Two-Dimensional Turbulence

8.1 Introduction

Let us begin by considering a fluid of uniform density ρ_0 in a frame which may be rotating with a constant rotation $\vec{\Omega}$. It obeys Eq. (2.70), where we recall that the "modified pressure" P also contains the gravity and centrifugal effects. This equation governs the motion of a rotating (or not) non-stratified flow in a laboratory experiment. Let us assume that the $\vec{z}$ axis of coordinates is directed along $\vec{\Omega}$, and look for two-dimensional solutions $\vec{u}(x, y, t)$ and $P(x, y, t)$. Let $u(x, y, t), v(x, y, t)$ and $w(x, y, t)$ be respectively the "horizontal" (that is perpendicular to $\vec{\Omega}$) and vertical components of the velocity. The continuity equation implies that the velocity field is horizontally non-divergent

$$\frac{\partial u}{\partial x} + \frac{\partial v}{\partial y} = 0 \tag{8.1}$$

and hence there exists a stream function $\psi(x, y, t)$ such that

$$u = \frac{\partial \psi}{\partial y}; \quad v = -\frac{\partial \psi}{\partial x}. \tag{8.2}$$

The Coriolis force in the equation of motion is then equal to $-2\Omega\vec{\nabla}\psi$ and can also be included in the pressure term, modified as $P'(x, y, t) = P(x, y, t) + 2\rho_0\Omega\psi$. The result is that the "horizontal" velocity field $\vec{u}_H(x, y, t)$ of components $(u, v, 0)$ satisfies a two-dimensional Navier–Stokes equation

$$\begin{aligned} \frac{\partial u}{\partial t} + u\frac{\partial u}{\partial x} + v\frac{\partial u}{\partial y} &= -\frac{1}{\rho_0}\frac{\partial P'}{\partial x} + \nu\nabla_H^2 u \\ \frac{\partial v}{\partial t} + u\frac{\partial v}{\partial x} + v\frac{\partial v}{\partial y} &= -\frac{1}{\rho_0}\frac{\partial P'}{\partial y} + \nu\nabla_H^2 v \end{aligned} \tag{8.3}$$

with the incompressibility condition Eq. (8.1). In the following, the suffix H refers to the horizontal coordinates: for instance $\nabla_H^2 = \partial^2/\partial x^2 + \partial^2/\partial y^2$ is the horizontal Laplacian operator. The vertical coordinate $w(x, y, t)$ obeys a two-dimensional passive scalar equation[1]

$$\frac{D_H w}{dt} = \frac{\partial w}{\partial t} + u\frac{\partial w}{\partial x} + v\frac{\partial w}{\partial y} = \nu\nabla_H^2 w. \tag{8.4}$$

This shows that the assumption of two-dimensionality does not imply a purely horizontal motion: a fluid particle will conserve during the motion (modulo the viscous dissipation) its initial vertical velocity. The components of the vorticity $\vec{\nabla} \times \vec{u}$ are: $\partial w/\partial y, -\partial w/\partial x, -\nabla_H^2\psi$. It can be easily checked, either directly from Eq. (8.1) or from the general vorticity equation Eq. (2.75) which is written

$$\begin{aligned}\frac{D_H\vec{\omega}}{dt} &= (\vec{\omega} + 2\vec{\Omega}).\vec{\nabla}_H\vec{u} + \nu\nabla_H^2\vec{\omega} \\ &= \frac{\partial w}{\partial y}\frac{\partial \vec{u}}{\partial x} - \frac{\partial w}{\partial x}\frac{\partial \vec{u}}{\partial y} + \nu\nabla_H^2\vec{\omega},\end{aligned}$$

that the vertical vorticity $-\nabla_H^2\psi$ (which is also the vorticity of the horizontal velocity $\vec{u}_H$) obeys the same equation as Eq. (8.4). However, the vertical vorticity is no longer a passive scalar, since a perturbation brought to it would affect ψ and hence $\vec{u}_H$. It has to be stressed that, although ω is not a passive scalar, any passive scalar which, in a two-dimensional flow, satisfies the same initial and boundary conditions as ω, will be identital to it (provided the scalar molecular diffusivity is equal to ν). In a spatial mixing layer for instance, a dye injected in the vortical layer just behind the splitter plate will allow to visualize the vorticity. This was done for instance by Winant and Browand [721] to characterize the pairing mechanism.

The equation of motion for the stream function is

$$\left[\frac{\partial}{\partial t} + J(., \psi)\right]\nabla_H^2\psi = \nu\nabla_H^2(\nabla_H^2\psi) \tag{8.5}$$

where the Jacobian operator $J(A, B)$ is defined by

$$J(A, B) = \frac{\partial A}{\partial x}\frac{\partial B}{\partial y} - \frac{\partial A}{\partial y}\frac{\partial B}{\partial x}. \tag{8.6}$$

Consider for example a two-dimensional purely horizontal flow ($w = 0$): this demonstrates that a constant rotation has no effect on the dynamics of such a

[1] "Passive", in the sense that any external perturbation modifying w will have no effect on the convective field $\vec{u}_H$.

flow.[2] But we have already seen in Chapter 3, and new examples will be given in the next chapter (see also Chapter 13), that a strong rotation prevents small vertical velocity fluctuations from developing, and hence plays a stabilizing role with respect to the two-dimensional solutions.

Is it then possible to speak of *two-dimensional turbulence*? Clearly, the conservation of the vertical vorticity (modulo viscous diffusion) following the motion of the fluid particle is a severe constraint which seems to prevent all the vortex-stretching effects associated to the finite inviscid kinetic energy dissipation features of three-dimensional turbulence. However, a lot of weakly-viscous two-dimensional flows share the *mixing* and *unpredictability* properties, proposed in Chapter 1 as characteristic of turbulence. It will be seen below that two-dimensional turbulence is characterized (for low but non-zero viscosity) by a conservation of kinetic energy, a finite dissipation of enstrophy, and an exponential increase of the palinstrophy,[3] already introduced in Chapter 6, and here equal to

$$P(t) = \frac{1}{2}\langle[\vec{\nabla} \times (\vec{\nabla} \times \vec{u}_H)]^2\rangle. \tag{8.7}$$

From a mathematical viewpoint, there is therefore no difficulty in studying turbulent solutions of the two-dimensional Navier–Stokes equations considered above. The problem lies in the physical possibility of realizing and maintaining such flows: indeed, and if one accepts the well-known concept of "return to three-dimensionality" (see e.g. Herring [275]), a two-dimensional turbulent flow extending in an infinite domain and submitted to small 3D perturbations will become three-dimensional if there is no external action tending to maintain the two-dimensionality. The first possibility is thus to consider in a laboratory a flow constrained between two planes of distance D: at scales much larger than D, one may expect the flow to be horizontal and two-dimensional. Nevertheless the boundary layers along the planes will develop, interact, and be responsible for active three-dimensional turbulence at scales smaller than D, which could rapidly dissipate the energy of the large two-dimensional scales. It is therefore necessary to limit the development of these boundary layers. This may be done with the aid of a rapid[4] rotation $\vec{\Omega}$ (Colin de Verdière [132], Hopfinger et al. [296], Morize, Moisy and Rabaud [523,524]) or (in M.H.D.turbulence) by imposing a magnetic field $\vec{B}$ (Somméria [660], Moreau [519], Messadek and Moreau [489]). In geophysical situations, the shallowness of the atmosphere or of the oceans (with respect to horizontal plan-

[2] If the boundary conditions concerning ψ are unchanged with respect to the non-rotating case.

[3] This word was introduced first in Pouquet et al. [584]. It is constructed with the aid of Greek derivatives: *strophy* stands for *rotation*, and *palin* for *again*, so that *palinstrophy* characterizes the *curl* of the *curl* (see Frisch [221]).

[4] "Rapid", that is with a low Rossby number.

etary scales) and the rotation of the earth corresponds to an analogous situation. In fact, the concept of two-dimensional turbulence and unpredictability was developed by meteorologists who could not predict the evolution of these planetary motions for more than a few days (Thompson [685], Leith [398], Lorenz [454]).

Let us mention also the experiments on two-dimensional turbulence and two-dimensional shear flows done in liquid soap films by Couder [149] and Gharib and Derango [253]. The latter authors show in particular impressive visualizations of Kelvin–Helmholtz vortices in the flow over a backwards-facing step, which resemble very much the two-dimensional direct-numerical simulations of this flow done by Silveira-Neto [648] and presented on Plate 3.

We stress that a very interesting series of experiments done in the group of Tabeling have confirmed most of the important theoretical predictions regarding forced two-dimensional turbulence. The experiments are done in two layers of NaCl solutions excited with electromagnetic forces. The velocity field is measured, allowing in particular the numerical determination of the fluid-particle trajectories. These results will be precised later on.

Finally, Chapter 13 will discuss how the influence of a stable stratification in an infinite fluid might lead in some cases to quasi two-dimensional flows organized in horizontal layers possessing some of the features of two-dimensional turbulence, but with a strong vertical variability.

In the present chapter, we focus on the dynamics of strictly two-dimensional turbulence. We will first look at it from a statistical point of view, and show how the double inviscid conservation of energy and enstrophy pushes these quantities to cascade respectively towards large and small scales. We will study also coherent vortices, pressure distributions, diffusion of passive scalars, and pair dispersion. The E.D.Q.N.M. theory will be also considered. All this concerns isotropic two-dimensional turbulence. We will end this chapter by examining the two-dimensional temporal mixing layer from a two-dimensional turbulence point of view.

Let us mention an interesting review on two-dimensional and quasi two-dimensional turbulence by Carnevale [100].

8.2 Spectral tools for two-dimensional isotropic turbulence

We consider purely two-dimensional isotropic turbulence obeying Eq. (8.3) (or equivalently Eq. (8.5)). The essential characteristics of the dynamics of such a turbulence from a statistical viewpoint are described in Kraichnan and Montgomery [359] and Lesieur [417]. As was the case in three dimensions, one can introduce the two-dimensional spatial Fourier transform of the velocity and stream function

$$\hat{u}_i(\vec{k},t) = \left(\frac{1}{2\pi}\right)^2 \int e^{-i\vec{k}.\vec{x}} \hat{u}_i(\vec{x},t)dxdy \tag{8.8}$$

$$\hat{\psi}(\vec{k},t) = \left(\frac{1}{2\pi}\right)^2 \int e^{-i\vec{k}.\vec{x}} \psi(\vec{x},t)dxdy \tag{8.9}$$

with $\vec{k} = (k_1, k_2)$ and $\vec{x} = (x, y), i = (1, 2)$. Let us define the function $\hat{\Psi}$ such that

$$\langle \hat{\psi}(\vec{k}',t)\hat{\psi}(\vec{k},t)\rangle = \hat{\Psi}(k,t)\delta(\vec{k}+\vec{k}'). \tag{8.10}$$

We recall from Chapter 5 that for isotropic two-dimensional turbulence:

$$\langle \hat{u}_i(\vec{k}',t)\hat{u}_j(\vec{k},t)\rangle = \frac{E(k,t)}{\pi k} P_{ij}(\vec{k})\delta(\vec{k}+\vec{k}'), \tag{8.11}$$

and one chan check that

$$E(k,t) = \pi k^3 \hat{\Psi}(k,t). \tag{8.12}$$

The kinetic energy and the enstrophy are still respectively

$$\int_0^{+\infty} E(k,t)dk \quad \text{and} \quad \int_0^{+\infty} k^2 E(k,t)dk.$$

As in three-dimensional turbulence, the kinetic energy is conserved by the nonlinear terms of the equations, and Eq. (8.3) yields in the unforced case

$$\frac{d}{dt}\int_0^{+\infty} E(k,t)dk = -2\nu \int_0^{+\infty} k^2 E(k,t)dk. \tag{8.13}$$

But since there is no vortex stretching, the enstrophy also obeys a conservation equation

$$\frac{d}{dt}\int_0^{+\infty} k^2 E(k,t)dk = -2\nu \int_0^{+\infty} k^4 E(k,t)dk. \tag{8.14}$$

This result will form the basis for all the phenomenological theories of two-dimensional turbulence. It has to be stressed however that an infinite family of "inviscid"[5] invariants can be constructed with the aid of the enstrophy: indeed, Eq. (8.5) expresses the "inviscid" conservation of the vorticity ω following the fluid motion, and hence of any functional $f(\omega)$. Since the motion is incompressible, the surface $\delta\Sigma$ of the horizontal sections of the fluid tubes is also conserved, and the integral $\int f(\omega)\delta\Sigma$ on the domain over which the

[5] "Inviscid" means here without considering the viscous dissipation terms, which however exist and may contribute to the dissipation of the quantities considered, even at small viscosity.

fluid extends is conserved with time.[6] This implies the invariance of $\langle f(\omega)\rangle$ with time, if one accepts identifying the ensemble and spatial averages. It is therefore possible that the existence of these invariants could modify the following dynamical conclusions, based on theories which generally preserve only the kinetic energy and enstrophy invariance.

8.3 Fjortoft's theorem

This theorem (which has no relation with Fjortoft's inviscid instability criterion demonstrated in Chapter 3) (Fjortoft [206]) serves as a basis for the two-dimensional turbulence phenomenology: let us consider the two-dimensional Euler equation in Fourier space, truncated in order to retain only three modes k_1, k_2 and k_3. For simplification we assume $k_2 = 2k_1$ and $k_3 = 3k_1$. Let $E(k_i, t)$ be the kinetic energy at the mode k_i (integrated upon a ring of radius k_i). Conservation of kinetic energy and enstrophy implies that between two times t_1 and t_2, the variation $\delta E_i = E(k_i, t_2) - E(k_i, t_1)$ satisfies two constraints

$$\delta E_1 + \delta E_2 + \delta E_3 = 0 \tag{8.15}$$

$$k_1^2 \delta E_1 + k_2^2 \delta E_2 + k_3^2 \delta E_3 = 0 \tag{8.16}$$

which yields

$$\delta E_1 = -\frac{5}{8}\delta E_2; \quad \delta E_3 = -\frac{3}{8}\delta E_2 \tag{8.17}$$

$$k_1^2 \delta E_1 = -\frac{5}{32} k_2^2 \delta E_2; \quad k_3^2 \delta E_3 = -\frac{27}{32} k_2^2 \delta E_2. \tag{8.18}$$

Therefore, if the intermediate wave number k_2 loses kinetic energy (which implies $\delta E_2 < 0$), more energy will go to k_1 than to k_3, and more enstrophy will go to k_3 than to k_1. These conclusions must, of course, be reversed if $\delta E_2 > 0$. But, it is the first case which has more physical significance when freely decaying two-dimensional turbulence is considered: indeed let us envisage now a continuous range of wave numbers, and an initial kinetic energy spectrum peaked about a wave number $k_i(0)$. Due to nonlinear interactions, it is expected that the peak will spread out towards other modes, and consequently the amount of kinetic energy in the vicinity of $k_i(0)$ will decrease; Fjortoft's result will then suggest that more kinetic energy (resp. less enstrophy) will go towards modes $k < k_i(0)$ than towards modes $k > k_i(0)$. The same result is obtained by considering the inviscid equations 8.13 and 8.14: a purely ultraviolet transfer of energy would heavily increase the enstrophy, and the only

[6] This is valid however only if the domain is compact, or if periodicity holds on the boundaries: the latter condition is fulfilled for homogeneous turbulence (fluid in a "square").

way of satisfying both kinetic-energy and enstrophy conservation is to have an infrared energy transfer larger than the ultraviolet one. Actually, this is what the direct numerical simulations show in this case. It has to be stressed that Fjortoft's result is not always true for individual triads of wave vectors $(\vec{k}_1, \vec{k}_2, \vec{k}_3)$ with an arbitrary relative orientation, as was shown by Merilees and Warn [487].

8.4 Enstrophy cascade

8.4.1 Forced case

We work in the context of a turbulence forced at a fixed wave number k_i by a stationary kinetic-energy forcing $F_o(k)$ concentrated about k_i. It injects kinetic energy and enstrophy at respective rates $\epsilon = \int_0^{+\infty} F_o(k)dk$ and $\beta = \int_0^{+\infty} k^2 F(k)dk \approx k_i^2 \epsilon$. Let us write the evolution equation for the enstrophy spectrum

$$\left(\frac{\partial}{\partial t} + 2\nu k^2\right) k^2 E(k,t) = k^2 T(k,t) + k^2 F_o(k), \tag{8.19}$$

where $T(k,t)$ is the kinetic energy transfer. Let

$$Z(k) = \int_k^{\infty} k^2 T(k) dk \tag{8.20}$$

be the enstrophy flux across k. We assume a stationary energy spectrum except at modes $k \ll k_i$, where it will be shown below that we do not have stationarity. Neglecting this spectral range in the enstrophy budget, Eq. (8.19) implies that

$$\beta = 2\nu \int_0^{+\infty} k^4 E(k) dk. \tag{8.21}$$

Now we assume that the Reynolds number is high enough, so that there exists a range of wave numbers $k_i < k \ll k_d$ whose dynamics is not affected by viscosity (k_d is an enstrophy-dissipative wave number, discussed below). Then a reasoning analogous to what was done for 3D isotropic turbulence allows to show an exact result in this range:

$$Z(k) \equiv \beta.$$

It has been proposed by Kraichnan [350] and Leith [398] that the kinetic-energy spectrum in this range is a function of β and k only. Then standard dimensional analysis yields the enstrophy cascade concept, where the kinetic energy spectrum is given by

$$E(k) = C' \beta^{2/3} k^{-3}. \tag{8.22}$$

8.4.2 Decaying case

The above reasoning assumes that turbulence is forced at k_i. The same k^{-3} enstrophy cascade was proposed by Batchelor [51] in the context of a freely-decaying two-dimensional turbulence, where a self-similar evolving spectrum of the form

$$E(k,t) = v^3 t F(kvt) \tag{8.23}$$

was assumed: with such a spectrum (where the kinetic energy $(1/2)v^2$ is supposed to be independent of time), the enstrophy is proportional to t^{-2} provided the integral $\int^{\infty} x^2 F(x)dx$ converges; the enstrophy dissipation rate

$$\beta = -\frac{dD(t)}{dt} \tag{8.24}$$

is proportional to t^{-3}, and the assumption of a range where $F(x) \propto x^{\alpha}$ with a coefficient independent of v leads to $\alpha = -3$ and a spectrum $E(k) \sim t^{-2}k^{-3}$ corresponding to Eq. (8.22).

Physically, the enstrophy-cascade concept corresponds to the fact that a fluid blob imbedded into a larger scale velocity strain will be elongated in the flow direction, and compressed in the transverse direction, yielding a decrease of its transverse characteristic dimension; since at the same time the vorticity of each fluid point is conserved, the result will be a steepening of the transverse vorticity gradients, with a flux of vorticity into the small scales. This may be understood more quantitatively in the following manner. Let us consider (in the Euler case) the vorticity gradient equation: since the vorticity ω is convected by the flow, its gradient satisfies an equation similar to Eq. (2.89), yielding

$$\frac{D}{Dt}\vec{\nabla}\omega = -\vec{\nabla}\vec{u}|^t : \vec{\nabla}\omega. \tag{8.25}$$

The same equation is also satisfied by the gradient $\vec{\nabla}\rho$ of a passive scalar. Here, we anticipate that coherent vortices of the Kelvin–Helmholtz or Karman type are going to appear as the result of strong inverse energy transfers processes (see below), producing large-scale intermittency. If we consider the stagnation regions in the braids between the vortices, and assume that the vorticity is much smaller than the deformation (as we did in Chapter 3 to understand the formation of longitudinal vortices in quasi two-dimensional mixing layers), one can replace in Eq. (8.25) the velocity gradient by the deformation tensor. Assuming that the (small) vorticity has no effect upon the deformation tensor elements, it implies that the vorticity gradient is increased in the direction of the second principal axis of deformation (direction normal to the braids reconnecting the vortices). This mechanism does not hold within the core of the vortices, and it is feasible that the enstrophy cascade will not be efficient there. This might be an explanation why kinetic-energy spectra observed in

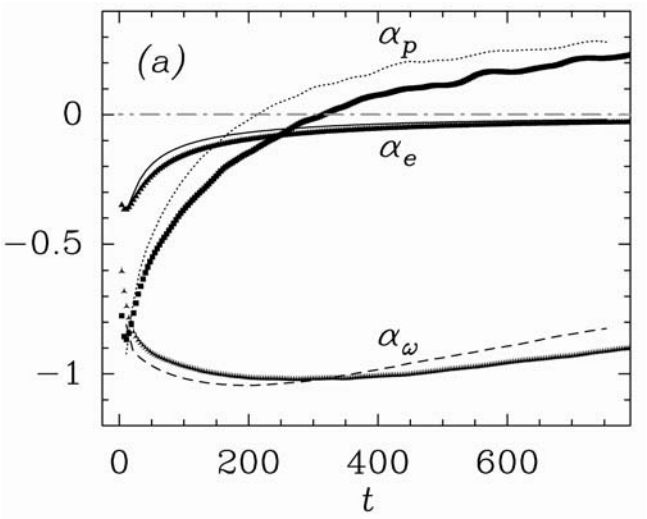

Figure 8.1. Time exponents characterizing enstrophy, energy and pressure in two LES' at resolutions 1024×1024 (full line) 256×256 (points). From Ossia and Lesieur [557].

two-dimensional turbulence are slightly steeper than k^{-3}. For the same reason (existence of coherent vortices), the t^{-2} decay law of enstrophy predicted by Batchelor's self-similar analysis is reduced significantly in the final stage of decay of the vortices (see in particular Carnevale et al. [99], Bartello and Warn [35], Chasnov [113], Ossia and Lesieur [557]). In the latter work, if one assumes that the energy and enstrophy decay respectively as $t^{-\alpha_E}$ and $t^{-\alpha_D}$, pseudo-spectral LES' yield the result that α_E tends to zero and α_D increases slightly above 1. This is shown in Figure 8.1, presenting respectively $\alpha_\omega = -\alpha_D, \alpha_e = -\alpha_E$ in runs at two different resolutions. The figure gives also the pressure time exponent α_p such that $\langle p'^2 \rangle \propto t^{\alpha_p}$. More on pressure in two-dimensional turbulence will be said at the end of this chapter.

8.4.3 Enstrophy dissipation wave number

When molecular-viscous effects are taken into account, and if the local vorticity gradients are high enough, the molecular viscosity dissipates the vorticity. Then an enstrophy dissipation wave number can be introduced, function of β and ν only. It has a different form from Eq. (6.39) and is now equal to

$$k_d = \left(\frac{\beta}{\nu^3}\right)^{1/6}. \tag{8.26}$$

On the other hand, the assumption of a $\beta^{2/3}k^{-3}$ energy spectrum extending from k_i to k_d permits to evaluate approximately the kinetic energy $(1/2)v^2$ and the enstrophy D. Neglecting the logarithmic corrections, one finds $k_i \sim \beta^{1/3}/v$ and

$$\beta^{1/3} \sim D(t)^{1/2}.$$

Estimating roughly D as $k_i^2 v^2$, one finally obtains

$$Re = \frac{v}{\nu k_i} \sim \left(\frac{k_d}{k_i}\right)^2, \tag{8.27}$$

which shows that the total number of degrees of freedom of two-dimensional turbulence is of the order of Re, at variance from the $Re^{9/4}$ value which has been determined for three-dimensional turbulence.

8.4.4 Discussion on the enstrophy cascade

DNS' of the enstrophy cascade were carried out by Lilly using finite-difference methods, both in the forced and freely-evolving cases [440–442]. He found a spectrum very close to k^{-3} on about one decade.[7] He confirmed also, by comparing the stream function and vorticity contours, the fact that vorticity tends to cascade towards small scales while kinetic energy goes to larger and larger scales, where it remains trapped if the fluid extends on a domain of finite extent. We reproduce in Figure 8.2 a sketch of Lilly [442] due to O. Carel during a summer school in 1971 in Lannion (France) organized by Morel [520] which the author attended, and where these results where presented.

Higher-resolution calculations (with 128^2 modes in a spectral-method calculation) in the decaying case, using spectral methods or finite-differences methods as well, were done by Herring et al. [275]. They found a k^{-4} spectrum instead of the law equation (8.22), and stressed that the extent of the spectral range was insufficient to describe properly the enstrophy cascade, due to the low resolution. They remark also that, at these resolutions, the dynamics of the large scales is Reynolds number independent. These calculations display also in the vorticity contours evidence of the presence of what will be called later on coherent vortices.

Other interpretations of the vorticity transfers towards small scales in two-dimensional isotropic turbulence have been given, in particular by Saffman [623], who proposes that the vorticity conservation following the motion will produce vorticity shocks, and that the resulting enstrophy spectrum consists of a random superposition of shocks, and is then proportional to k^{-2}; hence the energy spectrum should follow a k^{-4} inertial range. As a matter of fact, an inviscid numerical simulation done by Kida and Yamada [328], using time

[7] Numerical methods were however quite diffusive.

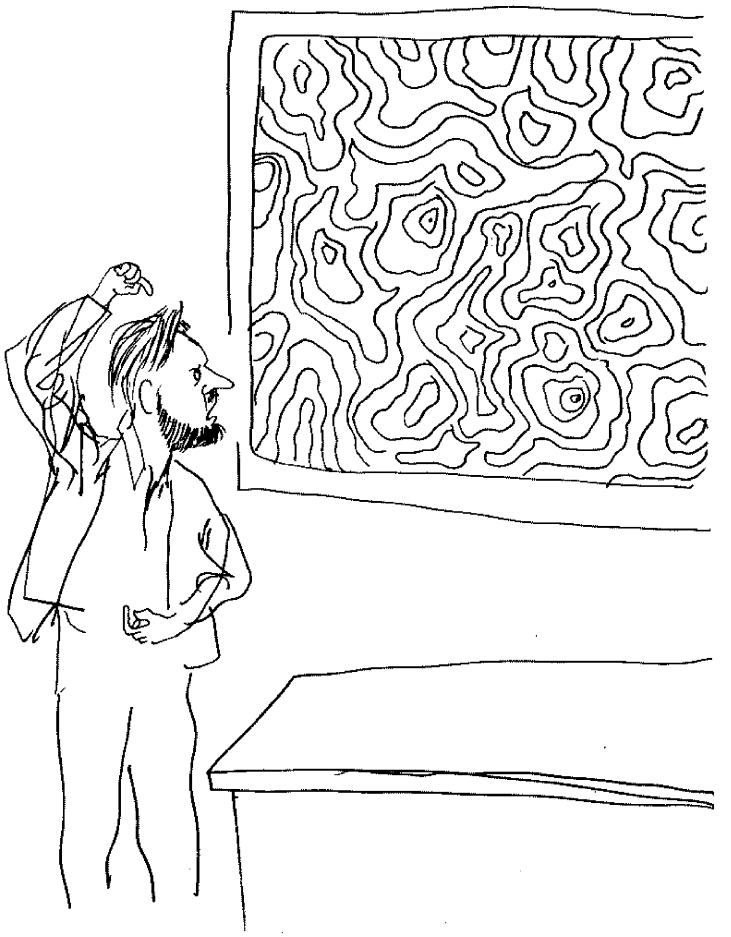

Figure 8.2. Stream function in DNS of two-dimensional turbulence presented by Lilly [442] in Lannion (courtesy O. Carel).

power series expansions, displays an energy spectrum proportional to $k^{-4.6}$. However, such a theory does not take into account the role of viscosity, which will be seen to be needed if one wants to dissipate the enstrophy at a finite rate.

A clear experimental checking of the enstrophy cascade in the forced case has been given more recently by Paret, Jullien and Tabeling [565]. They find a close to k^{-3} range on about one decade, and determine in Eq. (8.22) the constant as $C' = 1.4$. They find also in this range a close to Gaussian behaviour for the vorticity exponents.

Figure 8.3. Isovorticity lines in the isotropic two-dimensional direct numerical simulation of Brachet et al. [75], for a pseudo-spectral calculation with a resolution of 512^2 (courtesy M.E. Brachet).

8.5 Coherent vortices

As already pointed out, a very impressive feature of two-dimensional isotropic turbulence is the formation of Kelvin–Helmholtz type coherent vortices. These structures have been clearly identified in the numerical simulations of Fornberg [209] and McWilliams [479] in decaying situations (see also Babiano et al. [24], Brachet et al. [75, 76], Farge and Sadourny [195]), and in some stationary forced situations with a forcing spectrum at high wave numbers (Basdevant et al. [38], Herring and McWilliams [282]). Paret et al. [565] find in their forced experiment elongated vorticity contour in the enstrophy cascade.

These coherent vortices are visible in Figure 8.3, taken from Brachet et al. [75]. They carry both signs of vorticity, since (due to the circulation theorem) the integral of vorticity on a periodic square domain is zero. Vortices of same sign may undergo a pairing,[8] as observed in the numerical simulations of decaying two-dimensional isotropic turbulence done by Babiano et al. [24],

[8] That is, merging of two eddies of same sign which rotate around one another.

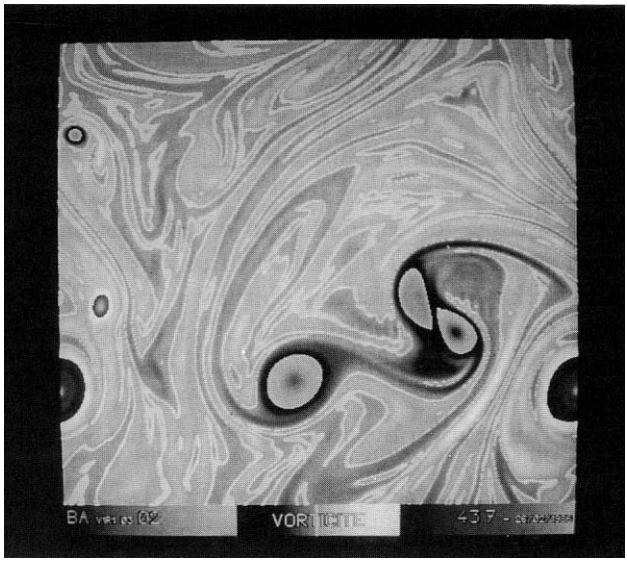

Figure 8.4. Vorticity distribution in a DNS of two-dimensional turbulence, showing in particular a pairing and a dipole (courtesy M. Farge, Paris).

Brachet et al. [76] and Farge and Sadourny [195]. Vortices of opposite sign may form dipoles. This is well illustrated by the DNS of Figure 8.4, due to Farge [196]. The origin of these vortices is a matter of debate. If one considers an initial-value problem with an initial field consisting of a weak random white noise, one sees in the numerical simulations small coherent vortices emerging from the initial "chaos". McWilliams [479] explains this phenomenon by the strong inverse energy transfers due to the double conservation of energy and enstrophy. They imply a significant growth of the integral scale, and hence some spatial organization. The formation of the initial vortices might also be due either to the development of inflectional instabilities of the initial velocity field. Afterwards, as already stressed, the scale of the structures grow, due in particular to pairings. Two-dimensional turbulence provides in fact a beautiful example of self-organization within a system which was initially totally disorganized. It was shown in the above-quoted reference that the large vortices survive much longer after the small-scale turbulence has been dissipated by viscosity. Their influence on the two-dimensional kinetic-energy spectrum may be multiple: firstly, they produce large-scale intermittency,[9] and it has been argued by Basdevant et al. [38] and Basdevant and Sadourny

[9] Indeed, if one considers the E.D.Q.N.M. model of two-dimensional turbulence (see below), it is possible to give in that frame an analytical derivation of the k^{-3} law (with a logarithmic correction), which also shows that the enstrophy interactions

[40] that this intermittency could restore the transfers localness and yield a kinetic energy spectrum steeper than the k^{-3} enstrophy cascade model presented above. Secondly, and as already stressed, they create strong vorticity gradients in the stagnation regions inbetween, as shown by Brachet et al. [76]: in the latter spectral calculation, performed in the decaying case at a resolution of 800^2 modes, there are two distinct phases: during a first period (when coherent eddies form), the energy spectrum is not submitted to viscosity (which affects the small scales), and seems to be close to k^{-4}, with formation of intense sheets of palinstrophy strained between the large eddies. Once the dissipative scales are excited[10] there is a transition towards a k^{-3} energy spectrum, corresponding to a "packing" of these sheets. This is apparent in Figure 8.3. A last theory of the kinetic-energy spectrum is to say that it results from spiral vortex distributions within the coherent vortices: Moffatt [512] and Gilbert [257] propose that a spiralling vortex should have a $k^{-11/3}$ spectrum, which is intermediate between k^{-3} and k^{-4}.

Let us finish this section by saying a few words about what is called Weiss criterion. On the basis of Eq. (8.25), Weiss [714] remarks that the eigenvalues λ of the operator $\vec{\nabla}\vec{u}|^t$ are the square roots of $(\sigma^2 - \omega^2)/4$, where ω is the vorticity and σ the strain defined by

$$\sigma^2 = \frac{1}{2} \sum_{i,j=1,2} \left(\frac{\partial u_i}{\partial x_j} + \frac{\partial u_j}{\partial x_i} \right)^2 . \tag{8.28}$$

Then he separates the space into elliptic and hyperbolic regions, where the quantity $\sigma^2 - \omega^2$ is respectively negative and positive. Assuming that the velocity gradients vary much slower than the vorticity gradients, he proposes that in the elliptic regions the vorticity gradients will rotate (since the eigenvalues are pure imaginary), while in the hyperbolic regions they will be stretched or compressed along the eigenvectors (since the eigenvalues are real and of opposite sign because of incompressibility). On the basis of various DNS of two-dimensional turbulence, Basdevant and Philipovitch [41] have checked that elliptic regions did correspond to coherent vortices (with spiral vorticity distributions), and satisfy Weiss criterion. On the other hand, hyperbolic regions do not. In fact this is a particular case in two dimensions of the Q criterion mentioned in Chapter 4, as discussed in Lesieur et al. [431]. Studies going beyond Weiss criterion's assumptions can be found in Lapeyre et al. [374,375] and Klein et al. [335].

---

in the enstrophy cascade are not local, but semi-local in the sense that $Z(k)$ is dominated by triads (k', p, q) such that $q \ll k' \approx k \approx p$.

[10] Time which corresponds to a maximum in the enstrophy-dissipation rate.

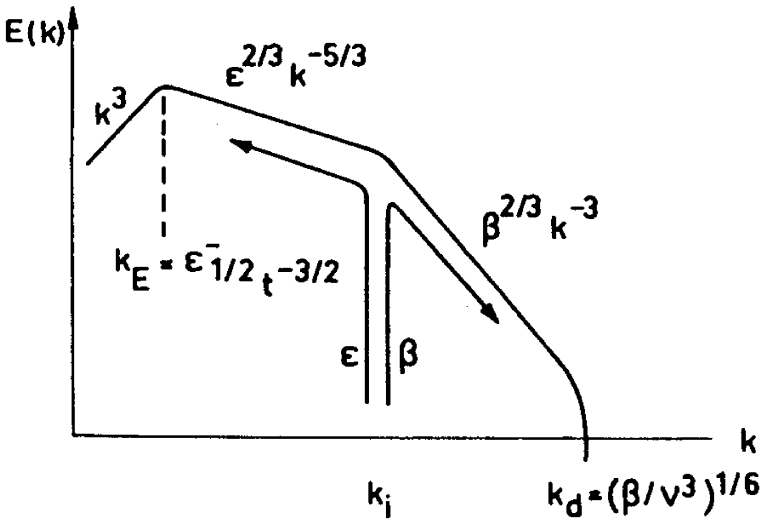

Figure 8.5. Schematic double cascading spectrum of forced two-dimensional turbulence (from Lesieur [417]).

8.6 Inverse energy transfers

8.6.1 Inverse energy cascade

This concept is from Kraichnan [350], and holds only when turbulence is forced at a fixed wave number k_i. Fjortoft's theorem has shown that kinetic energy could be transferred more easily towards large scales than towards small scales. In fact it will be shown below that, within the E.D.Q.N.M. model, the kinetic-energy flux through the enstrophy cascade is zero. So the kinetic energy injected at the rate ϵ at k_i can only cascade backwards towards small wave numbers. Kraichnan's argument is then the same as for the three-dimensional Kolmogorov kinetic energy cascade, except for the sign of the kinetic energy flux $\Pi(k)$ which is now negative. In this range ($k < k_i$) the kinetic energy spectrum is

$$E(k) = C'_K \epsilon^{2/3} k^{-5/3}. \tag{8.29}$$

Figure 8.5 shows schematically the kinetic energy spectrum obtained with such a forcing.

We will call this range Kolmogorov inverse energy cascade. It is not stationary at low wave numbers, since kinetic energy is continuously supplied at a rate ϵ, without any dissipation. Writing that the kinetic energy contained under the Kolmogorov spectrum is proportional to ϵt, it is then easy to show

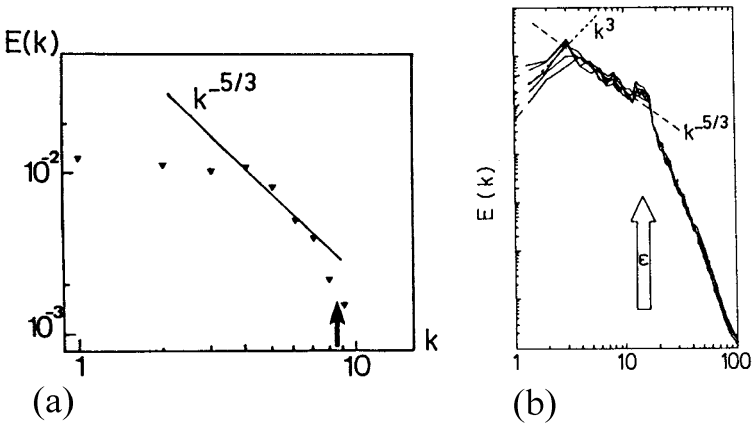

Figure 8.6. (a) Experimental kinetic energy spectrum obtained by Sommeria [660] in a forced two-dimensional turbulence in mercury. The arrow figures the energy injection wave number (courtesy *J. Fluid Mech.*). (b) Inverse energy cascade obtained in the numerical simulation of Frisch and Sulem (1984). The calculation shows also the k^3 infrared spectrum due to backscatter (courtesy *Physics of Fluids*).

that the wave number k_E characteristic of the spectrum maximum will decrease like (Pouquet et al. [584])

$$k_E(t) \sim \epsilon^{-1/2} t^{-3/2} \tag{8.30}$$

a Richardson law for the associated scale (which here is the integral scale of the turbulence, characteristic of the energetic eddies). For $k < k_E$, the spectrum is proportional to k^3, due to resonant non-local interactions of two energetic wave numbers $\approx k_E$, as shown in Basdevant et al. [37]. This k^3 spectral backscatter, which will be explained thanks to the E.D.Q.N.M. analysis, is the equivalent of the k^4 backscatter found in three dimensions (see Chapter 7). It exists also in decaying situations, as shown below.

Practically, there always exists in the numerical calculations or in the experiments a minimum non-zero wave number corresponding to the maximum extension of the domain: it has been shown in this case (forced turbulence) that the kinetic energy cannot increase indefinitely, as it would do for a $k^{-5/3}$ spectrum extending to $k = 0$, but will have an upper bound, due to the action of viscosity which will eventually play a role in the large scales when the latter will be extremely energetic (Pouquet et al. [584]). In order to prevent this excessive accumulation of energy on the lower wave number, it is possible to add to the r.h.s. of the equation of motion (8.5) a damping term proportional to $-\nabla_H^2 \psi$, which will dissipate the inverse cascading kinetic energy and limit the

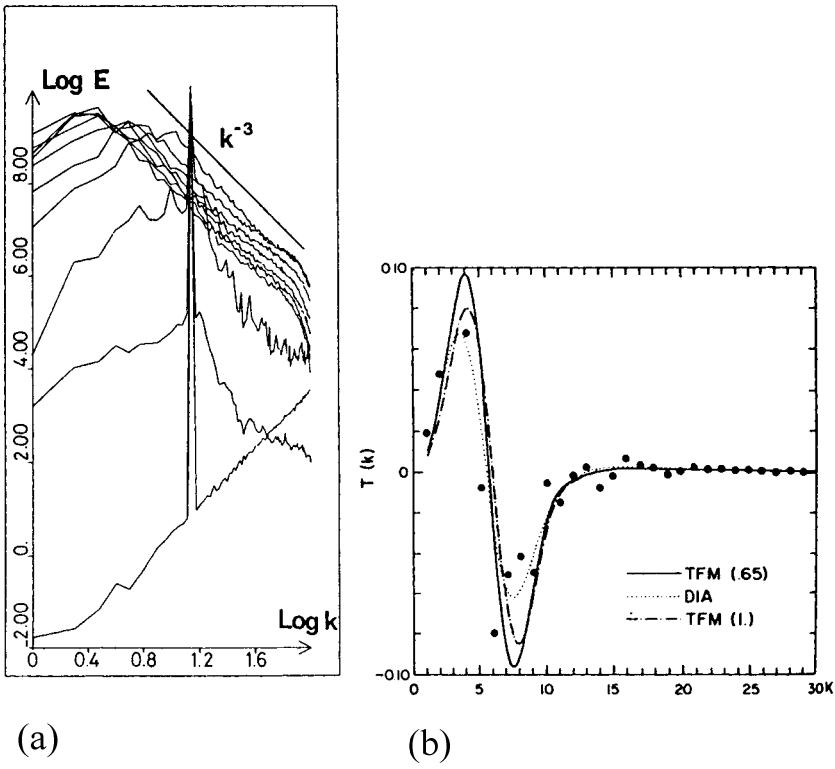

Figure 8.7. (a) Freely-decaying kinetic-energy spectrum obtained numerically in the LES of Staquet [668]. A self-similar k^{-3} Batchelor spectrum establishes, with an enstrophy cascade extending above $k_i(t)$, and no inverse $k^{-5/3}$ energy cascade. (b) Comparison between the two-dimensional turbulence kinetic energy transfers computed in a DNS (points), the D.I.A. approximation, and the Test-Field-Model with two different values of an adjustable parameter (from Herring et al. [276], courtesy *J. Fluid Mech.*).

infrared extent of the inverse energy cascade: this was done in particular in the numerical simulations of Lilly [440, 442]. Physically, such a damping may be provided by the Ekman layer dissipation for a rapidly-rotating flow above a flat plate (see next chapter), or by the Hartman layers in the two-dimensional M.H.D turbulence between two planes studied by Somméria [660]. In this case, where a stationary forcing is produced by two-dimensional Taylor–Green vortices driven electrically, a $k^{-5/3}$ inverse energy cascade has actually been measured in a certain range of the parameters characterizing the dissipation, and this seems to be the first experimental evidence of the inverse energy

cascade of two-dimensional turbulence (see Figure 8.6a). In fact more recent experiments by Paret and Tabeling [564] display a well-established inverse energy cascade with a constant $C'_K \approx 6.5$. They find also that two-dimensional turbulence organizes within this range into large-scale coherent vortices.

Direct numerical calculations done by Lilly [442], Fyfe et al. [235], Frisch and Sulem [226] and Herring and McWilliams [282] show some evidence of the inverse cascade (Figure 8.6b).

8.6.2 Decaying case

No such inverse energy cascade exists in the freely-decaying case, but only a stronger decrease (initially $\propto t^{-1}$, compared with the $t^{-0.3\approx0.5}$ law of three-dimensional turbulence) of the wave number $k_i(t)$ where the spectrum peaks. This situation, presented on the LES (using a bi-Laplacian dissipation operator as a subgrid model) of Figure 8.7a (from Staquet [669]), will be looked at from a statistical point of view in more details below.

Physically, the strong inverse transfers of decaying two-dimensional isotropic turbulence result undeniably from the pairing of large energetic eddies of same vorticity sign and therefore correspond to two-dimensional subharmonic instabilities similar to those leading to coherent-vortex pairing in the mixing layer. The latter were experimentally displayed by Winant and Browand [721].[11]

Let us now present in Figures 8.8 and 8.9 DNS and LES (resolution 1024×1024) of Ossia and Lesieur [557] in the decaying case, taking initially for $k \to 0$ a k^5 kinetic-energy spectrum. Both confirm very neatly during the major part of the evolution the infrared k^3 spectral backscatter. The LES has a short enstrophy cascade of slope -3.05. We show also in Figure 8.10 LES at resolution 512×512 starting with a k equipartioned energy spectrum at low wave numbers. First, the initial shape of the energy spectrum is preserved at the smallest numerical wave numbers ($k \approx k_{min}$). But the violent temporal growth of the integral scale is such that the energy spectrum rapidly steepens at low k, although the k^3 slope has not been reached yet. This behaviour is in agreement with the two-dimensional test-field model calculations of Lesieur and Herring [418].[12]

[11] However, things are less clear in the forced case where, as pointed out by Herring and McWilliams [282], a strong random forcing may suppress the formation of coherent vortices. It may also, in the case where these structures form, inhibit the various pairings, which are dependent upon the phases of the various subharmonic instabilities.

[12] It contrasts with the three-dimensional case discussed in Chapter 7, where a LES with $s_0 = 2$ yields an energy spectrum below $k \leq k_I(t)$ constant in time [427, 431, 556].

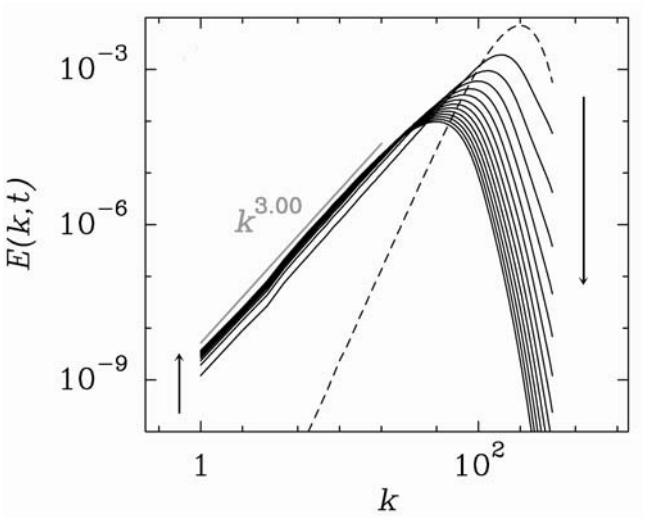

Figure 8.8. Temporal evolution of kinetic-energy spectra in DNS of decaying isotropic two-dimensional turbulence starting initially with a $\propto k^5$ energy spectrum at low k (dashed line). Arrows denote the time direction (from Ossia and Lesieur [557]).

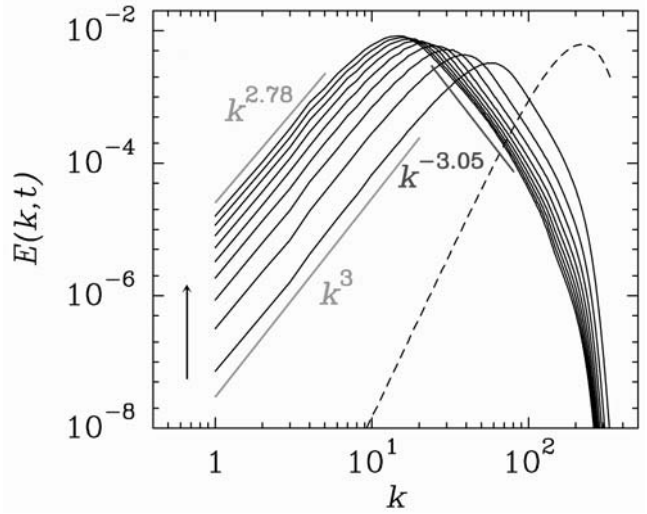

Figure 8.9. LES in conditions analogous to Figure 8.8 (from Ossia and Lesieur [557]).

8.7 The two-dimensional E.D.Q.N.M. model

The application of E.D.Q.N.M.-type techniques to two-dimensional isotropic turbulence was made in particular in Kraichnan [354], Leith [399], Herring et al. [276], Pouquet et al. [584], Holloway [289], Lesieur and Herring [418], and Métais and Lesieur [492]. Using the spectral tensor expression (5.79) in Eq. (7.21), one obtains the following expression for the kinetic-energy transfer $T(k,t)$

$$T(k,t) = \frac{2}{\pi} \iint_{\Delta_k} dp\ dq \theta_{kpq} \frac{k^2}{pq} b_2(k,p,q) \\ [kE(p,t)E(q,t) - pE(q,t)E(k,t)] \tag{8.31}$$

with the same notations as in Chapter 7, the coefficient b_2 being given by

$$b_2(k,p,q) = 2\frac{p}{k}(xy - z + 2z^3)(1-x^2)^{\frac{1}{2}} \\ = 2\frac{(k^2-q^2)(p^2-q^2)}{k^4}(1-x^2)^{\frac{1}{2}}. \tag{8.32}$$

The relaxation time for triple correlations θ_{kpq} has the same expression, in terms of the energy spectrum, as for three-dimensional turbulence. Only the numerical constant a_1 arising in Eq. (7.17) should change. Lesieur and Herring [418] take the value 0.40 (instead of 0.36 in Chapter 7) in order to recover the same Kolmogorov constant in the $k^{-5/3}$ inverse energy cascade, 6.69, as determined analytically by Kraichnan [354] in a stationary solution given by the Test-Field Model.[13] This is not far from the experimental results of Paret and Tabeling [564], and within the range of results given by the DNS of Lilly [440], Frisch and Sulem [226] and Herring and McWilliams [282] (which yield values comprised between 4 and 9). This relatively high value proves that the two-dimensional Kolmogorov inverse energy cascade is far less efficient than its three-dimensional direct counterpart.

The transfer given by Eq. (8.31) conserves kinetic energy and enstrophy, and it may be checked that

$$\int_0^{+\infty} T(k,t)dk = 0; \quad \int_0^{+\infty} k^2 T(k,t)dk = 0. \tag{8.33}$$

Such a transfer, as indicated by Fjortoft's theorem, is now positive in the large scales, as can be checked in Figure 8.7b, which shows both a direct and a closure calculation of the two-dimensional turbulence isotropic transfer determined by Herring et al. [276]. This behaviour is completely different from the three-dimensional transfer of Figure 6.2 which is negative in the

[13] Which has no adjustable parameter, contrary to E.D.Q.N.M. theory.

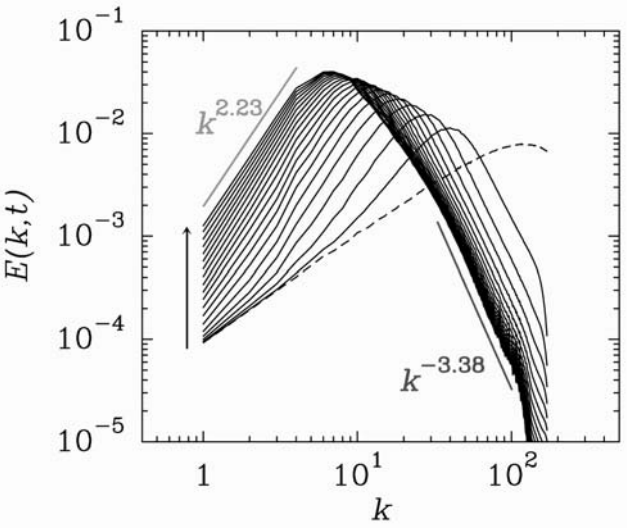

Figure 8.10. Kinetic-energy spectra in decaying LES starting initially with a $\propto k^1$ energy spectrum at low k (dashed line) (from Ossia and Lesieur [557]).

large scales, indicating thus the tendency for the kinetic energy to cascade up to the small scales.

The same techniques as proposed in Chapter 7 allow one to calculate the non-local flux of enstrophy (Kraichnan [354], Pouquet et al. [584], Basdevant et al. [37], Lesieur and Herring [418], Métais and Lesieur [492]), which is equal to

$$Z_{NL}(k,t) = -\frac{1}{4}\int_0^{ak} \theta_{kkq} q^2 E(q) dq k^3 \frac{\partial}{\partial k} kE(k)$$

$$+\frac{1}{2}\int_0^k k'^4 E(k') dk' \int_{\sup(k,k'/a}^{\infty} \theta_{k'pp} \frac{\partial}{\partial p} pE(p) dp$$

$$-\int_0^k k'^5 dk' \int_{\sup(k,k'/a)}^{\infty} \theta_{k'pp} \frac{E(p)^2}{p} dp \qquad (8.34)$$

where a is the non-localness parameter. The non-local kinetic energy flux calculated in the same way is

$$\Pi_{NL}(k,t) = -\frac{1}{4}\int_0^{ak} \theta_{kkq} q^2 E(q) dq k \frac{\partial}{\partial k} kE(k)$$

$$+\frac{1}{2}\int_0^k k'^2 E(k') dk' \int_{\sup(k,k'/a)}^{\infty} \theta_{k'pp} \frac{\partial}{\partial p} pE(p) dp$$

$$-\int_0^k k'^3 dk' \int_{\sup(k,k'/a)}^{\infty} \theta_{k'pp} \frac{E(p)^2}{p} dp. \tag{8.35}$$

Let us first consider the infrared region $k \to 0$: it can be checked (see Basdevant et al. [37]) that $\Pi_{NL}(k)$ reduces to the third term on the r.h.s. of Eq. (8.35), and that the corresponding energy transfer $-\partial \Pi_{NL}(k)/\partial k$ is itself of the order of

$$k^3 \int_{k_i}^{\infty} \theta_{kpp} \frac{E(p)^2}{p} dp$$

where k_i is the wave number where the energy spectrum peaks (i.e. $k_E(t)$ in a forced situation and $k_i(t)$ in a decaying situation). This term corresponds to k^3 two-dimensional backscatter, and provides an explanation for the infrared k^3 kinetic energy spectrum already mentioned on preceding figures.

In the enstrophy cascade, it turns out that the first term in the r.h.s. of Eq. (8.34) gives the essential contribution to the enstrophy flux. As already mentioned, it involves wave-number triads (k', p, q) such that $q \ll k' \approx k \approx p$, the same that are responsible for the k^{-1} viscous-convective range of the three-dimensional passive scalar at high Prandtl number, and which correspond to the creation of smaller scales through the straining of a larger-scale velocity shear. The enstrophy flux $Z(k)$ can then be approximated by (Kraichnan [354])

$$Z(k) = -\frac{1}{4} \left(k^3 \frac{\partial}{\partial k} [kE(k)] \right) \int_0^k \theta_{kk0} q^2 E(q) dq \tag{8.36}$$

which itself can be modified as (Pouquet et al. [584], Basdevant et al. [37])

$$Z(k) = -\frac{1}{4} k^3 \frac{\partial}{\partial k} \left[kE(k) \theta_{kk0} \int_0^k q^2 E(q) dq \right]. \tag{8.37}$$

This is not very different from Eq. (8.36) in the enstrophy cascade, but offers the further advantage of being both conservative of energy and enstrophy, and therefore able to approximate the enstrophy flux whatever the value of k (and not only in the enstrophy cascade). Eq. (8.37) can be solved analytically, assuming a constant enstrophy flux β. It leads to

$$E(k) \sim a_1^{2/3} \beta^{2/3} k^{-3} \left(\ln \frac{k}{k_1} \right)^{-1/3} \tag{8.38}$$

where the wave number k_1 is unknown. The constant in the r.h.s. of Eq. (8.38) can be determined analytically. An analogous logarithmic correction was originally proposed by Kraichnan [354] as a Test-Field Model steady solution of the kinetic-energy spectrum evolution equation. If one identifies both expressions as was done by Pouquet et al. [584] and Métais and Lesieur [492], one

finds $a_1 = 0.53$. This does not change much the level of $E(k)$ in the inverse energy cascade.

Let us now turn our attention to the kinetic energy flux in the enstrophy cascade: from Eq. (8.35) it is approximately equal to

$$\Pi(k) = \frac{Z(k)}{k^2} + 2\int_0^k \nu_t(k')k'^2 E(k')dk' \tag{8.39}$$

where

$$\nu_t = \frac{1}{4}\int_k^\infty \theta_{0pp}\frac{\partial}{\partial p}pE(p)dp. \tag{8.40}$$

Indeed, the third term in the r.h.s. of Eq. (8.35) can be neglected. Contrary to the three-dimensional turbulence case, this eddy viscosity, of the order of $-(1/4)kE(k)\theta_{kk0}$, is negative for any spectrum decreasing faster than k^{-1}. The total energy flux through the enstrophy cascade is composed of a positive term $Z(k)/k^2$ corresponding to the energy flux due to the semi-local interactions responsible for the enstrophy cascade, minus negative eddy-viscosity interactions which send back into the large scales the kinetic energy drained towards the small scales by the enstrophy cascade. The result turns out to be a zero kinetic energy flux for a k^{-3} kinetic energy spectrum. This implies for high Reynolds number two-dimensional turbulence a very peculiar dynamics, where the large scales (unaffected by molecular viscosity), conserve exactly their kinetic energy, while their vorticity is dissipated at a finite rate towards small scales through an enstrophy cascade. It is clear from that result that any system of inviscid dynamical equations which do not dissipate enstrophy cannot pretend to represent two-dimensional turbulence correctly.

Again one may wonder about the physical significance of this negative eddy-viscosity: the simplest physical mechanism is to invoke the pairing of small-scale eddies. It may also be due to other types of subharmonic instabilities displayed by Sinai and co-workers in the case of the Kolmogorov flow.[14] More generally, one can widen the concept of negative eddy viscosity and include in it all the larger-scales formation effects arising in two-dimensional turbulence and mainly due to the double constraint of energy and enstrophy conservation. One must emphasize, however, that, in the context of two-dimensional numerical LES for instance, the "negative eddy viscosity" effects described above are not represented at all by a negative eddy-viscosity, since the modelled scales need to conserve their kinetic energy, while dissipating their enstrophy at a finite rate in the subgrid scales (see Chapter 12).

[14] Which is a class of two-dimensional flows forced in the small scales by a periodic field (see Meshalkin and Sinai [488], Sivashinsky and Yakhot [646]).

8.7.1 Forced turbulence

It was this problem which was studied in the pioneering work of Pouquet, Lesieur, André and Basdevant [584]. Turbulence is forced by a narrow forcing peaking at k_i. The kinetic-energy and enstrophy injection rates are respectively ϵ and β. The parameter a_1 is adjusted in an infinite log-corrected enstrophy cascade (see above). Figure 8.11 shows the time evolution of kinetic-energy spectra once the k^{-3} enstrophy cascade has been built. One sees very clearly the progression to the left of the inverse energy cascade of the wave number $k_E(t)$ indicating the peak of the spectrum. The importance of this work lies in the fact that it shows in a time-dependent calculation the convergence towards stationary solutions consisting of the enstrophy cascade and the inverse-energy cascade. It shows also without debate that enstrophy goes to high wave numbers and kinetic energy to low wave numbers, in very good agreement with the scheme of Figure 8.5. Let us quote a remark by Lesieur and Herring [418]:

> It must be stressed, however, that only meagre evidence – experimental or theoretical – indicates this double cascade is really the dynamics of two-dimensional turbulence.

In fact, the numerous numerical and experimental works discussed above do show the reality of double enstrophy-energy cascades in two-dimensional turbulence.

8.7.2 Freely-decaying turbulence

Numerical results

We study now with the E.D.Q.N.M. model a freely-evolving two-dimensional turbulence having a spectrum initially concentrated at a wave number $k_i(0)$ (and a k^3 spectrum at low k). Let us first show in Figure 8.12 the analogous of Figure 8.11 in the decaying case, taken from Pouquet et al. [584]. A long enstrophy cascade establishes. However, the infrared behaviour is not clear due to an excessive accumulation of energy close to the smallest mode. Other decaying E.D.Q.N.M. calculations confirming the k^3 energy spectrum at small k will be presented in Chapter 11.

Analytical results

Here we will study the initial build-up period of the enstrophy cascade, and then show how one can derive the law $k_i(t) \sim (vt)^{-1}$ which underlies the Batchelor law equation (8.23).

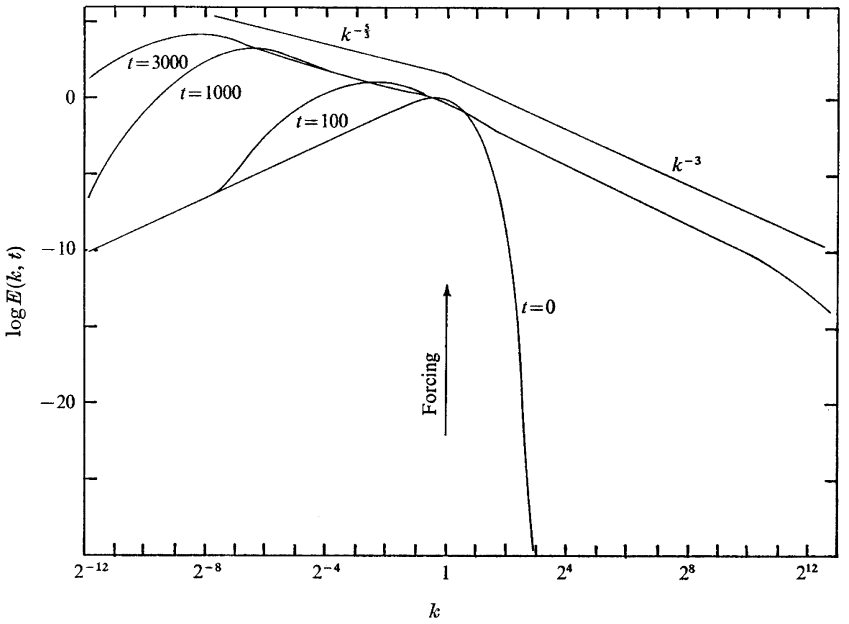

Figure 8.11. Double cascading spectrum of forced E.D.Q.N.M. two-dimensional calculations (from Pouquet et al. [584], courtesy A. Pouquet).

From Eq. (8.14) the enstrophy can only decay or remain constant, and is thus upper bounded by its initial value $D(0)$. Consequently, Eq. (8.13) implies that the kinetic-energy dissipation rate will always tend to zero with the viscosity: hence the kinetic energy of two-dimensional turbulence is conserved for any time at vanishing viscosity, at variance with the result of finite dissipation at finite time occurring in the case of the closures applied to three-dimensional turbulence.

The question now arises of the time-evolution of the enstrophy, which, because of Eq. (8.14), obliges one to look at the palinstrophy: from the expression (8.31) of the kinetic energy transfer, and the calculations of Pouquet et al. [584], the E.D.Q.N.M. evolution equation for the palinstrophy is found, with our notations, to be

$$\frac{dP(t)}{dt} = \frac{4}{\pi} \int_0^\infty \int_0^\infty p^4 q^2 E(p,t) E(q,t) \theta_{kpq} A(p,q) dp dq$$

$$-2\nu \int_0^{+\infty} k^6 E(k,t) dk \tag{8.41}$$

with

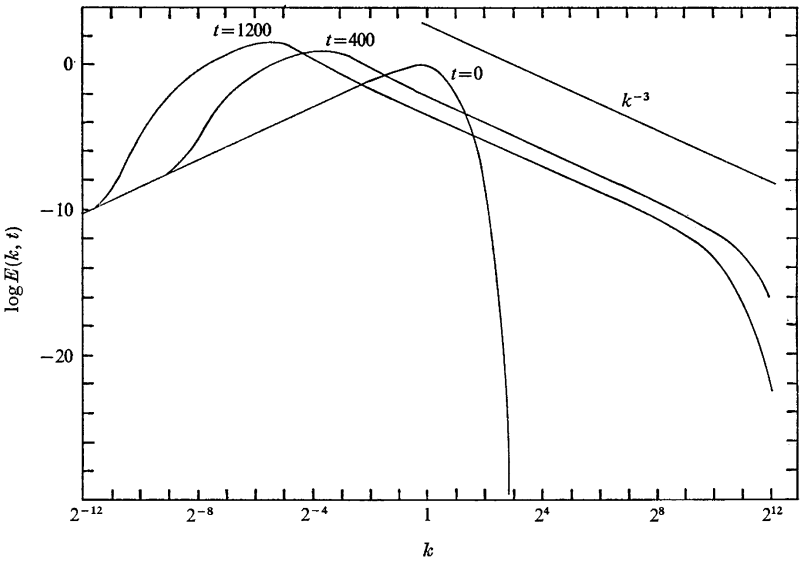

Figure 8.12. Decaying E.D.Q.N.M. two-dimensional calculations (from Pouquet et al., [584], courtesy A. Pouquet).

$$A(p,q) = \begin{cases} (\pi/2)[1-(q/p)^2], & \text{if } q \le p \\ (\pi 2)[1-(q/p)^2](p/q)^2, & \text{otherwise.} \end{cases}$$

We may then symmetrize the nonlinear term of Eq. (8.41) with respect to p and q, and obtain

$$\frac{dP(t)}{dt} = 2\int_0^{+\infty} dp \int_0^p q^2(p^4 - q^4)E(p,t)E(q,t)\theta_{kpq}dq$$

$$-2\nu\int_0^{+\infty} k^6 E(k,t)dk. \tag{8.42}$$

Since θ_{kpq} is majored by $(\mu_k + \mu_p + \mu_q)^{-1}$, itself majored by μ_q^{-1}, where μ_k is given by Eq. (7.17) with $a_1 = 0.4$, the nonlinear term of the r.h.s. of Eq. (8.42) is upper bounded by

$$2\int_0^{+\infty} dp \int_0^p p^4 q^2 E(p,t)E(q,t)\mu_q^{-1}dq =$$

$$\frac{4}{a_1}\int_0^{+\infty} dpp^4 E(p,t)\left[\int_0^p q^2 E(q,t)dq\right]^{\frac{1}{2}} \le \frac{4}{a_1}P(t)D(t)^{\frac{1}{2}}.$$

Finally Eq. (8.42) leads to the following inequality

$$\frac{dP(t)}{dt} \leq \frac{4}{a_1} P(t) D(t)^{\frac{1}{2}} - 2\nu \int_0^{+\infty} k^6 E(k,t) dk \tag{8.43}$$

which reduces to

$$\frac{dP(t)}{dt} \leq \frac{4}{a_1} P(t) D(t)^{\frac{1}{2}} \tag{8.44}$$

in the limit of a zero viscosity. The palinstrophy majoration corresponding to Eq. (8.44) is

$$P(t) \leq P(0) \exp\left(\frac{4}{a_1} D(0)^{\frac{1}{2}} t\right) \tag{8.45}$$

and is better than the one obtained in Pouquet et al. [584] which involved an exponential of t^2. The conclusion is, as already stressed in this paper, that for any fixed t the palinstrophy, even high, remains bounded when the viscosity goes to zero. This implies from Eq. (8.14) that, in the same conditions, the enstrophy dissipation rate goes to zero, and the enstrophy is conserved for any time. There is therefore no finite inviscid enstrophy dissipation at a finite time, similar to the finite kinetic energy dissipation of three-dimensional turbulence.

It would however be an error to think that, within the E.D.Q.N.M. frame, two-dimensional turbulence does not dissipate enstrophy when the viscosity is small but finite. This would contradict in particular the t^{-2} enstrophy dissipation law derived from Eq. (8.23). Actually, the E.D.Q.N.M. or direct calculations of freely-evolving two-dimensional turbulence all show that the palinstrophy starts increasing, following approximately an exponential of the type of Eq. (8.45) r.h.s., reaches a maximum, and then decreases under the action of viscosity. The maximum corresponds to a time t_c where the whole span of the energy spectrum, from $k_i(0)$ to $k_d(t_c)$ has been filled up. The enstrophy dissipation wave number $k_d(t_c)$ is defined from Eq. (8.26), with $\beta = t_c^{-3}$:

$$k_d(t_c) = (\nu t_c)^{-1/2}. \tag{8.46}$$

The palinstrophy $P(t_c)$ is thus approximately equal to

$$P(0) \exp\left(\frac{4}{a_1} D(0)^{1/2} t_c\right)$$

from the inviscid stage described by Eq. (8.45) (taken as an equality), and to $t_c^{-2} k_d(t_c)^2$ from the enstrophy cascade assumption. Noticing finally that the total kinetic energy $(1/2)v^2$ is proportional to $t_c^{-2} k_i(t_c)^{-2}$, and the initial palinstrophy to $k_i(0)^4 v^2$, one obtains approximately

$$t_c \approx D(0)^{-1/2} \ln \frac{k_d(t_c)}{k_i(t_c)} \tag{8.47}$$

which indicates that the "critical" time t_c is proportional to the logarithm of the Reynolds number given by Eq. (8.27). It is only after t_c that the enstrophy

will be dissipated at a finite rate $\sim t^{-2}$. The existence of such a time was first conjectured by Tatsumi and Yanase [678], and its correct determination $\propto \ln R$ was given by Basdevant [38]: before t_c, the palinstrophy grows "inviscidly" according to Eq. (8.45), and the enstrophy should decrease like

$$D(t) = A - \nu B \exp[CD(0)^{1/2}t] \tag{8.48}$$

where A, B, and C are three constants. The enstrophy dissipation rate is thus proportional to $\nu \exp[CD(0)^{1/2}t]$. After t_c, the kinetic energy spectrum decays self-similarly according to Eq. (8.23), and the enstrophy dissipation rate is proportional to t^{-3}. The critical time t_c goes to infinity with the Reynolds number, that is when the viscosity goes to zero: in this case, one recovers the above mentioned result of inviscid conservation of enstrophy for any time. Let us mention finally that the inviscid exponential evolution of $P(t)$ has been verified in the direct numerical Euler calculations of Kida and Yamada [328].

Batchelor's analysis (8.23) is based on a self-similar assumption of the type (6.68), with an integral scale $l \approx k_i(t)^{-1}$ proportional to vt. It is possible to justify such an assumption (Lesieur and Herring [418]) on the basis of two hypotheses which have been derived from the closures, i.e. the existence of an infrared k^3 energy spectrum, and of a k^{-3} enstrophy cascade. As shown in this paper, the k^3 spectrum for $k \to 0$ will appear whatever the slope s of the initial spectrum, due to the strong k^3 backscatter in low k. One assumes then that

$$\begin{aligned} E(k,t) &= C(t)k^3, k < k_i(t); \\ E(k) &= \beta^{2/3}k^{-3}, k > k_i(t). \end{aligned} \tag{8.49}$$

The enstrophy is negligibly contributed to by the k^3 range, which yields $\beta^{2/3} \approx D(t)$, and hence respectively a t^{-2} and t^{-3} behaviour for $D(t)$ and β. The total kinetic energy is proportional to $t^{-2}k_i(t)^{-2}$, which yields

$$k_i(t) \sim (vt)^{-1} \tag{8.50}$$

and demonstrates Batchelor's law. Finally, matching both spectral ranges at $k_i(t)$ gives

$$C(t) \sim v^6 t^4. \tag{8.51}$$

The law equation (8.50) has been verified by Rhines [593] in a DNS, with a wave number $\langle k(t) \rangle$ characteristic of the energy-containing eddies defined by

$$\langle k(t) \rangle = \frac{\int_0^{+\infty} kE(k,t)dk}{\int_0^{+\infty} E(k,t)dk}. \tag{8.52}$$

This calculation led to

$$\frac{1}{v}\frac{d}{dt}\langle k \rangle^{-1} = \frac{1}{30} \tag{8.53}$$

which shows that the "doubling time" of the "eddy" $\langle k \rangle^{-1}$ (that is the time necessary to form an eddy of size $2/\langle k \rangle$) is, in time units $(v\langle k \rangle)^{-1}$, equal to 30. As stressed by Staquet [669] on the basis of a similar two-dimensional isotropic calculation, this doubling time is 15 when evaluated with the aid of the wave number $k_i(t)$ where the kinetic energy spectrum peaks.

We have given above arguments based on the existence of large coherent vortices showing that at high times enstrophy decays slower than the self-similar t^{-2} law (see Figure 8.3). Therefore, closures of the E.D.Q.N.M. type applied to decaying two-dimensional turbulence should be used more for qualitative purposes

8.8 Diffusion of a passive scalar

The two-dimensional passive scalar diffusion is a significant problem when one is interested in the large-scale diffusion of tracers or pollutants in the atmosphere or the ocean, or by temperature fluctuations in two-dimensional laboratory experiments. It also gives information about the way vorticity (or potential vorticity in geostrophic turbulence) is transported by the flow. Since the vorticity and the passive scalar both obey equation (8.4), they have close analogies. However, the scalar, whose variance is an inviscid invariant, is not constrained to the double energy-enstrophy conservation like the velocity field. This will rule out the possibility of strong inverse scalar transfers, inverse scalar cascades and negative eddy-diffusivities.

The phenomenology of two-dimensional passive-scalar diffusion has been given in Lesieur et al. [414] and Lesieur and Herring [418]. Let $T(\vec{x}, t)$ be the scalar, $E_T(k, t)$ its spectrum such that

$$\frac{1}{2}\langle T(\vec{x})^2 \rangle = \int_0^{+\infty} E_T(k, t) dk. \tag{8.54}$$

$\epsilon_T = \int_0^{+\infty} k^2 E_T(k, t) dk$ is the scalar dissipation rate and κ the scalar diffusivity. The scalar dissipation wave number is now (Lesieur and Herring [418])

$$k_c = \left(\frac{\epsilon_T}{\kappa^3}\right)^{1/6}. \tag{8.55}$$

We start by considering the scalar in an enstrophy cascade. The corresponding inertial-convective, inertial-conductive and viscous-convective ranges are shown in Figure 8.13, taken from Lesieur and Herring [418]: if the scalar is injected in the enstrophy cascade, and for $k < \inf(k_c, k_d)$, an Oboukhov type analysis, already employed in the three-dimensional case, shows that the scalar spectrum is proportional to the cascading enstrophy spectrum and is consequently of the form

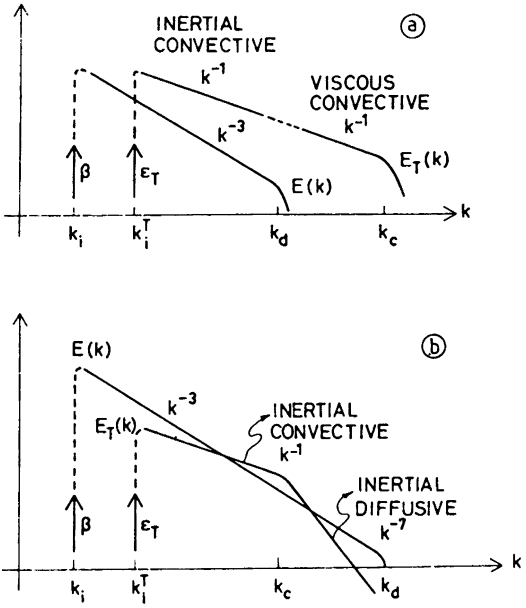

Figure 8.13. Schematic inertial-ranges of the kinetic energy and scalar spectra in the enstrophy cascade. The enstrophy is injected at k_i with a rate β, and the scalar at k_i^T with a rate ϵ_T. (a) Prandtl number > 1; (b) Prandtl number < 1. Inertial diffusive stands for inertial conductive in the present book (from Lesieur and Herring [418], courtesy *J. Fluid Mech.*).

$$E_T(k,t) \sim \frac{\epsilon_T}{\beta} k^2 E(k,t) \sim \epsilon_T \beta^{-1/3} k^{-1}. \tag{8.56}$$

The prediction of such a spectrum wa first done by Fasham [194]. It was also proposed by Lesieur et al. [414] (see also Lesieur and Sadourny [414] and Mirabel and Monin [508]). Here, the scalar spectrum is proportional to the spectrum of the cascading quantity, the enstrophy. The physics of this cascade is again provided by Eq. (8.25), valid also for the scalar gradient: the latter will be intensified in the second principal axis of deformation direction, normal to the weak vorticity braids reconnecting the large coherent vortices. Thus, these braids will form local scalar "fronts" with high $\partial\rho/\partial n$. The latter may induce high scalar Laplacians $\approx \partial^2\rho/\partial n^2$, and hence high scalar molecular diffusion. In combustion problems where reacting species may be in contact along this interface, this increased molecular mixing will favour the chemical reactions. These mechanisms of scalar-front formation might be also at hand in atmospheric frontogenenis (see next chapter).

An interesting experimental verification of the k^{-1} inertial-convective range in forced two-dimensional turbulence at high Peclet number has been carried out by Jullien et al. [323].

In the inertial-conductive range, it has already been mentioned in Chapter 6 that Eq. (6.117) is still valid (with a different value of the constant), that is

$$E_T(k,t) \sim \epsilon_T \kappa^{-3} k^{-4} E(k,t) \sim \epsilon_T \kappa^{-3} \beta^{2/3} k^{-7}. \tag{8.57}$$

Such a k^{-7} scalar law was predicted by Lesieur et al. [414].

As for the viscous-convective range, it is still proportional to k^{-1}.

8.8.1 E.D.Q.N.M. two-dimensional scalar analysis

This phenomenology is supported by an E.D.Q.N.M. analysis, whose spectral equation is written (from Eq. (7.126) which is still valid)

$$\left(\frac{\partial}{\partial t} + 2\kappa k^2\right) E_T(k,t) = \frac{4}{\pi} \iint_{\Delta_k} dp\ dq \theta_{kpq} \frac{p}{q} (1-x^2)^{\frac{1}{2}}$$
$$[kE_T(p,t)E(q,t) - pE(q,t)E_T(k,t)]. \tag{8.58}$$

Here we have taken the same triple-correlations relaxation time as for the velocity, which is certainly not justified but does not greatly influence the results. The use of a modified θ time of the form θ_{00q}, already considered in the three-dimensional case, has the advantage of allowing a return to physical space, yielding then Eq. (7.130) which is still valid (see Larchevêque and Lesieur [378], Lesieur and Herring [418]).

Using the same non-local techniques already employed above and in Chapter 7, one can calculate the non-local flux of scalar, equal to

$$\Pi_{NL}^T(k,t) = -\frac{1}{4} \int_0^{ak} \theta_{kkq} q^2 E(q) dq k^3 \frac{\partial}{\partial k} \frac{E_T(k)}{k}$$
$$+ \int_0^k k'^2 E_T(k') dk' \int_{\sup(k,k'/a)}^{\infty} \theta_{k'pp} E(p) dp$$
$$- \int_0^k k'^3 dk' \int_{\sup(k,k'/a)}^{\infty} \theta_{k'pp} \frac{E(p)E_T(p)}{p} dp. \tag{8.59}$$

This expansion shows again, as for the energy spectrum, the existence of a k^3 scalar backscatter in the infrared region $k \to 0$. The second term in the r.h.s. of Eq. (8.59) corresponds to an eddy diffusivity

$$\kappa_t = \frac{1}{2} \int_{k/a}^{\infty} \theta_{0pp} E(p) dp \tag{8.60}$$

which, contrary to the eddy viscosity, is always positive. The first term in the r.h.s. of Eq. (8.59) is identical to the enstrophy flux in the enstrophy cascade if $E_T(k)$ is replaced by $k^2E(k)$. This allows to show

$$E_T(k,t) = \frac{\epsilon_T}{\beta} k^2 E(k,t) \tag{8.61}$$

in the enstrophy cascade inertial-convective range (Lesieur and Herring [418]), provided the local scalar transfer may, as for the enstrophy, be neglected.[15]

When the scalar is forced into the $k^{-5/3}$ *inverse* kinetic energy cascade, it is going to cascade to higher wave numbers along a *direct* $k^{-5/3}$ inertial-convective range, as shown in Lesieur and Herring [418].

Curiously, and when compared with the DNS which have been done for this passive-scalar problem, the conclusions of this statistical analysis for the k^{-1} inertial-convective range seem to work quite well, though the enstrophy spectra determined in these (low resolution) computations are steeper than k^{-1} (Babiano et al. [24]). It has also been noticed by Holloway and Kristmannsson [291] that the scalar is more easily diffused by turbulence than is the vorticity. It would be interesting to verify the discrepancy between the enstrophy and scalar spectra on higher resolution computations. It might be that such an effect results simply from the absence of pressure term in the scalar equation,[16] and that, as in the three-dimensional case, the k^{-1} scalar spectra observed in the numerical simulations are the result of a random shearing of the scalar by the large eddies, corresponding to Eq. (6.140).

8.8.2 Particles-pair dispersion in 2D

To end this section, let us consider the diffusion problem from a Lagrangian point of view, by looking for instance at the particles-pair dispersion problem already studied in Chapters 6 and 7 for the three-dimensional case. As shown in Larchevêque and Lesieur [378] and Lesieur and Herring [418] with the aid of the E.D.Q.N.M. theory, the probability density $P(r,t)$ that the pair should be a distance $\vec{r}$ apart admits a similarity solution of the form

$$P(r,t) = R^{-2} f\left(\frac{r}{R}\right) \tag{8.62}$$

where R is the r.m.s. pair separation.

• Inverse energy cascade:

[15] This assumption should however be verified, either with the aid of the E.D.Q.N.M. theory or DNS.

[16] There is no pressure in the vorticity equation as well, but the deformation of vorticity by the velocity reacts on the velocity field and may inhibit the vorticity diffusion, compared with the scalar diffusion.

R satisfies a Richardson law $dR^2/dt \sim \epsilon^{1/3} R^{4/3}$, yielding $R^2 = g\epsilon t^3$. This law has been recovered experimentally by Jullien et al. [322] with $g \approx 0.5$.

• Enstrophy cascade:

we obain the dispersion law

$$\frac{1}{2}\frac{dR^2}{dt} \sim \beta^{1/3} R^2 \tag{8.63}$$

which was proposed originally by Lin [449] on a phenomenological basis. Such a law leads to an exponential dispersion for a stationary forced enstrophy cascade. It has been recovered experimentally in an initial regime by Jullien [324].

Eq. (8.63) implies also that $dR/dt \sim \beta^{1/3} R$. This gives the order of magnitude $\beta^{2/3} r^2$ for the second-order velocity structure function. It is then tempting to relate such a dispersion law (resp. structure function) to the kinetic-energy spectrum, as was done for three-dimensional turbulence when the Richardson law was equivalent to the Kolmogorov law for the kinetic-energy spectrum. This poses however some problems, as stressed in Babiano et al. [23, 25], where it has been shown that a r^2 structure function could correspond to spectra decreasing faster than k^{-3}. Thus, the determination of diffusion or dispersion statistics in a two-dimensional turbulent flow, as was for instance experimentally done for the EOLE experiment in the atmosphere (see Morel and Larchevêque [521]), could not be sufficient to characterize the flow dynamically.

Let us finally mention the work by Zouari and Babiano, [738] where DNS are used in order to study pair dispersion. Separating the flow into elliptic and hyperbolic regions, as was done above for Weiss criterion, they find that the tracers disperse following Lin's law within the hyperbolic zones, while they remain trapped in the vortices (elliptic zones).

8.9 Pressure spectrum in two dimensions

We recall that such a spectrum allows to calculate the sound pressure level. We will give here the predictions of the Q.N./E.D.Q.N.M. analyses, which, as already stressed, are equivalent [380].

8.9.1 "Ultraviolet" case

Larchevêque [380] did not consider the pressure spectrum. noise The same derivation as done above in the three-dimensional case yields again for the latter (Lesieur et al. [427]) $E_{pp}(k) \sim k[E(k)]^2$ which gives

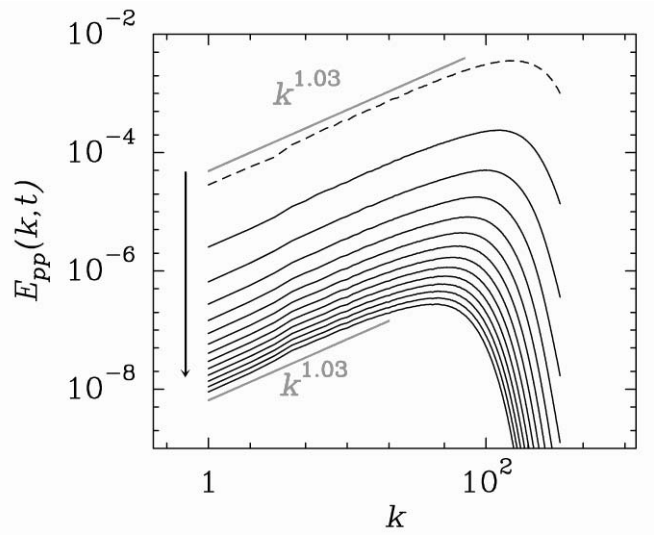

Figure 8.14. Temporal evolution of pressure spectra in the DNS of Figure 8.8. The dashed line corresponds for the intial time (from Ossia and Lesieur [557]).

$$E_{pp}(k) \sim \epsilon^{4/3} k^{-7/3} \tag{8.64}$$

in the inverse-energy cascade, and

$$E_{pp}(k) \sim \beta^{4/3} k^{-5} \tag{8.65}$$

in the enstrophy cascade. The latter law is feasible, since we recall that experiments of Paret et al. [565] demonstrating the existence of a k^{-3} enstrophy cascade indicate a close to Gaussian vorticity distribution in this range. Compared to the $k^{-7/3}$ ultraviolet pressure spectrum in three-dimensions, it implies that the noise emitted in 2D is more determined by large scales and coherent vortices than in 3D.

8.9.2 Infrared case

As for the three-dimensional case (see Chapter 7), a Q.N./E.D.Q.N.M. analysis yields now [427, 557]

$$E_{pp}(k,t) = \frac{3}{2} \left(\int_0^{+\infty} \frac{E(q,t)^2}{q} dq \right) k. \tag{8.66}$$

One may check the validity of this law in DNS' and LES', except for the numerical constant (3/2). In the DNS' however, there is a lot of kinetic-energy

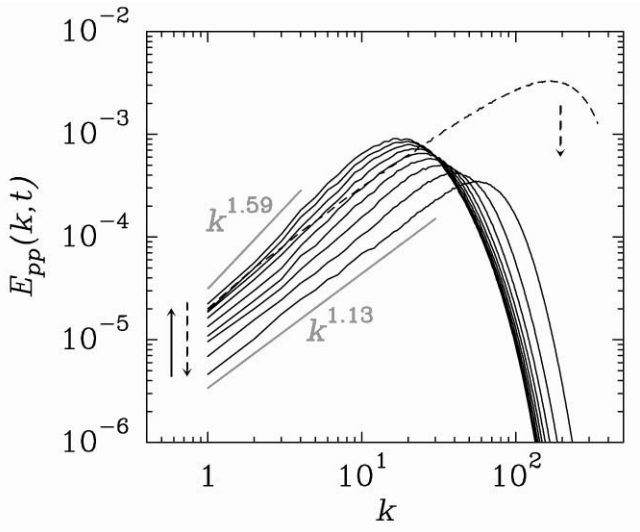

Figure 8.15. Pressure spectra in the LES of Figure 8.9 (from Ossia and Lesieur [557]).

dissipation, and the k infrared pressure spectrum, once formed, will decay as in in three dimensions. This is clear in Figure 8.14, which corresponds to the DNS of Figure 8.8. The corresponding pressure variance will also decay with time.

The pressure spectrum corresponding to the LES of Figure 8.9 is displayed in Figure 8.15. Here, we have first a time decay of the infrared pressure spectrum, followed by an increase. The associated pressure-variance time exponent α_p such that $\langle p'^2 \rangle \propto t^{\alpha_p}$ can be found in Figure 8.1. One can see that it is first negative, corresponding to a decay of $\langle p'^2 \rangle$, then it become positive and the turbulence noise will increase.

In [557], the pressure p.d.f.'s have been determined. They are not far from analytic predictions made by Holzer and Siggia [295] on the basis of a shell model.

It seems that two-dimensional turbulence is more noisy than three-dimensional one, and breaking up two-dimensional vortices may constitute a good way to reduce the aerodynamic noise in turbulence.

8.10 Two-dimensional turbulence in a temporal mixing layer

In reviewing the various physical mechanisms which may contribute to the enstrophy cascade, let us mention the work of Staquet et al. [668, 669], Lesieur et al. [420], and Comte et al. [134], concerning the longitudinal spatial energy spectra in a two-dimensional temporal mixing layer, which could shed some light on the build up of the enstrophy cascade. Figure 8.16, taken from Lesieur et al. [420], shows the evolution of a two-dimensional temporal mixing layer initiated by a hyperbolic-tangent velocity profile $U \tanh(2y/\delta_i)$, upon which is superposed a weak white noise in the rotational region. The longitudinal extent of the domain corresponds to $4\lambda_a$, where $\lambda_a = 7\delta_i$ is the most-amplified wavelength. Four primary vortices are therefore expected to develop. The figure presents simultaneously vorticity contours and longitudinal spatial spectra. At $t = 20\delta_i/U$, the spectrum corresponds to a sharp peak at the fundamental mode ($k_4 = 2\pi/\lambda_a$), which is responsible for smaller peaks at its harmonics $2k_4$ and $3k_4$. The background spectrum corresponds to more complex interactions involving the first and second subharmonic $k_4/2$ and $k_4/4$. At $t = 40\delta_i/U$, that is at the end of the first pairing, the two distinct parts of the spectrum collapse to form a continuous range of exponent close to k^{-4}. Then the flow can really be called "turbulent", since it possesses a broad-band spectrum. If one accepts the association of this range to an enstrophy-cascading inertial range of two-dimensional turbulence, this indicates clearly the importance of the pairing interactions for the establishment of the enstrophy cascade. At time $t = 80\delta_i/U$, at the end of the second pairing, the second subharmonic $k_1 = \pi/2\lambda_a$ has grown and rejoins the inertial range. In this temporal calculation, a layer of size δ will double its size in a time of $10\delta/U$. These calculations also show that the first fundamental eddies which appear have a vorticity thickness of $2\delta_i$, and are formed at a time of $15\delta_i/U$. Then the first pairing will occur approximately at $35\delta_i/U$, and the subsequent[17] pairing at $75\delta_i/U$. Another result of these temporal mixing layer calculations (done with a larger number of vortices) is that the vorticity thickness stops growing when there remains approximately two eddies in the computational square domain, due to the longitudinal periodicity.[18] This does not prevent the last pairing to occur, but it does so without any vorticity thickness growth.

[17] This reasoning is simply based on the assumption that the vorticity thickness will have doubled after each pairing.

[18] And not to the parallel boundaries, as erroneously stressed in the first edition of this monograph; this point has been verified in Lesieur et al. [420].

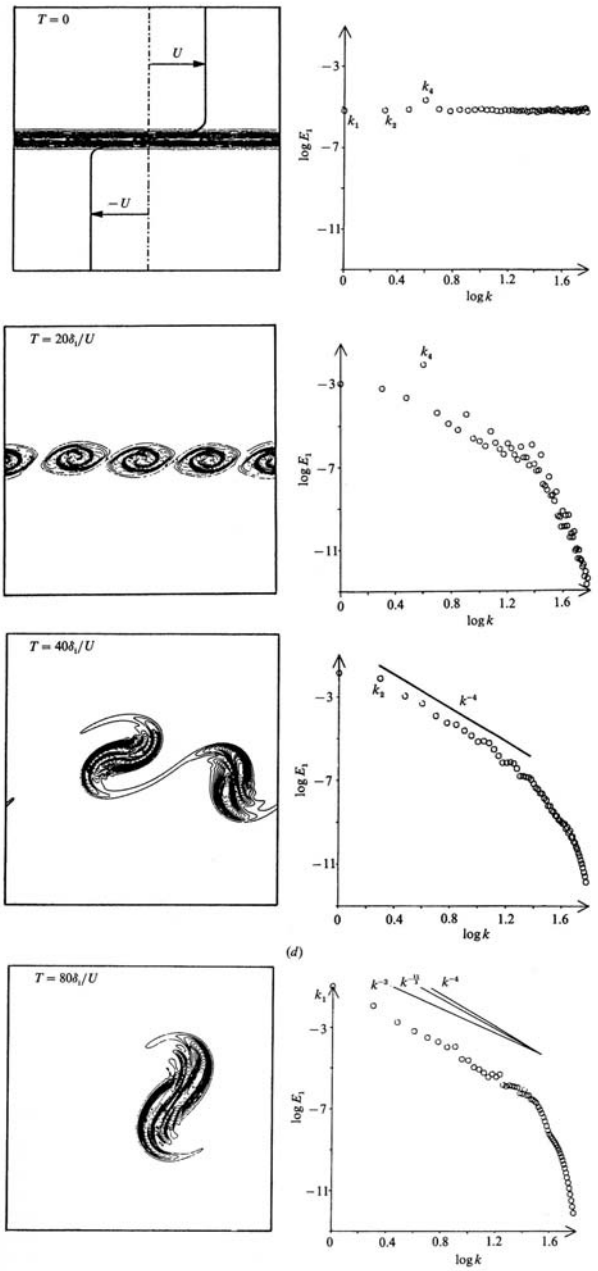

Figure 8.16. Isovorticity lines and longitudinal kinetic energy spectra in the temporal mixing layer at times $0, 20, 40$ and $80\delta_i/U$ (from Lesieur et al. [420], courtesy *J. Fluid Mech.*).

We will present in Chapter 11 another two-dimensional turbulence behaviour in two-dimensional mixing layers: the chaotic character of two-dimensional subharmonic instabilities in the two-dimensional pairing.

9

Beyond Two-Dimensional Turbulence in GFD

9.1 Introduction

The former chapter dealt with strictly two-dimensional turbulence, which is a sort of zero-order approximation for the dynamics of large-scale flows in Geophysical Fluid Dynamics (GFD). In fact these motions, although in thin layers, are strongly influenced by stratification effects which are three-dimensional. A first step in this study is the quasi geostrophic theory, allowing one to write quasi two-dimensional evolution equations for the large scales of a stably-stratified shallow flow on a rapidly-rotating sphere. We will see how the two-dimensional dynamics is modified by quasi geostrophy. We will also try to explain the main mechanisms of baroclinic instability, resulting from the existence of horizontal thermal fronts, which is at the origin of storms in the atmosphere. This will necessitate to look at non-geostrophic effects. We will give a version of quasi geostrophic theory in a fluid with N layers of different density which is currently used for ocean-circulation modelling. We will study the interaction of geostrophic layers with Ekman layers close to boundaries. At a smaller scale, we will provide a model of tornado generation in the atmospheric boundary layer in the presence of localized thermal convection. We will also present a description of waves such as Rossby waves. We will discuss Jupiter external atmosphere made of alternate zonal jets. Finally the statistical concept of geostrophic turbulence will be discussed.

More details on the topics presented here may be found in Holton [294], Pedlosky [567] and McWilliams [480]. Some other aspects of geophysical turbulence are developed in Chapter 13.

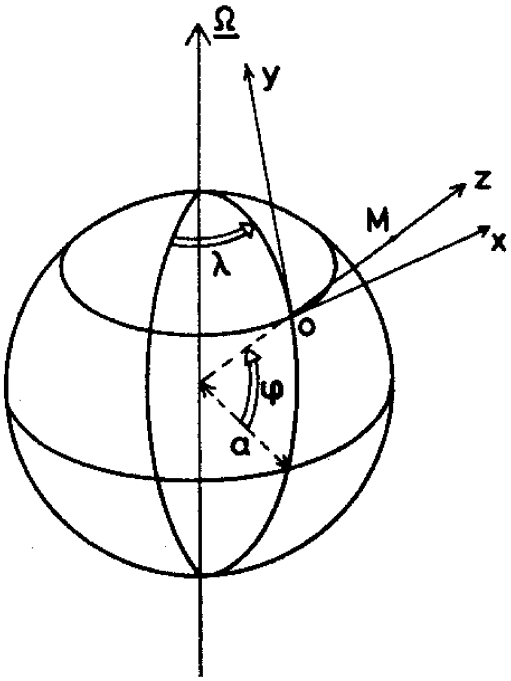

Figure 9.1. Local frame on the rotating sphere.

9.2 Geostrophic approximation

The mathematical details of this theory, proposed by Charney [109], are given in [567]. Here we will give the main physical ingredients of the approximation. Consider a rotating sphere (of angular rotation vector $\vec{\Omega}$) of radius a. A given point of the flow M is defined by its vertical projection O on the sphere, and by its "altitude" z. To O is associated the local frame $(\vec{x}, \vec{y}, \vec{z}), \vec{x}$ being directed along a parallel of latitude φ and $\vec{y}$ along a meridian of longitude λ (see Figure 9.1). The components of the velocity field $\vec{u}$ in the local frame are (u, v, w). The point O will be assumed to be close to a reference point O_0 of longitude and latitude λ_0 and φ_0, in order to neglect the sphericity corrections. The "horizontal" coordinates of M are defined by

$$x = a(\lambda - \lambda_0)\cos\varphi_0$$

$$y = a(\varphi - \varphi_0). \tag{9.1}$$

Let D be the average depth of the fluid, L and U characteristic horizontal lengths and velocities, W a characteristic vertical velocity. We introduce the

local Rossby number $R_o = U/f_0 L$, and the Froude number $F = U/(ND) = U/\sqrt{g_* D}$ (where $g_* = N^2 D$ is a reduced gravity). The scope of the present study is to write an approximate evolution equation for the quasi horizontal large-scale velocity field, using expansions with respect to the small parameters $D/L, R_o$, and F. The theory will consist of two major ingredients: the first one is called the geostrophic approximation, and the second is the application of Ertel's potential vorticity conservation in the special case of the geostrophic approximation.

In order to treat both a liquid and a gas, we utilize the Boussinesq approximation on a rotating sphere, within the same approximation as done in Eq. (2.137), that is:

$$\begin{aligned} \frac{Du}{dt} &= -\frac{\partial \tilde{p}}{\partial x} + fv + \nu_e \nabla^2 u \\ \frac{Dv}{dt} &= -\frac{\partial \tilde{p}}{\partial y} - fu + \nu_e \nabla^2 v \\ \frac{Dw}{dt} &= -\frac{\partial \tilde{p}}{\partial z} - \tilde{\rho} g + \nu_e \nabla^2 w. \end{aligned} \tag{9.2}$$

In fact, the velocity field in Eqs. (9.2) represents a filtered velocity field, averaged over a horizontal box of size δL, which is the smallest characteristic scale for which the following geostrophic approximation will be valid. Therefore, ν_e represents an eddy viscosity corresponding to momentum exchanges with the "sub-geostrophic scales" smaller than δL. This is a very rough way of modelling the effect of these small scales, but ν_e will not play any role in the following geostrophic approximation. However, this coefficient will be essential for the understanding of the Ekman layer (see below). The continuity equation is approximated as

$$\frac{\partial u}{\partial x} + \frac{\partial v}{\partial y} + \frac{\partial w}{\partial z} = 0. \tag{9.3}$$

9.2.1 Hydrostatic balance

The smallness of D/L justifies an assumption of hydrostatic balance along the vertical, as was done in Chapter 2. This leads to

$$\tilde{\rho} = -\frac{1}{g}\frac{\partial \tilde{p}}{\partial z}. \tag{9.4}$$

This corresponds to

$$\rho' = -\frac{1}{g}\frac{\partial p'}{\partial z}, \tag{9.5}$$

for the density and pressure fluctuations about the basic hydrostatic profile $\bar{\rho}(z), \bar{p}(z)$. This implies that the instantaneous density $\rho = \bar{\rho} + \rho'$ and pressure $p = \bar{p} + p'$ are also hydrostatically related:

$$\rho = -\frac{1}{g}\frac{\partial p}{\partial z}. \tag{9.6}$$

9.2.2 Geostrophic balance

In the horizontal velocity equations, the Coriolis force is of the order of $f_0 U$, the nonlinear terms $\partial \vec{u}_H/dt$ of the order of U^2/L, and the dissipative term of the order of $\nu_e U/L^2$, where f_0 the value of the Coriolis parameter (defined by Eq. (2.87) at φ_0). From the Ekman layer study done below, $\nu_e \sim f_0 \delta_E^2$, where $\delta_E \ll D$ characterizes the vertical thickness of the Ekman layers between which the fluid evolves (see below). Hence the dissipative term is $\sim f_0 U \delta_E^2/L^2$. The ratio of the nonlinear to the Coriolis term is of the order of the Rossby number $U/f_0 L$, and that of the dissipative to the Coriolis term of the order of $(\delta_E/L)^2 \ll 1$. Then, as soon as the Rossby number $U/f_0 L$ is small compared with one, and if O is close to O_0, the momentum equation in the rotating shallow layer on the sphere reduces to

$$-\vec{\nabla}_H \tilde{p} = f_0 \vec{z} \times \vec{u}_H. \tag{9.7}$$

Since $\bar{p}$ is a function of z only, Eq. (9.7) is equivalent[1] to

$$-\frac{1}{\rho_0}\vec{\nabla}_H p = f_0 \vec{z} \times \vec{u}_H, \tag{9.8}$$

where ρ_0 is the average value of the density across the fluid layer. Eq. (9.8) corresponds to the geostrophic balance between the pressure gradient and the Coriolis force. It shows that the horizontal flow follows the isobaric lines in a horizontal plane, in the cyclonic direction (that is the positive rotation imposed by $\vec{\Omega}$) in the vicinity of a pressure trough, and in the anticyclonic direction around a pressure peak. Eq. (9.8) implies also that

$$\vec{u}_H = -\vec{z} \times \vec{\nabla}_H \psi(x, y, z, t) \tag{9.9}$$

$$\psi(x, y, z, t) = -\frac{1}{\rho_0 f_0} p(x, y, z, t)$$

where ψ acts like a stream function for the horizontal motion, but depends on the vertical coordinate z. Let us remark also, from Eq. (9.6), that

[1] These relations might also have been obtained using the Navier–Stokes equations directly.

$$\rho = \frac{\rho_0 f_0}{g} \frac{\partial \psi}{\partial z}. \tag{9.10}$$

We will define the *geostrophic velocity* $\vec{u}_G$ by Eq. (9.9). Introducing a fluctuating stream function

$$\psi'(x, y, z, t) = -\frac{1}{\rho_0 f_0} p'(x, y, z, t), \tag{9.11}$$

with

$$\psi = -\frac{1}{\rho_0 f_0} \bar{p}(z) + \psi',$$

the above relations write

$$\vec{u}_H = -\vec{z} \times \vec{\nabla}_H \psi'(x, y, z, t) \tag{9.12}$$

$$\tilde{\rho} = \frac{f_0}{g} \frac{\partial \psi'}{\partial z}.$$

Hence, ψ' may also play the role of a stream function for the geostrophic field.

9.2.3 Generalized Proudman-Taylor theorem

We remark also that the geostrophic velocity is horizontally non-divergent. This has important consequences for the vertical velocity of the actual flow: indeed, let us write the real (dimensional) velocity field as

$$\vec{u}(\vec{x}, t) = \vec{u}_G(\vec{x}, t) + \frac{U}{f_0 L}\ \vec{u}^{(1)}(\vec{x}, t) + \left[\frac{U}{f_0 L}\right]^2 O(\vec{u}), \tag{9.13}$$

where $\vec{u}^{(1)}$ has a modulus of the order of U. Since $\vec{u}_G$ is horizontal, the vertical characteristic velocity W is of the order of $R_o W^{(1)}$, where $W^{(1)}$ is a typical vertical component of $\vec{u}^{(1)}$. Since the three-dimensional incompressibility condition (9.3) is valid at any order of the expansion, it implies

$$\frac{\partial w^{(1)}}{\partial z} = -\left(\frac{\partial u^{(1)}}{\partial x} + \frac{\partial v^{(1)}}{\partial y}\right),$$

which yields

$$\frac{W^{(1)}}{D} = O\left[\frac{U}{L}\right]; \quad \frac{W}{U} = O\left[\left(\frac{D}{L}\right)\left(\frac{U}{f_0 L}\right)\right]. \tag{9.14}$$

These results show that a rapid rotation diminishes the ratio W/U from the value D/L (imposed by the shallowness of the layer and the continuity equation) to $(U/f_0 L)(D/L)$. This is a generalization of the Proudman–Taylor theorem to a shallow flow on a rotating sphere, and goes in favour of the limitation of the vertical fluctuations of the flow under the action of a rapid rotation, as seen in Chapter 2 for a flow of uniform density in a layer of arbitrary depth.

9.2.4 Atmosphere versus oceans

The local Rossby number is infinite at the equator, and so the geostrophic balance holds only in the medium and high latitudes. More specifically, and as already discussed in Chapter 1, the Rossby number is of the order of 0.3 in Earth atmosphere in medium latitudes ($f = 10^{-4}$ rd/s) for tropospheric jets of velocity 30 m/s and length scales 1000 km. Since the geostrophic balance theory is valid at the lowest order with respect to the Rossby number, the latter fixes the precision of the determination of the actual velocity field using the geostrophic velocity inferred from the pressure field. In the ocean, a velocity of 5 cm/s and a length scale of 100 km yields a Rossby number of 5.10^{-2} at the same latitude. So the ocean is much more geostrophic than the atmosphere. This explains why quasi geostrophic models are used much more in the oceans than in the atmosphere.

9.2.5 Thermal wind equation

By differentiating Eq. (9.9) with respect to z, and using Eq. (9.6), one obtains the so-called thermal wind equation

$$\frac{\partial \vec{u}_H}{\partial z} = -\frac{g}{\rho_0 f_0} \vec{z} \times \vec{\nabla}_H \rho. \tag{9.15}$$

This shows a tendency for the horizontal density gradients to induce, under the action of a rapid rotation, zonal currents with a vertical gradient: in Earth atmosphere, for instance, the meridional density gradients are directed towards the poles, and the thermal-wind equation is therefore in good agreement with the zonal westerly jet streams in medium latitudes and the circumpolar vortices. Notice also that Eq. (9.15) is equivalent to

$$\frac{\partial \vec{u}_H}{\partial z} = -\frac{g}{f_0} \vec{z} \times \vec{\nabla}_H \tilde{\rho} = -\frac{g}{f_0} \vec{z} \times \vec{\nabla}_H \rho_*. \tag{9.16}$$

9.3 Quasi geostrophic potential vorticity equation

The geostrophic approximation is a "diagnostic" equation, allowing one to approximate the velocity by a horizontal field, the geostrophic velocity, and to calculate it from the pressure field, using Eq. (9.9). With the aid of the hydrostatic approximation, the velocity and the temperature can thus be completely determined from the pressure, with a precision of the order of the Rossby number. Therefore we need a "prognostic" equation allowing one to predict the evolution in time of the pressure field, or the vertical geostrophic vorticity $\omega_G = -\nabla_H^2 \psi$. Such an equation may be derived with the aid of systematic

expansions with respect to the small parameters (Rossby number R_o, Froude number and D/L), as was done by Charney [109], see also Pedlosky [567]). Here, we will derive this equation using the *potential-vorticity conservation principle*, expanding the potential-vorticity equation.

One still works within the Boussinesq approximation, neglecting molecular diffusion. As shown in Chapter 2, the potential vorticity

$$\zeta = (\vec{\omega} + 2\vec{\Omega}).\vec{\nabla}\rho_* \tag{9.17}$$

is conserved following the three-dimensional motion. We will expand this equation to the first order with respect to the above-mentioned small parameters. Therefore, the vorticity $\vec{\omega}$ in Eq. (9.17) may be replaced by the geostrophic vorticity $\vec{\omega}_G$, since it is of order R_o with respect to $2\vec{\Omega}$. Writing

$$\vec{\nabla}\rho_* = \frac{\partial \rho_*}{\partial z}\vec{z} + \vec{\nabla}_H \rho_*,$$

the potential vorticity is:

$$\zeta = (\omega_G + f)\frac{\partial \rho_*}{\partial z} + (\vec{\omega}_G + 2\vec{\Omega}).\vec{\nabla}_H \rho_*. \tag{9.18}$$

Let us consider the orders of magnitude of the second term in the r.h.s. of Eq. (9.18), which is, due to the thermal-wind equation (9.16), of the order of or smaller than $(f_0^2/g)\ \|\partial \vec{u}_H/\partial z\| \sim (f_0^2 U/gD)$. The first term in Eq. (9.18) is minored (in modulus) by $\sim (U/L)|d\bar{\rho}_*/dz|$. Hence, the ratio of the second to the first term is of the order of $(f_0/N)^2(L/D)$, where N is the Brunt-Waisala frequency. The magnitude of this parameter can be specified by noticing that

$$\frac{f_0}{N} = \frac{F}{R_0}\frac{D}{L}.$$

Hence

$$\left(\frac{f_0}{N}\right)^2 \frac{L}{D} = \left(\frac{F}{R_o}\right)^2 \frac{D}{L}$$

will be small if the Froude number is of the order of or smaller than the Rossby number. In this case, the potential vorticity Eq. (9.18) writes

$$\zeta = (\omega_G + f)\frac{\partial \rho_*}{\partial z}. \tag{9.19}$$

We have

$$\rho_* = \bar{\rho}_*(z) + \tilde{\rho}, f = f_0 + f'$$

and assume that

$$\left|\frac{\tilde{\rho}}{\bar{\rho}_*}\right|, \left|\frac{\partial \tilde{\rho}}{\partial z}/\frac{d\bar{\rho}_*}{dz}\right|, \frac{f'}{f_0}$$

are small parameters of the order of or smaller than R_o. To the first order, it is obtained

$$\zeta = f_0 \frac{d\bar{\rho}_*}{dz} + (\omega_G + f') \frac{d\bar{\rho}_*}{dz} + f_0 \frac{\partial \tilde{\rho}}{\partial z}. \tag{9.20}$$

Dividing by $d\bar{\rho}_*/dz$, and using Eqs. (2.127), (9.12), and (9.20) writes:

$$\zeta = \frac{d\bar{\rho}_*}{dz} \left[-\nabla_H^2 \psi' + f - \left(\frac{f_0}{N} \right)^2 \frac{\partial^2 \psi'}{\partial z^2} \right]. \tag{9.21}$$

The conservation of potential vorticity is thus expressed as

$$\frac{D}{Dt}\zeta = \frac{D_H}{Dt}\zeta + w \frac{\partial}{\partial z}\zeta = 0, \tag{9.22}$$

where w is the vertical velocity. In Eq. (9.22), the magnitude of $w\partial\zeta/\partial z$ relative to $D_H\zeta/Dt$ is, from Eq. (9.14), equal to the Rossby number. Then it is easy to check that, to the lowest order, Eq. (9.22) reduces to

$$\frac{D_H}{Dt}\zeta + f_0 w \frac{d^2 \bar{\rho}_*}{dz^2} = 0 \ . \tag{9.23}$$

We assume for simplicity that N^2 is a constant. Hence the potential vorticity equation writes:

$$\frac{D_H}{Dt}\omega'_P = 0, \tag{9.24}$$

with

$$\omega'_P = -\nabla_H^2 \psi'(x, y, z, t) + f - \left(\frac{f_0}{N} \right)^2 \frac{\partial^2 \psi'}{\partial z^2}. \tag{9.25}$$

At this point, and since $\psi - \psi'$ is a function of z only, the quasi geostrophic potential vorticity equation may be replaced by:

$$\frac{D_H}{Dt}\omega_P = 0$$

$$\omega_P = -\nabla_H^2 \psi(x, y, z, t) + f - \left(\frac{f_0}{N} \right)^2 \frac{\partial^2 \psi}{\partial z^2}. \tag{9.26}$$

More details may be found in Pedlosky [567].[2]

The three terms of the r.h.s. of Eq. (9.26) correspond to three different physical processes: $\omega_{BT} = -\nabla_H^2 \psi$, the barotropic potential vorticity, will give rise to the two-dimensional turbulence introduced in the previous chapter; the variations of f with the latitude will generate Rossby waves (see below);

[2] The reader is warned that our stream function has an opposite sign compared to Pedlosky's.

finally the baroclinic potential vorticity $\omega_{BC} = -(f_0/N)^2\partial^2\psi/\partial z^2$, which, from Eq. (9.10), is proportional to $-\partial\rho/\partial z$, will be responsible for the so-called "baroclinic instability", due to the simultaneous action of a rotation and a density gradient.

There ought to be a sub-geostrophic diffusion term in the r.h.s. of Eq. (9.26a), due both to the small-scale turbulent diffusion of momentum and temperature. The simplest form for such an operator could be an eddy-viscous dissipation $\nu_e\nabla_H^2\omega_G$ (which however ignores the temperature diffusion). Actually, oceanographers prefer to utilize a biharmonic diffusion operator proportional to $-(\nabla_H^2)^2\omega_G$ (Holland [287, 288]). Higher-order Laplacian operators have been proposed by Basdevant and Sadourny [40]. In the numerical LES of quasi geostrophic turbulence, these higher-order turbulent dissipation operators cause the dissipative effects to shift towards the smallest resolved scales, leaving the large scales unaffected by viscosity (see Chapter 12).

9.4 Baroclinic instability

It is an instability due to the conjugation of rotation and temperature gradients (horizontal and vertical) in thermal fronts which is at the origin of storms in the atmosphere, and the development of vortices in the ocean. Here we assume $f = f_0$. There are several interpretations of this instability.

9.4.1 Eady model

We consider a flow in a rotating stably-stratified channel of width L and depth H. It is differentially heated in the y direction with a constant non-dimensionalized "density" gradient $\partial\rho_*/\partial y$. Geostrophy is also assumed, as well as thermal-wind balance. We find as solution of Boussinesq equations a basic zonal flow of uniform vertical gradient A, where A is a constant related to $\partial\rho_*/\partial y$. If one takes a zero velocity at the ground, we have $\bar{u}(y,z) = Az$. This is the simplest model of atmospheric jet stream, represented by the lid moving at velocity AH.

Afterwards one performs a linear-stability analysis of the equations about this state. One recovers the same equation as when linearizing Eqs. (9.24) and (9.25) about the same state: neglecting differential rotation, it is obtained

$$\left(\frac{\partial}{\partial t} + Az\frac{\partial}{\partial x}\right)\left[\nabla_H^2\psi'(x,y,z,t) + \left(\frac{f_0}{N}\right)^2\frac{\partial^2\psi'}{\partial z^2}\right] = 0, \qquad (9.27)$$

equivalent to Eq. (45-28) of the Eady model given in Drazin and Reid [173]. The latter provide a solution of this equation by normal modes, with free-slip boundary conditions on the lateral boundaries, the bottom and the lid,

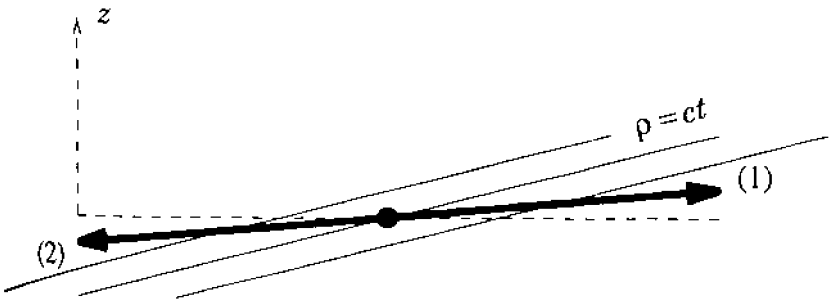

Figure 9.2. Schematic view of quasi horizontal thermal convection in baroclinic instability (ρ stands here for ρ_* introduced in Boussinesq approximation).

and periodicity in the longitudinal direction. It is found that unstable modes appear when the Burger number

$$B_u = \left(\frac{HN}{Lf_0}\right)^2 = \left(\frac{R_o}{F}\right)^2 = \left(\frac{r_I}{L}\right)^2 \tag{9.28}$$

is smaller than 0.58, equivalent to $L > 1.31 r_I$, which shows that the baroclinic instability develops at horizontal wavelengths larger than r_I.

9.4.2 Displaced fluid particle

Let us now recall a displaced fluid-particle argument in order to understand more physically baroclinic instability (see e.g. Holton [294]). We consider a fluid particle located on some isopycnic surface, which is not horizontal, but raised to the North due to the thermal front[3] (see Figure 9.2). We remember that the flow motion is quasi horizontal because of Eq. (9.14). If a fluid parcel is displaced to the North following a quasi horizontal path slightly rising (trip 1 in the figure), it will feel a positive buoyancy, since it has been brought into a denser fluid. Hence it will tend to rise and keep on this motion, which will further increase the positive buoyancy. The same reasoning may be applied to a fluid parcel descending towards the South slightly under the horizontal (trip 2 in the figure). Thus, baroclinic instability is a sort of quasi horizontal thermal convection, rendered possible because the isopycnals are raised in the front.

[3] Resulting for instance from the differential heating between the poles and the equator.

9.4.3 Hyperbolic-tangent front

The above reasoning does not give informations about the sign of the vertical vorticity. Let us consider now the following hyperbolic-tangent front studied by Peltier, Polavarapu et al. [568,581,582], Garnier et al. [241–243] and Lesieur et al. [429]. They consider an ideal gas and take as basic potential temperature the following distributions: linear and positive along the vertical, hyperbolic-tangent profile of width δ along the horizontal (see Figure 9.3):

$$\Theta = \bar{\Theta}(z) - \frac{\Delta\Theta}{2} \tanh \frac{2y}{\delta}. \tag{9.29}$$

Posing

$$2V = \frac{gH}{f_0 \delta} \frac{\Delta\Theta}{\Theta_0}, \tag{9.30}$$

the thermal-wind balance writes

$$\frac{\partial \vec{u}}{\partial z}(y,z) = \frac{2V}{H \cosh^2(2y/\delta)} \vec{x},$$

which yields

$$\bar{u}(y,z) = \frac{2V}{H \cosh^2(2y/\delta)} z + L(y),$$

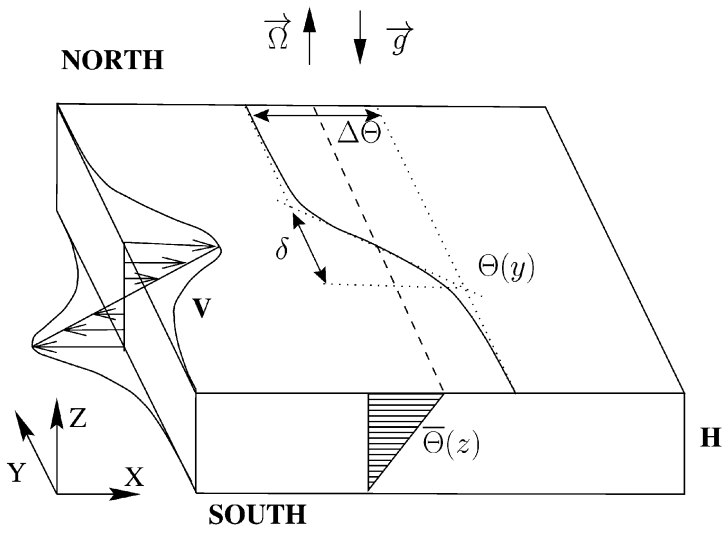

Figure 9.3. Initial velocity and potential temperature distributions in the baroclinic jet configuration studied by Garnier [241] and corresponding to Eq. (9.31) (courtesy E. Garnier).

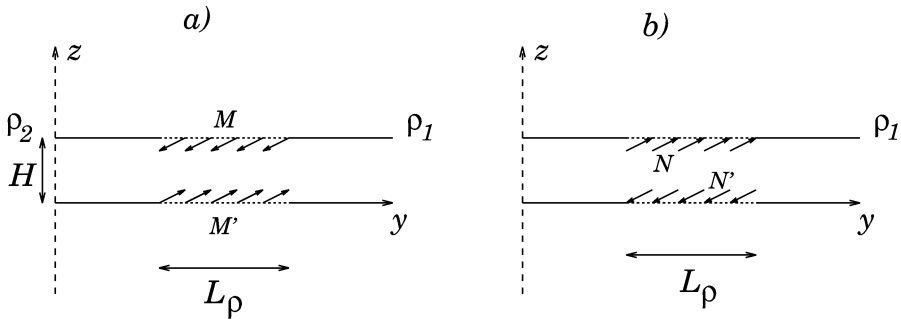

Figure 9.4. Possible lateral motions of the upper and lower flow in a front.

where $L(y)$ is a function we will choose such that $u(y,H) = -u(y,0)$, giving $L(y) = -V/\cosh^2(2y/\delta)$. The final baroclinic-jet velocity profile is

$$\bar{u}(y,z) = \frac{V}{\cosh^2(2y/\delta)}\left[\frac{2z}{H} - 1\right]. \tag{9.31}$$

It is a double Bickley jet linearly varying with the vertical, from $-V$ on the ground to $+V$ on the top ($y = 0$). The same initial state had been taken by Peltier, Polavarapu et al. [568, 581, 582] for the numerical resolution of Navier–Stokes with differential rotation within anelastic dynamics.

In fact one may take also $L(y) = 0$ in the above integration, to give

$$\bar{u}(y,z) = \frac{2V}{H\cosh^2(2y/\delta)}z, \tag{9.32}$$

which is a single Bickley jet with zero velocity at the ground and $2V$ on the top ($y = 0$).

The Rossby and Froude numbers are respectively $V/f\delta$ and V/NH.

9.4.4 Dynamic evolution of the baroclinic jets

Garnier et al. [243] have shown by DNS that the flow given by Eq. (9.31) is linearly unstable for $R_o/F < 1.5$. We assume now that this basic flow is perturbed, and write the evolution equation for the vertical relative vorticity ω_z

$$\frac{D}{Dt}\omega_z = \vec{\omega}_H.\vec{\nabla}_H w + (f_0 + \omega_z)\frac{\partial w}{\partial z}. \tag{9.33}$$

Suppose that baroclinic instability develops. Let M be a fluid parcel located initially close to the upper surface (see Figure 9.4a). Assuming the fluid

cannot cross the wall, it can descend to the South, due to the baroclinic-instability mechanism of Figure 9.2. It will thus acquire a positive $\partial w/\partial z$, since $w = 0$ on the upper lid and is negative lower. DNS and LES due to Garnier et al. and reported in [243] and Lesieur et al. [429, 431] have shown that the term $\vec{\omega}_H.\vec{\nabla}_H w$ of Eq. (9.33) is in fact negligible, so that the equation reduces to

$$\frac{D}{Dt}\omega_z \approx (f_0 + \omega_z)\frac{\partial w}{\partial z}. \tag{9.34}$$

In this equation, the r.h.s. is positive. Hence, the fluid parcel M will see its vorticity increase by vertical stretching. This shows that in the upper jet cyclonic vorticity will increase, and anticyclonic decrease in modulus. In the same way, a fluid parcel M' close to the ground will rise to the North, with again respectively increase and diminishing of the cyclonic and anticyclonic vorticity modulus.

In fact, we have to consider also a motion corresponding to reversal of velocity in Figure 9.4a. It is shown in Figure 9.4b, where the fluid parcel N rises to the North up to the lid, which implies a negative $\partial w/\partial z$ and decrease of the vertical vorticity, that is to say creation of anticyclonic vorticity modulus. The same occurs for N'. This anticyclonic production is less intense than the cyclonic one, due to the $f_0 + \omega_z$ term in Eq. (9.34). The ratio of anticyclonic to cyclonic production is in fact initially of the order of $(1 - R_o)/(1 + R_o)$, and will diminish with the growth of anticyclonic vorticity.

Numerical solutions of Boussinesq equations starting initially with the above barolinic jets corresponding to Eq. (9.31) have been performed by Garnier et al. [243] (DNS and LES). The simulations of Garnier are carried out at initial Rossby and Froude numbers of respectively 0.1 and 0.2. An animation of the DNS[4] is presented in Lesieur et al. [431]. It shows that the jets oscillate horizontally at the most-unstable mode predicted by a linear baroclinic instability analysis. In fact, both jets become a sort of Karman street as in a regular Bickley jet,[5] with an out of phase oscillation of the top and bottom jets. In the upper jet cyclonic vorticity grows and rolls up in the northern part, and anticyclonic vorticity in the southern part. The intensity of the latter is lower than the cyclonic one, in agreement with the above reasoning of Figure 9.4. In the lower jet, cyclonic vorticity grows in the southern part, and anticyclonic vorticity in the northern part. Then the upper and lower cyclones move towards each other and align vertically to form a nearly two-dimensional vortex. This is certainly due to the intense entrainment rotation which favours cyclonic vorticity (see Chapter 13). On the contrary, the upper and lower anticyclones are vertically decorrelated. Simultaneously, intense

[4] With $R_o = F = 0.1$, but phenomena are the same.

[5] The difference with a Bickley jet is that, in two-dimensions, the vorticity modulus of the latter cannot grow.

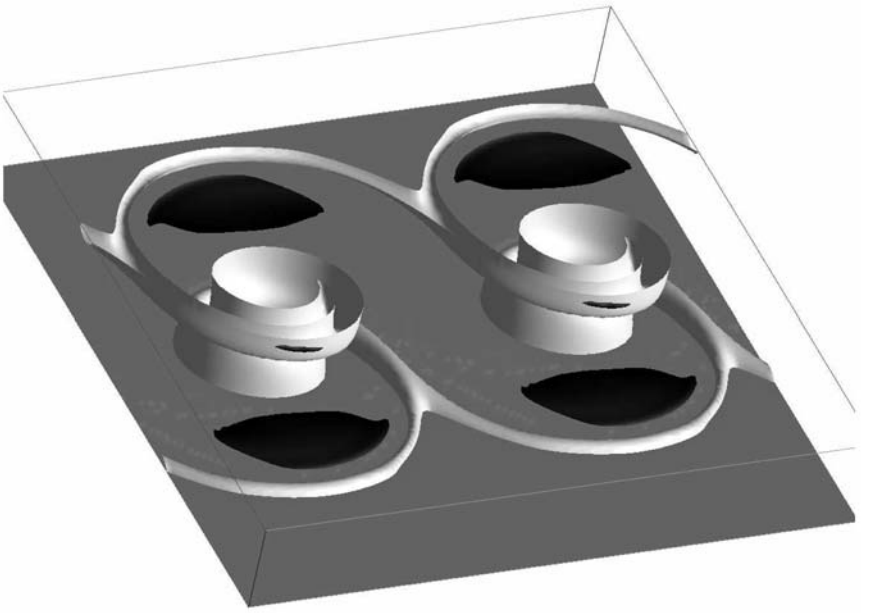

Figure 9.5. Strong cyclonic depressions resulting from three-dimensional DNS of the baroclinic jet; white (resp. black) corresponds to positive (resp. negative) vertical relative vorticity (courtesy E. Garnier).

cyclonic vorticity keeps on growing in the "braids" reconnecting the cyclones on the lower and upper boundaries. The resulting state is shown in Figure 9.5. It displays isosurfaces of vertical vorticity (cyclonic in white, anticyclonic in black), at a threshold $6V/\delta$. One does observe the two-dimensional cyclonic vortices, which are about 8 times stronger than the initial maximal cyclonic vorticity. As for the braids, they are 30 times stronger, which corresponds to intense local horizontal mixing layers along the front. Anticyclonic vortices exist only at the top and the bottom of the domain. They are more diffused than the cyclonic ones, and weaker (6 times the initial value). This figure resembles strikingly cyclonic disturbances which form currently at medium latitudes in the atmosphere.

The intense production of vertical vorticity in the braids inbetween the cyclones may again be explained with the aid of Eq. (9.34). Indeed, the cyclonic vortex close to the ground will pump from the South fluid which will be warmer than fluid coming from the North. We will have a thin cold front formation to the South, where one may expect that the southern warm flow will rise above the northern cold one within some local thermal convection. We have $\partial w/\partial z > 0$. Since the Rossby number is low, we are sure that $f_0 + \omega_z > 0$

whatever the sign of ω_z. Then ω_z will grow: if it is positive, cyclonic vorticity will be intensified, while if it is negative, anticyclonic vorticity modulus will decay. The same reasoning may be carried out on the lid, where the cyclonic vortex will pump from the North fluid which will be colder than fluid coming from the South with formation of a thin warm front to the North. The northern cold flow will sink under the southern warm one, and we will still have $\partial w/\partial z > 0$.

LES of Garnier et al. [243], less dissipative than the DNS, show secondary instabilities developing on the braids, with production of two secondary cyclonic vortices in two days as one can see in Figure 9.6. The latter represents an evolution with time of the potential temperature at the ground. These vortices have a vorticity of 2 to 3 times that of primary vortices. It is clear that the same vortices should form on the lid. One of these vortices had been found at the ground by Polavarapu and Peltier [581, 582] in their anelastic simulations with β-effect. So the work of Garnier et al. [243] indicates that these small-scale cyclones are not due to differential rotation.

It is interesting to note that these simulations, published in 1998, have strong analogies with the two devastating storms which struck Europe on December 26th and 28th 1999 (see Lesieur et al. [429, 431]). Indeed, satellite meteorological observations on the 25th show a big cyclonic perturbation hitting Scandinavia after having crossed Great-Britain. The winds are of the order of 120 km/h (33 m/s). This is typical of regular storms above northern Atlantic. A cold front forms in France at the level of Brittany. It is there that the first intense storm developed on 26th morning, in the form of a vortex of diameter 400 km which was observed to travel eastward at a velocity of 100 km/h. Since winds of $\approx$200 km/h were reported, the only explanation is that the vortex had an external rotational velocity of 100 km/h, which gives a total velocity of 200 km/h to its south, and 0 to its north.

A second vortex of the same type, although less intense, appeared two days after.

To finish with storms, a few words on the one which crossed northern Europe on January 18th 2007, and where winds of 160 km/h were recorded in London, and 200 in Germany. Maps and animations published on the internet site "www.wunderground.com", and coming from the ANV model results, show a strong negative temperature gradient oriented South-West/North-East along the line Spain-France-Scandinavia. The jet stream (data at the level corresponding to 300 hpa) evolution is shown from the 16th to the 19th. It oscillates quasi hozizontally, and hits on the 19th values of about 360 km/h. We recall that 4 days before the storm of December 26th 1999, the jet stream had a velocity of 400 km/h (see Lesieur et al. [429]). In the above model of single baroclinic jet, the maximal jet stream velocity is from Eqs. (9.30) and (9.32)

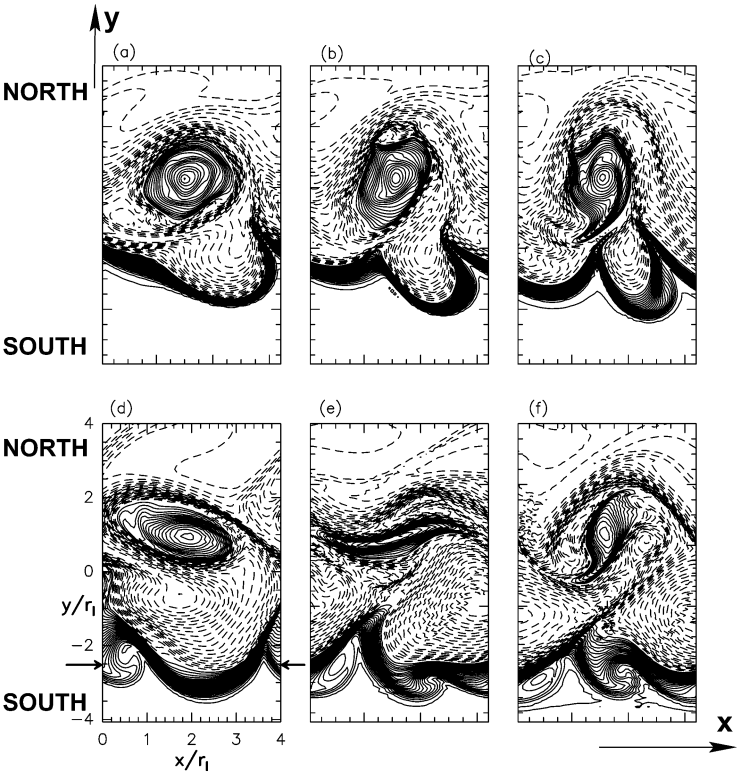

Figure 9.6. Time evolution (corresponding to letters) of the potential temperature at the ground in LES of the baroclinic jets (courtesy E. Garnier).

$$2V = \frac{gH}{f_0}\left|\frac{\partial \rho_*}{\partial y}\right|, \tag{9.35}$$

where $\partial\rho_*/\partial y$ is taken at $y = 0$. It is on this velocity that the winds velocity will scale when the storm will have developed.[6] It is feasible in real Earth atmosphere that fast jet streams due to high horizontal temperature gradients will lead to severe storms, if the parameter R_o/F is in the unstable range. But the amplitude of V is unimportant in the stability criterion from which V is eliminated.

9.4.5 Baroclinic instability in the ocean

We present now an example of baroclinic instability coming from a three-dimensional numerical solution of Boussinesq equations applied by Chanut et

[6] This is at least what happens in the present model.

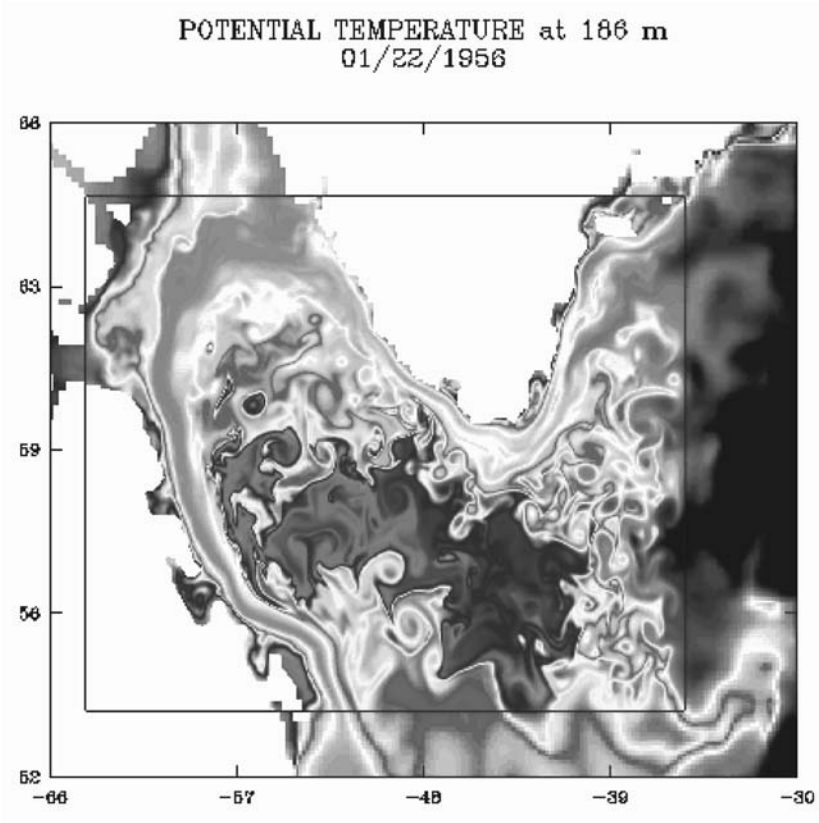

Figure 9.7. Temperature field at a depth of 186 m in the Labrador sea in a numerical simulation carried out by Chanut et al. [108] (see text for details, courtesy B. Barnier).

al. [108] to Labrador sea in the framework of the initialization of an ocean-modelling code forced by a wind.[7] The horizontal resolution is 4 km. A temperature field at a depth of 186 m is presented in Figure 9.7. It corresponds to a hypothetic day January 22nd 1956, with a a cold wind of $-30°$C blowing from the North-West. This wind cools the surface of the sea, which dives by thermal convection.[8] The central dark part of the sea (deep blue in reality) corresponds to a temperature of 3°C. The grey part (including the coastal current, red in reality) has a temperature of 4.5°C. The right part (deep red

[7] See below in the Ekman-layer section for details on these forcings.

[8] This happens for instance in the Golfe du Lion (Mediterranean sea) when the north wind (mistral) blows.

in reality) is warmer. One sees very neatly the formation in thermal fronts of vortices, in particular along the Greenland western coast. These vortices have both signs. They are due to baroclinic instability and to thermal convection. The latter has been studied with LES by Padilla-Barbosa and Métais [558].

9.5 The N-layer quasi geostrophic model

The quasi geostrophic potential-vorticity equation derived in Section 9.3 can be generalized to a variable $d\bar{\rho}/dz$, the Brunt-Vaisala frequency being function of z (see Pedlosky [567]). However, it is valid within the interior of the geostrophic fluid, and requires knowledge of boundary conditions at the bottom and the top of the fluid layer. In the Earth atmosphere, the bottom boundary conditions are due to the orography, and to the existence of a turbulent Ekman layer[9] (see below). In the Ocean, there is also an upper Ekman layer due to wind stress. In order to understand the role of these boundary conditions, it may be useful to consider the particular case of a flow composed of N quasi horizontal layers of fluids of uniform densities $\rho_1, \ldots, \rho_N$. We stress that N is in this section an integer which has nothing to do with the Brunt-Vaisala frequency. This model will be used more for the ocean than the atmosphere for two reasons: density vertical distribution of in the ocean may vary by steps, and ocean has a much lower Rossby number. More details on the following derivation can be found in Pedlosky [567]. The fluid is assumed to be perfect (no viscosity), and a superposition of homogeneous layers of density ρ_n (increasing with n), instantaneous thickness $h_n(x, y, t)$, and average thickness H_n (see Figure 9.8). The Coriolis parameter f may vary.

The hydrostatic approximation is done on the vertical, permitting to calculate the instantaneous pressure at an altitude z as:

$$\begin{aligned} p(x, y, z, t) = p_A + g(\rho_1 h_1 + \rho_2 h_2 + \cdots + \rho_{n-1} h_{n-1}) \\ + \rho_n g(\eta_n + H_n + H_{n+1} + \cdots - z), \end{aligned} \tag{9.36}$$

where p_A is the pressure at a free surface, if any, and η_n the denivellation of the upper surface of the layer n. Using the following relations

$$\sum_i h_i(x, y, t) + \tau(x, y) - \eta_1 = \sum_i H_i = H$$

$$h_n - \eta_n + \eta_{n+1} = H_n$$

$$\bar{p}(z) = p_A + g(\rho_1 H_1 + \rho_2 H_2 + \cdots + \rho_{n-1} H_{n-1})$$

[9] Where an appreciable part of the geostrophic kinetic energy is dissipated.

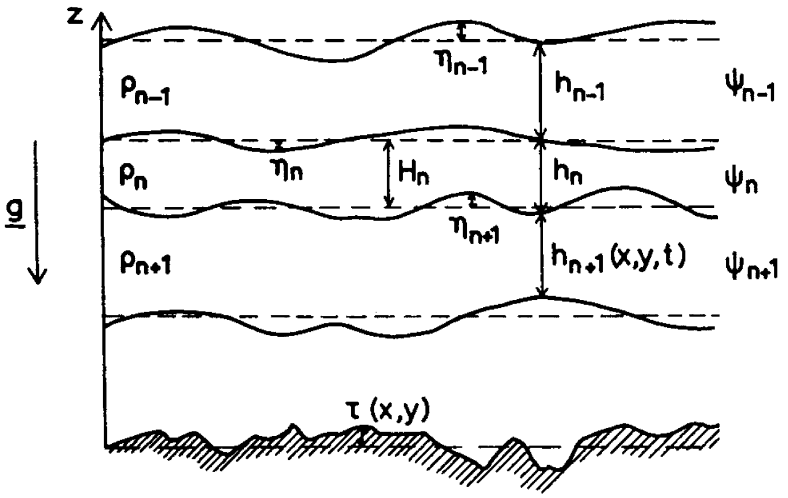

Figure 9.8. Schematic vertical section of a N-layer geostrophic flow: η_n and η_{n+1} are the deviations of the interface of the layer n with respectively the layers $(n-1)$ and $(n+1)$.

$$+\rho_n g(H_n + H_{n+1} + \cdots - z),$$

where $\tau(x,y)$ is the bottom topography, and $\bar{p}(z)$ the hydrostatic pressure (without any motion), it is obtained for the fluctuating[10] pressure $p'_n(x,y,t)$ in the layer n:

$$p'_n(x,y,t) = g[\rho_1\eta_1 + (\rho_2 - \rho_1)\eta_2 + \cdots + (\rho_n - \rho_{n-1})\eta_n. \tag{9.37}$$

We remark that this pressure fluctuation in each layer does not depend upon z. This allows to simplify the motion equations within layer n. More specifically, and as we did for Barré de Saint-Venant equation, we will look for solutions where the horizontal velocity field is z independent. We have

$$\frac{D_H^{(n)}}{Dt}u = -g\frac{\partial\eta}{\partial x} + fv \tag{9.38}$$

$$\frac{D_H^{(n)}}{Dt}v = -g\frac{\partial\eta}{\partial y} - fu \tag{9.39}$$

where $\vec{u}_n$ (of components u and v) is the horizontal velocity components in layer n, $D_H^{(n)}/Dt$ the derivative following the horizontal motion $\vec{u}_n$, and

[10] With respect to $\bar{p}(z)$.

$$\eta = p'/g\rho_n.$$

Integrating the continuity equation along the vertical in this layer, we have

$$h_n \vec{\nabla}_H . \vec{u}_n + w_n - w_{n+1} = 0,$$

where w_n and w_{n+1} are the vertical velocities at the top and bottom of the layer. This yields

$$\frac{D_H^{(n)}}{Dt} h_n = -h_n \vec{\nabla}_H . \vec{u}_n.$$

As for a single layer, one can easily show the conservation of potential vorticity $(\omega_n + f)/h_n$ following the horizontal motion, where ω_n is the vorticity of $\vec{u}_n$.

Afterwards we consider Eqs. (9.38) and (9.39) (Euler equations for the layer of density ρ_n), and assume a geostrophic balance. This enables to associate to the layer a stream function of the horizontal velocity field $\vec{u}_n(x, y, t)$ equal to:

$$\psi_n(x, y, t) = -\frac{p'_n(x, y, t)}{\rho_n f_0}.$$

Therefore, the conservation of potential vorticity reduces here to the conservation of $(-\nabla_H^2 \psi_n + f)/h_n$ following the horizontal motion $\vec{u}_n$. Let the constant H_n be the mean thickness of the layer n. The potential vorticity can be approximated by

$$\frac{1}{H_n} \left[-\nabla_H^2 \psi_n + f - (\eta_n - \eta_{n+1}) \frac{f_0}{H_n} \right].$$

Note that the quasi geostrophic equation for the nth layer can also be written as

$$\frac{D_H^{(n)}}{Dt} \left[-\nabla_H^2 \psi_n(x, y, t) + f \right] = \frac{f_0}{H_n} (w_n - w_{n+1})$$

In order to calculate η_n, one writes ψ_n and ψ_{n-1} using Eq. (9.37), which gives

$$\eta_n(x, y, t) = \frac{f_0}{g(\rho_n - \rho_{n-1})} (\rho_{n-1}\psi_{n-1} - \rho_n \psi_n). \tag{9.40}$$

In the upper layer, $\eta_1 = -f_0 \psi_1 / g$.

9.5.1 One layer

Let us consider first a one-layer fluid over a topography $\tau(x, y)$. The quasi geostrophic potential vorticity equation is thus

$$\frac{D_H}{Dt} \left[-\nabla_H^2 \psi(x, y, t) + f + \frac{f_0}{H} (\tau - \eta) \right] = 0,$$

that is

$$\frac{D_H}{Dt}\left[-\nabla_H^2\psi(x,y,t)+f+\frac{f_0}{H}\tau+\frac{f_0^2}{gH}\psi\right]=0. \tag{9.41}$$

This very simple case allows one to understand the role of the bottom topography, which can be included in the potential vorticity of the bottom. Another remark concerns the topographic Rossby waves, which will be generated by the variations of τ with y in the same way as Rossby waves are generated by the variations of f (see below). Notice also that the contribution to the potential vorticity due to the free surface is proportional to ψ/r_E^2, where r_E is the external Rossby radius of deformation: if the horizontal wavelength L is much smaller than r_E, this term is negligible in front of $\nabla_H^2\psi$, which constitutes the rigid-lid approximation.

9.5.2 Two layers

For a two-layer fluid above a topography τ (with a free surface of denivellation η) we get

$$\eta_1=-\frac{f_0}{g}\psi_1;\quad \eta_2=\frac{f_0}{g\delta\rho}(\rho_1\psi_1-\rho_2\psi_2);\quad \eta_2-\eta_1=\frac{f_0}{g\delta\rho}\rho_2(\psi_1-\psi_2),$$

where $\delta\rho=\rho_2-\rho_1$ is the density difference (positive, since we are in a stable situation and the heaviest fluid is at the bottom). Because of Eq. (9.10), $\psi_1-\psi_2$ is characteristic of the temperature difference between the two layers. The two potential vorticity equations are (within the rigid lid approximation)

$$\frac{D_H^{(1)}}{Dt}\left[-\nabla_H^2\psi_1(x,y,t)+f+\frac{\psi_1-\psi_2}{R_1^2}\right]=0$$

$$\frac{D_H^{(2)}}{Dt}\left[-\nabla_H^2\psi_2(x,y,t)+f+\frac{\psi_2-\psi_1}{R_2^2}+f_0\frac{\tau}{H_2}\right]=0, \tag{9.42}$$

where $R_1=N_1H_1/f_0$ and $R_2=N_2H_2/f_0$ are two internal radii of deformation analogous to Eq. (9.12), the local Brunt-Vaisala frequencies being defined by

$$N_1^2=\frac{g}{\rho_2}\frac{\delta\rho}{H_1};\quad N_2^2=\frac{g}{\rho_2}\frac{\delta\rho}{H_2}. \tag{9.43}$$

This two-layer model was first introduced by Phillips [570–572]. In fact the latter was present in Lannion 1971 summer school already mentioned in Chapter 8 (Morel [520]), and it is interesting to reproduce in Figure 9.9 another picture by O. Carel of N. Philips' lectures in Lannion, showing the audience, composed partly of former Paris Ecole Polytechnique students, sinking with swords drawn and cocked hats in the sea of large-scale atmospheric equations.

Figure 9.9. Lecture of N. Phillips in Lannion (courtesy O. Carel).

The model can be interpreted in a different way displaying the interaction between a mean horizontal field (the "barotropic" mode)

$$\psi_{BT} = \frac{\psi_1 + \psi_2}{2} \tag{9.44}$$

and the "baroclinic" mode

$$\psi_{BC} = \frac{\psi_1 - \psi_2}{2} \tag{9.45}$$

which has been seen to characterize the temperature. To simplify matters, let us assume that there is no topography, and that both internal radii of deformation are equal

$$\frac{1}{R_1^2} = \frac{1}{R_2^2} = \frac{\mu^2}{2}. \tag{9.46}$$

A good exercise is to check that these modes satisfy the two following equations (where ∇^2 stands for the operator ∇_H^2, and $J(.,.)$ for the Jacobian)

$$\frac{\partial}{\partial t}\nabla^2\psi_{BT} + J(\nabla^2\psi_{BT}, \psi_{BT}) + J(\nabla^2\psi_{BC}, \psi_{BC}) + \beta\frac{\partial \psi_{BT}}{\partial x} = 0$$

$$\frac{\partial}{\partial t}[(\nabla^2 - \mu^2)\psi_{BC}] + J[(\nabla^2 - \mu^2)\psi_{BC}, \psi_{BT}] + J(\nabla^2\psi_{BT}, \psi_{BC})$$

$$+\beta \frac{\partial \psi_{BC}}{\partial x} = 0 \tag{9.47}$$

where the "β-plane approximation"

$$f = f_0 + \beta y \tag{9.48}$$

has been made (β is assumed to be constant, this is the same as Eq. (3.24)). We recall the value of β

$$\beta = \frac{2\Omega}{a} \cos \varphi_0; \quad \frac{f}{\beta} = a \tan \varphi_0.$$

At a latitude of 45°, we have $f \approx 10^{-4}$ rd s^{-1} and $\beta \approx 1.6 \times 10^{-11}$ m^{-1}s^{-1}.

9.5.3 Spectral vertical expansion

An alternative way of obtaining these N-layer equations is to perform a spectral vertical expansion of the original quasi geostrophic equation (9.26) (with a constant Brunt-Vaisala frequency), which involves a three-dimensional fluid with a continuous density profile: for a vertical two-mode truncation of a layer of thickness H extending from $z = -H/2$ to $z = H/2$ for instance, one can look for solutions of the form (cf. Hoyer and Sadourny [300])

$$\psi(x, y, z, t) = \psi_{BT}(x, y, t) + \sqrt{2} \psi_{BC}(x, y, t) \sin \frac{\pi z}{H} \tag{9.49}$$

where the barotropic mode corresponds to a horizontal two-dimensional basic flow, and the baroclinic mode is the amplitude of a vertical sine perturbation describing the departure from two-dimensionality. The potential vorticity in Eq. (9.26) is thus equal to

$$\omega_p = -\nabla_H^2 \psi_{BT} + f + \sqrt{2}(-\nabla_H^2 + \mu^2) \psi_{BC} \sin \frac{\pi z}{H} \tag{9.50}$$

with

$$\mu = \pi \frac{f_0}{NH}$$

(N is again the Brunt-Vaisala frequency). The spectral expansion can then be performed in the following way: one integrates the potential vorticity conservation equation successively from $z = -H/2$ to $+H/2$, then from $z = 0$ to $H/2$: one obtains exactly for ψ_{BT} and ψ_{BC} the same equations as Eq. (9.47). It is remarkable to see here how a two-mode vertical spectral expansion of a fluid with a continuous density can be identified with a flow involving two homogeneous fluids of different densities.

The physical interpretation of this two-layer (or two-mode) model in terms of quasi geostrophic turbulence will be given below.

Now, we will look at the interaction of a quasi geostrophic flow with an Ekman layer, and also study some barotropic and baroclinic quasi geostrophic waves.

9.6 Ekman layer

When a quasi geostrophic flow $\vec{u}_G$ is close to a boundary, the latter will tend to diminish the velocity (which must be zero on the boundary), in such a way that the geostrophic balance will be lost. The consequence will be a rotation of the horizontal velocity in the boundary layer (the so-called Ekman spiral), and a vertical fluid flux at the top of the boundary layer, due to the loss of horizontal non-divergence. To study this important problem which controls the dissipation of a geostrophic flow in the presence of a boundary and the forcing of oceans by the wind, the simplest model to consider is that of a fluid of constant density ρ_0 rotating with a constant angular velocity $f_0/2$ about a vertical axis (see Figure 9.10)

$$\frac{Du}{Dt} = -\frac{1}{\rho_0}\frac{\partial P}{\partial x} + f_0 v + \nu_e \nabla^2 u \tag{9.51}$$

$$\frac{Dv}{Dt} = -\frac{1}{\rho_o}\frac{\partial P}{\partial y} - f_0 u + \nu_e \nabla^2 v \tag{9.52}$$

$$\frac{Dw}{Dt} = -\frac{1}{\rho_0}\frac{\partial P}{\partial z} + \nu_e \nabla^2 w \tag{9.53}$$

where the gravity and centrifugal force have been included in the pressure. The velocity field is a filtered velocity defined as in Eq. (9.2). This permits one to assume that the fluid is geostrophic and equal to $\vec{u}_G$ of components u_G and v_G at the top or the bottom of the layer. Furthermore, the hydrostatic approximation is made in Eq. (9.53), showing that the pressure P is a function of x and y only, and is then equal to its geostrophic value such that

$$f_0 v_G = \frac{1}{\rho_0}\frac{\partial P}{\partial x}; \quad -f_0 u_G = \frac{1}{\rho_0}\frac{\partial P}{\partial y}. \tag{9.54}$$

It justifies the above argument that the geostrophic balance will be lost in the boundary layer if the velocity modulus decreases. Thus the equations of motion become

$$\frac{Du}{Dt} = f_0(v - v_G) + \nu_e \nabla^2 u$$

$$\frac{Dv}{Dt} = -f_0(u - u_G) + \nu_e \nabla^2 v. \tag{9.55}$$

In the outer geostrophic region, the inertial and viscous terms were neglected, so that the equation reduced to $v = v_G$ and $u = u_G$. In the Ekman layer on the contrary, dissipation is significant and cannot be neglected, while the inertial terms D/Dt are still discarded, since it is still assumed that the Rossby number is small. Let $\vec{\tilde{u}} = \vec{u}_H - \vec{u}_G$ of components $\tilde{u}$ and $\tilde{v}$, and the complex

velocity fields $Z = \tilde{u} + i\tilde{v}$, $Z_G = u_G + iv_G$. We have, when taking into account only the z-dependence

$$0 = f_0\tilde{v} + \nu_e \frac{d^2\tilde{u}}{dz^2}$$

$$0 = -f_0\tilde{u} + \nu_e \frac{d^2\tilde{v}}{dz^2}$$

which leads to

$$\frac{d^2Z}{dz^2} = i\frac{f_0}{\nu_e}Z. \tag{9.56}$$

We pose

$$\delta_E = \sqrt{\frac{2\nu_e}{f_0}}. \tag{9.57}$$

It is a scale which will be characteristic of the Ekman layer thickness. Remarking that the square roots of if_0/ν_e are $\pm(1+i)/\delta_E$, solutions are

$$Z = A\exp\frac{(1+i)z}{\delta_E} + B\exp -\frac{(1+i)z}{\delta_E},$$

where A and B are two complex constants to be determined in terms of boundary conditions.

9.6.1 Geostrophic flow above an Ekman layer

It is the case envisaged in Figure 9.10: the boundary conditions are $Z(0) = -Z_G$ (no-slip condition on the lower boundary) and $Z(\infty) = 0$ (geostrophic flow on the top), and the solution of Eq. (9.56) is

$$Z = -Z_G\left(\exp -\frac{z}{\delta_E}\right)\left(\exp -\frac{iz}{\delta_E}\right). \tag{9.58}$$

This shows both the exponential decrease of the horizontal velocity modulus, as well as the clockwise rotation (with increasing altitude) of the velocity direction in the Ekman layer. Assuming that $v_G = 0$, it is obtained

$$u = u_G\left[1 - (e^{-z/\delta_E})\cos(z/\delta_E)\right] \tag{9.59}$$

$$v = u_G(e^{-z/\delta_E})\sin(z/\delta_E). \tag{9.60}$$

which leads to the famous Ekman spiral for the horizontal velocity profile. More details can be found in, e.g., Greenspan [265] and Pedlosky [567].

The Ekman layer thickness is defined by

$$D_E = \pi\delta_E, \tag{9.61}$$

and corresponds to a velocity equal to 1.04% of the geostrophic velocity.[11] In practice, the Ekman layer thickness can be determined experimentally, and allows one to calculate the eddy-viscosity ν_e. D_E is about 1 km in Earth atmosphere,[12] and a few tenths of a meter in the ocean. One can then define the *Ekman number* for a fluid layer of width D

$$E_k = \frac{\nu_e}{f_0 D^2} = \frac{\delta_E^2}{2D^2}, \tag{9.62}$$

which characterizes the relative importance of the viscous to the Coriolis forces in Eqs. (9.51) and (9.52). If $E_k \ll 1$, one is back to the case of the above geostrophic analysis.

This analysis did not take into account the horizontal variation of the geostrophic velocity: let us consider at the top of the layer a closed isobaric contour C, to which the geostrophic velocity is tangential, and let Σ be a cylinder of section C and of generating lines parallel to $\vec{z}$ (see Figure 9.10). The fluid flux through Σ per unit length of C is equal, from Eq. (9.60), to

$$\Phi = \int_0^{+\infty} v(z)dz = u_G \frac{\delta_E}{2}.$$

Thus the total fluid flux through Σ is

$$\Phi_t = \frac{\delta_E}{2} \oint_C \vec{u}_G.\vec{\delta l} = \frac{\delta_E}{2} \iint_S \vec{\omega}_G.\vec{z}dS, \tag{9.63}$$

where $\vec{\omega}_G$ is the geostrophic vorticity, and S the surface enclosed by C. If the variations of $\vec{\omega}_G$ on S are ignored, the horizontal flux across Σ is equal to $(\delta_E/2)S$ times the vorticity of the geostrophic motion at the top of the Ekman layer. Since, for the sake of continuity, this horizontal flux has to be balanced by a vertical flux of velocity w_∞ at the top of the layer, we obtain the important relation

$$w_\infty = \frac{\delta_E}{2}\omega_G \tag{9.64}$$

which fixes for the geostrophic flow the vertical velocity coming from the interaction with the Ekman layer. One can also notice that a cyclonic geostrophic motion will imply a positive w_∞ (Ekman pumping), while an anticyclonic motion will bring outer fluid into the Ekman layer. Hence, there is a secondary circulation within the geostrophic flow, which is induced by the Ekman layer.

[11] It looks odd to find a velocity higher than the velocity at infinity, but this is one of the effects of rotation.

[12] An intense turbulence accompanied with clouds is often felt at this elevation while landing in a plane.

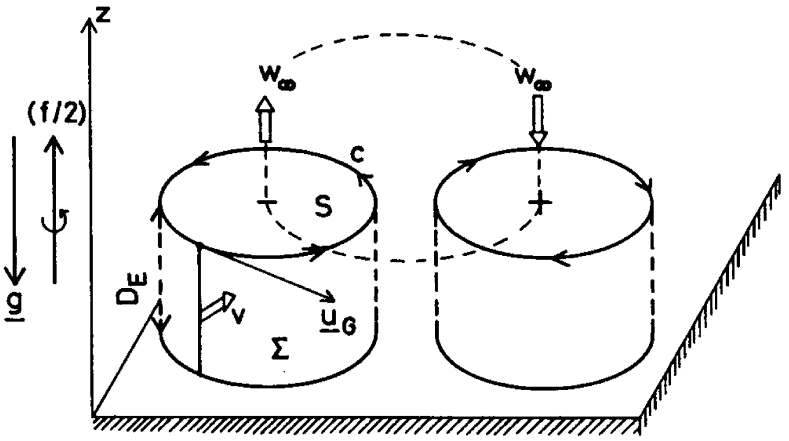

Figure 9.10. Schematic view of the bottom Ekman layer.

One can for instance write the quasi geostrophic potential-vorticity equation for one layer above an Ekman layer extending over a topography τ. Potential vorticity conservation is then written

$$\frac{D_H}{Dt}\left[-\nabla_H^2\psi(x,y,t)+f\right]=\frac{f_0}{H}(w_s-w_i) \tag{9.65}$$

where w_s and w_i are the vertical velocities respectively at the top and bottom of the layer. It has been shown by Pedlosky [567] that the effects of topography and free surface could be decoupled from the Ekman layer effects, in such a way that, from Eq. (9.64):

$$w_i=\frac{D_H\tau}{Dt}-\frac{\delta_E}{2}\nabla_H^2\psi(x,y,t) \tag{9.66}$$

$$w_s=\frac{D_H\eta}{Dt},$$

where $\eta(x,y,t)$ is the elevation of the free surface, equal to $-(f_0/g)\psi$. It is found

$$\frac{D_H}{Dt}\left[-\nabla_H^2\psi+f+\frac{f_0}{H}\tau+\frac{f_0^2}{gH}\psi\right]=\frac{f_0\delta_E}{2H}\nabla_H^2\psi. \tag{9.67}$$

The new term introduced by comparison to Eq. (9.41) is the Ekman layer damping term, which dissipates the vorticity linearly, and hence in the large eddies.[13]

[13] There ought to be also in the r.h.s. of Eq. (9.67) a turbulent damping due to sub-geostrophic scales, as discussed above: it will dissipate in the small scales the vorticity carried there along the enstrophy cascade (see below).

9.6.2 The upper Ekman layer

When a geostrophic ocean is driven by a wind exerting a strain $\vec{\sigma}$ on the surface, this strain is transmitted to the geostrophic circulation through an upper Ekman layer, to which the above calculation applies with appropriate boundary conditions. The Ekman layer is still described by Eq. (9.56), with boundary conditions which are now $Z = U - Z_G$ on the top $z = 0$ ($\vec{U} = U\vec{x}$ is the ocean surface velocity driven by the wind), and $Z = 0$ on the bottom $z \to -\infty$. It is found

$$Z = (U - Z_G)e^{z/\delta_E}e^{iz/\delta_E}.$$

If one assume $U_G \ll U$, it is easily found that

$$u = U\cos\frac{z}{\delta_E}\exp\frac{z}{\delta_E},$$

$$v = U\sin\frac{z}{\delta_E}\exp\frac{z}{\delta_E}.$$

Let us now look at the effect of an upper wind above the ocean surface. Let $\vec{n}$ be a vector normal to the surface and directed to the air. The stress exerted by the wind upon the ocean is $\vec{\sigma} = \overline{\overline{\sigma}}_a \otimes \vec{n}$, where $\overline{\overline{\sigma}}_a$ is the stress tensor in air. The stress exerted by the ocean upon the air is $\overline{\overline{\sigma}}_w \otimes (-\vec{n})$, where $\overline{\overline{\sigma}}_w$ is the stress tensor in water. Writing the mechanical balance of a portion of the surface,[14] one finds that both stress tensors are equal at the surface. We have

$$\vec{\sigma} = \overline{\overline{\sigma}}_w \otimes \vec{n}$$

whose components are

$$\sigma_1 = \mu_e\left(\frac{\partial u}{\partial z} + \frac{\partial w}{\partial x}\right) \approx \mu_e\frac{\partial u}{\partial z}$$

$$\sigma_2 = \mu_e\left(\frac{\partial v}{\partial z} + \frac{\partial w}{\partial y}\right) \approx \mu_e\frac{\partial v}{\partial z}$$

which writes

$$\vec{\sigma}_H \approx \rho\nu_e\left(\frac{\partial\vec{u}}{\partial z}\right)_{z=0} = \rho_0\nu_e\frac{U}{\delta_E}(\vec{x} + \vec{y}), \tag{9.68}$$

which shows that, due to Coriolis force, the water at the ocean surface is deviated 45° right (in the northern hemisphere) of the wind stress.

On the other hand, the vertical integration of u and v show (see Pedlosky [567]) that the horizontal flux across the Ekman layer is:

$$\vec{m}_E = \frac{U\delta_E}{2}(\vec{x} - \vec{y}) = \frac{\vec{\sigma}\times\vec{z}}{\rho_0 f_0}\ .$$

[14] Without considering any surface-tension effect.

Hence, a vertical integration of the three-dimensional continuity equation yields, for the vertical velocity $w_{-\infty}$ at the bottom of the Ekman layer:

$$w_{-\infty} = \vec{\nabla}_H . \vec{m}_E = \frac{1}{f_0 \rho_0} \vec{z} . \vec{\nabla} \times \vec{\sigma}. \tag{9.69}$$

When applied to a quasi geostrophic layer of an ocean forced by the wind, the complete potential vorticity equation is:

$$\frac{D_H}{Dt} \left[-\nabla_H^2 \psi + f + \frac{f_0 \tau}{H} + \frac{f_0^2}{gH} \psi \right]$$

$$= \frac{1}{\rho_0 H} \vec{z} . \vec{\nabla} \times \vec{\sigma} + \frac{f_0 \delta_E}{2H} \nabla_H^2 \psi. \tag{9.70}$$

When a multi-layer model is considered (within the rigid-lid approximation), the forcing terms are introduced in the upper layer, and the orographic and Ekman dissipation terms in the bottom layer.

9.6.3 Oceanic upwellings

Let us mention finally that Eq. (9.68) permits an understanding of the phenomenon called *upwelling*: when a wind blows along a coast – with the water to the right in the northern hemisphere (and left in the southern hemisphere) – the warm ocean surface layer will be entrained offshore, and, by continuity, deep cold water will upwell to the surface. The result is a cold coastal current going in the same direction as the wind. Famous examples are the Californian current in the northern hemisphere, which goes southward, and the Humboldt current in the southern hemisphere, which goes northwards: they are initiated by the anticyclonic winds west of the American Pacific coast. Due to the horizontal thermal gradients thus created in water, the current may be subject to a baroclinic instability, which might explain the eddies observed in the Californian current.[15] LES of this region using Boussinesq equations have been carried out by Tseng and Ferziger [692]. A very famous (but not yet really understood) anomaly of the Humboldt current corresponds to the so-called *El Nino* phenomenon, where this current chaotically reverses its direction every 2 or 3 years, transforming into a southward current of warm water. This catastrophic[16] event is accompanied with climatic anomalies such as the reversal of trade winds, and might involve extremely complicated nonlinear couplings between the atmosphere and the oceans.

[15] However, eddies found in the ocean may have other causes, such as horizontal shear instabilities or topographic trapping for instance.

[16] For the local fish industries.

9.7 Tornadoes

As stressed in Lesieur [424], tornadoes are an evil which strikes in particular farmers in the US Middle West. They develop generally in summer[17] within the atmospheric boundary layer during intense stormy episodes,[18] above plains over-heated by the sun. In fact, at the initiation of the tornado, their are two vertical eddy branches, one cyclonic and one anticyclonic. But afterwards, the latter disappears in 90% of the cases.

9.7.1 Lilly's model

We present here Lilly's helical model for tornadoes generation. Lilly [448] explains the growth of positive vertical vorticity in tornadoes and storms as the interaction of thermal convection with a helical wave of vertical axis (see Chapter 4) in the atmospheric boundary layer. More specifically, let $\bar{\rho}(z)$ and $\vec{u}_B(z)$ be respectively basic density and velocity profiles. The latter has the following components

$$\bar{u}(z) = -U\cos\lambda z, \quad \bar{v}(z) = U\sin\lambda z, \quad \bar{w} = 0. \tag{9.71}$$

Its vorticity is $\vec{\omega}_B = \lambda\vec{u}_B$. One can easily check that it is a stationary solution of Boussinesq equations in a perfect fluid without entrainment rotation (use Eq. (2.113)). With λ positive, the basic velocity vector rotates clockwise with height, as in the atmospheric Ekman layer.[19] Now we consider departures from the basic state. The exact perturbed vertical vorticity equation writes

$$\frac{D}{Dt}\omega_z = \vec{\omega}_H.\vec{\nabla}_H w + \omega_z\frac{\partial w}{\partial z},$$

where w is the vertical velocity. A linearization to the lowest order yields

$$\frac{\bar{D}}{\bar{D}t}\omega_z = \vec{\omega}_B.\vec{\nabla}_H w = \lambda\vec{u}_B.\vec{\nabla}_H w, \tag{9.72}$$

$\bar{D}/\bar{D}t$ standing for the derivative following the basic flow. Suppose that we travel with the wind at a given altitude z, and encounter a thermal updraft

[17] Notice however that, on February 3rd 2007, a tornado in Florida killed 20 people and was at the origin of considerable damages. It was initiated by heavy storms coming from Mexico gulf, which hit the land where the tornado was created. The latter progressed from West to East at a velocity of 80 km/h. In fact tornadoes had already struck Florida in February 1998, killing 42 people.

[18] On July 6th 2001, the fall of a tree due to a tornado killed 13 people in a park in Strasbourg.

[19] However, no variation of the velocity modulus is considered.

due to thermal convection: then the r.h.s. of Eq. (9.72) will be positive, and cyclonic vorticity will be generated on the thermal front.

Remark that this model might apply also to thermal convection in the upper Ekman layer in the ocean, when the water surface is cooled by the wind. This question has already been discussed above. Now, the Ekman velocity profile rotates anticlockwise when approaching the surface, so that one has to take $\lambda\langle 0$. Eq. (9.72) is still valid, and a sinking of cold surface waters will give rise to a negative $\vec{u}_B.\vec{\nabla}_H w$, and hence cyclonic vorticity again.

9.7.2 A hairpin-vortex based model

Lesieur [424] presents the following model (with different numbers): let us consider a developed turbulent boundary layer (without rotation). A quasi longitudinal hairpin will travel following the motion as seen in Chapter 4. Suppose that it encounters a very hot area: the head of the hairpin will tend to rise vertically due to thermal convection. Let us evaluate the Rossby number at this stage, before the development of the tornado: taking a low fluctuating velocity of 5 m/s and a vortex of diameter 1000 m at medium latitude ($f \approx 10^{-4}$) yields a Rossby of 50. It is then possible that rotation destroys anticyclonic vortices and stabilizes the cyclonic ones (see Chapter 13). The latter will be stretched vertically by thermal convection, which will increase the velocity. In a developed tornado of velocity 60 m/s, the Rossby number will be ≈ 600.

Once the tornado has formed in the atmosphere, its vorticity is approximately vertical, and thermal convection induces a vertical transport within it. So its helicity is important. As noticed by Lilly [444, 445] and already stressed in Chapter 7, this might explain the strong coherence of these phenomena, due to a time delay in the kinetic-energy dissipation.

Returning to the last Florida case already mentioned, the existence of storms above the ocean indicates that the temperature of the latter was high. Thermal convection was obviously present within the storms. But temperature was higher above the land than on the ocean. So the amplification of thermal convection above Earth may have intensified catastrophically vortex stretching to the point of creating the tornado.

9.8 Barotropic and baroclinic waves

9.8.1 Planetary Rossby waves

Up to now, we have mentioned the propagation of many waves due to gravity, constant rotation, compressibility. Here we focus our interest on Rossby waves,

which are obtained within the geostrophic approximation applied to a shallow fluid on a rotating sphere, and are due to the variation in the latitude of the "effective" Coriolis force $-f\vec{z}\times\vec{u}_H$. These waves are extremely significant in Earth atmosphere and oceans. The simplest model to study them is Eq. (9.41) with no topography, using the rigid-lid approximation, and with the β-plane approximation (9.48), that is

$$\frac{\partial}{\partial t}\nabla^2\psi + J(\nabla^2\psi,\psi) + \beta\frac{\partial\psi}{\partial x} = 0. \tag{9.73}$$

A linearization about a basic state at rest yields the famous Rossby equation [618]

$$\frac{\partial}{\partial t}\nabla^2\psi + \beta\frac{\partial\psi}{\partial x} = 0. \tag{9.74}$$

We look for wave solutions of the form

$$\psi(x,y,t) = \psi_0 \exp i(\vec{k}.\vec{x} - \varpi t), \tag{9.75}$$

ψ_0 being complex, with $\vec{k} = (k_1, k_2, 0)$ (real) and $\vec{x} = (x, y, 0)$. In fact, the solutions ψ sought in the form of Eq. (9.75) have to be complex, since ψ is a stream function. Otherwise, velocity components would not be real. As already stressed, this is not a problem because we are in front of a real linear partial-differential equation: a complex solution ψ yields two real solutions, its real and imaginary parts.

One finds the following dispersion relation

$$\varpi = -\frac{\beta k_1}{k_1^2 + k_2^2}. \tag{9.76}$$

Since $\beta > 0$, and assuming that $\varpi > 0$, we have $k_1 < 0$. The phase velocity in direction x is

$$c_x = \frac{\varpi}{k_1} = -\frac{\beta}{k_1^2 + k_2^2},$$

which shows that waves travel to the West.

The components of the group velocity $\vec{V}_G$ are

$$\frac{\partial\varpi}{\partial k_1} = \frac{\beta}{k^2}\frac{k_1^2 - k_2^2}{k_1^2 + k_2^2} = \frac{\beta}{k^2}\cos 2\theta$$

$$\frac{\partial\varpi}{\partial k_2} = \frac{\beta}{k^2}\sin 2\theta$$

where θ is the angle $\vec{x}, \vec{k}$. In fact one can build the group velocity from he circle $\varpi(k_1, k_2) = \varpi_0$, which writes

$$\left(k_1 + \frac{\beta}{2\varpi_0}\right)^2 + k_2^2 = \frac{\beta^2}{4\varpi_0^2}.$$

The centre of this circle is the point O of coordinates $(-\beta/2\varpi_0, 0)$. If we plot on this circle the vector $\vec{k}$ as a bipoint of origine the axes and extremity M, the group-velocity is a vector parallel to $\overrightarrow{MO}$ and of modulus β/k^2.

9.8.2 Reflection of Rossby waves

We consider a fluid initially at rest, and a Rossby waves packet travelling towards a vertical western boundary (see Figure 9.11). We suppose that the waves are going to be reflected on this boundary. Here we will write the waves as

$$\psi_i = A_i \cos(\vec{k}_i.\vec{x} - \varpi_i t + \phi_i)$$

for the incident one, and

$$\psi_r = A_r \cos(\vec{k}_r.\vec{x} - \varpi_r t + \phi_r)$$

after reflection. The fact that the incident wave packet goes to the West implies that $\vec{V}_{G_i}$ has a negative zonal component. Writing the free-slip boundary conditions on the western boundary (taken as $x = 0$) yields $\partial\psi/\partial y = 0$, with $\psi = \psi_i + \psi_r$, that is

$$A_i k_{i_2} \sin(k_{i_2} y - \varpi_i t + \phi_i) + A_r k_{r_2} \sin(k_{r_2} y - \varpi_r t + \phi_r) = 0.$$

Since this must be satisfied for arbitrary y and t, it implies

$$k_{i_2} = k_{r_2}, \varpi_i = \varpi_r, \phi_i = \phi_r \ , A_i = -A_r.$$

In Figure 9.11, the circle is the one envisaged above for the pulsation ϖ_i. Vectors $\vec{k}_i, \vec{k}_r, \vec{V}_{G_i}, \vec{V}_{G_r}$ are as indicated in the figure. Let

$$k_i = |\vec{k}_i|, k_r = |\vec{k}_r|, V_{G_i} = |\vec{V}_{G_i}|, V_{G_r} = |\vec{V}_{G_r}|.$$

We have

$$\beta = k_i^2 V_{G_i} = k_r^2 V_{G_r}. \tag{9.77}$$

Since $k_i < k_r$, $V_{G_i} > V_{G_r}$. The group velocity is reduced by the reflection. Let us consider now the kinetic energy (per unit mass) of the fluid where a wave

$$\psi = A \cos(\vec{k}.\vec{x} - \varpi t + \phi)$$

propagates. We have

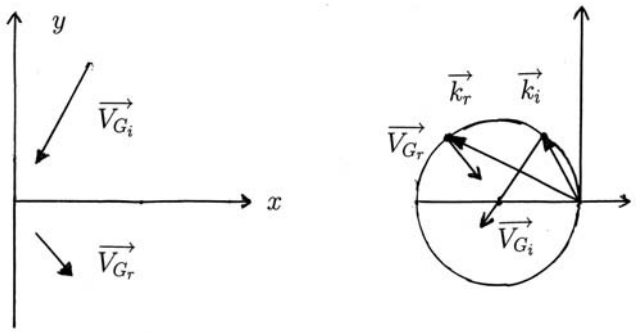

Figure 9.11. Schematic representation of Rossby-waves packet reflection on a western boundary.

$$E_c = \frac{1}{2}\left[\left(\frac{\partial\psi}{\partial x}\right)^2 + \left(\frac{\partial\psi}{\partial y}\right)^2\right] = \frac{1}{2}A^2k^2\sin^2(\vec{k}.\vec{x} - \varpi t + \phi).$$

Remarking that

$$2\sin^2(\vec{k}.\vec{x} - \varpi t + \phi) = 1 - \cos 2(\vec{k}.\vec{x} - \varpi t + \phi),$$

is a function of temporal period π/ϖ, the average kinetic energy on a period $T = 2\pi/\varpi$ is

$$\bar{E}_c = \frac{1}{2}A^2k^2\frac{1}{T}\int_0^T \sin^2(\vec{k}.\vec{x} - \varpi t + \phi)dt = \frac{A^2k^2}{4}.$$

If we pose $A_i = A$, the incident average kinetic energy is $\bar{E}_i = A^2k_i^2/4$, and the reflected one $\bar{E}_r = A^2k_r^2/4$. The latter is increased by reflection.

In fact Eq. (9.77) expresses that the average energy flux $\bar{E}_cV_G$ is conserved during the reflection. So a western frontier in an oceanic basin will intensify the variability of the currents. This applies in particular to the Gulf Stream and Kuroshio.

9.8.3 Topographic Rossby waves

Let us go back to the quasi geostrophic potential vorticity equation (9.41), assuming a rigid lid with $f = f_0$ constant. It writes

$$\frac{D_H}{Dt}\left[-\nabla_H^2\psi(x,y,t) + \frac{f_0}{H}\tau\right] = 0.$$

We suppose that we are in a channel whose bottom is raised in the y direction (see Figure 9.12). We pose

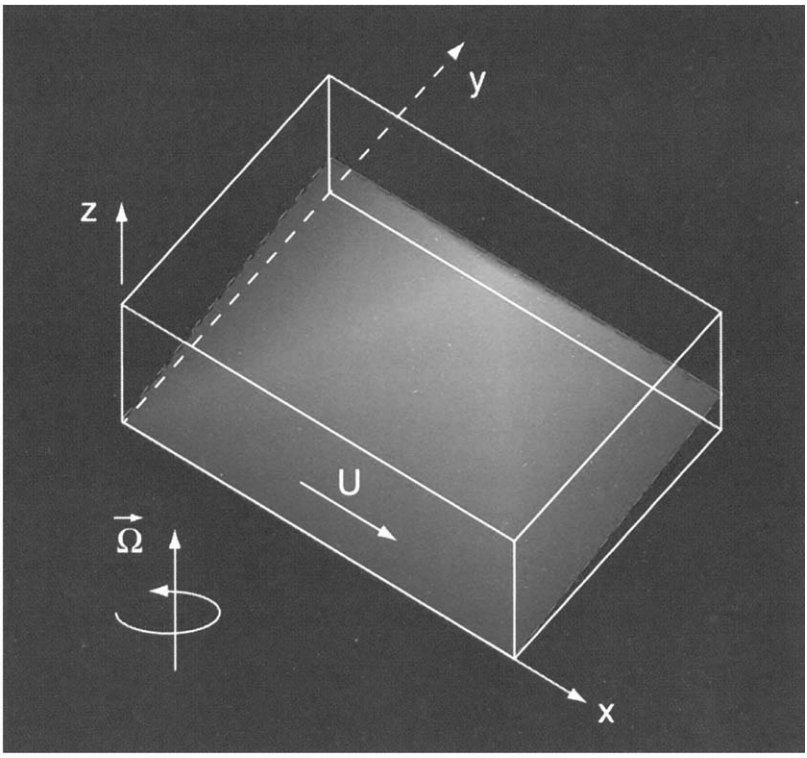

Figure 9.12. Rotating channel with an inclined bottom, where topographic Rossby waves propagate (From Lesieur [424], courtesy EDP-Springer).

$$\frac{f_0}{H}\tau(x,y) = \beta_1 y$$

and are back to the former case. If the flow has a velocity $\vec{U}$, and working in a frame moving with it, the waves will travel in the direction opposite to $\vec{U}$. They are called "topographic Rossby waves", and can be easily obtained in rapidly rotating fluid experiments in a laboratory (Colin de Verdière, [131]).

9.8.4 Baroclinic Rossby waves

It is interesting to perform the analogous wave analysis on a two-layer geostrophic fluid, with the linearized equations (9.47):

$$\frac{\partial}{\partial t}\nabla^2\psi_{BT} + \beta\frac{\partial\psi_{BT}}{\partial x} = 0 \tag{9.78}$$

$$\frac{\partial}{\partial t}[(\nabla^2 - \mu^2)\psi_{BC}] + \beta\frac{\partial \psi_{BC}}{\partial x} = 0. \tag{9.79}$$

The linearized equation for the barotropic mode is the classical Rossby equation. We look for solutions where ψ_{BT} and ψ_{BC} are proportional to $\exp i(\vec{k}.\vec{x} - \varpi t)$. For the barotropic mode, there is no change with respect to the one-layer model. The dispersion relation for the baroclinic equation is

$$\varpi_{BC} = -\frac{\beta k_1}{k_1^2 + k_2^2 + \mu^2}. \tag{9.80}$$

For wave lengths much larger than the internal radius of deformation $\approx \mu^{-1}$, these "baroclinic Rossby waves" will have a frequency much smaller than the barotropic frequency given by Eq. (9.76). Consequently the characteristic times will be much larger: this is particularly true in the oceans, where the typical velocity spin-up times are of 100 to 200 days, while the thermal spin-up time (corresponding to the baroclinic mode) is of several years.

9.8.5 Other quasi geostrophic waves

Let us briefly summarize an analysis, taken from Pedlosky [567], showing how the baroclinic instability can be understood in the frame of the two-layer model: we take a basic flow corresponding to a constant westerly zonal velocity U_0, that is

$$\psi_{BT} = U_0 y \tag{9.81}$$

and a temperature ψ_{BC} decreasing (with a constant gradient) towards the North, that is

$$\psi_{BC} = U_1 y. \tag{9.82}$$

Then, after linearization of Eqs. (9.47), one obtains for the fluctuations $\tilde{\psi}_{BT}$ and $\tilde{\psi}_{BC}$ about the basic state:

$$\frac{\partial}{\partial t}\nabla^2\tilde{\psi}_{BT} + J(\nabla^2\tilde{\psi}_{BT}, U_0 y) + J(\nabla^2\tilde{\psi}_{BC}, U_1 y) = 0$$

$$\frac{\partial}{\partial t}(\nabla^2 - \mu^2)\tilde{\psi}_{BC} + J[(\nabla^2 - \mu^2)\tilde{\psi}_{BC}, U_0 y] + J[(\nabla^2 - \mu^2)U_1 y, \tilde{\psi}_{BT}]$$
$$+J(\nabla^2\tilde{\psi}_{BT}, U_1 y) + J(\nabla^2 U_0 y, \tilde{\psi}_{BC}) = 0.$$

It writes

$$\frac{\partial}{\partial t}\nabla^2\tilde{\psi}_{BT} + U_0\frac{\partial}{\partial x}\nabla^2\tilde{\psi}_{BT} + U_1\frac{\partial}{\partial x}\nabla^2\tilde{\psi}_{BC} = 0$$

$$\frac{\partial}{\partial t}(\nabla^2 - \mu^2)\tilde{\psi}_{BC} + U_0\frac{\partial}{\partial x}(\nabla^2 - \mu^2)\tilde{\psi}_{BC} + U_1\frac{\partial}{\partial x}(\nabla^2 + \mu^2)\tilde{\psi}_{BT} = 0.$$

One looks for solutions of the form

$$\tilde{\psi}_{BT} = A \exp i(\vec{k}.\vec{x} - \varpi t)$$

$$\tilde{\psi}_{BC} = B \exp i(\vec{k}.\vec{x} - \varpi t)$$

which gives

$$A(\varpi - k_1 U_0) i k^2 - B U_1 i k_1 k^2 = 0$$

$$[\varpi(k^2 + \mu^2) - k_1 U_0 (k^2 + \mu^2)] iB - i k_1 U_1 (k^2 - \mu^2) A = 0.$$

It yields the homogeneous system

$$(\varpi - k_1 U_0) A - k_1 U_1 B = 0$$

$$-k_1 U_1 (k^2 - \mu^2) A + (\varpi - k_1 U_0)(k^2 + \mu^2) B = 0.$$

It has non-zero solutions only if

$$(k^2 - \mu^2)(k_1 U_1)^2 - (\varpi - k_1 U_0)^2 (k^2 + \mu^2) = 0,$$

which leads to the dispersion relation

$$\varpi = k_1 \left(U_0 \pm |U_1| \left[\frac{k^2 - \mu^2}{k^2 + \mu^2} \right]^{1/2} \right), \tag{9.83}$$

where k is the modulus of the horizontal wave vector $\vec{k}$ of components k_1 and k_2. This shows that for wave numbers $k \geq \mu$ (hence wave lengths inferior to $2\pi\mu^{-1}$, of the order of the internal radius of deformation), ϖ is real and waves can propagate. For larger scales, ϖ has a non-zero imaginary part and the perturbations can amplify exponentially. This is an aspect of baroclinic instability in the frame of this model.

Let us notice also that

$$\left| \frac{A}{B} \right|^2 = \frac{k^2 + \mu^2}{|k^2 - \mu^2|}$$

Since $\tilde{\psi}_{BT}$ is in complex form, the stream function of the associated real velocity field is $(1/2)(\tilde{\psi}_{BT} + \tilde{\psi}^*_{BT})$. The horizontal velocity components are

$$u = \frac{i}{2} k_2 (\tilde{\psi}_{BT} - \tilde{\psi}^*_{BT}), v = -\frac{i}{2} k_1 (\tilde{\psi}_{BT} - \tilde{\psi}^*_{BT}),$$

and the kinetic energy

$$E_{BT} = -\frac{k^2}{8} (\tilde{\psi}_{BT} - \tilde{\psi}^*_{BT})^2 = -\frac{k^2}{8} [\tilde{\psi}^2_{BT} + (\tilde{\psi}^*_{BT})^2 - 2|A|^2].$$

The average kinetic energy on a period $2\pi/\varpi$ is

$$\bar{E}_{BT} = \frac{k^2}{4}|A|^2.$$

We have seen in Chapter 2 that the available potential energy is proportional to the squared density fluctuations. Here we will define the baroclinic energy by

$$E_{BC} = \frac{1}{8}(\tilde{\psi}_{BC} + \tilde{\psi}^*_{BC})^2 = \frac{1}{8}[\tilde{\psi}^2_{BC} + (\tilde{\psi}^*_{BC})^2 + 2|B|^2].$$

So the average baroclinic energy on a period $2\pi/\varpi$ is

$$\bar{E}_{BC} = \frac{1}{4}|B|^2.$$

We have

$$\frac{\bar{E}_{BT}}{\bar{E}_{BC}} = k^2 \frac{k^2 + \mu^2}{|k^2 - \mu^2|}. \tag{9.84}$$

It is thus for $k \to \mu^-$ that the instability is the more efficient, with a sort of resonance. It confirms that forcing due to baroclinic instability involves horizontal scales of the order of the internal radius of deformation.

9.9 Quasi geostrophic turbulence

This is a turbulence obeying the quasi geostrophic theory. The main effects which can cause the dynamics of such a turbulence to differ from the two-dimensional turbulence looked upon in the previous chapter are the density stratification (responsible for baroclinic effects), the β-effect (responsible for Rossby waves propagation), the bottom topography, the dissipation by an Ekman layer, and possibly the existence of a finite external Rossby radius of deformation.[20] It is, of course, difficult to study the influence of these physical effects all together, and preferable to consider separately the influence of each on two-dimensional turbulence:

9.9.1 Turbulence and topography

The influence of topography in geostrophic flows has been studied extensively, and a review can be found in Verron and Le Provost [699]: in order to conserve its potential vorticity $(\omega + f)/h$, a flow of initially zero relative vorticity will react to the decrease of h due to a topography of positive height by creating negative relative vorticity. This explains the trapping of anticyclonic vortices by a topography, and hence the existence of fair weather associated to anticyclones in the atmosphere close to mountains. The same reasoning would

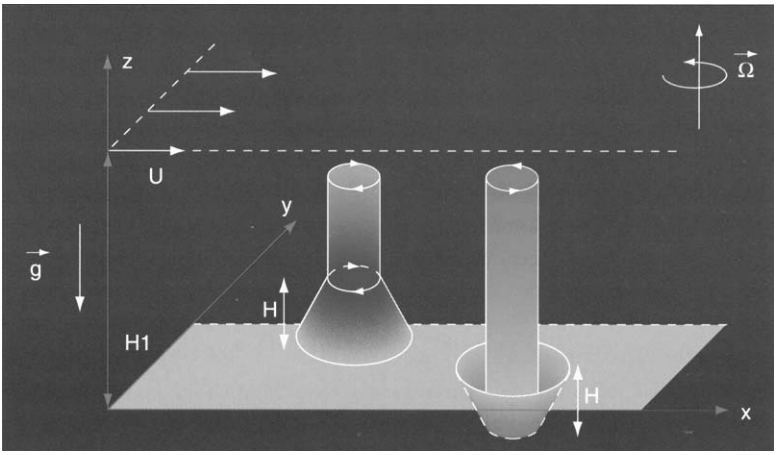

Figure 9.13. Generation of anticyclonic (resp. cyclonic) vortices above a topography (resp. a trough) in a rotating flow. (From Lesieur [424], courtesy EDP-Springer).

lead to the formation of cyclonic vortices over a trough. This is illustrated in Figure 9.13, taken from Lesieur [424].

When the topography is complex and chaotic-like, numerical simulations of decaying geostrophic turbulence show that its spatial features eventually lock on the topography (see Holloway [292]). We recall also the analogy between Rossby waves caused by topography and differential rotation.

The dissipation by a bottom Ekman layer has been seen to damp linearly the vorticity. This large-scale dissipation can limit or even prevent the formation of the inverse energy cascade, as occurs for instance in Earth atmosphere.

9.9.2 Turbulence and Rossby waves

The interaction of Rossby waves with two-dimensional turbulence has been studied by Rhines [593,594] with the aid of DNS, and by Holloway and Hendershott [290], Legras [397] and Bartello and Holloway [33] using stochastic closures. An important length, introduced by Rhines [593], corresponds in the potential vorticity equation to a balance between the relative vorticity $\omega = \partial v/\partial x - \partial u/\partial y$ and the βy term due to differential rotation. If U is a characteristic scale of turbulence, let us consider a sort of circular eddy of radius L_R and velocity U at the exterior. If the vorticity is assumed to be uniform (relative solid-body rotation), it is equal to $\omega = 2U/L_R$. Writing that $\omega \approx \beta L_R$, it is found

[20] The effect of the latter is weak, and will not be considered here.

$$l_R = \left(\frac{2U}{\beta}\right)^{1/2}. \tag{9.85}$$

At scales smaller than Rhines length l_R, one has $\beta y \ll \omega$, and turbulence is not affected by Rossby waves: if one imagines for instance a kinetic energy forcing at scales much smaller than l_R, the inverse energy cascade is going to build isotropic eddies up to the scale $\approx l_R$, where the Rossby waves start propagating. As shown by Rhines [593] on the basis of DNS, the wave propagation will induce a strong anisotropy by blocking the growth of the structures in the meridional direction, and hence producing elongated structures in the zonal direction.[21] This has been proposed as a possible explanation for the zonal jets observed on Jupiter's outer surface (Williams [717, 718]) and perhaps Saturn. Indeed the width of these jets one can see on Plate 6 is about 10,000 km on Jupiter, of the same order as the Rhines's length which can be approximately measured (see below). Such an explanation supposes however that there exists an energy forcing at smaller scales: this forcing is certainly not of baroclinic origin, since measurements have shown there is no meridional temperature gradient on Jupiter, but could be due to agitation from below arising from the turbulent thermal convection caused by the intense heating in the interior of the planet.

Another theory of Jupiter's zonal structure, put forward by Busse [90], proposes that it is a surface manifestation of internal thermal convection columns parallel to the axis of rotation and turning in the same sense (see Figure 9.14). This poses however some problems, since the existence of such columns would imply meridional transports at the surface which are not apparent on Plate 6. In fact these vortices might exist under the surface, and contribute to the external-layers forcing. The same type of vortices might be present within Earth outer core, and contribute to the dynamo effect.

In Earth atmosphere and oceans in medium latitudes, Rhines's length is of 2000 km and 100 km respectively. This is not far from the internal radius of deformation where kinetic energy is provided by baroclinic instability. In the atmosphere, where this forcing can be considered as approximately stationary, this could be one of the reasons for the non-existence of a $k^{-5/3}$ inverse energy cascade in the planetary scales.[22]

As an exercise, let us determine Rhines's length l_R in Earth atmosphere and oceans, and Jupiter. We will assume we are on the 45th parallel (close to Grenoble for instance). So $f = a\beta$, where a is the planet radius.

[21] This may be associated with the inhibition of the pairing in a mixing layer submitted to a differential rotation, when β exceeds a critical value, mentioned in Chapter 3: thus, Eq. (9.85) is a statistical analogue of Eq. (3.27) if the latter is replaced by an equality.

[22] Another one being the Ekman dissipation in the atmospheric boundary layer.

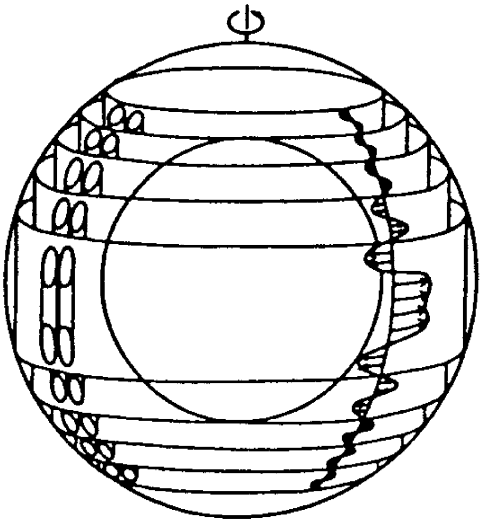

Figure 9.14. Convective columns obtained in a rapidly rotating spherical atmosphere such as Jupiter, and the associated surface zonal flows, from Busse [90] (courtesy *Geophys. Astrophys. Fluid Dyn.*).

• Earth atmosphere: we take $a \approx 6400$ km. With $f = 10^{-4}$, we find $\beta = 1.56 \times 10^{-11}$ m^{-1}s^{-1}. With a velocity of 30 m/s, $l_R = 1960$ km.

• Earth oceans: β has the same value. Taking a velocity of 0.1 m/s, one finds $l_R = 113$ km.

• Jupiter: we have seen in Chapter 1 that $f = 10^{-4} \times 24/10$. Taking a radius of 64,000 km, we have $\beta = 3.75 \times 10^{-12}$. With a velocity of 100 m/s, $l_R = 7300$ km. This is close to the scale of 10,000 km charasteristic of Jupiter zonal jets width.

9.9.3 Charney's theory

A theory of geostrophic turbulence including baroclinic effects has been proposed by Charney [110], with the concept of potential enstrophy cascade generalizing the two-dimensional enstrophy cascade: one considers the potential vorticity conservation equation (9.26), and rescales x and y by the internal radius of deformation, z by the vertical height of the layer, and t using the horizontal scale and velocity. Forgetting about the differential rotation term βy, one obtains

$$\frac{D_H}{Dt}\left(\frac{\partial^2\psi}{\partial x^2}+\frac{\partial^2\psi}{\partial y^2}+\frac{\partial^2\psi}{\partial z^2}\right)=\frac{1}{Re}\nabla_H^2(\nabla_H^2\psi), \tag{9.86}$$

where Re is a horizontal turbulent Reynolds number representing the "sub-geostrophic diffusion" of potential vorticity already discussed above. The rescaled stream function $\psi(x, y, z, t)$ characterizes the horizontal velocity through its horizontal derivatives $\partial\psi/\partial y$ and $-\partial\psi/\partial x$, and the density through $\partial\psi/\partial z$. One can consider a random homogeneous three-dimensionally isotropic stream function, whose three-dimensional spatial Fourier transform is $\hat{\psi}(k_1, k_2, k_3, t)$. The potential enstrophy is defined by

$$D_p = \frac{1}{2}\left\langle \left(\frac{\partial^2\psi}{\partial x^2} + \frac{\partial^2\psi}{\partial y^2} + \frac{\partial^2\psi}{\partial z^2}\right)^2 \right\rangle \tag{9.87}$$

and is conserved with time[23] (modulo the horizontal turbulent diffusion). The other quadratic invariant is the total energy

$$E_t = \frac{1}{2}\left\langle \left(\frac{\partial\psi}{\partial x}\right)^2 + \left(\frac{\partial\psi}{\partial y}\right)^2 + \left(\frac{\partial\psi}{\partial z}\right)^2 \right\rangle \tag{9.88}$$

sum of the mean horizontal kinetic energy

$$\frac{1}{2}\left\langle \left(\frac{\partial\psi}{\partial x}\right)^2 + \left(\frac{\partial\psi}{\partial y}\right)^2 \right\rangle$$

(barotropic energy) and of the mean "available potential energy"

$$\frac{1}{2}\left\langle \left(\frac{\partial\psi}{\partial z}\right)^2 \right\rangle$$

(baroclinic energy). Let $\hat{\Psi}(k, t)$ such as

$$\langle\hat{\psi}(\vec{k}', t)\hat{\psi}(\vec{k}, t)\rangle = \hat{\Psi}(k, t)\delta(\vec{k} + \vec{k}') \tag{9.89}$$

$$E(k, t) = 2\pi k^4\hat{\Psi}(k, t). \tag{9.90}$$

Thus one can check that the total energy is $\int_0^{+\infty} E(k, t)dk$, and the potential enstrophy $\int_0^{+\infty} k^2 E(k, t)dk$. This can also be verified from the point of view of the "turbulence in a box" considered in Chapter 5. We expand now ψ in Fourier series:

$$\psi(\vec{x}, t) = \sum_{\vec{k}} e^{i\vec{k}.\vec{x}}\hat{\psi}(\vec{k}, t). \tag{9.91}$$

We have

[23] The conservation holds also for the squared potential vorticity spatially averaged on any horizontal plane.

$$\left\langle \left(\frac{\partial \psi}{\partial x}\right)^2 \right\rangle = \left\langle \left(\frac{\partial \psi}{\partial x}\right)\left(\frac{\partial \psi}{\partial x}\right)^* \right\rangle = \sum_{\vec{k}} k_1^2 \langle |\hat{\psi}|^2 \rangle,$$

$$E_t = \frac{1}{2}\sum_{\vec{k}} k^2 \langle |\hat{\psi}|^2 \rangle, \tag{9.92}$$

$$\frac{\partial^2 \psi}{\partial x^2} + \frac{\partial^2 \psi}{\partial y^2} + \frac{\partial^2 \psi}{\partial z^2} = -\sum_{\vec{k}} e^{i\vec{k}.\vec{x}} k^2 \hat{\psi}(\vec{k}, t),$$

$$D_p = \frac{1}{2}\sum_{\vec{k}} k^4 \langle |\hat{\psi}|^2 \rangle. \tag{9.93}$$

Within this formalism, the energy spectrum is such that

$$E(k) = \frac{2\pi k^4}{\Delta k^3} \langle |\hat{\psi}|^2 \rangle, \tag{9.94}$$

and we do have

$$E_t = \int_0^{+\infty} E(k)dk, D_p = \int_0^{+\infty} k^2 E(k)dk.$$

As for two-dimensional turbulence, both quantities are conserved by the non-linear terms of the equations, the difference being here that $E(k,t)$ is a three-dimensional spectrum. Nevertheless, the conclusions are the same. The double conservation of energy and potential enstrophy will force the energy to go to large scales, and potential enstrophy to cascade to small scales. If potential enstrophy is injected at a given wave number k_i at a rate β, it will cascade towards large wave numbers along a $\beta^{2/3}k^{-3}$ potential enstrophy cascade. Since isotropy is assumed, this cascade will correspond to a simultaneous k^{-3} cascade of the enstrophy of the horizontal motion (barotropic enstrophy) and of the density $\partial\psi/\partial z$ (baroclinic enstrophy). The injection wave number corresponding to the alimentation of this potential enstrophy cascade will have non-dimensional components of the order of one, since r_I turns out to be the scale where the horizontal kinetic energy is, through the baroclinic instability, fed into the system from the available potential energy. Let us mention also the work of Herring [279].

Charney did not consider scales larger than r_I. They have been studied by Salmon [628] and Hoyer and Sadourny [300] with a two-layer geostrophic model to which the E.D.Q.N.M. theory was applied. They provide a stochastic version of the baroclinic instability: the latter show for instance that if the energy is fed into the system under a baroclinic form at a scale[24] larger than

[24] This scale, determined by the differential heating between the equator and the pole, is about 3000 km for Earth atmosphere, while one recalls that the internal radius of deformation is about 1000 km.

r_I, it will cascade down a $k^{-5/3}$ spectrum[25] up to the internal radius of deformation, where a part of it will be transformed into barotropic energy: the potential enstrophy will cascade to higher wave numbers under a double barotropic and baroclinic form, according to Charney's theory; the barotropic energy produced at r_I^{-1} will cascade back to smaller wave numbers along a $k^{-5/3}$ inverse energy cascade, in the opposite direction of the baroclinic energy. The situation for the $k^{-5/3}$ inverse horizontal kinetic energy cascade is thus the same as for the two-dimensional turbulence, where we have shown that the temperature flux is positive in the inverse energy cascade. Therefore, the horizontal kinetic energy of geostrophic turbulence can be approximated by that of a two-dimensional turbulence which would be alimented in energy at the internal radius of deformation, at a rate corresponding to the conversion of baroclinic into barotropic energy.

Multi-layer numerical simulations of geostrophic turbulence with a high vertical resolution (up to 7 layers) (Hua and Haidvogel [301]) have confirmed Charney's isotropy assumption, and shown also that a large part of the geostrophic dynamics is captured by two-layer models. Geostrophic turbulence, especially with a small number of vertical modes, is a very useful model towards understanding the physics of rapidly-rotating stably-stratified flows. Nevertheless, the approximation discards a lot of important physical effects, such as thermal convection or the interaction of turbulence with the internal gravity waves considered in Chapter 2. It is clear that a deeper understanding of the atmospheric and oceanic dynamics requires the recourse to three-dimensional equations such as Boussinesq or full Navier–Stokes equations.[26] This is rendered easier with the continuous strong development of scientific calculation facilities.

[25] k is here a horizontal wave number.

[26] The use of the so-called "primitive equations", which are not geostrophic but where the hydrostatic approximation is done along the vertical, may not be sufficient, since they filter out internal-gravity waves.

10

Statistical Thermodynamics of Turbulence

In this chapter, we will present a theoretical approach of turbulence close to statistical thermodynamics, which has interesting applications for two-dimensional turbulence.

10.1 Truncated Euler equations

We go back to the flow within a box, that is to say which can be expanded into an infinite serie of discrete wave vectors $\vec{k}_n$ with velocity amplitudes $\underline{\hat{u}}(\vec{k}_n, t)$, as introduced earlier. Let us first consider Navier–Stokes equations in Fourier space, relating this infinite set of modes. The equation is truncated by retaining the modes lower than a cutoff wave number $k_{\max}$, and properly normalized:

$$\left(\frac{\partial}{\partial t} + \nu k^2\right) \hat{u}_i(\vec{k}, t) = -\frac{i}{2} P_{ijm}(\vec{k}) \sum \hat{u}_j(\vec{p}, t) \hat{u}_m(\vec{q}, t), \tag{10.1}$$

where the sum $\sum$ only keeps modes such that $\vec{k} = \vec{p} + \vec{q}$ and whose modulus is smaller than $k_{\max}$.

10.1.1 Application to three-dimensional turbulence

Let us consider the three-dimensional case. If $k_{\max}$ is superior or equal to the Kolmogorov wave number, it is expected that the truncated equations will correctly represent turbulence. This is precisely what is done in the DNS. If this condition is not fulfilled, and if we start initially with an energy spectrum sharply peaked at an initial energetic wave number k_0 (in a freely decaying turbulence), Eq. (10.1) will properly describe the evolution of turbulence in the early stage, when the cascade has not yet reached $k_{\max}$. But as soon as

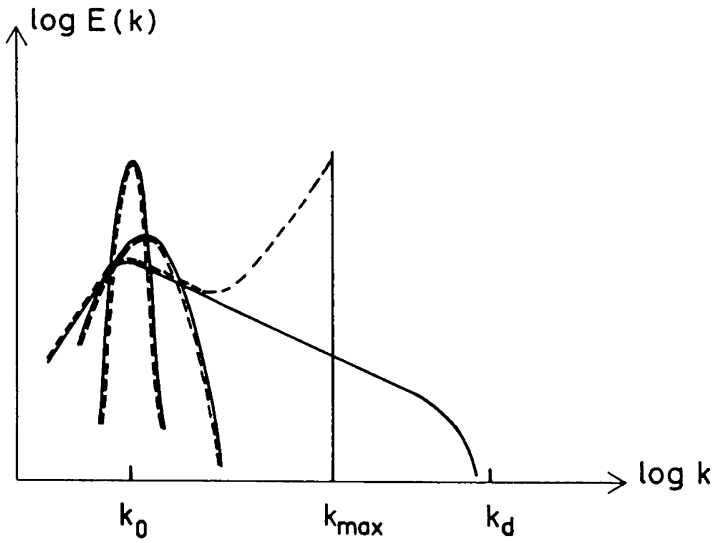

Figure 10.1. Schematic comparison in three dimenions of the evolution of a kinetic-energy spectrum obeying Navier–Stokes equations (straight line) and truncated Navier–Stokes equations (dashed line).

the Kolmogorov energy cascade forms (that is, from Chapter 7, at a time of about 5 initial large-eddy turnover times), energy will tend to go beyond $k_{\max}$ in the dissipative scales, which is not permitted by the truncated equation (10.1). Instead, energy will then accumulate at $k_{\max}$, which may be a source of numerical instability, and in any case does not give an acceptable description of turbulence (cf. Figure 10.1). The question posed to LES is to model kinetic-energy fluxes towards *subgrid scales* $k > k_{\max}$. This problem will be looked at in Chapter 12.

In the present chapter, we consider the equation

$$\frac{\partial}{\partial t}\hat{u}_i(\vec{k},t) = -\frac{i}{2}P_{ijm}(\vec{k})\sum \hat{u}_j(\vec{p},t)\hat{u}_m(\vec{q},t) \tag{10.2}$$

with the same conditions $k, p, q \leq k_{\max}$. This system does not provide an accurate description of Euler equations, since the latter require an infinite set of wave numbers, except in the early stage of the evolution described in Figure 1. It will however be seen that the study of equilibrium statistical mechanics of such a system will provide useful information for turbulence, especially in two-dimensions. Further details on this analysis can be found for instance in Rose and Sulem [617] and Orszag [550, 551, 553].

Now we are going Liouville theorem in phase space. To each mode $\underline{\hat{u}}(\vec{k}_n, t)$ one associates two real vectors, the real and imaginary part, which are both

in the plane perpendicular to $\vec{k}_n$ and can therefore be represented each by their two real components in that plane; let

$$y_{n_1}(t), y_{n_2}(t), y_{n_3}(t), y_{n_4}(t)$$

be these real components. One can remark that

$$\underline{\hat{u}}(\vec{k}_n, t)^* . \underline{\hat{u}}(\vec{k}_n, t) = \sum_{i=1}^{4} y_{n_i}(t)^2. \tag{10.3}$$

Then if N wave vectors are retained in the truncation, the system can be represented by a point of $m = 4N$ coordinates $y_{n_i}(t)$ (i from 1 to 4) in a phase space determined by $y_a(t)$ (a from 1 to $4N$). In a similar way to what has been done in Chapter 6, it is easy to show that Eq. (10.2) conserves the kinetic energy

$$\frac{1}{2} \sum_{\vec{k}_n} \underline{\hat{u}}(\vec{k}_n, t)^* . \underline{\hat{u}}(\vec{k}_n, t) = \frac{1}{2} \sum_{a=1}^{m} y_a(t)^2 \tag{10.4}$$

and then that the system evolves in phase space on a sphere of radius determined by the initial kinetic energy. From Eq. (10.2) a system describing the evolution of the $y_a(t)$ can be written

$$\frac{d}{dt} y_a(t) = \sum_{b,c=1}^{m} A_{abc} y_b(t) y_c(t), \tag{10.5}$$

where the A_{abc} are complicated coupling coefficients which do not need to be written here: indeed, the kinetic energy conservation Eq. (10.5) implies, if only three "modes" (a, b, c) are considered, a detailed conservation property

$$A_{abc} + A_{bca} + A_{cab} = 0. \tag{10.6}$$

As mentioned in Rose and Sulem [617], it can be shown also that A_{abc} is zero as soon as two of the indices (a, b, c) are equal. This allows to write an "incompressibility" condition for the generalized velocity field of components $dy_a(t)/dt$ in phase space:

$$\frac{\partial}{\partial y_a} \frac{dy_a(t)}{dt} = 0. \tag{10.7}$$

The following analysis can be made either by considering the *microcanonical ensemble* (systems all lying on a given energy sphere)[1] or the *canonical ensemble* (systems of arbitrary energy). Here we adopt the latter point of view,

[1] Such an analysis has been carried out by Basdevant and Sadourny [36] in the case of two-dimensional turbulence.

considering in the phase space a collection of systems of density $\rho(y_1, \dots y_m, t)$. Since the total number of systems is obviously preserved in the motion, and the volumes are preserved as well, a generalized continuity equation can be written

$$\frac{D\rho}{Dt} = \frac{\partial \rho}{\partial t} + \sum_{a=1}^{4N} \frac{dy_a}{dt} \frac{\partial \rho}{\partial y_a} = 0 \tag{10.8}$$

which is Liouville theorem for the problem considered.

We now look for *equilibrium solutions* of Eq. (10.7), that is solutions $P(y_1, \dots y_m)$ which do not depend explicitly on t. This is the case for any function of a conserved quantity. Since kinetic energy $(1/2)\sum_{a=1}^{m} y_a^2$ is conserved with the motion, and by analogy with statistical thermodynamics at the equilibrium, one will consider the particular Boltzmann–Gibbs equilibrium distribution

$$P(y_1, \dots y_m) = \frac{1}{Z} \exp -\frac{1}{2}\sigma \sum_{a=1}^{m} y_a^2, \tag{10.9}$$

where Z is the partition function of the system

$$Z = \int \int .. \int \exp -\frac{1}{2}\sigma \sum_{a=1}^{m} y_a^2 dy_1 dy_2 \dots dy_{4N} \tag{10.10}$$

and σ a positive constant.[2] Eq. (10.9) can be interpreted as a Gaussian probability distribution of the systems in phase space. One then assumes that the ensemble average $\langle \rho(y_1, \dots y_m, t) \rangle$ of an ensemble of given systems $\rho(y_1, \dots y_m, t)$ obeying Eqs. (10.5) and (10.8) will eventually relax towards the distribution (10.9). Such a behaviour has been numerically checked by Lee [394]. This allows us to calculate the "mean energy" of the mode "a":

$$\langle y_a(t)^2 \rangle = \frac{1}{Z} \int \int .. \int y_a^2 [\exp -\frac{1}{2}\sigma \sum_{b=1}^{4N} y_b^2] dy_1 \dots dy_m \tag{10.11}$$

which turns out to be independent of a. There is then equipartition of energy between the modes $a = 1, \dots, 4N$, and also between the wave vectors $\vec{k}_n$. The kinetic-energy spectrum, proportional to

$$2\pi k^2 \langle \vec{\hat{u}}(\vec{k}, t)^* . \vec{\hat{u}}(\vec{k}, t) \rangle,$$

[2] In statistical thermodynamics, σ is related to the temperature by the Boltzmann relation $\sigma = 1/KT$, T being the temperature and K the Boltzmann constant. So in our problem, σ characterizes the inverse of the "temperature" of the inviscid truncated system. It has of course no relation with the physical temperature of turbulence.

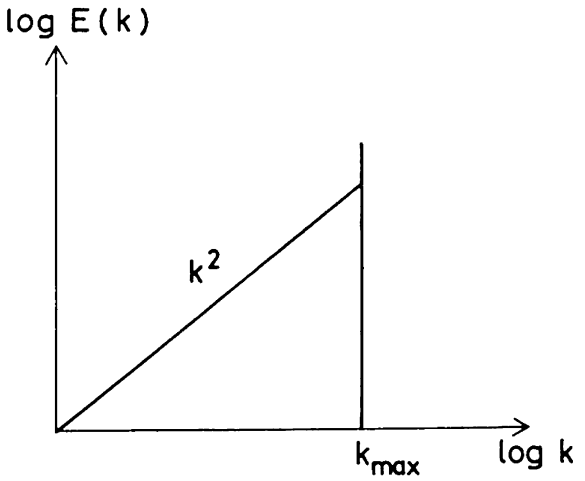

Figure 10.2. Equipartition kinetic energy spectrum of truncated three-dimensional Euler equations.

is then proportional to k^2, and we obtain a spectrum of equipartition of kinetic energy among the modes. This result is from Lee [392], and expresses in some way for the energy spectrum an accumulation of energy at the maximum wave number, characteristic of the ultraviolet energy transfers of three-dimensional turbulence (Figure 10.2).

One might object to this analysis the fact that kinetic energy is not the only invariant, and that the conservation of helicity might alter the equipartition k^2 spectrum: such a study has been made by Kraichnan [355], but the qualitative conclusions (ultraviolet energy transfer) are not fundamentally modified. As stressed in Rose and Sulem [617], this is no longer true for three-dimensional strong M.H.D. helical turbulence, where a study of equilibrium-ensemble solutions done by Frisch et al. [222] led to the conjecture of an inverse cascade of magnetic helicity.[3] This was later on verified in the frame of the E.D.Q.N.M. closure by Pouquet et al. [585].

10.1.2 Application to two-dimensional turbulence

The best way to build the phase space is to use the stream function $\hat{\psi}(\vec{k}, t)$, y_a being now its real or imaginary parts. One has here two invariants to consider, the kinetic energy

[3] Scalar product of the potential vector with the magnetic field.

$$\frac{1}{2}\sum_{\vec{k}_n} k_n^2 |\hat{\psi}(\vec{k}_n,t)|^2 = \frac{1}{2}\sum_{a=1}^{m} k_a^2 y_a(t)^2 \tag{10.12}$$

and the enstrophy

$$\frac{1}{2}\sum_{\vec{k}_n} k_n^4 |\hat{\psi}(\vec{k}_n,t)|^2 = \frac{1}{2}\sum_{a=1}^{m} k_a^4 y_a(t)^2 \tag{10.13}$$

which implies that the system moves on the intersection of the kinetic-energy sphere and the enstrophy ellipsoid. The invariant to consider is a linear combination of the kinetic energy and enstrophy, and the equilibrium distribution (10.9) has now to be replaced by (Kraichnan [350, 357])

$$P(y_1, \ldots y_m) = \frac{1}{Z}\exp -\frac{1}{2}\sum_{a=1}^{m} k_a^2(\sigma + \mu k_a^2) y_a^2 \tag{10.14}$$

where σ and μ are two constants. Again the validity of such a distribution has been verified by Fox and Orszag [215] and Basdevant and Sadourny [36]. The "mean" stream function variance at mode "a" is now

$$\langle y_a(t)^2 \rangle = \frac{1}{Z}\int\int .. \int y_a^2 \exp -\frac{1}{2}\sum_{b=1}^{m} k_b^2(\sigma + \mu k_b^2) y_b^2 dy_1 \ldots dy_m$$

which reduces to

$$\langle y_a(t)^2 \rangle = \frac{1}{Y}\int_{-\infty}^{+\infty} y^2 \exp -\frac{1}{2} k_a^2(\sigma + \mu k_a^2) y^2 dy \tag{10.15}$$

with

$$Y = \int_{-\infty}^{+\infty} \exp -\frac{1}{2} k_a^2(\sigma + \mu k_a^2) y^2 dy. \tag{10.16}$$

With the change of variable

$$y' = k_a(\sigma + \mu k_a^2)^{1/2} y,$$

Eqs. (10.15) and (10.16) can easily be calculated, to yield

$$\langle y_a(t)^2 \rangle = [k_a^2(\sigma + \mu k_a^2)]^{-1} \tag{10.17}$$

and hence

$$\langle |\hat{\psi}(k)|^2 \rangle = \frac{2}{k^2(\sigma + \mu k^2)} \tag{10.18}$$

$$E(k) = \pi k^3 \langle |\hat{\psi}(k)|^2 \rangle \sim \frac{k}{\sigma + \mu k^2}. \tag{10.19}$$

The constants σ and μ can be determined from Eq. (10.19) in terms of the mean kinetic energy and enstrophy. If σ and μ are both positive, the wave number $(\sigma/\mu)^{1/2}$ may easily be shown to be of the order of

$$k_i = \left(\frac{\int_0^\infty k^2 E(k) dk}{\int_0^\infty E(k) dk} \right)^{1/2}$$

characteristic of an average wave number of the spectrum (Basdevant and Sadourny [36]). Then if $k_{\max}$ is much larger than k_i, the energy spectrum will be a k^{-1} enstrophy equipartioning[4] spectrum for $k \gg k_i$ and a k energy equipartition spectrum for $k \to 0$. The possibility of a negative σ (with a positive μ) is permitted if there exists a lower wave number bound $k_{\min}$ such that

$$k_{\min} > \left(\frac{-\sigma}{\mu} \right)^{1/2} .$$

Therefore, and if $k_{\min}$ is very close to $(-\sigma/\mu)^{1/2}$, one can obtain an arbitrarily high kinetic energy spectrum in the vicinity of $k_{\min}$. This is what Kraichnan called *negative temperature* states", since the "temperature" of the system is characterized by σ, which is here negative. Such a behaviour could of course be considered as an indication of the inverse energy cascade in the viscous problem.

Let us now consider the two-dimensional passive scalar: since it possesses only one quadratic invariant (the scalar variance), the same analysis will lead to equipartition of scalar variance among the wave vectors $\vec{k}$, and thus to a scalar spectrum proportional to k. If $\sigma > 0$, scalar and kinetic-energy spectra will be both proportional to k at low wave numbers, while the enstrophy spectrum will be $\propto k^3$. Consequently, there will be more scalar than enstrophy in this infrared spectral range: such a behaviour was verified by Holloway and Kristmannsson [291] with an inviscid truncated direct numerical simulation, and shows the dynamical difference of the scalar and the enstrophy in this range.

10.2 Two-dimensional turbulence over topography

One must first stress that the existence of a differential rotation (β-effect) does not modify the results of Section 3, since the conservation of kinetic energy and enstrophy is not changed. It yields then isotropy, in contradiction with the anisotropic effects of differential rotation displayed in the viscous calculations

[4] Indeed the equipartition of enstrophy yields $k^2 E(k) \propto k$.

of Rhines [593] and Bartello and Holloway [33]:[5] this is an example where the predictions of inviscid truncated systems are strongly at variance with the real viscous flows dynamics.

An interesting problem, the solution of which is given in Holloway [292], is that of a geostrophic turbulence over a random topography: from Eq. (9.41), the potential vorticity (within the rigid-lid approximation) is $-\nabla^2\psi+h$, where $h(x,y)$ is the topography, properly normalized. Let $\hat{h}(\vec{k})$ be the spatial Fourier transform of $h(\vec{x})$, and let h_a be the real and imaginary parts of the various $\hat{h}(\vec{k}_n)$. With the same notations as in Section 10.1.2, the quadratic invariants are the kinetic energy Eq. (10.12) and the potential enstrophy

$$\frac{1}{2}\sum_{\vec{k}_n}|k_n^2\hat{\psi}+\hat{h}|^2=\frac{1}{2}\sum_{a=1}^{m}(k_a^2y_a+h_a)^2. \tag{10.20}$$

The probability distribution corresponding to a linear combination of kinetic energy and potential enstrophy is then

$$P(y_1,\dots y_m)=\frac{1}{Z}\exp-\frac{1}{2}\sum_{a=1}^{m}k_a^2(\sigma+\mu k_a^2)y_a^2+2\mu k_a^2h_ay_a+\mu h_a^2.$$

This permits to calculate $\langle y_a^2\rangle$, equal to

$$\langle y_a(t)^2\rangle=\frac{1}{Y'}\int_{-\infty}^{\infty}y^2\exp-\frac{1}{2}[k_a^2(\sigma+\mu k_a^2)y^2+2\mu k_a^2h_ay+\mu h_a^2]dy \tag{10.21}$$

with

$$Y'=\int_{-\infty}^{\infty}\exp-\frac{1}{2}[k_a^2(\sigma+\mu k_a^2)y^2+2\mu k_a^2h_ay+\mu h_a^2]dy. \tag{10.22}$$

Expressing

$$k_a^2(\sigma+\mu k_a^2)y^2+2\mu k_a^2h_ay+\mu h_a^2$$

under the form

$$k_a^2(\sigma+\mu k_a^2)\left[\left(y+\mu\frac{h_a}{\sigma+\mu k_a^2}\right)^2+\sigma\mu\frac{h_a^2}{k_a^2(\sigma+\mu k_a^2)^2}\right]$$

and with the change of variable

$$y'=y+\mu\frac{h_a}{\sigma+\mu k_a^2},$$

[5] More precisely, it was shown by Shepherd [644] that the ergodic property was lost if β is high.

Eq. (10.21) can be written as

$$\langle y_a(t)^2\rangle = \frac{1}{Y}\int_{-\infty}^{+\infty} y^2 \exp -\frac{1}{2}k_a^2(\sigma+\mu k_a^2)y^2 dy$$

$$+\mu^2 \frac{h_a^2}{(\sigma+\mu k_a^2)^2} \tag{10.23}$$

where Y is still given by Eq. (10.16). Then, if one considers the topography as random, the modal vorticity variance at wave vector $\vec{k}$ is

$$\langle \hat{\omega}(-\vec{k})\hat{\omega}(\vec{k})\rangle = k^4\langle|\hat{\psi}(k)|^2\rangle = 2\frac{k^2}{\sigma+\mu k^2} + \mu^2 k^4 \frac{\langle \hat{h}(-\vec{k})\hat{h}(\vec{k})\rangle}{(\sigma+\mu k^2)^2}$$

which shows that the resulting flow is the superposition of the classical two-dimensional turbulence equilibrium solution found in the preceding section, and of a contribution due to the topography. This topographic component can be clearly understood when looking at the vorticity topography correlation $\langle \hat{\omega}(-\vec{k})\hat{h}(\vec{k})\rangle$ which turns out to be equal to $2\langle h_a y_a\rangle$ for an arbitrary a. The same changes of variable as above yield

$$\langle h_a y_a\rangle = \frac{h_a}{Y}\int_{-\infty}^{+\infty}\left(y-\mu\frac{h_a}{\sigma+\mu k_a^2}\right)\exp -\frac{1}{2}k_a^2(\sigma+\mu k_a^2)y^2 dy$$

$$= -\mu\frac{h_a^2}{\sigma+\mu k_a^2} \tag{10.24}$$

and hence

$$\langle \hat{\omega}(-\vec{k})\hat{h}(\vec{k})\rangle = -\langle \hat{h}(-\vec{k})\hat{h}(\vec{k})\rangle \frac{k^2}{\sigma+\mu k^2}. \tag{10.25}$$

The topographic component of the vorticity is then locked on to the topography, with a sign corresponding to the potential vorticity conservation phenomenology, that is in the anticyclonic direction above a positive topography (compression of relative vortex tubes), and in the cyclonic direction above a trough (stretching of relative vortex tubes).

This is a quite remarkable result, which has been observed also in the viscous DNS of Holloway [292]. It seems therefore one might oppose a *maximum entropy principle* (leading to the Boltzmann–Gibbs equilibrium distribution), which yields in this case[6] the formation of organized eddies locked to the topography, to the *minimum enstrophy principle* of Bretherton and Haidvogel [81] (see also Leith [402]) which assumes that the flow is going to evolve under the action of viscosity towards a state of minimal enstrophy. Though the example of inviscid truncated solutions for two-dimensional turbulence above

[6] Here one recalls that the system is *non-dissipative*.

topography is quite impressive, it has to be remembered that turbulence is an essentially *dissipative* phenomenon (of enstrophy in two dimensions), and that results closer to reality will certainly be obtained with theories allowing dissipation to act. But absolute equilibrium ensembles are a useful qualitative tool to explore the direction of the transfers among the various scales of motion.

10.3 Inviscid statistical mechanics of two-dimensional point vortices

Up to now we have considered inviscid systems of a finite number of wave vectors. Another point of view (in two dimensions) is to consider a large number of individual point vortices located at $\vec{r}_i(t)$ and of circulation c_i, so that the vorticity field is given by

$$\omega(\vec{r},t) = \sum_i \delta[\vec{r} - \vec{r}_i(t)]. \tag{10.26}$$

A review of this approach can be found in Chorin [123, 124], Frisch [229], and Cottet and Koumoutsakos [148].[7] Such a problem permits a Hamiltonian formulation. In a pioneering study, Onsager [549] showed the possibility of negative temperature states (in the statistical thermodynamics sense), with clustering of same-sign vortices. Later on, various works (see e.g. Joyce and Montgomery [321], Montgomery and Joyce [517], Kraichnan and Montgomery [359]) could relate the average vorticity $-\nabla^2\psi$ of the solution to the stream function ψ. Let us quote for instance the sinh-Poisson equation of Joyce and Montgomery [321] (see also Montgomery et al. [518]). Robert and Sommeria [605, 606, 662] (see also Miller et al. [506]) have performed an analysis based on mutually exclusive patches of vorticity, instead of delta-functions points and find a different equation. Yin et al. [733] has carried out DNS of decaying Navier–Stokes equations in a periodic square, and stress that the dipole-like eventual state confirms the sinh-Poisson solution.

[7] The latter study also the three-dimensional case with vortex filaments, and include viscosity effects.

11

Statistical Predictability Theory

11.1 Introduction

The concepts of predictability and unpredictability have been widely used throughout the preceding chapters, and are one of the major ingredients in our definition of turbulence. When turbulence is examined from the point of view of "chaos" in dynamical systems, predictability is studied by looking at the sign of the Liapounov exponent l, with $d(t) \propto e^{lt}$, where $d(t)$ is an appropriate measure of the distance between two points representing the system and initially very close in phase space: a positive exponent means then an exponential separation, and implies loss of predictability.

When developed (and hence *dissipative*) turbulence is envisaged, the concept of predictability is *a priori* more vague, since no evident phase space exists. It took about 15 years for this concept to find a satisfactorily mathematical formulation, through the works of Thompson, Novikov, Lorenz, Charney, Leith and Kraichnan for instance. The reader is referred to the paper of Thompson [686] for a historical overview of the subject: the problem was pointed out by meteorologists concerned with the amplification in the forecast models, as time was going on, of the errors contained in the initial conditions. The latter are due to the inaccuracy of the measurements and interpolation of the observing net data. Let us quote Thompson [686]:

> Suppose that the prediction model were perfect, and that the model equations could be integrated without error. Then there would still be a practical limitation on the accuracy of prediction, owing to the fact that the initial analysis is subject to (...) errors (...). The working hypothesis was (...) that the growth of error was a distinctively nonlinear phenomenon and that (...) the (...) prediction model (...) would amplify errors.

As recalled in Chapter 1, the unpredictability concept pioneers are certainly Poincaré [579] and Laplace [376].

At the beginning of unpredictability studies applied to fluid mechanics, the problem was posed more as a stability problem, where one looks at the evolution of a "perturbation" (actually the initial departure from the real flow) superposed to the flow one desires to forecast. Then a statistical formalism was proposed by Novikov [539], and used in Fourier space by Lorenz [454], Leith [399] and Leith and Kraichnan [400]: instead of considering one given realization of the flow $\vec{u}^{(\alpha)}(\vec{x},t)$ where α stands for the particular realization of the random field studied, perturbed by $\delta\vec{u}^{(\alpha)}(\vec{x},t)$, one considers two ensembles of flows defined by the random functions

$$\vec{u}_1(\vec{x},t) = \{\vec{u}^{(\alpha)}(\vec{x},t)\} \tag{11.1}$$

$$\vec{u}_2(\vec{x},t) = \{\vec{u}^{(\alpha)}(\vec{x},t) + \delta\vec{u}^{(\alpha)}(\vec{x},t)\}. \tag{11.2}$$

The statistical formalism restricts the study to random functions $\vec{u}_1$ and $\vec{u}_2$ having the same statistical properties. This implies in particular that $\langle\delta\vec{u}\rangle$ is zero, and that the two random flows have the same spectrum. The statistical predictability will study the statistical properties of $\delta\vec{u} = \vec{u}_1 - \vec{u}_2$. Of particular interest will be the relative energy of the error

$$r(t) = \frac{\langle(\vec{u}_1 - \vec{u}_2)^2\rangle}{2\langle\vec{u}_1^2\rangle} \tag{11.3}$$

also called the error rate: when the two fields are initially very close, $|\delta\vec{u}^{(\alpha)}| \ll |\vec{u}^{(\alpha)}|$ in each of the realizations α considered, and $r(0)$ is consequently much smaller than 1. The two fields are then almost completely correlated. On the contrary, if the error between the two fields grows in such a way that they become decorrelated (and hence that $\langle\vec{u}_1.\vec{u}_2\rangle = 0$), one will have $r = 1$.

Let us consider isotropic turbulence and work in Fourier space. One considers the kinetic-energy spectrum $E(k,t)$ of $\vec{u}_1$ and $\vec{u}_2$, such that

$$\frac{1}{2}\langle\vec{u}_1^2(\vec{x},t)\rangle = \int_0^{+\infty} E(k,t)dk \tag{11.4}$$

$$E(k,t) = (D-1)\pi k^{D-1}\hat{U}(k,t) \tag{11.5}$$

where $\hat{U}(k,t)$ is the trace of the spectral tensor, spatial Fourier transform of

$$\langle u_{1_i}(\vec{x},t)u_{1_j}(\vec{x}+\vec{r},t)\rangle$$

(or of the spectral tensor built with $\vec{u}_2$). D is the dimension of space (2 or 3). In the same way one can introduce the *correlated energy spectrum*

$$E_W(k,t) = (D-1)\pi k^{D-1}\hat{W}(k,t) \tag{11.6}$$

where $\hat{W}(k,t)$ is the trace of the tensor Fourier transformed of

$$\langle u_{1_i}(\vec{x},t)u_{2_j}(\vec{x}+\vec{r},t)\rangle,$$

and such that

$$\frac{1}{2}\langle \vec{u}_1(\vec{x},t).\vec{u}_2(\vec{x},t)\rangle = \int_0^{+\infty} E_W(k,t)dk. \tag{11.7}$$

It is very easy to check that

$$\frac{1}{2}\langle (\vec{u}_1-\vec{u}_2)^2\rangle = \int_0^{+\infty} 2E_\Delta(k,t)dk$$

with

$$E_\Delta(k,t) = E(k,t) - E_W(k,t). \tag{11.8}$$

$E_\Delta(k,t)$ is called the *decorrelated energy spectrum*, or *error spectrum*. The error rate defined in Eq. (11.3) is thus equal to

$$r(t) = \frac{\int_0^{+\infty} E_\Delta(k,t)dk}{\int_0^{+\infty} E(k,t)dk}. \tag{11.9}$$

Due to a Schwarz inequality, $|E_W(k,t)| < E(k,t)$, and $E_\Delta(k,t)$ is positive and majored by $2E(k,t)$. The case $E_\Delta(k) = E(k)$ corresponds to a complete decorrelation between the two fields. Although it is not mathematically ruled out, the situations with $E_\Delta(k) > E(k)$ are physically irrealistic, since they would correspond to a correlation of the field $\vec{u}_1$ with $-\vec{u}_2$.

Because of their meteorological motivations, the people who initiated these studies were mainly concerned with two-dimensional or quasi geostrophic turbulence. But the predictability problem may be posed for three-dimensional turbulence as well, and has important implications concerning the relevance of the large-eddy simulations of these flows (see next chapter). Thus we will consider here both cases of three and two dimensions. On the other hand, the numerical prediction frame in which the predictability problem is posed usually leads one to assume that the error between the two flows $\vec{u}_1$ and $\vec{u}_2$ is confined to the small scales corresponding to the inaccuracy of the initial state or the smallest resolved scale in the numerical model: this will imply an initial error spectrum equal to zero for $k < k_e(0)$, and comprised between 0 and $E(k,0)$ for $k > k_e(0)$. The corresponding correlated energy spectrum is equal to $E(k,0)$ for $k < k_e(0)$, and comprised between $E(k,0)$ and 0 for $k > k_e(0)$. An example of an initial situation is shown in Figure 11.1. The questions which are posed concern the time evolution of the wave number $k_e(t)$ characterizing the "front" of the error spectrum, and of $r(t)$. A decrease of $k_e(t)$ as well as an increse of $r(t)$ will mean loss of predictability. Notice that in some of the situations envisaged below, the wave number $k_e(t)$ may be hard

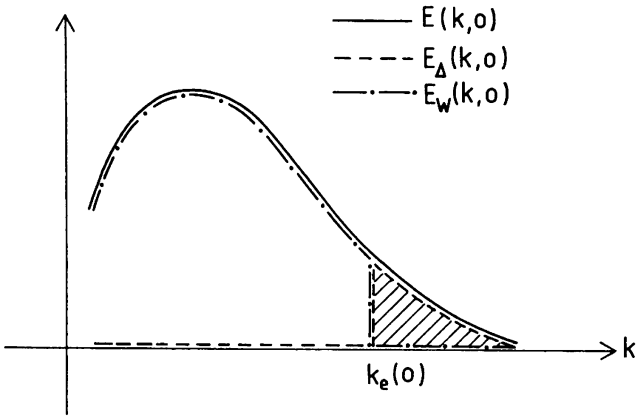

Figure 11.1. Initial kinetic, correlated and decorrelated energy spectra in a typical statistical predictability study where complete uncertainty (corresponding to the shaded area) is assumed at wave numbers $k > k_e(0)$. $k_e(0)$ characterizes the initial front of the error.

to define, and thus $r(t)$ seems to give the best measure of the error. Notice also that, even if it has been less investigated, the statistical predictability problem could also be envisaged with an initial error affecting the energy-containing eddies. We will return to that point later. Notice finally that the statistical predictability problem has nothing to do with the problem where the kinetic-energy spectrum of turbulence is perturbed by an energy supply: in the case where for instance a small-scale kinetic energy peak is superposed at a wave number k_P upon the three-dimensional Kolmogorov inertial range, it is easy to show with the aid of dimensional arguments or via two-point closures that the peak will spread out through the whole spectrum in a few turnover times $[k_P^3 E(k_P)]^{-1/2}$ of the turbulence at the wave number k_P. In the predictability problem on the contrary, the kinetic energy spectrum $E(k,t)$ is the same for the two velocity fields considered.

In this chapter we will mainly be concerned with the closure results, particularly closures of the E.D.Q.N.M. family, and will summarize the results obtained by Leith [399], Leith and Kraichnan [400], Métais [490] and Métais and Lesieur [492] for three and two-dimensional isotropic turbulence. Let us also mention the two-dimensional Quasi-Normal study of Lorenz [454] which concluded to an upper limit of 8 days for the deterministic forecast of Earth atmosphere. We must point out the pioneering study of Lilly [442], who looked at statistical predictability with the aid of two-dimensional DNS.

The chapter is organized as follows: Section 2 will give the E.D.Q.N.M. statistical predictability equations. Sections 3 and 4 will present respectively

the three-dimensional turbulence and two-dimensional isotropic turbulence results. Section 5 will consider unpredictability in a two-dimensional temporal mixing layer.

11.2 E.D.Q.N.M. predictability equations

At the present point of progress of this book, the reader might not welcome new lengthy calculations giving the $E.D.Q.N.M.$ spectral equations for $E(k,t)$ and $E_W(k,t)$. We will therefore skip such a derivation, which is at hand for any reader having mastered the $E.D.Q.N.M.$ techniques described in Chapter 7. The essence of the calculation is to write the Navier–Stokes equations in Fourier space simultaneously for $\underline{\hat{u}}_1(\vec{k},t)$ and $\underline{\hat{u}}_2(\vec{k},t)^*$, in order to obtain for the correlated spectral tensor an evolution equation which can be written formally as

$$\left(\frac{\partial}{\partial t}+2\nu k^2\right)\langle\underline{\hat{u}}_1(\vec{k},t).\underline{\hat{u}}_2(\vec{k},t)^*\rangle=\langle\hat{u}_1\hat{u}_1\hat{u}_2\rangle+\langle\hat{u}_2\hat{u}_2\hat{u}_1\rangle \tag{11.10}$$

where the r.h.s. of Eq. (11.10) involves triple moments of the two fields. First, the Quasi-Normal procedure is applied at the level of the equation for the triple moments (see Lorenz [454]). A new problem which arises with the eddy damping is the choice of the triple-correlations relaxation time, which might differ from the time θ_{kpq} introduced in Chapter 7, since it now involves two *distinct* velocity fields. In fact all the studies quoted above have chosen the same time. With this choice, the resulting equations for $E(k,t)$ and $E_\Delta(k,t)$ read (see Métais and Lesieur [492])

$$\left(\frac{\partial}{\partial t}+2\nu k^2\right)E(k,t)=\iint_{\Delta_k}dp\;dqS_E(k,p,q)+F(k) \tag{11.11}$$

$$\left(\frac{\partial}{\partial t}+2\nu k^2\right)E_W(k,t)=\iint_{\Delta_k}dp\;dqS_W(k,p,q)+F(k) \tag{11.12}$$

$$\begin{aligned}S_E(k,p,q)&=A_D(k,p,q)\theta_{kpq}a(k,p,q)k^{D-1}E(p)E(q)\\&-\frac{1}{2}b(k,p,q)p^{D-1}E(q)E(k)-\frac{1}{2}b(k,q,p)q^{D-1}E(p)E(k)\end{aligned} \tag{11.13}$$

$$\begin{aligned}S_W(k,p,q)&=A_D(k,p,q)\theta_{kpq}a(k,p,q)k^{D-1}E_W(p)E_W(q)\\&-\frac{1}{2}b(k,p,q)p^{D-1}E(q)E_W(k)-\frac{1}{2}b(k,q,p)q^{D-1}E(p)E_W(k)\end{aligned} \tag{11.14}$$

$$A_3(k,p,q)=\frac{k}{pq};\quad A_2(k,p,q)=\frac{2}{\pi}\frac{k^2}{pq}. \tag{11.15}$$

In these equations, D is still the space dimension (3 or 2). The coefficient $b(k,p,q)$ has already been introduced in Chapters 7 (three dimensions) and 8 (two dimensions), and $a(k,p,q)$ is in both cases given by Eq. (7.12). The kinetic-energy transfers corresponding to Eq. (11.13) are of course the same as those arising in Eqs. (7.22) (three dimensions) and (8.31) (two dimensions), but put under a slightly different form closer to the expression of the correlated energy transfer Eq. (11.14). $F(k)$ comes from a possible forcing term $\underline{\hat{f}}(\vec{k},t)$ in the r.h.s. of the Navier–Stokes equations written in Fourier space: the modelling of this forcing through the closure has been already envisaged in Chapter 7, and we recall the main result: when a spectral tensor trace evolution equation of the form Eq. (6.1) is written, a force-velocity correlation $\langle \underline{\hat{f}}(\vec{k},t).\underline{\hat{u}}(\vec{k},t)^* \rangle$ appears. If the random function $\vec{f}(\vec{x},t)$ is a Gaussian white noise with respect to the time, such that

$$\langle \underline{\hat{f}}(\vec{k}',t).\underline{\hat{f}}(\vec{k},t) \rangle = \hat{F}(k)\ \delta(\vec{k}+\vec{k}')\delta(t-t') \tag{11.16}$$

and statistically independent of the initial velocity field, then it may be shown (Lesieur et al. [410])[1] that the forcing term in the r.h.s. of Eq. (11.11) is

$$F(k) = 2\pi k^2 \hat{F}(k)(D=3); \quad F(k) = \pi k \hat{F}(k)(D=2). \tag{11.17}$$

This analysis is also valid for the correlations $\langle f u_2 \rangle$ and $\langle f u_1 \rangle$ if the same forcing functions are taken for the two fields $\vec{u}_1$ and $\vec{u}_2$. This is what we will call *correlated forcing*, which yields the same forcing term $F(k)$ in the r.h.s. of Eqs. (11.11) and (11.12). As in the above chapters, emphasis will be given to the decaying cases where $F(k)$ is zero.

The above equations can be solved numerically with the same techniques that are described in Chapter 7. This was done in Leith [399] and Leith and Kraichnan [400] assuming a stationary kinetic energy spectrum, and in Métais and Lesieur [492] in a decaying turbulence: most of the results quoted in the next two sections come from these references. Let us also mention the E.D.Q.N.M. predictability study performed for a quasi geostrophic two-layer model by Herring [281].

11.3 Predictability of three-dimensional turbulence

Let us assume that the Reynolds number of the turbulence is high enough so that a $k^{-5/3}$ Kolmogorov inertial range exists. Let $k_e(t)$ be a wave number over which most of the error is confined, and such that complete uncertainty exists for $k > k_e(t)(E_\Delta(k) = E(k))$. A non-local analysis of the equation for

[1] The model used in this reference was the R.C.M., but the analysis can be generalized to Markovian models.

$E_\Delta(k)$ derived from Eqs. (11.11) and (11.12) leads, for $k < k_e(t)$ to (Leith and Kraichnan [399], Métais and Lesieur [492]:

$$\frac{\partial}{\partial t}E_\Delta(k,t) = \frac{14}{15}k^4 \int_{k_e(t)}^{\infty} \theta_{kpp}\frac{E^2(p,t)}{p^2}dp \tag{11.18}$$

which reduces, due to the inertial range expression of the energy spectrum, to

$$\frac{\partial}{\partial t}E_\Delta(k,t) \sim \epsilon k_e^{-5}(t)k^4. \tag{11.19}$$

This shows the existence of a strong error backscatter, responsible for a k^4 error spectrum for $k < k_e$. It is then possible to develop an analysis resembling the one we did in Chapter 7 for the passive scalar when it was injected in the small scales of turbulence: assuming that

$$E_\Delta(k,t) = C_\Delta(t)k^4; \quad k \to 0 \tag{11.20}$$

and matching the error and energy spectra at k_e yields

$$C_\Delta(t) \sim \epsilon^{2/3}k_e^{-17/3} \tag{11.21}$$

while Eq. (11.19) writes

$$\frac{dC_\Delta(t)}{dt} \sim \epsilon k_e^{-5}. \tag{11.22}$$

For a stationary kinetic energy spectrum where ϵ is a constant, it is then easy to show that the scale k_e^{-1} follows an *à la* Richardson law

$$\sigma_\Delta = \frac{1}{2}\frac{d}{dt}k_e^{-2}(t) \sim \epsilon^{1/3}k_e^{-4/3} \tag{11.23}$$

which leads to

$$k_e^{-2/3}(t) \sim \epsilon^{1/3}t + k_e^{-2/3}(t_0),$$

where t_0 is the time at which the error has been injected in the small scales of the inertial range. This shows that k_e is going to decrease following a $(t - t_0)^{-3/2}$ law, as soon as $k_e(t)$ will be sufficiently small compared with $k_e(0)$. The initial location of this wave number can then be forgotten, and the necessary time for the error, starting from very high wave numbers, to reach a given wave number k, is proportional to $\epsilon^{-1/3}k^{-2/3}$, that is the local turnover time of turbulence at k. In an infinite Reynolds number turbulence, it would therefore take a finite time for the error, injected at infinitely large wave numbers, to reach a given mode k.

Figures 11.2a, b and 11.3c, taken from Métais and Lesieur [492], show an E.D.Q.N.M. calculation of the inverse error cascade for three cases: a stationary turbulence forced at a mode $k_i(0)$ (and thus developing a k^2 equipartition

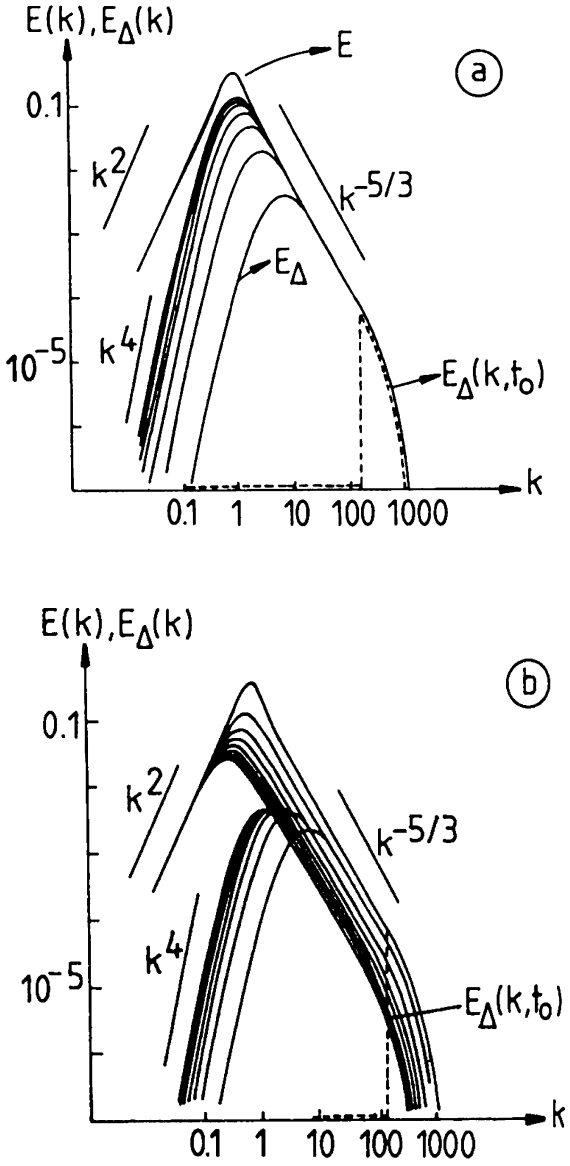

Figure 11.2. Inverse cascade of the error spectrum in isotropic turbulence for: (a) a stationary three-dimensional turbulence; (b) a decaying three-dimensional turbulence with $E(k) \propto k^2, k \to 0$.

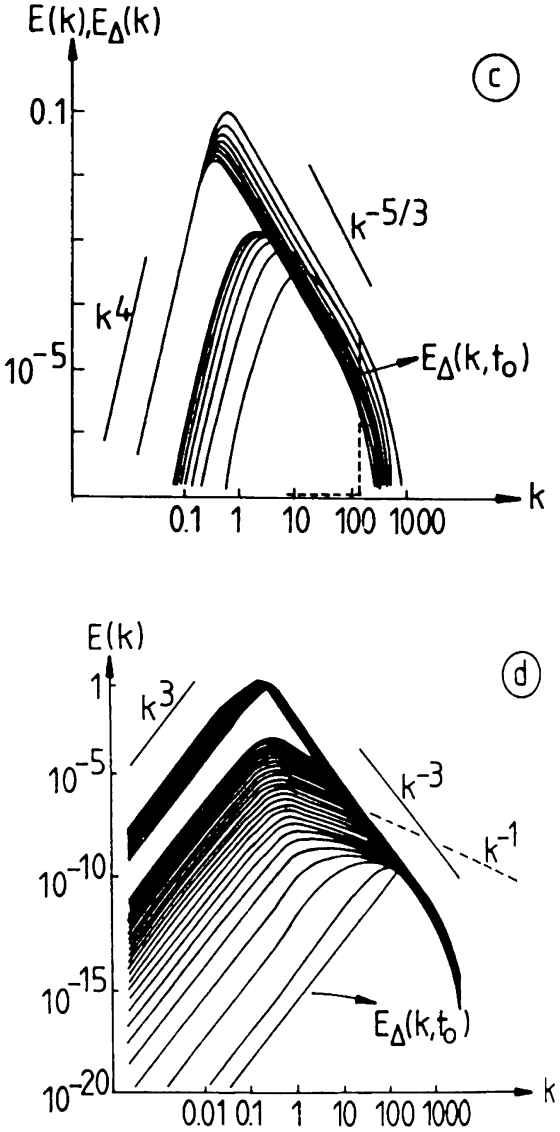

Figure 11.3. Inverse cascade of the error spectrum for: (c) a decaying three-dimensional turbulence with $E(k) \propto k^4, k \to 0$; (d) a decaying two-dimensional turbulence (from Métais and Lesieur [492], courtesy *J. Atmos. Sci.*).

energy spectrum at low k), and a decaying energy spectrum in both situations of a k^2 or a k^4 infrared energy spectrum. The initial (at $t = t_0$) energy spectrum in the decaying situation (case b) is identical to the stationary energy spectrum of case a). In the three cases the initial error spectrum is the same, and corresponds to the typical situation described in Figure 11.1. One clearly sees the inverse cascade of error which gradually contaminates larger and larger scales. The time evolution of the error rate $r(t)$ can be understood from the approximate relation

$$r(t) \approx \frac{\int_{k_e}^{\infty} E(k)dk}{\int_{k_i}^{\infty} E(k)dk} \approx \left(\frac{k_e}{k_i}\right)^{-2/3}. \tag{11.24}$$

Thus, in the stationary turbulence case, and because of the analogous Richardson law satisfied by $k_e(t)$, $r(t) \propto t$. In decaying turbulence, analytical expressions for k_e (and hence for $r(t)$) can be found in Métais and Lesieur [492]: in this case, $k_e(t)/k_i(t)$ is initially (for t close to t_0) equivalent to $(t - t_0)^{-3/2}$ and $r(t)$ also starts growing like $t - t_0$, then slows down when k_e reaches the vicinity of k_i. The *predictability time*, defined such that $r(t) = 1/2$, is equal respectively to

$$\begin{aligned} T_{r=1/2} &= 17\tau_0; \quad \text{case a} \\ T_{r=1/2} &= 33\tau_0; \quad \text{cases b and c,} \end{aligned} \tag{11.25}$$

where τ_0 is the large-eddy turnover time $(\langle \vec{u}^2 \rangle^{1/2} k_i)^{-1}$ of the initial (in cases b and c) energy spectrum. This predictability time is, as already stressed, independent of the initial position of $k_e(0)$ if far enough in the inertial range. This result has important implications for the LES of three-dimensional turbulence, since it shows in principle that no deterministic numerical simulation is then possible at times greater than $20 \approx 30\tau_0$. We will come back to that in the next chapter on large-eddy simulations. Let us also mention that the statistical predictability of three-dimensional turbulence has been studied by Chollet and Métais [120] using LES with a spectral eddy-viscosity (see next chapter). The calculations confirm that $k_e(t)$ decreases and $r(t)$ increases with time, but the resolution of the calculation (32^3) modes is too low to confirm the above theoretical predictions. In the same paper, the authors look also at the predictability of a passive scalar.

We stress finally that Sandham and Kleiser [631] have carried out predictability studies of a turbulent channel with the aid of DNS'.

11.4 Predictability of two-dimensional turbulence

Since Chapter 8, we are used to the fact that the dynamics of two-dimensional turbulence may be as intricate as in three dimensions, and this will also be

the case for the predictability problem. In particular, even though some of the analytical derivations of Section 3 can be applied in the inverse energy cascade, they have no validity at all in the enstrophy cascade because of the strong non-localness of the transfers. Let us first suppose, on a dimensional ground, that in the enstrophy cascade dk_e/dt is function of β (the enstrophy dissipation rate) and k_e only. This yields

$$\frac{d}{dt} \ln k_e \sim \beta^{\frac{1}{3}} \tag{11.26}$$

and k_e would then decrease exponentially. The error rate, approximated by $(k_e/k_i)^{-2}$ in a k^{-3} energy spectrum, would increase exponentially as

$$r(t) = r(t_0) \exp \frac{t - t_0}{\Lambda \tau_0}, \tag{11.27}$$

where the large-eddy turnover time τ_0 is of the order of $\beta^{-1/3}$ and Λ is a constant. Since $r(t_0) \approx [k_e(t_0)/k_i(t_0)]^{-2}$, the predictability time tends to infinity with $k_e(t_0)$ in an infinite k^{-3} enstrophy cascade inertial range.

In fact, E.D.Q.N.M. calculations made in Métais and Lesieur [492] have shown that, due to the strong non-local error transfers, the exponential decrease of k_e is only valid for the early stages of the evolution, where the error is very quickly transferred from high wave numbers to the energy containing eddies. This is shown in Figure 11.3d: in about 5 turbulence turnover times, the error spreads out through the whole spectrum, and the situation is as if the error had been injected directly in the energy containing eddies. Then the error rate grows exponentially, still following approximately the law equation (11.27) (though Eq. (11.26) is no more valid).[2] Notice also in Figure 11.3d the existence of a k^3 backscatter both in the energy and error spectra. The value of the constant Λ is equal to 2.6 for a stationary kinetic energy spectrum, and to 4.8 in the decaying turbulence case. The predictability time $T_{r=1/2}$ is now given by

$$T_{r=1/2} = \Lambda \tau_0 \ln[1/2r(t_0)]. \tag{11.28}$$

As shown in Métais and Lesieur [492], this can be used to estimate the predictability times in the atmosphere and the ocean.

11.4.1 Predictability time in the atmosphere

If this model of two-dimensional turbulence is applied to Earth's atmosphere, one may take $\tau_0 \approx 1$ day. We have

[2] The same behaviour for the error spectrum has been found qualitatively by Lilly [442] in the two-dimensional isotropic DNS already quoted above, and in the DNS of the temporal mixing layer done by Lesieur et al. [420].

$$\frac{k_e(t_0)}{k_i(t_0)} = \frac{100 \text{ km}^{-1}}{1000 \text{ km}^{-1}} = 10$$

$$r(t_0) = \left(\frac{k_e}{k_i}\right)^{-2} \approx 10^{-2};$$

then the predictability time would be of 10 or 18 days whether we consider the atmosphere as a stationary turbulence or as a decaying turbulence. These values are in good agreement with predictions based on other predictability theories. In fact the atmospheric circulation is forced by thermal heating, in such a way that 10 days is a better estimate. So, within this model, no precise numerical forecast of the atmosphere is possible beyond this limit.

This poses some questions about the validity of climate models, which solve approximately during periods of years coupled Navier–Stokes and energy equations for the atmosphere and the ocean.[3] The atmospheric model in these works is not two-dimensional nor even quasi geostrophic. However, it is obvious that it keeps this character of total unpredictability for forecast periods of more than 20 days. This is crucial, since it is from these model predictions that Earth's temperature should increase in an alarming fashion in the following tenths of years.

11.4.2 Predictability time in the ocean

In the ocean, where the large-eddy turnover time is about 20 days, the predictability times are then 20 times greater. Notice that the propagation of Rossby waves in the case of turbulence on a β-plane or on a sphere seems to slightly increase the predictability of the flow, as shown by Basdevant et al. [38].

11.4.3 Unpredictability and coherence

To finish this chapter, it is of interest to discuss the signification of these predictability times, based on statistical estimations, with respect to the dynamics of the flow itself when only one realization is considered. It could be an error to consider that, for times greater than the predictability time, the flow is going to look different, and in particular will lose any kind of spatial organization in the case where it would possess some well identified *coherent vortices*. In fact, the predictability time could in some occasions (for two-dimensional turbulence for instance) be much shorter than the life time of the organized eddies: this is in no way a contradiction, but simply means that the two flows $\vec{u}_1$ and $\vec{u}_2$ studied in the predictability problem both possess the

[3] These difficult studies include clouds, greenhouse effect gases and ice.

same sort of spatially-organized structures, whose spatial location ("phase") could differ appreciably from one flow to the other. Similar situations occur in meteorology at planetary scales, where one often encounters the same "mushroom" shaped [cyclonic-anticyclonic] dipole structures, whose exact location cannot be predicted accurately, in such a manner that one will never know in advance whether we will fall inside the anticyclonic part (which means fair weather) or the cyclonic one (and then bad weather). Another question which is still widely brought up concerns the role for predictability played by the actual external forces applied to a real flow, and by the boundaries. It is obvious of course that the models of isotropic three and two-dimensional homogeneous turbulence are so idealized that they cannot pretend to represent the whole reality. Nevertheless these models show that the nonlinearities of Navier–Stokes equations may be a source of unpredictability for high Reynolds number flows, and this mechanism has to be included (among others) in the physical principles and processes gear we use to try to understand turbulence in fluid dynamics.

11.5 Two-dimensional mixing-layer unpredictability

Such a study has been performed numerically in the case of the temporal mixing layer by Lesieur et al. [420]. Two velocity fields $\vec{u}_1(x, y, t)$ and $\vec{u}_2(x, y, t)$ are considered: they are supposed to be two solutions of the Navier–Stokes equations in the same domain D_N, with the boundary conditions of the temporal mixing layer. The error rate $r(t)$ is defined as a properly spatially averaged (in a test domain) kinetic energy of the difference between the two flows, divided by the average kinetic energy of one of the flows. The two fields are prepared in such a way that they initially (at time 0) differ only by a white-noise perturbation, superposed in both cases to the same basic hyperbolic-tangent velocity shear to which a small deterministic longitudinal sine perturbation at the fundamental wave length has been added: at the time t_0 of the rollup, the difference existing between $\vec{u}_1$ and $\vec{u}_2$ will therefore have lost the artificial character it had initially due to the white noise, and the two fields thus generated at t_0 will be mainly composed of coherent vortices extremely close from one field to the other. The simultaneous numerical calculation of the evolution of $\vec{u}_1$ and $\vec{u}_2$ allows one to determine $r(t)$, which has roughly an exponential growth of characteristic time $15\delta_0/U$. The error saturates together with the vorticity thickness, due to the longitudinal periodicity constraints already mentioned above. Hence, it can be concluded that the error grows as long as the vorticity thickness grows. In fact, one of the main reasons for such unpredictability growth is here the initial subharmonic perturbation. If its phase is chosen properly, it will be responsible for an important decorrelation

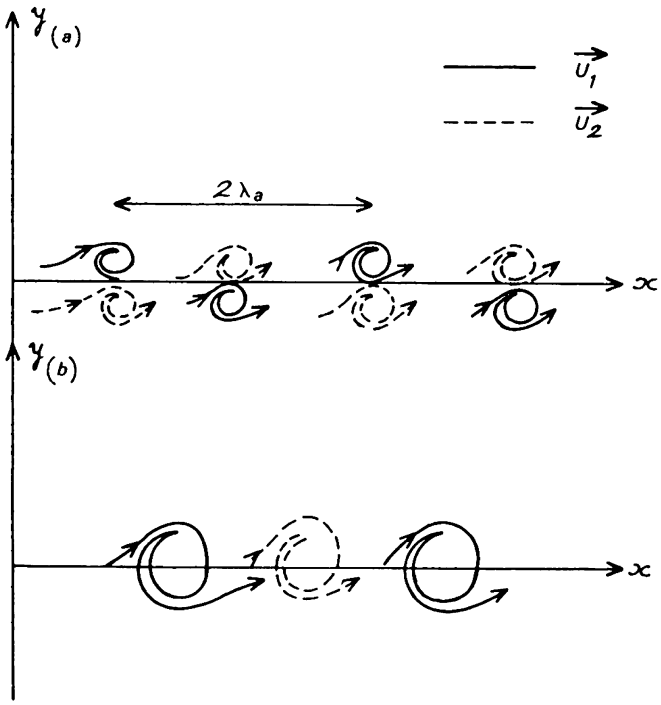

Figure 11.4. Growth of unpredictability in a two-dimensional mixing layer; (a) initial fields $\vec{u}_1(x, y, 0)$ and $\vec{u}_2(x, y, 0)$, modulated by two subharmonic perturbations in phase opposition; (b) the fields after the pairing.

between the two fields at the time of the first pairing. Indeed, let us consider for $\vec{u}_1$ and $\vec{u}_2$ two rows of vortices, each of them being modulated by out of phase subharmonic perturbations (of wave length $2\lambda_a$) (see Figure 11.4a). From what we have seen in Chapter 3 concerning the pairing, the resulting fields after the pairing will consist in two rows of Kelvin–Helmholtz vortices of wave length $2\lambda_a$ in phase opposition (Figure 11.4b), which corresponds to a high decorrelation rate between the two fields.

11.5.1 Two-dimensional unpredictability and three-dimensional growth

As an exercise, we will develop here a two-mode[4] nonlinear approach allowing one to relate the above two-dimensional predictability study to the three-

[4] One mode is the two-dimensional flow, and the second is obtained through a one-mode spectral spanwise truncation of the flow.

dimensionalization of the layer. This analysis is taken from Lesieur et al. [420], and has some analogies with the linear studies of Pierrehumbert and Widnall [573], Corcos and Lin [144] and Herbert [272] mentioned previously in this monograph: let us consider a quasi two-dimensional flow, whose velocity and pressure fields $\vec{u}(\vec{x},t)$ and $p(\vec{x},t)$ are expanded as

$$\vec{u}(x,y,z,t) = \vec{u}_{2D}(x,y,t) + \sqrt{2}\vec{u}_{3D}(x,y,t)\sin\beta z \tag{11.29}$$

$$p(x,y,z,t) = p_{2D}(x,y,t) + \sqrt{2}p_{3D}(x,y,t)\sin\beta z \tag{11.30}$$

where $\vec{u}_{2D}$ and $\vec{u}_{3D}$ are two horizontal (in the $x-y$ direction) non-divergent velocity fields, and β the wave-number of the spanwise perturbation. The flow is non-divergent, since the spanwise velocity is zero. $\vec{u}_{2D}$ corresponds more or less to a basic Kelvin–Helmholtz billow, while $\vec{u}_{3D}$ is the amplitude of a spanwise oscillation of the billow, initially small. The following decomposition is analogous to the two-mode spectral vertical decomposition of the quasi geostrophic potential-vorticity equation presented in Chapter 9. Projection of Navier–Stokes equation (with constant density) on these two modes may be performed either as was done in Chapter 9, or in the following manner: one substitutes the particular expansions (11.29) and (11.30) into three-dimensional Navier–Stokes equations (without rotation). One obtains

$$\frac{\partial\vec{u}_{2D}}{\partial t} + \vec{u}_{2D}.\vec{\nabla}\vec{u}_{2D} + 2\sin^2\beta z\vec{u}_{3D}.\vec{\nabla}\vec{u}_{3D} +$$

$$\sqrt{2}\sin\beta z\left(\frac{\partial\vec{u}_{3D}}{\partial t} + \vec{u}_{2D}.\vec{\nabla}\vec{u}_{3D} + \vec{u}_{3D}.\vec{\nabla}\vec{u}_{2D}\right) = -\frac{1}{\rho}\vec{\nabla}p_{2D}$$

$$-\sqrt{2}\sin\beta z\frac{1}{\rho}\vec{\nabla}p_{3D} + \nu[\nabla^2\vec{u}_{2D} + \sqrt{2}\sin\beta z(\nabla^2\vec{u}_{3D} - \beta^2\vec{u}_{3D})]. \tag{11.31}$$

Since $2\sin^2\beta z = 1 - \cos 2\beta z$, and eliminating the $\cos 2\beta z$ term (which corresponds to the truncation), we obtain after identification of the $\sin\beta z$ terms

$$\frac{\partial\vec{u}_{2D}}{\partial t} + \vec{u}_{2D}.\vec{\nabla}\vec{u}_{2D} + \vec{u}_{3D}.\vec{\nabla}\vec{u}_{3D} = -\frac{1}{\rho}\vec{\nabla}p_{2D} + \nu\nabla^2\vec{u}_{2D} \tag{11.32}$$

$$\frac{\partial\vec{u}_{3D}}{\partial t} + \vec{u}_{2D}.\vec{\nabla}\vec{u}_{3D} + \vec{u}_{3D}.\vec{\nabla}\vec{u}_{2D} = -\frac{1}{\rho}\vec{\nabla}p_{3D} + \nu\nabla^2\vec{u}_{3D}. \tag{11.33}$$

Notice that, in Eq. (11.33), the $\sim \nu\beta^2\vec{u}_{3D}$ term arising in Eq. (11.31) has been neglected in the dissipation term; we think this term would have only a negligible influence on the following results. Now let

$$\vec{u}_1(x,y,t) = \vec{u}_{2D} + \vec{u}_{3D}, \vec{u}_2(x,y,t) = \vec{u}_{2D} - \vec{u}_{3D} \tag{11.34}$$

and similarly for p_1 and p_2. It can be easily checked from Eqs. (11.32) and (11.33) that $\vec{u}_1$ and $\vec{u}_2$ both satisfy independent two-dimensional Navier–Stokes equations, with the same boundary conditions as $\vec{u}(x, y, z, t)$ for $y = \pm\infty$. Therefore, and since initially $\vec{u}_1$ and $\vec{u}_2$ are very close, the growth of this particular three-dimensional perturbation can be expressed in terms of the predictability problem studied above: the study of $\frac{1}{2}(\vec{u}_1 - \vec{u}_2) = \vec{u}_{3D}$ in the predictability problem will give access to the three-dimensional perturbation amplitude, the error rate being identified with the kinetic energy of the three-dimensional perturbation, averaged over a wave length $2\pi/\beta$ in the spanwise direction (see Lesieur et al. [420]).

Such an analysis is of course subject to criticism, since there is no spanwise velocity in the velocity field. The discarding of the $\cos 2\beta z$ term eliminates the harmonic spanwise wave length π/β which contains certainly some important three-dimensional characteristics of the flow, such as the existence of secondary streamwise vortices mentioned in Chapter 3, or small-scale three-dimensional turbulence. However, this analysis could take into account certain three-dimensional characteristics of the large coherent eddies, such as helical-pairing for instance.

12

Large-Eddy Simulations

12.1 DNS of turbulence

As already stressed in previous chapters, there is *a priori* no difficulty in envisaging a numerical solution of unstationary Navier–Stokes equations for rotational flows: the various operators are represented by discrete systems relating the values taken by velocity or vorticity components, pressure, density, temperature, etc., on a space-time grid. This grid may be spatially regular or irregular, with finite-difference, finite-volume or finite-element methods.[1] Often an orthogonal decomposition of the flow allows a spectral method to be used (see e.g. Canuto et al. [95]). For incompressible two-dimensional flows, the use of the stream function permits the elimination of the pressure. It is not the aim of the present monograph to describe the various numerical methods used in the so-called *Computational Fluid Dynamics*. We will insist rather on the physical limitations which arise when such a simulation is performed on a turbulent flow.

We recall that a DNS of turbulence has to take into account explicitly all scales of motion, from the largest (imposed by the existence of boundaries or the periodicities) to the smallest (the Kolmogorov dissipation scale for instance).

We have already seen that the total number of degrees of freedom necessary to represent a turbulent flow through this whole span of scales is of the order of $R_l^{9/4} \sim R_\lambda^{9/2}$ in three dimensions, and R_l^2 in two dimensions, where R_l is the turbulent Reynolds number based on the integral scale. As stressed in Chapter 1, one can in three-dimensional computations multiply by ten every ten years the number of computational points in each space direction. Thus, the improvement is very slow, and Reynolds numbers attained are still several orders of magnitude lower than the huge Reynolds numbers

[1] On the latter method applied to fluid dynamics, see Pironneau [578].

encountered in natural situations: there is no hope in the near future, even with the present unprecedented computer revolution, to envisage for instance a direct-numerical simulation of Earth atmosphere from the planetary scales (several thousands of kilometers horizontally) to the dissipation scale (1 mm), since it would require about 10^{20} degrees of freedom to put on the computer, all these modes interacting nonlinearly. Things get even worse on Jupiter, or in a star like the sun. Even in a wind tunnel, whith an integral scale of 5 cm and a Kolmogorov scale of 0.1 mm, about 10^8 degrees of freedom are needed (5×10^2 in each direction). As already stressed above, this is at hand now. The situation is improving with the development of parallel computers using a large number of processors simultaneously. We must also mention again that the simulation of the Kolmogorov cascade in the limit of zero viscosity requires an infinite number of degrees of freedom, and is out of reach of any DNS.

The conclusion we draw is that, for a high-Reynolds number turbulent flow, it is not possible in the near future (and perhaps not in the distant future either) to simulate explicitly all the scales of motion from the smallest to the largest. Generally, scientists or engineers are more interested in the description of the large scales of the flow, which often contain the desired information about turbulent transfers of momentum or heat for example: it is these large scales which will be simulated on the computer. The problem is no longer that of a DNS of turbulence, but of a LES. The latter, as will be seen, need the representation in some way (at least statistically) of the energy exchanges with the small scales which are not explicitly simulated.[2]

12.2 LES formalism in physical space

12.2.1 Large and subgrid scales

We present here the formalism for constant-density flows, and will give below some indications of the way compressibility may be handled.

Let us first look at the LES philosophy in physical space: suppose for sake of simplification that the numerical method chosen involves a discretization of the fields on a regular cubic array of points, Δx being the grid mesh. To the fields defined in the continuous space $\vec{x}$, one will associate filtered fields (*large-scale fields*), through the convolution with a filter $\bar{G}_{\Delta x}$. The filtered velocity and temperature are thus given by

$$\underline{\bar{u}}(\vec{x},t) = \int \vec{u}(\vec{y},t)\bar{G}_{\Delta x}(\vec{x}-\vec{y})d\vec{y} \tag{12.1}$$

[2] It should be stressed that in combusting or reacting flows, some important phenomena or reactions take place at the molecular-diffusion scales level. This is a further difficulty for the LES of these flows.

$$\bar{T}(\vec{x},t) = \int T(\vec{y},t)\bar{G}_{\Delta x}(\vec{x}-\vec{y})d\vec{y}. \tag{12.2}$$

In fact, one has, for any quantity f (scalar or vectorial)

$$\bar{f}(\vec{x},t) = \int f(\vec{y},t)\bar{G}_{\Delta x}(\vec{x}-\vec{y})d\vec{y} = \int f(\vec{x}-\vec{y},t)\bar{G}_{\Delta x}(\vec{y})d\vec{y}.$$

The filter has to be chosen in the best way to eliminate the small spatial scales. If one sees the motion as a superposition of sort of sine waves, then the sharp cutoff low-pass filter in Fourier space will be preferable (see below).

One can easily check that such a filter commutes with temporal and spatial derivatives, so that the continuity equation for the filtered field holds.[3] Let $\vec{u}'$ and T' be the fluctuations of the actual fields with respect to the filtered fields (density is taken constant and equal to ρ_0)

$$\vec{u} = \underline{\bar{u}} + \vec{u}'; \quad T = \bar{T} + T' \tag{12.3}$$

and more generally $f = \bar{f} + f'$. The fields "prime" concern fluctuations at scales smaller than Δx (the "grid scale"), and will then be referred to as *subgrid-scale fields*.

One now considers Navier–Stokes equations in the form:

$$\frac{\partial u_i}{\partial t} + \frac{\partial}{\partial x_j}(u_i u_j) = -\frac{1}{\rho_0}\frac{\partial p}{\partial x_i} + \frac{\partial}{\partial x_j}\left\{\nu\left(\frac{\partial u_i}{\partial x_j} + \frac{\partial u_j}{\partial x_i}\right)\right\}. \tag{12.4}$$

After applying the filter, one gets

$$\frac{\partial \bar{u}_i}{\partial t} + \frac{\partial}{\partial x_j}(\bar{u}_i \bar{u}_j) = -\frac{1}{\rho_0}\frac{\partial \bar{p}}{\partial x_i} + \frac{\partial}{\partial x_j}\left\{\nu\left(\frac{\partial \bar{u}_i}{\partial x_j} + \frac{\partial \bar{u}_j}{\partial x_i}\right) + T_{ij}\right\}, \tag{12.5}$$

where the subgrid-scale tensor T_{ij} is given by

$$T_{ij} = \bar{u}_i \bar{u}_j - \overline{u_i u_j}. \tag{12.6}$$

The filtered fields do not need to be resolved at scales smaller than Δx, since they have been constructed in a way to eliminate all the fluctuations under this scale. Therefore, they can be properly represented by the computer.[4] But a new problem arises, since the averaging procedure has produced in the

[3] Notice that this commutation property will not be any more true when employing a variable mesh Δx, which implies a variable width for the filter. Errors will thus be introduced, superposing to other errors done in the LES modelling.

[4] At this level, the filtered fields are still defined upon continuous space-time variables. It is only later that they will be discretized by proper numerical schemes. Thus, new errors will be introduced at this level.

equations of motion new terms. Indeed, let us write the subgrid-scale tensor as

$$T_{ij} = \bar{u}_i\bar{u}_j - \overline{\bar{u}_i\bar{u}_j} - (\overline{\bar{u}_i u'_j} + \overline{\bar{u}_j u'_i}) - \overline{u'_i u'_j}. \tag{12.7}$$

The r.h.s. of Eq. (12.7) can be split in three terms: $\bar{u}_i\bar{u}_j - \overline{\bar{u}_i\bar{u}_j}$ is the Leonard term, $-(\overline{\bar{u}_i u'_j} + \overline{\bar{u}_j u'_i})$ is "cross term", and $-\overline{u'_i u'_j}$ the "Reynolds-stress like term", following the terminology given by Clark et al. [128]. The latter reference is an attempt to evaluate these respective terms by a comparison between a coarse mesh and a fine mesh calculation.

Here we prefer to model the subgrid scales as a whole. Leonard's tensor is an explicit term which can be computed in terms of the filtered field, but the other terms are unknown. The equations of motion for the filtered field have analogies with Reynolds equations for the mean flow in non-homogeneous turbulence, but other terms than $-\overline{u'_i u'_j}$ arise in the LES, due to fact that the operator "bar" is not idempotent, that is to say $\overline{\overline{f}} \neq \overline{f}$. Another difference between LES and Reynolds equations is that LES deal usually with rapidly-fluctuating fields in space and time if Δx is small enough, while the solutions of Reynolds equations vary very smoothly with space, and generally not with time. The reader will find in Lesieur et al. [431] (Chapter 1) a discussion on unstationary RANS with respect to LES.

In the LES, we have to solve Navier–Stokes equations for the filtered field (large scales) modified by supplementary subgrid-scale terms which we do not know. Reviews of the LES methods may be found for instance in Rogallo and Moin [612], Lesieur and Métais [426], and Lesieur et al. [431].

12.2.2 LES of a transported scalar

Let us now consider a scalar T (called temperature) convected by the flow, κ being the molecular diffusivity. It satisfies

$$\frac{\partial T}{\partial t} + \frac{\partial}{\partial x_j}(T u_j) = \frac{\partial}{\partial x_j}\left\{\kappa \frac{\partial T}{\partial x_j}\right\}. \tag{12.8}$$

If the filter $\bar{G}_{\Delta x}$ is applied to this equation, one finds

$$\frac{\partial \bar{T}}{\partial t} + \frac{\partial}{\partial x_j}(\bar{T}\bar{u}_j) = \frac{\partial}{\partial x_j}\left\{\kappa \frac{\partial \bar{T}}{\partial x_j} + \bar{T}\bar{u}_j - \overline{T u_j}\right\}. \tag{12.9}$$

Here again, is posed the question of modelling the subgrid temperature fluxes.

The problem of the *subgrid-scale modelling*[5] is then to express the subgrid-scale terms as functions of the large-scale field. This is in no way an academic

[5] Also called *parameterization of subgrid scales.*

problem: indeed, at least for three-dimensional developed turbulence, we absolutely need in the equations some terms allowing the kinetic energy in the large scales to be transferred towards the subgrid scales where it will eventually be dissipated by molecular viscosity. In the absence of any subgrid-scale transfer, the energy of the large scales would tend to equipartition, from the results of Chapter 10.

This kind of problem (subgrid-scale modelling) is sometimes referred to, in mathematics, as a problem of *homogenization*, where the laws governing a medium are known at a microscopic level, and one seeks evolution laws at a macroscopic level. Here in turbulence, the "microscopic" level corresponds to the individual fluid particle for which we were able to write Navier–Stokes equations (see Chapter 2). The "macroscopic" level corresponds to the filtered field (large scales, or *supergrid scales*). Let us mention that homogenization methods applied to turbulence have been developed (see Bègue et al. [54], Dubrulle and Frisch [177, 229], Laval and Dubrulle [390]). They give a more rigorous basis to the concept of eddy viscosity and diffusivity when there exists a separation of scales between the large and subgrid scales. But they are not, up to now, exactly applicable to a turbulence having a continuous distribution of energy from the large to the small scales.

12.2.3 LES and the predictability problem

Mathematically, the subgrid-scale modelling problem is not a well-posed problem, due to propagation to the large scales of the uncertainty contained initially in the subgrid-scales: we suppose that at the initial time t_0 of the large-eddy simulation, the flow possesses fluctuations in the subgrid scales.[6] The large-scale fields initializing this computation ignore totally these small-scale fluctuations, and we are then in a situation of complete uncertainty at wave numbers greater than $\sim (\Delta x)^{-1}$. Let us now consider two possible realizations of the flow, identical in the large scales $> \Delta x$, and completely decorrelated in the subgrid scales $< \Delta x$. If one accepts the results on the propagation of unpredictability given in Chapter 11, the difference between the two fields will contaminate the large scales by error backscatter, and the two flows will in reality separate in these scales. Now let us assume that we have been able to solve the subgrid-scale modelling problem, and dispose of "closed" large-scale equations where everything is expressed in terms of these scales. Then the LES performed on the two fields will be unable to propagate any kind of difference between them. This implies that a turbulence LES, however good the subgrid-scale modelling may be, will not describe exactly the large-scale

[6] This is not the case if one considers initial energy spectra sharply peaked at a given mode k_i corresponding to the large scales.

evolution from a deterministic viewpoint, at last for times greater than the predictability time. This point was noted in particular by Herring [278].

Does that mean that LES are useless at large times? Certainly not: one might interpret then the calculated flow as a different realization of the actual flow, and hope that it could possess at least the same statistical properties (in space or time), and may be the same spatially-organized structures, though at a different location from the reality: this last point is of course very frustrating in meteorology, as mentioned already in Chapter 11, since it is certainly of some interest for the populations to know whether a cyclonic or anticyclonic perturbation will come. It might not be too crucial in a lot of engineering flows, as soon as the statistics resulting from the computed flow[7] are correct. Remark however that certain industrial applications require to kow the position of vortices and the deterministic amplitude of the perturbations (for thermal fatigue or corrosion of a material in contact with the flow in nuclear engineering or hypersonic aerodynamics for instance).

From these remarks we could try to propose criteria of what one could call a "good" LES of turbulence, according to the specifications we require:

- **low-grade definition**: the simulation must predict correctly the statistical properties of turbulence (spectral distributions, turbulent exchange coefficients, etc.)
- **high-grade definition**: moreover, the simulation must be able to predict the shape and topology (but not the phase) of coherent vortices existing in the flow at the scales of the simulation.[8]

There could have been a third definition proposed, namely the objective of predicting exactly the actual flow (in the supergrid scales). This is certainly not possible at large times, due to the inverse cascade of unpredictability mentioned above. Another remark is that the notion of *actual flow* is highly questionable for a turbulent flow in a laboratory or in a wide range of engineering situations, where no repeatable (from a deterministic viewpoint) realization can be obtained.

12.2.4 Eddy-viscosity assumption

In the rest of the chapter, we will prefer not to split the subgrid-scale tensor T_{ij} into parts, and rather model it as a whole.[9] Most operational (in terms of

[7] These statistics will generally be evaluated in the computation with the aid of a spatial averaging.

[8] In fact, it often occurs that LES can predict qualitatively the topology of the vortices, but make substantial errors on the statistics.

[9] This has the further advantage of accounting for non-regular grids, where we recall that Eqs. (12.6) and (12.9) are no more valid.

practical applications) subgrid-scale models make an eddy-viscosity assumption (Boussinesq's hypothesis) in order to model the subgrid-scale tensor:

$$T_{ij} = 2\nu_t \bar{S}_{ij} + \frac{1}{3} T_{ll} \delta_{ij} \ , \tag{12.10}$$

where

$$\bar{S}_{ij} = \frac{1}{2} \left(\frac{\partial \bar{u}_i}{\partial x_j} + \frac{\partial \bar{u}_j}{\partial x_i} \right)$$

is the deformation tensor of the filtered field. The LES momentum equation becomes

$$\frac{\partial \bar{u}_i}{\partial t} + \bar{u}_j \frac{\partial \bar{u}_i}{\partial x_j} = -\frac{1}{\rho_0} \frac{\partial \bar{P}}{\partial x_i} + 2 \frac{\partial}{\partial x_j} \left\{ (\nu + \nu_t) \bar{S}_{ij} \right\} . \tag{12.11}$$

Here, we have introduced a modified pressure[10] $\bar{P} = \bar{p} - (1/3)\rho_0 T_{ll}$ which will be determined with the help of the filtered continuity equation, by taking the divergence of Eq. (12.11). This allows in particular to take into account in the resulting Poisson equation for the pressure spatial variations of ν_t.

12.2.5 Eddy-diffusivity assumption

For the temperature (or another transported scalar), one introduces an eddy diffusivity κ_t such that

$$\bar{T}\bar{u}_j - \overline{T u_j} = \kappa_t \frac{\partial \bar{T}}{\partial x_j} \tag{12.12}$$

which yields

$$\frac{\partial \bar{T}}{\partial t} + \bar{u}_j \frac{\partial \bar{T}}{\partial x_j} = \frac{\partial}{\partial x_j} \left\{ (\kappa + \kappa_t) \frac{\partial \bar{T}}{\partial x_j} \right\} . \tag{12.13}$$

The eddy diffusivity is related to the eddy viscosity by the relation

$$P_r^{(t)} = \frac{\nu_t}{\kappa_t},$$

where $P_r^{(t)}$) is a turbulent Prandtl number which has to be specified (see below).

12.2.6 LES of Boussinesq equations

Eqs. (12.11) and (12.13) may be generalized to Navier–Stokes equations in a rotating frame within the Boussinesq approximation for a density-stratified fluid in the following way. One starts with Eq. (2.108), which is equivalent to Eq. (12.4) plus Coriolis acceleration, with an added gravity term $(\rho/\rho_0)\vec{g}$ on

[10] Called macropressure in Lesieur et al. [431].

its r.h.s., p being the static pressure, and ρ the total density. After applying the filter $\bar{G}$ to this equations, and introducing an eddy viscosity, one obtains the generalized LES Boussinesq equations, with a term $(\bar{\rho}/\rho_0)\vec{g}$ on the r.h.s. of Eq. (12.11), as well as Coriolis acceleration relative to the filtered velocity.

For a liquid, ρ satisfies Eq. (12.8) where T has been replaced by ρ. Applying the filter $\bar{G}$ to this equation, and using an eddy diffusivity, the filtered total density $\bar{\rho}$ still satisfies Eq. (12.13). Remark that $\bar{\rho}$ has here nothing to do with the basic density profile considered when establishing Boussinesq approximation. The case of an ideal gaz is discussed in Lesieur et al. [431].

12.2.7 Compressible turbulence

For compressible turbulence (see applications in the next chapter), one will assume that the subgrid-scales are not far from incompressibility. This point has been discussed at length in Lesieur et al. [431]. Here, it is preferable to work using Favre filters, which are weighted by density. In fact, Favre [198,199] considers Favre averages, which are Reynolds averages weighted by density.

In compressible turbulence LES, Lesieur et al. [431] introduce a macrotemperature related to the macropressure (see also Ducros et al. [178]). The filtered fields obey compressible Navier–Stokes equations with variable density, where the molecular viscosity $\mu = \rho\nu$ is replaced by $\mu + \bar{\rho}\nu_t$ (except in the energy equation). The molecular conductivity $\rho C_p \kappa = C_p \mu P_r^{-1}$ is replaced by $C_p(\mu P_r^{-1} + \bar{\rho}\nu_t P_r^{(t)})$, where P_r is the molecular Prandtl number.

The question is now to determine the eddy viscosity $\nu_t(\vec{x}, t)$. It is well known (see e.g. the discussion in Lesieur et al. [431]) that this eddy-viscosity assumption, in the framework of which we are going to work here, is rather questionable. One expects, however, that the information derived using this concept may help to improve it. For instance this is the philosophy of the dynamic model, discussed below.

12.2.8 Smagorinsky model

The most widely used eddy-viscosity model was proposed by Smagorinsky [653]. The latter was simulating a two-layer quasi-geostrophic model, in order to represent large (synoptic) scale atmospheric motions. He introduced an eddy viscosity which was supposed to model three-dimensional turbulence that follows approximately a three-dimensional Kolmogorov $k^{-5/3}$ cascade in the subgrid scales. In fact, Smagorinsky model turned out to be too dissipative for quasi two-dimensional turbulence. On the other hand, it is still very popular for engineering applications (with wall laws), starting with the pioneering work of Deardorff [162] for the channel flow.

In Smagorinsky model, a sort of mixing-length assumption is made, in which the eddy viscosity is assumed to be proportional to the subgrid-scale characteristic length scale Δx, and to a characteristic turbulent velocity $v_{\Delta x} = \Delta x|\bar{S}|$. Here $|\bar{S}| = \sqrt{2\bar{S}_{ij}\bar{S}_{ij}}$ is a typical velocity gradient at Δx, determined with the aid of the filtered-field deformation tensor $\bar{S}_{ij}$ defined in Eq. (12.10). The model is

$$\nu_t = (C_S \Delta x)^2 |\bar{S}|. \tag{12.14}$$

If one assumes that $k_C = \pi/\Delta x$, the cutoff wavenumber in Fourier space, lies within a $k^{-5/3}$ Kolmogorov cascade, one can adjust the constant C_S so that the ensemble averaged subgrid kinetic-energy dissipation is identical to ϵ. It is found (Lilly [446], see also Lesieur et al. [431]):

$$C_S \approx \frac{1}{\pi}\left(\frac{3C_K}{2}\right)^{-3/4}. \tag{12.15}$$

This yields $C_S \approx 0.18$ for a Kolmogorov constant $C_K = 1.4$. Most people prefer $C_S = 0.1$ (which represents a reduction by nearly a factor of 4 of the eddy viscosity), a value for which Smagorinsky's model behaves reasonably well for isotropic turbulence, free-shear flows, and channel flow (Moin and Kim [513]) with a damping function at the wall. In the latter case, it gives qualitatively good results in terms of coherent hairpins and streaks at the wall. But quantitative experimental agreement cannot be reached without DNS such as those of Kim et al. [330]. More recently, Rodi et al. [610] recommend Smagorinsky model with a wall law for LES of turbulence around obstacles.

In fact, it is well known that plain Smagorinsky model is too dissipative close to a wall. This can be shown through expansions of the velocity components in powers of the wall distance y (see for a review Lesieur et al. [431]). So the model does not work for transition in a boundary layer on a flat plate, starting with a laminar profile to which a small perturbation is added: the flow remains laminar, due to an excessive eddy viscosity coming from the mean shear.[11]

More elaborate subgrid-scale models, adopting the second-order one-point closure modelling point of view (with evolution equations for the subgrid-scale stresses), have been developed by Deardorff [163] (see also Somméria [659], Schumann [640], and Schmidt and Schumann [636]).

A nice alternative to Smagorinsky model is its dynamic version (see below).

[11] It works however for by-pass transition, with a high level of upstream perturbation (Yang and Voke [731]).

12.3 LES in spectral space

In this section, we present a point of view based on the concepts of spectral eddy viscosity and spectral eddy diffusivity introduced in Chapter 7. Related to the two definitions given in Section 12.2.3, we will try to propose a subgrid-scale procedure for the kinetic energy and temperature fluctuations predicting at least correct spectra and decay laws.

12.3.1 Sharp filter in Fourier space

We will work in Fourier space, introduce a cutoff[12] wave number $k_C \sim \Delta x^{-1}$ and define the filtered field in Fourier space as

$$\bar{\hat{u}}(\vec{k},t) = \begin{cases} \hat{u}(\vec{k},t), & \text{if } |\vec{k}| \leq k_C; \\ 0, & \text{otherwise.} \end{cases} \tag{12.16}$$

and the same relation for the temperature $\bar{\hat{T}}$. This is a sharp filter in Fourier space.[13]

12.3.2 Spectral eddy viscosity and diffusivity

Details on the following results can be found in Chollet and Lesieur [116,117], Pouquet et al. [586], and Métais and Lesieur [493]. They use E.D.Q.N.M. as a tool to model the subgrid-scale transfers.

Let us first look back at the kinetic-energy and temperature transfers given by the E.D.Q.N.M. theory in Chapter 7.

Case k small in front of k_C

One assumes first $k \ll k_C$ (both modes being larger than k_i). Then one can write the spectral evolution equations for the supergrid scale spectra $\bar{E}(k,t)$ and $\bar{E}_T(k,t)$ as

$$\left(\frac{\partial}{\partial t} + 2\nu k^2\right) \bar{E}(k,t) = T_{<k_C}(k,t) + T_{sg}(k,t) \tag{12.17}$$

$$\left(\frac{\partial}{\partial t} + 2\kappa k^2\right) \bar{E}_T(k,t) = T^T_{<k_C}(k,t) + T^T_{sg}(k,t), \tag{12.18}$$

[12] This wave number should not be confused with the conductive wave number k_c of the passive scalar problem.

[13] The effects of such a filter on the definition of the eddy viscosity in physical space have been studied by Leslie and Quarini [433].

with

$$T_{sg}(k,t) = -2\nu_t^{\infty} k^2 \bar{E}(k,t) \tag{12.19}$$

$$\nu_t^{\infty} = \frac{1}{15}\int_{k_C}^{\infty} \theta_{0pp}\left[5E(p,t) + p\frac{\partial E(p,t)}{\partial p}\right] dp \tag{12.20}$$

$$T_{sg}^{T}(k,t) = -2\kappa_t^{\infty} k^2 \bar{E}_T(k,t) \tag{12.21}$$

$$\kappa_t^{\infty} = \frac{2}{3}\int_{k_C}^{\infty} \theta_{0pp}^{T} E(p,t)dp. \tag{12.22}$$

The supergrid-scale transfers $T_{<k_C}(k,t)$ and $T^T_{<k_C}(k,t)$ correspond to triad interactions whose wave numbers lie in the supergrid range, and hence do not need any modelling, since they can be calculated exactly in the LES. Here, non-local transfers from the supergrid to the subgrid scales have been evaluated with the aid of Eqs. (7.76) (for the kinetic energy) and (7.143) (for the temperature), with a small parameter $a = k/k_C$. At this point, the $O(k^4)$ backscatter term has been discarder. Indeed, its relative importance in terms of transfers is, according to E.D.Q.N.M. theory, $(k/k_C)^2[E(k_C)/E(k)]$, which is very small since $E(k_C) \ll E(k)$. This is true in particular if k_C lies in the Kolmogorov cascade. More details can be found in Lesieur et al. [431].

Notice that if k_C is in the energy-containing range, the k^4 backscatter plays an important role in the subgrid exchanges, and further investigations are needed in this direction. The problem is that, in practice, these scales are not isotropic nor even homogeneous. Leith [403] proposes that, in a mixing layer, turbulence confined in small scales can, by backscatter, inject energy into the larger scales, where it may grow via Kelvin-Helmholtz instability. This could apply to other types of instabilities as well, such as Rayleigh-Taylor for instance.

The asymptotic eddy viscosity Eq. (12.20) and eddy diffusivity Eq. (12.22) may be calculated analytically if the kinetic-energy spectrum is given for $k \geq k_C$. Assuming for instance a $k^{-5/3}$ inertial range at wave numbers greater than k_C, we obtain:

$$\nu_t^{\infty} = 0.441 {C_K}^{-3/2}\left[\frac{E(k_C)}{k_C}\right]^{1/2} \tag{12.23}$$

$$\kappa_t^{\infty} = \frac{\nu_t^{\infty}}{P_r^{(t)}}, \tag{12.24}$$

where the turbulent Prandtl number $P_r^{(t)}$ has been determined in Chapter 7. If one assumes for instance a Kolmogorov constant of 1.4 in the energy cascade, the constant in front of Eq. (12.23) will be 0.267. As already stressed, the highest possible value of $P_r^{(t)}$ permitted by the E.D.Q.N.M. is 0.6.

If one considers a kinetic-energy spectrum $\propto k^{-m}$ for $k > k_C$, the eddy viscosity given by Eq. (12.20) is now

$$\nu_t^\infty = \frac{1}{15a_1}\frac{5-m}{m+1}\sqrt{3-m}\left[\frac{E(k_C)}{k_C}\right]^{1/2}, \tag{12.25}$$

for $m \leq 3$. The constant $1/(15a_1)$ in front of Eq. (12.25), coming from the E.D.Q.N.M. (see Chapter 7), is equal to $0.31{C_K}^{-3/2}$. This expression was shown by Métais and Lesieur [496]. It was used by Lamballais [366] for channel-flow LES (see below). The associated eddy diffusivity is

$$\kappa_t^\infty = \frac{4}{3a_3}\frac{\sqrt{3-m}}{m+1}\left[\frac{E(k_C)}{k_C}\right]^{1/2}, \tag{12.26}$$

and the turbulent Prandtl number

$$P_r^{(t)} = \frac{5-m}{20}\frac{a_3}{a_1}.$$

Remembering that the constants a_1 and a_3 are such that one recovers $P_r^{(t)} = 0.6$ for $m = 5/3$, it is finally found

$$P_r^{(t)} = 0.18(5-m). \tag{12.27}$$

For $m > 3$, the eddy viscosity scales as $[E(k_C)/k_C]$, and becomes negative for $m > 5$. This might explain the results of Domaradzki et al. [170], who evaluate this asymptotic eddy viscosity in a DNS,[14] and find (small) negative values: indeed, the kinetic energy spectrum in such a simulation is much steeper than $k^{-5/3}$.

Case k close k_C

When k is close to k_C, the above concept of spectral eddy coefficients can be generalized for a $k^{-5/3}$ inertial range at wave numbers greater than k_C. Following Kraichnan's theory of eddy viscosity in spectral space [358], it is possible, with the aid of the E.D.Q.N.M. approximation, to calculate the subgrid-scale transfers, corresponding to triadic interactions where at least one of the wave numbers p and q is greater than k_C. This allows us to define two functions $\nu_t(k|k_C)$ and $\kappa_t(k|k_C)$, respectively the eddy viscosity in spectral space (Kraichnan [358]) and the eddy diffusivity in spectral space (Chollet and Lesieur [117]) given by

[14] This is done by defining a fictitious cutoff k_C, and evaluating the transfers across k_C.

$$T_{sg}(k,t) = -2\nu_t(k|k_C)k^2\bar{E}(k,t) \tag{12.28}$$

$$T^T_{sg}(k,t) = -2\kappa_t(k|k_C)k^2\bar{E}(k,t). \tag{12.29}$$

The functions $\nu_t(k|k_C)$ and $\kappa_t(k|k_C)$ are such that

$$\nu_t(k|k_C) = K(k/k_C)\nu_t^\infty \tag{12.30}$$

$$\kappa_t(k|k_C) = C(k/k_C)\kappa_t^\infty, \tag{12.31}$$

where ν_t^∞ and κ_t^∞ are the asymptotic values Eq. (12.23) and Eq. (12.24). The functions $K(x)$ and $C(x)$ (displayed in Lesieur et al. [431]) are approximately constant and equal to 1, except in the vicinity of $k/k_C = 1$ where they display a strong overshoot (called the *cusp*-behaviour), due to the predominance of semi-local transfers across k_C. In fact, the function $K(x)$ can be put under the form

$$K(x) = 1 + \nu_n^* x^{2n}, \tag{12.32}$$

with $2n \approx 3.7$ (Chollet [118]). Métais [499] has proposed to determine ν_n^* by considering the energy balance between explicit and subgrid-scale transfers. This yields:

$$\int_0^{k_C} 2\nu_t k^2 E(k,t)dk = \epsilon,$$

which, in an infinite Kolmogorov inertial range, leads to

$$1 + \frac{1}{1+(3n/2)}\nu_n^* = \frac{2}{3\times 0.441}. \tag{12.33}$$

Developments of this type of model in physical space in terms of hyperviscosities have been proposed by Lesieur and Métais [426] (see also Lesieur et al. [431]).

As for the turbulent Prandtl number $\nu_t(k|k_C)/\kappa_t(k|k_C)$, it depends upon the choice of the two E.D.Q.N.M. scalar adjustable constants: in the *à la L.H.D.I.A.* case, it remains approximately equal to 0.6, even in the vicinity of k_C; in the *à la D.I.A.* case, it has a plateau value of 1/3, and a cusp close to k_C where it rises to 0.6. We mention finally that the use of subgrid-scale transfers given by Eqs. (12.28) and (12.29) allows one to solve numerically E.D.Q.N.M. kinetic-energy and passive-scalar Eqs. (7.22) and (7.128) at zero molecular viscosity and conductivity in the self-similar decaying regime (for $k \leq k_C$), as shown by Chollet and Lesieur [116, 117].

12.3.3 LES of isotropic turbulence

Let us now come back to the evolution equations (in spectral space) of the filtered field (for $|\vec{k}| < k_C$)

$$\left(\frac{\partial}{\partial t}+\nu k^2\right)\bar{\hat{u}}_i(\vec{k},t)=t_{<k_C}(\vec{k},t)+t_{sg}(\vec{k},t) \tag{12.34}$$

$$\left(\frac{\partial}{\partial t}+\kappa k^2\right)\bar{\hat{T}}(\vec{k},t)=t^T_{<k_C}(\vec{k},t)+t^T_{sg}(\vec{k},t) \tag{12.35}$$

with the usual distinction between the explicit supergrid transfers, still calculated by a truncation for $k,p,q\le k_C$ of the r.h.s. of Eqs. (5.18) and (5.19), and the unknown subgrid-scale transfers. We propose to model the latter with the aid of $\nu_t(k|k_C)$ and $\kappa_t(k|k_C)$ introduced in Eqs. (12.30) and (12.31), namely

$$t_{sg}(\vec{k},t)=-\nu_t(k|k_C)k^2\overline{\hat{u}}_i(\vec{k},t) \tag{12.36}$$

$$t^T_{sg}(\vec{k},t)=-\kappa_t(k|k_C)k^2\overline{\hat{T}}(\vec{k},t). \tag{12.37}$$

The only justification of this subgrid-scale modelling is that, when one writes the exact evolution equations for the spectra of $\overline{\underline{\hat{u}}}$ and $\overline{\hat{T}}$ as they arise from Eqs. (12.34) and (12.35), one obtains the E.D.Q.N.M. subgrid-scale transfers calculated in Eqs. (12.28) and (12.29). It is then natural, if we trust the spectral predictions of the E.D.Q.N.M. theory, to use these eddy-viscosity and eddy-diffusivity coefficients in spectral space for subgrid-scale modelling purposes. The main criticisms which may be brought to this modelling concern the fact that the same results, as far as the energetics are concerned, could be obtained by multiplying the velocity in Fourier space by any complex number of modulus 1. Indeed, the interactions with the subgrid scales may affect the phase of the velocity vector $\underline{\hat{u}}(\vec{k},t)$. However, when $k\ll k_C$, and due to the separation of space and time scales, it is difficult (in isotropic turbulence) to believe that the subgrid scales will instantaneously affect the phase of the velocity field at $\vec{k}$: this would require a finite time, comparable to the time taken by an error in the small scales to contaminate the large scales in the predictability problem. On the contrary, the validity of this spectral eddy viscosity is questionable if k lies in the vicinity of k_C. But this is shared with other theories such as the Renormalization Group (Yakhot and Orszag [728], Mc Comb [476]) or homogenization (Bègue et al. [54], Frisch [229]) techniques.

As already stressed in Chapter 7, the R.N.G. analysis[15] developed by Yakhot and Orszag [728] yields a k_C-dependent eddy viscosity, also proportional to $[E(k_C)/k_C]^{1/2}$ as in Eq. (12.23), and without any cusp. As mentioned in Chapter 7, the constant ν_0 in front of $[E(k_C)/k_C]^{1/2}$ is equal to 0.388, and the Kolmogorov constant found in the theory is 1.617.

Now, let us consider the E.D.Q.N.M. eddy viscosity with no cusp, and adjust the constant ν_0 as proposed by Leslie and Quarini [433], by balancing (in the inertial range) the subgrid-scale flux with the kinetic-energy flux ϵ

[15] There was an earlier attempt made by Rose [616] for the passive scalar problem.

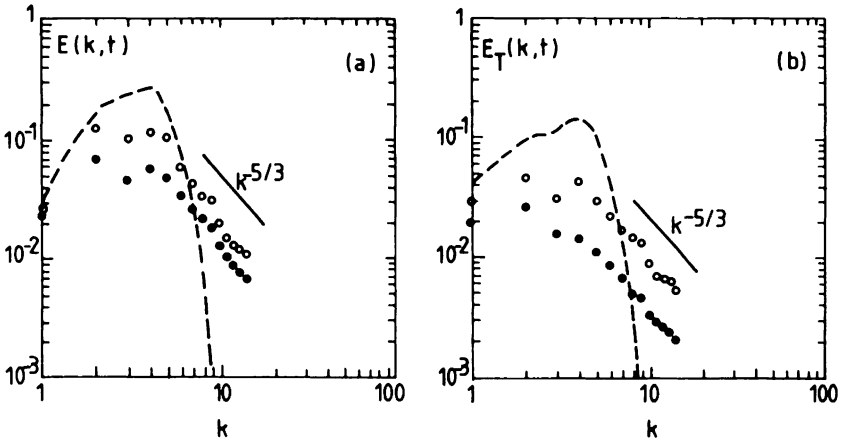

Figure 12.1. Decaying kinetic-energy (a) and temperature spectra (b) in a LES of three-dimensional isotropic turbulence using a spectral eddy viscosity and diffusivity. The resolution is 32^3 in a spectral code (from Chollet and Lesieur [117] courtesy "La Météorologie").

in the energy spectrum evolution equation, as was done in order to obtain Eq. (12.33). This yields

$$\nu_t(k_C) = \frac{2}{3} C_K^{-3/2} \left[\frac{E(k_C)}{k_C} \right]^{1/2} , \tag{12.38}$$

where C_K is the Kolmogorov constant. A Kolmogorov constant of 1.4 leads to $\nu_0 = 0.402$.

The results of the E.D.Q.N.M. spectral plateau-peak eddy viscosity applied to three-dimensional isotropic turbulence LES are satisfactory when it is implemented on a spectral code directly in Fourier space and at a low resolution: Figure 12.1, taken from Chollet and Lesieur [117], shows the evolution of the kinetic-energy and temperature spectra in a 32^3 modes spectral calculation, starting from initial conditions corresponding to sharply peaked spectra. Kolmogorov and Corrsin-Oboukhov $k^{-5/3}$ cascades establish in times comparable with the critical times estimated in Chapter 7. Then the spectra decay self-similarly, with $k^{-5/3}$ slopes extending up to k_C. Notice that during the early stage of the calculation, the $\sim [E(k_C)/k_C]^{1/2}$ expression of the eddy coefficients automatically sets their value to zero as long as the ultraviolet cascade has not reached k_C and that $E(k_C)$ is negligible. This is an advantage compared to other eddy-viscosity methods which dissipate the energy more uniformly, since it permits a simulation of the inviscid stage preceding the establishment of the Kolmogorov energy cascade. The same calculations allow

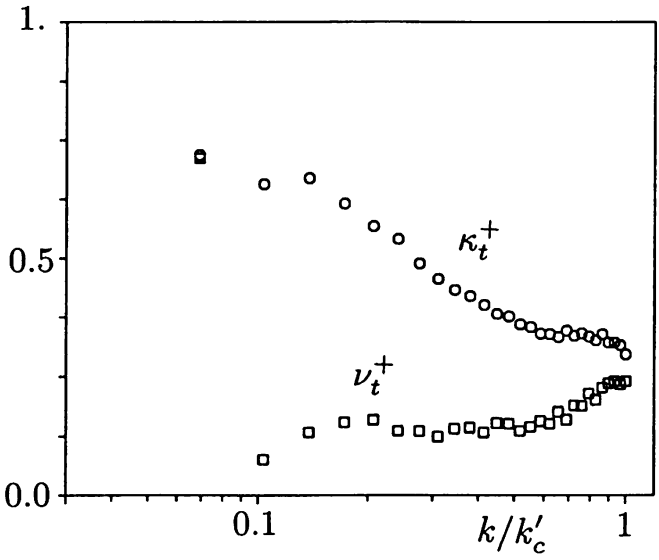

Figure 12.2. Three-dimensional isotropic decaying turbulence, resolution 128^3; spectral eddy viscosity and diffusivity, calculated from the LES of Métais and Lesieur [496].

one to compute the kinetic-energy and temperature-variance decay, extrapolating the total energy and temperature from the supergrid scales values by assuming that infinite $k^{-5/3}$ spectra extend beyond k_C. This yields

$$\frac{1}{2} < \vec{u}^2 >= \int_0^{k_C} \bar{E}(k,t)dk + \frac{3}{2} k_C E(k_C,t)$$

and the same expression for the temperature. It is found that both kinetic energy and temperature variance decay as $t^{-1.2}$, according to the Saffman law[16] derived in Chapter 7 This might be due to the coarse resolution of the large-eddy simulation in the low wave numbers, which could yield equipartition of energy in these modes, and hence a k^2 infrared spectrum.

However, we have already mentioned in Chapter 6 results concerning the same E.D.Q.N.M. subgrid-scale modelling,[17] but with a higher resolution (128^3, see Lesieur and Rogallo [421], and Lesieur et al. [422]. In these calculations, the kinetic-energy spectrum at the cutoff is closer to k^{-2} than to

[16] The result is the same for the "supergrid" kinetic energy and temperature variance, corresponding only to modes $< k_C$.

[17] That is, a plateau at 0.267 followed by a cusp.

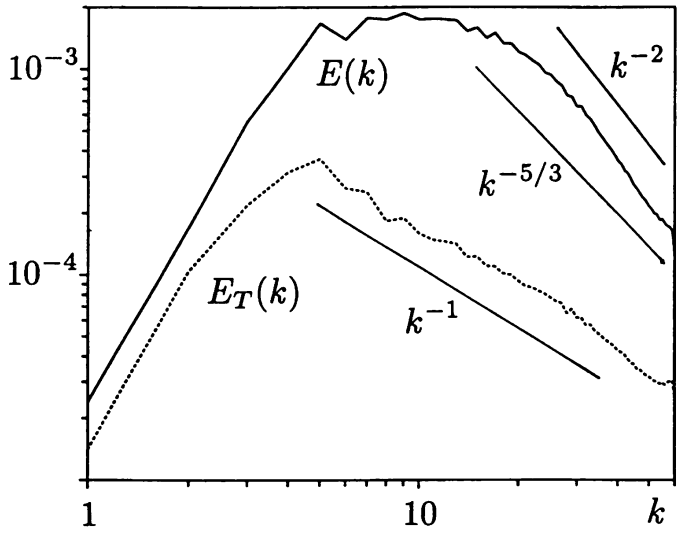

Figure 12.3. Kinetic energy and temperature spectra corresponding to the calculation of Figure 12.2.

$k^{-5/3}$. We will present below a local generalization of this spectral eddy viscosity to physical space (structure-function model), which gives better results for isotropic turbulence. But beforehand we will look at some anomalous aspects of the spectral eddy diffusivity, related to the large-scale intermittent character of the passive temperature already mentioned in Chapters 6 and 7.

12.3.4 The anomalous spectral eddy diffusivity

Figure 6.12b (from Lesieur and Rogallo [421]) is the passive-scalar LES counterpart of Figure 6.12a, at a turbulent Prandtl number of 0.6. It shows an anomalous large-scale passive scalar range close to k^{-1}, which might be due to the direct shearing of the temperature fluctuations by the large-scale velocity gradients (see Chapter 6). In these simulations, the spectral eddy viscosity and diffusivity may be evaluated in the following manner: one defines a fictitious cutoff wave number k'_C (for instance $k'_C = k_C/2$). The transfers between $k < k'_C$ and the range $[k'_C, k_C]$ are evaluated directly in the simulation, while the transfers between k and the range $[k_C, +\infty]$ are calculated analytically using the E.D.Q.N.M. approximation. This is in fact the philosophy followed by the dynamic model in physical space (see below).

Figure 12.2, taken from Métais and Lesieur [496], shows the spectral eddy viscosity and diffusivity normalized by $[E(k'_C)/k'_C]^{1/2}$, in a 128^3 spectral LES

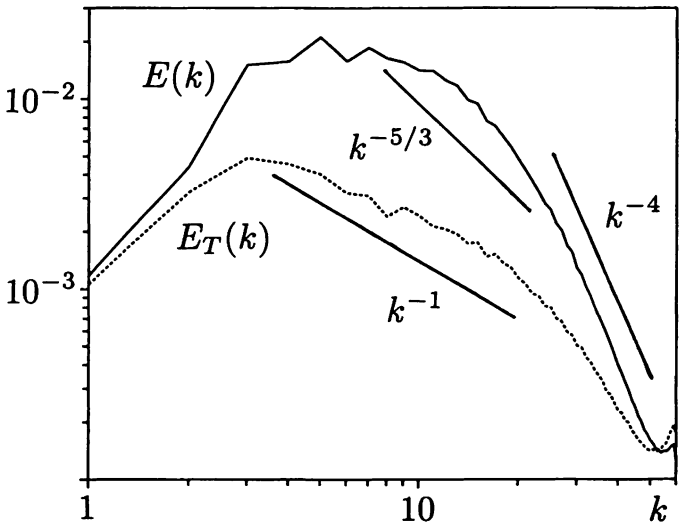

Figure 12.4. Three-dimensional isotropic decaying turbulence, resolution 128^3; kinetic energy and scalar spectra, calculated from the DNS of Métais and Lesieur [496].

of decaying isotropic turbulence.[18] The eddy viscosity displays a plateau at a value which, once corrected in order to take into account the transfers across k_C (see Métais and Lesieur [496]) is very close to the 0.267 theoretical E.D.Q.N.M. value. The cusp is somewhat eroded, due to the proximity of k_i with respect to k_C. Notice that this result is at variance with the so-called multiscale formulation of Hughes et al. [304], where a zero-plateau eddy viscosity is assumed.

The eddy diffusivity, on the contrary, has no plateau and decreases logarithmically with k. The same behaviour had been found in the calculations of Lesieur and Rogallo [421]. Figure 12.3 shows the kinetic energy and scalar spectra corresponding to Figure 12.2. Figure 12.4 shows a DNS done by Métais and Lesieur [496] in the same conditions: the k^{-1} scalar spectral range is still visible, since the shearing due to the large-scale velocity gradients may still act. Figure 12.5 shows the spectral eddy viscosity and diffusivity corresponding to Figure 12.4: the plateau of the eddy viscosity is now zero (and even slightly negative as in Domaradzki et al. [170], but the eddy diffusivity is non-zero with the same logarithmic behaviour.

[18] $k_C = 60, k_i = 20, k'_C = 30$, same parameters as for Figure 6.12. Only the explicit transfers are shown here. The molecular viscosity and conductivity are set equal to zero.

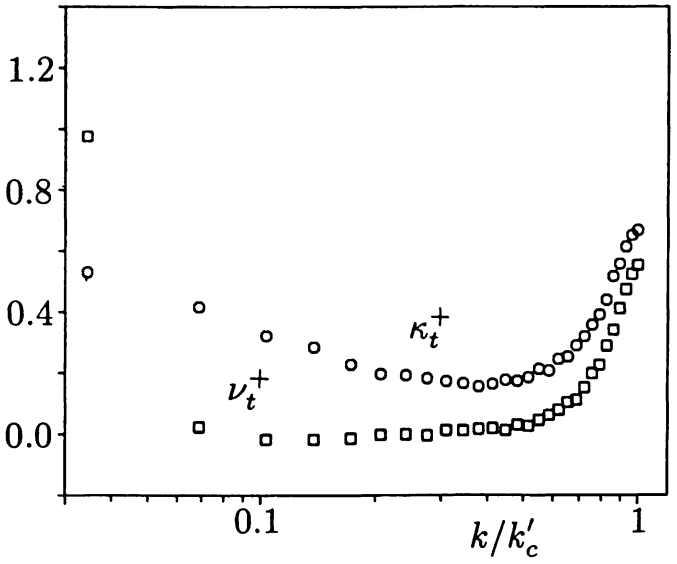

Figure 12.5. Same calculation as Figure 12.4; spectral eddy viscosity and diffusivity.

More recent LES of isotropic turbulence with animations of various fields can be found in Lesieur et al. [431].

12.3.5 Alternative approaches

Let us stress first that this eddy-viscosity subgrid-scale model is completely compatible with the energy-conservation constraints arising in the E.D.Q.N.M. equations, since it represents the whole transfers across k_C. These transfers reduce finally to an energy flux from the large eddies to the subgrid scales, which is quite expected in three-dimensional isotropic turbulence, and, as already stressed, necessary to simulate the dissipation of the energy by molecular viscosity in the dissipative scales.

Most of the above subgrid-scale modelling methods (with or without a "cusp") assume that an inertial range at modes greater than k_C exists. However, this imposes a quite high k_C, and therefore costly calculations. When k_C lies in the energy containing eddies range, the method is certainly no more valid. Other more sophisticated methods, still based on an E.D.Q.N.M. calculation of the transfers, have been developed (see Aupoix and Cousteix [22] and Chollet [119]): it is a coupled method which solves simultaneously Navier–Stokes equations in the large scales, and the E.D.Q.N.M. evolution equation for $E(k,t)$. This enables to recalculate at each step a spectral eddy viscosity

based on the actual flow spectrum, instead of assuming a fictitious Kolmogorov spectrum. The method is nevertheless quite heavy to implement, and it is perhaps not a safe horse to bet on, since it assumes also isotropy in the large scales.

An alternative formalism to derive a subgrid-scale modelling in spectral space exists, utilizing the stochastic Langevin model point of view (see e.g. Herring and Kraichnan [273]). This has been done by Bertoglio [59] who retrieves the same results as Chollet [119] in the isotropic case, and shows in the case of a homogeneous turbulence submitted to a constant shear (and thus anisotropic) the appearance of a new class of interactions sending back energy from the subgrid to the supergrid scales.[19] This could then render the use of the isotropic spectral eddy viscosity questionable in non-isotropic situations. Further comparisons between both methods have to be made in order to reach a decision. Let us mention finally the work of Yoshizawa [734], based on D.I.A. approximation, which allows also an extension of the isotropic eddy viscosity to anisotropic situations.

These LES's allow predictability studies in the isotropic case, in the following manner: Chollet [119] and Chollet and Métais [120] have considered LES of two flows $\vec{u}_1$ and $\vec{u}_2$, differing either by the resolution of the calculation (16^3 and 32^3) or by a perturbation involving modes close to k_C. Bertoglio [59] was able, with the Langevin model method, to let the error come from the subgrid scales to the large scales. Both studies show an inverse cascade of error qualitatively analogue to the closure predictions of Chapter 11, with a k^4 infrared ($k \to 0$) error spectrum. This result is very encouraging, displaying both the performances of LES and the validity of closures.

12.3.6 Spectral LES for inhomogeneous flows

The spectral eddy viscosity may be used also for inhomogeneous turbulence when pseudo-spectral methods can be employed. This was the case for the temporal mixing layers shown on Plates 9 and 10 and Figure 3.11 (see also Silvestrini [652]), with the classical plateau-cusp eddy viscosity given by Eq. (12.28). It confirms that such LES can handle the stretching of longitudinal hairpins between the big vortices. Even for the channel flow, Lamballais [367] could develop a *spectral dynamic model*: the code, already mentioned in Chapters 3 and 4, uses pseudo-spectral methods in the horizontal directions (streamwise and spanwise), and compact schemes (Padé approximants) of sixth order in the vertical direction. The eddy viscosity was calculated in each plane parallel to the walls, with the aid of Eq. (12.25), multipled by the non-dimensional plateau-cusp eddy viscosity $K(x)$ of the isotropic Kolmogorov

[19] This might be a manifestation in Fourier space of the streak growth seen in Chapter 4.

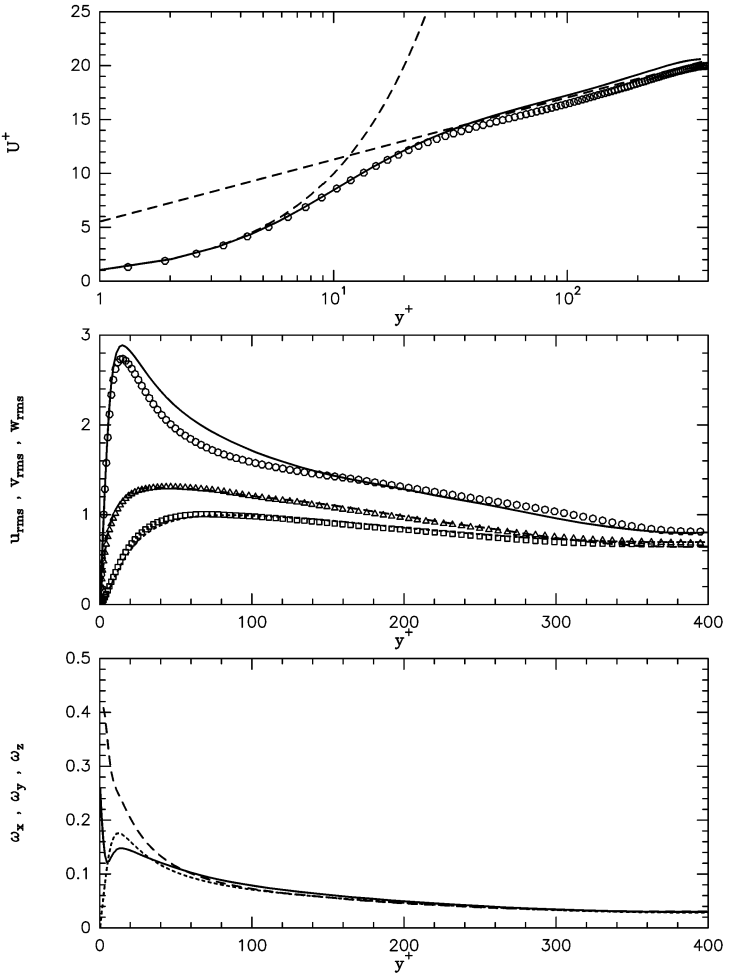

Figure 12.6. Turbulent channel flow, comparaison of Lamballais' spectral-dynamic LES (straight lines, $h^+ = 389$) with the DNS of Antonia et al. (symbols, $h^+ = 395$); (a) mean velocity, (b) r.m.s. velocity components, (c) r.m.s. vorticity components (courtesy E. Lamballais).

case (see Eq. (12.30)). This allows to take into account spectra decreasing faster than Kolmogorov, which is always the case close to the wall. At low Reynolds numbers (subcritical with respect to the linear-stability analysis), the results agree very well with experiments and DNS, both from a statistical and topological point of view (see Lesieur et al. [431]). Concerning the

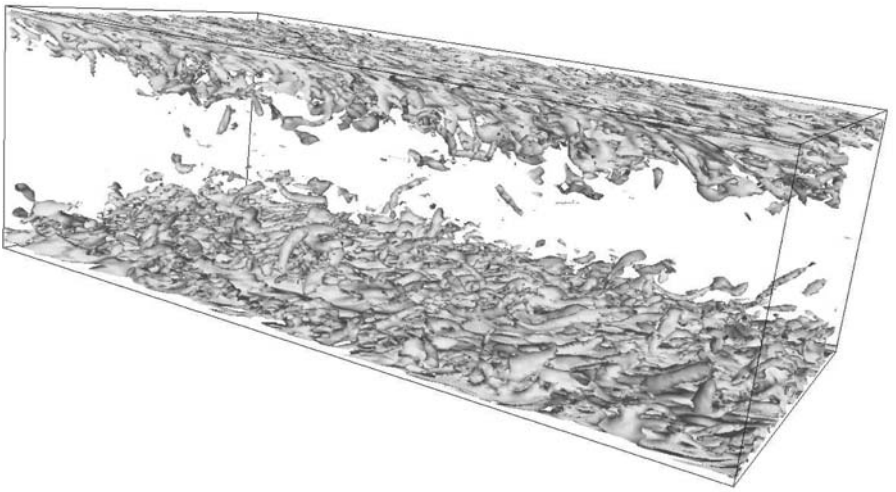

Figure 12.7. Same LES as in Figure 12.6; isosurface of the vorticity modulus; the flow goes from left to right (courtesy E. Lamballais).

supercritical case, Figure 12.6 (a and b) shows a comparison of the LES (at $h^+ = 389$) with a DNS ($h^+ = 395$) published in Antonia et al. [11]. The agreement is very good, and the LES allows to reduce the computational cost by a factor of the order of 100. Figure 12.6c displays the r.m.s. vorticity components in Lamballais' LES, with the usual behaviour already discussed above in this monograph. Remark also that LES at these Reynolds numbers display much more vortical activity in the small scales than the simulations at lower Reynolds, as Figure 12.7 shows. The small-scale activity thus predicted is susceptible of enhancing mixing or chemical reactions in LES of turbulent transport or combustion for instance.

More informations on this spectral-dynamic model may be found in Lesieur et al. [431].

12.4 New physical-space models

12.4.1 Structure-function model

This model is due to Métais and Lesieur [496]. In most practical situations, the geometry of the computational domain is too complex to permit the use of pseudo-spectral or spectral methods. One is obliged to work in physical space.

Let us consider how the spectral eddy viscosity (without cusp) can be employed in physical space. The inconvenient of an eddy viscosity of the type

(12.38) is that it is uniform in space when used in physical space. Obviously, the eddy viscosity should take into account the intermittency and inhomogeneity of turbulence: there is no need for any subgrid-scale modelling in regions of space where the flow is calm or transitional. On the other hand, it is essential to dissipate in the subgrid scales local bursts of turbulence if they become too intense. Considering also that turbulence in small scales may not be too far from isotropy, we propose to come back to the classical formulation (12.10) in physical space, the eddy viscosity being determined with the aid of Eq. (12.38), where $E(k_C, \vec{x})$ is now a local kinetic energy spectrum: this spectrum corresponds to a fictitious homogeneous turbulence which would be obtained by filling the whole space periodically with small boxes containing the flow in the neighbourhood of $\vec{x}$. The local spectrum at k_C is calculated in terms of the local second-order velocity structure function of the filtered field

$$F_2(\vec{x}, \Delta x) = \left\langle \|\overline{\vec{u}}(\vec{x}, t) - \overline{\vec{u}}(\vec{x} + \vec{r}, t)\|^2 \right\rangle_{\|\vec{r}\| = \Delta x} \tag{12.39}$$

as if turbulence is three-dimensionally isotropic, with Batchelor's formula [47]

$$F_2(\vec{x}, \Delta x) = 4 \int_0^{k_C} E(k) \left(1 - \frac{\sin(k\Delta x)}{k\Delta x}\right) dk. \tag{12.40}$$

In the original Batchelor relation (6.49), the k integral was carried out from 0 to ∞, but, here, one works with a filtered field $\bar{u}$ whose spectrum is zero above k_C. This yields, for a Kolmogorov spectrum (see Mtais and Lesieur [496], and Ducros [178])

$$\nu_t^{SF}(\vec{x}, \Delta x) = 0.105 C_K^{-3/2} \Delta x [F_2(\vec{x}, \Delta x)]^{1/2}. \tag{12.41}$$

F_2 is calculated with a local statistical average of square velocity differences between $\vec{x}$ and the six closest points surrounding $\vec{x}$ on the computational grid. In some cases, the average may be taken over four points parallel to a given plane; in a channel, for instance, the plane is parallel to the boundaries. When a scalar transported by turbulence is considered, an eddy diffusivity corresponding to a Prandtl number of 0.6 is chosen.

The structure-function model (SF) works well for isotropic turbulence, where it yields a fairly good Kolmogorov spectrum, as attested by Figure 12.8 (Métais and Lesieur [496]). It shows the compensated spectrum $\epsilon^{-2/3} k^{5/3} E(k, t)$ in the decaying case (resolution 96^3). It is approximately constant between $k = 10$ and $k = 40$, with $C_K \approx 1.4$. However the spectrum rises too much at k_C. This is certainly due to the absence of a cusp in the eddy viscosity. The kinetic-energy spectrum obtained with Smagorinsky's model ($C_S = 0.2$) is steeper than the SF spectrum and close to a k^{-2} slope. The SF pressure spectrum E_{pp} is also reported in Figure 12.8. It is compensated according to Batchelor's $k^{-7/3}$ law equation (6.91). The constant C_P is given by

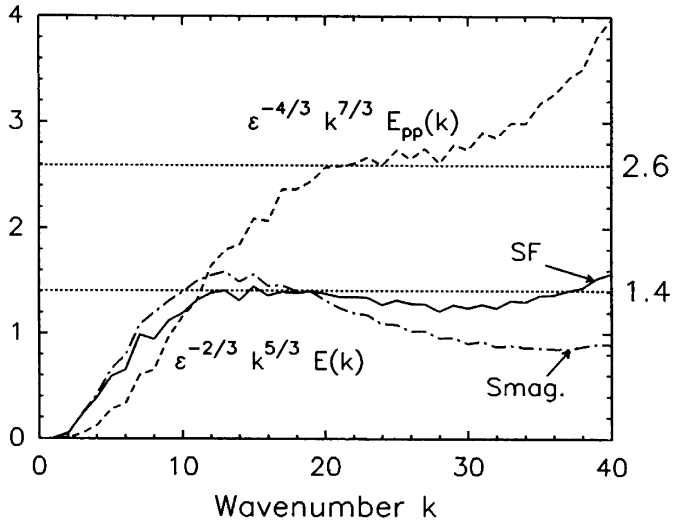

Figure 12.8. Structure-function model based LES of decaying isotropic turbulence; compensated spectra of velocity (straight line) and pressure (dashed line); Smagorinsky's ($C_S = 0.2$) velocity spectrum is also reported (courtesy O. Métais).

Eq. (6.95). In the figure, there is a tiny plateau of the compensated pressure spectrum at the right value C_P corresponding to $C_K = 1.4$. LES (or DNS) at higher resolution should be performed to elucidate the nature of the pressure spectrum in the inertial range.

The SF model gives also good qualitative results for free-shear flows: in the incompressible spatially-growing wake calculations of Gonze [261], a Karman street stretching intense longitudinal vortices was formed (see Figure 4.3 in Chapter 4). We will show in the next chapter other applications of the SF model to separated or rotating flows, and supersonic temporal boundary layers.

As with Smagorinsky's model, however, the SF model is too dissipative for transition in a boundary layer at low Mach number. This is still true within the four-point formulation in planes parallel to the wall, which eliminates the effect of the mean shear at the wall on the eddy viscosity. In fact, the spectrum $E_{\vec{x}}(k_C)$ determined by the isotropic formula (12.40) is too sensitive to the inhomogeneous low-frequency oscillations caused by the TS waves.

To overcome the difficulty with transition, two improved versions of the SF model have been developed: the selective structure-function model (SSF), and the filtered structure-function model (FSF). The dynamic procedure is another way of adapting the eddy viscosity to the local conditions of the flow. We will review the three types of models in the following subsections.

We show first how the SF model may account for the effect of non-uniform (but orthogonal) grids: let $\Delta c = (\Delta x_1 \Delta x_2 \Delta x_3)^{1/3}$ be a (geometric) mean mesh in the three spatial directions. Remembering Kolmogorov's 1941 law in physical space, which states that the second-order velocity structure-function scales like $(\epsilon r)^{2/3}$, one can in Eq. (12.41) replace Δx by Δc, with (in the six-point formulation)

$$F_2(\vec{x}, \Delta c) = \frac{1}{6} \sum_{i=1}^{3} F_2^{(i)} \left(\frac{\Delta c}{\Delta x_i} \right)^{2/3}, \tag{12.42}$$

with

$$F_2^{(i)} = \left[\|\vec{u}(\vec{x}) - \vec{u}(\vec{x} + \Delta x_i \vec{e}_i)\|^2 + \|\vec{u}(\vec{x}) - \vec{u}(\vec{x} - \Delta x_i \vec{e}_i)\|^2 \right],$$

where $\vec{e}_i$ is the unit vector in direction x_i.

One can also look at the relation of Smagorinsky's and the structure-function models when the differences in the structure-function are replaced (within a first-order approximation!) by spatial derivatives. It is found for the six-point formulation (see Comte [139]), in the limit of $\Delta x \to 0$:

$$\nu_t^{SF} \approx 0.777 (C_S \Delta x)^2 \sqrt{2 \bar{S}_{ij} \bar{S}_{ij} + \bar{\omega}_i \bar{\omega}_i}, \tag{12.43}$$

where $\overline{\vec{\omega}}$ is the vorticity of the filtered field, whereas C_S is Smagorinsky's constant defined by Eqs. (12.14) and (12.15). As stressed in Lesieur et al. [431], it shows that within stagnation regions between vortices, the SF model is about 20% less dissipative that Smagorinsky, which may favour the stretching of hairpin vortices.

12.4.2 Selective structure-function model

The selective structure-function model (SSF) was developed by David [157]. The idea is to switch off the eddy viscosity when the flow is not three-dimensional enough. The three-dimensionalization criterion is the following: one measures the angle between the vorticity at a given grid point and the average vorticity at the six closest neighbouring points (or the four closest points in the four-point formulation). If this angle exceeds 20°, the most probable value according to simulations of isotropic turbulence at a resolution of $32^3 \sim 64^3$, the eddy viscosity is turned on. Otherwise, only the molecular dissipation is active. The constant arising in Eq. (12.41) is changed, and determined with the aid of LES of freely-decaying isotropic turbulence: one requires that the eddy viscosity averaged over the computational domain should be the same in a selective structure-function model and a SF model simulation. It is found that the constant in Eq. (12.41) has to be multiplied by 1.56. A

discussion on this choice can be found in Ackerman and Métais [1] and Lesieur et al. [431]. However, it seems in practice that the original version should be preferred, as stressed by Münch et al. [527] in LES of heated channels.

The SSF model works very well for isotropic turbulence, free-shear flows, and wall flows (without or with thermal transfers). The reader is referred to Lesieur et al. [431] for more details. Examples of application to a backward-facing step and a compression ramp at Mach 2.5 will be given in Chapter 13.

The SSF model depends however upon the most probable angle of the next neighbours average vorticity, chosen above equal to 20°. In fact, this angle is a function of the resolution of the simulation, since it should go to zero with Δx, and may be with the type of flow considered. Progresses in this model should be made by adjustment of this angle to the local grid.

12.4.3 Filtered structure-function model

This FSF model was developed by Ducros [178] and applied to transition in a spatially-developing boundary layer on an adiabatic flat plate at Mach 0.5. Here, the filtered field $\bar{u}_i$ is submitted to a high-pass filter in order to get rid of low-frequency oscillations which affect $E_{\vec{x}}(k_C)$ in Eq. (12.41). The high-pass filter is a Laplacian discretized by second-order centered finite differences and iterated three times. It was shown by Ducros [178] that, for some three-dimensional random or turbulent isotropic test fields, the spectrum of the high-pass filtered field is

$$\frac{\tilde{E}(k)}{E(k)} \approx 40^3 \left(\frac{k}{k_C}\right)^9 . \tag{12.44}$$

This is different from the $(k^4)^3$ law one should expect from an iterated Laplacian, the loss being due to the finite-difference scheme.[20] On the other hand, the second-order velocity structure function of the filtered field satisfies an equation analogous to Eq. (12.40):

$$\tilde{F}_2(\vec{x}, \Delta x) = 4 \int_0^{k_C} \tilde{E}(k) \left(1 - \frac{\sin(k\Delta x)}{k\Delta x}\right) dk. \tag{12.45}$$

Substituting Eq. (12.44) into Eq. (12.45), and replacing $E(k)$ by a Kolmogorov spectrum, one can determine $\tilde{F}_2(\vec{x}, \Delta x)$ in terms of a spectrum $E(k_C)$ which is no more sensitive to the low wavenumber fluctuations, which yields

$$\nu_t^{FSF}(\vec{x}, \Delta x) = 0.0014 C_K^{-3/2} \Delta x [\tilde{F}_2(\vec{x}, \Delta x)]^{1/2}. \tag{12.46}$$

[20] This shows that finite-difference methods up to the fourth order (the latter being used by Ducros [178]) cannot deal with high-order Laplacian operators.

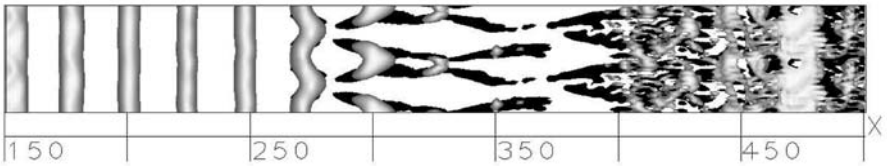

Figure 12.9. FSF structure-function based LES of a weakly-compressible spatially-developing boundary layer; isosurfaces of pressure ($p = 0.999p_\infty$, grey) and longitudinal vorticity ($\omega_1 = \pm 0.1 U_\infty \delta_i$, dark) are shown (courtesy F. Ducros).

This works well for both isotropic turbulence and transition in a spatially-developing boundary layer. This simulation (see Ducros et al. [180]) was done in a weakly-compressible case at $M_\infty = 0.5$, for an adiabatic plate. The upstream boundary conditions consist in the superposition of a Blasius velocity profile and TS waves plus a three-dimensional white noise of same amplitude as the waves. The Reynolds number based upon the upstream displacement thickness Reynolds is 1000. The numerical methods are the fourth-order Mac Cormack scheme (see Normand and Lesieur [538] for details). The resolution is $650 \times 32 \times 20$ in the streamwise, transverse and spanwise directions. A top view of the low pressure and longitudinal vorticity in the transitional region is shown in Figure 12.9: just before the transition, TS waves give rise to straight lower pressure quasi two-dimensional rolls. During the transition, these rolls evolve into a staggered pattern which breaks down into turbulence. Meanwhile the longitudinal velocity organizes into the low- and high-speed streaks already discussed in Chapter 4 (see Figure 12.10).

We have seen in Chapter 4 (Plate 18) examples of hairpin vortices ejected away from the wall in this simulation. Plate 20 presents an enlarged view of the turbulence structure just after transition, with (weak) longitudinal haipins above the wall. A longitudinal vertical cross section shows the spanwise vorticity distribution. An animations in Lesieur et al. [431] proves that these vortices travel downstream with the flow.

We recall that Kleiser and Zang [336] have been able to carry out a DNS in order to simulate the early stages of transition above a flat plate, but afterwards the simulation blows up due to insufficient resolution. As already stated, the flow remains laminar with the classical Smagorinsky or SF models. The FSF model is however not "perfect" for the prediction of average quantities. In Ducros et al. [180], the calculation overestimates of about 15% the mean velocity in the logarithmic profile.[21] The same happens when it is

[21] An analogous calculation at Mach 0.3 with a finer resolution at the wall was done by Briand [82]. Details are given in Lesieur et al. [431].

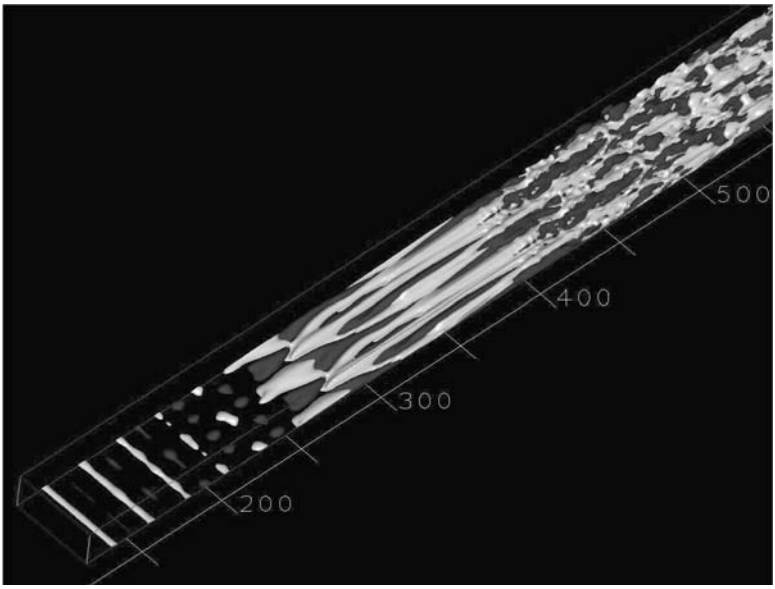

Figure 12.10. Same calculation as Figure 12.9; isosurfaces of longitudinal velocity fluctuations ($u_1' = 0.024U_\infty$, grey).

applied to the incompressible channel (see Lesieur et al. [431]). In the latter case, the spectral dynamic model presented above works better.

We have shown in Plate 17 and Figure 4.2 examples of applications of the FSF model to a spatially-developing incompressible mixing layer, with at the inflow a hyperbolic-tangent velocity profile plus a weak quasi two-dimensional (Plate 17) or three-dimensional (Figure 4.2) random perturbation. Here the molecular Reynolds number is infinite. We come back now to the simulation of Plate 17, and compare it to a SF simulation done in the same conditions. The comparison is shown in Figure 12.11, presenting isosurfaces of the vorticity modulus (threshold: two-thirds of the maximum initial spanwise vorticity). Kelvin-Helmholtz vortices are produced, and stretch intense longitudinal hairpins. However, in the FSF case, the upstream vortex sheet is about half as long as for the SF, pairing occurs much faster, and there are more longitudinal vortices in the spanwise direction. Other comparisons of this type can be found in Lesieur et al. [431].

12.4.4 Scale-similarity and mixed models

The eddy-viscosity closures assume a one to one correlation between the subgrid-scale stress and the large-scale deformation tensors. The analysis

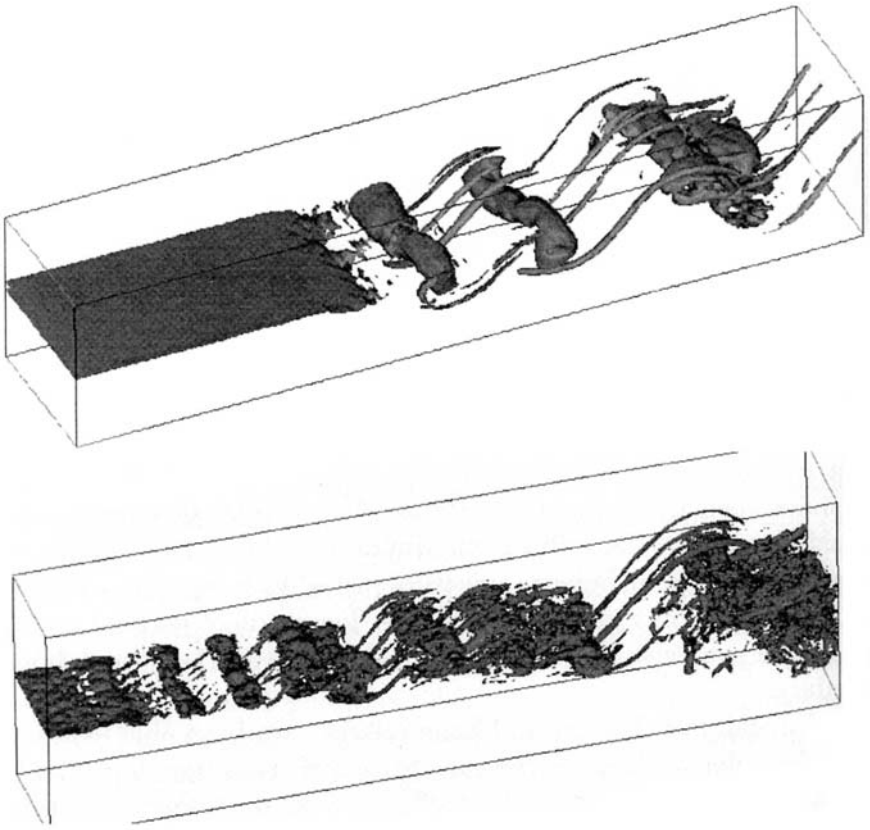

Figure 12.11. (a) SF simulation vs (b) FSF simulation of a spatially-developing mixing layer (courtesy J. Silvestrini).

of fields obtained from DNS has, however, displayed very little correlation between the two tensors (see e.g. Clark et al. [128], McMillan and Ferziger [477]). This has led Bardina et al. [32] to propose an alternative subgrid-scale model called the scale-similarity model. This is based upon a double filtering approach and on the idea that the important interactions between the resolved and unresolved scales involve the smallest eddies of the former and the largest eddies of the latter. They suggest to evaluate the subgrid tensor as:

$$T_{ij} = \bar{\bar{u}}_i \bar{\bar{u}}_j - \overline{\bar{u}_i \bar{u}_j}. \tag{12.47}$$

DNS and experiments (Bardina et al. [32], Liu et al. [452]) show that the modelled subgrid-scale stress deduced from Eq. (12.47) is well correlated with

the real stress. However, it is only weakly dissipative as far as the kinetic energy is concerned. It was thus combined with an eddy-viscosity type model such as Smagorinsky's model to produce the mixed model. In the line of Bardina's model, new formulations have been proposed to correct this lack of dissipation. Goutorbe et al. [263] and Liu et al. [452] have proposed the following models:

$$T_{ij} = C_L \left(\tilde{\bar{u}}_i \tilde{\bar{u}}_j - \widetilde{\bar{u}_i \bar{u}_j} \right), \tag{12.48}$$

where C_L is a dimensionless coefficient. The models differ through the operator $\tilde{\cdot}$ which consists either in a space average (Goutorbe et al. [263]) or in a second filter of different width (Liu et al. [452]). This concept of double filtering is not far from the dynamic models presented below.

12.4.5 Dynamic model

We have already noted for Kraichnan's spectral eddy viscosity that the parameters defining it could be computed from a LES with a cutoff k_C, by defining a fictitious cutoff $k'_C = k_C/2$, and explicitly calculating the transfers across k'_C (Lesieur and Rogallo [421]). This is the underlying philosophy of the dynamic model (Germano et al. [247], see also Germano [248]), when transposed in physical space. The method relies on a LES using a "base" subgrid-scale model such as Smagorinsky's model,[22] with a grid mesh Δx. The computed fields $\bar{f}$ are filtered by a "test filter" $\tilde{\cdot}$ of larger width $\alpha \Delta x$ (for instance $\alpha = 2$), to yield the field $\widetilde{\bar{f}}$. If one applies the double filter to Navier–Stokes equations (with constant density), the subgrid-scale tensor of the field $\widetilde{\bar{u}}$ is readily obtained from Eq. (12.6) with the replacement of the filter "bar" by the double filter "bar-tilde", that is:

$$\mathcal{T}_{ij} = \widetilde{\bar{u}}_i \widetilde{\bar{u}}_j - \widetilde{\overline{u_i u_j}} \, . \tag{12.49}$$

We consider now the following resolved turbulent stress corresponding to the test-filter applied to the field $\bar{u}$:

$$\mathcal{L}_{ij} = \widetilde{\bar{u}}_i \widetilde{\bar{u}}_j - \widetilde{\bar{u}_i \bar{u}_j}. \tag{12.50}$$

Finally we apply the filter "tilde" to Eq. (12.6), to yield

$$\widetilde{T_{ij}} = \widetilde{\bar{u}_i \bar{u}_j} - \widetilde{\overline{u_i u_j}}. \tag{12.51}$$

Adding Eqs. (12.50) and (12.51) gives, using Eq. (12.49)

$$\mathcal{L}_{ij} = \mathcal{T}_{ij} - \widetilde{T_{ij}}, \tag{12.52}$$

[22] However it may be used with other subgrid models such as the SF model (see Lesieur et al. [431] for details).

called Germano's identity. In this expression, $\mathcal{T}_{ij}$ and $\widetilde{T_{ij}}$ have to be modelled, while $\mathcal{L}_{ij}$ can be explicitly calculated by applying the test filter to the base LES results. Using Smagorinsky's model, we have from Eqs. (12.10) and (12.14)

$$\widetilde{T_{ij}} - \frac{1}{3}\widetilde{T_{ll}}\delta_{ij} = 2\widetilde{\mathcal{A}_{ij}C}, \tag{12.53}$$

whith $C = C_S^2$ and

$$\mathcal{A}_{ij} = (\Delta x)^2 |\bar{S}| \bar{S}_{ij}. \tag{12.54}$$

Still using Smagorinsky, we have

$$\mathcal{T}_{ij} - \frac{1}{3}\mathcal{T}_{ll}\delta_{ij} = 2\mathcal{B}_{ij}C, \tag{12.55}$$

whith

$$\mathcal{B}_{ij} = \alpha^2(\Delta x)^2 |\tilde{\bar{S}}| \tilde{\bar{S}}_{ij}. \tag{12.56}$$

$|\tilde{\bar{S}}|$ and $\tilde{\bar{S}}_{ij}$ are the quantities analogous to $|\bar{S}|$ and $\bar{S}_{ij}$ built with the doubly-filtered field $\tilde{\bar{u}}$. Substracting Eq. (12.53) from Eq. (12.55) yields with the aid of Eq. (12.52)

$$\mathcal{L}_{ij} - \frac{1}{3}\mathcal{L}_{ll}\delta_{ij} = 2\mathcal{B}_{ij}C - 2\widetilde{\mathcal{A}_{ij}C}. \tag{12.57}$$

In order to obtain C, many people remove it from the filtering as if it were constant, leading to

$$\mathcal{L}_{ij} - \frac{1}{3}\mathcal{L}_{ll}\delta_{ij} = 2CM_{ij}, \tag{12.58}$$

with

$$M_{ij} = \mathcal{B}_{ij} - \widetilde{\mathcal{A}_{ij}}. \tag{12.59}$$

Now, all the terms of Eq. (12.58) can be determined with the aid of $\bar{u}$. There are however five independent equations for only one variable C, and the problem is overdetermined.

Two alternatives have been proposed to deal with this undeterminacy. A first solution (Germano [247]) is to contract Eq. (12.58) by $\bar{S}_{ij}$ to obtain

$$C = \frac{1}{2}\frac{\mathcal{L}_{ij}\bar{S}_{ij}}{M_{ij}\bar{S}_{ij}}, \tag{12.60}$$

since, due to incompressibility, $\bar{S}_{ij}$ is traceless. This permits in principle to "dynamically" determine the "constant" C as a function of space and time, to be used in the LES of the base field $\bar{u}$. In tests using channel flow data obtained from direct numerical simulations, it was however shown by Germano et al. (1991) that the denominator in Eq. (12.60) could locally vanish or become sufficiently small to yield computational instabilities. To get rid of this problem, Lilly [447] chose to determine the value of C which "best satisfies"

the system (12.58) by minimizing the error using a least squares approach. It yields

$$C = \frac{1}{2}\frac{\mathcal{L}_{ij}M_{ij}}{M_{ij}^2}. \tag{12.61}$$

This removes the undeterminacy of Eq. (12.58). Under this form, the dynamic model has been used by Piomelli [574] and Sreedhar and Ragab [664].

The analysis of DNS (Lund et al. [457]) and experimental (Liu et al. [452]) data revealed, however, that the C field predicted by the models (12.60) and (12.61) varies strongly in space and contains a significant fraction of negative values, with a variance which may be ten times higher than the square mean. So, the removal of C from the filtering operation is not really justified and the model exhibits some mathematical inconsistencies (see Ghosal et al. [254]). The possibility of negative C is an advantage of the model since it allows a sort of backscatter in physical space, but very large negative values of the eddy viscosity is a destabilizing process in a numerical simulation, and a non-physical growth of the resolved scale energy has been often observed (Lund et al. [457]). The cure which is often adopted to avoid excessively large values of C consists in averaging the numerators and denominators of Eqs. (12.60) and (12.61) over space and/or time, thereby losing some of the conceptual advantages of the "dynamic" local formulation. Averaging over direction of flow homogeneity has been a popular choice, and good results have been obtained by Germano et al. [247] and Piomelli [574], who took averages in planes parallel to the walls in their channel flow simulation.[23] They showed that the dynamic model gives a zero subgrid-scale stress at the wall, where L_{ij} vanishes, which is a great advantage with respect to the original Smagorinsky model; it gives also the proper asymptotic behavior near the wall. Comparisons with DNS at Reynolds number 3300 (based upon the centerline velocity and the channel half-width) and with experiments at high Reynolds number are very good. Notice again that the use of Smagorinsky's model as a base for the dynamic procedure is not compulsory, and any of the models described in the present paper can be a candidate. As examples, Zang et al. [737] have applied the dynamic procedure to the "mixed" model (see above). El-Hady and Zang [185] have done it for the structure-function model applied to a compressible boundary layer above a long cylinder.

As stressed in Lesieur et al. [431],

> Meneveau et al. [485, 486] adopted a Lagrangian viewpoint, and obtained good results in a dynamic Smagorinsky approach where the constants C was averaged following the flow motion (see also Piomelli

[23] Remark that the same thing has been done, with success, when averaging the spectral eddy viscosity (see the above-mentioned work of Lamballais [366]).

et al. [576, 577]). This is in fact more physical as far as coherent vortices are concerned.

12.4.6 Other approaches

Some details on hyperviscosities (plain and generalized) may be found in Lesieur et al. [431]. For other developments using in particular de-filtering approaches, the reader is referred to Geurts [251, 252].

A very important application of numerical simulations concerns combustion. For the non-premixed case, interesting reviews can be found in Vervisch and Poinsot (DNS) [700] and Riley (LES) [604]. Veynante and Vervisch [701] have also carried out a complete review of turbulent combustion modeling, including RANS and LES approaches.

The three-dimensional numerical simulations modelling the interaction of vortex filaments via Biot and Savart laws and already mentioned in Chapter 2 (Leonard [407], Chorin [123], Meiburg [483]) need also some sort of subgrid-scale modelling, necessary when a vortex tube is too much distorted and develops oscillations of length scale smaller than the spatial resolution of the calculation: these small scales are removed by a smoothing, whose dynamical significance in terms of subgrid-scale parameterization is not completely clear. Developments in this direction have been done by Cottet and Koumoutsakos [148], with applications to wake control.

We mention also the cellular automata methods, which are based on the statistical mechanics of a *lattice gas* (see e.g. Frisch et al. [227,229], d'Humières et al. [167]): instead of discretizing the real continuous flow equations on a grid, as was done in the classical techniques of direct or large-eddy simulations, the method calculates explicitly the motions of the particles of a fictitious gas, these particles being allowed to travel on a regular grid from one point to one of its neighbours with the same velocity modulus V. Sometimes they may also remain stationary on the same site. The above quoted two-dimensional calculations are made with a triangular array of points. The collision laws between the particles are chosen in such a way that a "macroscopic velocity" $\bar{u}$, calculated as an average on all the particles lying at a given time inside a " macroscopic site" including a given number of individual grid points, should follow Navier–Stokes equations.[24] When programmed on classical vectorial computers, these methods allow one to reproduce Karman vortex streets in times of the order (larger, however) of the finite-differences

[24] This result supposes however certain validity conditions, as the assumption of a "Mach number" of the theory $\bar{u}/V$ small compared with one, which are not fulfilled in the numerical applications. Then, and since the "macroscopic velocities" do not in practice follow exactly Navier–Stokes equations, the philosophy of the lattice-gas method could be closer to the LES one than to the DNS.

or spectral-methods computational times. Three-dimensional calculations of this type are now at hand, and are used in car industry.

12.5 LES of two-dimensional turbulence

Since meteorologists played a great role in the development of computational fluid dynamics in quasi two-dimensional situations, it is in this context that the subgrid-scale modelling problem was posed, by Smagorinsky [653] for instance. The problem is far from being solved, but empirical recipes have been developed, which seem to work quite well (if the cutoff is in the enstrophy cascade) in comparison with the other physical processes to be parameterized in the global atmospheric prediction models.

Let us consider a flow which, for some reason, is quasi two-dimensional in the large scales and three-dimensional in the small scales, and assume that the cutoff wave number k_C in the LES corresponds to quasi two-dimensional scales. Then the subgrid-scale modelling to be developed has to take into account the two-dimensional dynamics of the large scales (conservation of kinetic energy and enstrophy) on the one hand, and also possible interactions with small-scale three-dimensional turbulence on the other hand. It is then difficult at this level to know whether the subgrid-scale modelling to use has to consider the small-scale three-dimensional point of view (and then employ methods presented above), or the two-dimensional point of view. Smagorinsky's example illustrates this point, and it has been remarked by Herring [278] that

> N.A. Phillips [571], in one of the first numerical experiments treating the general circulation of the atmosphere, introduced an eddy viscosity A whose value was chosen in accordance with Richardson's empirical law $A = 0.2(\Delta x)^{4/3}$.

This law concerns three-dimensional turbulence, and it is clear that such a subgrid-scale model was not much concerned with the still unknown enstrophy cascade dynamics.

Let us take now the point of view of strictly two-dimensional turbulence in the context of two-dimensional Navier–Stokes equations: if k_C lies in the enstrophy cascade, the parameterization of the small scales needs to ensure both a constant enstrophy flux and a zero kinetic energy flux through k_C. The two constraints are very difficult to satisfy: a method calculating the fluxes with the aid of the E.D.Q.N.M. approximation, and paralleling the one developed above in three dimensions, was proposed by Basdevant et al. [37]. The resulting LES gave "satisfactory" spectral results,[25] but appeared to strongly affect the

[25] Satisfactory, for those who believe in the enstrophy-cascade concept.

shape of the spatially-organized eddies characteristic of two-dimensional turbulence (Basdevant and Sadourny [40]). More empirical techniques were then developed, generalizing the *biharmonic dissipation* operator $-\nu_1(\nabla^2)^2\omega$ used by the oceanographers in the r.h.s. of the vorticity equation (Holland [287]). Thus Basdevant and Sadourny [40] performed a systematic study of LES with a subgrid-scale diffusion operator (in the vorticity equation) proportional to $-(-\nabla^2)^\alpha\omega$, and came to the conclusion that the "optimal value" of α was of the order of $4 \sim 8$ (the value of 2 already giving much better results than the "viscous" value $\alpha = 1$). An application to the simulation of a mixing layer has been presented in Chapter 8. The consequence of these modified dissipativities is, with an adjustment of the numerical constant, to push the effects of dissipation in the neighbourhood of k_C, as can be understood easily when looking at the expression $\sim -k^{2\alpha}\hat{\omega}$ of the dissipative term in Fourier space. It seems difficult for numerical reasons at these quite low resolution calculations to increase the value of α above 8. Let us mention also another method, called the *anticipated potential vorticity method* (Sadourny and Basdevant [620]), which may be useful in quasi-geostrophic turbulence when the mesh size Δx is larger than the internal Rossby radius of deformation.

To conclude this section, it seems that the development of computers allows DNS of two-dimensional flows at high Reynolds numbers. But we have also shown in the chapter devoted to two-dimensional turbulence that LES using hyperviscosities may be very helpful as well.

13

Towards "Real World Turbulence"

13.1 Introduction

Up to now, the analytical statistical theories we have considered concerned mainly[1] what one could call *ideal turbulence*, in the sense that isotropy was nearly always assumed, either in three or in two dimensions. We have, however, also discussed in Chapter 3, 4 and 12 the dynamics of more realistic flows, in the context of transition and coherent vortices in particular. We have chosen in this last chapter to consider four examples of turbulent flows which have a great practical importance, and which may be considered as prototypes for the applications of certain concepts, analysis and techniques developed in the preceding chapters.

The first problem envisaged here will be that of a three-dimensional homogeneous turbulence submitted to a stable stratification. This is no longer an isotropic turbulence, and we will mainly focus on what happens if an isotropic turbulence is created in a stably-stratified fluid, through some external device which afterwards will be suddenly turned off. This problem has important applications in meteorology and oceanography. The study of this question will permit the use of some of the isotropic phenomenological results derived above, and also enable us to see how three-dimensional isotropic dynamics is modified by buoyant forces. In particular we will show how the spectral eddy viscosity and eddy diffusivity derived in Chapter 12 can be used during the initial stage of decay.

The second problem will be the effect of a solid-body rotation upon turbulence. The effects of rotation on flows have been already looked upon at several occasions in the book. Here we will consider both homogeneous or

[1] Except for the mixing-length theory of turbulent shear flows considered in Chapter 6.

sheared turbulence. This has applications in geophysical flows as well as in engineering (turbomachinery).

The third problem will deal with separated flows, such as the backward-facing step, extremely frequent in aerodynamics. Large-eddy simulation techniques are now able to handle these flows both statistically and from the coherent-vortex point of view.

Finally we will look at the effects of compressibility and density differences upon turbulence, with some applications to subsonic and supersonic aerodynamics.

We will also provide a tentative conclusion of this monograph.

13.2 Stably-stratified turbulence

13.2.1 The so-called "collapse" problem

The problem of the evolution of an initially three-dimensional isotropic turbulence submitted to the action of a stable stratification is of essential concern for the *mesoscale atmosphere*,[2] and the ocean, where it governs the vertical fluxes of temperature for instance.

To illustrate this point, let us consider the experiment where a grid is pulled horizontally with a velocity U through a channel initially containing a stably-stratified fluid with a constant Brunt-Vaisala frequency, or equivalently when the stratified fluid flows through a fixed grid with the velocity U (Stillinger et al. [672]). The phenomenological theory of what happens first has been given by Riley et al. [600]. The grid produces in its close neighbourhood a three-dimensional turbulence of typical velocity and scale U_1 and D_1, and one can assume that this turbulence is negligibly affected by stratification. This corresponds to an initial Froude number[3] $F_1 = U_1/ND_1$ which is large with respect to 1. Further from the grid, the turbulent velocity will decay with time t, due to the dissipative action of turbulence. The characteristic scale D will increase. It was shown in Chapter 6 that the ratio U/D decays like t^{-1} for isotropic three-dimensional turbulence at high Reynolds number. Therefore the instantaneous Froude number U/ND will be proportional to $(Nt)^{-1}$, as far as tubulence is not significantly affected by stratification. It will reach

[2] That is, the atmospheric motions between one km to a few hundred kilometers.

[3] In a flow of dimension D and velocity U, the Froude number $F = U/(ND)$, already introduced at numerous occasions before, measures the relative importance of inertial effects (characterized by a frequency U/D) over stratification effects (characterized by the Brunt-Vaisala frequency of gravity waves N). Thus, high Froude numbers correspond to a negligible influence of stratification, while the latter is preponderant at low Froude.

values of order unity in a time of the order of N^{-1}. Stratification effects will then appear, with the propagation of internal-gravity waves.

The characteristic scales of the problem are the integral scale $l = v^3/\epsilon$, and a characteristic scale of stratification l_B. The latter is obtained by defining a turbulent velocity $(\epsilon l_B)^{1/3}$ such that the associated Froude number $(\epsilon l_B)^{1/3}/N l_B = 1$. This yields

$$l_B = \left(\frac{\epsilon}{N^3}\right)^{1/2}. \tag{13.1}$$

This scale is generally referred to as the Osmidov scale (Osmidov [555]), and corresponds to a balance between inertial and buoyant effects. Since the local Froude number of turbulence $F = v/Nl$ is equal to $\epsilon^{1/3}/Nl^{2/3}$, one obtains the important relation

$$F = \left(\frac{l_B}{l}\right)^{2/3} \tag{13.2}$$

which shows that stratification has a negligible effect on turbulence if $l \ll l_B$, and becomes dynamically important when the eddies are of the order of or greater than the Osmidov scale. During this evolution, the integral scale of turbulence will grow, according to the laws derived in Chapter 7 ($t^{0.3} \approx t^{0.5}$), and Osmidov scale will decay like $\epsilon^{1/2}$. Both scales will collapse when the Froude number is one. Further evolution is difficult to predict by phenomenology.

At low Froude number, stratification becomes preponderant. It is understandable that it will limit the amplitude of vertical fluctuations at a value $\approx l_B$. On the other hand, stratification has no effect on quasi two-dimensional motions which develop horizontally. One may then expect at high Reynolds numbers important horizontal nonlinear transfers. Riley et al. [600] carried out an expansion of Boussinesq equations with respect to the Froude number. If the latter is sufficiently small, this procedure may lead, in certain conditions, to two-dimensional Navier–Stokes equations for a given horizontal level. One is then led to the concept of "gravitational collapse of turbulence" into horizontal "pancake-shaped eddies" (Maxworthy [475]) of thickness l_B. This turbulence is not, properly speaking, a two-dimensional turbulence as was defined in Chapter 8, since it is not independent of z. Here, the correct term should be *horizontal turbulence*, since these horizontal layers are more or less vertically decorrelated, and hence depend upon the z direction. Some authors call this *quasi two-dimensional turbulence*.

Thus, in the atmosphere, small-scale three-dimensional turbulence, produced e.g. by the breaking of lee waves behind the mountains or by convective storms, may find itself afterwards imbedded in a stably-stratified density field and collapse into quasi two-dimensional turbulence. This idea has been used by

Gage [236] and Lilly [443] to envisage the existence of a small-scale (a few kilometers) quasi two-dimensional forcing in the atmosphere, which would feed an inverse horizontal $k^{-5/3}$ energy cascade responsible for the atmospheric mesoscale energy spectrum and extending up to several hundred kilometers. Such a spectrum has been measured experimentally by Gage and Nastrom [237], on the basis of velocity records statistics provided by commercial aircrafts. This is at variance with the EOLE[4] experiment conclusions of a k^{-3} spectrum extending from 1000 to 100 km (Morel and Larchevêque [521]). This question of atmospheric mesoscale turbulence structure is extremely open: vertical soundings of the atmosphere seem to confirm the fact that turbulence is concentrated into multiple extremely thin horizontal layers, which could be an argument favouring the inverse cascade theory. Notice however that such a structure is sometimes interpreted by the physicists of the "middle atmosphere" as due to the vertical propagation of gravity waves.

In the ocean, the interaction of gravity waves with three-dimensional turbulence involves various complex phenomena which contribute to the formation of the mixed layer and are responsible for vertical exchanges arising in this layer and at the level of the thermocline. Among these mechanisms are again the breaking of internal waves into small-scale turbulence, and the reorganization of this turbulence into waves and possibly horizontal motions. Notice that in the experiment of Gargett et al. [240], already quoted as an evidence of a small-scale Kolmogorov energy spectrum in the ocean, turbulence was actually due to the breaking of internal waves. The evolution of this turbulence under stratification was then examined, in such a way that these measurements are an oceanic counterpart of the grid-stratified turbulence experiments done by Stillinger et al. [672], Itsweire et al. [312], Lienhard and Van Atta [437] and Thoroddsen and Van Atta [687].

Many other laboratory experiments have been carried out on this problem (see e.g. Hopfinger [297], for a review). A particularly impressive result was obtained by Pao [561], who showed that the wake of a spherical obstacle in a stably-stratified flow, initially three-dimensional behind the obstacle, would suddenly collapse into a thin horizontal Karman-like vortex street.

In LES (using hyper-viscosity and conductivity) of Boussinesq equations (see details below) forced quasi two-dimensionally (no z dependence except for a small three-dimensional white noise), Herring and Métais [283] showed a quasi two-dimensional behaviour of the flow with the development of pancake-like horizontal layers characterized by strong vertical gradients of horizontal velocity. This is shown in Figure 13.1, which presents isosurfaces of horizontal

[4] In this experiment, 500 constant-level 200 mb balloons were released in the southern hemisphere, and tracked with the aid of the EOLE satellite: statistics on their relative dispersion then allowed approximate measurements of the energy spectrum.

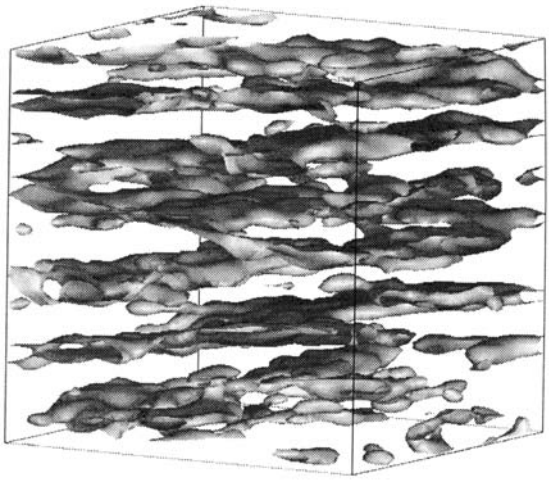

Figure 13.1. Horizontal vorticity isosurfaces in LES of stratified turbulence forced quasi two-dimensionally (courtesy O. Métais).

vorticity obtained in such a simulation at a Froude number 0.1. The vertical mixing layers thus created cause a strong vertical dissipation which inhibits any important inverse energy cascade within the horizontal layers, as can be checked in the simulations.[5] A similar structure of quasi horizontal vortex sheets was found in experiments by Fincham et al. [205], where a rake of vertical rods was towed through a horizontal stratified tank. In this experiment, the vorticity was determined with the aid of DPIV techniques.[6] More recent experiments of the same type in a stratified flow by Praud et al. [588] carried out in Grenoble large Coriolis rotating platform facility[7] confirm the pancake structure. Notice the strong resemblance between the horizontal vorticity layers of Figure 13.1 and the cirrus clouds which form in a stably-stratified atmosphere.

It was also shown by Métais et al. [500], still with LES, that the combination of solid-body rotation and stratification imposed upon a forced three-dimensional isotropic turbulence (at Rossby and Froude 0.1) led to a very strong $k^{-5/3}$ inverse kinetic energy cascade. This cascade is highly three-dimensional, and has all the characteristics of Charney's quasi geostrophic turbulence discussed in Chapter 9. Vertical-vorticity measurements of Praud et al. [588] in the rotating case show how the rake wake, formed initially of

[5] Remark that an analogous non-stratified simulation with the same initial state leads to an inverse cascade of two-dimensional turbulence.

[6] Digital particle image velocimetry.

[7] In the non-rotating case.

vertical vortices of both signs, evolves into large three-dimensional vortices. At low Rossby number, they find a k_h^{-3} kinetic-energy spectrum for the horizontal wave number.

13.2.2 Numerical approach to the collapse

We consider a fluid satisfying Boussinesq equations in their simplest form. Let $\vec{g} = -g\vec{z}$ be the gravity. We suppose that $\bar{\rho}_*$ is only function of z, with a constant Brunt-Vaisala frequency N, and neglect rotation. It is easy to check from Eq. (2.112) that the fluid satisfies

$$\begin{aligned} \frac{D\vec{u}}{Dt} &= -\vec{\nabla}\tilde{p} + \vartheta\vec{z} + \nu\nabla^2\vec{u} \\ \vec{\nabla}.\vec{u} &= 0 \\ \frac{D\vartheta}{Dt} + N^2 w &= \kappa\nabla^2\vartheta, \end{aligned} \tag{13.3}$$

where $\vartheta = -\tilde{\rho}g$. The assumption that N is a constant is certainly not fulfilled in the atmospheric or oceanic situations mentioned above, but is a very useful step in order to understand the physics of these complex interactions between turbulence and waves.

Now statistical homogeneity is assumed. The potential energy is

$$E_p = \frac{1}{2}N^{-2}\langle\vartheta^2\rangle$$

and it is very easy to check from Eqs. (13.3) that the total energy

$$\frac{1}{2}\langle\vec{u}^2\rangle + E_p$$

is conserved by nonlinear terms of the equations. But, as in three-dimensional isotropic turbulence, these quantities might be dissipated at a finite rate by viscosity and conductivity. Notice in particular that when the Froude number is large and that buoyancy may be neglected, the potential energy is proportional to the variance of the passive scalar ϑ, and decays according to the laws derived in Chapter 7.

This problem has first been studied, at a Prandtl number ν/κ of one, with the aid of DNS by Riley et al. [600], using a spectral code of 32^3 modes, and starting initially with an isotropic velocity field. The Reynolds number was of course much smaller than in laboratory experiments. It turned out that kinetic energy kept on being dissipated, as in isotropic turbulence, for times greater than N^{-1}, without any marked transition (or "collapse") at N^{-1}.

More specifically, the kinetic energy decay curve exhibited a wavy tendency, which could be attributed to the appearance of waves.

The same calculation was performed by Métais [491] within a LES in spectral space using the plateau-cusp eddy viscosity and diffusivity defined in Chapter 12, and starting initially from a turbulent Froude number of 3, close to the experimental value of Itsweire et al. [312]. The use of such an isotropic subgrid-scale parameterization can be justified in the early stage of the evolution,[8] since then subgrid-scale turbulence is negligibly affected by stratifiction. The results thus obtained have been interpreted in terms of the vortex-wave decomposition (or Craya decomposition) presented in Chapter 5, and in particular the "vortex kinetic energy" and the "wave kinetic energy", respectively

$$\bar{\Phi}_1(t) = \int (e - Z_1) d\vec{k}; \bar{\Phi}_2(t) = \int (e + Z_1) d\vec{k},$$

introduced after Eq. (5.113) for axisymmetric turbulence.[9] We recall that the total kinetic energy is equal to $\bar{\Phi}_1(t) + \bar{\Phi}_2(t)$. Figure 13.2 shows in this calculation the evolution of these normalized energies and of the potential energy $\langle \vartheta^2 \rangle$ both in an isotropic calculation (no stratification) and in the stratified case: in the isotropic case, the various kinetic energies (horizontal kinetic $\langle \vec{u}_H^2 \rangle/2$, vertical kinetic $\langle w^2 \rangle/2$, vortex kinetic, wave kinetic) properly normalized are all equal, and decay within the LES like $t^{-1.2}$, as stressed in Chapter 12. This is also true for the temperature variance[10] $\langle \vartheta^2 \rangle$, which represents an analogous "potential" energy. All these isotropic energies – plus the total (kinetic + potential) energy – are represented by curve A. In the stratified case, the vortex kinetic energy (curve B) differs negligibly from the isotropic case. The wave kinetic energy (C) presents oscillations of period $\approx \pi/N$. The potential energy (D), initially weak, starts building up, then decays with oscillations of the same period, in phase opposition with the wave kinetic energy. It has been checked that the total energy (kinetic plus potential) presents no oscillations and decays following the $t^{-1.2}$ law, exactly as in the non-stratified case. In this particular calculation, it seems that the vortex and wave kinetic energies are very close to respectively the horizontal and vertical kinetic energies.

The wavy behaviour of the "wave kinetic" and "potential" components of the energy in the stratified case is the same as found by Riley et al. [600], even if the initial Froude number is now higher. The period π/N found numerically seems to characterize the horizontal propagation of gravity waves: indeed, a wave of energy

[8] When the integral scale is smaller than Osmidov scale.

[9] Since the initial conditions are axisymmetric, this condition will be preserved with time.

[10] At this low resolution of 32^3.

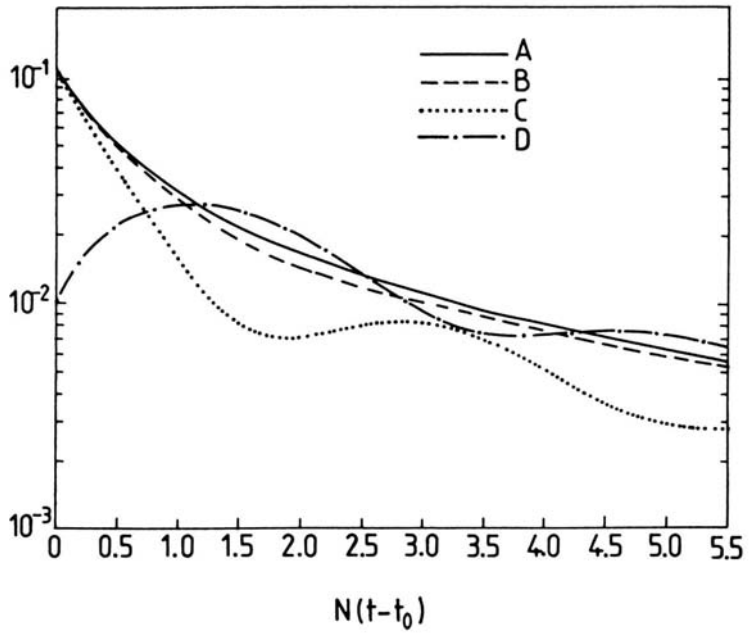

Figure 13.2. Time evolution of the normalized energies in a non-stratified and stratified spectral LES (resolution 32^3). A: kinetic or potential energy (isotropic case). B: "vortex" kinetic energy (stratified case). C: "wave" kinetic energy (stratified case). D: potential energy (stratified case) (from Métais [491]).

$$|\phi|^2 \propto \sin(2Nt + \alpha)$$

corresponds to a fluctuation $\phi \propto \sin(Nt + \gamma)$ (α and γ are arbitrary phases), and hence a pulsation $\varpi = N$ in Eq. (2.128). This implies $k_3 = 0$. These waves affect the large scales of the flow, as shown by the spectra of these various energies (averaged on a sphere of radius $k = |\vec{k}|$) presented in Figure 13.3: the vortex spectrum in the stratified case (B) does not differ very much from the isotropic one (A); the waves are clearly displayed on the spectra C and D for modes $k <\sim k_i$, the small scales $k > k_i$ behaving in the same way as in A and B with a $k^{-5/3}$ spectrum extending up to the cutoff k_C. It is not clear whether these waves are physically realistic, or are due to the artificial periodic boundary conditions[11] of the *turbulence within a box* which has been considered. But even if these waves are strongly amplified by the numerical model, they do not seem to significantly affect the dynamics of the "vortex component", nor to reduce the total energy dissipation rate.

[11] Which indeed put in phase the fluctuations at the boundaries, thus forcing waves at the scale of the computing box.

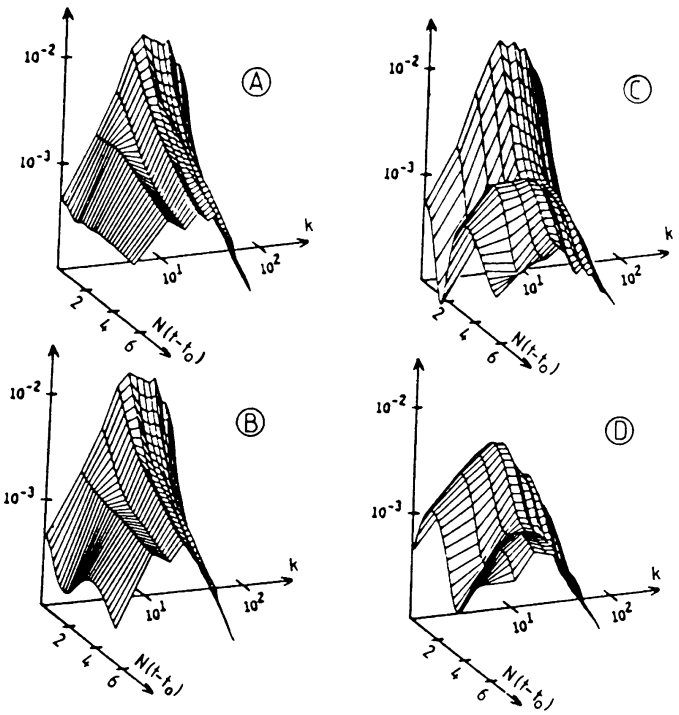

Figure 13.3. Time evolution of energy spectra in the same conditions as in Figure 13.2 (from Métais [491]).

These calculations show also that the integral scale and Osmidov scale cross at about $t = N^{-1}$, as predicted by the phenomenology. At that time, the turbulent Froude number has decreased from its initial value of 3 to 1. Afterwards it continues to decrease and is about 0.15 after $5N^{-1}$. This is quite a low value, but there is not yet any two-dimensional turbulence inverse-cascade tendency when considering the kinetic energy spectra. DNS at a higher resolution (64^3) and for longer times ($50N^{-1}$) were made by Métais and Herring [494]. Their results are qualitatively similar to those of Riley et al. [600] and Métais [491] for $t < 5N^{-1}$. However, they find a clear slowdown in the decay of the vortex kinetic energy at $t \approx 6N^{-1}$, while the other energies (wave and potential) continue to decay at the same rate. Before this time,[12] the vortex and wave spectra are identical in the small scales. Afterwards, the wave

[12] The existence of this collapse time was confirmed simultaneously in a spectral LES (at a resolution of 32^3) carried out for longer times done by Métais and Chollet [495]. This calculation shows also that the vertical diffusion of a thin

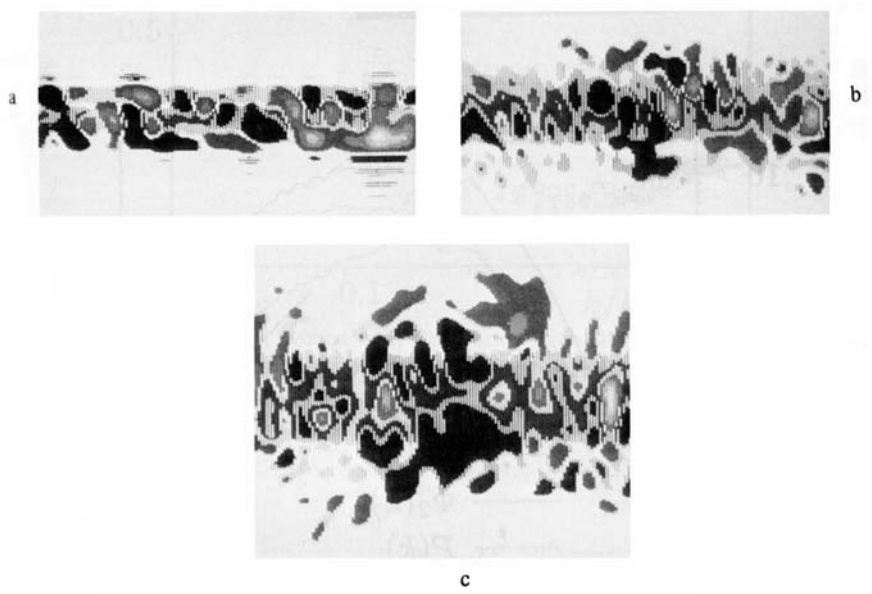

Figure 13.4. Spectral LES of the vertical diffusion of passive scalar done by Métais and Chollet [495]. A vertical section is shown: initially (a); at $t = 12.85N^{-1}$ in the stratified case (b); at the same time in the isotropic case (c).

energy cascades faster to high k than the vortex energy, and it seems that there is a tendency for the vortex energy to be trapped in the large scales. It is found that the "collapse time" $6N^{-1}$ is such that Osmidov and Kolmogorov scales are equal, which implies that all the scales of motion are influenced by buoyancy, including the smallest ones. But the vortex kinetic energy dissipation rate is still important, even though it has decreased, and the situation is in no way that of a two-dimensional turbulence, although Métais and Herring [494] find that the isopycnal surfaces become quasi two-dimensional after the collapse.

Still in the decaying case, other initial situations can be considered: for instance a completely horizontal field where all the energy is under its vortex form, with a strong vertical decorrelation (Métais and Herring [494]). Such a state implies important vertical gradients of the horizontal velocity. In this case, two possibilities exist: if the stratification is sufficiently high, the local Richardson number will be everywhere greater than its local critical value 0.25, and no instability will develop: the flow remains in horizontal layers,

initially horizontal layer of passive scalar is strongly inhibitted by stratification after the collapse, as shown in Figure 13.4.

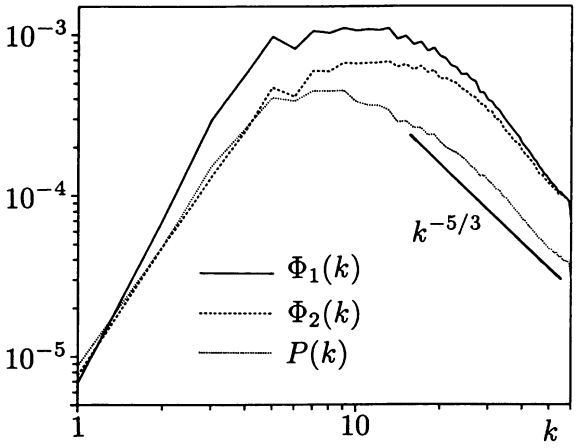

Figure 13.5. Vortex kinetic energy spectrum $\Phi_1(k)$, wave kinetic energy spectrum $\Phi_2(k)$ and potential energy spectrum $P(k)$ at $t = 1.48N^{-1}$ in the stratified LES of Métais and Lesieur [496].

and is not affected by gravity waves which propagate; but again the vortex kinetic energy dissipation is important, due to the strong vertical gradients of the horizontal velocity. Otherwise, internal Kelvin–Helmholtz waves will emerge, and possibly break up into small-scale three dimensional turbulence. This is a mechanism which converts vortex energy into wave energy.[13]

Returning to the above-considered problem of the collapse of initially isotropic turbulence under stratification, we mention finally the more recent spectral LES performed by Métais and Lesieur [496] at a resolution of 128^3 and up to $t = 7.5N^{-1}$: it confirms the existence of the collapse time at $6N^{-1}$, by considering the instantaneous time-decay exponent α_V of the vortex kinetic energy ($\propto t^{-\alpha_V}$), which is appreciably reduced after the collapse. The exponent α_W corresponding to the potential and wave energy seems, after some adjustment time, to become of the same order as α_V, which shows a strong difference with the anomalous behaviour of the passive temperature found in Chapter 12 for the same calculation. Here, in the stratified case, the potential energy spectrum loses the k^{-1} large-scale range displayed in the non-stratified case of Figure 12.3. This is shown in Figure 13.5, presenting respectively the vortex, wave and potential energy spectra at $t = 1.48N^{-1}$.

[13] Though there does not seem to be any doubt about the fact that the "vortex" energy is a good indicator of horizontal kinetic energy, it is on the contrary more difficult to distinguish, in the "wave" kinetic energy, the gravity wave contribution from the small-scale three-dimensional turbulence contribution.

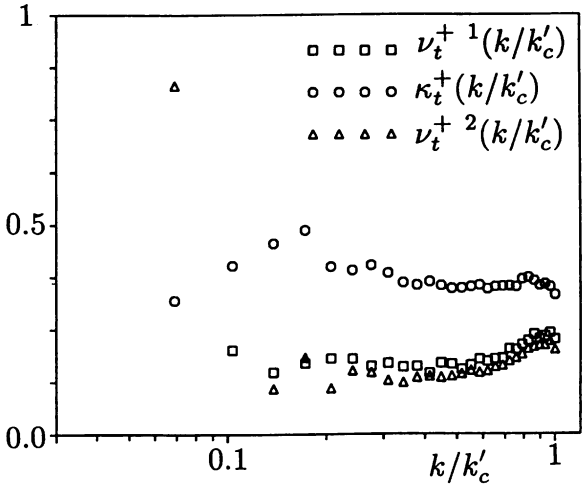

Figure 13.6. Spectral vortex and wave eddy viscosity, and eddy diffusivity, corresponding to the calculation of Figure 13.5.

Figure 13.6, to be compared with Figure 12.2 in the isotropic case, shows that, now, the eddy diffusivity has also lost its logarithmic k dependency, and is approximately constant, with an eddy-Prandtl number of the order of 0.45. At the same time, the p.d.f. of the temperature is now Gaussian, as was the velocity in the isotropic case (see Chapter 6). Hence, the coupling between temperature and velocity due to buoyancy seems to have suppressed the large-scale intermittency of the temperature which we had mentioned in isotropic turbulence. This is confirmed by Figure 13.7, taken from Métais and Lesieur [496], which shows the temperature p.d.f. in spectral LES and DNS,[14] determined respectively in the isotropic and stratified case. The strong temperature intermittency in the isotropic case is illustrated in Plate 19. At the later times of the stratified LES and DNS calculation of Métais and Lesieur [496], various spectra confirm that the vortex kinetic energy tends to be trapped in the large scales.

More recent DNS of this problem at Froude numbers of the order of one have been carried out by Riley and De Bruyn Kops [603].

13.2.3 Other configurations

Let us mention also that stratified-shear flow three-dimensional DNS have been performed by Gerz et al. [250] in the case of a constant shear, and by

[14] See also Métais and Lesieur [493].

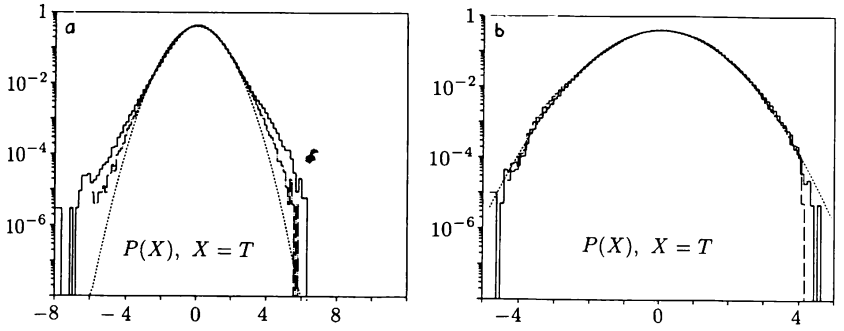

Figure 13.7. Temperature p.d.f. determined at $t = 1.48N^{-1}$ in the DNS (continuous line) or LES by Métais and Lesieur [496]; (a) isotropic calculation; (b) stratified calculation. The dashed line indicates a Gaussian distribution.

Staquet and Riley [670,671] for a mixing layer. In the latter case, stratification produces a sort of horizontal collapse of the Kelvin–Helmholtz billows, at the origin of vertical vorticity. Experiments (see e.g. Koop and Browand [343]) show this collapse of the mixing layer under stratification.

A very complete numerical and experimental review may be found in Riley and Lelong [602] (see also Riley and De Bruyn Kops [603]).

Finally, Plate 21 presents a gravity wave developing in a strongly-stratified flow behind an obstacle, in a three-dimensional finite-volume calculation.

13.3 Rotating turbulence

We will look here at the action of a solid-body rotation of constant instantaneous rotation vector $\vec{\Omega} = (f/2)\vec{z} = \Omega\vec{z}$ upon a flow of uniform density ($f > 0$). Two cases will be considered: first, a shear flow of basic (or mean, if turbulence has developed) parallel velocity $\bar{u}(y)\vec{x}$, and second, an initially isotropic turbulence (quasi two-dimensional or three-dimensional).

13.3.1 From low to high Rossby number

As already stressed, the influence of rotation is measured by the Rossby number, which may have a wide range of variation. We recall that in geophysical and astrophysical phenomena, typical values are by increasing order:
(a) 10^{-5} for Earth outer core (velocity 10^{-3} m/s, length 1000 km);
(b) 0.04 for Jupiter great red spot;
(c) 0.05 for mesoscale oceanic eddies;

(d) 0.3 for large synoptic atmospheric perturbations;
(e) 3 for the atmospheric wake of a small island in mid-latitudes (15 m/s, 50 km);
(f) 5 for a developed hurricane in the tropics (60 m/s, 200 km);
(g) 600 for a tornado in mid-latitudes (60 m/s, 1 km).

We anticipate from the following results that rotation will have a two-dimensionalizing effect in the 4 first cases. For case (e), rotation will stabilize cyclonic vortices and disrupt anticyclonic ones. In case (g), and if one considers the hairpin-based model discussed in Chapter 9, rotation may disrupt the anticyclonic branch of the tornado during its development.

Rotating turbulence finds also numerous industrial applications in turbomachinery. As quoted in Lesieur et al. [425]:

> The turbulent characteristics of the flow in blade passages of radial pumps and compressor impellers determine the efficiency of these devices. Turbulence is also of great importance for the cooling by the fluid inside the blades. Depending upon the magnitude of the radial velocity, the Rossby number within rotating machines can range from values close to unity to very small ones (≈ 0.05).

13.3.2 Linear instability

Let us introduce

$$R_o(y) = -\frac{1}{f}\frac{d\bar{u}}{dy} \tag{13.4}$$

as the local Rossby number, which may be positive or negative depending upon the sign of $d\bar{u}/dy$. A positive (resp. negative) Rossby number will correspond to a cyclonic (resp. anticyclonic) region. We have already shown in Chapter 3 that in the inviscid case exist unstable longitudinal modes (in the sense of normal-mode analysis) if and only if $R_o(y)$ is smaller than -1 somewhere in the flow (see Pedley [566]).

13.3.3 Mixing layers and wakes

Instability

A three-dimensional viscous linear-stability study was carried out for the mixing layer and the wake by Yanase et al. [730]. We present here some of the results obtained for the mixing layer at Reynolds 150. Figure 13.8 shows the contours of constant amplification rate σ in the k_x, k_z plane.[15]

[15] These longitudinal and spanwise wave numbers were called α and β in Chapter 3. These quantities are here respectively normalized by U/δ_0 and δ_0^{-1}.

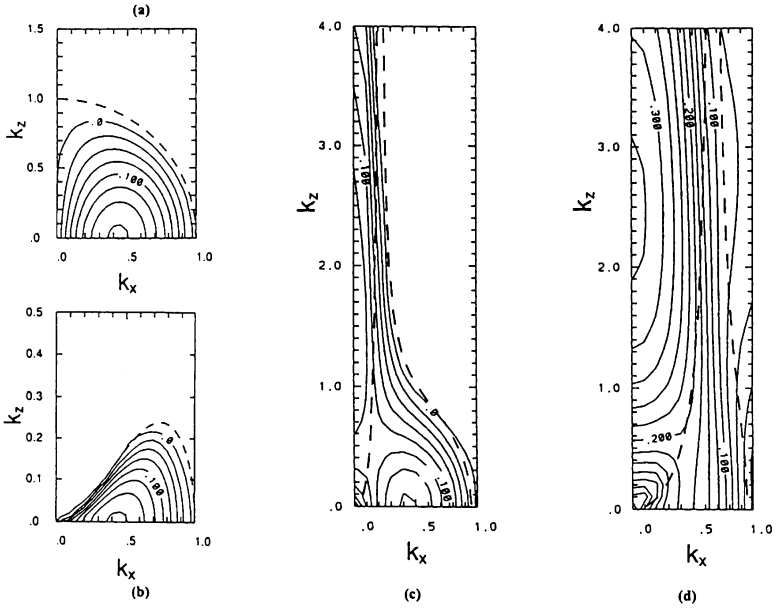

Figure 13.8. Iso-amplification rates in the three-dimensional linear-stability analysis of a rotating mixing layer carried out by Yanase et al. [730], at Reynolds 150; (a) no rotation, (b) $R_o^{(i)} = 1$, (c) $R_o^{(i)} = -20$, (d) $R_o^{(i)} = -2$ (courtesy *Phys. Fluids*).

Case (a) corresponds to no rotation: the most-amplified mode is purely spanwise ($k_x = 0.433, k_z = 0, \sigma = 0.180$), and is very close to the inviscid Michalke mode ($k_x = 2\pi/14 = 0.449$). Case (b) corresponds to $R_o^{(i)} = 1$, where $R_o^{(i)}$ is the minimum initial Rossby number defined by Eq. (13.4), and is associated with the inflection point. It is a cyclonic situation, and the migration of the iso$-\sigma$ curves towards the $\vec{x}$ axis shows a two-dimensionalization due to cyclonic rotation. The spanwise most-amplified mode is unchanged, as one can show easily since Orr–Sommerfeld equation is not affected by rotation in two dimensions. Case (c) ($R_o^{(i)} = -20$), is anticyclonic. A new window of instability is now opened, corresponding to longitudinal modes. But Michalke mode is still the most amplified. At $R_o^{(i)} = -2$ (d), the most-amplified mode is now purely longitudinal ($k_x = 0, k_z = 2.5, \sigma = 0.332$). This shear-Coriolis instability, as it was named by Yanase et al. [730] is of course related to the inviscid longitudinal modes mentioned in Chapter 3, and resembles centrifugal instabilities such as Couette–Taylor or Görtler. It can be checked that the maximal rate of longitudinal amplification is for $R_o^{(i)} \approx -2.5$. At Reynolds 150, the shear-Coriolis instability dominates Kelvin–Helmholtz' in the range

$\approx -10 < R_o^{(i)} < -1$. The lower bound is pushed to ≈ -20 at Reynolds 800. These calculations show also that shear-Coriolis instability disappears for $R_o^{(i)} \geq -1$, which proves in particular that the flow is two-dimensionalized at high rotation rates $|R_o^{(i)}| \ll 1$, in good agreement with Proudman–Taylor theorem.

In the case of the wake, the relevant initial Rossby number is the modulus of the Rossby number at the inflection points. It was shown by Yanase et al. [730] that at $|R_o^{(i)}| = 20$ and for Reynolds 150, the same diagram as Figure 13.8c is obtained, with occurrence of longitudinal modes. They become more amplified than the Karman mode for $1 < |R_o^{(i)}| <\approx 7$. The shear-Coriolis instability is here also maximum at $|R_o^{(i)}| = 2.5$. At Reynolds 800, the instability dominates for $1 < |R_o^{(i)}| <\approx 12$.

Real flows

For free-shear flows, the drastically different effects of solid-body rotation on the eddies, depending on their cyclonic or anticyclonic nature, have been investigated in several laboratory experiments. The rotating mixing-layer experiment (rotation axis oriented along the span) by Bidokhti and Tritton [63] (see also Tritton and Davies [690]) have confirmed the stabilization of cyclonic eddies. Conversely, Kelvin–Helmoltz vortices seem to be completely disrupted, even by a weak anticyclonic rotation. Destabilization and stabilization can be simultaneously observed in flows like rotating wakes or jets. Witt and Joubert [722] found that the wake of a cylinder whose axis is parallel to $\vec{\Omega}$ exhibits asymmetry for the mean flow as well as for the turbulent quantities. This is confirmed by Chabert d'Hières et al. [103]: they show that, at moderate rotation rates, the cyclonic vortices of the wake are reinforced while the anticyclonic ones are destroyed. Conversely, the wake reorganizes into a very regular two-dimensional Karman street of alternate vortices at high rotation rates.[16] Satellite observations of atmospheric wakes displayed by clouds exhibit also strong asymmetrical eddy structures (Etling [189]).

We will here give some details on three-dimensional rotating free-shear layer simulations, both for mixing layers and wakes.

We start with mixing-layer DNS presented in Lesieur et al. [423]. They use pseudo-spectral methods (with lateral boundaries to infinity treated using a coordinate mapping) at a resolution of $48 \times 48 \times 24$ (two longitudinal fundamental modes) starting initially with a three-dimensional random perturbation superposed on the basic flow $U \tanh 2y/\delta_i$. Figure 13.9 shows the growth of spanwise kinetic energy[17] for values of the Rossby number modulus ranging

[16] Although the Karman street becomes highly three-dimensional in the non-rotating case.

[17] Which is a good indicator of three-dimensionality.

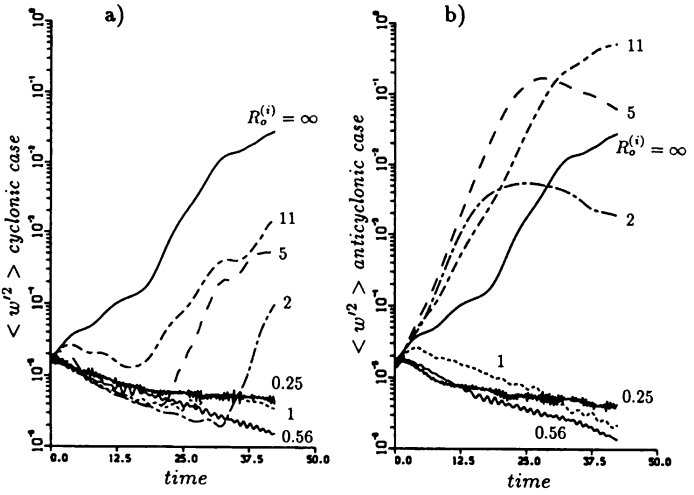

Figure 13.9. Growth of the three-dimensional kinetic energy in the rotating mixing layer; (a) cyclonic case; (b) anticyclonic case (from Lesieur et al. [423], courtesy S. Yanase).

from infinity (no rotation) to 0.25. In the cyclonic case (where the solid-body vorticity is of same sign as the primary coherent vortices), rotation is always stabilizing with respect to the non-rotating case: an interesting feature may be noticed, that is, the initial decay of the three-dimensional perturbation, followed by a growth which is delayed as the rotation increases. In the anticyclonic case, and at $t = 25\delta_i/U$ (slightly before the pairing in the non-rotating case), the highest three-dimensional energy is for $R_o^{(i)} = -4 \approx -5$. The ageostrophic component of the pressure at $t = 25$ is displayed in Figure 13.10. For $R_o^{(i)} = \infty$ (no rotation, Figure 13.10a), the flow possesses strong quasi two-dimensional billows. At $R_o^{(i)} = 11$ (cyclonic, Figure 13.10b), the vortices are strongly two dimensionalized. The $R_o^{(i)} = -11$ anticyclonic case indicates that the billows are three-dimensionally distorted, but remain coherent (Figure 13.10c). On the other hand, the $R_o^{(i)} = -5$ case shows extremely elongated hairpins, without any Kelvin–Helmholtz roller (Figure 13.10d). Still in the anticyclonic case, rotation is stabilizing again for $R_o^{(i)} \geq -1$, as attested by Figure 13.10e (at $R_o^{(i)} = -0.25$), where very straight two-dimensional vortices are obtained, in good agreement with Proudman–Taylor theorem.

New DNS of rotating temporal mixing layers and wakes have been carried out by Métais et al. [498] (see also Flores [207]) using pseudo-spectral methods at a resolution of 64^3 collocation points. The initial velocity consists respectively in a hyperbolic-tangent and a Gaussian profile, to which is

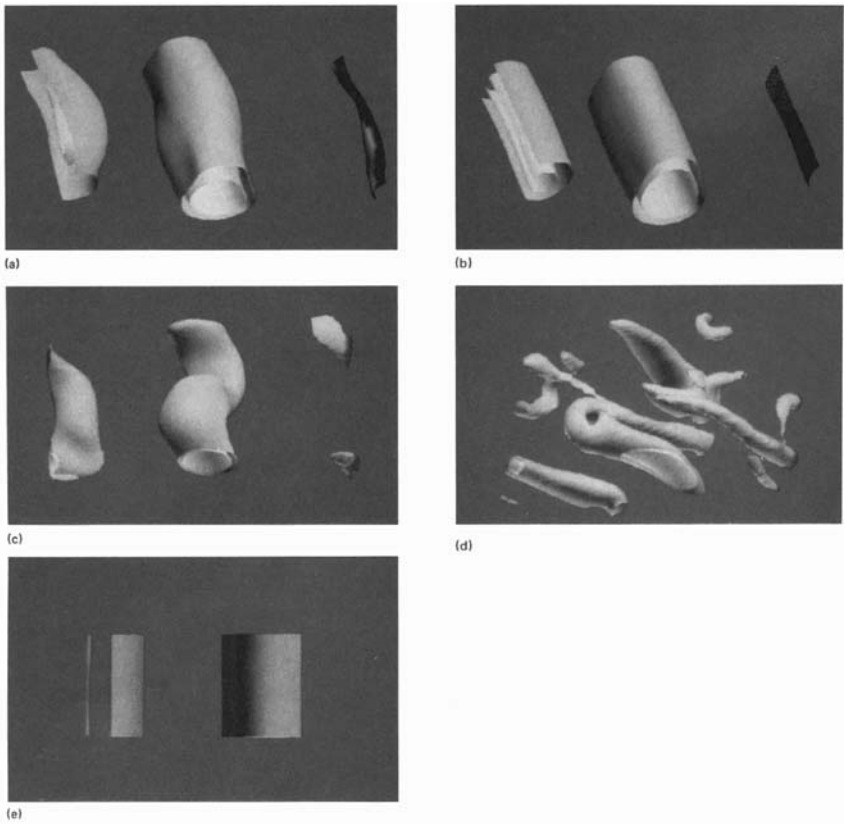

Figure 13.10. Pressure plots in DNS of a rotating mixing layer at $t = 25$, for (a) $R_o^{(i)} = \infty$, (b) $R_o^{(i)} = 11$, (c) $R_o^{(i)} = -11$, (d) $R_o^{(i)} = -5$, and (e) $R_o^{(i)} = -0.25$ (from Lesieur et al. [423], courtesy S. Yanase).

superposed a low-amplitude random perturbation. The simulations confirm the global trends observed in the experiments, some of which were predicted by the linear-stability analysis: the Kelvin–Helmoltz and Karman vortices are two-dimensionalized by the rotation when they are cyclonic, whatever the Rossby number; this is also true for all vortices (cyclonic or anticyclonic) in the case of rapid rotation (in the sense of the linear-stability analysis, that is, $|R_o^{(i)}| \leq 1$). Conversely, a moderate anticyclonic rotation ($1 < |R_o^{(i)}| <\approx 10$) in mixing layers disrupts the primary vortices. The latter are stretched into intense longitudinal absolute-vorticity hairpins,[18] as shown in Figure 13.11. It concerns an anticyclonic mixing layer at initial $R_o^{(i)} = -5$, forced initially by

[18] That is to say coherent structures where absolute vorticity is condensed.

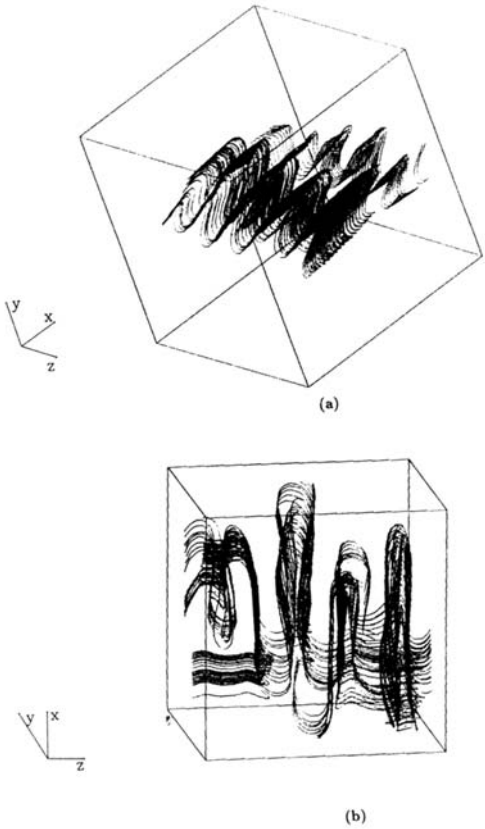

Figure 13.11. Absolute vortex filaments in the DNS of a rotating mixing layer at $R_o^{(i)} = -5$ carried out by Métais et al. [498]; (a) initial linear stage, (b) nonlinear stretching of absolute vorticity hairpins (courtesy *J. Fluid Mech.*).

a three-dimensional isotropic perturbation. The absolute vortex filaments[19] are shown, and undergo two distinct stages in their evolution. Figure 13.11a corresponds to the linear stage ($t = 18\delta_i/V$), where the filaments oscillate in phase and grow according to the longitudinal mode predicted by the linear theory. Their local Rossby (based upon the spanwise relative vorticity averaged in the spanwise direction) is ≈ -2.5, that is to say the most-amplified initial Rossby of the linear theory. They form with the horizontal an angle of $\approx 45°$, not far from the predictions of the velocity-sheets model (see below). Figure 13.11b is at $t = 22.5$. The absolute-vortex filaments are now very

[19] Chosen as passing through points where the longitudinal vorticity is maximum.

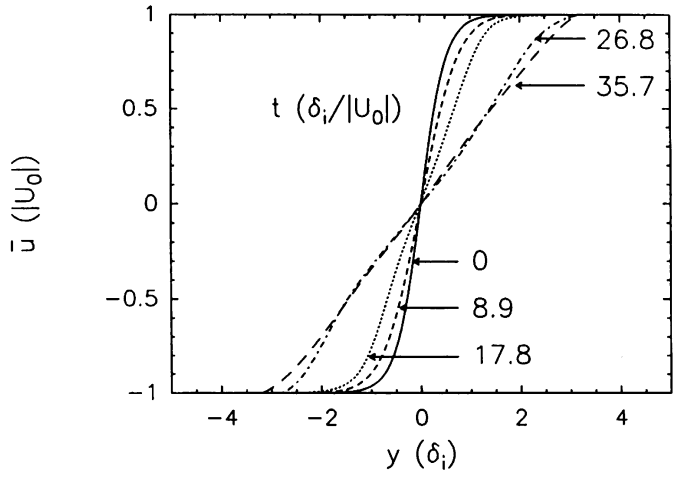

Figure 13.12. Same calculation as in Figure 13.11; time evolution of the mean longitudinal velocity profile (courtesy *J. Fluid Mech.*).

elongated, and have condensed into a hairpin shape.[20] They are raised of 20° with respect to the horizontal, and their spanwise wavelength corresponds to the fastest-growing mode of the linear-instability theory. Since the spanwise component of the absolute vorticity is approximately zero for these hairpins, they are in a zone where the local Rossby number is ≈ -1, which corresponds to a spanwise-averaged longitudinal velocity gradient equal to f:

$$\frac{d\bar{u}}{dy} = f. \tag{13.5}$$

This is obvious in Figure 13.12, presenting the time-evolution of this average velocity profile $\bar{u}(y)$ in terms of y/δ_i. One can see how it evolves from the initial hyperbolic-tangent profile to a constant-shear profile. It was checked in Métais et al. [498] (see also Lesieur et al. [431]) that at $t = 35.7$, we do have a local Rossby number close to -1 on the interval $[-2, +2]$.

Let us mention also the experimental measurements done by Tarbouriech and Renouard [674] in a rotating turbulent wake, using DPIV techniques. They find a local Rossby number of the order of -1 within the anticyclonic side. Such a result is verified in the DNS of a temporal wake (see Lesieur et al. [431]).

[20] The same results are obtained for a wake. At initial Rossby corresponding to the dominance of shear-Coriolis instability, the structure is made of longitudinal absolute-vorticity hairpins on the anticyclonic side, and quasi two-dimensional Karman vortices on the cyclonic side.

This stresses the importance of both the linear-stability analysis (existence of an unstable longitudinal mode) and the longitudinal stretching of absolute vorticity. These results show also that, in mixing layers or separated flows, an anticyclonic solid-body rotation of spanwise axis may be a very efficient mechanism to destroy the primary coherent vortices,[21] as already noticed experimentally. We have finally predicted the existence of longitudinal coherent vortices in anticyclonic mixing layers.[22] These vortices have not yet been observed in the experiments, but have analogies with longitudinal vortices observed in centrifugal instabilities.

This provides a mechanism of cyclonic preference for atmospheric or oceanic vortices in wakes and jets, at Rossby numbers moduli between unity and ≈ 10. It might apply in particular to the generation of cyclonic subtropical perturbations in the atmosphere on the western coasts of the continents. These perturbations travel to the west across the oceanic basins. Some of them will, by conversion of latent evaporation heat in kinetic energy, transform into hurricanes when passing above a water of temperature superior to 26°C. These hurricanes cause huge damages when they hit the eastern coasts of continents. The most impressive in the last decades is certaily Katrina, which hit the city of New Orleans end of August 2005. About 80% of the city was flooded because several levees protecting the city from Mississippi river and Lake Pontachartrain were destroyed. In fact the water of the latter was pumped up by the very low pressure induced by the hurricane.

Returning to the problem of rotating shear flows, we have observed above that anticyclonic mixing layers of moderate Rossby number modulus organize into regions were the mean absolute spanwise vorticity is zero. In fact, this remarkable result, discovered by Métais et al. [498], had already been found experimentally in a channel by Jonhston et al. [319]. So there is a universality of rotating shear flows.

We will first present a review of the channel case, then try to explain this longitudinal alignment of absolute vorticity in anticyclonic regions by the so-called weak absolute vorticity stretching principle.

13.3.4 Channels

The flow configuration is given in Figure 13.13. The vorticity vector associated with the basic velocity profile $\vec{\omega} = (0, 0, -d\bar{u}/dy)$ is parallel to $\vec{\Omega}$ near the upper wall and antiparallel near the lower wall: we refer to the two particular walls as cyclonic and anticyclonic. Various other terms are currently used, such as "suction and pressure sides", or "trailing and leading sides".

[21] Conversely, cyclonic rotation may be used to stabilize the two-dimensional vortices.

[22] And the anticyclonic sides of wakes.

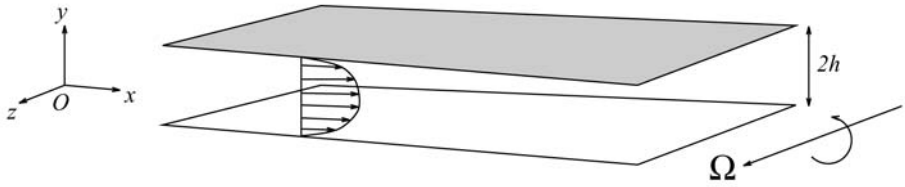

Figure 13.13. Rotating channel (courtesy E. Lamballais).

Let us take in Figure 13.13 the origin $y = 0$ at the channel centerplane. If $\bar{u}$ is parabolic (at the initial instant), the basic Rossby number $R_o(y, 0)$ is linear in y and antisymmetric. The minimum value $R_o^{(i)} = R_o(-h, 0)$ is negative. The flow is anticyclonic in its bottom part, and cyclonic in its upper part.

Instability

As recalled in Lesieur et al. [431], Lezius and Johnston [436] have shown that this flow is inviscidly unstable if $R_o^{(i)}$ is lower than -1. This is analogous to Pedley's result.

Real flows

Laboratory experiments (Johnston et al. [319]) have shown that the cyclonic side is stabilized: as compared to the non-rotating case, the turbulence energy production decreases with increasing rotation rate and fast rotation can lead to the total suppression of turbulent transition. Conversely, the anticyclonic side is destabilized for moderate rotation rates (moderate means here a Rossby number modulus high enough, see below), and develops an instability in the form of large periodic longitudinal rolls.

DNS of rotating channel flows have been carried out (see e.g. Kim [329], Kristoffersen and Andersson [361], Lamballais [366]). Other references are given in Lesieur et al. [431]. LES have been done with the aid of the dynamic model by Piomelli and Liu [575], and the spectral-dynamic model by Lamballais et al. [366, 369]. These simulations have complemented the experimental investigations by studying in particular the influence of rotation on the three-dimensional coherent structures.

The above-quoted DNS of Lamballais allow to recover on the anticyclonic side the presence of a constant-shear profile, as attested by Figure 13.14. It shows in a DNS at a moderate Reynolds number of 5000 (based on $2h$ and the bulk velocity across the channel, which is set constant with time in these simulations), the mean-velocity profile as a function of $|R_o^{(i)}|$, the

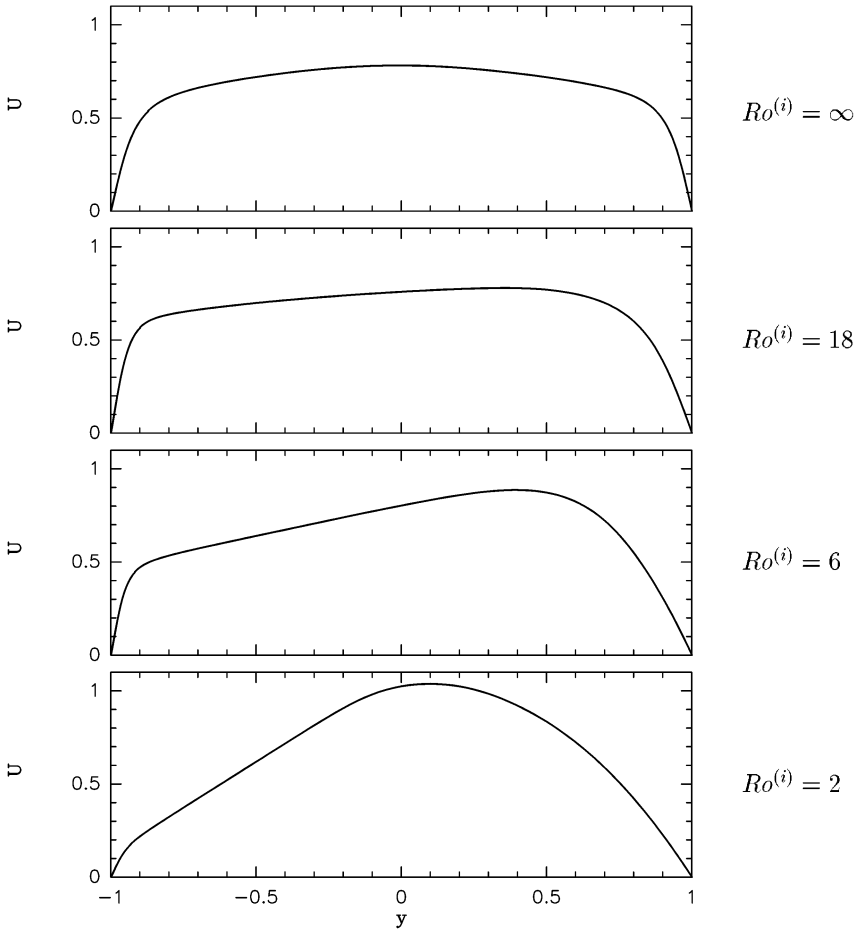

Figure 13.14. Mean longitudinal velocity profiles as a function of the initial Rossby number modulus in DNS of a rotating channel (courtesy E. Lamballais).

initial Rossby number.[23] Whatever the initial Rossby, the linear-velocity range does correspond to a local Rossby $R_o(y) \approx -1$, as checked in Lesieur et al. [431]. The latter reference shows also the same result in LES of Lamballais et al. [369]. In both cases, it is at $R_o^{(i)} = -5$ that this range is the more extended. Figure 13.15 shows in the same calculation as Figure 13.14 iso-surfaces of the vorticity modulus. It is clear that the flow is quasi laminar

[23] All these simulations are initiated by a Poiseuille velocity profile, slighly perturbed, and $R_o^{(i)}$ is based upon the vorticity at the wall of this profile.

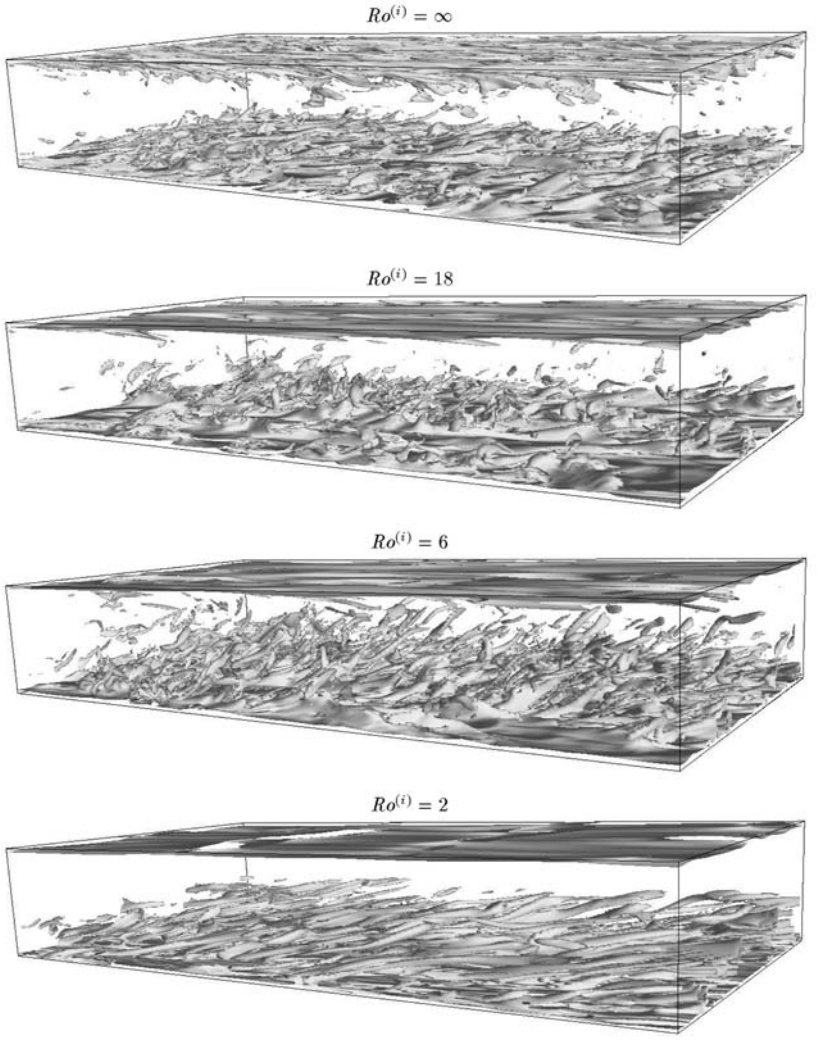

Figure 13.15. Same calculation as Figure 13.14; iso-surfaces of relative vorticity modulus (courtesy E. Lamballais).

on the cyclonic side, while hairpins on the anticyclonic side are more and more inclined with respect to the wall as rotation is increased. It was also checked that longitudinal velocity fluctuations on this side are reduced when the Rossby number is increased, and that the corresponding streaks have disappeared at $R_o^{(i)} = -2$.

The replacement of the famous logarithmic velocity profile by a linear profile due to anticyclonic spanwise rotation is certainly an extremely important result for turbulent boundary layers. The fact that the linear profile exists also in anticyclonic free-shear flows adds further importance to it.

To our knowledge, no experimental data seem to be available for high-rotation rates in the anticyclonic case. It was shown by Lamballais [366] that at Rossby -0.1, and for a bulk Reynolds number of 10,666, the flow is two-dimensionalized, in agreement with Proudman–Taylor theorem, and evolves into alternate large rolls of spanwise axis, as obtained by Jimenez [315, 316] in two-dimensional channel DNS.

It should be stressed that most people who work on this rotating channel problem use a parameter called *rotation number*, equal to 3 times the inverse of $|R_o^{(i)}|$.

A study having analogies with the rotating channel is the rotating plane Couette flow, investigated with DNS by Bech and Andersson [52].

13.3.5 Some theoretical considerations

Rotating velocity-sheets model

As an exercise, we come back to the "velocity-sheets model" in a constant shear $\lambda = \bar{u}'(y)$ within an infinite domain, already looked at in Chapter 3. Here we assume also a spanwise rotation. The perturbed velocity (with respect to the basic flow) is still assumed of the form

$$\underline{\tilde{u}} = U(z)[X(t)\vec{x} + Y(t)\vec{y}],$$

with a zero spanwise velocity w. A basic pressure gradient balances the Coriolis force corresponding to the basic flow, and the perturbed pressure is assumed uniform. Eq. (3.47) writes now

$$U(z)\left(\frac{dX}{dt} + \lambda Y\right) = fYU(z) + \nu U''(z)X$$

$$U(z)\frac{dY}{dt} = -fXU(z) + \nu U''(z)Y \tag{13.6}$$

Taking $U(z) = \sin k_3 z$, we have

$$\frac{dY}{\partial t} + fX = -\nu k_3^2 Y, \frac{dX}{\partial t} + (\lambda - f)Y = -\nu k_3^2 X. \tag{13.7}$$

This system was solved in Métais et al. [496] without viscosity. The Rossby number is here $-\lambda/f$. In the anticyclonic case, it was found for $R_o < -1$ that

the fluctuating vorticity vector projected in the (x, y) plane was stretched exponentially with time,[24] and made eventually with the horizontal an angle of tangent $\sqrt{-(1+R_o)}$. The highest amplification rate was obtained for $R_o = -2$, which corresponds to an angle of 45°. At $R_o = -1$, the system Eq. (13.7) is equivalent to a non-rotating problem, with the exchange of X and Y. Thus, the velocity sheets oscillate now weakly along $\vec{x}$ with a velocity $\tilde{u}$ exponentially-damped by viscous dissipation, while the oscillations along $\vec{y}$ become very strong, the velocity $\tilde{v}$ scaling (in modulus) like $ft \exp -\nu k_3^2 t$. The absolute vorticity becomes purely longitudinal. This is an algebraic mode, stable from the point of view of normal-mode analysis. The former longitudinal high and low-speed streaks of the non-rotating case have now become intense alternate vertical currents. However, and as for the non-rotating case, the uniform perturbed pressure assumption is a severe drawback of the model.

Weak absolute-vorticity stretching principle

The following analysis was proposed in Lesieur et al. [423], as well as in the second edition of this book in 1990, before the linear-stability study of Yanase et al. [730] was performed. We call it the *weak absolute-vorticity stretching principle*. It predicts that, in the anticyclonic case at moderate rotation rates, absolute vorticity will condense into coherent longitudinal hairpin structures. We first reproduce it mainly as it was stated, then will discuss it in the light of the stability and numerical results.

We assume that at some instant the relative vorticity writes locally $\vec{\omega} = \omega_{2D}\vec{z} + \vec{\omega}^{(1)}$, with the norm of $\vec{\omega}^{(1)}$ much smaller than $|\omega_{2D}|$. We recall that Helmholtz theorem applies to the absolute vorticity, here equal to $(\omega_{2D} + f)\vec{z} + \vec{\omega}^{(1)}$. Absolute vortex filaments are (neglecting viscosity) material, with respect to the flow. We will assume that the stretching of the absolute vortex filaments is mainly due to the basic two-dimensional flow characterized by ω_{2D}. It is only by a longitudinal straining of the initial absolute vortex filament that longitudinal relative vorticity (corresponding to three-dimensionalization) may be produced. It is therefore essential to look at the initial distribution of the absolute vorticity. We assume $\omega_{2D} < 0$. In the subsection only we suppose that Ω may have both signs (see Figure 13.16). The following situations may be envisaged:

(a) cyclonic rotation ($\Omega < 0$): the absolute vortex filament corresponding to the relative vorticity distribution $\omega_{2D}\vec{z} + \vec{\omega}^{(1)}$ will be less inclined with respect to the z axis than the associated relative vortex filament. Therefore, the straining (if any) of the absolute vortex will be delayed, and a cyclonic rotation will have a stabilizing effect (compared with the non-rotating case).

[24] The spanwise fluctuating vorticity component is here conserved.

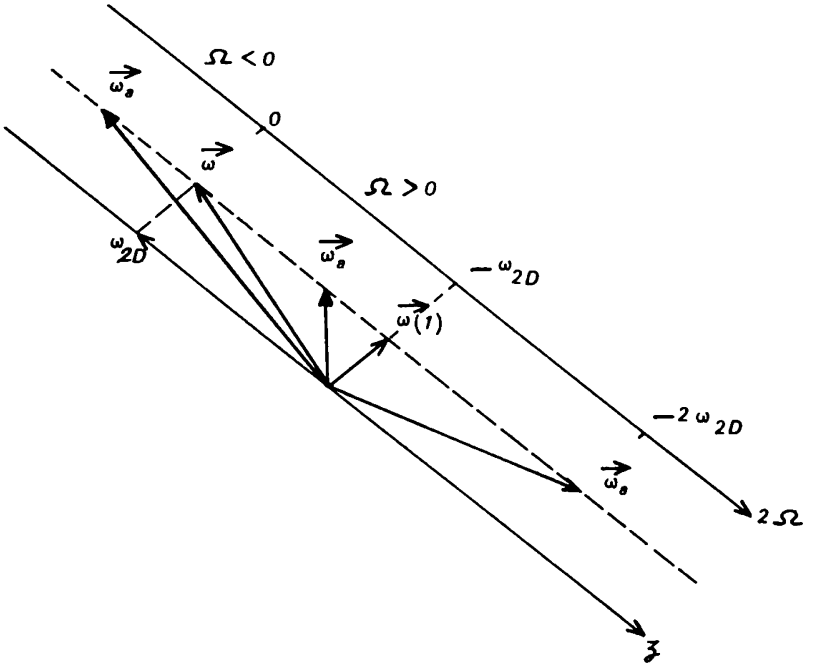

Figure 13.16. Distribution of relative and absolute vorticity in a quasi two-dimensional shear flow submitted to a solid-body rotation.

(b) anticyclonic rotation ($\Omega > 0$): when Ω increases by positive values starting from 0, the initial absolute vortex filament is more perturbed three-dimensionally than the relative one. Hence, rotation is destabilizing with respect to the non-rotating case. An intense three-dimensionalization of the layer occurs when $\omega_{2D} + 2\Omega \approx 0$, that is when the local Rossby number is of the order of -1: indeed, the initial absolute vortex filament corresponds approximately to the vorticity distribution associated with $\vec{\omega}^{(1)}$, and is highly three-dimensional if $\vec{\omega}^{(1)}$ corresponds to a three-dimensionally turbulent perturbation. Hence, it is going to be immediately stretched by the basic shear, and intense longitudinal vorticity will be produced everywhere throughout the layer, as a highly distorted filament of dye would be mixed within the shear layer. Then, it is feasible that the longitudinal vorticity thus created by mixing of the absolute vorticity will strongly affect the basic flow, which will very quickly lose its two-dimensionality. This explosive mechanism is certainly extremely efficient to disrupt the coherent vortices. When $\omega_{2D}+2\Omega > |\vec{\omega}^{(1)}|$, the initial absolute vortex filament will see its orientation reversed with respect to the relative one. For

$$\omega_{2D} + 2\Omega > -\omega_{2D}, \tag{13.8}$$

that is $R_o > -0.5$, the absolute vortex is again less three-dimensional than its relative counterpart, and the anticyclonic rotation becomes stabilizing again.

The weak absolute-vorticity stretching principle is certainly not valid in the context of linear-stability analysis starting with infinitesimal perturbations, since we have seen already that the flow is stable at $R_o = -1$. But it is of interest from a nonlinear point of view, considering the above numerical simulations.

The reader will find in Lesieur et al. [431] a theoretical explanation based on nonlinear reorientation of absolute vorticity in an x-independent flow, which confirms the tendency of absolute vorticity to realign in the flow direction.

13.3.6 Initially three-dimensional turbulence

Let us look now at the effect of solid-body rotation upon a decaying three-dimensional turbulence, with an initial isotropic state. A review may be found in Bartello et al. [34]. In fact, DNS pose certain problems, specially at low Rossby numbers. Indeed, it may take many initial turnover times for turbulence to reorganize under the action of rotation, and DNS dissipate most of the energy before rotation effects become dominant. This is why it is preferable to use LES for this study, since they dissipate kinetic energy much slower than DNS. Bartello et al. [34] used the structure-function or hyperviscosity models. The main results were obtained with pseudo-spectral methods at a resolution of 64^3 in a cubic box. The rotation axis is parallel to the vertical. The Rossby number is here defined as $\omega_0/2\Omega$, where ω_0 is the initial r.m.s. of the vertical vorticity (Ω is taken positive). Two calculations were carried out, respectively with quasi two-dimensional and three-dimensional isotropic initial states.

In the quasi two-dimensional case, the initial state consists in developed two-dimensional turbulence with formed coherent vortices, to which is superposed a weak three-dimensional random perturbation. At an initial Rossby number $R_o^{(i)} = 0.1$, the perturbation rapidly dies out, and the flow remains two-dimensional with both cyclonic and anticyclonic vortices. At $R_o^{(i)} = 1$ on the contrary, cyclonic vortices are stabilized, while anticyclonic vortex filaments are stretched into transverse hairpin vortices, exactly as described above, and afterwards are dispersed all over the flow. The eventual coherent state is made of quasi two-dimensional cyclonic vortices, in such a way that the initial symmetry cyclones/anticyclones has been broken by rotation.

In the three-dimensional case, the initial state consists in isotropic three-dimensional turbulence which has developed a Kolmogorov cascade (without

rotation). Then rotation is applied. At $R_o^{(i)} = 1$, quasi two-dimensional cyclonic vortices appear, without any well-formed anticyclonic vortex. This is confirmed by the consideration of the vertical vorticity p.d.f. $P(\omega_z)$: initially, it is symmetric, with quasi exponential wings both for positive and negative values of ω_z. At the end, it is highly skewed towards positive values (that is, cyclonic), while the anticyclonic side becomes Gaussian. The vertical vorticity skewness reaches important values. The physical explanation might be that rotation has stabilized the initial cyclonic vortex filaments (of direction close to the axis of rotation), and disrupted the anticyclonic ones. At $R_o^{(i)} = 0.1$, anticyclonic vortices reform, although they are weaker than the cyclonic ones.

Analogous results were found experimentally by Morize et al. [523], and Morize and Moisy [524].

An interesting numerical study resembling Bartello's [34] but with a stationary three-dimensional forcing by inertial waves has been carried out by Smith and Waleffe [655]. They display very neatly the formation of two-dimensional cyclonic vortices.

13.4 Separated flows

As already stressed, separated flows are very common in external aerodynamics of cars, trains, planes, ships or submarines. They are also encountered in hydraulics, thermohydraulics of nuclear reactors, or internal aerodynamics of combustors (rocket solid-propergol boosters for instance).

The flow behind a two-dimensional backward-facing step is a prototype of separated flow. The simplest example is given by a uniform flow of velocity U_0 in a domain whithout upper boundary, passing above a step of infinite height. This is very close to a spatial mixing layer between two currents of velocity U_0 and 0. This configuration was for instance studied experimentally at high Reynolds number by Wygnanski and Fiedler [725], who performed an extensive study of large-scale intermittency. This work did show by statistical means the existence of large-scale fluctuations, which correspond in fact to the shedding of coherent vortices visualized by Brown and Roshko [88] a few years later. It is also in such a step configuration that Chandrsuda et al. [107] proposed the possibility for helical pairing in a mixing layer (see Chapter 3).

Let us now assume a step of finite height H, with an upstream velocity field corresponding to a boundary layer (turbulent or possibly laminar) developing upstream of the step. The phenomenology of what happens is described in Figure 13.17. Kelvin–Helmholtz type vortices are shed in the mixing layer behind the step. They grow by pairing and are three-dimensionalized in a way which will be discussed below. These vortices have already been shown in the two-dimensional simulation of Plate 3. The shear layer bends towards the

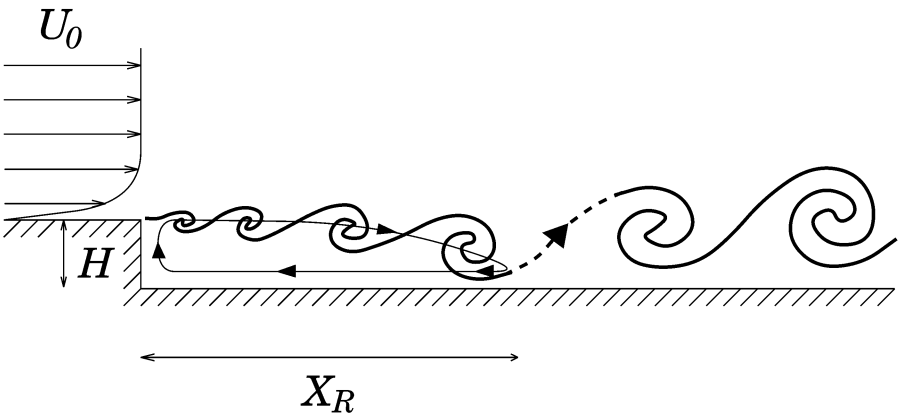

Figure 13.17. Schematic view of a backward-facing step flow.

wall and impinges it. Let X_R be a mean reattachment length, which may be defined as a line where the longitudinal velocity has an equal probability of being positive or negative. A recirculation zone forms upstream of X_R, where vortices may be trapped and reinjected in the upstream mixing layer. Other vortices are shed from the reattachment region and carried away downstream by the mean flow.

We do not intend here to make a complete review of the topic. Most of the following informations come from:

(a) Experiments by Eaton and Johnston [184], Driver et al. [174], Kiya et al. [332, 333], Bandyopadhyay [31], and Jovic and Driver [320].

(b) LES of Silveira-Neto et al. [648–650], Arnal and Friedrich [17], Akselvoll and Moin [4], Danet and Aider [3, 155]. The latter work in a weakly-compressible situation, with an upper free boundary (see Lesieur et al. [431] for more details on this work with animations).

(c) DNS of Le et al. [391]. They use a free-slip upper boundary condition, with an expansion ratio of 1.2. It simulates the experiment of Jovic and Driver [320] in a double-expansion channel at a Reynolds number $R_e = U_0 H/\nu = 5100$.

Let us mention that a recent review on the backward-facing step can be found in Lesieur et al. [431].

13.4.1 Mean reattachment length

A very rough estimate of the mean reattachment length may be obtained in the following way. We remind (see Chapter 4) that the growth rate of an

incompressible turbulent mixing layer between two flows of velocities U_1 and U_2 (and same densities) is given by the law

$$\frac{U_1 + U_2}{U_1 - U_2} \frac{d\delta}{dx} = A, \tag{13.9}$$

where δ is the vorticity thickness and A a non-dimensional coefficient of the order of 0.20. In the case of the mixing layer just behind the step, we take $U_1 = U_0$ and $U_2 = 0$, which yields $d\delta/dx \approx 0.2$. If one assumes that X_R is the downstream distance such that $\delta(X_R) = H$, it is obtained

$$X_R = 5H.$$

In fact, it was found by Armaly et al. [15] that X_R increases with the Reynolds number for $R_e < 1200$, then decreases up to $R_e = 6600$, then remains constant above. The reattachment length increases also with the expansion ratio. Typical values at high Reynolds range from $5H$ to $8H$. For low expansion ratios, numerical simulations may have difficulties to get a correct X_R if the velocity just upstream of the step consists for instance in a mean turbulent boundary layer profile to which a random fluctuation is superposed.[25]

It was shown by Le et al. [391] and Akselvoll and Moin [4] that realistic deterministic turbulent boundary-layer fields using a "precursor calculation" (see Lund et al. [458]), as well as grid refinement in the shear layer behind the step and at the lower wall are needed in order to get the right X_R. In the precusor calculation, a time-dependent flow having the same scalings as the outer and inner boundary layer is computed.

13.4.2 Coherent vortices

In his visualizations of the flow in a blunt plate separation bubble, Kiya [333] could identify quasi two-dimensional Kelvin–Helmholtz (KH) vortices shed behind the leading edge of the plate, and then stretched longitudinally into Λ-structures. Silveira-Neto et al. [648–650] were the first to study the topology of coherent vortices in a backstep flow with the aid of LES. They found evidence for helical pairing of the KH vortices at an expansion ratio of 1.67 corresponding to the experiment of Eaton and Johnston [184], but a more quasi two-dimensional structure (with longitudinal hairpins stretched between the KH billows, see Plate 22) at an expansion ratio of 5. However, this was only a transient state, as found by Fallon et al. [193], who recovered for longer times the helical-pairing configuration in the latter case.

[25] But average quantities such as the velocity profile, r.m.s. velocity fluctuations or Reynolds stresses are well predicted, provided the downstream distance from the step is renormalized by X_R (Fallon et al. [193]).

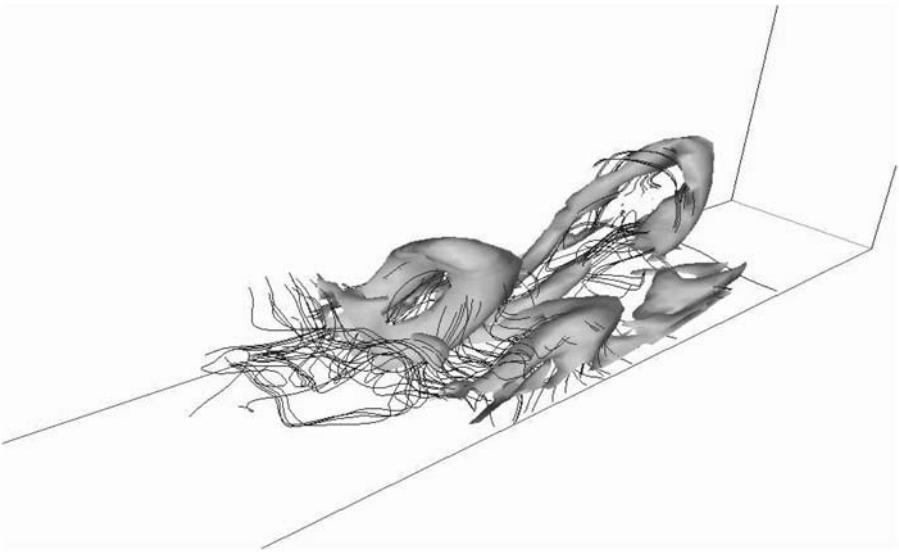

Figure 13.18. LES showing a close up of the vorticity field corresponding to reattaching Λ-vortices behind a backward-facing step (courtesy F. Delcayre, Grenoble).

Figure 13.18 shows the behaviour of coherent vortices in a LES done by Delcayre [165] in the same configuration as Le et al. [391]: uniform density, Reynolds number 5100, free-slip upper boundary, grid refinement at the wall and in the shear layer downstream of the step. Delcayre uses, together with finite-volume methods (which are numerically diffusive), the selective structure-function model (see Chapter 9), without any wall law, and with a very short inlet channel of length H where the experimental mean velocity profile of Jovic and Driver's [320] experiment is assumed. As already stressed, this does not give a good mean reattachment length, since the computed X_R is $7.5H$ (instead of $6.1H$ in the experiment). But there is no reason why the dynamics of the coherent vortices should not be properly represented. The figure shows a big Λ vortex which impinges the lower wall and is carried away downstream, while transforming into an arch-like vortex resembling the hairpins ejected in a turbulent boundary layer (see Plate 18). In fact, examination of the pressure plots in the simulation just behind the step indicates that helical pairing is at hand. It seems then that a good scenario for coherent vortex dynamics is here:

(a) quasi two-dimensional KH coherent vortices are shed behind the step;
(b) they undergo helical-pairing interactions;
(c) a staggered pattern of big Λ-vortices forms;
(d) they impinge the wall;

(e) they are either carried away downstream and transform into archs, or trapped into the recirculation bubble.

Let us quote Lesieur et al. [431], who mention the weakly-compressible LES of Danet and Aider [3, 155], and provide animations of these flows:

> In a more recent LES study of the (...) step at Mach 0.3, Lesieur et al. [430] compare flows resulting from two sets of upstream conditions:
> (A) a mean velocity profile corresponding to Spalart's boundary-layer DNS [663] perturbed by a weak three-dimensional white noise.
> (B) a more realistic time-dependent velocity field (precursor calculation) generated through an extension to the compressible case of the method developed by Lund et al. [458].
>
> In case B, the upstream boundary layer contains quasi longitudinal vortices propagating before the step. The first grid point in the direction nomal to the wall is at a distance of 1.3 in wall units relative to the upstream turbulent boundary layer. Periodicity is assumed in the spanwise direction, and the boundary condition at the top and the exit of the domain is non-reflective. This makes a difference with respect to the DNS of Le et al. [391] where free-slip conditions are taken. (...) Q isosurfaces (threshold $0.6U_0^2/H^2$) for the two classes of upstream conditions are presented. For case A, one sees the regular shedding of straight quasi two-dimensional Kelvin–Helmholtz vortices, which appear at a distance of $1.5 \approx 2H$ downstream of the step. They undergo helical pairing, and transform into big Λ vortices (arch vortices) which impinge the lower wall and are carried away from the step. (For case B, one sees) qualitatively the same events, but vortices appear very close to the step, and the flow is much more three-dimensional. Helical pairing seems to be triggered by the passage of upstream longitudinal vortices passing above the step. The side views of figures (...) confirm that the flow reattaches sooner in this case than in the noised case. This is confirmed by the determination of the reattachment length, which is of $5.80H$ for (A) and $5.29H$ for (B). The latter value is different from the value of $\approx 6.1H$ found by Le et al. [391] with equivalent upstream conditions. This discrepancy may be attributed to the differences in the boundary conditions above and downstream of the computational domain.

13.4.3 Instantaneous reattachment length

In fact, one can define in this problem an instantaneous reattachment line, for instance by considering the instantaneous streamlines in the neighbourhood of the lower wall. It will oscillate in the spanwise direction, due to the three-dimensional structure of the vortices which impinge the wall. It will also

oscillate in the flow direction, with a frequency determined by the velocity and spacing of vortices originating from the upstream mixing layer which pass in the reattachment region. This frequency is measured as $f_{KH} \approx 2U_0/X_R$. In their experiment (where $X_R = 7.8H$), Eaton and Johnston [184] show also evidence for an oscillation of the reattachment length at a "flapping frequency" $f_F \approx 0.07U_0/H \approx 0.55U_0/X_R$. A three-dimensional high-resolution LES of Silveira-Neto et al. [650] recovers a peak at the same frequency in the kinetic-energy spectra, for two downstream positions $10H$ and $12H$. It was checked by these authors that this low-frequency oscillation of the backstep flow may be recovered also in two-dimensional DNS. What is observed in these two-dimensional DNS is the following: KH vortices generated behind the step are caught in the recirculation region which, from time to time, sheds bigger vortices downstream at the frequency f_F. As a result, the recirculation region shortens abruptly as soon as a big eddy detaches, then slowly increases until the next eddy separates. Notice that in Silveira-Neto's two-dimensional simulations of Eaton and Johnston's experiment, the upper boundary (with a no-slip condition) was shown to play an important role, since the associated boundary layer detaches and sheds downstream a row of vortices of opposite sign with respect to the step vortices. The latter organise themselves in phase opposition with respect to the former, as in a two-dimensional jet. Remark finally that the flapping frequency was also found in the three-dimensional DNS of Le et al. [391], whith a free-slip upper boundary condition and hence no possibility for such an upper boundary-layer detachment. In fact, this flapping phenomenon is general to most of recirculation bubbles, as stressed by Kiya [333].

13.4.4 Rotating backstep

This exercise is an interesting combination of rotation and separation.

Deep flow

Let us assume that the flow in Figure 13.17 is submitted to a rotation of spanwise axis, and that the fluid is very deep in this direction.

It is clear from the upper results that if rotation is cyclonic (same sense as detached vortices), the latter will be strongly two-dimensionalized whatever the Rossby number upstream of the reattachment region. Downstream, it is probable they will keep their coherence, and travel as straight two-dimensional billows above the wall.

If rotation is anticyclonic, and if the Rossby number modulus is not too low, the vortices detached behind the step should give rise to purely longitudinal alternate vortices of same type as those encountered in rotating anticyclonic mixing layers. They will impinge the lower wall and keep on travelling

in the turbulent boundary layer above the wall. Before reattachment, one should have a linear mean velocity profile, corresponding to regions of zero absolute spanwise vorticity. If Rossby number modulus is low enough, one should observe a two-dimensional flow structure similar to the cyclonic case.

Shallow flow in the Mediterranean

A geophysical example of backstep in a shallow flow is given by the vortices shed in the Algerian current, which detach periodically from the recirculation region induced by surface Atlantic water passing through Gibraltar straight to the Mediterranean. Here, rotation is anticyclonic, but the very low Rossby numbers of oceanic vortices (≈ 0.05) imply a two-dimensionalization by rotation.

In fact the Algerian current is made of water fresher and colder than the bottom current coming from the Mediterranean to the Atlantic and which will give rise to the so-called meddies. Here, warm salty water is heavier than cold freshier water. It is also well known that water exchanges between the Atlantic and the Mediterranean are positive, since water lost by evaporation in the Mediterranean is not compensated by the supply due to rivers.

13.5 Compressible flows

The development of hypersonic planes and bodies has boosted research on free-shear or wall turbulent flows in supersonic or hypersonic conditions. Some of these studies might be easier numerically than experimentally. Since one-point closure models have some difficulties to capture the effects of Mach number on turbulence,[26] works using DNS or LES are of interest.

We review here some particular aspects of compressible turbulent shear flows. Other topics related to compressible turbulence may be found in Lele [405], Smits and Dussauge [656], as well as Krishnan and Sandham [360].

13.5.1 Compressible mixing layer

In compressible mixing layers between two flows of parallel velocities U_1 and U_2 in unbounded domains, the relevant Mach numbers are the convective Mach numbers $M_c^{(1)}$ and $M_c^{(2)}$, built with the velocity difference of each layer with respect to U_c, the velocity of the large vortices (Bogdanoff [69]), and respectively c_1 and c_2, the sound velocities in the two external flows. It can be shown by assuming a uniform pressure that

[26] See however Gerolymos and Vallet [249].

$$U_c = \frac{U_1 c_2 + U_2 c_1}{c_1 + c_2}. \tag{13.10}$$

Then, within this assumption, the convective Mach numbers

$$M_c^{(1)} = \frac{U_1 - U_c}{c_1}, \quad M_c^{(2)} = \frac{U_c - U_2}{c_2},$$

are both equal to

$$M_c = \frac{U_1 - U_2}{c_1 + c_2} = \frac{U}{\bar{c}}, \tag{13.11}$$

where $2U$ is the velocity difference, and $\bar{c}$ an average speed of sound between the two layers. Note that Eq. (13.10) writes also as

$$U_c = U_1 \frac{1 + (U_2/U_1)\sqrt{\rho_2/\rho_1}}{1 + \sqrt{\rho_2/\rho_1}}. \tag{13.12}$$

This expression allows to recover the value $U_c = (U_1 + U_2)/2$ in the incompressible uniform-density case. It may also be useful in an incompressible mixing layer with density differences, since it takes into account density effects which are not of gravitational type.

Returning to compressible mixing layers, laboratory experiments (Papamoschou and Roshko [562]) show that this hypothesis (identity of the two convective Mach numbers) is valid up to $M_c \approx 0.6$. Experiments show also a dramatic decrease of the spreading rate of the mixing layer, with respect to the incompressible value, between $M_c \approx 0.5$ and $M_c \approx 1$ (what we call M_c is now the highest of the two convective Mach numbers). Above, it saturates at about 40% of the incompressible case (see Figure 13.19).

The inviscid linear-stability analysis of the compressible mixing layer in the temporal case was performed by Lessen et al. [434,435] and Blumen [68]. The stability diagram found by the latter (for $\gamma = 1.4$) shows that the maximum-amplification rate is a decreasing function of the initial Mach number $M_c^{(i)} = U/\bar{c}$, with a drastic change in the slope at $M_c^{(i)} = 0.6$.

Two-dimensional DNS of Normand [537] show an inhibition of Kelvin–Helmholtz instability for $M_c^{(i)} > 0.6$: there is hardly any roll-up of the vortices, which remain extremely flat and merge "longitudinally", without turning around each other. On the contrary, for $M_c^{(i)} \leq 0.6$, the roll-up and pairing occur qualitatively in the same fashion as in the incompressible case, although they are delayed by factors corresponding exactly to the amplification rates predicted by Blumen [68]. Another interesting characteristic feature in two dimensions is the occurrence of shocklets on the edge of the vortices at $M_c^{(i)} \approx 0.7 \sim 0.8$. Figure 13.20 presents the vorticity and pressure fields in the two-dimensional DNS of Normand [537] at a convective Mach number of

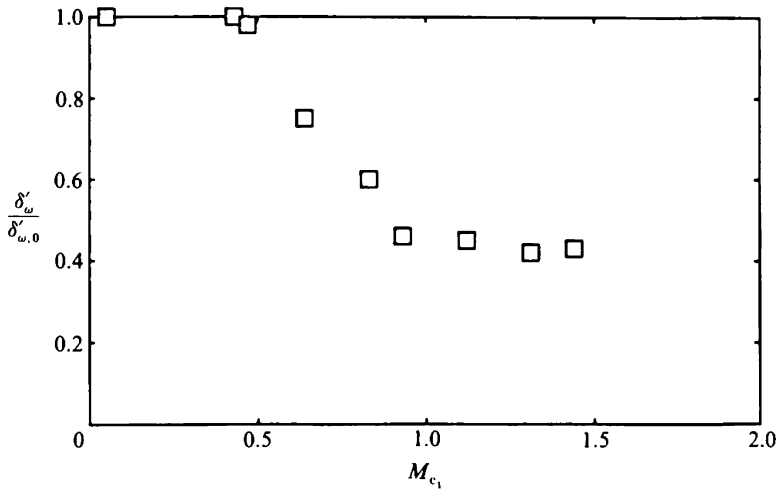

Figure 13.19. Experimental growth rate of the compressible mixing layer (normalized by the incompressible value) in terms of the largest convective Mach number (from Papamoschou and Roshko [562], courtesy *J. Fluid Mech.*).

0.8. They are visible as discontinuities in the pressure field, and leave weak traces on the vorticity. They are exactly analogous to shocks arising on a transsonic wing, and due to the fact that the flow is accelerated on the side of the vortex and becomes locally supersonic. Similar results were found by Soetrisno et al. [657, 658] and Lele [404]. This occurs both in the temporally and spatially-growing cases. It was however checked by Fouillet (1992) that at higher convective Mach number (still in two-dimension), these shocklets disappear, due to the very elongated character of the vortices.

A three-dimensional linear-stability analysis of the compressible temporal mixing layer was carried out by Sandham and Reynolds [629, 630]. It turned out that oblique waves are more amplified than two-dimensional waves when $M_c^{(i)}$ exceeds 0.6. Another result shown with the aid of DNS by Fouillet [211] is that the helical pairing found in the incompressible case (with a three-dimensional random forcing superposed to the hyperbolic-tangent profile) is inhibitted above $M_c^{(i)} = 0.6 \approx 0.7$. The vortex structure of the mixing layer is then made of staggered Λ vortices, as shown in Figure 13.21a, where the basic flow in the upper layer goes from left to right.[27] The corresponding pressure is displayed in Figure 13.21b. It indicates a longitudinal reconnexion of pressure

[27] The same structure was also found in the DNS of Sandham and Reynolds [630] with a quasi two-dimensional initial forcing.

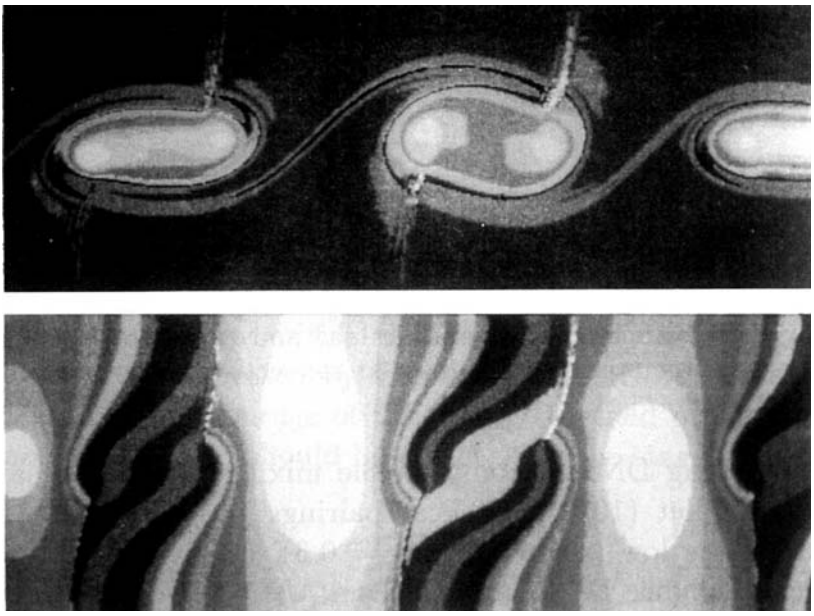

Figure 13.20. Vorticity (a) and pressure (b) maps obtained in the DNS of a compressible temporal mixing layer at $M_c^{(i)} = 0.8$ (courtesy X. Normand).

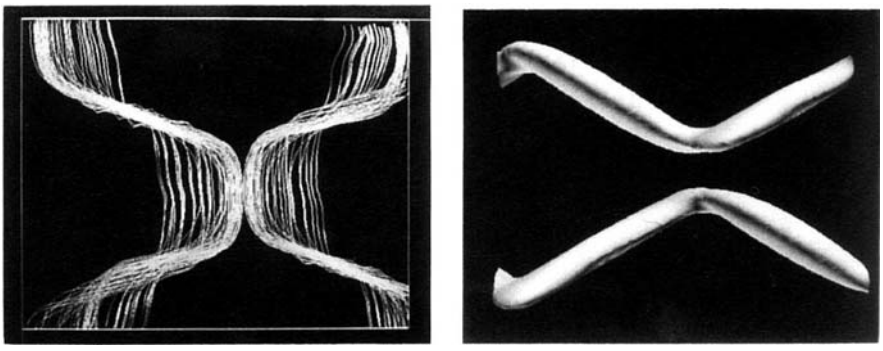

Figure 13.21. Top view of vortex lines (left) and pressure (right) in the DNS of a compressible temporal mixing layer at convective Mach number 1 (from Fouillet [211]).

into tubes following the legs of the Λ's. This is an example where low pressure ceases to follow the coherent vortices.

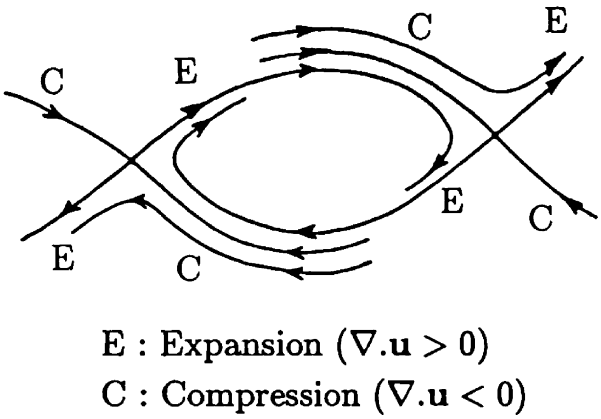

Figure 13.22. Compression and expansion of fluid particles in the stagnation region of mixing layers.

As stressed in Lesieur et al. [431], these large structures do not persist for higher resolution simulations of the temporal mixing layer at higher Reynolds number (see Pantano and Sarkar [560] and Beer [53]).

Spatially-growing DNS of compressible mixing layers were also performed by Fouillet [211]. Helical pairings was observed when the compressibility is low (upstream $M_c = 0.3$), as in the incompressible simulations of Chapter 4. At upstream $M_c = 0.7$ on the contrary, a pattern of very elongated staggered Λ vortices is obtained. The same pattern was found by Gathmann et al. [244] in a supersonic mixing layer confined between parallel planes. More recent LES of compressible spatial mixing layers are due to Doris [171]. Let us mention also the experiments of De Bisschop et al. [164] and Chambres [104].

Recent results concerning spatially-growing compressible free and forced round jets can be found in Lesieur et al. [431].

The saturation of spreading rates observed experimentally when M_c exceeds 0.6 might be due to two causes. The first one is the reflexion of Mach waves on the walls of the facility. The second is the inhibition of Kelvin–Helmholtz instability at this cross-over convective Mach number 0.6. Such an inhibition may be physically explained as follows (see Figure 13.22). We first consider an incompressible mixing-layer, where the vortex cores correspond to pressure troughs, while pressure highs are located in the stagnation regions. We assume now that compressibility is present, but is not too high so that the same type of pressure distribution is preserved. We suppose also that the fluid is a barotropic ideal gas, where p/ρ^γ is conserved with the motion. Therefore, fluid parcels travelling from low to high pressures (region C in Figure 13.22) will see their density increase when arriving at the stagnation

points (which means convergence, that is, $D\rho/Dt > 0$ and $\vec{\nabla}.\vec{u} < 0$). Afterwards they will expand (region E on the figure, $D\rho/Dt < 0$ and $\vec{\nabla}.\vec{u} > 0$). Let us now consider the vorticity equation (2.76), which reduces, in this compressible two-dimensional case, to

$$\frac{D}{Dt}\frac{\omega}{\rho} = \frac{1}{\rho^3}(\vec{\nabla}\rho \times \vec{\nabla}p).\vec{z} + \frac{\nu}{\rho}\nabla^2\omega. \tag{13.13}$$

Lele [404] and Fouillet [211] have verified in their numerical simulations that the baroclinic and the viscous terms are negligible, so that the vorticity dynamics reduces to the conservation of the "potential vorticity" ω/ρ. Thus, the convergence and divergence zones will be respectively a source and a sink of vorticity. This will work against Kelvin–Helmholtz instability, which tends to diminish the vorticity at the stagnation points, and to increase it in the low-pressure regions. As an illustration, Plate 23 presents a two-dimensional DNS of an initially isothermal supersonic spatially-developing mixing layer: the Mach numbers of the two streams are respectively 2 and 1.2. Hence, the convective Mach number is 0.4, still under the critical value of 0.6, but the divergence field already behaves as indicated by Figure 13.22. Note on Plate 23 an error concerning the montage of the divergence-field picture, since the "quadrupole structures" should be centered on the stagnation regions.

13.5.2 Baroclinic effects in free-shear flows

On the basis of Eq. (2.76), various interesting baroclinic vorticity production effects may be considered, even at low Mach. We take first a mixing layer between two flows of densities and velocities ρ_1, ρ_2, U_1, U_2. Suppose for instance $\rho_1 > \rho_2$ (see Figure 13.23). The braids between the vortices correspond to a density interface, and the vector $\vec{\nabla}\rho$ will be normal to the braid all along it. Since vortices are low-pressure regions, the pressure gradient $\vec{\nabla}p$ will be oriented as indicated on the figure. Therefore, the baroclinic torque will be a source (resp. a sink) of vorticity in the lower (resp. the upper) part of the braid. If $\rho_1 < \rho_2$, the reverse occurs between the lower and upper braids.

In fact, this is valid only when ρ is conserved, that is, for a liquid. For an ideal gas, the potential temperature Θ is conserved, and the baroclinic torque in Eq. (2.76) is equal to $(1/\rho^2\Theta)(\vec{\nabla}p \times \vec{\nabla}\Theta)$. Thus the above reasoning still holds when replacing ρ by $-\Theta$. This yields "comma-shape vortices", where the part of the braid on the warm side is intensified, while the other one disappears. This phenomenon is obvious in the gas mixing layers DNS presented in Figures 13.23a and 13.23b (taken from Fouillet [211]), at a temperature ratio of 2.

Such phenomena might be at hand in an axisymmetric round jet strongly heated, in a flame for instance. The upper results indicate that vorticity in the

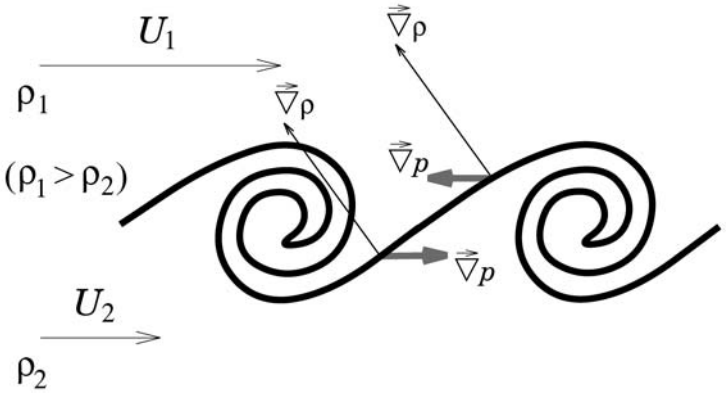

Figure 13.23. Baroclinic torque in a mixing layer with density differences ($\rho_1 > \rho_2$).

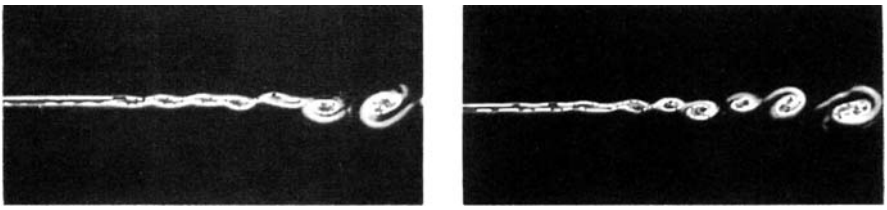

Figure 13.24. Two-dimensional DNS of a gas mixing layer at convective Mach number $M_c^{(i)} = 0.375$, with $U_1 > U_2$; a) $T_2 = 2T_1$, b) $T_1 = 2T_2$ (courtesy Y. Fouillet, Grenoble).

external part of the jet is reduced, while it is increased in the inner part. This is a situation favourable for a good combustion, since one may expect reduction of instabilities on the surface of the flame, and enhanced turbulent mixing (favouring chemical reactions) inside the jet. The same problem was looked at with three-dimensional DNS of a temporal mixing layer by McMurtry et al. [478] (see also Riley [601]), taking into account in the flow dynamics heat release due to the chemical reaction. They obtain slower roll-up and less entrainment of unmixed fluid, due in particular to the baroclinic torque. All these arguments contribute to explain why turbulent jets in a gas combustor are more steady than a non-heated jet (Mariasine, private communication).

Remark finally that such effects are absent from Boussinesq equations, where in the configuration of Figure 13.3 the baroclinic torque is proportional to $\vec{\nabla}\rho \times \vec{g}$, and constant along the braid. In the stable case ($\rho_2 > \rho_1$), it gives rise to a vorticity intensification on the braid which may be at the origin of a secondary Kelvin–Helmholtz instability. The latter was identified by Staquet

and Riley [670] (see also Staquet [671]) in the case of a mixing layer, and by Fallon et al. [193] for a stratified backstep flow.

13.5.3 Compressible wake

We have seen that compressibility inhibits the development of inflectional instabilities. This is true in particular for a wake. DNS of a three-dimensional compressible temporal plane wake, developing from a Gaussian deficit-velocity profile, were carried out by Chen et al. [114]. They show that, at a relative Mach number[28] of 0.462, the growth rate of the wake is reduced by a factor of 60% compared with an incompressible calculation. As time evolves and the deficit velocity decays, the wake becomes less and less compressible.

For a spatial wake developing behind a real object, things are extremely different in the supersonic case: visualizations (see e.g. Van Dyke [698]) show that, behind the front shock, the turbulent wake has become very narrow, with small-scale three-dimensional turbulence and without any large-scale vortex street.

13.5.4 Boundary layer upon a heated plate

We show now LES done by David [157] of transition to turbulence for an ideal gas without gravity effects in a heated boundary layer inclined 10° with respect to the incoming flow. The wall is isothermal, at a temperature three times larger than the temperature at infinity: the flow is uniform upstream ($M_\infty = 0.5$), with a small three-dimensional random white-noise perturbation superposed upon it. A curvilinear system of coordinates is used, at a resolution $237 \times 30 \times 32$ grid points respectively in the streamwise, transverse and spanwise directions. Here, the heating accelerates the transition, due to the generalized inflection-point criterion.[29] Staggered Λ vortices are visible in Figure 13.25, showing the vorticity modulus. In this calculation, it is the selective-structure function model (see Chapter 9) which is used. As for the transition on a flat plate, this calculation is not possible either within a DNS at reasonable cost or utilizing subgrid models like Smagorinsky's or the standart structure-function model.

It must be stressed also that the structure of this particular boundary layer has analogies with that of an incompressible boundary layer once turbulence has developed.

[28] Based on half the initial deficit velocity at the centre.

[29] This necessary condition for linear stability in a compressible parallel flow stresses that $\rho d\bar{u}/dy$ should have at least one extremum in the layer. If the wall is sufficiently heated, $\rho d\bar{u}/dy$ may increase with y, then decrease to zero at infinity, in such a way that it will have a maximum. These instabilities resemble Kelvin–Helmholtz instability.

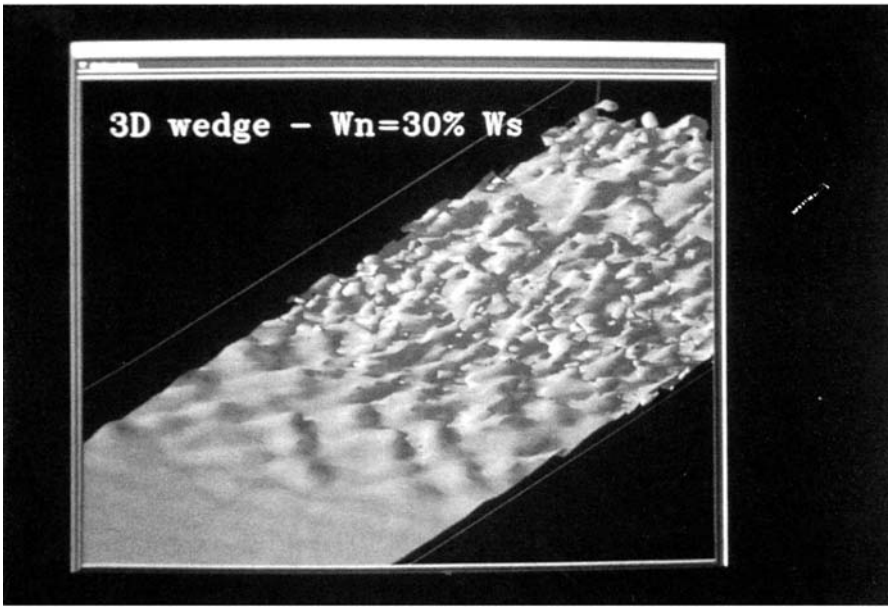

Figure 13.25. Vorticity modulus in the LES of a boundary layer at low Mach number upon a heated inclined plate (courtesy E. David).

Let us mention finally that important LES of heated channels (straight and curved) with applications to rocket engines (Ariane V in particular) are reported in Lesieur et al. [431]. This concerns the work of Salinas-Vazquez and Métais [625–627], and Münch et al. [527].

13.5.5 Compression ramp

We present here LES related to studies concerning the rear flap during the atmospheric reentry of HERMES, the former European space shuttle project. Indeed, there was some concern that coherent vortices (e.g. Görtler vortices) created in this region would produce temperature fluctuations overheating the flap, and possibly damaging the material. A three-dimensional LES of HERMES' rear flap, in conditions corresponding to a laboratory experiment carried out at the ONERA (with in particular a Mach number of 2.5), has been performed by David [157] with the same code as for the boundary layer upon a heated plate shown above. The calculation predicts both the λ shock characteristic of compression ramps and the presence of quasi stationary counter-rotating longitudinal Görtler type vortices. They are visible in Figure 13.26, which shows a spanwise section of the vorticity and the temperature field, with

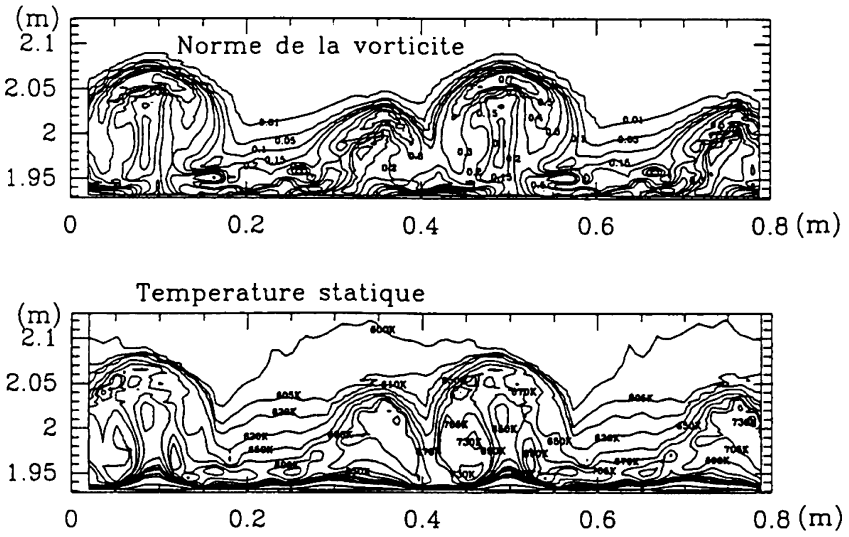

Figure 13.26. LES of HERMES' rear flap; spanwise section of the longitudinal vorticity (a) and temperature (b) (courtesy E. David, Grenoble).

characteristic mushroom shaped structures. More detailed on this calculation can be found in Lesieur et al. [431].

In fact, the longitudinal vortices induce a heat transfer at the wall which is five times larger than the average values. As stressed in Lesieur et al. [431], of particular importance is the notion of

> adiabatic temperature T_a (...), defined as the temperature reached at the wall (where the velocity is zero) by a fluid parcel travelling adiabatically from the exterior of the boundary layer (for a time-independent perfect fluid), and given by

$$T_a = T_\infty \left(1 + \frac{\gamma - 1}{2} M_\infty^2\right). \tag{13.14}$$

So T_a is greater than T_∞: longitudinal vortices take very hot external fluid at a temperature T_∞, and bring it close to the wall at a lower velocity and higher temperature. For a real hypersonic shuttle, we have $T_\infty \approx 3000°$K, and the temperature at the wall may be increased. This is susceptible of destroying any material.

This is an example of the interest of LES with respect to modelling methods, which might never predict this type of fluctuations. These calculations were still in progress when HERMES' project was cancelled, which is a pity

since we will never know about the potential dangers of these vortices. However, the unfortunate crash of US shuttle Columbia in 2003 might be due to a problem of this type.

13.5.6 Compressible boundary layer

A review of the stability studies concerning a compressible boundary layer above an adiabatic wall may be found in Mack [461] and Arnal [16]. Here, we summarize the results of the linear-stability calculations done by Arnal [16] for two-dimensional waves: the stability diagram resembles the incompressible one, up to a first critical Mach number of 1.3. The waves which propagate are analogous to the incompressible T.S. waves, and driven by a viscous instability. However, their amplification rates are smaller. For $1.3 < M < 2.2$, a new class of unstable modes appear at high Reynolds numbers, corresponding to an inviscid instability. For instance, at $M = 2.2$, these modes dominate for $R = U\delta_1/\nu > 7000$, while the viscous T.S. modes are dominant for $R < 7000$. This critical Reynolds number separating the viscous from the inviscid instability diminishes when the Mach number is increased, up to $M = 3$, where the viscous instabilities disappear. Another important characteristic is that the stability diagram splits for $M > 2.2$, with the appearance of a second class of instabilities of higher amplification rates and much higher wave numbers, compared with the unstable modes described previously. This Mack's second mode sees however its characteristic wave number decrease when M is further increased, up to $M = 4.8$ where the two unstable regions collapse. There is only one unstable region at higher Mach number.

As in the mixing layer, three-dimensional oblique waves appear, which, for $0.9 < M < 2.2$, grow faster than the two-dimensional ones (Arnal [16]). In the range of Mach numbers where the stability diagram opens out ($2.2 < M < 4.8$), it seems that the oblique waves corresponding to the lower unstable region of the stability diagram are more amplified than the corresponding two-dimensional waves (Arnal [16]).

The problem is of course extremely intricate, but nothing indicates that any inhibition of the instabilities will occur when the Mach number is increased. On the contrary, and because the structure of a boundary layer is highly three-dimensional, it is possible that turbulent boundary layers may exist even at very high Mach numbers, of the order of 15 (Morkovin [525]).

LES of temporal boundary layer at Mach 4.5

We finish by presenting numerical results concerning the transition to turbulence in a a temporal boundary layer developing upon an adiabatic flat plate at a Mach number $M = 4.5$ and a Reynolds number 10.000. A three-dimensional

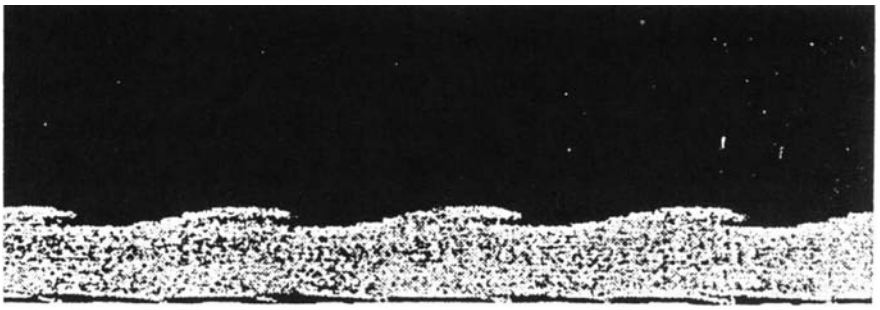

Figure 13.27. Two-dimensional DNS of a temporal boundary layer at Mach 4.5; vorticity field corresponding to rope-like vortices developing from the second mode (courtesy F. Ducros, Grenoble).

linear-stability analysis of the laminar boundary profile shows that the most-unstable mode is the two-dimensional second mode, due to the generalized inflection-point instability. Three-dimensional DNS of such a boundary layer were carried out by Ng and Erlebacher [533]. They first generate a basic two-dimensional state, starting with the laminar profile to which a perturbation consisting of the eigenmode corresponding to the second mode is added. The resulting evolved basic state is made of the so-called "rope-like vortices", sort of very flat Kelvin–Helmholtz vortices developing close to the exterior of the boundary layer. Let $(2, 0)$ be the components of the corresponding Fourier wavevector in the (α, β) space. Afterwards, they add a three-dimensional perturbation as a pair of oblique subharmonic waves,[30] which puts energy on the wavevector $(1, 1)$, which is a staggered mode. The DNS shows the growth of energy in this mode, but blows up before the development of turbulence. Ducros et al. [179] have redone these DNS in a slightly different manner: they first generate the rope-like vortices through two-dimensional DNS starting with the laminar profile to which a two-dimensional white noise is superposed. This basic state is displayed in Figure 13.27. Then a three-dimensional white noise is added. As for Ng and Erlebacher [533], the DNS blows up before the end of transition. Figure 13.28a shows the evolution with time of the kinetic energies of the various modes (integrated on the height of the layer) in Ducros et al.'s [179] DNS: it confirms the growth of the subharmonic $(1, 1)$, but also of a purely longitudinal mode $(0, 2)$. In the same paper, a LES using the structure-function model within the four-point formulation in planes parallel to the wall is carried out. The initial conditions are the same as for the DNS. The agreement between DNS and LES is good, as far

[30] Which are the most-amplified within a secondary-instability analysis of the second mode.

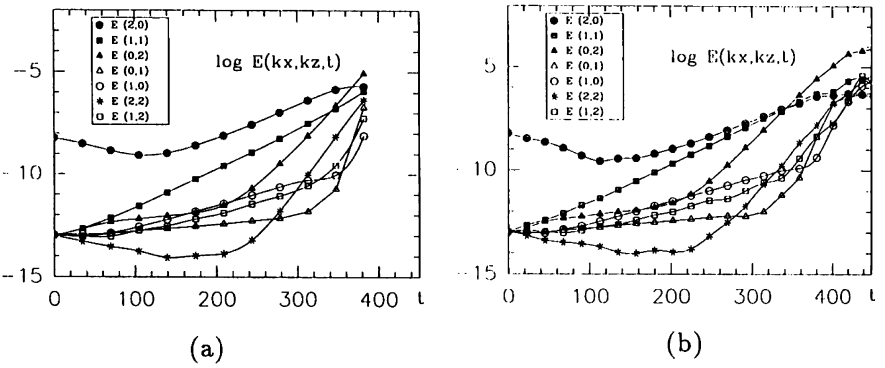

Figure 13.28. Growth of modal energies in three-dimensional DNS (a) and LES (b) of a temporal boundary layer at Mach 4.5 (courtesy F. Ducros, Grenoble).

as the modal energies are concerned (see Figure 13.28b). However, the LES allows to go beyond the transition to developed turbulence. One sees that, during transition, the mode $(0, 2)$ has initially a very slow growth (may be linear, as in the models looked at in Chapter 3), then shoots up and eventually overwhelms the other modes. Up to $t \approx 350\delta_i/U_\infty$, the rope-like vortices undergo an out-of-phase spanwise deformation, corresponding to the subharmonic mode $(1, 1)$. This is close to the topology of the compressible mixing layer, and of the inclined heated boundary layer of Figure 13.25. Meanwhile, the longitudinal mode is physically associated to weak low- and high-speed streaks of longitudinal velocity located close to the wall. They are also visible when looking at the vertical vorticity ω_y. But the streaky pattern does not persist after $t = 400\delta_i/U_\infty$, in the final stage of transition. Such a structure has also been observed by Adams and Kleiser [2] with better-resolved DNS permitting to go beyond transition. More details on the flow evolution may be found in Adams and Kleiser [2]. They also find an important growth of the $(0, 2)$ mode, and attribute it to a *strongly nonlinear interaction between the dominant modes*. Indeed, a nonlinear resonant interaction between two $(1, 1)$ modes may, if longitudinal periodicity is assumed, amplify the $(0, 2)$ mode.

Other configurations

Let us mention also the work of Maeder et al. [462], which is a "parabolized" DNS of a spatially-growing boundary layer without pressure gradient above an isothermal flat plate, at Mach M_∞ ranging from 3 to 6. It gives an interesting review on numerical and experimental aspects of compressible boundary layers.

13.6 Book's conclusions

The world of *turbulence* is very wide, and it was not our aim to cover all its aspects, some of which are already presented in excellent textbooks or reviews. Therefore we have chosen to present only a limited number of issues.

In Chapter 1, we give a broad presentation of turbulence in fluids, with experimental and numerical illustrations. We provide numerous engineering, geophysical or astrophysical applications. We propose a new definition of turbulence based upon the properties of *unpredictability, mixing*, and the existence of a wide band of scales. Such a definition does not require three-dimensionality nor vortex stretching in the flow, and allows us to accept the concept of *two-dimensional turbulence*. We propose also definitions for *coherent vortices* and *coherent structures*. The concept of *fully-developed turbulence* and the *isotropy assumption* are discussed. We introduce both *deterministic approaches* such as *direct-numerical simulations* (DNS), and *stochastic tools* such as one-point or two-point *closure models*. In this respect, *large-eddy simulations* (LES) are a very promising compromise, allowing to provide informations regarding both the deterministic structure and the statistical properties of turbulence.

Chapter 2 presents basic dynamics and thermodynamics of fluids, with *Euler* and *Navier–Stokes equations* for liquids and gases. Gravity, ensemble rotation and compressibility are taken into account in a very complete fashion. We look at vorticity dynamics, and present both *Helmholtz and Kelvin's theorems*. We derive also *Ertel's theorem for potential vorticity*, with applications to atmospheric and oceanic dynamics. We derive *Proudman–Taylor theorem* for rapidly-rotating non-stratified flows. Density stratification effects are looked at with the aid of *Boussinesq equations*, with a formulation valid both for liquids and gases. This allows us to study internal *inertial-gravity waves* in geophysical flows. External inertial-gravity effects in shallow layers are considered with the aid of *Barré de Saint-Venant equations*. We develop in particular the *shallow-water analogy* between gravity waves at the surface of a liquid and sound waves in a barotropic gas. We look also at the interesting problem of *Kelvin waves and tides*. Finally we consider surface gravity waves in a fluid of arbitrary depth.

In Chapter 3 we study *transition to turbulence*. We first introduce the *Reynolds number*, then present the *linear-instability theory* for a parallel basic flow, both in two and three dimensions. We demonstrate *Orr–Sommerfeld equation* for a viscous fluid, and *Rayleigh equation* for a perfect flow. *Squires' theorem* permits to relate the three- and two-dimensional approaches. The effect of a solid-body rotation is looked at, with the presentation of *shear-Coriolis instability*, and how it relates to *centrifugal instabilities*. In the non-rotating case, we present very simple *non-normal models* having some analogies with *low- and high-speed streaks* observed in turbulent boundary layers.

Afterwards we discuss transition in free-shear flows, using both laboratory experiments and numerical simulations. We present physically the *roll up* and *pairing* of *Kelvin–Helmholtz vortices*, as well as the formation of *longitudinal hairpin vortices*. We show also the possibility for *helical pairing interactions*, yielding *dislocations of the coherent vortices*. We describe transition in wall flows, with *Klebanoff's harmonic mode* and *Herbert's staggered mode*. Finally, thermal convection is discussed, mainly from the viewpoint of *Rayleigh–Bénard convection*.

Chapter 4 is devoted to free or wall-bounded *turbulent shear flows*, both from a statistical and coherent-structure point of view. We first present *Reynolds equations*, as well as the *mixing-length theory*. The latter allows to calculate the mean velocity profiles of plane and round jets or wakes, and of mixing layers. For wall flows, we introduce *wall units* and derive the mean logarithmic velocity profile for *turbulent boundary layers*, plane *Poiseuille and Couette flows*. We discuss *Blasius law of skin friction*, and *Dean analogy*. We show how coherent vortices may be characterized by the Q criterion. Then we discuss the topology of vortices in *turbulent mixing layers*, jets and wakes, with primary vortices, secondary longitudinal vortices stretched between the latter, or helical reconnections. For round jets, the equivalent of helical pairing is *alternate pairing of vortex rings*. We finally review the coherent topology of turbulent wall flows, with longitudinal *low- and high-speed streaks* close to the wall, and *propagation of hairpins* above the low-speed streaks. The latter dynamics is supported by animations of LES given in Lesieur et al. [431].

In Chapter 5, we introduce spectral tools which are very useful for the study of statistically *homogeneous turbulence*. We present two Fourier transforms of a flow: the discrete and integral representations, for respectively periodic and non-periodic flows. Afterwards, we write Navier–Stokes and Boussinesq equations in Fourier space, and introduce *Craya decomposition*, which is shown to be equivalent to *Riley's vortex-wave decomposition*. We present also the *complex helical wave decomposition*. We discuss how *random functions* may be applied to turbulence. A particular emphasis is put on *spectral tensors*. In the case of *isotropic turbulence*, we introduce the spectra of kinetic energy, *enstrophy, helicity* and passive scalar. We study also *axisymmetric turbulence*. Finally, we present the basic lines of *rapid-distorsion theory*, which applies to homogeneous turbulence submitted to a mean constant shear.

Chapter 6 is devoted to three-dimensional isotropic turbulence. We first look at *triad interactions* in Fourier space, and *quadratic invariants* in physical space. Afterwards we present the so-called *Kolmogorov's 1941 theory*, both in Fourier space (*Oboukhov's theory*) and in physical space. *Structure functions* of arbitrary order are considered. We discuss also *Richardson's law* concerning the relative dispersion of particles pairs. Afterwards, the question of the

dimension of the attractor of turbulence is looked at. A discussion relating the *skewness factor* to a possible *enstrophy divergence* is carried out. The second part of the chapter deals with coherent vortices in three-dimensional isotropic turbulence. One looks also at the vorticity and pressure p.d.f.'s, and derive *Batchelor's law for the pressure spectrum*. We indicate how to calculate the turbulence noise from this spectrum. Afterwards, we present the phenomenology of passive-scalar diffusion, very important for combustion modelling. The chapter ends with a discussion on *internal intermittency*, and some anomalous data found for the passive scalar in the large scales.

Chapter 7 is concerned with *two-point closures* of isotropic turbulence. It presents first the *Quasi-Normal approximation*, then the *Eddy-Damped Quasi-Normal Markovian approximation* (E.D.Q.N.M.). Equivalent stochastic models are proposed. These tools are extremely effective to understand the energy transfers between different scales of motion. They are applied to kinetic energy, helicity, pressure and diffusion of passive scalars. For the helicity spectrum, they allow to predict a $k^{-5/3}$ cascade which superposes to the $k^{-5/3}$ kinetic-energy cascade, and delays it. This helicity cascade has been recovered by LES, which shows the quality of E.D.Q.N.M. type statistical closures. The *non-local interaction theory* is derived, and interpreted in terms of *spectral backscatter* (recovered also by DNS and LES) and *kinetic-energy decay*. We present also the formalism of *Renormalization-Group techniques* (R.N.G.), with a discussion on their validity.

Most of Chapter 8 deals with two-dimensional isotropic turbulence, which has applications to large-scale atmospheric and mesoscale oceanic dynamics, as well as to MHD turbulence, plasma physics and fusion-produced energy. We start with *Fjortoft's theorem*, then explain the concepts of *enstrophy cascade* and *inverse energy cascade*. We provide experimental validations of these cascades, and discuss their relation with coherent vortices. We present *Weiss criterion* (see also Herring [277]), which turns out to be a particular case in two dimensions of the Q criterion, and is anterior. The E.D.Q.N.M. model is also applied to kinetic energy, passive scalar and pressure. It allows to recover the upper phenomenology. New DNS and LES of kinetic-energy and pressure spectra are shown. Finally, we look at some two-dimensional mixing-layer simulations from the point of view of two-dimensional turbulence.

Chapter 9 is devoted to some aspects of *Geophysical turbulence*. It presents the *geostrophic approximation* for the large-scale motions, and associated discrete-layer models. *Baroclinic instability* developing from thermal fronts is looked at using both theoretical considerations and DNS-LES based upon Boussinesq equations. One shows in particular how cyclonic vorticity is favoured throughout the process, specially in braids reconnecting the vortices. We present Rossby waves (environmental and topographic). We discuss also

the Ekman layer separating the geostrophic flows from a solid boundary or (for the ocean) the upper wind. We present *Lilly's model of tornado generation*, as well as a model based on thermal convection of a hairpin. Finally, *Charney's theory of geostrophic turbulence* is studied.

Chapter 10 is related to statistical thermodynamics of *inviscid truncated systems*. In fact the use of these tools for real turbulent flows is limited.

Chapter 11 presents *unpredictability growth* from a two-point closure point of view, both in three and two dimensions. We show how inverse cascades of unpredictability from small to large scales may occur. We have related this phenomenon to an *error backscatter*. There are important applications of this problem in meteorology, since it is found that one cannot predict weather numerically for periods overtaking $10 \approx 15$ days. It turns out that climate numerical models of the atmosphere which make predictions for much longer periods are subject to errors.

Chapter 12 presents modern basis of *large-eddy simulations* (LES). We first introduce the formalism of LES in physical space, with *Smagorinsky's model*. We derive *Kraichnan's spectral eddy viscosity* and eddy diffusivity from the E.D.Q.N.M. approach, using the non-local interaction theory. This model is extended to spectra decreasing faster than Kolmogorov at the cutoff (*spectral dynamic model*). We present also the *structure-function model*, as an attempt to extend the spectral eddy coefficients to physical space. Filtered or selective versions of this model are developed, in order to get rid of the influence of large-scale velocity gradients in the evaluation of the eddy viscosity. We discuss *Smagorinsky's dynamic model*. Various applications are provided concerning isotropic turbulence, free-shear flows and wall flows.

Chapter 13 concerns four important practical applications of turbulence, dealing with the effects of *stratification, rotation, separation and compressibility*. They are studied with the aid of experiments, DNS and LES. We show in particular how stratified turbulence may collapse into *pankake-shaped structures*. Rotating turbulence concerns first shear flows, where DNS and LES, show in certain anticyclonic regions the formation of longitudinal hairpins where absolute vorticity condenses. This is associated with a local Rossby number equal to -1. We discuss also LES of initially isotropic turbulence submitted to rotation. Afterwards, separated flows behind a backward-facing step are looked at, both from a statistical and topological viewpoint. Finally, compressibility effects in free-shear flows and boundary layers are considered, with aerospace applications.

It is of course not possible to give a definitive conclusion to this monograph, which poses certainly more questions than it provides answers. Therefore we will leave the reader to draw his own conclusions, hoping that we have been able to propose some new trails to his imagination.

A continuous preoccupation throughout the book concerned the question of the existence of *coherent vortices* as a part of the turbulence itself, and how they interact with smaller scales in the flow. It is an appealing prospect than trying develop a *Mechanics of elementary vortices*, involving modes such as *spirals, pairings, dipoles, dislocations, alternate pairings, hairpins, streaks*, etc.

What will be the near future of Fluid Mechanics? It seems that, taking into account the huge increase of computer ressources, a period has come in which three-dimensional DNS and LES of flows of reasonable complexity[31] are not only at hand, but are even less expensive than laboratory experiments.[32] These numerical simulations (in case of LES) need an efficient subgrid-scale modelling in order to take into account the small-scale turbulence. They need also to be devised in such a way as to reproduce perfectly the results of the linear-instability theory.[33] The numerical codes have to be validated on simpler cases such as isotropic turbulence, on experiments if possible, and must be consistent with the physical principles which have emerged from the theory, like the existence of inertial cascades, the correct decay laws or the unpredictability. It is then important in this context to maintain and develop the stochastic modelling tools, and make them as simple as possible to handle.

The LES will serve as an invaluable tool to assess the classical methods of turbulence modelling in the industry. They will also permit a *dynamic control of turbulence*, for instance in aerodynamics, acoustics or combustion. Let us mention that right now, methods for coupling one-point closure modelling in the large scales with LES in the small scales are rapidly developing for industrial applications.

Such a trend in Fluid Dynamics research will in no way exclude the recourse to theory. Laboratory experiments will of course be necessary, either for a better understanding of fundamental physics, or in complex situations where developing a calculation is not realistic. As already stressed, they are also needed in order to validate the numerical codes.

Of course, all these ambitious projects will be rendered possible only with a proper development of the computing, data processing and visualization facilities. Parallel calculations performed simultaneously on a large number of processors will play an important role in this development.

---

[31] "Reasonable", in the sense of the large eddies around a wing or within a combustor, or the planetary scales of atmospheres and oceans, or the convective cells in a heated flow. But certain extremely complex industrial flows (like within the core of a fast-breeder reactor for instance) do not fall into this category.

[32] In some situations such as in very high speed or high temperature flows, the experiment (or measurements) may even be impossible (or too dangerous).

[33] This point is extremely important in the context of the study of large coherent vortices.

It might finally happen that this would be only a necessary transition stage towards the definition of new fluid dynamical concepts which would render obsolete and useless the complicated analytical and numerical techniques which helped create them.

References

1. Ackermann, C. and Métais, O. (2001) A modified selective structure function subgrid-scale model. J. Turbulence, **2**, 011
2. Adams, N.A. and Kleiser, L. (1996) Subharmonic transition to turbulence in a flat-plate boundary layer at Mach number 4.5. J. Fluid Mech., **317**, 301-335
3. Aider, J.L. and Danet, A. (2006) Large-eddy simulation study of upstream boundary conditions influence upon a backward-facing step flow. C.R. Acad. Sci. Mécanique, **334**, 447-453
4. Akselvoll, K. and Moin, P. (1995) Large-eddy simulation of turbulent confined coannular jets and turbulent flow over a backward-facing step. Stanford University, Rep. MD-43
5. Allègre, C. (1983) L'écume de la Terre, Fayard
6. André, J.C. (1974) Irreversible interaction between cumulants in homogeneous, isotropic, two-dimensional turbulence theory. Phys.Fluids, **17**, 15-21
7. André, J.C. and Lesieur, M. (1977) Influence of helicity on high Reynolds number isotropic turbulence. J. Fluid Mech., **81**, 187-207
8. André, J.C. (1988) Private communication
9. Anselmet, F., Gagne, Y., Hopfinger, E.J. and Antonia, R.A. (1984) High-order velocity structure functions in turbulent shear flows. J. Fluid Mech., **140**, 63-89
10. Antonia, R.A., Hopfinger, E.J., Gagne, Y. and Anselmet, F. (1984) Temperature structure functions in turbulent shear flows. Phys. Rev. A, **30**, 2704-2707
11. Antonia, R.A., Teitel, M., Kim, J. and Browne, L.W.B. (1992) Low Reynolds number effects in a fully-developed turbulent channel flow. J. Fluid Mech., **236**, 579-605
12. Aref, H. (1983) Integrable, chaotic and turbulent vortex motion in two-dimensional flows. Ann. Rev. Fluid Mech., **15**, 345-389
13. Aref, H. (1985) Chaos in the dynamics of few vortices – Fundamentals and applications. In Theoretical and Applied Mechanics, F.L. Niordson and N. Olhoff eds, Elsevier Science Publishers, 43-68
14. Argoul, F., Arnéodo, A., Grasseau, G., Gagne, Y. Hopfinger, E.J. and Frisch, U. (1989) Wavelet analysis of turbulence reveals the multifractal nature of the turbulent cascade. Nature, **338**, 51-53

15. Armaly, B.F., Durst, F., Pereira, J.C.F. and Schönung, B. (1983) Experimental and theoretical investigation of backward-facing step. J. Fluid Mech., **127**, 473-496
16. Arnal, D. (1988) Stability and transition of two-dimensional laminar boundary layers in compressible flow over an adiabatic wall. Rech. Aérosp., **4**, 15-32
17. Arnal, M. and Friedrich, R. (1993) Large-eddy simulation of a turbulent flow with separation. In Turbulent Shear Flows VIII, Springer-Verlag, 169
18. Ashurst, W.T. (1979) Numerical simulation of turbulent mixing layers via vortex dynamics. in Turbulent Shear Flows I, Springer-Verlag, 402-413
19. Ashurst, W.T. and Meiburg, E. (1988) Three-dimensional shear layers via vortex dynamics. J. Fluid Mech., **189**, 87-116
20. Atten, P., Caputo, J.G., Malraison, B. and Gagne, Y. (1984) Determination of attractor dimension of various flows. in Bifurcations and chaotic behaviours, J. Mec. Theor. Appl., Suppl., G. Iooss and R. Peyret ed., 133-156
21. Aubry, N., Holmes, P., Lumley, J.L. and Stone, E. (1988) The dynamics of coherent structures in the wall region of a turbulent-boundary layer", J. Fluid Mech., **192**, 115-173
22. Aupoix, B. and Cousteix, J. (1982) Modèles simples de tension sous-maille en turbulence homogène et isotrope. La Recherche Aérospatiale, **4**, 273-283
23. Babiano, A., Basdevant, C. and Sadourny, R. (1985) Structure functions and dispersion laws in two-dimensional turbulence. J. Atmos. Sci., **42**, 941-949
24. Babiano, A., Basdevant, C., Legras, B. and Sadourny, R. (1987) Vorticity and passive-scalar dynamics in two-dimensional turbulence. J. Fluid Mech., **183**, 379-397
25. Babiano, A., Basdevant, C., Leroy, P. and Sadourny, R. (1990) Relative dispersion in 2-dimensional turbulence. J. Fluid Mech., **214**, 535-557
26. Balarac, G. and Metais, O. (2005) The near field of coaxial jets: a numerical study. Phys. Fluids, **17**, 169-182
27. Balarac, G. (2006) Etude numérique de la dynamique tourbillonnaire et du mélange dans les jets coaxiaux turbulents. PhD Grenoble Institute of Technology
28. Balarac, G., Si-Ameur, M., Lesieur, M. and Métais, O. (2006) Direct numerical simulations of high-velocity ratio coaxial jets: mixing properties and influence of upstream conditions. J. Turbulence, **8**(22), 1-27
29. Balint, J.L., Vukoslavcevic, P. and Wallace, J.M. (1986) A study of the vortical structure of the turbulent-boundary layer, in Advances in turbulence, G. Comte-Bellot and J. Mathieu eds, Springer-Verlag, 456-464
30. Balint, J.L., Vukoslavcevic, P. and Wallace, J.M. (1991) The velocity and vorticity vector fields of a turbulent boundary layer. Part 2. Statistical properties. J. Fluid Mech., **228**, 53-86
31. Bandyopadhyay, P.R. (1991) Instabilities and large structures in re-attaching boundary layers. AIAA J., **29**, 1149-1155
32. Bardina J., Ferziger J.H. and Reynolds W.C. (1980) Improved subgrid model for large-eddy simulation. AIAA paper 80-1357
33. Bartello, P. and Holloway, C. (1991) Passive scalar transport in β-plane turbulence. J. Fluid Mech., **223**, 521-536

34. Bartello, P., Métais, O. and Lesieur, M. (1994) Coherent structures in rotating three-dimensional turbulence. J. Fluid Mech., **273**, 1-29
35. Bartello, P. and Warn, T. (1996) Self-similarity of decaying two-dimensional turbulence. J. Fluid Mech., **326**, 357-372
36. Basdevant, C. and Sadourny, R. (1975) Ergodic properties of inviscid truncated models of two dimensional incompressible flows. J. Fluid Mech., **69**, 673-688
37. Basdevant, C., Lesieur, M. and Sadourny, R. (1978) Subgrid-scale modelling of enstrophy transfer in two dimensional turbulence. J. Atmos. Sci., **35**, 1028-1042
38. Basdevant, C., Legras, B., Sadourny, R. and Beland, B. (1981) A study of barotropic model flows: intermittency, waves and predictability. J. Atmos. Sci., **38**, 2305-2326
39. Basdevant, C. (1981) Contribution à l'étude numérique et théorique de la turbulence bidimensionnelle. Thèse de doctorat d'Etat, Université Pierre et Marie Curie, Paris
40. Basdevant, C. and Sadourny, R. (1983) Parameterization of virtual scale in numerical simulation of two-dimensional turbulent flows. in Two-dimensional turbulence, J. Mec. Theor. Appl., Suppl., R. Moreau ed., 243-270
41. Basdevant, C. and Philipovitch, T. (1994) On the validity of the "Weiss criterion" in two-dimensional turbulence. Physica D, **73**, 17-30
42. Batchelor, G.K. and Townsend, A.A. (1947) Decay of vorticity in isotropic turbulence. Proc. Roy. Soc., Vol A **191**, 534-550
43. Batchelor, G.K. and Townsend, A.A. (1949) The nature of turbulent motion at large wave-numbers. Proc. Roy. Soc., Vol A **199**. 238-255
44. Batchelor, G.K. (1949) Diffusion in a field of homogeneous turbulence: I. Eulerian analysis. Austral. J. Sci. Res., **2**, 437-450
45. Batchelor, G.K. (1951) Pressure fluctuations in isotropic turbulence. Proc. Camb. Phil. Soc., **47**, 359-374
46. Batchelor, G.K. (1952) Diffusion in a field of homogeneous turbulence: II. The relative motion of particles. Proc. Camb. Phil. Soc., **48**, 345-362
47. Batchelor, G.K. (l953) The theory of homogeneous turbulence. Cambridge University Press
48. Batchelor, G.K. (1959) Small scale variation of convected quantities like temperature in turbulent fluid. Part 1. General discussion and the case of small conductivity. J. Fluid Mech., **5**, 113-134
49. Batchelor, G.K., Howells, I.D. and Townsend, A. (1959) Small scale variation of convected quantities like temperature in turbulent fluid. Part 2. The case of large conductivity. J. Fluid Mech., **5**, 135-139
50. Batchelor, G.K. (1967) An introduction to fluid dynamics. Cambridge University Press
51. Batchelor, G.K. (1969) Computation of the energy spectrum in homogeneous two-dimensional turbulence. Phys. Fluids Suppl., II **12**, 233-239
52. Bech, K.H. and Andersson, H.I. (1997) Turbulent plane Couette flow subject to strong system rotation. J. Fluid Mech., **347**, 289-314
53. Beer, A. (2003), Etude par simulation numérique temporelle des effets de compressibilité en couche de mélange plane turbulente, Grenoble Institute of Technology

54. Bègue, C., Chacón, T., Ortegón, F. and Pironneau, O. (1987) 3D simulation of two length scales turbulent flows by homogenization. In Advances in turbulence, G. Comte-Bellot and J. Mathieu eds, Springer-Verlag, 135-142
55. Bergé, P., Pomeau, Y. and Vidal, C. (1984) L'ordre dans le chaos, Hermann, Paris
56. Bernal, L.P. and Roshko, A. (1986) Streamwise vortex structure in plane mixing layer. J. Fluid Mech. **170**, 499-525
57. Bernard, S. and Wallace, J. (2002) Turbulent flow, Wiley
58. Bernoulli, D. (1738) Hydrodynamica, sive de viribus et motibus fluidorum commentarii
59. Bertoglio, J.P. (1986) Thèse de Doctorat d'Etat, Université Claude Bernard, Lyon
60. Betchov, R. (1957) On the fine structure of turbulent flows. J. Fluid Mech., **3**, 205-216
61. Betchov, R. and Szewczyk, G. (1963) Stability of a shear layer between parallel streams. Phys. Fluids, **6**, 1391-1396
62. Bewley T.R., Moin P., Temam R. (2001) DNS-based predictive control of turbulence: an optimal benchmark for feedback algorithms J. Fluid Mech., **447**, 179-225
63. Bidokhti, A. and Tritton, D.J. (1992) The structure of a turbulent free shear layer in a rotating fluid. J. Fluid Mech., **241**, 469-502
64. Biringen, S. (1984) Final stages of transition to turbulence in plane channel flow. J. Fluid Mech., **148**, 413-442
65. Blackwelder, R.F. (1979) Boundary-layer transition. Phys. Fluids, **22**, 583-584
66. Blanc-Lapierre, A. and Picinbono, B. (1981) Fonctions aléatoires, Masson
67. Blasius, H. (1913) Das Ähnlichkeitsgesetz bei Reibungsvorgängen in Flüssigkeiten, Forschg. Arb. Ing.-Wes, **134**
68. Blumen, W. (1970) Shear-layer instability of an inviscid compressible fluid. J. Fluid Mech., **40**, 769-781
69. Bogdanoff, D.W. (1983) Compressibility effects in turbulent shear layers. AIAA J., **21**, 926-927
70. Bogey C. and Bailly C. (2006) Investigation of downstream and sideline subsonic jet noise using large eddy simulation. Theor. Comp. Fluid Dyn., **20**, 23-40
71. Boratav, O.N. and Pelz, R.B. (1994) Direct-numerical simulation of transition to turbulence from a high-symmetry initial condition. Phys. Fluids, **6**, 2757-2784
72. Borue, J. and Orszag, S.A. (1997) Spectra in helical three-dimensional isotropic turbulence. Phys. Rev. E., **55**, 7005-7009
73. Brachet, M.E. (1982) Intégration numérique des équations de Navier–Stokes en régime de turbulence développée. C.R. Acad. Sci. Paris, Ser. B, **294**, 537-540
74. Brachet, M.E., Meiron, D.I., Orszag, S.A., Nickel, B.G., Morf, R.H. and Frisch, U. (1983) Small scale structure of Taylor Green vortex. J. Fluid Mech., **130**, 411-452
75. Brachet, M.E., Ménéguzzi, M. and Sulem, P.L. (1986) Small scale dynamics of high Reynolds number two-dimensional turbulence. Phys. Rev. Lett., **57**, 683

76. Brachet, M.E., Ménéguzzi, M., Politano, H. and Sulem, P.L. (1988) The dynamics of freely decaying two-dimensional turbulence. J. Fluid Mech., **194**, 333-349
77. Brachet, M.E. (1990) Géométrie des structures à petite échelle dans le vortex de Taylor–Green. C.R. Acad. Sci. Paris, Ser. B., **311**, 775-780
78. Bradshaw, P. (1969) The analogy between streamline curvature and buoyancy in turbulent shear flow. J. Fluid Mech., **36**, 177-191
79. Braud, C., Heitz, D., Arroyo, G., Perret, L., Delville, J. and Bonnet, J.P. (2004) Low-dimensional analysis, using POD, for two mixing layer-wake interactions. Int. J. Heat and Fluid Flow **25** (3), 351-363
80. Breidenthal, R. (1981) Structure in turbulent mixing layers and wakes using a chemical reaction. J. Fluid Mech., **109**, 1-24
81. Bretherton, F.P. and Haidvogel, D.B. (1976) Two-dimensional turbulence above topography. J. Fluid Mech., **78**, 129-154
82. Briand, E. (1999) Dynamique des structures cohérentes en couche limite transitionnelle et turbulence étudiée par simulation des grandes échelles. PhD Grenoble Institute of Technology
83. Brissaud, A., Frisch, U., Léorat, J., Lesieur, M., Mazure, A., Pouquet, A., Sadourny, R. and Sulem, P.L. (1973) Catastrophe énergétique et nature de la turbulence. Annales de Géophysique (Paris), **29**, 539-546
84. Brissaud, A., Frisch, U., Léorat, J., Lesieur, M. and Mazure, A., (1973) Helicity cascades in fully developed isotropic turbulence. Phys. Fluids, **16**, 1366-1367
85. Browand, F.K. and Latigo, B.O. (1979) Growth of the two-dimensional mixing layer from a turbulent and non-turbulent boundary layer. Phys. Fluids, **22**, 1011-1019
86. Browand, F.K. and Troutt, T.R. (1980) A note on spanwise structure in the two-dimensional mixing layer. J. Fluid Mech., **93**, 325-336
87. Browand, F.K. and Ho, C.M. (1983) The mixing layer: an example of quasi two-dimensional turbulence. In Two-dimensional turbulence, J. Mec. Theor. Appl., Suppl., R. Moreau ed., 99-120
88. Brown, G. and Roshko, A. (1974) On density effects and large structure in turbulent mixing layers. J. Fluid Mech., **64**, 775-816
89. Busse, F.H. (1981) Transition to turbulence in Rayleigh–Bénard convection. In Hydrodynamic instabilities and the transition to turbulence, edited by H.L. Swinney and J.P. Gollub, Springer-Verlag, 97-137
90. Busse, F.H. (1983) A model of mean zonal flows in the major planets. Geophys. Astrophys. Fluid Dynamics, **23**, 153-174
91. Cadot, O., Douady, S. and Couder, Y. (1995) Characterization of very low pressure events in 3-D turbulence. Phys. Fluids, **7**, 630
92. Cambon, C., Jeandel, D. and Mathieu, J. (1981) Spectral modelling of homogeneous non isotropic turbulence. J. Fluid Mech., **104**, 247-262
93. Cambon, C. (1983) Etude spectrale de la turbulence: rotation pure et introduction à la décomposition modale. Contract DRET-Ecole Centrale de Lyon 83225
94. Cambon, C., Tesseidre, C. and Jeandel, D. (1985) Effets couplés de déformation et de rotation sur une turbulence homogène. J. Mec. Theor. Appl., **4**, 629-657

95. Canuto, C., Hussaini, M.Y., Quarteroni, A. and Zang, T.A. (1987) Spectral methods in fluid dynamics, Springer
96. Capéran, P. (1982) Contribution à l'étude expérimentale de la turbulence homogène *M.H.D.* Première caractérisation de son anisotropie, PhD Grenoble Institute of Technology
97. Cardin, P. (2002) Private communication
98. Carnevale, G.F. (1982) Statistical features of the evolution of two dimensional turbulence. J. Fluid Mech., **122**, 143-153
99. Carnevale, G.F., McWilliams, J.C., Pomeau, Y., Weiss, J.B. and Young, W.R. (1991) Evolution of vortex statistics in two-dimensional turbulence. Phys. Rev. Lett., **66**, 2735-2738
100. Carnevale, G.F. (2007) Two-dimensional turbulence, an overview. In Mathematical and physical theory of turbulence, edited by J. Cannon and B. Shivamoggi, Chapman & Hall/CRC, 47-68
101. Casalis, G. (1990) Instabilités primaire et secondaire dans la couche limite laminaire pour un fluide incompressible. PhD Toulouse Institute of Technology
102. Castaing, B., Gunaratne, G., Heslot, F., Kadanoff, L., Libchaber, A., Thomae, S., Wu, X.Z., Zaleski, S. and Zanetti, G. (1989) Scaling of hard thermal turbulence in Rayleigh–Bénard convection. J. Fluid Mech., 204, 1-30
103. Chabert d'Hières, G., Davies, P.A. and Didelle, H. (1988) Laboratory studies of pseudo-periodic forcing due to vortex shedding from an isolated solid obstacle in a homogeneous rotating fluid. 20th Int. Liège Colloquium on Ocean Hydrodynamics, 2-6 May 1988, Elsevier
104. Chambres, O. (1997) Analyse expérimentale de la modélisation de la turbulence en couche de mélange supersonique. PhD Thesis, Poitiers
105. Champagne, F.H., Friehe, C.A., LaRue, J.C., Wyngaard, J.C. (1977) Flux measurements, flux estimation techniques and fine-scale turbulence measurements in the unstable surface layer over land. J. Atmos. Sci., **34**, 515-530
106. Chandrasekhar, S. (1950) The theory of axisymmetric turbulence. Phil. Trans. A, **242**, 557-577
107. Chandrsuda, C., Mehta, R.D., Weir, A.D. and Bradshaw, P. (1978) Effect of free-stream turbulence on large structure in turbulent mixing layers. J. Fluid Mech., **85**, 693-704
108. Chanut J., Barnier B., Large W., Debreu, L., Penduff, T. and Molines J.M. (2007) Mesoscale eddies in the Labrador Sea and their contribution to convection and re-stratification. J. Phys. Oceanography, in press.
109. Charney, J.G. (1947) The dynamics of long waves in a baroclinic westerly current. J. Meteor., **4**, 135-163
110. Charney, J.G. (1971) Geostrophic turbulence. J. Atmos. Sci., **28**, 1087-1095
111. Chasnov, J., Canuto, V.M. and Rogallo, R.S. (1988) Turbulence spectrum of a passive temperature field: results of a numerical simulation. Phys. Fluids, **31**, 2065-2067
112. Chasnov, J. (1994) Similarity states of passive-scalar transport in isotropic turbulence. Phys. Fluids, **6**, 1036-1051
113. Chasnov, J. (1997) On the decay of two-dimensional homogeneous turbulence. Phys. Fluids, **9**, 171-180

114. Chen, J.H., Cantwell, B.J. and Mansour, N.N. (1991) The effect of Mach number on the stability of a plane supersonic wake. Phys. Fluids A, **2**, 984-1004
115. Choi, H., Moin, P. and Kim. J. (1993) Direct-numerical simulation of turbulent flow over riblets. J. Fluid Mech., **225**, 503-539
116. Chollet, J.P. and Lesieur, M. (1981) Parameterization of small scales of three-dimensional isotropic turbulence utilizing spectral closures. J. Atmos. Sci., **38**, 2747-2757
117. Chollet, J.P. and Lesieur, M. (1982) Modélisation sous-maille des flux de quantité de mouvement et de chaleur en turbulence tridimensionnelle isotrope. La Météorologie, **29-30** , 183-191
118. Chollet, J.P. (1983) Turbulence tridimensionnelle isotrope: modélisation statistique des petites échelles et simulation numérique des grandes échelles. Thèse de Doctorat d'Etat, Grenoble
119. Chollet, J.P. (1984) Two-point closures as a subgrid scale modelling for large eddy simulations. In Turbulent Shear Flows IV, edited by F. Durst and B. Launder, Lecture Notes in Physics, Springer-Verlag
120. Chollet, J.P. and Métais, O. (1989) Predictability of three-dimensional turbulence in large-eddy simulations. Eur. J. Mech., B/Fluids, **8**, 523-548
121. Chomaz, J.M. (2005) Global instabilities in spatially developing flows: Non-normality and nonlinearity An. Rev. Fluid Mech., *37*, 357-2005
122. Chorin, A.J. (1973) Numerical study of slightly viscous flow. J. Fluid. Mech., **57**, 785-796
123. Chorin, A.J. (1993) Vorticity and turbulence. Springer
124. Chorin, A.J. (1996) Vortex methods. In Computational Fluid Dynamics 1993, Les Houches Summer School of Theoretical Physics, M. Lesieur, P. Comte and J. Zinn Justin eds, North-Holland, 65-109
125. Chou, P.Y. (1940) On an extension of Reynolds' method of finding apparent stress and the nature of turbulence. Chin. J. Phys. **4**, 1-33
126. Christensen, T. and Adrian, R. (2000) The velocity and acceleration signatures of small-scale vortices in turbulent channel flow, J. Turbulence, **3** 023
127. Cimbala, J.M., Nagib, H.M. and Roshko, A. (1988) Large structure in the far wakes of two-dimensional bluff bodies. J. Fluid Mech., **190**, 265-298
128. Clark, R.A., Ferziger, J.H. and Reynolds, W.C. (1979) Evaluation of subgrid scale models using an accurately simulated turbulent flow. J. Fluid Mech., **91**, 1-16
129. Coantic, M. and Lasserre J. J. (1999) On pre-dissipative 'bumps' and a Reynolds-number dependent spectral parameterization of turbulence. Eur. J. Mech. B/Fluids, **18**, 1027-47
130. Coleman, G. N., Kim, J. and Moser, R. D. (1995) A numerical study of turbulent supersonic isothermal-wall channel flow. J. Fluid Mech., **305**, 159-83
131. Colin de Verdière, A. (1979) Mean flow generation by topographic Rossby waves. J. Fluid Mech., **94**, 39-64
132. Colin de Verdière, A. (1980) Quasi geostrophic turbulence in a rotating homogeneous fluid. Geophys. Astrophys. Fluid Dynamics, **15**, 213-251
133. Comte, P., Lesieur, M. and Chollet, J.P. (1987) Simulation numérique d'un jet plan turbulent. C.R. Acad. Sci., ser. II, **305**, 1037-1044

134. Comte, P. (1989) Etude par simulation numérique de la transition à la turbulence en écoulement cisaillé libre. PhD Grenoble Institute of Technology
135. Comte, P., Lesieur, M. Laroche, H. and Normand, X. (1989) Numerical simulations of turbulent plane shear layers. In Turbulent Shear Flows VI, Springer-Verlag, 360-380
136. Comte, P. and Lesieur, M. (1989) Coherent structures of mixing layers in large-eddy simulation. In Topological Fluid Dynamic, Cambridge University Press, H.K. Moffatt, 649-658
137. Comte, P., Fouillet, Y., Gonze, M.A., Lesieur, M., Métais, O. and Normand, X. (1991) Large-eddy simulations of free-shear layers. In Turbulence and coherent structures, O. Métais and M. Lesieur eds, Kluwer, 45-73
138. Comte, P., Lesieur, M. and Lamballais, E. (1992) Large and small-scale stirring of vorticity and a passive scalar in a 3D temporal mixing layer. Phys. Fluids A, **4**, 2761-2778
139. Comte, P. (1994) Structure-function based models for compressible transitional shear flows. ERCOFTAC Bull., **22**, 9-14.
140. Comte P, Silvestrini J and Bégou P (1998) Streamwise vortices in large eddy simulation of mixing layers. Eur. J. Mech. B, **17**, 615-37
141. Comte, P. (2005) Private communication
142. Comte-Bellot, G. and Corrsin, S. (1966) The use of a contraction to improve the isotropy of a grid generated turbulence. J. Fluid Mech., **25**, 657-682
143. Constantin, P., Foias, C., Manley, O.P. and Temam, R. (1985) Determining modes and fractal dimension of turbulent flows. J. Fluid Mech., **150**, 427-440
144. Corcos, G.M. and Lin, S.J. (1984) The mixing layer: deterministic models of a turbulent flow. Part 2. The origin of the three-dimensional motion. J. Fluid Mech., **139**, 67-95
145. Corrsin, S. (1951) J. Appl. Phys. **22**, 469
146. Corrsin, S. (1962) Turbulent dissipation fluctuations. Phys. Fluids, **5**, 1301
147. Corrsin, S. (1964) The isotropic turbulent mixer: Part II. Arbitrary Schmidt number. A.I.Ch.E.J. **10**, 870-877
148. Cottet, G.H. and Koumoutsakos, P. (2000) Vortex methods: theory and practice. Cambridge University Press
149. Couder, Y. (1984) Two-dimensional grid turbulence in a thin liquid film. J. Phys. Lett., **45**, 353-360
150. Couder, Y. and Basdevant, C. (1986) Experimental and numerical study of vortex couples in two-dimensional flows. J. Fluid Mech., **173**, 225-251
151. Cousteix, J. (1989) Turbulence et couche limite. CEPADUES (Toulouse)
152. Coustols, E. and Cousteix, J. (1994) Performances of riblets in the supersonic regime. *AIAA J.*, **32**, 431-433
153. Craya, A. (1958) Contribution à l'analyse de la turbulence associée à des vitesses moyennes. P.S.T. Ministère de l'Air, **345**
154. Crow, S.C. and Champagne, F.H. (1971) Orderly structure in jet turbulence. J. Fluid Mech., **48**, 547-591
155. Danet, A. (2001) Influence des conditions amont sur l'écoulement derrière une marche par la simulation des grandes échelles. PhD Grenoble Institute of Technology

156. Dannevik, W.P., Yakhot, V. and Orszag, S.A. (1988) Analytical theories of turbulence and the ϵ expansion. Phys. Fluids, **30**, 2021-2029
157. David, E. (1993) Modélisation des écoulements compressibles et hypersoniques: une approche instationnaire. PhD Grenoble Institute of Technology
158. da Silva, C. and Métais, O. (2002) Vortex control of bifurcating jets: A numerical study, Phys. Fluids, **14**, 3798-3819
159. da Silva, C.B., Balarac, G. and Métais, O. (2003) Transition in high velocity ratio coaxial jets analysed from direct numerical simulations. J. Turbulence, **4**, 024
160. Davidson, P.A. (2000) Was Loitsyansky correct? A review of the arguments. J. Turbulence, **1**, 006
161. Dean, R.B. (1978) Reynolds number dependance of skin friction and other bulk flow variables in two-dimensional rectangular duct flow, Trans. ASME I: J. Fluids Eng., **100**, 215-223.
162. Deardorff, J.W. (1970) A numerical study of three-dimensional turbulent channel flow at large Reynolds number. J. Fluid Mech., **41**, 453-480
163. Deardorff, J.W. (1973) The use of subgrid transport equations in a three-dimensional model of atmospheric turbulence. J. Fluids Eng., **95**, 429-438
164. Debisschop, J., Chambres, O. and Bonnet, J.P. (1994) Velocity field characteristics in supersonic mixing layers. Exp. Therm. and Fluid Science, **9**, 147-155
165. Delcayre, F. (1996) private communication
166. Delville, J., Bellin, S. and Bonnet, J.P. (1991) Use of proper orthogonal decomposition in a plane turbulent mixing layer. In Turbulence and coherent structures, O. Métais and M. Lesieur eds, Kluwer, 75-90
167. d'Humières, D., Lallemand, P. and Frisch, U. (1986) Simulations d'allées de Von Karman bidimensionnelles à l'aide d'un gaz de réseau, C.R. Acad. Sci. Paris, B **301**, 11
168. Dimotakis, P., Miakelye, R. and Papantoniou, D. (1983) Structure and dynamics of round turbulent jets. Phys. Fluids, **26**, 3185-3192
169. Dimotakis, P. (2000) The mixing transition in turbulent flows. J. Fluid Mech., **409**, 69-97
170. Domaradzki, J.A., Metcalfe, R.W., Rogallo, R.S. and Riley, J. (1987) Analysis of subgrid-scale eddy viscosity with the use of the results from direct numerical simulations. Phys. Rev. Lett. **58**, 547-550
171. Doris, L. (2001) Simulation des grandes échelles du développement spatial d'une couche de mélange turbulente compressible, PhD Thesis, Paris
172. Drazin, P.G. and Howard, L.N. (1966) Hydrodynamic stability of parallel flow of inviscid fluid. Adv. Appl. Mech., **7**, 142-250
173. Drazin, P.G. and Reid, W.H. (1981) Hydrodynamic stability, Cambridge University Press
174. Driver, D.M., Seegmiller, H.L. and Marvin, J.G. (1987) Time-dependent behavior of a reattaching shear layer. AIAA J., **25**, 914-919
175. Druault P., Delville, J. and Bonnet J.P. (2005) Experimental 3D analysis of the large scale behaviour of a plane turbulent mixing layer. Flow Turb. and Comb., **74** (2), 207-233
176. Dubief, Y. and Delcayre, F. (2000) On coherent-vortex identification in turbulence. J. Turbulence, **1**, 011

177. Dubrulle, B. and Frisch, U. (1991) The eddy-viscosity of parity-invariant flow. Phys. Rev. A, **43**, 5355-5364
178. Ducros, F. (1995) Simulations numériques directes et des grandes échelles de couches limites compressibles. PhD Grenoble Institute of Technology
179. Ducros, F., Comte, P. and Lesieur, M. (1995) Direct and large-eddy simulations of a supersonic boundary layer. In Turbulent Shear Flows IX, Springer-Verlag, 283-300
180. Ducros, F., Comte, P. and Lesieur, M. (1996) Large-eddy simulation of transition to turbulence in a boundary layer developing spatially over a flat plate. J. Fluid Mech. **326**, 1-36
181. Dumas, R. (1962) Contribution à l'étude des spectres de turbulence. Thèse de Doctorat d'Etat, Université d'Aix-Marseille
182. Durbin, P. and Pettersson Reif Chichester, B. (2001) Statistical Theory and Modeling For Turbulent Flows. Wiley
183. Dziomba, B. and Fiedler, H.E. (1985) Effect of initial conditions on two-dimensional free shear layers. J. Fluid Mech., **152**, 419-442
184. Eaton J.K. and Johnston J.P. (1980) Turbulent flow reattachment: an experimental study of the flow and structure behind a backward-facing step. Stanford University, Rep. MD-39
185. El-Hady, N. and Zang, T.A. (1995) Large-eddy simulation of nonlinear evolution and breakdown to turbulence in high-speed boundary layers. Theor. and Comp. Fluid Dynamics, **7**, 217-240
186. Elliott, F. and Majda, J. (1996) Pair dispersion over an inertial range spanning many decades. Phys. Fluids, **8**, 1052-1060
187. Emmons, H.W. and Bryson, A.E. (1951) The laminar-turbulent transition in a boundary layer. Part 1. J. Aeronaut. Sci., **18**, 490-498
188. Eswaran, V. and O'Brien, E.E. (1989) Simulations of scalar mixing in grid turbulence using an eddy-damped closure model. Phys. Fluids A, **1** , 537-548
189. Etling, D. (1990) Mesoscale vortex shedding from large islands: a comparison to laboratory experiments in rotating stratified flows. Met. Atmos. Phys., **43**, 145
190. Eyink, G. and Thompson, D. (2000) Free decay of turbulence and breakdown of self-similarity. Phys. Fluids, **12**, 477-479
191. Falkovich, G. and Shafarenko, A.V. (1988) Blow-up in weak-acoustic turbulence. Preprint N 393, Institute of Aut. and Elec., Sib. USSR Acad. Sci.
192. Falkovich, G., Gaweddzki, K. and Vergassola, M. (2001) Lagrangian description of turbulence. In New trends in turbulence 2000, Les Houches Summer School of Theoretical Physics, M. Lesieur, A. Yaglom and F. David eds, EDP-Springer, 505-554
193. Fallon, B., Lesieur, M., Delcayre, F. and Grand, D. (1997) Large-eddy simulations of stable-stratification effects upon a backstep flow. Eur. J. Mech. B/Fluids, **16**, 525-644
194. Fasham, M. J. (1978) Oceanogr. Mar. Biol. A. Rev., **16**, 43-**XX**
195. Farge, M. and Sadourny, R. (1989) Wave-vortex dynamics in rotating shallow water. J. Fluid Mech., **206**, 433-462
196. Farge, M. (1994) Private communication

197. Fauve, S., Laroche, C. and Castaing, B. (1993) Pressure fluctuations in swirling turbulent flows. J. Phys II, **3**, 271-278
198. Favre, A. (1958) Equations statistiques des gaz turbulents, C.R.Acad. Sci., Paris, **246**: masse, quantité de mouvement, 2576-2579; énergie cinétique du mouvement macroscopique, énergie cinétique de la turbulence, 2839-2842; enthalpies, entropie, températures, 3216-3219
199. Favre A. (1965) Equations des gaz turbulents compressibles, J. de Mécanique, **4**, 361
200. Favre, A., Kovasznay, L., Dumas, R., Gaviglio, J. and Coantic, M. (1976) La turbulence en mécanique des fluides: bases théoriques et expérimentales, méthodes statistiques. Gauthier-Villars
201. Favre, A., Guitton, H., Guitton, J., Lichnerowicz, A. and Wolf, E. (1988) De la causalité à la finalité: à propos de la turbulence, Maloine, Paris
202. Favre, A., Guitton, H., Guitton, J., Lichnerowicz, A. and Wolf, E. (1995) Chaos and determinism: turbulence as a paradigm for complex systems converging toward final states. Johns Hopkins University Press
203. Favre-Marinet, M., Camano-Schettini, E. and Sarboch., J. (1999) Near-field of coaxial jets with large density differences. Ex. Fluids, **26**, 97-106
204. Favre-Marinet, M. and Camano-Schettini, E. (2001) The density field of coaxial jets with large velocity ratio and large density differences. Int. J. Heat and Fluid Flow. **14**, 1913-1924
205. Fincham, A.M., Maxworthy, T. and Spedding, G.R. (1996) Energy dissipation and vortex structure in freely decaying stratified grid turbulence. Dyn. Atmos. Oceans, **23**, 155-169
206. Fjortoft, R. (1953) On the changes in the spectral distribution of kinetic energy for two-dimensional non-divergent flow. Tellus, **5**, 225-230
207. Flores, C. (1993) Etude numérique de l'influence d'une rotation sur les écoulements cisaillés libres. PhD Grenoble Institute of Technology
208. Foias, C. and Penel, P. (1975) Dissipation totale de l'énergie dans une équation non linéaire liée à la théorie de la turbulence. C.R. Acad. Sci., Paris, A **280**, 629-632
209. Fornberg, B. (1977) A numerical study of two-dimensional turbulence. J. Comp. Phys., **25**, 1
210. Forster, D., Nelson, D.R. and Stephen, M.J. (1977) Large distance and long time properties of a randomly stirred field. Phys. Rev. A, **16**, 732-749
211. Fouillet, Y. (1992) Contribution à l'étude par expérimentation numérique des écoulements cisaillés libres. Effets de compressibilité. PhD Grenoble Institute of Technology
212. Fournier, J. D. (1977) Quelques méthodes systématiques de développement en turbulence homogène. Thèse, Université de Nice
213. Fournier, J.D. and Frisch, U. (1983) L'équation de Burgers déterministe et statistique. J. Mec. Theor. Appl., **2**, 699-750
214. Fournier, J.D. and Frisch, U. (1983) Remarks on the renormalization group in statistical fluid dynamics. Phys. Rev. A, **28**, 1000-1002
215. Fox, D.G. and Orszag, S.A. (1973) Inviscid dynamics of two dimensional turbulence. Phys. Fluids, **16**, 167-171

216. Franc, J.P. Michel, J.M. and Lesieur, M. (1982) Structures rotationnelles bi et tri-dimensionnelles dans un sillage cavitant. C.R. Acad. Sci., Paris, Ser II, **295**, 773-776
217. Freund, J.B., Lele, S.K. and Moin, P. (2000) Compressibility effects in a turbulent annular mixing layer. Part 1. Turbulence and growth rate. J. Fluid Mech., **421**, 229-267
218. Freund, J.B. (2001) Noise sources in a low-Reynolds-number turbulent jet at Mach 0.9. J. Fluid Mech., **438**, 277-305
219. Friehe, C.A., Van Atta, C.W. and Gibson, C.H. (1971) Jet turbulence: dissipation rate measurements and correlations. Proc. A.G.A.R.D. Spec. Meeting on Turbulent Shear Flow, London
220. Frisch, U., Lesieur, M. and Brissaud, A. (1974) A Markovian Random Coupling Model for turbulence. J. Fluid Mech., **65**, 145-152
221. Frisch, U. (1974) Private communication
222. Frisch, U., Pouquet, A., Léorat, J. and Mazure, A. (1975) Possibility of an inverse cascade of magnetic helicity in magneto hydrodynamic turbulence. J. Fluid Mech., **68**, 769-778
223. Frisch, U., Sulem, P.L. and Nelkin, M. (1978) A simple dynamical model of intermittent fully developed turbulence. J. Fluid Mech., **87**, 719-736
224. Frisch, U. and Fournier, J.D. (1978) in Nice Winter School on Turbulence and non-linear Physics, Nice Observatory, January 1978 (unpublished)
225. Frisch, U., Lesieur, M. and Schertzer, D. (1980) Comment on the Quasi Normal markovian approximation for fully developed turbulence. J. Fluid Mech., **97**, 181-192
226. Frisch, U. and Sulem, P.L. (1984) Numerical simulation of the inverse cascade in two-dimensional turbulence. Phys. Fluids, **27**, 1921-1923
227. Frisch, U., Hasslacher, B. and Pomeau, Y. (1986) Lattice gas automata for the Navier Stokes equation. Phys. Rev. Lett., **56**, 1505
228. Frisch, U. and Orszag, S.A. (1990) Turbulence: challenges for theory and experiment. Physics Today, **24**, 24-32
229. Frisch, U. (1995) Turbulence, the legacy of A.N. Kolmogorov. Cambridge University Press
230. Frisch, U. and Bec, J. (2001) Burgulence. In New trends in turbulence 2000, Les Houches Summer School of Theoretical Physics, M. Lesieur, A. Yaglom and F. David eds, EDP-Springer, 341-383
231. Frisch, U., Khanin, K. and Matsumoto, T. (2005) Multifractality of the Feigenbaum attractor and fractional derivatives. J. Stat. Physics, **121**, 671-695
232. Frisch, U., Afonso, M.M. and Mazzino A. (2005) Does multifractal theory of turbulence have logarithms in the scaling relations? J. Fluid Mech., **542**, 97-103
233. Fulachier, L. and Dumas, R. (1976) Spectral analogy between temperature and velocity fluctuations in a turbulent boundary layer. J. Fluid Mech., **77**, 257-277
234. Fung, J.C., Hunt, J.C., Malik, N.A. et Perkins, R.J. (1992) Kinematic simulation of homogeneous turbulence by unsteady random Fourier modes. J. Fluid Mech., **236**, 281-318
235. Fyfe, D., Montgomery, D. and Joyce, G. (1977) Phys. Fluids, **117**, 369
236. Gage, K.S. (1979) Evidence for a $k^{-5/3}$ law inertial range in meso scale two dimensional turbulence. J. Atmos. Sci., **36**, 1950-1954

237. Gage, K.S. and Nastrom, G.D. (1986) Theoretical interpretation of atmospheric spectra of wind and temperature observed by commercial aircraft during GASP. J. Atmos. Sci., **47**, 729-740
238. Gagne, Y. (1978) Contribution à l'étude expérimentale de l'intermittence de la turbulence à petite échelle. Thèse de Docteur-Ingénieur, Grenoble
239. Gagne, Y. (1987) Etude expérimentale de l'intermittence et des singularités dans le plan complexe en turbulence développée. Thèse de Doctorat d'Etat, Grenoble.
240. Gargett, A.E., Osborn, T.R. and Nasmyth, T.W. (1984) Local isotropy and the decay of turbulence in a stratified fluid. J. Fluid Mech., **144**, 231-280
241. Garnier, E. (1996) Etude numérique des instabilités de jets baroclines. PhD Grenoble University
242. Garnier, E., Métais, O. and Lesieur, M. (1996) Instabilités primaires et secondaires dans un jet barocline. C.R. Acad. Sci., Paris, Ser II b, **323**, 161-168
243. Garnier, E., Métais, O. and Lesieur, M. (1998) Synoptic and frontal-cyclone scale instabilities in baroclinic jet flows. J. Atmos. Sci., **55**, 1316-1335
244. Gathmann, R., Si-Ameur, M. and Mathey, F. (1993) Numerical simulation of three-dimensional natural transition in the compressible confined shear layer. Phys. Fluids A, **5**, 2946-2968
245. Gayon, J. (1998) Le déterminisme: origines d'un mot, évaluation d'une idée. In Turbulence et déterminisme, Collection Grenoble-Sciences, M. Lesieur ed., EDP-Springer
246. Germain, P. (1962) Mécanique des milieux continus. Masson
247. Germano, M., Piomelli, U., Moin, P. and Cabot, W. (1991) A dynamic subgrid-scale eddy-viscosity model. Phys. Fluids A., **3**, 1760-1765
248. Germano, M. (1992) Turbulence, the filtering approach. J. Fluid Mech., **238**, 325-336
249. Gerolymos, G. and Vallet, I. (2001) Wall-normal-free Reynolds-stress closure for three-dimensional compressible separated flows. AIAA J., **39**, 1833-1841
250. Gerz, T., Schumann, U. and Elghobashi, S.E. (1989) Direct numerical simulation of stratified homogeneous turbulent shear flows. J. Fluid Mech., **200**, 563-594
251. Geurts, B. (1997) Inverse modelling for large-eddy simulation. Phys. Fluids, **9**, 3585-3587
252. Geurts, B. (2003) Elements of Direct and Large-Eddy Simulation. R.T. Edwards Publ
253. Gharib, M. and Derango, P. (1989) A liquid film (soap film) tunnel to study laminar and turbulent shear flows. Physica D, **37**, 406-416
254. Ghosal, S., Lund, T.S., Moin, P. and Akselvoll, K. (1995) A dynamic localization model for large-eddy simulation of turbulent flows. J. Fluid Mech., **286**, 229-255
255. Gibson, M.M. (1963) Spectra of turbulence in a round jet. J. Fluid Mech., **15**, 161-173
256. Giger, M., Jirka, G.H. and Dracos, Th. (1985) Meandering jets in a shallow fluid layer. Turbulent Shear Flows V, Cornell University, edited by J.L. Lumley
257. Gilbert, A.D. (1988) Spiral structures and spectra in two-dimensional turbulence. J. Fluid Mech., **193**, 475-498

258. Gill, A., E. (1982) Atmosphere-Ocean dynamics. Academic Press
259. Glauser, M., Zheng, X. and Doering, C.R. (1991) The dynamics of organized structures in the axisymmetric jet mixing layer. In Turbulence and coherent structures, O. Métais and M. Lesieur eds, Kluwer, 253-265
260. Golanski, F., Fortuné, V. and Lamballais, E. (2005) Noise radiated by a non-isothermal, temporal mixing layer. Theor. Comp. Fluid. Dyn. **19(6)**, 391-416
261. Gonze, M.A. (1993) Simulation numérique des sillages en transition à la thurbulence. PhD Grenoble Institute of Technology
262. Gottlieb, D. and Turkel, E. (1976) Dissipative two-four methods for time-dependent problems. Math. Comp., **30**, 703-723
263. Goutorbe, T., Laurence, D., Maupu, V. (1994) A priori test of a subgrid scale stress tensor model including anisotropy and backscatter effects. In Direct and Large-Eddy Simulation I, P. Voke et al. eds, Kluwer, 121-131
264. Grant, H.L., Stewart, R.W. and Moilliet, A. (1962) Turbulent spectra from a tidal channel. J. Fluid Mech., **12**, 241-268
265. Greenspan, H.P. (1968) The theory of rotating fluids. Cambridge University Press
266. Gurbatov, S., Simdyankin, S., Aurell, E., Frisch, U. and Toth, G. (1997) On the decay of Burgers turbulence. *J. Fluid Mech.*, **344**, 339-374
267. Guyon, E., Hulin, J. and Petit, L. (1981) Hydrodynamique physique, Inter-Editions, Editions du CNRS (Paris)
268. Hama, F.R., Long, J.D., Hegarty, J.C. (1957) On transition from laminar to turbulent flow. J. Applied. Phys., **27**, 388-394
269. Hamilton, J.M., Kim, J. and Waleffe, F. (1995) Regeneration mechanisms of near-wall turbulence structures. J. Fluid Mech., **287**, 317-348
270. Hauët, G. (2003) Contrôle de la turbulence par simulation des grandes échelles en transport supersonique. PhD Grenoble Institute of Technology
271. Herbert, T. (1984) Stability and transition of laminar flows. Von Karman Institute for Fluid Dynamics, Special Course on Stability and transition of laminar flows, March 1984, Brussels
272. Herbert, T. (1988) Secondary instability of boundary layers. Ann. Rev. Fluid Mech., **20**, 487-526
273. Herring, J.R. and Kraichnan, R.H. (1972) Comparison of some approximations for isotropic turbulence. In Statistical models and turbulence, edited by M. Rosenblatt and C. Van Atta, Springer Verlag, **12**, 148-194
274. Herring, J.R., Riley, J.J., Patterson, G.S. and Kraichnan, R.H., 1973) Growth of uncertainty in decaying isotropic turbulence. J. Atmos. Sci., **30**, 997-1006
275. Herring, J.R. (1974) Approach of an axisymmetric turbulence to isotropy. Phys. Fluids, **17**, 859-872
276. Herring, J.R., Orszag, S.A., Kraichnan, R.H. and Fox, D.G. (1974) Decay of two-dimensional homogeneous turbulence. J. Fluid Mech., **66**, 417-444
277. Herring, J.R. (1975) Theory of two-dimensional anisotropic turbulence. J. Atmos. Sci., **32**, 2254-2271
278. Herring, J.R. (1979) Subgrid scale modeling – An introduction and overview. In Turbulent Shear Flows I, edited by F. Durst et al., Springer Verlag, 347-352
279. Herring, J.R. (1980) Statistical theory of quasi-geostrophic turbulence. J. Atmos. Sci., **37**, 969-977

280. Herring, J.R., Schertzer, D., Lesieur, M., Newman, G.R., Chollet, J.P. and Larchevêque, M. (1982) A comparative assessment of spectral closures as applied to passive scalar diffusion. J. Fluid Mech., **124**, 411-437
281. Herring, J. R. (1984) The predictability of quasi-geostrophic flows. In *Predictability of fluid motions*, La Jolla Institute 1983, AIP Conference Proceedings **106**, G. Holloway and B.J. West eds, 321-332
282. Herring, J.R. and McWilliams, J.C. (1985) Comparison of direct-numerical simulation of two-dimensional turbulence with two-point closure: the effects of intermittency. J. Fluid Mech., **153**, 229-242
283. Herring, J.R. and Métais, O. (1989) Numerical experiments in forced stably stratified turbulence. J. Fluid Mech., **202**, 97-115
284. Hill, R. (1996) Pressure-velocity statistics in isotropic turbulence, Phys. Fluids, **8**, 3085-3093
285. Hinze, J.O. (1975) Turbulence, McGraw-Hill
286. Ho, C.M. and Huerre, P. (1984) Perturbed free shear layers. Ann. Rev. Fluid Mech., **16**, 365-424
287. Holland, W.R. (1978) The role of mesoscale eddies in the general circulation of the ocean. J. Phys. Ocean., **8**, 363-392
288. Holland, W.R. (1996) Ocean circulation modelling. In Computational Fluid Dynamics 1993, Les Houches Summer School of Theoretical Physics, M. Lesieur, P. Comte and J. Zinn Justin eds, North-Holland, 375,441
289. Holloway, G. (1976) Statistical hydromechanics: application in mesoscale ocean circulation. PhD Thesis, Univ. Calif. San Diego
290. Holloway, G. and Hendershott, M.C. (1977) Stochastic closure for non-linear Rossby waves. J. Fluid Mech., **82**, 747-765
291. Holloway, G. and Kristmannsson, S. (1984) Stirring and transport of tracer fields by geostrophic turbulence. J. Fluid Mech., **141**, 27-50
292. Holloway, G. (1986) Eddies, waves, circulation and mixing: statistical geofluid mechanics. Ann. Rev. Fluid Mech., **18**, 91-147
293. Holmes, P., Lumley, J. and Berkooz, G. (1998) Turbulence, coherent structures, dynamical systems and symmetry. Cambridge University Press
294. Holton, J.R. (1979) An introduction to dynamic meteorology. Academic Press
295. Holzer, M. and Siggia, E. (1993) Skewed exponential pressure distributions from Gaussian velocities. Phys. Fluids A, **5**, 2525-2532
296. Hopfinger, E.J., Browand, F.K. and Gagne, Y. (1982) Turbulence and waves in a rotating tank. J. Fluid Mech., **125**, 505-534
297. Hopfinger, E.J. (1987) Turbulence in stratified fluids: a review. J. Geophys. Research, **92** (C5), 5287-5303
298. Howard, L.N. (1961) Note on a paper of John W. Miles. J. Fluid Mech., **10**, 509-512
299. Howard, L.N. and Drazin, P.G. (1964) On instability of parallel flow of inviscid fluid in rotating system with variable Coriolis parameter. J. Math. Phys., **43**, 83-99
300. Hoyer, J.M. and Sadourny, R. (1982) Closure modeling of fully developed baroclinic instability. J. Atmos. Sci., **39**, 707-721
301. Hua, B.L. and Haidvogel, D.B. (1986) Numerical simulations of the vertical structure of quasi-geostrophic turbulence. J. Atmos. Sci., **43**, 2923-2936

302. Huang, L.S. and Ho, C.M. (1990) Small-scale transition in a plane mixing layer. J. Fluid Mech., **210**, 475-500
303. Huerre P. and Monkewitz, P.A.(1990) Local and global instabilities in spatially developing flows. Ann. Rev. Fluid Mech., **22**, 473-537
304. Hughes, T., Mazzei, L., Oberai, A. and Wray, A. (2001) the multiscale formulation of large-eddy simulation: decay of homogeneous isotropic turbulence. Phys. Fluids, **13**, 505-512
305. Hunt, J. (1985) Turbulent diffusion from sources in complex flows. Ann. Rev. Fluid Mech., **17**, 447-485
306. Hunt, J., Wray, A. and Moin, P. (1988) Eddies, stream and convergence zones in turbulent flows. Center for Turbulence Research Rep., **CTR-S88**, 193
307. Hunt, J. (2006) Private communication
308. Husain, H.S. and Hussain, A.K.M.F. (1995) Experiments on subharmonic resonance in a shear layer. J. Fluid Mech., **304**, 343-372
309. Hussain, A.K.M.F. and Zaman, K.B.M.Q. (1981) The preferred mode of the axisymmetric jet. J. Fluid Mech., **110**, 39-71
310. Iooss, G. and Joseph, D.D. (1980) Elementary stability and bifurcation theory. Springer-Verlag
311. Ishida, T., Davidson, P.A. and Kaneda, Y. (2006) On the decay of isotropic turbulence. J. Fluid Mech. **564**, 455-475
312. Itsweire, E.C., Helland, K.N. and Van Atta, C.W. (1986) The evolution of a grid generated turbulence in a stably stratified fluid. J. Fluid Mech., **162**, 299-338
313. Jayesh and Warhaft, Z. (1992) Probability distribution, conditional dissipation, and transport of passive-temperature fluctuations in grid-generated turbulence. Phys. Fluids A, **4**, 2292-2307
314. Jimenez, J. (1983) A spanwise structure in the plane shear layer, J. Fluid Mech., **132**, 319-336
315. Jimenez, J. (1987) Bifurcations and bursting in two-dimensional Poiseuille flow. Phys. Fluids, **30**, 3644-3646
316. Jimenez, J. (1990) Transition to turbulence in two-dimensional Poiseuille flow. J. Fluid Mech., **218**, 265-297
317. Jimenez J. and Wray A. A. (1998) On the characteristics of vortex filaments in isotropic turbulence. J. Fluid Mech. **373**, 255-285
318. Jimenez, J. (2000) Turbulence. In Perspectives in Fluid Mechanics, G.K. Batchelor, H.K. Moffatt and M.G. Woster eds, Cambridge University Press, 231-283
319. Johnston, J.P., Halleen, R.M. and Lezius, D.K. (1972) Effects of spanwise rotation on the structure of two-dimensional fully developed turbulent channel flow. J. Fluid Mech., **56**, 553-557
320. Jovic, S. and Driver, M. (1994) Backward-facing step measurements at low Reynolds number $Re_h = 5000$. NASA Tech. Mem. 108807, Ames Research Center
321. Joyce, G. and Montgomery, D. (1973) Negative temperature states for the two-dimensional guiding center plasma. J. Plasma Physics, **10**, 107-121
322. Jullien, M.C., Paret, J. and Tabeling, P. (1999) Richardson pair dispersion in two-dimensional turbulence Phys. Rev. Let., **82**, 2872-2875

323. Jullien, M.C., Castiglione P. and Tabeling P. (2000) Experimental observation of Batchelor dispersion of passive tracers. Phys. Rev. Let., **85**, 3636-3639
324. Jullien, M.C. (2003) Dispersion of passive tracers in the direct enstrophy cascade: Experimental observations. Phys. Fluids **15**: 2228-2237
325. Kachanov, Y. and Levchenko, V. (1984) The resonant interaction of disturbances at laminar-turbulent transition in a boundary layer. J. Fluid Mech., **138**, 209-247
326. Karman, T. and Howarth, L. (1938) On the statistical theory of isotropic turbulence. Proc. Roy. Soc., Vol A **164**, 192-215
327. Kerr, R.M. (1993) Evidence for a singularity of the three-dimensional, incompressible Euler equations. Phys. Fluids A, **5**, 1725-1746
328. Kida, S. and Yamada, M. (1984) Singularity and energy spectrum in a two-dimensional incompressible inviscid flow. in Turbulence and chaotic phenomena in fluids, edited by T. Tatsumi, North-Holland, 275-280
329. Kim, J. (1983) The effect of rotation on turbulence structure. In Proc. 4th Symp. on Turbulent Shear Flows, Karlsruhe, 6.14-6.19
330. Kim, J., Moin, P. and Moser, R. (1987) Turbulent statistics in fully developed channel flow at low Reynolds number. J. Fluid Mech., **177**, 133-166
331. Kim, J. and Moser, R.D. (1989) On the secondary instability in plane Poiseuille flow. Phys. Fluids A, **1**, 775-777
332. Kiya, M. and Sasaki, K. (1983) Structure of turbulent separation bubbles. J. Fluid Mech., **137**, 83-113
333. Kiya, M. (1989) Separation bubbles. In Theoretical and Applied Mechanics, P. Germain et al. eds, North-Holland, 173-191
334. Klebanoff, P.S., Tidstrom, K.D. and Sargent, L.M. (1962) The three-dimensional naure of boundary layer instability. J. Fluid Mech., **12**, 1-34
335. Klein, P., Hua, B.L. and Lapeyre, G. (2000) Alignment of tracer gradient vectors in 2D turbulence. Physica D-Nonlinear phenomena, **146**, 246-260
336. Kleiser, L. and Zang, T.A. (1991) Numerical simulation of transition in wall-bounded shear flows. Ann. Rev. Fluid Mech., **23**, 495-537
337. Kline, S.J., Reynolds, W.C., Schraub, F.A. and Runstadler, P.W. (1967) The structure of turbulent-boundary layers. J. Fluid Mech., **30**, 741-773
338. Kolmogorov, A.N. (1941) The local structure of turbulence in incompressible viscous fluid for very large Reynolds numbers. Dokl. Akad. Nauk SSSR, **30**, 301-305
339. Kolmogorov, A.N. (1941) On degeneration of isotropic turbulence in an incompressible viscous liquid. Dokl. Akad. Nauk. SSSR, **31**, 538-541
340. Kolmogorov, A.N. (1962) A refinement of previous hypotheses concerning the local structure of turbulence in a viscous incompressible fluid at high Reynolds number. J. Fluid Mech., **12**, 82-85
341. Konrad, J.H. (1976) An experimental investigation of mixing in two-dimensional turbulent shear flows with applications to diffusion-limited chemical reactions. PhD California Institute of Technology
342. Koochesfahani, M.M. and Dimotakis, D.E. (1986) Mixing and chemical reactions in a turbulent liquid mixing layer. J. Fluid Mech., **170**, 83-112
343. Koop, C.G. and Browand, F.K. (1979) Instability and turbulence in a stratified fluid with shear. J. Fluid Mech., **93**, 135

344. Kourta, A., Boisson, H.C., Chassaing, P. and Ha Minh, H. (1987) Non-linear interaction and the transition to turbulence in the wake of a circular cylinder. J. Fluid Mech., **181**, 141-162
345. Kraichnan, R.H. (1959) The structure of isotropic turbulence at very high Reynolds number. J. Fluid Mech. **5**, 497-543
346. Kraichnan, R.H. (1961) Dynamics of nonlinear stochastic systems. J. Math. Phys., **2**, 124-148
347. Kraichnan, R.H. (1965) Lagrangian history closure approximation for turbulence, Phys. Fluids, **8**, 575-598
348. Kraichnan, R.H. (1966) Isotropic turbulence and inertial range structure. Phys. Fluids., **9**, 1728-1752
349. Kraichnan, R.H. (1966) Dispersion of particle pairs in homogeneous turbulence. Phys. Fluids, **9**, 1937-1943
350. Kraichnan, R.H. (1967) Inertial ranges in two-dimensional turbulence. Phys. Fluids, **10**, 1417-1423
351. Kraichnan, R.H. (1968) Lagrangian History statistical theory for Burgers turbulence. Phys. Fluids, **11**, 265-277
352. Kraichnan, R.H. (1968) Small-scale structure convected by turbulence. Phys. Fluids, **11**, 945-953
353. Kraichnan, R.H. (1971) An almost markovian Galilean invariant turbulence model. J. Fluid Mech., **47**, 513-524
354. Kraichnan, R.H. (1971) Inertial-range transfer in two and three-dimensional turbulence. J. Fluid Mech., **47**, 525-535
355. Kraichnan, R.H. (1973) Helical turbulence and absolute equilibrium. J. Fluid Mech., **59**, 745-752
356. Kraichnan, R.H. (1975) Remarks on turbulence theory. Advances in Mathematics, **16**, 305-331
357. Kraichnan, R.H. (1975) Statistical dynamics of two dimensional flows. J. Fluid Mech., **67**, 155-175
358. Kraichnan, R.H. (1976) Eddy viscosity in two and three dimensions. J. Atmos. Sci., **33**, 1521-1536
359. Kraichnan, R.H. and Montgomery, D. (1980) Two-dimensional turbulence. Reports Progr. Phys., **43**, 547-619
360. Krishnan L. and Sandham, N.D. (2006) Effect of Mach number on the structure of turbulent spots. J. Fluid Mech., **566**, 225-234
361. Kristoffersen, R. and Andersson, H.I. (1993) Direct simulations of low-Reynolds-number turbulent flow in a rotating channel. J. Fluid Mech. **256**, 163-197
362. Kuroda, A. (1990) Direct-numerical simulation of Couette-Poiseuille flows. PhD Tokyo University
363. Lafon, A. (1985) Etude des attracteurs pour des écoulements bidimensionnels de fluides visqueux incompressibles. PhD Paris University
364. Laizet, S. and Lamballais, E. (2006) Direct-numerical simulation of the splitting-plate downstream-shape influence upon a mixing layer. C.R. Acad. Sci. Paris, **334** (7), 454-460
365. Lamb, H. (1932) Hydrodynamics. Dover, New York (sixth edition)

366. Lamballais, E. (1995) Simulations numériques de la turbulence dans un canal plan tournant. PhD Grenoble Institute of Technology
367. Lamballais, E., Lesieur, M. and Métais, O. (1996) Influence d'une rotation d'entraînement sur les tourbillons cohérents dans un canal. C.R. Acad. Sci. Paris, Ser II, **323**, 95-101
368. Lamballais, E., Lesieur, M., Métais, O. (1996) Effects of spanwise rotation on the vorticity stretching in transitional and turbulent channel flow. Int. J. Heat and Fluid Flow, **17**, 324-332
369. Lamballais, E., Métais, O. and Lesieur, M. (1998) Spectral-dynamic model for large-eddy simulations of turbulent rotating channel flow, Theor. Comp. Fluid Dyn., **12**, 149-177
370. Lamballais, E., Lesieur, M. and Métais, O. (1998) Probability distribution functions and coherent structures in a turbulent channel. Phys. Rev. E, **56**, 6761-6766
371. Landau, L. and Lifchitz, E. (1971) Fluid Mechanics. Mir, Moscow
372. Landhal, M. and Mollo-Christensen, E. (1986) Turbulence and random processes in fluid mechanics. Cambridge University Press
373. Lanford, O.E. (1977) Computer pictures of the Lorenz attractor, in Turbulence seminar, Berkeley 76-77, A. Dold and B. Eckmann eds, Springer-Verlag Lecture Notes in Mathematics, **615**, 113-116
374. Lapeyre, G., Klein, P. and Hua, B.L. (1999) Does the tracer gradient vector align with the strain eigenvectors in 2D turbulence? Phys. Fluids, **11**, 3729-3737
375. Lapeyre, G., Hua, B.L. and Klein, P. (2001) Dynamics of the orientation of active and passive scalars in two-dimensional turbulence. Phys. Fluids, **13**, 251-264
376. Laplace, Pierre Simon de (1814) Essai philosophique sur les probabilités, Paris, Mme Ve Courcier. (Fac-similé: Bruxelles, Culture et civilisation, 1967)
377. Larchevêque, M., Chollet, J.P., Herring, J.R., Lesieur, M., Newman, G.R. and Schertzer, D. (1980) Two-point closure applied to a passive scalar in decaying isotropic turbulence. In Turbulent Shear Flows II, edited by L.J.S. Bradbury et al., Springer Verlag, 50-65
378. Larchevêque, M. (1981) Contribution à l'étude de la diffusion d'un contaminant passif par une turbulence homogène. Thèse de doctorat d'Etat, Université Pierre et Marie Curie, Paris
379. Larchevêque, M. and Lesieur, M. (1981) The application of eddy-damped markovian closures to the problem of dispersion of particle pairs. J. de Mécanique, **20**, 113-134
380. Larchevêque, M. (1990) Pressure fluctuations and Lagrangian accelerations in two-dimensional incompressible isotropic turbulence. Eur. J. Mech. B, **9**, 109-128
381. Laroche, H. (1991) Simulations numériques directes des écoulements d'un fluide tournant ou stratifié en densité de façon stable, autour d'un obstacle, PhD Grenoble Institute of Technology
382. La Rue, J.C. and Libby, P.A. (1981) Thermal mixing layer downstream of a half heated turbulence grid. Phys. Fluids, **24**, 597-603

383. Lasheras, J.C., Cho, J.S. and Maxworthy, T. (1986) On the origin and evolution of streamwise vortical structures in a plane, free shear layer. J. Fluid Mech., **172**, 231-258
384. Lasheras, J.C. and Choi, H. (1988) Three-dimensional instability of a plane free shear layer: an experimental study of the formation and evolution of streamwise vortices. J. Fluid Mech., **189**, 53-86
385. Lasheras, J.C. and Meiburg, E. (1990) Three-dimensional vorticity modes in the wake of a flat plate. Phys. Fluids A, **3**, 371-380
386. Lasheras, J.C. and Meiburg, E. (1991) On the three-dimensional dynamics of coherent vortical structures forming in Free, shear flows. in Turbulence and coherent structures, O. Métais and M. Lesieur eds, Kluwer, 91-111
387. Laufer, J., Kaplan, R.E. and Chu, W.T. (1973) On the generation of jet noise. AGARD Specialists Meeting Noise Mechanisms, Brussels
388. Launder, B.E. and Spalding, D.B. (1972) Mathematical models of turbulence. Academic Press
389. Launder, B.E. (1996) An introduction to single-point closure methodology. In Computational Fluid Dynamics 1993, Les Houches Summer School of Theoretical Physics, M. Lesieur, P. Comte and J. Zinn Justin eds, North-Holland, 257-323
390. Laval, JP and Dubrulle B. (2006) A LES-Langevin model for turbulence. Eur. Phys. J. B, **49**, 471-481
391. Le H., Moin, P. and Kim J. (1997) Direct numerical simulation of turbulent flow over a backward-facing step. J. Fluid Mech., **330**, 349-374
392. Lee, T.D. (1952) On some statistical properties of hydrodynamical and magneto hydrodynamical fields. Q. Appl. Math., **10**, 69-74
393. Lee, J. (1979) Dynamical behaviour of the fundamental triad-interaction system in three-dimensional homogeneous turbulence. Phys. Fluids, **22**, 40-53
394. Lee, J. (l982) Development of mixing and isotropy in inviscid homogeneous turbulence. J. Fluid Mech., **120**, 155-183
395. Lee, M.J., Kim, J. and Moin, P. (1990) Stucture of turbulence at high shear rate. J. Fluid Mech., **216**, 561-583
396. Legras, B. (1978) Turbulence bidimensionnelle sur une sphère en rotation, simulations directes et modèles stochastiques. Thèse, Université Pierre et Marie Curie, Paris
397. Legras, B. (1980) Turbulent phase shift of Rossby waves. Geophys. Astrophys. Fluid Dyn., **15**, 253-281
398. Leith, C.E. (1968) Diffusion approximation for two-dimensional turbulence. Phys. Fluids, **11**, 671-673
399. Leith, C.E. (1971) Atmospheric predictability and two-dimensional turbulence. J. Atmos. Sci., **28**, 145-161
400. Leith, C.E. and Kraichnan, R.H. (1972) Predictability of turbulent flows. J. Atmos. Sci., **29**, 1041-1058
401. Leith, C.E. (1980) Private communication
402. Leith, C.E. (1984) Minimum enstrophy vortices. Phys. Fluids, **27**, 1388-1395
403. Leith (1990) Stochastic backscatter in a subgrid-scale model: plane shear mixing layer. Phys. Fluids A. **2**, 297-300

404. Lele, S.K. (1989) Direct-numerical simulation of compressible free-shear flows. AIAA paper 89-0374
405. Lele, S.K. (1994) Compressibility effects on turbulence. Ann. Rev. Fluid Mech., **26**, 211-254
406. Le Mouël, J.L. (2006) Private communication
407. Leonard, A. (1985) Computing three dimensional incompressible flows with vortex elements, Ann. Rev. Fluid Mech. **17**, 523-559
408. Léorat, J., Pouquet, A. and Frisch, U. (1981) Fully-developed MHD turbulence near critical magnetic Reynolds number. J. Fluid Mech., **104**, 419-443
409. Leray, J. (1934) Sur le mouvement d'un fluide visqueux emplissant l'espace. J. Acta Math., **63**, 193-248
410. Lesieur, M., Frisch, U. and Brissaud, A. (1971) Théorie de Kraichnan de la turbulence, application à l'étude d'une turbulence possédant de l'hélicité. Ann. Geophys., **27**, 151-165
411. Lesieur, M. (1972) Décomposition d'un champ de vitesse non divergent en ondes d'hélicité, Turbulence (Observatoire de Nice)
412. Lesieur, M. (1973) Contribution à l'étude de quelques problèmes en turbulence pleinement développée. Thèse de Doctorat d'Etat, Université de Nice
413. Lesieur, M. and Schertzer, D. (1978) Amortissement auto similaire d'une turbulence à grand nombre de Reynolds. Journal de Mécanique, **17**, 609-646
414. Lesieur, M., Somméria, J. and Holloway, G. (1981) Zones inertielles du spectre d'un contaminant passif en turbulence bidimensionnelle. C.R. Acad. Sci. Paris, Ser II, **292**, 271-274
415. Lesieur, M. and Sadourny, R. (1981) Satellite-sensed turbulent ocean structure. Nature, **294**, 673
416. Lesieur, M. (1982) La turbulence développée. La Recherche, **139**, 1412-1425
417. Lesieur, M. (1983) Introduction to two-dimensional turbulence. in Two-dimensional turbulence, J. Mec. Th. Appl., Suppl., R. Moreau ed., 5-20
418. Lesieur, M. and Herring, J.R. (1985) Diffusion of a passive scalar in two-dimensional turbulence. J. Fluid Mech., **161**, 77-95
419. Lesieur, M., Montmory, C. and Chollet, J.P. (1987) The decay of kinetic energy and temperature variance in three-dimensional isotropic turbulence. Phys. Fluids, **30**, 1278-1286
420. Lesieur, M., Staquet, C., Le Roy, P. and Comte, P. (1988) The mixing layer and its coherence examined from the point of view of two-dimensional turbulence. J. Fluid Mech., **192**, 511-534
421. Lesieur, M. and Rogallo, R. (1989) Large-eddy simulation of passive-scalar diffusion in isotropic turbulence. Phys. Fluids A, **1**, 718-722
422. Lesieur, M., Métais, O. and Rogallo, R. (1989) Etude de la diffusion turbulente par simulation des grandes échelles. C.R. Acad. Sci., Paris, Ser II, **308**, 1395-1400
423. Lesieur, M., Yanase, S. and Métais, O. (1991) Stabilizing and destabilizing effects of a solid-body rotation on quasi-two-dimensional shear layers. Phys. Fluids A, **3**, 403–407
424. Lesieur, M. (1994) La turbulence, Collection Grenoble-Sciences, EDP-Springer
425. Lesieur, M., Comte, P. and Métais,O. (1995) Numerical simulations of coherent vortices in turbulence. Appl. Mech. Rev., **48**, 121-149

426. Lesieur, M. and Métais, O. (1996) New trends in large-eddy simulations of turbulence. Ann. Rev. Fluid Mech., **28**, 45-82
427. Lesieur, M., Ossia, S. and Métais, O. (1999) Infrared pressure spectra in two- and three-dimensional isotropic incompressible turbulence. Phys. Fluids, **11**, 1535-1543
428. Lesieur, M. and Ossia, S. (2000) 3D isotropic turbulence at very high Reynolds numbers: EDQNM study. J. Turbulence, **1**, 007
429. Lesieur, M., Métais, O. and Garnier, E. (2000) Baroclinic instability and severe storms, J. Turbulence, **1**, 02
430. Lesieur, M., Begou, P., Briand, E., Danet, A., Delcayre, F. and Aider, J.L. (2003) Coherent-vortex dynamics in large-eddy simulations of turbulence. J. Turbulence, **4**, 016
431. Lesieur, M., O. Métais and Comte, P. (2005) Large-eddy simulations of turbulence. Cambridge University Press
432. Leslie, D.C. (1973) Developments in the theory of turbulence. Clarendon Press, Oxford
433. Leslie, D.C. and Quarini, G.L. (1979) The application of turbulence theory to the formulation of subgrid modelling procedures. J. Fluid Mech., **91**, 65-91
434. Lessen, M., Fox, J.A. and Zien, H.M. (1965) On the inviscid stability of the laminar mixing of two parallel streams of a compressible fluid. J. Fluid Mech., **23**, 355-367
435. Lessen, M., Fox, J.A. and Zien, H.M. (1966) Stability of the laminar mixing of two parallel streams with respect to supersonic disturbances. J. Fluid Mech., **25**, 737-742
436. Lezius, D.K. and Johnston, J.P. (1976) Roll-cell instabilities in rotating laminar and turbulent channel flows, J. Fluid Mech., **77**, 153-175
437. Lienhard, V.J. and Van Atta, C.W. (1990) The decay of turbulence in thermally stratified flow. J. Fluid Mech., **210**, 57-112
438. Lighthill, J. (1952) On sound generated aerodynamically I. General theory. Proc. Roy. Soc. A., **211**, 564-587
439. Lighthill, J. (1978) Waves in fluids. Cambridge University Press
440. Lilly, D.K. (1969) Numerical simulation of two-dimensional turbulence. Phys. Fluids Suppl. II **12**, 240-249
441. Lilly, D.K. (1971) Numerical simulation of developing and decaying two-dimensional turbulence. J. Fluid Mech., **45**, 395
442. Lilly, D.K. (1973) Lectures in sub-synoptic scales of motion and two-dimensional turbulence. in Dynamic Meteorology, Proceedings of the Lannion 1971 C.N.E.S. Summer School of Space Physics, P. Morel ed., Reidel, 355-418
443. Lilly, D.K. (1983) Stratified turbulence and the mesoscale variability of the atmosphere. J. Atmos. Sci., **40**, 749-761
444. Lilly, D.K. (1984) Some facets of the predictability problem for atmospheric mesoscales. in Predictability of fluid motions, La Jolla Institute 1983, AIP Conference Proceedings **106**, edited by G. Holloway and B.J. West, 287-294
445. Lilly, D.K. (1986) The structure, energetics and propagation of rotating convective storms. Part II: helicity and storm stabilization. J. Atmos. Sci., **43**, 126-140

446. Lilly, D.K. (1987) in *Lecture Notes on Turbulence*, edited by J.R. Herring and J.C. McWilliams, World Scientific, 171-218
447. Lilly, D.K. (1992) A proposed modification of the Germano subgrid-scale closure method. Phys. Fluids A., **4**, 633-635
448. Lilly, D.K. (1996) Numerical simulation and prediction of atmospheric convection. In Computational Fluid Dynamics 1993, Les Houches Summer School of Theoretical Physics, M. Lesieur, P. Comte and J. Zinn-Justin eds, North-Holland, 325-374
449. Lin, J.T. (1972) Relative dispersion in the enstrophy cascading inertial range of homogeneous two-dimensional turbulence. J. Atmos. Sci., **29**, 394-396
450. Lions, J.L. (1969) Quelques méthodes de résolution des problèmes aux limites non linéaires. Dunod
451. Lions, J.L. (1991) Remarks on turbulence. In Turbulence and coherent structures, M. Lesieur and O. Métais eds, Kluwer
452. Liu, S., Meneveau, C. and Katz, J. (1994) On the properties of similarity subgrid-scale models as deduced from measurements in turbulent jet. J. Fluid Mech., **275**, 83-119
453. Lorenz, E.N. (1963) Deterministic nonperiodic flow. J. Atmos. Sci., **20**, 130-141
454. Lorenz, E.N. (1969) The predictability of a flow which possesses many scales of motion. Tellus, **21**, 289-307
455. Lowery, P.S. and Reynolds, W.C. (1986) Numerical simulation of a spatially-developing, forced, plane mixing layer. Report TF-26, Stanford University
456. Lumley, J.L. (1978) Advances in Appl. Mech., **18**, 123-175
457. Lund, T.S., Ghosal, S. and Moin, P. (1993) Numerical experiments with highly-variable eddy-viscosity models. in Engineering applications to large eddy simulation, U. Piomelli and S. Ragab eds, ASME, New York, 7-11
458. Lund, T., Wu, X. and Squires, K.D. (1998) Generation of turbulent inflow data for spatially-developing boundary-layer simulations. J. Comp. Phys., **140**, 233-258
459. Lundgren, T.S. (1981) Turbulent pair dispersion and scalar diffusion. J. Fluid Mech., **111**, 27-57
460. MacCormack, R. (1969) The effect of viscosity in hypervelocity impact cratering, AIAA paper, **69** 354
461. Mack, L.M. (1969) Boundary-layer stability theory (2 volumes), Jet Propulsion Laboratory
462. Maeder, T. Adams, N. and Kleiser, L. (2001) Direct simulation of turbulent supersonic boundary layers by an extended temporal approach. J. Fluid Mech., **429**, 187-216
463. Maekawa, H., Mansour, N. and Buell, J.C. (1991) Instability mode interactions in a spatially-developing plane wake. J. Fluid Mech., **235**, 223-254
464. Maidi M. and Lesieur, M. (2005) Large eddy simulations of spatially growing subsonic and supersonic turbulent round jets. J. Turbulence, **6** (38), 1-20
465. Maidi M., Lesieur M. and Métais, O. (2006) Vortex control in large-eddy simulations of compressible round jets. J. Turbulence, **7** (49), 1-22
466. Maidi, M. (2006) Estimation of aerodynamic noise generated by forced compressible round jets. C.R. Acad. Sci. Paris,**334**, 285-291

467. Mandelbrot, B. (1975) Les objets fractals: forme, hasard et dimension. Flammarion, Paris
468. Mandelbrot, B. (1976) Intermittent turbulence and fractal dimension. In Turbulence and Navier–Stokes equations, R. Temam ed., Lecture Notes in Mathematics, **565**, Springer-Verlag, 121-145
469. Mandelbrot, B. (1977) The fractal geometry of nature. W.H. Freeman and Company, New York
470. Mankbadi, R. (2001) Computational aeroacoustics, in New trends in turbulence 2000, Les Houches Summer School of Theoretical Physics, M. Lesieur, A. Yaglom and F. David eds, EDP-Springer, 259-317
471. Maréchal, J. (1972) Etude expérimentale de la déformation plane d'une turbulence homogène. J. Mécanique, **11**, 263-294
472. Martin, J.E. and Meiburg, E. (1991) Numerical investigation of three-dimensionally evolving jets subject to axisymmetric and azimuthal perturbations. J. Fluid Mech., **230**, 271-318
473. Martin, J.E. and Meiburg, E. (1992) Numerical investigation of three-dimensionally evolving jets under helical perturbations. J. Fluid Mech., **243**, 457-487
474. Maslowe, S.A. (1981) Shear-flow instabilities and transition, in Hydrodynamic instabilities and the transition to turbulence, edited by H.L. Swinney and J.P. Gollub, Springer-Verlag, 181-228
475. Maxworthy, T. (1983) Private communication
476. Mc Comb, W.D. (1990) The physics of fluid turbulence, Oxford University Press
477. McMillan, O.J. and Ferziger, J.H. (1980) Tests of new subgrid scale models in strained turbulence. AIAA paper 80-1339
478. McMurtry, P.A., Riley, J.J. and Metcalfe, R.W. (1989) Effects of heat release on the large-scale structure of turbulent mixing layers. J. Fluid Mech., **199**, 297-332
479. McWilliams, J. (1984) The emergence of isolated coherent vortices in turbulent flow. J. Fluid Mech., **146**, 21-43
480. McWilliams, J. (2006) Fundamendals of geophysical fluid dynamics. Cambridge University Press
481. Meiburg, E. (1986) Numerische Simulation der Zwei- und Dreidimensionalen Strukturbildung in Scherschichten un Nachläufen, DFVLR Forschungsbericht FB 86-10
482. Meiburg, E. and Lasheras, J.C. (1988) Experimental and numerical investigation of the three-dimensional transition in plane wakes. J. Fluid Mech., **190**, 1-37
483. Meiburg, E. (1995) Three-dimensional vortex dynamics simulations. In *Fluid vortices*, S. Green ed., Springer
484. Melander, M. and Hussain, F. (1993) Polarized vorticity dynamics on a vortex column, Phys. Fluids A., **5**, 1992-2003
485. Meneveau C., Lund T.S. and Cabot W.H. (1996) A Lagrangian dynamic subgrid-scale model of turbulence. J. Fluid Mech., **319**, 353
486. Meneveau, C. and Katz, J. (2000) Scale-Invariance and turbulence models for large-eddy simulations. Ann. Rev. Fluid Mech., **32**, 1-32

487. Merilees, P.E. and Warn, H. (1975) On energy and enstrophy exchanges in two-dimensional non-divergent flow. J. Fluid Mech., **69**, 625-630
488. Meshalkin, L.D. and Sinai, Y.G. (1961) J. Appl. Math. Mech., **25**, 1700
489. Messadek, K. and Moreau R. (2002) An experimental investigation of MHD quasi-two-dimensional turbulent shear flows, J. Fluid. Mech., **456**, 137-159
490. Métais, O. (1983) La prédicibilité des écoulements turbulents évoluant librement. PhD Grenoble Institute of Technology
491. Métais, O. (1985) Evolution of three-dimensional turbulence under stratification. Proceedings of "Turbulent Shear Flows V", Cornell University, edited by J.L. Lumley
492. Métais, O. and Lesieur, M. (1986) Statistical predictability of decaying turbulence. J. Atmos. Sci., **43**, 857-870
493. Métais, O. and Lesieur, M. (1989) Large-eddy simulation of isotropic and stably-stratified turbulence. In Advances in Turbulence 2, H.H. Fernholz and H.E. Fiedler eds, Springer-Verlag, 371-376
494. Métais, O. and Herring, J.R. (1989) Numerical simulations of freely-evolving turbulence in stably-stratified fluids. J. Fluid Mech., **202**, 117-148
495. Métais, O. and Chollet, J.P. (1989) Turbulence submitted to a stable density stratification: large-eddy simulation and statistical theory. In Turbulent Shear Flows VI, Springer-Verlag, 398-416
496. Métais, O. and Lesieur M. (1992) Spectral large-eddy simulations of isotropic and stably-stratified turbulence. J. Fluid Mech., **239**, 157-194
497. Métais, O., Yanase, S., Flores, C., Bartello, P. and Lesieur, M. (1992) Reorganization of coherent vortices in shear layers under the action of solid-body rotation. in Turbulent Shear Flows VIII, Springer-Verlag, 415-430
498. Métais, O., Flores, C., Yanase, S., Riley, J. and Lesieur, M. (1995) Rotating free-shear flows. Part 2. Numerical simulations. J. Fluid Mech., **293**, 47-80
499. Métais, O. (1995) private communication
500. Métais, O., Bartello, P., Garnier, E., Riley, J. and Lesieur, M. (1996) Inverse cascade in stably stratified rotating turbulence. Dyn. Atmos. Oceans, **23**, 193-203
501. Metcalfe, R.W., Orszag, S.A., Brachet, M.E., Menon, S. and Riley, J. (1987) Secondary instability of a temporally growing mixing layer. J. Fluid Mech., **184**, 207-243
502. Meyer, Y. (1992) Wavelets and operators. Cambridge University Press
503. Michalke, A. (1964) On the inviscid instability of the hyperbolic tangent velocity profile. J. Fluid Mech., **19**, 543-556
504. Michalke, A. and Hermann, G. (1982) On the inviscid instability of a circular jet with external flow. J. Fluid Mech., **114**, 343-359
505. Miles, J. (1961) On the stability of heterogeneous shear flows. J. Fluid Mech., **10**, 496-508
506. Miller, J., Weichman, P. and Cross, M. (1992) Statistical mechanics, Euler's equation, and Jupiter's red spot. Phys. Rev. A., **45**, 2328-2359
507. Millionshtchikov, M. (1941) On the theory of homogeneous isotropic turbulence. Dokl. Akad. Nauk. SSSR, **32**, 615-618
508. Mirabel, A.P. and Monin, C.A. (1982) Physics of the atmosphere and oceans, **19**, 902

509. Moffatt, H.K. (1970) Dynamo action associated with random inertial waves in a rotating conducting fluid. J. Fluid Mech., **44**, 705-719
510. Moffatt, H.K. (l978: Magnetic field generation in electrically conducting fluids. Cambridge University Press
511. Moffatt, H.K. (1985) Magnetostatic equilibria and analogous Euler flows of arbitrarily complex topology. Part 1. Fundamentals. J. Fluid. Mech., **159**, 359-378
512. Moffatt, H.K. (1986) Geophysical and astrophysical turbulence. In Advances in turbulence, G. Comte-Bellot and J. Mathieu eds, Springer-Verlag, 228-244
513. Moin, P. and Kim, J. (1982) Numerical investigation of turbulent channel flow. J. Fluid Mech., **118**, 341-377
514. Monchaux, R., Berhanu, M., Bourgoin, M., et al. (2007) Generation of a magnetic field by dynamo action in a turbulent flow of liquid sodium. Phys. Rev. Let., **98**, (4) Art. No. 044502
515. Monin, A.S. and Yaglom, A.M. (1975) Statistical Fluid Mechanics: Mechanics of Turbulence. Vol. 2, M.I.T. Press, Cambridge
516. Monkewitz, P.A., Bechert, D.W., Barsikow, B. and Lehmann, B. (1990) Self-excited oscillations and mixing in a heated round jet. J. Fluid Mech., **213**, 611-639
517. Montgomery, D. and Joyce, G. (1974) Statistical mechanics of negative temperature states, Phys. Fluids, **17**, 1139-1145
518. Montgomery, D., Matthaeus, W.H., Stribling, W.T., Martinez, D. and Oughton, S. (1992) Relaxation in two dimensions and the sinh-Poisson equation. Phys. Fluids A, **4**, 3-6
519. Moreau, R. (1990) Magneto-hydrodynamic turbulence. Springer
520. Morel, P. (1973) Dynamic meteorology. Proceedings of the Lannion 1971 C.N.E.S. Summer School of Space Physics. Lectures by Charney, J., Lilly, D., Monin, A., Morel, P., Phillips and Queney, P., Reidel
521. Morel, P. and Larchevêque, M. (1974) Relative dispersion of constant level balloons in the 200 mb general circulation. J. Atmos. Sci., **31**, 2189-2196
522. Morf, R.H., Orszag, S.A. and Frisch, U. (1980) Spontaneous singularity in three-dimensional inviscid, incompressible flow. Phys. Rev. Letters., **44**, 572
523. Morize, C., Moisy, F. and Rabaud, M. (2005) Decaying grid-generated turbulence in a rotating tank. Phys. Fluids, **17**: No. 095105
524. Morize, C. and Moisy, F. (2006) Energy decay of rotating turbulence with confinement effects, Phys. Fluids, **18**: No. 065107
525. Morkovin, M. (1988) private communication
526. Moses, H. E. (1971) Eigenfunctions of the curl operator, rotationally invariant Helmholtz theorem and applications to electromagnetic theory and fluid mechanics. SIAM J. Appl, **21**, 114-144
527. Münch, C., Hébrard, J. and Métais, O. (2003) Large-Eddy Simulations of curved and S-shape squared ducts, Direct and Lare-Eddy Simulation 5, Münich, 27-29 August 2003
528. Munk, W.H. and MacDonald, G.J.F. (1975) The rotation of the Earth. Cambridge University Press
529. Nassef, H. and Browand, F.K. (1993) On the initial formation of a defect structure in a two-dimensional mixing layer. Phys. Fluids, **5**, 979-983

530. Nelkin, M. and Kerr, R.M. (1981) Decay of scalar variance in terms of a modified Richardson law for pair dispersion. Phys. Fluids, **24**, 1754-1756
531. Neu, J.C. (1984) The dynamics of stretched vortices. J. Fluid Mech., **143**, 253-276
532. Newman, G.R. and Herring, J.R. (1979) A test field model study of a passive scalar in isotropic turbulence. J. Fluid Mech., **94**, 163-194
533. Ng, L.L. and Erlebacher, G. (1992) Secondary instabilities in compressible boundary layers. Phys. Fluids A, **4**, 710-726
534. Nikuradse, J. (1932) Gesetzmässigkeit der turbulenten Strömung in glatten Rohren. Forschungsheft, **356**
535. Nishioka, M., Iida, S. and Ichikawa, Y. (1975) An experimental investigation of the stability of plane Poiseuille flow. J. Fluid Mech., **72**, 731-751
536. Normand, X., Comte, P. and Lesieur, M. (1988) Numerical simulation of a spatially-growing mixing layer. La Recherche Aérospatiale, **6**, 45-52
537. Normand, X. (1990) Transition à la turbulence dans les écoulements cisaillés libres et pariétaux. PhD Grenoble Institute of Technology
538. Normand, X. and Lesieur, M. (1992) Direct and large-eddy simulation of transition in the compressible boundary layer. Theor. and Comp. Fluid Dynamics, **3**, 231-252
539. Novikov, E.A. (1959) Izv. Acad. Sci. USSR, Geophys. Ser. **11**
540. Novikov, E.A. and Stewart, R.W. (1964) Intermittency of turbulence and spectrum of fluctuations in energy dissipation. Izv. Akad. Nauk. SSSR, Ser. Geophys., **3**, 408
541. Nygaard, K.J. and Glezer, A.(1990) Core instability of the spanwise vortices in a plane mixing layer. Phys. Fluids A, **2**, 461
542. Oboukhov, A.M. (1941) On the distribution of energy in the spectrum of turbulent flow. Dokl. Akad. Sci. Nauk SSSR, **32 A**, 22-24
543. Oboukhov, A.M. (1941) Spectral energy distribution of a turbulent flow. Izv. Akad. Nauk SSSR, Ser. Geogr. Geophys., **5**, 453-466
544. Oboukhov, A.M. (1949) Pressure fluctuations in a turbulent flow. Dokl. Akad. Sci. Nauk SSSR, **66**, 17-20
545. Oboukhov, A.M. (1949) Structure of the temperature field in turbulent flows. Isv. Akad. Nauk SSSR, Ser. Geogr. Geophys., **13**, 58-69
546. Oboukhov, A.M. (1962) Some specific features of atmospheric turbulence. J. Fluid Mech., **12**, 77-81.
547. 0'Brien, E.F. and Francis, G.C. (1963) A consequence of the zero fourth cumulant approximation. J. Fluid Mech., **13**, 369-382
548. Ogura, Y. (1963) A consequence of the zero fourth cumulant approximation in the decay of isotropic turbulence. J. Fluid Mech., **16**, 33-40
549. Onsager, L. (1949) Statistical hydrodynamics. Nuovo Cimento, **6**, 279-287
550. Orszag, S.A. (1970) The statistical theory of turbulence. (This monograph was unfortunately never published, though excerpts are contained in Orszag [553]. I am greatly indebted to the author for having let copies of his manuscript available.)
551. Orszag, S. A. (1970) Analytical theories of turbulence. J. Fluid Mech., **41**, 363-386

552. Orszag, S.A. and Patterson, G.S. (1972) Numerical simulations of turbulence. In Statistical models and turbulence, edited by M. Rosenblatt and C. Van Atta, Springer Verlag, **12**, 127-147
553. Orszag, S.A. (1977) Statistical theory of turbulence. In Fluid Dynamics 1973, Les Houches Summer School of Theoretical Physics, R. Balian and J.L. Peube eds, Gordon and Breach, 237-374
554. Orszag, S.A. and Patera, A.T. (1983) Secondary instability of wall-bounded shear flows. J. Fluid Mech., **128**, 347-385
555. Osmidov, R.V. (1975) On the turbulent exchange in a stably stratified ocean. Izvestiya, Academy of Sciences, USSR, Atmospheric and Oceanic Physics, **1**, 493-497
556. Ossia, S. and Lesieur, M. (2000) Energy backscatter in large-eddy simulations of three-dimensional incompressible isotropic turbulence. J. Turbulence, **1**, 010
557. Ossia, S. and Lesieur, M. (2001) Large-scale energy and pressure dynamics in decaying 2D incompressible isotropic turbulence. J. Turbulence, **2**, 1-34
558. Padilla-Barbosa, J. and Métais, O. (2000) Large-eddy simulations of deep-ocean convection: analysis of the vorticity dynamics. J. Turbulence, **1**, 009
559. Panchev, S. (1971) Random functions and turbulence. Pergamon Press, Oxford
560. Pantano, C. and Sarkar, S. (2002) A study of compressibility effects in the high-speed turbulent shear layer using direct simulation. J. Fluid Mech., **451**, 329-371
561. Pao, Y.H. (1973) Measurements of internal waves and turbulence in two-dimensional stratified shear flows. Boundary-Layer Met., **5**, 177
562. Papamoschou, D. and Roshko, A. (1988) The compressible turbulent shear layer: an experimental study. J. Fluid Mech., **197**, 453-477
563. Papoulis, A. (1965) Probability, random variables and stochastic processes, McGraw-Hill
564. Paret, J. and Tabeling, P. (1997) Experimental observation of the two-dimensional inverse energy cascade. Phys. Rev. Let., **79**, 4162-4165
565. Paret, J., Jullien, M.C. and Tabeling, P. (1999) Vorticity statistics in the two-dimensional enstrophy cascade. Phys. Rev. Let., **83**, 3418-3421
566. Pedley, T.J. (1969) On the stability of viscous flow in a rapidly rotating pipe. J. Fluid Mech., **35**, 97-115
567. Pedlosky, J. (1979) Geophysical Fluid Dynamics. Springer Verlag
568. Peltier, W.R., Moore, G.W.K. and Polavarapu, S. (1990) Cyclogenesis and frontogenesis, Tellus, **42-A**, 3-13
569. Pelz, R.B. (2001) Symmetry and the hydrodynamic blow-up problem. J. Fluid Mech., **444**, 299-320
570. Phillips, N.A. (1954) Energy transformations and meridional circulations associated with simple baroclinic waves in a two-level, quasi-geostrophic model. Tellus, **6**, 273-286
571. Phillips, N.A. (1956) The general circulation of the atmosphere: a numerical experiment. Q. J. R. Meteorol. Soc., **82**, 123-140
572. Phillips, N.A. (1973) Principles of large scale numerical weather prediction. in Dynamic Meteorology, Proceedings of the Lannion 1971 C.N.E.S. Summer School of Space Physics, P. Morel ed., Reidel, 3-96

573. Pierrehumbert, R.T. and Widnall, S.E. (1982) The two- and three-dimensional instabilities of a spatially periodic shear layer. J. Fluid Mech., **114**, 59-82
574. Piomelli, U. (1993) High Reynolds number calculations using the dynamic subgrid-scale stress model. Phys. Fluids A, **5**, 1484-1490
575. Piomelli, U. and Liu, J. (1995) Large-eddy simulations of rotating channel flows using a localized dynamic model. Phys. Fluids, **7**, 839-848
576. Piomelli, U., Balaras, E. and Pascarelli, A. (2000) Turbulent structures in accelerating boundary layers, J. Turbulence, **1**, 001
577. Piomelli, U.and Balaras, E. (2002) Wall-layer models for large-eddy simulations. Ann. Rev. Fluid. Mech., **34**, 349-374.
578. Pironneau, O. (1989) Finite-elements methods in fluids. Wiley-Masson
579. Poincaré, H. (1889) Sur le problème des trois corps et les équations de la dynamique, Mémoire présenté à l'Académie Royale de Suède
580. Poinsot, T. and Lele, S.K. (1992) Boundary conditions for direct simulations of compressible viscous flows, J. Comp. Phys., **101**, 104-129
581. Polavarapu, S.M., Peltier, W.R. (1993) Formation of small-scale cyclones in numerical simulations of synoptic-scale baroclinic wave life-cycles- secondary instability at the cusp. J. Atmos. Sci., **50**, 1047-1057
582. Polavarapu, S.M., Peltier, W.R. (1993) The structure and nonlinear evolution of synoptic-scale cyclones .2. wave mean flow interaction and asymptotic equilibration. J. Atmos. Sci., **50**, 3164-3184
583. Pope, S. (2000) Turbulent flows. Cambridge University Press
584. Pouquet, A., Lesieur, M., André, J.C. and Basdevant, C. (1975) Evolution of high Reynolds number two-dimensional turbulence. J. Fluid Mech., **72**, 305-319
585. Pouquet, A., Frisch, U. and Léorat, J. (1976) Strong MHD helical turbulence and the non-linear dynamo effect. J. Fluid Mech., **77**, 321-354
586. Pouquet, A., Frisch, U. and Chollet, J.P. (1983) Turbulence with a spectral gap. Phys. Fluids., **26**, 877-880
587. Prandtl, Z.A. (1925) Bericht über Untersuchugen zur Ausgebildeten Turbulenz. Z. Angew. Math. Mech., **5**, 136-169
588. Praud O., Sommeria, J. and Fincham, A.M. (2006) Decaying grid turbulence in a rotating stratified fluid. J. Fluid. Mech., **547**, 389-412
589. Prigogine, I. (1980) From being to becoming, Freeman
590. Proudman, I. and Reid, W.H. (1954) On the decay of a normally distributed and homogeneous turbulent velocity field. Phil. Trans. Roy. Soc., Vol A **247**, 163-189
591. Rehab, H., Villermaux, E. and Hopfinger, E.J. (1997) Flow regimes of large-velocity-ratio coaxial jets. J. Fluid Mech., **345**, 357-381
592. Reynolds, O. (1883) An experimental investigation of the circumstances which determine whether the motion of water shall be direct and sinuous, and the law of resistance in parallel channels. Phil. Trans. Roy. Soc., 51-105
593. Rhines, P.B. (1975) Waves and turbulence on a β-plane, J. Fluid Mech., **69**, 417-443
594. Rhines, P.B. (1979) Geostrophic turbulence. Ann. Rev. Fluid Mech., **11**, 401-441
595. Richardson, L.F. (1922) Weather prediction by numerical process, Cambridge University Press

596. Richardson, L.F. (1926) Atmospheric diffusion shown on a distance neighbor graph. Proc. Roy. Soc. London, Ser. A, **110**, 709-737
597. Richardson, L.F. and Stommel, H. (1948) Note on eddy diffusion in the sea. J. Meteorology, **5**, 238-240
598. Richardson, L.F. (1993) Collected papers. Volume 1 Meteorology and numerical analysis. O. Ashford, H. Charnock, P. Drazin, J. Hunt, P. Smoker and I. Sutherland. Cambridge University Press
599. Riley, J.J., Metcalfe, R.W. (1980) Direct-numerical simulations of perturbed turbulent mixing layers. AIAA paper 80-0274
600. Riley, J.J., Metcalfe, R.W. and Weissman, M.A. (1981) Direct numerical simulations of homogeneous turbulence in density stratified fluids. In Non linear properties of internal waves, La Jolla Institute, AIP Conference Proceedings **76**, edited by B.J. West, 79-112
601. Riley, J.J. (1996) Numerical simulation of variable-density, reacting flows. In Computational Fluid Dynamics 1993, Les Houches Summer School of Theoretical Physics, M. Lesieur, P. Comte and J. Zinn Justin eds, North-Holland, 221-255
602. Riley J.J., Lelong M.P. (2000) Fluid motions in the presence of strong stable stratification Ann. Rev. Fluid Mech., **32**, 613-657
603. Riley J.J. and De Bruyn Kops S.M. (2003) Dynamics of turbulence strongly influenced by buoyancy. Phys. Fluids, **15**, 2047-2059
604. Riley, J.J. (2006) Review of large-eddy simulation of non-premixed turbulent combustion. J. Fluids Engineering-Transactions ASME, **128**, 209-215
605. Robert, R. and Somméria, J. (1991) Statistical equilibrium states for two-dimensional flows. J. Fluid. Mech., **229**, 291-310
606. Robert, R. and Somméria, J. (1992) Relaxation towards a statistical equilibrium in two-dimensional perfect flui dynamics. Phys. Rev. Lett., **69**, 291-310
607. Roberts, P.H. (1961) Analytical theory of turbulent diffusion. J. Fluid Mech., **11**, 257-283
608. Robertson, H.P. (1940). Proc. Cambridge Phil. Soc., **36**, 209
609. Robinson, S.K. (1991) Coherent motions in the turbulent boundary layer. Ann. Rev. Fluid Mech., **23**, 601-639
610. Rodi W., Ferziger J., Breuer, M. and Pourquié, M. (1997) Status of large eddy simulation: results of a workshop Workshop on LES of Flows Past Bluff Bodies (Rottach-Egern, Tegernsee, 1995) J. Fluids Eng., **119**, 248-62
611. Rogallo, R.S. (1981) Numerical experiments in homogeneous turbulence. NASA TM 81315
612. Rogallo, R.S. and Moin, P. (1984) Numerical simulation of turbulent flows. Ann. Rev. Fluid Mech., **16**, 99-137
613. Rogers, M.M. and Moin, P. (1987) The structure of the vorticity field in homogeneous turbulent flows. J. Fluid Mech., **176**, 33-66
614. Rogers, M.M. and Moin, P. (1987) Helicity fluctuations in incompressible turbulent flows. Phys. Fluids, **30**, 2662-2671
615. Rogers, M. and Moser, R. (1992) The three-dimensional evolution of a plane mixing layer: the Kelvin–Helmholtz roll up. J. Fluid Mech., **243**, 183-226
616. Rose, H.A. (1977) Eddy diffusivity, eddy noise and subgrid scale modelling. J. Fluid Mech., **81**, 719-734

617. Rose, H. and Sulem, P.L. (1978) Fully developed turbulence and statistical mechanics. Journal de Physique (Paris), **39**, 441-484
618. Rossby, C.G. et al. (1939) Relation between variations in the intensity of the zonal circulation of the atmosphere and the displacements of the semi permanent centers of action. J. Marine Res., **2**, 38-55
619. Rouse, H. and Ince, S.(1957) History of Hydraulics. Iowa Institute of Hydraulic Research
620. Sadourny, R. and Basdevant, C. (1985) Parameterization of subgrid scale barotropic and baroclinic eddies in quasi geostrophic models: anticipated potential vorticity method. J. Atmos. Sci., **42**, 1353-1363
621. Saffman, P. G. (1967) The large-scale structure of homogeneous turbulence. J. Fluid Mech., **27**, 581-593
622. Saffman, P.G. (1967) Note on decay of homogeneous turbulence. Phys. Fluids, **10**, 1349
623. Saffman, P.G. (1971) On the spectrum and decay of random two-dimensional vorticity distributions of large Reynolds number. Stud. Appl. Math., **50**, 377-383
624. Sagaut, P. (2005) Large-eddy simulations for incompressible flows: an introduction. Springer
625. Salinas-Vazquez, M. (1999) Simulations des grandes échelles des écoulements turbulents dans les canaux de refroidissement des moteurs fusée. PhD Grenoble Institute of Technology
626. Salinas-Vazquez, M. and Métais, O. (1999) Large-eddy simulation of the turbulent flow in a heated square duct. In Direct and Large Simulation III, P.R. Voke et al. eds, Kluwer, 13-24
627. Salinas-Vazquez, M. and Métais, O. (2002) Large Eddy Simulation of the turbulent flow through a heated square duct. J. Fluid Mech., **453**, 201-238
628. Salmon, R. (1978) Two-layer quasi-geostrophic turbulence in a simple special case. Geophys. Astrophys. Fluid Dyn., **10**, 25-52
629. Sandham, N.D. and Reynolds, W.C. (1989) The compressible mixing layer: linear theory and direct simulation. AIAA paper 89-0371
630. Sandham, N.D. and Reynolds, W.C. (1991) Three-dimensional simulations of large eddies in the compressible mixing layer. J. Fluid Mech., **224**, 133-158
631. Sandham, N.D. and Kleiser, L.K. (1992) The late stages of transition to turbulence in channel flow. J. Fluid Mech., **245**, 319-348
632. Sato, H. and Kuriki, K. (1961) The mechanism of transition in the wake of a thin flat plate placed parallel to a uniform flow. J. Fluid Mech., **11**, 321-352
633. Schaeffer, N. and Cardin, P. (2006) Quasi-geostrophic kinematic dynamos at low magnetic Prandtl number. Earth and Planetary Science Let.,**245**, 595-604
634. Schertzer, D. and Lovejoy, S. (1984) The dimension and intermittency of atmospheric dynamics. In Turbulent Shear Flows IV, edited by B. Launder, Springer-Verlag
635. Schlichting, H. (1968) Boundary-layer theory. Pergamon Press, London
636. Schmidt, H. and Schumann, U. (1989) Coherent structure of the convective boundary layer derived from large eddy simulations. J. Fluid Mech., **200**, 511-562

637. Schmidt, P.J. and Henningson, D.S. (2001) Stability and transition in shear flows. Sringer
638. Schubauer, G.B. and Skramstad, H.K. (1948) Laminar boundary layer oscillations and transition on a flat plate. N.A.C.A. Report 909
639. Schubauer, G.B. and Klebanoff, P.S. (1955) Contributions on the mechanics of boundary layer transition. N.A.C.A. TN 3489
640. Schumann, U. (1975) Subgrid-scale model for finite-difference simulations of turbulent flows in plane channels and annuli. J. Comput. Phys., **18**, 376-404
641. Schwartz, L. (1950) Théorie des distributions. Hermann, Paris
642. Serres, M. (1977) La naissance de la Physique dans le texte de Lucrèce, fleuves et turbulences. Editions de Minuit
643. She, Z.S., Jackson, E. and Orszag, S. A. (1990). Nature, **344**, 226
644. Shepherd, T. (1987) Non-ergodicity of inviscid two-dimensional flow on a beta-plane and on the surface of a rotating sphere. J. Fluid Mech., **184**, 289-302
645. Shtilman, L., Levich, E., Orszag, S.A., Pelz, R.B. and Tsinober, A. (1985) On the role of helicity in complex fluid flows. Phys. Let., **113 A**, 32-37
646. Sivashinsky, G. and Yakhot, V. (1985) Negative viscosity effect in large-scale flows. Phys. Fluids, **28**, 1040-1042
647. Siggia, E.D. (1981) Numerical study of small-scale intermittency in three-dimensional turbulence. J. Fluid Mech. **107**, 375-406
648. Silveira, A. (1991) Simulation numérique des grandes échelles d'un écoulement turbulent décollé en aval d'une marche. PhD Grenoble Institute of Technology
649. Silveira-Neto, A., Grand, D., Métais, O. and Lesieur, M. (1991) Large-eddy simulation of the turbulent flow in the downstream region of a backward-facing step. Phys. Rev. Lett., **66**, 2320-2323
650. Silveira-Neto, A., Grand, D., Métais, O. and Lesieur, M. (1993) A numerical investigation of the coherent vortices in turbulence behind a backward-facing step. J. Fluid Mech., **256**, 1-25
651. Silvestrini, J., Comte, P. and Lesieur, M. (1995) DNS and LES of spatial incompressible mixing layer. 10th Symposium on Turbulent Shear Flows, Penn State University
652. Silvestrini, J. (1996) Simulation des grandes échelles des zones de mélange: application à la propulsion solide des lanceurs spatiaux. PhD Grenoble Institute of technology
653. Smagorinsky, J. (1963) General circulation experiments with the primitive equations. Mon. Weath. Rev., **91, 3**, 99-164
654. Smith, C.R. and Walker, J.D. (1995) Turbulent wall-layer vortices. In Fluid vortices, S. Green ed., Kluwer
655. Smith, L.M. and Waleffe, F. (1999) Transfer of energy to two-dimensional large scales in forced, rotating three-dimensional turbulence. Phys. Fluids, **11**, 1608-1622
656. Smits, L. and Dussauge, J.P. (1996) Turbulent shear layers in supersonic flows. American Institute of Physics
657. Soetrisno, M., Eberhardt, S., Riley, J. and McMurtry, P. (1988) A study of inviscid, supersonic mixing layers using a second-order TVD scheme. AIAA/ASME/SIAM/APS 1st Nat. Fluid Dynamics Congress, Cincinnati, AIAA paper 88-3676-CP

658. Soetrisno, M., Greenough, J.A., Eberhardt, S. and Riley, J. (1989) Confined compressible mixing layers: part I. Three-dimensional instabilities. AIAA 20 Fluid Dynamics, Plasma Dynamics and Lasers Conference, Buffalo, Nat. Fluid Dynamics Congress, Cincinnati, AIAA paper 89-1810
659. Somméria, G. (1976) Three-dimensional simulation of turbulent processes in an undisturbed trade wind boundary layer. J. Atmos. Sci., **33**, 216-241
660. Somméria, J. (1986) Experimental study of the two-dimensional inverse energy cascade in a square box. J. Fluid Mech., **170**, 139-168
661. Somméria, J., Meyers, S.D. and Swinney, H.L. (1988) Laboratory simulation of Jupiter's Great Red Spot. Nature, **331**, 689-693
662. Somméria, J. (2001) Two-dimensional turbulence. In New trends in turbulence 2000, Les Houches Summer School of Theoretical Physics, M. Lesieur, A. Yaglom and F. David eds, EDP-Springer, 385-447
663. Spalart, P.R. (1988) Direct Simulation of a Turbulent Boundary Layer up to $R_\theta = 1410$. J. Fluid Mech., **187**, 61-98
664. Sreedhar, M. and Ragab, S. (1994) Large-eddy simulation of longitudinal stationary vortices. Phys. Fluids, **6**, 2501-2514
665. Sreenivasan, K.R., Tavoularis, S., Henry, S. and Corrsin, S. (1980) Temperature fluctuations and scales in grid-generated turbulence. J. Fluid Mech., **100**, 597-621
666. Sreenevasan, K.R. and Strykowski, P.J. (1984) On analogies between turbulence in open flows and chaotic dynamical systems. in Turbulence and chaotic phenomena in fluids, edited by T. Tatsumi, North-Holland, 191-196
667. Stapountzis, B., Sawford, B.L., Hunt, J.C. and Britter, R.E. (1986) Structure of the temperature field downwind of a line source in grid turbulence. J. Fluid Mech., **165**, 401-424
668. Staquet, C., Métais, O. and Lesieur, M. (1985) Etude de la couche de mélange et de sa cohérence du point de vue de la turbulence bidimensionnelle. C.R. Acad. Sci., Paris, Ser II, **300**, 833-838
669. Staquet, C. (1985) Etude numérique de la transition à la turbulence bidimensionnelle dans une couche de mélange. PhD Grenoble University
670. Staquet, C. and Riley, J. (1989) A numerical study of a stably-stratified mixing layer. In Turbulent Shear Flows VI, Springer-Verlag, 381-397
671. Staquet, C. (1995) Two-dimensional secondary instabilities in a strongly-stratified shear layer. J. Fluid Mech., **296**, 73-126
672. Stillinger, D.C., Helland, K.N., and Van Atta, C.W. (1983) Experiments on the transition of homogeneous turbulence to internal waves in a stratified fluid. J. Fluid Mech., **131**, 691-722
673. Sulem, P.L., Lesieur, M. and Frisch, U. (1975) Le Test Field Model interprété comme méthode de fermeture des équations de la turbulence. Ann. Géophys. (Paris), **31**, 487-495
674. Tarbouriech, L. and Renouard, D. (1996) The effect of rotation in destabilizing a turbulent plane wake. C.R. Acad. Sci. Ser II, **323**, 391-396
675. Tatsumi, T. (1957) The theory of decay process of incompressible isotropic turbulence. Proc. Roy. Soc. London, Ser. A **239**, 16-45
676. Tatsumi, T., Kida, S. and Mizushima, J. (1978) The multiple scale turbulent expansion for isotropic turbulence. J. Fluid Mech., **85**, 97-142

677. Tatsumi, T. (1980) Theory of homogeneous turbulence. Adv. Appl. Mech., **20**, 39-133
678. Tatsumi, T. and Yanase, S. (1981) The modified cumulant expansion for two-dimensional isotropic turbulence. J. Fluid. Mech., **110**, 475-496
679. Taylor, G.I. (1921) Proc. London Math. Soc., **20**, 126
680. Taylor, G.I. (1922) The motion of a sphere in a rotating liquid. Proc. Roy. Soc. London, Ser. A, **102**, 213-215
681. Taylor, G.I. and Green, A.E. (1937) Proc. Roy. Soc. London, Ser. A, **158**, 499
682. Temam, R. (1977) Navier–Stokes equations. North Holland (revised edition 1984)
683. Tennekes, H. (1968) Simple model for the small-scale structure of turbulence. Phys. Fluids, **11**, 669-671
684. Tennekes, H. and Lumley, J.L. (1972) A first course in turbulence. MIT Press, Cambridge, Mass
685. Thompson, P.D. (1957) Uncertainty of initial state as a factor in the predictability of large-scales atmospheric flow patterns. Tellus, **9**, 275-295
686. Thompson, P.D. (1984) A review of the predictability problem. In Predictability of fluid motions, La Jolla Institute 1983, AIP Conference Proceedings **106**, G. Holloway and B.J. West eds, 1-10
687. Thoroddsen, S.T. and Van Atta, C.W. (1992) Exponential tails and skewness of density-gradient probability density functions in stably-stratified turbulence. J. Fluid Mech., **244**, 547-566
688. Thorpe, S.A. (1968) A method of producing a shear-flow in a stratified fluid. J. Fluid Mech., **32**, 693-704
689. Townsend, A.A. (1976) The structure of turbulent shear flow. Cambridge University Press.
690. Tritton, D.J. and Davies, P.A. (1985) Instabilities in Geophysical Fluid Dynamics. In Hydrodynamic instabilities and the transition to turbulence, edited by H.L. Swinney and J.P. Gollub, Springer-Verlag, 181-228 (second edition)
691. Tritton, D. (1988) Physical fluid dynamics. Clarendon Press, Oxford
692. Tseng, Y. and Ferziger, J. (2001) Effects of coastal geometry and the formation of cyclonic/anti-cyclonic eddies on turbulent mixing in upwelling simulation. J. Turbulence, **2** 014
693. Tsinober, A. and Levitch, E. (1983) On the helical nature of three-dimensional coherent structures in turbulent flows. Phys. Letters, **99 A**, 321-324
694. Tsinober, A., Kit, E. and Dracos, T. (1992) Experimental investigation of the field of velocity gradients in turbulent flows. J. Fluid Mech., **242**, 169-192
695. Tso, J. and Hussain, F. (1989) Organized motions in a fully-developed turbulent axisymmetric jet. J. Fluid Mech., **203**, 425-448
696. Urbin, G. (1995) Calcul par simulation des grandes échelles de la transition turbulente d'un jet libre rond. Report CEA-Grenoble STR/LML/95-335.
697. Van Atta, C.W. and Chen, W.Y. (1970) Stucture functions of turbulence in the atmospheric boundary layer over the ocean. J. Fluid Mech., **44**, 145-159
698. Van Dyke, M. (1982) An album of fluid motion, The Parabolic Press, Stanford, California
699. Verron, J. and Le Provost, C. (1985) A numerical study of quasi-geostrophic flow over isolated topography. J. Fluid Mech., **154**, 231-252

700. Vervisch, L. and Poinsot, T. (1998) Direct numerical simulation of non-premixed turbulent flames. Ann. Rev. Fluid. Mech., **30**, 655-691
701. Veynante, D. and Vervisch, L. (2002) Turbulent combustion modeling. Progr. En. Comb. Sci., **28**, 193-266
702. Villermaux, E. and Rehab, H. (2000) Mixing in coaxial jets. J. Fluid Mech., **425**, 161-185
703. Villermaux, E., Innocenti, C. and Duplat, J. (2001) Short circuits in the Corrsin-Oboukhov cascade. Phys. Fluids, **13**, 284-289
704. Vincent, A. and Meneguzzi, M. (1991) The spatial structure of homogeneous turbulence. In Turbulence and coherent structures, O. Métais and M. Lesieur eds, Kluwer, 191-201
705. Vincent, A. and Meneguzzi, M. (1991) The spatial structure and statistical properties of homogeneous turbulence. J. Fluid Mech., **225**, 1-20
706. Vincent, A. and Meneguzzi, M. (1994) The dynamics of vorticity tubes in homogeneous turbulence. J. Fluid Mech., **258**, 245-254
707. Virk, D. Melander, M. and Hussain, F. (1994) Dynamics of a polarized vortex ring. J. Fluid Mech., **260**, 23-56
708. Vukoslavcevic, P., Balint, J.L. and Wallace, J.M. (1991: The velocity and vorticity vector fields of a turbulent boundary layer. Part 1. Simultaneous measurements by hot-wire anemometry. J. Fluid Mech., **228**, 25-51
709. Waleffe, F. (1992) The nature of triad interactions in homogeneous turbulence. Phys. Fluids, A, **4**, 350-363
710. Wallace, D. and Redekopp, L.G. (1992) Linear-instability character of wall-shear layers. Phys. Fluids, **4**, 189-191
711. Wang M., Freund, J.B. and Lele, S.K. (2006) Computational prediction of flow-generated sound. Ann. Rev. Fluid Mech., **38**, 483-512
712. Warhaft, Z. and Lumley, J.L. (1978) An experimental study of the decay of temperature fluctuations in grid generated turbulence. J. Fluid Mech., **88**, 659-684
713. Warhaft, Z. (1984) The interference of thermal fields from line sources in grid turbulence. J. Fluid Mech., **144**, 363-387
714. Weiss, J. (1981) The dynamics of enstrophy transfers in two-dimensional hydrodynamics. La Jolla Institute preprint LJI-TN-121ss. See also Physica D (1991), **48**, 273-294
715. Werlé, H. (1974) Courants et couleurs. ONERA
716. Widnall, S.E., Bliss, D.B. and Tsai, C. (1974) The instability of short waves on vortex ring. J. Fluid Mech., **66** (1), 35-47
717. Williams, G.P. (1978) Planetary circulations: 1. barotropic representation of Jovian and terrestrial turbulence. J. Atmos. Sci., **35**, 1399-1426
718. Williams, G.P. (1979) Planetary circulations: 2. The Jovian quasi-geostrophic regime J. Atmos. Sci., **36**, 932-968
719. Williamson C. and Prasad, A. (1993) Acoustic forcing of oblique wave resonance in the far wake. J. Fluid Mech., **256**, 315-341
720. Williamson, C. (1996) Vortex dynamics in the cylinder wake. Ann. Rev. Fluid Mech., **28**, 477-539
721. Winant,C.D. and Browand,F.K. (1974) Vortex pairing, the mechanism of turbulent mixing layer growth at moderate Reynolds number. J. Fluid Mech., **63**, 237-255

722. Witt, H.T. and Joubert, P.N. (1985) Effect of rotation on a turbulent wake. Proceedings of "Turbulent Shear Flows V", Cornell University, edited by J.L. Lumley
723. Wray, A. (1988) Private communication
724. Wurtele, M.G., Sharman, R.D. and Datta, A. (1996) Atmospheric lee waves. Ann. Rev. Fluid Mech., **28**, 429-476
725. Wygnanski, I. and Fiedler, H.E. (1970) The two-dimensional mixing region. J. Fluid Mech., **41**, 327-361
726. Yaglom, A.M. (1966) Effect of fluctuations in energy dissipation rate on the form of turbulence characteristics in the inertial range. Dokl. Akad. Nauk. SSSR, **166**, 49
727. Yaglom, A.M. (2000) Private communication
728. Yakhot, V. and Orszag, S. (1986) Renormalization Group (RNG) methods for turbulence closure. J. Scientific Computing, **1**, 3-52
729. Yamada, H. and Matsui, T. (1978) Preliminary study of mutual slip-through of a pair of vortices. Phys. Fluids, **21**, 292-294
730. Yanase, S., Flores, C., Métais, O. and Riley, J. (1993) Rotating free-shear flows. I. Linear stability analysis. Phys. Fluids, **5**, 2725-2737
731. Yang, Z. and Voke, P.R. (1993) In Engineering turbulence modelling and measurements, W. Rodi and F. Martelli eds, North-Holland, 603-611
732. Yeh, T.T. and Van Atta, C.W. (1973) Spectral transfer of scalar and velocity fields in heated-grid turbulence. J. Fluid Mech., **48**, 41-71
733. Yin, Z., Montgomery, D. and Clercx, H. (2003) Alternative mechanical-statistical description of decaying two-dimensional turbulence in terms of patches and points. Phys. Fluids, **15**, 1937-1953
734. Yoshizawa, A. (1982) A statistically derived subgrid model for the large eddy simulations of turbulence. Phys. Fluids, **225**, 1532-1538
735. Zabusky, N.J. and Deem, G.S. (1971) Dynamical evolution of two-dimensional unstable shear flows. J. Fluid Mech., **47**, 353-379
736. Zang, T.A. and Krist, S.E. (1989) Numerical experiments on stability and transition in plane channel flow. Theor. and Comp. Fluid Dynamics, **1**, 41-64
737. Zang, T.A., Street, R.L. and Koseff, J.R. (1993) A dynamic mixed subgrid scale model and its application to turbulent recirculating flows. Phys. Fluids, **5**, 3186-3196
738. Zouari, N. and Babiano, A. (1994) Derivation of the relative dispersion law in the inverse energy cascade of two-dimensional turbulence. Physica D, **76**, 318-328

Index

β-plane approximation, 371

absolute instability, 107
absolute-vorticity hairpin, 472
Ackerman, 444
Adams, 501
adiabatic equilibrium, 57
aerodynamics, 23
aeronautics, 10, 23
Aider, 484
aircraft (commercial), 458
aircraft turbojets, 145
airfoil, 1, 21, 32
Akselvoll, 484
Alboran sea, 11
Algerian current, 489
Allègre, 28
alternate pairing, 22, 104, 140, 143, 144
analytical statistical theories, 20, 237
Andersson, 476, 479
André, 83, 239, 250, 334
Anselmet, 230
anticyclonic, cyclonic vortices, 9, 11, 352, 361
Antonia, 232, 438
apex vortices, 8
Archimedeus, 58
Aref, 16
Argoul, 232
Ariane V, 497
Arnal, 484, 499
Ashurst, 97
astrophysics, 23
Atten, 206
Aubry, 15, 206
Aupoix, 437
available potential energy, 390
axisymmetric turbulence, 155, 182, 461
Ayrault, 4, 5

Bénard–Marangoni convection, 118
Bègue, 423, 432
Babiano, 322, 342
backscatter spectrum, 234
backward-facing step, 10, 483
Bailly, 144
Balarac, 104, 145
Balint, 4–6
balls lift, 32
bananas, 217
Bandyopadhyay, 484
Bardina, 447
baroclinic energy, 386
baroclinic instability, 11, 22, 62, 349, 357, 384, 385
baroclinic vector, 41
barotropic, 35, 41
barotropic energy, 390
Barré de Saint-Venant equations, 62, 367
Bartello, 319, 387, 399, 482

Basdevant, 8, 168, 255, 322, 324, 326, 334, 338, 357, 395, 398, 414, 452
Batchelor, 8, 25, 41, 92, 169, 171, 183, 202, 209, 220, 225, 276, 303, 318, 338, 441
Batchelor's constant, 227
Bech, 479
Beltrami flow, 163
Bergé, 15, 118
Bernal, 97, 136
Bernard, 6
Bernoulli (Daniel), 30, 31
Bernoulli's theorem (first), 32
Bernoulli's theorem (second), 35
Bertoglio, 438
Betchov, 91, 198
Bewley, 151
Bickley jet, 105, 361
Bickley jet (turbulent), 125
Bidokhti, 470
bifurcation, 18
big bang, 235
Biot and Savart, 44
Biringen, 112
black holes, 94
Blackwelder, 149
Blanc-Lapierre, 239
Blasius, 75
Blasius velocity profile, 81, 108
Blumen, 490
Bogdanoff, 489
Bogey, 144
Boltzmann constant, 396
Boltzmann–Gibbs equilibrium distribution, 396, 401
Bonnet, 137
Boratav, 215
Borue, 269
boundary layer, 1
boundary layer (turbulent), 130, 145
Boussinesq approximation, 25, 52, 114
Boussinesq equations (Fourier space), 160
Brachet, 215, 232, 320
Bradshaw, 86
brain, 95
Brault, 16
Breidenthal, 97, 107
Bretherton, 401
Briand, 445
Brissaud, 214, 264
Browand, 104, 129, 136, 198, 312, 328, 467
Brown, 4, 119, 136, 483
Brownian motion, 203, 306
Brunt–Vaisala frequency, 57, 161
Bryson, 111
buoyancy, 25
Burger number, 358
Burgers equation, 264
Busse, 13, 116, 118, 388
by-pass transition, 112, 427

Cadot, 219
Californian current, 377
Cambon, 161, 164, 167, 181, 244
canonical ensemble, 395
Canuto, 419
Capéran, 183
Cardin, 171
Carel, 320, 369
Carnevale, 152, 314, 319
Casalis, 85
Castaing, 235
Catherine the 1st, 30
Catherine the great, 30
cavitating wake, 138
cells, convective, 117
cellular automata method, 451
centrifugal force, 28
Chabert d'Hières, 470
Champagne, 104, 119, 198, 224, 234, 286
Chandrasekhar, 183
Chandrsuda, 103, 483
channel sea ("Manche"), 69
Chanut, 364
chaos, 14, 22, 403
chaotic advection, 16
Charney, 349, 355, 389, 403, 459
Chasnov, 227, 297, 319
chemical engineering, 23
Chen, 107, 232, 496

Choi, 97, 151
Chollet, 286, 297, 412, 428, 463
Chorin, 44, 102, 402, 451
Chou, 239
Chu, 104
Cimbala, 138
circumpolar vortices, 354
cirrus, 459
Clark, 422, 447
clear-air turbulence, 57
climate, 28
climate models, 414
closure problem, 121, 122
Coantic, 208
coaxial jets, 145
coherent structure, 8
coherent vortex, 7, 8, 10, 19, 135, 320
Colin de Verdière, 313, 383
collapse to quasi two-dimensional turbulence, 162, 456
combustion, 23, 451
combustion (non-premixed), 95
compensated spectrum, 208
complex helical wave, 163
compressibility, 23
compressible turbulence, 426
Comte, 7, 93, 100, 102, 137, 219, 346, 443
Comte-Bellot, 270, 274
conductive wave number, 222
Constantin, 206
continuity equation, 27
convective instability, 107
conveyor belt, 13, 118
cooking oven, 30
Corcos, 100, 417
Coriolis force, 9, 27, 48
Coriolis parameter, 46
correlated energy spectrum, 404
Corrsin, 43, 198, 224, 270, 274, 297
Corrsin–Oboukhov's constant, 224
Cottet, 44, 402, 451
Couder, 8, 314
Couette flow (plane), 76, 114
Couette flow (plane, turbulent), 135
Cousteix, 132, 151, 437
Coustols, 151
Craya, 164, 167, 182
Craya decomposition, 22, 161, 461
Craya space, 172
critical points, 80
Crow, 104, 119
cumulant, 240

d'Humières, 451
da Silva, 104, 144, 145
Danet, 484
Dannevik, 238, 282
Daviaud, 171
David, 443, 496
Davies, 470
De Bruyn Kops, 466
Dean, 133
Deardorff, 426
decorrelated energy spectrum, 405
Deem, 44
deformation tensor, 28, 425
degrees of freedom, 14, 16, 320, 419
Delcayre, 486
Delta wing, 8
Delville, 16
Derango, 314
desert, 112
detailed conservation of kinetic energy, 188, 395
deterministic, 2, 18
diffusion (coherent), 204
diffusion (incoherent), 204
diffusion coefficient, 309
Dimotakis, 95, 215
dipole, 8, 322, 323, 415
Dirac function, 157
Direct-Interaction Approximation (D.I.A.), 247
direct-numerical simulation, 10, 18
dislocation, 5, 22
dispersion coefficient, 202
displacement thickness, 108
dissipative scale, 14
dissipative structure, 43
dissipative system, 14, 23
DNS, 18, 19, 21
Domaradzki, 430

double-diffusive convection, 118
drag, 1
Drazin, 76, 81, 82, 86, 105, 108, 116, 204, 357
Driver, 484
Druault, 16
dry adiabatic lapse rate, 57
Dubrulle, 423
Ducros, 8, 110, 148, 426, 500
Dumas, 198, 287
dune, 112
Durbin, 21
Dussauge, 489
dynamic viscosity, 28
dynamic model, 448
dynamical system, 14, 16, 20, 403
dynamo effect, 170, 266, 388
Dziomba, 130

E.D.Q.N.M. approximation, 237
Eady model, 357
Earth, 1, 10, 13, 14, 20, 25, 27, 46, 61, 374, 388
Earth atmosphere, 67
Eaton, 484
eddy conductivity, 286
eddy diffusivity, 310
eddy diffusivity in spectral space, 295
eddy viscosity, 21, 123, 124, 286, 351
eddy viscosity in spectral space, 271
Eddy-Damped Quasi-Normal approximation (E.D.Q.N.), 244
Eddy-Damped Quasi-Normal Markovian approximation (E.D.Q.N.M), 245
ejection, 133, 145
Ekman pumping, 374
Ekman layer, 22, 366, 371
Ekman layer thickness, 374
Ekman number, 374
Ekman spiral, 372, 373
El Nino, 377
El-Hady, 450
Elliott, 205
Emmons, 111
energy cascade, 16, 197
ensemble average, 121, 166
enstrophy, 177
enstrophy cascade, 16, 317, 346
enstrophy dissipation wave number, 319
enthalpy, 34
entropy, 37
EOLE experiment, 343, 458
equipartition of energy, 396
ergodic hypothesis, 168
Erlebacher, 500
error backscatter, 409, 423
error function, 129
error rate, 404
error spectrum, 405
Ertel's theorem, 45, 55
Eswaran, 288
Etling, 470
Euler, 23, 30, 31, 100
Euler equation, 30, 41
external forces, 168
Eyink, 271

Falkovich, 205, 290
Fallon, 485, 496
Farge, 162, 322
Fasham, 340
Fauve, 171, 219
Favre, 16
Favre average, 426
Favre filter, 426
Favre-Marinet, 145
Ferziger, 377, 447
Fick's equation, 204
Fiedler, 129, 483
filtered fields, 420
filtered structure-function model, 444
Fincham, 459
Fjortoft, 325
Fjortoft criterion, 81
Fjortoft's theorem, 316
flash, 114
Flores, 471
flow within a box, 155, 393
fluid particle, 25
Foias, 265
Fornberg, 322
Forster, 238, 277

Foucault pendulum, 46
Fouillet, 7, 8, 140, 491
Fourier law, 34
Fourier representation (integral), 158
Fourier space, 155, 157
Fournier, 238, 264, 277
Fox, 168, 398
fractal, 43
fractal dimension of Hausdorff, 230
Franc, 138
Francis, 242
Freund, 144
friction velocity, 130
Friedrich, 484
Friehe, 231
Frisch, 197, 229, 243, 246, 253, 266, 277, 313, 328, 330, 397, 402, 423, 451
front (cold), 362
front (warm), 363
Froude number, 61, 96, 351, 360, 456
Fulachier, 287
fully-developed turbulence, 10, 13, 14, 20, 155, 187
Fung, 204
Fyfe, 328

Gage, 458
Gagne, 166, 198, 224, 229, 240
galaxies, 94
Galilean, 25
Galilean invariance, 4
Galilean transformation, 106
Gargett, 198, 458
Garnier, 360
Gathmann, 493
Gaussian random function, 239, 240
Gayon, 17
generalized functions (distributions), 157
Geophysical-Fluid Dynamics, 21
geostrophic, 22
geostrophic approximation, 351
geostrophic balance, 8, 49, 352, 368
geostrophic turbulence, 12, 13, 349, 389
geostrophic velocity, 352
Germain, 43
Germano, 448
Gerolymos, 489
Gerz, 466
Geurts, 19, 451
Gharib, 314
Ghosal, 450
Gibraltar, 489
Gibson, 198
Giger, 198
Gilbert, 324
Gill, 25, 56, 60
Glauser, 16
Glezer, 136
Golfe du Lion, 365
Gonze, xxxii, 107, 138, 442
Goutorbe, 448
Grant, 198
gravity waves, 21
great red spot, 13, 467
Green's function, 247
greenhouse effect gas, 414
Greenspan, 373
grid turbulence, 4, 270
Gulf Stream, 11, 382
Gurbatov, 271
Guyon, 118

H-mode, 111, 112
Haidvogel, 392, 401
hairpin vortex, 5, 8, 98, 103, 109, 167
Hama, 110
Hamilton, 138
harmonic oscillator, 59
Hauët, 151
helical pairing, 5, 22, 102, 138, 483, 485, 487
helical spectral tensor, 191
helical wave, 163, 378
helical-waves decomposition, 22, 163
helicity, 163, 170, 191, 265, 266, 397
helicity spectrum, 176, 268
Helmholtz decomposition, 162
Helmholtz theorem, 42
Hendershott, 387
Henningson, 150
Herbert, 109, 111, 112, 140, 417
Hermann, 104, 140

Herring, 183, 234, 245, 284, 296, 297, 313, 320, 327, 328, 330, 342, 391, 408, 423, 438, 452, 458, 504
Hill, 277
Hinze, 109, 110, 169, 173, 188, 207
Hiroshige, 94
Ho, 97, 98, 130, 136, 198
Holland, 357, 453
Holloway, 330, 342, 387, 399
Holmes, 15
Holton, 46, 57, 60, 349, 358
Holzer, 345
homogeneous turbulence, 167
homogenization, 423
Hopfinger, 10, 153, 313, 458
horizontal turbulence, 457
Howard, 82, 96, 105
Hoyer, 371, 391
Hua, 392
Huang, 98, 130, 136
Huerre, 97, 107
Hughes, 436
Humboldt current, 377
Hunt, 204
hurricane, 468, 475
Husain, 136
Hussain, 104, 136, 140, 165
hydraulics, 23
hydrodynamic instability theory, 22, 76
hydrostatic balance, 49, 351
hydrostatic state, 52
hypersonic, 16, 23, 489
hyperviscosity, 431

immersed boundary method, 108
Ince, 28
incompressibility, 27, 40
incompressibility plane, 160
inertial force, 3, 48
inertial range, 14, 201
inertial-conductive range, 225, 227, 339, 341
inertial-convective range, 224, 292, 339, 340
inflection-point instability, 119
infrared pressure, 276, 344
integral scale, 2, 199
intermittency (external), 228
intermittency (internal), 43, 228
internal energy, 34
internal-gravity wave, 57, 162, 457
internal-inertial gravity wave, 55
inverse cascade of error, 20
inverse energy cascade (2D), 324, 399
inviscid instability, 73
Iooss, 18
Ishida, 19, 276
isobaric surface, 41
isopycnal surface, 41
isotropic turbulence, 10, 19, 22, 155, 169
Itsweire, 458

Jayesh, 232
jet (plane, laminar), 104
jet (plane, turbulent), 104, 123, 138
jet stream, 354
Jimenez, 44, 97, 114, 207
Johnston, 476, 484
Joseph, 18
Joubert, 470
Jovic, 484
Joyce, 402
Jullien, 321, 341
Jupiter, 1, 13, 14, 83, 388

K-mode, 111, 113, 149
Kachanov, 112
Kaplan, 104
Karman constant, 131
Karman street, 106, 107
Karman vortices, 8, 107, 138
Karman-Howarth solution, 207
Katrina, 475
Kelvin theorem, 42
Kelvin wave, 68
Kelvin–Helmholtz instability, 5, 82, 93
Kelvin–Helmholtz vortex, 7, 8, 93, 96, 136, 137, 215, 314, 322, 483
Kerr, 215, 298
Kida, 320, 338
Kim, 8, 113, 145, 427, 476
kinematic simulation, 204
kinetic-energy flux, 193

kinetic-energy spectrum, 176
kinetic-energy theorem, 31, 33
kinetic-energy transfer, 193
Kiya, 484
Klebanoff, 8, 110, 111
Klein, 324
Kleiser, 110, 112, 412, 445, 501
Kline, 8, 145
Kolmogorov, 16, 102, 119, 203, 228
Kolmogorov cascade, 138, 420
Kolmogorov constant, 197, 198
Kolmogorov dissipative scale, 17, 18, 198
Kolmogorov flow, 333
Kolmogorov inverse energy cascade, 325
Kolmogorov wave number, 198, 199, 393
Kolmogorov's 1941 theory, 196
Konrad, 97
Koochesfahani, 95
Koop, 467
Koumoutsakos, 44, 402, 451
Kourta, 107
Kraichnan, 16, 20, 189, 194, 237, 241, 245, 264, 268, 271, 288, 295, 303, 314, 325, 330, 397–399, 403, 430, 438
Krishnan, 489
Krist, 112
Kristmannsson, 342, 399
Kristoffersen, 476
Kuo equation, 78, 82
Kuriki, 106
Kuroda, 133
Kuroshio, 11, 382

Léorat, 266
La Rue, 174
Labrador sea, 364
Lafon, 206
Lagrange, 67
Lagrangian History Direct Interaction Approximation (L.H.D.I.A.), 248
Lagrangian correlation time, 306
Lagrangian derivative, 26
Laizet, 108
Lamb, 26
Lamballais, 87, 108, 113, 133, 145, 430, 438, 450
laminar, 3, 74
Landau, 133, 201, 273
Landhal, 88, 150
Lanford, 15, 17
Langevin equation, 246, 278
Langevin model (stochastic), 438
Lapeyre, 324
Laplace, 17
Laplace equation, 70
Larchevêque, 221, 284, 297, 341–343, 458
large-eddy simulation, 19, 20, 419
large-eddy turnover time, 244
Laroche, 83
Lasheras, 97, 107, 142
Lasserre, 208
lattice gas, 451
Lattigo, 129
Laufer, 104, 198
Launder, 21
Laval, 423
Le, 484, 485
Le Mouël, 171
Le Provost, 386
leapfrog, 104
Lee, 150, 162, 168, 396
lee wave, 57, 457
Legras, 244, 387
Leith, 204, 245, 314, 330, 401, 403, 429
Lele, 489, 491
Lelong, 467
Leonard, 44, 451
Leonard term, 422
Leray, 18, 214
LES, 19, 21, 420
Lesieur, 19, 71, 92, 100, 104, 110, 111, 135, 138, 142, 163, 165, 181, 183, 217, 219, 227, 232, 238, 245, 252, 264, 272, 275, 290, 296, 297, 324, 334, 339, 360, 379
Leslie, 20, 222, 225, 227, 237, 278, 428
Lessen, 490
Levchenko, 112

Levich, 269
Liapounov exponent, 14, 403
Libby, 174
Lienhard, 458
Lifchitz, 133, 201, 273
lift, 33
Lighthill, 60, 144
Lighthill analogy, 39
Lilly, 267, 320, 327, 406, 450, 458
Lin, 100, 343, 417
Lions, 18, 214
Liouville theorem, 394, 396
liquid sodium, 171
Liu, 447, 476
local turnover time, 8, 201
logarithmic velocity profile, 131
Loitzianskii integral, 272
long-wave approximation, 71
longitudinal hairpins, 100, 107
longitudinal vortices, 22, 86, 97, 98, 103, 107, 136, 138, 143, 146, 151
Lorentz force, 27
Lorenz, 15, 20, 314, 403
Lorenz attractor, 17
Lovejoy, 232
low- and high-speed streaks, 88, 110, 133, 145, 147
low-Mach number expansions, 39
Lowery and Reynolds, 97
Lucretius, 152
Lumley, 15, 21, 200, 206, 207, 222, 270, 293
Lund, 450, 485
Lundgren, 303

M.H.D. helical turbulence, 397
M.H.D. turbulence, 22, 42, 170, 266, 313, 504
Münch, 497
Métais, 44, 68, 87, 90, 104, 144, 194, 217, 232, 252, 275, 296, 330, 366, 406, 422, 458, 471
MacCormack, 143
MacDonald, 28
Mach number, 17, 39
Mach number (convective), 490
Mack, 499
macropressure, 425
macrotemperature, 426
Maeder, 501
Maekawa, 107
magnetic helicity, 397
Magnus effect, 32
Maidi, 143
Majda, 205
mammoth, 208
Mandelbrot, 43, 229
Mankbadi, 220
Maréchal, 167
Markovian Random Coupling Model (M.R.C.M.), 246
Martin, 142
Maslowe, 80
Matsui, 104
maximum entropy principle, 401
Maxworthy, 457
Mc Comb, 432
McMillan, 447
McMurtry, 495
McWilliams, 322, 328, 330, 349
meddies, 489
Mediterranean, 11, 365
Meiburg, 44, 97, 103, 107, 142, 451
Melander, 165
Meneguzzi, 44, 216
Meneveau, 450
Merilees, 317
Meshalkin, 333
mesoscale atmosphere, 62, 456
Messadek, 313
Metcalfe, 7, 97
meteorology, 23
METEOSAT II, 11
Meyer, 16
Michalke, 92, 104, 140, 469
Michel, 138
microcanonical ensemble, 395
Miles, 96
Miller, 402
Millionshtchikov, 239
minimum enstrophy principle, 401
Mirabel, 340

mirror symmetry, 170
mistral, 365
mixed model, 448
mixing layer, 1, 4, 73, 76, 96
mixing layer (compressible), 489
mixing layer (plane, turbulent), 128
mixing length, 21, 22, 121, 123
mixing transition, 215
Moffatt, 42, 163, 170, 219, 324
Moin, 8, 145, 167, 270, 422, 427, 484
Moisy, 313, 483
molecular conductivity, 2, 37
molecular viscosity, 2
Mollo-Christensen, 88, 150
momentum flux, 124, 126
Monchaux, 171
Monin, 221, 229, 340
Monkewitz, 107
Montgomery, 314, 402
Moreau, 42, 170, 313
Morel, 320, 343, 369, 458
Morf, 215
Morize, 313, 483
Morkovin, 40, 499
Moser, 97, 113
Moses, 164
most-amplified mode, 85
most-amplified wave number, 91
Mount Saint-Michel, 69
multiscale formulation, 436
Munk, 28

Nagib, 138
Nassef, 136
Nastrom, 458
natural transition, 111
Navier, 30
Navier–Stokes equations, 30
Navier–Stokes (Fourier space), 159
negative eddy-viscosity, 333
negative temperature, 399
Nelkin, 298
Nelson, 277
Neptune, 13
Neu, 100
neutral modes, 80
New Orleans, 475
Newman, 287
Newton, 28, 58
Newtonian fluid, 28
Newtonian gravity, 28
Newtonian mechanics, 27
Ng, 500
Nikuradse, 131
Nishioka, 112
noise, 39, 145, 220, 343
non-local interactions, 255, 270
non-local transfers, 255
nonlinear interactions, 18
Normand, 6, 96, 110, 445, 490
Novikov, 229, 403
nuclear engineering, 23
numerical dye, 94
Nygaard, 136

O'Brien, 242, 288
Oboukhov, 196, 200, 204, 220, 224, 228
oceanography, 23
Ogura, 242
olympic swimmer, 132
one-point closure modelling, 21, 122
ONERA, 198
Onsager, 402
Orr–Sommerfeld equation, 108
Orr–Sommerfeld equation (2D), 79
Orr–Sommerfeld equation (3D), 84
Orszag, 20, 112, 160, 168, 197, 200, 202, 209, 210, 215, 216, 237, 238, 242, 244, 269, 272, 394, 398, 432
Osmidov scale, 457
Ossia, 259, 276, 319
outer core, 171, 467
ozone hole, 60

p.d.f., 303, 310
Padilla–Barbosa, 366
pair of Lagrangian tracers, 42
pairing, 5, 8, 10, 97, 104, 106, 136, 312, 322, 323, 328, 333, 346, 388
palinstrophy, 209, 313, 335
pancake, 457, 458
Panchev, 214
Pao, 458

Papamoschou, 490
Papoulis, 165
Paret, 321, 328, 330
particles-pair dispersion, 203, 303, 342
passive scalar, 21, 94, 221
passive tracers, 16
passive vector, 42
passive-scalar equation, 41
Patera, 112
Patterson, 160, 209, 216
Peclet number, 2, 36
Pedley, 86, 476
Pedlosky, 41, 45, 50, 349, 355, 366, 384
Peltier, 360, 361
Pelz, 215
Penel, 265
perfect barotropic fluid, 41
perfect fluid, 3, 35, 41
Pettersson Reif Chichester, 21
phase space, 14, 395
phenomenological theories, 22
Philipovitch, 324
Phillips, 370, 452
Picinbono, 239
Pierrehumbert, 98, 103, 138, 417
Pinton, 171
Piomelli, 450, 476
Pironneau, 419
planetary scales, 1, 10, 14
planetary vorticity, 46
plasma physics, 22, 504
Poincaré, 15, 403
Poinsot, 451
point vortices, 16
Poiseuille flow (circular), 74, 114
Poiseuille flow (plane), 75, 81, 112
Poiseuille flow (plane, turbulent), 132
Polavarapu, 360
Pope, 19, 21, 310
potential enstrophy cascade, 389
potential energy, 460
potential temperature, 37
potential vorticity, 21, 45, 55, 355
potential vorticity (quasi geostrophic), 356
potential vorticity conservation, 64
Pouquet, 194, 243, 255, 266, 313, 330, 334, 397, 428
Prandtl, 21, 123, 124
Prandtl number (turbulent), 286
Prandtl number, 37, 116, 221
Prandtl number (turbulent), 425, 429
Prandtl's mixing-length theory, 104
Prasad, 140
Praud, 459
precursor calculation, 485
predictability, 403
predictability of a passive scalar, 412
predictability time, 412
predictability time (atmosphere), 414
pressure (static), 28
pressure cooker, 30
pressure spectrum, 220
Prigogine, 153
primitive equations, 392
proper orthogonal decompositions, 16
Proudman, 239, 263
Proudman–Taylor theorem, 50
Proudman–Taylor theorem (generalized), 353
pseudo-spectral methods, 102, 160

Q criterion, 135, 324
Quarini, 428
quasi geostrophic theory, 349
quasi two-dimensional topology, 103
Quasi-Normal approximation (Q.N.), 239, 240

R.N.G., 432
Rabaud, 313
Ragab, 450
Random Coupling Model (R.C.M.), 247
random function, 19, 121, 165
random Galilean transformation, 248
random walk, 203, 306
rapid-distorsion theory, 149, 155, 167, 184
Rayleigh, 116
Rayleigh criterion for centrifugal instability, 87
Rayleigh discriminant, 87
Rayleigh equation, 105

Rayleigh equation (2D), 80
Rayleigh inflection-point criterion, 81
Rayleigh number, 96, 115, 117
Rayleigh–Bénard convection, 114, 117
Rayleigh–Bénard instability, 22
reacting flows, 420
realizability, 244
realization, 121
reattachment length, 484
Redekopp, 107
Rehab, 145
Reid, 76, 81, 86, 105, 108, 116, 239, 263, 357
relative vorticity, 9
Renormalization Group techniques, 22, 238, 277
Renouard, 474
residual turbulence, 76, 111
Reynolds, 74, 95, 96, 100, 114, 491
Reynolds equations, 21, 122, 422
Reynolds number, 2, 74, 200, 207
Reynolds stresses, 122, 129
Rhines, 13, 338, 387, 399
Rhines length, 388
riblets, 151
Richardson, 197, 275, 297, 298, 452
Richardson law, 203, 326, 409
Richardson number, 96
Richardson's constant, 204
rigid lid, 50, 369, 377
Riley, 7, 39, 48, 162, 183, 451, 456, 466, 495
Robert, 402
Roberts, 303
Robertson, 171
Robinson, 8
rocket, 497
Rodi, 427
Rogallo, 167, 233, 275, 422, 448
Rogers, 97, 167, 270
rolls, convective, 117
Rose, 187, 201, 237, 394, 432
Roshko, 4, 6, 97, 119, 136, 138, 483, 490
Rossby waves (planetary), 380
Rossby equation, 380
Rossby number, 12, 48
Rossby number (local), 86, 351
Rossby radius of deformation (internal), 60
Rossby radius of deformation (external), 66, 67, 369
Rossby wave, 13, 46, 349, 369
Rossby wave (baroclinic), 383
Rossby wave (topographic), 383
rotating backstep, 489
rotating turbulence, 467
rotation number, 479
round jet, 104, 198
round jet (turbulent), 4, 126, 140
round wake, 104
round wake (turbulent), 128
Rouse, 28
Ruelle, 140

Sadourny, 162, 168, 322, 340, 357, 371, 391, 395, 398, 452
Saffman, 274, 320
Sagaut, 19
Salmon, 391
salt fingers, 118
Sandham, 100, 112, 412, 489, 491
Sato, 106
Saturn, 1, 14, 388
sawtooth profile, 264
scalar backscatter, 341
scalar spectrum, 178
scalar-velocity correlation, 173
scale-similarity model, 447
Schertzer, 232, 254, 272
Schlichting, 21, 104, 108, 109, 124, 129, 135
Schmidt, 150, 427
Schmidt number, 221
Schon, 4, 5
Schubauer, 109, 111
Schumann, 427
Schwartz, 157
Schwarz inequality, 405
secondary-instability analysis, 98, 111, 112
selective structure-function model, 443
separated flows, 483
separation bubble, 485

Serres, 152
Shafarenko, 290
shallow-water analogy, 68
shallow-water equations, 62
shark-skin swimming costumes, 151
She, 43, 216
shear-Coriolis instability, 86, 469
shell model, 250, 345
Shepherd, 399
Shtilman, 270
side jets, 104
Siggia, 44, 216, 345
Silveira-Neto, 314, 484
Silvestrini, 100, 137, 438
Sinai, 333
Sivashinsky, 333
skewness factor, 209, 257
skin-friction coefficient, 75
Skramstad, 109
slug, 114
Smagorinsky model, 426
Smith, 149, 483
Smits, 489
smoke ring, 7
Soetrisno, 491
solar granulation, 117
solid-body rotation, 23, 25
Somméria, 13, 83, 313, 327, 402, 427
sound pressure level, 220
sound velocity, 39, 67
sound wave, 68
space shuttle, 30
Spalart, 8, 132
Spalding, 21
spatial average, 167, 168
spatial mixing layer, 91, 95
spatial mixing layer (turbulent), 136
spectral backscatter, 271, 275, 326, 328
spectral eddy diffusivity, 428
spectral eddy viscosity, 428
spectral tensor, 187
spike, 110
spiral galaxy, 7
splitter plate, 74
Squire's theorem, 85, 101
Sreedhar, 450
Sreenivasan, 206, 298
stable stratification, 23
stably-stratified turbulence, 162, 456
stagnation region, 100
Stapountzis, 299
Staquet, 7, 9, 48, 328, 339, 346, 466
stationary, 168
statistical thermodynamics, 393
statistical unpredictability, 23
Stephen, 277
Stewart, 229
Stillinger, 456
stochastic model, 20–22, 237
Stokes, 31
Stommel, 204
strange attractor, 15
structure-function model, 441
Strykowski, 206
Stuart vortex, 98
subcritical instability, 112
subgrid scales, 19, 394
subgrid-scale fields, 421
subgrid-scale modelling, 422
subharmonic instability, 94, 416
subharmonic instability (3D), 103
subsonic plane, 132
Sulem, 187, 201, 237, 238, 328, 330, 394
sun, 117
supergrid scales, 423
supergrid-scale transfer, 429
supersonic, 23, 489
surface gravity wave, 67
surface inertial wave, 67
Sutherland law, 29
Swift, 197
synoptic perturbations, 67
Szewczyk, 91

Tabeling, 314, 321, 328, 330
Takens, 140
Taneda, 3
Tarbouriech, 474
Tatsumi, 239, 249, 264, 275, 338
Taylor, 51
Taylor column, 51
Taylor microscale, 207
Taylor's diffusion law, 305

Taylor–Green vortex, 214, 327
Temam, 18, 214
temperature backscatter, 295
temperature enstrophy, 223, 290
temperature integral scale, 295
temporal mixing layer, 4, 7, 81, 91
Tennekes, 43, 198, 200, 207, 222
Test-Field Model (T.F.M.), 248
thermal convection, 15, 22, 57, 96
thermal diffusivity, 37
thermal fronts, 349, 357
thermal wind equation, 354
thermohaline convection, 118
Thompson, 314, 403
Thomson, 271
Thoroddsen, 458
Thorpe, 96
tidal range, 69
tide, 68
time average, 168
Tollmien–Schlichting wave, 109
topography, 63
tornado, 267, 349, 468
Townsend, 167, 183, 209
transition to turbulence, 22, 73, 74
translative instability, 98, 103
Tritton, 114, 118, 470
Troutt, 136
truncated Euler equations, 394
Tseng, 377
Tsinober, 6, 269
Tso, 140
tsunami, 67
turbomachine, 25
turbomachinery, 456, 468
turbulent boundary layer, 130
turbulent diffusion, 2, 22
turbulent jet, 4
turbulent spot, 111, 114
two-dimensional passive scalar, 339
two-dimensional turbulence, 22, 313
two-point closures, 20–22, 122, 187, 237

unpredictability, 2, 7, 10, 16, 19, 20, 119, 403
upwelling, 377
Urbin, 142
Utagawa school, 94

Vallet, 489
Van Atta, 232, 301
Van Dyke, 104, 496
van Gogh, 94
velocity correlation tensor, 167, 171
velocity induction, 94
velocity spectral tensor, 174
velocity structure function, 201
velocity-sheets model, 91, 479
Verron, 386
Vervisch, 451
Veynante, 451
Villermaux, 145, 235
Vincent, 44, 216
Virk, 165
viscous forces, 3
viscous instability, 73
viscous thickness, 131
viscous-convective range, 227, 292, 339–341
Voke, 427
vortex dynamics, 44
vortex lattice, 102
vortex line, 42
vortex methods, 451
vortex ring, 7, 104, 140, 142, 144
vortex street, 4, 119
vortex surface, 42
vortex tube, 42
vortex-filament method, 103
vortex-lattice topology, 103
vortex-tube stretching, 43
vorticity, 3, 31
vorticity dynamics, 54
Voyager 2, 13
Vukoslavcevic, 6

wake (plane), 106, 107
wake (plane, turbulent), 127, 138
Waleffe, 165, 483
Walker, 149
wall units, 131
Wallace, 6, 107
Wang, 144

Warhaft, 174, 232, 270, 293
Warn, 317, 319
water wave, 112
wavelet, 16
weak absolute-vorticity stretching principle, 480
Weiss criterion, 324
Werlé, 107
Widnall, 98, 103, 104, 138, 417
Williams, 13, 388
Williamson, 107, 140
Winant, 104, 312, 328
Witt, 470
Wray, 44, 212
Wurtele, 57
Wygnanski, 129, 483

Yaglom, 204, 221, 229
Yakhot, 238, 282, 333, 432
Yamada, 104, 320, 338
Yanase, 86, 338, 468
Yang, 427
Yeh, 301
Yin, 402
Yoshizawa, 438

Zabusky, 44
Zaman, 104
Zang, 110, 112, 445, 450
Zouari, 343

Mechanics

FLUID MECHANICS AND ITS APPLICATIONS

Series Editor: R. Moreau

Aims and Scope of the Series

The purpose of this series is to focus on subjects in which fluid mechanics plays a fundamental role. As well as the more traditional applications of aeronautics, hydraulics, heat and mass transfer etc., books will be published dealing with topics which are currently in a state of rapid development, such as turbulence, suspensions and multiphase fluids, super and hypersonic flows and numerical modelling techniques. It is a widely held view that it is the interdisciplinary subjects that will receive intense scientific attention, bringing them to the forefront of technological advancement. Fluids have the ability to transport matter and its properties as well as transmit force, therefore fluid mechanics is a subject that is particularly open to cross fertilisation with other sciences and disciplines of engineering. The subject of fluid mechanics will be highly relevant in domains such as chemical, metallurgical, biological and ecological engineering. This series is particularly open to such new multidisciplinary domains.

1. M. Lesieur: *Turbulence in Fluids.* 2nd rev. ed., 1990 ISBN 0-7923-0645-7
2. O. Métais and M. Lesieur (eds.): *Turbulence and Coherent Structures.* 1991 ISBN 0-7923-0646-5
3. R. Moreau: *Magnetohydrodynamics.* 1990 ISBN 0-7923-0937-5
4. E. Coustols (ed.): *Turbulence Control by Passive Means.* 1990 ISBN 0-7923-1020-9
5. A.A. Borissov (ed.): *Dynamic Structure of Detonation in Gaseous and Dispersed Media*. 1991 ISBN 0-7923-1340-2
6. K.-S. Choi (ed.): *Recent Developments in Turbulence Management.* 1991 ISBN 0-7923-1477-8
7. E.P. Evans and B. Coulbeck (eds.): *Pipeline Systems.* 1992 ISBN 0-7923-1668-1
8. B. Nau (ed.): *Fluid Sealing.* 1992 ISBN 0-7923-1669-X
9. T.K.S. Murthy (ed.): *Computational Methods in Hypersonic Aerodynamics.* 1992 ISBN 0-7923-1673-8
10. R. King (ed.): *Fluid Mechanics of Mixing*. Modelling, Operations and Experimental Techniques. 1992 ISBN 0-7923-1720-3
11. Z. Han and X. Yin: *Shock Dynamics.* 1993 ISBN 0-7923-1746-7
12. L. Svarovsky and M.T. Thew (eds.): *Hydroclones*. Analysis and Applications. 1992 ISBN 0-7923-1876-5
13. A. Lichtarowicz (ed.): *Jet Cutting Technology*. 1992 ISBN 0-7923-1979-6
14. F.T.M. Nieuwstadt (ed.): *Flow Visualization and Image Analysis*. 1993 ISBN 0-7923-1994-X
15. A.J. Saul (ed.): *Floods and Flood Management*. 1992 ISBN 0-7923-2078-6
16. D.E. Ashpis, T.B. Gatski and R. Hirsh (eds.): *Instabilities and Turbulence in Engineering Flows*. 1993 ISBN 0-7923-2161-8
17. R.S. Azad: *The Atmospheric Boundary Layer for Engineers.* 1993 ISBN 0-7923-2187-1
18. F.T.M. Nieuwstadt (ed.): *Advances in Turbulence IV.* 1993 ISBN 0-7923-2282-7
19. K.K. Prasad (ed.): *Further Developments in Turbulence Management.* 1993 ISBN 0-7923-2291-6
20. Y.A. Tatarchenko: *Shaped Crystal Growth.* 1993 ISBN 0-7923-2419-6
21. J.P. Bonnet and M.N. Glauser (eds.): *Eddy Structure Identification in Free Turbulent Shear Flows.* 1993 ISBN 0-7923-2449-8
22. R.S. Srivastava: *Interaction of Shock Waves*. 1994 ISBN 0-7923-2920-1

Mechanics

FLUID MECHANICS AND ITS APPLICATIONS

Series Editor: R. Moreau

23. J.R. Blake, J.M. Boulton-Stone and N.H. Thomas (eds.): *Bubble Dynamics and Interface Phenomena*. 1994 ISBN 0-7923-3008-0
24. R. Benzi (ed.): *Advances in Turbulence V.* 1995 ISBN 0-7923-3032-3
25. B.I. Rabinovich, V.G. Lebedev and A.I. Mytarev: *Vortex Processes and Solid Body Dynamics.* The Dynamic Problems of Spacecrafts and Magnetic Levitation Systems. 1994 ISBN 0-7923-3092-7
26. P.R. Voke, L. Kleiser and J.-P. Chollet (eds.): *Direct and Large-Eddy Simulation I.* Selected papers from the First ERCOFTAC Workshop on Direct and Large-Eddy Simulation. 1994 ISBN 0-7923-3106-0
27. J.A. Sparenberg: *Hydrodynamic Propulsion and its Optimization.* Analytic Theory. 1995 ISBN 0-7923-3201-6
28. J.F. Dijksman and G.D.C. Kuiken (eds.): *IUTAM Symposium on Numerical Simulation of Non-Isothermal Flow of Viscoelastic Liquids*. Proceedings of an IUTAM Symposium held in Kerkrade, The Netherlands. 1995 ISBN 0-7923-3262-8
29. B.M. Boubnov and G.S. Golitsyn: *Convection in Rotating Fluids*. 1995 ISBN 0-7923-3371-3
30. S.I. Green (ed.): *Fluid Vortices*. 1995 ISBN 0-7923-3376-4
31. S. Morioka and L. van Wijngaarden (eds.): *IUTAM Symposium on Waves in Liquid/Gas and Liquid/Vapour Two-Phase Systems*. 1995 ISBN 0-7923-3424-8
32. A. Gyr and H.-W. Bewersdorff: *Drag Reduction of Turbulent Flows by Additives.* 1995 ISBN 0-7923-3485-X
33. Y.P. Golovachov: *Numerical Simulation of Viscous Shock Layer Flows.* 1995 ISBN 0-7923-3626-7
34. J. Grue, B. Gjevik and J.E. Weber (eds.): *Waves and Nonlinear Processes in Hydrodynamics.* 1996 ISBN 0-7923-4031-0
35. P.W. Duck and P. Hall (eds.): *IUTAM Symposium on Nonlinear Instability and Transition in Three-Dimensional Boundary Layers.* 1996 ISBN 0-7923-4079-5
36. S. Gavrilakis, L. Machiels and P.A. Monkewitz (eds.): *Advances in Turbulence VI.* Proceedings of the 6th European Turbulence Conference. 1996 ISBN 0-7923-4132-5
37. K. Gersten (ed.): *IUTAM Symposium on Asymptotic Methods for Turbulent Shear Flows at High Reynolds Numbers.* Proceedings of the IUTAM Symposium held in Bochum, Germany. 1996 ISBN 0-7923-4138-4
38. J. Verhás: *Thermodynamics and Rheology.* 1997 ISBN 0-7923-4251-8
39. M. Champion and B. Deshaies (eds.): *IUTAM Symposium on Combustion in Supersonic Flows.* Proceedings of the IUTAM Symposium held in Poitiers, France. 1997 ISBN 0-7923-4313-1
40. M. Lesieur: *Turbulence in Fluids.* Third Revised and Enlarged Edition. 1997 ISBN 0-7923-4415-4; Pb: 0-7923-4416-2
41. L. Fulachier, J.L. Lumley and F. Anselmet (eds.): *IUTAM Symposium on Variable Density Low-Speed Turbulent Flows.* Proceedings of the IUTAM Symposium held in Marseille, France. 1997 ISBN 0-7923-4602-5
42. B.K. Shivamoggi: *Nonlinear Dynamics and Chaotic Phenomena.* An Introduction. 1997 ISBN 0-7923-4772-2
43. H. Ramkissoon, *IUTAM Symposium on Lubricated Transport of Viscous Materials*. Proceedings of the IUTAM Symposium held in Tobago, West Indies. 1998 ISBN 0-7923-4897-4
44. E. Krause and K. Gersten, *IUTAM Symposium on Dynamics of Slender Vortices.* Proceedings of the IUTAM Symposium held in Aachen, Germany. 1998 ISBN 0-7923-5041-3

Mechanics

FLUID MECHANICS AND ITS APPLICATIONS

Series Editor: R. Moreau

45. A. Biesheuvel and G.J.F. van Heyst (eds.): *In Fascination of Fluid Dynamics.* A Symposium in honour of Leen van Wijngaarden. 1998 ISBN 0-7923-5078-2
46. U. Frisch (ed.): *Advances in Turbulence VII.* Proceedings of the Seventh European Turbulence Conference, held in Saint-Jean Cap Ferrat, 30 June–3 July 1998. 1998 ISBN 0-7923-5115-0
47. E.F. Toro and J.F. Clarke: *Numerical Methods for Wave Propagation.* Selected Contributions from the Workshop held in Manchester, UK. 1998 ISBN 0-7923-5125-8
48. A. Yoshizawa: *Hydrodynamic and Magnetohydrodynamic Turbulent Flows*. Modelling and Statistical Theory. 1998 ISBN 0-7923-5225-4
49. T.L. Geers (ed.): *IUTAM Symposium on Computational Methods for Unbounded Domains*. 1998 ISBN 0-7923-5266-1
50. Z. Zapryanov and S. Tabakova: *Dynamics of Bubbles, Drops and Rigid Particles*. 1999 ISBN 0-7923-5347-1
51. A. Alemany, Ph. Marty and J.P. Thibault (eds.): *Transfer Phenomena in Magnetohydrodynamic and Electroconducting Flows*. 1999 ISBN 0-7923-5532-6
52. J.N. Sørensen, E.J. Hopfinger and N. Aubry (eds.): *IUTAM Symposium on Simulation and Identification of Organized Structures in Flows*. 1999 ISBN 0-7923-5603-9
53. G.E.A. Meier and P.R. Viswanath (eds.): *IUTAM Symposium on Mechanics of Passive and Active Flow Control*. 1999 ISBN 0-7923-5928-3
54. D. Knight and L. Sakell (eds.): *Recent Advances in DNS and LES*. 1999 ISBN 0-7923-6004-4
55. P. Orlandi: *Fluid Flow Phenomena.* A Numerical Toolkit. 2000 ISBN 0-7923-6095-8
56. M. Stanislas, J. Kompenhans and J. Westerveel (eds.): *Particle Image Velocimetry*. Progress towards Industrial Application. 2000 ISBN 0-7923-6160-1
57. H.-C. Chang (ed.): *IUTAM Symposium on Nonlinear Waves in Multi-Phase Flow*. 2000 ISBN 0-7923-6454-6
58. R.M. Kerr and Y. Kimura (eds.): *IUTAM Symposium on Developments in Geophysical Turbulence* held at the National Center for Atmospheric Research, (Boulder, CO, June 16–19, 1998) 2000 ISBN 0-7923-6673-5
59. T. Kambe, T. Nakano and T. Miyauchi (eds.): *IUTAM Symposium on Geometry and Statistics of Turbulence*. Proceedings of the IUTAM Symposium held at the Shonan International Village Center, Hayama (Kanagawa-ken, Japan, November 2–5, 1999). 2001 ISBN 0-7923-6711-1
60. V.V. Aristov: *Direct Methods for Solving the Boltzmann Equation and Study of Nonequilibrium Flows*. 2001 ISBN 0-7923-6831-2
61. P.F. Hodnett (ed.): *IUTAM Symposium on Advances in Mathematical Modelling of Atmosphere and Ocean Dynamics.* Proceedings of the IUTAM Symposium held in Limerick, Ireland, 2–7 July 2000. 2001 ISBN 0-7923-7075-9
62. A.C. King and Y.D. Shikhmurzaev (eds.): *IUTAM Symposium on Free Surface Flows*. Proceedings of the IUTAM Symposium held in Birmingham, United Kingdom, 10–14 July 2000. 2001 ISBN 0-7923-7085-6
63. A. Tsinober: *An Informal Introduction to Turbulence*. 2001 ISBN 1-4020-0110-X; Pb: 1-4020-0166-5
64. R.Kh. Zeytounian: *Asymptotic Modelling of Fluid Flow Phenomena*. 2002 ISBN 1-4020-0432-X
65. R. Friedrich and W. Rodi (eds.): *Advances in LES of Complex Flows.* Prodeedings of the EUROMECH Colloquium 412, held in Munich, Germany, 4–6 October 2000. 2002 ISBN 1-4020-0486-9

Mechanics

FLUID MECHANICS AND ITS APPLICATIONS

Series Editor: R. Moreau

66. D. Drikakis and B.J. Geurts (eds.): *Turbulent Flow Computation*. 2002 ISBN 1-4020-0523-7
67. B.O. Enflo and C.M. Hedberg: *Theory of Nonlinear Acoustics in Fluids*. 2002 ISBN 1-4020-0572-5
68. I.D. Abrahams, P.A. Martin and M.J. Simon (eds.): *IUTAM Symposium on Diffraction and Scattering in Fluid Mechanics and Elasticity*. Proceedings of the IUTAM Symposium held in Manchester, (UK, 16–20 July 2000). 2002 ISBN 1-4020-0590-3
69. P. Chassaing, R.A. Antonia, F. Anselmet, L. Joly and S. Sarkar: *Variable Density Fluid Turbulence.* 2002 ISBN 1-4020-0671-3
70. A. Pollard and S. Candel (eds.): *IUTAM Symposium on Turbulent Mixing and Combustion.* Proceedings of the IUTAM Symposium held in Kingston, Ontario, Canada, June 3–6, 2001. 2002 ISBN 1-4020-0747-7
71. K. Bajer and H.K. Moffatt (eds.): *Tubes, Sheets and Singularities in Fluid Dynamics*. 2002 ISBN 1-4020-0980-1
72. P.W. Carpenter and T.J. Pedley (eds.): *Flow Past Highly Compliant Boundaries and in Collapsible Tubes*. IUTAM Symposium held at the Univerity of Warwick, Coventry, United Kingdom, 26–30 March 2001. 2003 ISBN 1-4020-1161-X
73. H. Sobieczky (ed.): *IUTAM Symposium Transsonicum IV.* Proceedings of the IUTAM Symposium held in Göttingen, Germany, 2–6 September 2002. 2003 ISBN 1-4020-1608-5
74. A.J. Smits (ed.): *IUTAM Symposium on Reynolds Number Scaling in Turbulent Flow*. Proceedings of the IUTAM Symposium held in Princeton, NJ, U.S.A., September 11–13, 2002. 2003 ISBN 1-4020-1775-8
75. H. Benaroya and T. Wei (eds.): *IUTAM Symposium on Integrated Modeling of Fully Coupled Fluid Structure Interactions Using Analysis, Computations and Experiments*. Proceedings of the IUTAM Symposium held in New Jersey, U.S.A., 2–6 June 2003. 2003 ISBN 1-4020-1806-1
76. J.-P. Franc and J.-M. Michel: *Fundamentals of Cavitation*. 2004 ISBN 1-4020-2232-8
77. T. Mullin and R. Kerswell (eds.): *IUTAM Symposium on Laminar-Turbulent Transition and Finite Amplitude Solutions*. 2005 ISBN 978-1-4020-4048-1
78. R. Govindarajan (ed.): *Sixth IUTAM Symposium on Laminar-Turbulent Transition*. Proceedings of the Sixth IUTAM Symposium on Laminar-Turbulent Transition, Bangalore, India, 2004. 2006 ISBN 978-1-4020-3459-6
79. S. Kida (ed.): *IUTAM Symposium on Elementary Vortices and Coherent Structures: Significance in Turbulence Dynamics*. Proceedings of the IUTAM Symposium held at Kyoto International Community House, Kyoto, Japan, 26–28 October 2004. 2006 ISBN 978-1-4020-4180-8
80. S. Molokov, R. Moreau and H.K. Moffatt (eds.): *Magnetohydrodynamics*. Historical Evolution and Trends. 2007 ISBN 978-1-4020-4832-6
81. S. Balachandar and A. Prosperetti (eds.): *IUTAM Symposium on Computational Approaches to Multiphase Flow*. Proceedings of an IUTAM Symposium held at Argonne National Laboratory, October 4–7, 2004 2006 ISBN 978-1-4020-4976-7
82. A. Gyr and K. Hoyer: *Sediment Transport*. A Geophysical Phenomenon. 2006 ISBN 978-1-4020-5015-2
83. I.N. Ivchenko, S.K. Loyalka and R.V. Tompson Jr.: *Analytical Methods for Problems of Molecular Transport*. 2007 ISBN 978-1-4020-5864-6

Mechanics

FLUID MECHANICS AND ITS APPLICATIONS

Series Editor: R. Moreau

84. M. Lesieur: *Turbulence in Fluids*, Fourth Revised and Enlarged Edition. 2008

ISBN 978-1-4020-6434-0